Petrological, Geochemical and Field Studies of Fluid Infiltration during Regional Metamorphism of the Dalradian of the SW Scottish Highlands

Alasdair David Lister Skelton

Thesis submitted for the degree of Doctor of Philosophy

Edinburgh University 1992

DECLARATION

I declare that the work and results reported in this thesis are my own except where otherwise acknowledged.

I further declare that no part of this thesis has been submitted for any other degree or qualification at any other university.

For my family...
...with love

ACKNOWLEDGEMENTS

First, and foremost, my thanks are due to Colin Graham, for his hard work and his enthusiastic and inspiring guidance. My thanks are also due to Mike Bickle, for his lively and informative assistance.

I would next like to thank everyone who assisted me in the field: John Hunt on North Jura, Kevin Clyne and Justin Scott on Scarba, Yani Najman on Islay and in Knapdale, Alison Skelton in Knapdale and Ned Pegler at Tayvallich.

In Edinburgh, my thanks are due to Bob for making my "fizz-o-meter", Pete Hill and Stuart Kearns for teaching me to use the electron microprobe, Dodie James for teaching me XRF-preparation, grinding and rock-sawing, Yvonne and Diana for photography, Geoff Angel for teaching me XRD procedures, Nicky, Nikki, Helena, Heather and Denise for lots of little things, Gordon Waugh for always saying "yes" and Shane for killing the virus that otherwise may have eaten my thesis!

In East Kilbride, special thanks are due to Tony Fallick for his enthusiastic support, also to Alison and the two Julies for teaching me how to use the most horrible chemical on Earth.

I am also grateful to Tim Holland, Jeremy Fein, John Valley, Bruce Yardley, Dan Orange, Marion Holness, Ben Harte and John Dixon for useful discussions, help and advice towards developing the ideas put forward in this project.

My special thanks are due to all those who helped me in the final weeks, days and hours of writing up. Particularly to Yani Najman who co-ordinated my "back-up team". Also thanks to Alison Skelton, Kevin Clyne, Ewan Laws, Frazer McAllister and John Hunt who all made the task considerably easier.

Second to last, I wish to thank all those from Islay, Jura and Knapdale for a true West Highland welcome (including "Dudes" of Port Ellen who "borrowed" my 8-pound hammer, under the plausible misconception that it washed up on the beach...and thanks to his Mum for giving it back!).

Lastly, my thanks to the Natural Environment Research Council (and the DHSS) for financial support of this project.

ABSTRACT

The Dalradian of the SW Scottish Highlands consists of a regionally folded sequence of calc-phyllites, phyllites, psammites, marbles and metabasites which have undergone greenschist to epidote-amphibolite facies metamorphism and three successive phases of fluid infiltration: (1) pre-metamorphic spilitisation; (2) syn-metamorphic fiuid infiltration of a CO_2-bearing hydrous fluid into the margins of metabasic sills and dykes, driving mineral-fluid and isotope exchange reactions; (3) retrograde dolomitic veining, ankerite porphyroblast growth and isotopic exchange.

(1) Pre-metamorphic Spilitisation: Qualitative and semi-quantitative interpretations of pre-metamorphic spilitisation and associated Na/Ca exchange reactions are based on (i) $Na_2O/(Na_2O+CaO)$ profiles constructed across spilitised metabasic sills and (ii) Regional distribution patterns of spilitic metabasites. Observations are consistent with spilitisation having resulted from hydrothermal circulation of seawater driven by sill emplacement and volcanic activity during ensialic rifting.

(2) Syn-metamorphic Fluid Infiltration: Infiltration metamorphism at metabasic sill (and dyke) margins has been quantified in terms of advection of $\delta^{18}O$ isotopic fronts and carbonation reaction fronts. Measured advection distances from isotopic and reaction fronts have been found to be mutually consistent with theoretical predictions from recent one-dimensional front advection models. A simple geochemical field technique was adapted to quantify reaction progress, enabling efficient and effective identification of reaction fronts in the field. One-dimensional time-integrated fluid flux vectors were calculated from these measurements and flow direction was constrained from the asymmetry across individual metabasites. Regional fluid flux maps and regional fluid flow patterns were identified, from which regional-scale focusing of fluid along the axial surfaces of the Ardrishaig and Port Ellen anticlines was identified. Detailed analysis of a suite of metabasites in a variety of orientations demonstrated that the three-dimensional fluid flow direction was parallel to the axial surface of the Ardrishaig Anticline. The magnitude of this three-dimensional flux vector was estimated from one-dimensional fluxes by vector mathematics. It was concluded that syn-metamorphic fluid flow was (i) channelled through phyllites; and (ii) strongly focused along the axial surfaces of the Ardrishaig and Port Ellen Anticlines within which fluxes may have been in excess of 10^5 m^3/m^2. Psammites were effectively impermeable. Fluid flow within psammites was limited to zones of intensive deformation associated with emplacement of metabasites or phyllitic intercalations. The average three-dimensional time-integrated fluid flux was estimated to be $\approx 670 m^3/m^2$ which is consistent with fluid having been derived from devolatilisation of ≈5.5km of underlying phyllite.

(3) Post metamorphic Veining and Porphyroblast Growth: Retrograde fluid infiltration was developed as (i) fracture-controlled dolomite-Kfeldspar-chlorite-quartz and pyritic veining; and (ii) pervasive growth of ankerite porphyroblasts and disseminated pyrites in metabasites and phyllites. Retrograde infiltration is unambiguously identified by an anomalously high $\delta^{18}O$ signature. Fracture-controlled infiltration predominated in higher grade rocks (proximal to the Islay Anticline and Cowal Antiform) and pervasive infiltration was predominant in lower grade rocks (proximal to the Loch Awe Syncline). This anomalous distribution was attributed to differential uplift rates during D_4 metamorphism. Uplift of the Loch Awe Syncline was sluggish due to the overburden of the igneous complex, whereas uplift of the Cowal Antiform and Islay Anticlines was more rapid.

TABLE OF CONTENTS

1. INTRODUCTION 2
1.1 The Fluid Cycle 2
1.2 Deep-crustal Fluids 2
1.2.1 Direct Observation of Deep-crustal Fluids as Fluid Inclusions 2
1.2.2 Indirect Geological Evidence of Deep-crustal Fluids 4
1.3 Source Mechanism for Derivation of Deep-crustal Fluid 5
1.4 Implications 7
1.5 Modelling of Deep-crustal Fluid Behaviour 7
1.6 Thesis Rationale 8
1.6.1 Thesis Aim 8
1.6.2 Thesis Outline 8

2. QUANTIFICATION OF FLUID FLOW 10
2.1 Rationale 10
2.2 Zero-dimensional Models for Quantification of Fluid Flow 10
2.2.1 Stable Isotope Models 10
2.2.2 Petrological Models 13
2.2.3 The Significance of High Fluid:Rock Ratios 24
2.3 One-dimensional Models for Quantification of Fluid Flow 29
2.3.1 One-dimensional Modelling of Fluid Flow along a Temperature or Gradient under conditions of Internal-buffering 29
2.3.2 One-dimensional Modelling of Fluid Flow, from Advection of an Isotopic Front 40
2.3.3 One-dimensional Modelling of FluidFlow from Advection of an (Externally-Buffered) Reaction Front 47
2.3.4 Comparison of the Gradient Flow and Front Advection Models 50
2.3.5 The early works of Hoffman and Korzhinskii 51
2.4 Grain-Scale Mechanisms of Fluid Flow 52
2.5 Conclusion 59

PRELUDE TO CHAPTERS 3, 4 & 5 60

THE STUDY AREA: *The Dalradian of the SW Scottish Highlands* 62
3.1 Introduction 62
3.2 Location of Study Area 62
3.3 Lithostratigraphy and Depositional Facies 62
3.3.1 The Appin Group 65
3.3.2 The Argyll Group 65
3.3.3 General Interpretations of Depositional Facies 69
3.3.4 Implications of Lithostratigraphy to Modelling of Fluid Flow 69
3.4 Deformation and Metamorphism 70
3.4.1 Deformation History 71
3.4.2 Regional Metamorphic History 79
3.4.3 Pressure-Temperature Conditions of Metamorphism 83
3.4.4 Relative Timing of Deformation and Metamorphism 94
3.4.5 Implications of Deformation and Metamorphism to Modelling of Fluid Flow 95
3.5 Summary 95

4. THE STUDY AREA: *Fluid Infiltration History* **98**
4.1 Rationale 98
4.2 Qualitative Model of Fluid Infiltration in the SW Highland Dalradian 98
4.2.1 Pre-metamorphic Spilitisation 99
4.2.2 Syn-metamorphic Fluid Infiltration 105
4.2.3 Post-metamorphic Veining and Porphyroblast growth 111
4.2.4 Relative Timing of Phases of Isotopic Modification 117
4.3 Conclusion 118

5. THE STUDY AREA: *Lithological Descriptions* **119**
5.1 Introduction 119
5.2 Calc-phyllites 119
5.2.1 Distribution of Calc-phyllites 119
5.2.2 Field relations of Calc-phyllites 119
5.2.3 Mineralogy of Calc-phyllites 120
5.2.4 Petrogenesis and Deformation of Calc-phyllites: Phyllosilicates 132
5.2.5 Petrogenesis and Deformation of Calc-phyllites: Porphyroblast Phases 133
5.3 Metabasites 147
5.3.1 Distribution of Metabasites 147
5.3.2 Mineral Assemblages and Petrogenesis of Metabasites 148
5.3.3 Type I Metabasites 151
5.3.4 Type III Metabasites 154
5.3.5 Type II Metabasites 155
5.3.6 Deformation of Metabasites and Timing of Fluid Infiltration 158
5.3.7 Type I Metabasites 164
5.3.8 Summary 169
5.4 Marbles 170
5.5 Psammites 175
5.6 High X_{CO_2} Assemblages 183
5.7 Implications arising from Lithological Descriptions relating to Modelling of Fluid Flow 188

CONCLUSIONS TO CHAPTER 3, 4 & 5: The Study Area **190**

6. TECHNIQUES **193**
6.1 Rationale 193
6.2 Geological Mapping 193
6.3 Petrography 194
6.4 Field Geochemistry 196
6.5 Stable Isotope Geochemistry 201
6.5.1 Stable Isotope Analysis of Whole Rock Silicates 201
6.5.2 Stable Isotope Analysis of Carbonates 202
6.6 Electron Microprobe Analysis 203
6.7 Application of THERMOCALC and AX 204
6.8 XRF Analysis 204
6.9 Analytical Strategy 205

7. INTERPRETATION OF REACTION FRONT PROFILES 207
7.1 Rationale 207
7.2 Geological Setting 207
7.3 Reaction Front Modelling 210
7.4 Reaction Porgress Profiles 215
7.5 Interpretations and Conclusions 216

8. CORRELATION OF REACTION AND ISOTOPE FRONTS 218
8.1 Rationale 218
8.2 Theory 220
8.3 Geological Setting 221
8.4 Calculation of the Time-integrated Fluid Flux from the Adevection Distance of an Isotope Front 224
8.5 Calculation of the Time-integrated Fluid Flux from the Adevection Distance of an Reaction Front 224
8.6 The Correlation of Reaction and Isotope Fronts 227

PRELUDE TO CHAPTERS 9, 10 & 11: *Quantitative Modelling and Regional Mapping of Fluid Flow in the Dalradian of the SW Scottish Highlands* 229

9. QUANTITATIVE MODELLING AND REGIONAL MAPPING OF FLUID FLOW: *Pre-metamorphic Spilitisation* 231
9.1 Introduction 231
9.2 Background Rationale 231
9.3 Quantification of Pre-metamorphic Spilitisation 232
9.4 XRF Data 232
9.4.1 Na_2O-CaO Compositional Plots 233
9.4.2 $Na_2O/(Na_2O+CaO)$-distance Plots 233
9.5 Qualitative Interpretation of XRF Data 236
9.6 Spatial Distribution of Metabasites 237
9.7 Summary 238

10. QUANTITATIVE MODELLING AND REGIONAL MAPPING OF FLUID FLOW: *Syn-metamorphic Fluid Infiltration* 239
10.1 Introduction 239
10.2 Rationale 240
10.3 Quantification of Syn-metamorphic Fluid Infiltration 240
10.3.1 Identification of Mineral Reaction Fronts 241
10.3.2 Claculation of Time-integrated Fluid Fluxes 241
10.3.3 Regional Fluid Flux Mapping 244
10.4 Modal Profile Data 244
10.4.1 Port Cill Maluaig 245
10.4.2 North Jura 251
10.4.3 Clachbreac 254
10.4.4 Carsaig 257
10.4.5 Loch Stornoway 263
10.4.6 Traigh Gheighsgeir 263
10.4.7 Summary of Modal Profile Data 268

10.5 Quantification of Fluid Flow from Modal Profile Data 269
10.6 Comparison of the Modal and Reaction Progress approaches to the Identification of Mineral Reaction Fronts 270
10.7 Reaction Progress Profile Data 271
10.8 Quantification of Syn-metamorphic Fluid flow 273
10.8.1 Constraint of R_{CO_2} and R_{H_2O} 273
10.8.2 Constraint of $X_{CO_2,1}$ and $X_{CO_2,2}$ 277
10.8.3 Calculation of Time-integrated Fluid Fluxes 279
10.8.4 Errors in calculation of Time-integrated Fluid Flux 284
10.9 Interpretation of Regional Time-integrated Fluid Flux Maps 288
10.9.1 Regional Fluid Flow Patterns: The Ardrishaig Anticline 289
10.9.1.1 Interpretation of 1-D Time-integrated Fluid Flux Data 289
10.9.1.2 Evaluation of the 3-D Geometry of Fluid Flow 292
10.9.1.3 Quantitative constraint of 3-D Time-integrated Fluid Fluxes 296
10.9.1.4 Misfitting Data 307
10.9.2 Local Fluid Flow Patterns: Port Ellen Anticline 310
10.9.3 Regional Fluid Flow Patterns: The Loch Awe Syncline 315
10.9.4 Regional Fluid Flow Patterns: The Gulf of Corryvreckan 319
10.10 Syn-metamorphic Fluid Infiltration of the SW Highlands Regional Metamorphic Terrain 321
10.10.1 Structural and Lithological Controls of Syn-metamorphic Fluid Infiltration 323
10.10.2 Grain-scale Mechanism of Syn-metamorphic Fluid Flow 325
10.10.3 The Volume of Syn-metamorphic Fluid 326
10.10.4 The Source of Syn-metamorphic Fluid 328
10.10.5 A Quantitative Model of Syn-metamorphic Fluid Infiltration in Dalradian Rocks of the SW Highlands 329

11. QUANTITATIVE MODELLING AND REGIONAL MAPPING OF FLUID FLOW: *Post-metamorphic Veining and Porphyroblast Growth* **334**
11.1 Introduction 334
11.2 Dolomite-veining and Ankerite Porphyroblasts 334
11.3 Spatial Distribution of Dolomitic Veining and Ankerite Porphyroblast Growth 336
11.4 Pyritisation 340
11.5 Summary 343

12. CONCLUSIONS **344**
12.1 Layout of Conclusions 344
12.2 Thesis Objectives 344
12.3 Project Strategy 344
12.4 A Quantitative Model of Deep-crustal Fluid Flow in the SW Highlands 347
12.5 Concluding Statements 350
12.7 Future Work 351

REFERENCES **352**

Appendix 1: Geobarometry Data A1
Appendix 2: Geothermometry Data A7
Appendix 3: T-XCO2 Calculations A41
Appendix 4: Modal Profiles A71
Appendix 5: Reaction Progress Profiles A84
Appendix 6: Stable Isotope Data A101
Appendix 7: Electron Microprobe Data A107
Appendix 8: XRF Data A126

FIELD SLIPS and REFERENCE CARD are at the back of the thesis.

Petrological, Geochemical and Field Studies of Fluid Infiltration during Regional Metamorphism of the Dalradian of the SW Scottish Highlands

There are three stable states of matter; solid, fluid and gas. On the Earth's surface, transition from one such state to another occurs by melting, boiling or fusion, at, or near, a specific temperature. Yet, in the depths of the Earth's crust, the immense pressure of the over-bearing rock load can induce some species to remain in the fluid state at temperatures much in excess of their surface boiling point. The result is a super-critical liquid, an extremely reactive fluid phase, which can itself alter the minerals of the rock through which it passes. This is infiltration metamorphism and is the subject of this thesis.

CHAPTER 1

INTRODUCTION

1.INTRODUCTION

1.1 The Fluid Cycle

The planetary "budget" of fluid and gaseous species is fairly constant and therefore the planetary fluid cycle may be considered as a partially closed system. The most abundant fluid and gaseous species are H_2O, CO_2, CO, O_2, N_2, H_2S, H_2 and CH_4 and at any one time these species are distributed among several ephemeral "reservoirs" (figure 1.1); (1) the atmosphere, (2) the hydrosphere, (3) the crust and (4) the mantle. This thesis explores fluid behaviour in the third of these ephemeral reservoirs; the crust.

1.2 Deep-crustal Fluids

The presence and mobility of super-critical fluids in the deep-crust has been implied both by direct observation and indirect geological evidence.

1.2.1 Direct Observation of Deep-crustal Fluids as Fluid Inclusions

Deep-crustal fluids have been directly observed, trapped in partially healed fractures within mineral grains, as fluid inclusions.

Boyle (1672) referred to a large moving bubble in quartz. This was the first reference to fluid inclusions in the literature. Later, it was found that fluid inclusions are in such great abundance that they are solely reponsible for the opacity of milky quartz. In the early nineteenth century, several workers, including Breislak (1818) and Davy (1822), analysed these inclusions and found them to be water-rich in composition. Gas bubbles within fluid inclusions were identified by Sorby (1858) and later shown to be CO_2-rich. More recently fluid inclusions have been employed for

Figure 1.1:The Fluid Cycle

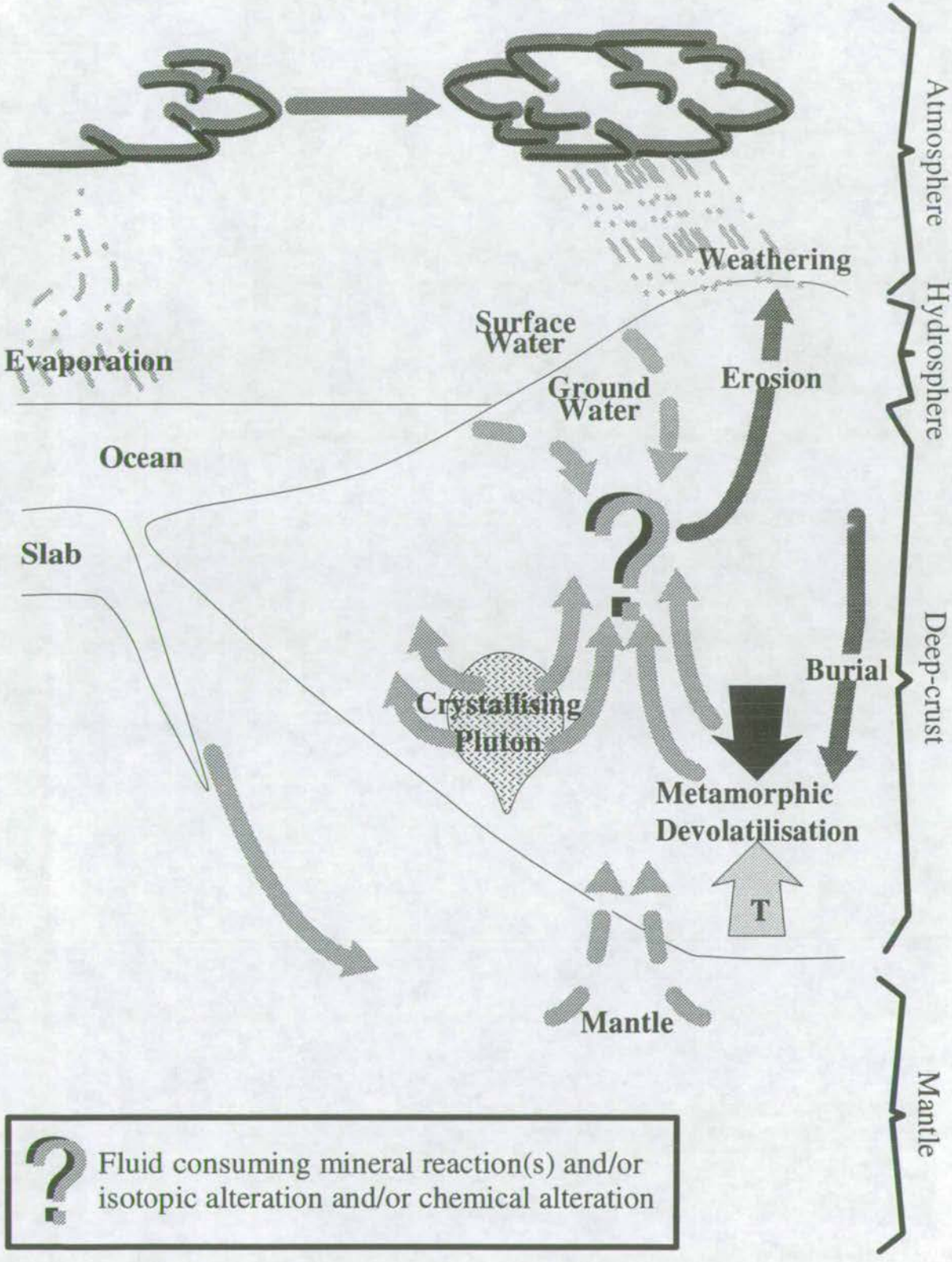

geothermometry, geobarometry and to constrain the composition of deep-crustal fluids (Roedder 1984).

The value of fluid inclusions as indicators of crustal fluid composition has been cast in to doubt by a number of workers. Roedder (1984) reviewed the problem of leakage and re-filling of fluid inclusions. Fluid may escape from an inclusion along dislocations within individual mineral grains which are developed most extensively at high pressures (e.g. in a metamorphic environment). The amount of leakage is a function of the diffusivities of the individual fluid species and therefore the fluid composition which is recorded from an inclusion may be affected by leakage. Furthermore it is often difficult to constrain the entrappment time for an individual fluid inclusion where a number of cross-cutting inclusion phases are present. Finally no information is given regarding the direction or magnitude of fluid flow. For these reasons fluid inclusions are not generally useful or reliable as indicators of deep-crustal fluid behaviour.

1.2.2 Indirect Geological Evidence of Deep-crustal Fluids

Korzhinskii (1946, 1947, 1948) predicted that the commonly observed regular metasomatic zonation of skarns developed in the presence of fluid which acted as a transport medium for 'perfectly mobile' components. Sales & Meyer (1950) posed a similar interpretation for the development of metasomatic zonation around veins.

Indeed the mere presence of veins testifies to the former presence and mobility of fluid in the crust. However, perhaps the most compelling evidence for the presence of fluids in the deep-crust is that the progress of many **prograde** metamorphic reactions is accompanied by the liberation of significant quantities of fluid. Mineralogical, petrological, thermodynamic and micro-textural evidence imply that such fluids play a critical role in the processes of deep-crustal mineral reactions.

Deep-crustal Mineral Reactions

Most metamorphic rocks contain hydrous, carbonate or sulphide minerals whose formation and stability requires the presence of a C-O-H-S bearing fluid phase. The stability of such minerals provides a means whereby the composition of the metamorphic fluid phase may be calculated or deduced when one or more of the intensive variables of metamorphism (P,T) are independently known. For example, in the simplified case where minerals equilibriate with an H_2O-CO_2 fluid phase, some reactions which generate CO_2-rich fluid are infact buffered by an H_2O-rich fluid. If P and T remain constant, such a reaction will only progress to a significant extent or to completion if additional H_2O is added to the system (figure 1.2). If P and T are known, the quantity of fluid may be constrained. Much petrological research has been directed towards identifying possible source mechanisms which could be responsible for the derivation of such fluid.

1.3 Source Mechanisms for Derivation of Deep-crustal Fluids

There are a variety of postulated mechanisms and pathways by which fluid enters the deep-crust, many of which are subject to controversy; for example:

(1) Unmetamorphosed pelites consist largely of clay minerals which contain structurally bound volatiles (dominantly H_2O and CO_2). During metamorphism, such pelites undergo successive devolatilisation reactions, liberating the structurally-trapped fluid into the crust.

(2) An igneous melt contains a significant quantity of dissolved fluid. On crystallisation there are insufficient minerals which can accomodate fluid within their structures, and the fluid must therefore be released into the surrounding rocks.

(3) Large-scale hydrothermal convection has been proposed as a potential mechanism by which surface fluids (oceans, ground-water) may be brought to deep crustal levels

Figure 1.2: T-X_{CO_2} Pathways

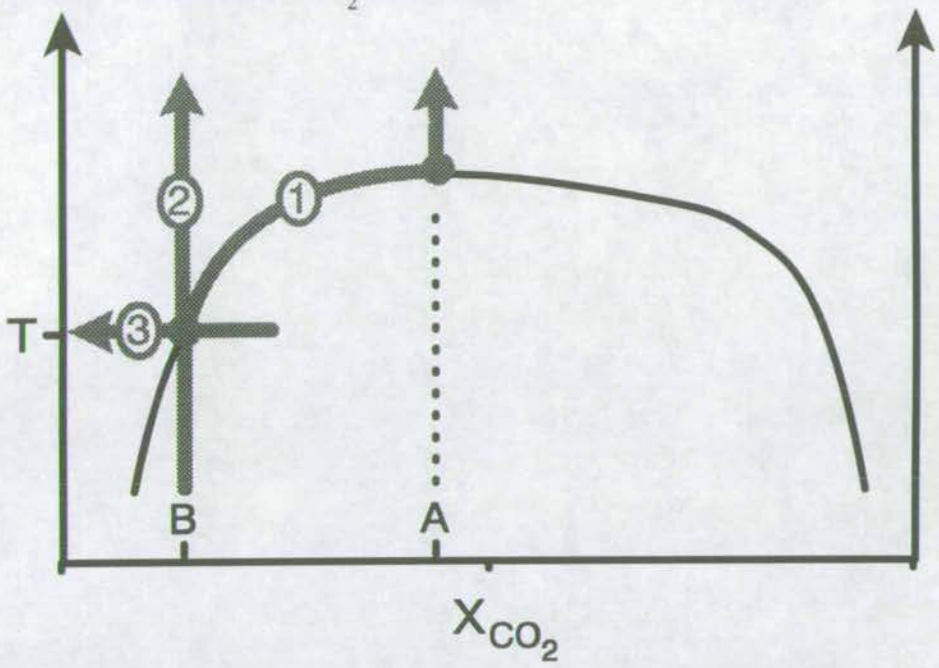

(1) The reaction is thermally-driven and buffers the fluid composition internally. It need not reach completion.

(2) The reaction is thermally-driven to completion. The fluid composition is maintained by external buffering.

(3) The reaction is driven to completion by infiltration of an externally derived fluid.

The reaction generates CO_2-rich fluid of composition (A), but in examples (2) and (3) the reaction is in equilibrium with an H_2O-rich fluid of composition (B). Therefore the reaction can only proceed to completion where there is an external source of H_2O.

(e.g. Wickham & Taylor 1985, 1987). However, Wood & Walther (1984) have demonstrated that this type of convection is physically implausible. This is discussed in detail in chapter 2.

(4) The mantle has been proposed as a potential source of deep-crustal fluid by several authors. However, this has been difficult to substantiate with evidence from crustal rocks.

1.4 Implications

Regardless of how fluid reaches the deep-crust, both its presence and its mobility are evident and the consequences of its mobility are of major geological significance. Mobile fluids are able to transport heat and mass, and to control the strength of the rocks. They are therefore critical in controlling many tectonic processes. The importance of developing a quantitative understanding of deep-crustal fluid behaviour can therefore not be under-estimated.

1.5 Modelling of Deep-crustal Fluid Behaviour

Over the past forty years, a number of models have been developed to evaluate the volume, composition, source and transport characteristics of deep-crustal fluids.

A number of models offered constraints on the physical properties (e.g. P, T and composition) of "fossilised" deep-crustal fluids trapped in fluid inclusions, whereas other models constrained the volume, source and transport characteristics of deep-crustal fluids by quantification of fluid-driven chemical, mineralogical and/or isotopic alteration of crustal rocks. The later approach was initially adopted by Korzhinskii (1951, 1952) and later by Hofmann (1972) and forms the basis of the most recent quantitative modelling techniques which have evolved over the past

decade from simplistic mass-balance approaches, which quantify the ***fluid volumes*** required to cause observed (isotopic or mineralogical) alterations (e.g. Taylor 1977, Ferry 1980), towards more mathematically complex and more generally applicable, one-dimensional models which quantify fluid flow as the ***time-integrated fluid flux*** required to cause observed (isotopic or mineralogical) alterations (e.g. Bickle & McKenzie 1987, Lassey & Blattner 1988, Ferry 1989 and Bickle & Baker 1990). One-dimensional modelling techniques are applied in this thesis to measure and map fluid fluxes and to constrain fluid flow directions thereby enabling identification of fluid sources, transport mechanisms and controls. The modelling techniques are described in detail, in the context of their historical and mathematical development in chapter 2, but first, the aim and outline of the thesis are presented.

1.6 Thesis Rationale

1.6.1 Thesis Aim

An initial aim of this thesis was to devise a practical method by which a one-dimensional modelling approach can be implemented to measure time-integrated fluid fluxes during regional metamorphism. This was achieved enabing construction of the first regional scale map of deep-crustal fluid flow. It was then possible to calculate the true 3-dimensional time-integrated fluid flux, to identify the fluid source reservoir and to establish the structural, lithological, mineralogical and textural controls on both regional and microscopic transport of fluids in the deep crust.

1.6.2 Thesis Outline

Initially, the modelling approach employed in this study is described and the reasons for its selection are explained. The study area is then presented and the reasons for its selection are discussed. Our qualitative understanding of fluid infiltration history of the study area is outlined. The techniques available for the

measurement of fluid flux are compared and contrasted, and the field and laboratory strategy of the project is justified and outlined.

This is followed by two short case-studies. The former case study discusses the general interpretation of the morphology of reaction front profiles in a view to quantification of fluid flux. The latter case study develops a theoretical foundation for quantitative modelling and regional mapping of fluid flow by testing the fundamental assumptions of the one-dimensional models employed in this study. Having achieved the necessary theoretical ground-work, the calculated time-integrated fluid flux data is presented and then compiled to produce a regional map of fluid flow. Furthermore, limiting constraints are placed upon the three-dimensional geometry and magnitude of fluid flow. One- and three-dimensional time-integrated fluid fluxes are implimented to constrain the structural, lithological, and grain-scale controls on fluid transport and to identify the fluid source. An novel and exciting model emerges, which has important implications for the interpretation of fluid flow in thus and other metamorphic terrains.

CHAPTER 2

QUANTIFICATION OF FLUID FLOW

2. QUANTIFICATION OF FLUID FLOW

2.1 Rationale

The quantification of fluid flow through crustal rocks during metamorphism has been a major objective of metamorphic petrology and geochemistry for more than a decade. Quantitative modelling of fluid flow has advanced from the early zero-dimensional mass-balance calculations which quantified fluid flow as a **volume** (Ferry 1980 and Taylor 1977) towards considerably more sophisticated one-dimensional mass-balance calculations which quantify fluid-flow as a time integrated fluid flux (Bickle & McKenzie 1987, Lassey & Blattner 1988, Ferry 1989 and Bickle & Baker 1990b) by adopting the theoretical reasoning which was introduced by Korzhinskii (1951, 1952) and clarified by Hoffman (1972).

The work in this thesis employs the one-dimensional models of Bickle & McKenzie (1987) and Bickle & Baker (1990b) to quantify fluid flow in the crust. Therefore, in this chapter, these models are described in the context of their historical and mathematical development from the early zero-dimensional (box) models and the essential links with the theoretical reasoning of Korzhinskii (1951, 1952, 1970) and Hoffman (1972) are outlined.

2.2 Zero-dimensional Models for Quantification of Fluid Flow

2.2.1 Stable Isotope Models

Local or regional changes in the isotopic signatures of crustal rocks have often been attributed to fluid infiltration. Taylor (1977) realised the potential of using such isotopic shifts for the quantification of fluid volumes by mass balance of isotopic species. He calculated the volume of fluid of known, or assumed, isotopic

composition required to achieve an observed isotopic shift. The model is illustrated in figure 2.1 and is given by:

$$\frac{W}{R} = \frac{\delta_{rock,i} - \delta_{rock,f}}{\delta_{H_2O,f} - \delta_{H_2O,i}} \qquad (2.1)$$

where $\delta_{rock,i}$ and $\delta_{rock,f}$ are the initial and final $\delta^{18}O$ of the rock respectively and therefore $\delta_{rock,i}$ - $\delta_{rock,f}$ is the isotopic shift of the rock. $\delta_{H_2O,i}$ and $\delta_{H_2O,f}$ are the initial and final $\delta^{18}O$ of the water respectively. $\delta_{rock,f}$ can be measured directly from the rock and $\delta_{rock,i}$ is assumed to be the original (e.g. sedimentary or igneous) signature of the rock. $\delta_{H_2O,i}$ and $\delta_{H_2O,f}$ may be estimated by combining $\delta_{rock,i}$ and $\delta_{rock,f}$ with the oxygen isotope fractionation between the rock and the fluid, $\alpha_{rock\text{-}fluid}$ (where $1000\ln\alpha = \delta_{rock} - \delta_{fluid}$), W is the atom % of water oxygen in the system and R is the atom % of rock oxygen in the system. W/R is therefore the ratio of water oxygen to rock oxygen. The volumetric water:rock ratio is given by dividing W and R by their respective total molecular weight proportions of oxygen. The water:rock ratio given by equation 2.1 is integrated over the lifetime of the hydrothermal system, assuming continuous convection (closed system). Taylor (1977) went on to model open system behaviour, where each increment of fluid passes through the rock once, during which time isotopic equilibrium between fluid and rock is attained (single-pass flow, figure 2.2). He derived the relationship:

$$\frac{W}{R} = \log_e\left[\left(\frac{W}{R}\right)_{\substack{closed \\ system}} + 1\right] \qquad (2.2)$$

Applications of the Water:Rock Ratio Model (Taylor 1977)

Wickham & Taylor (1985, 1987) employed these models in an extensive isotopic study of the Trois Seigneurs Massif in the French Pyrenees. A 12 km section

Figure 2.1: Zero-dimensional Mass Balance Model (Taylor 1977): Closed System Approximation

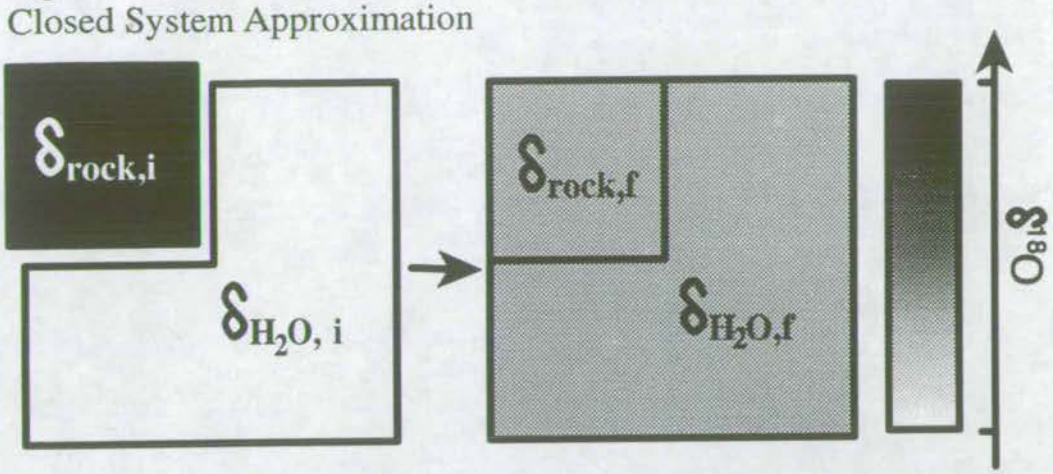

In the closed system approximation described above, a unit volume of rock with isotopic signature $\delta_{rock,i}$ completely equilibrates with a volume of fluid (defined by the fluid:rock ratio) with isotopic signature $\delta_{H_2O,i}$ such that the isotopic signature of the rock is $\delta_{rock,f}$ and the isotopic signature of the fluid is $\delta_{H_2O,f}$. The shading accounts for partitioning of oxygen between solid and fluid such that similar shading of rock and fluid indicates complete isotopic equilibrium, not identical isotopic signatures.

Figure 2.2: Zero-dimensional Mass Balance Model (Taylor 1977) Open System Approximation

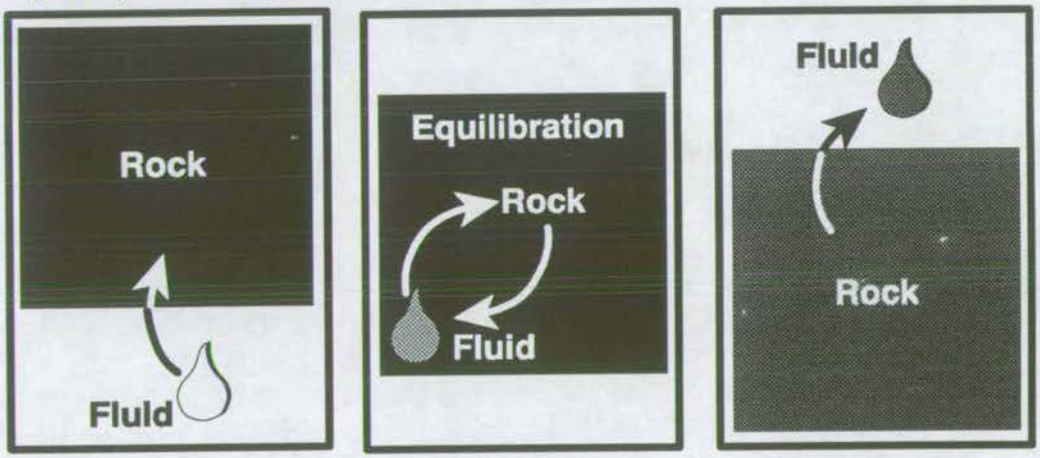

Each increment of fluid attains complete isotopic equilibrium with the rock. Shading refers to the isotopic signature as detailed in figure 2.1.

of crust is exposed at Trois Seigneurs where a sequence which is dominated by pelites is metamorphosed from chlorite-grade at the top to migmatite grade at the base. They observed km-scale isotopic homogenisation of the upper 4-6 km of the crustal section. They stated that the observed extent of isotopic modification was best described by a closed system approximation (equation 2.1) in which fluid was derived from surface reservoirs such as the oceans and/or ground-waters, and estimated the volumetric fluid:rock ratio to be 0.3-0.5 from equations 2.1. This interpretation would require convection of surface water to 12 km depth (figure 2.3). The implications of this conclusion will be discussed later in this chapter.

2.2.2 Petrological Models

The importance of significant quantities of mobile fluid as a potential driving force for metamorphic reactions, as opposed to the passive by-product which it had previously been considered, was first recognised by Greenwood (1967, 1975). Based on experimental studies of mineral-fluid equilibria in the system MgO-SiO_2-H_2O-CO_2, he noted that many univariant reactions which generate a CO_2-rich fluid progress ***only*** in the presence of extremely H_2O-rich fluids. That such reactions are often observed to go to completion in the crust can ***only*** be attributed to an, often large, external source of fluid (figure 1.2). Ferry (1980) built upon these observations by attempting to devise a model by which the required volume of fluid could be calculated. The model is simplistic but elegant and represented a major advance in our understanding of this important variable in the complex processes of metamorphism.

The Fluid:Rock Ratio Model (Ferry 1980)

The minimum amount of fluid which infiltrated a metacarbonate rock may be estimated, assuming knowledge of (i) the mineral reactions which progressed as a

Figure 2.3: Data and Interpretation of Wickham & Taylor (1985, 1987) Describing Fluid Infiltration of the Trois Seigneurs Massif based on the Open system Water:Rock Ratio Model of Taylor (1977)

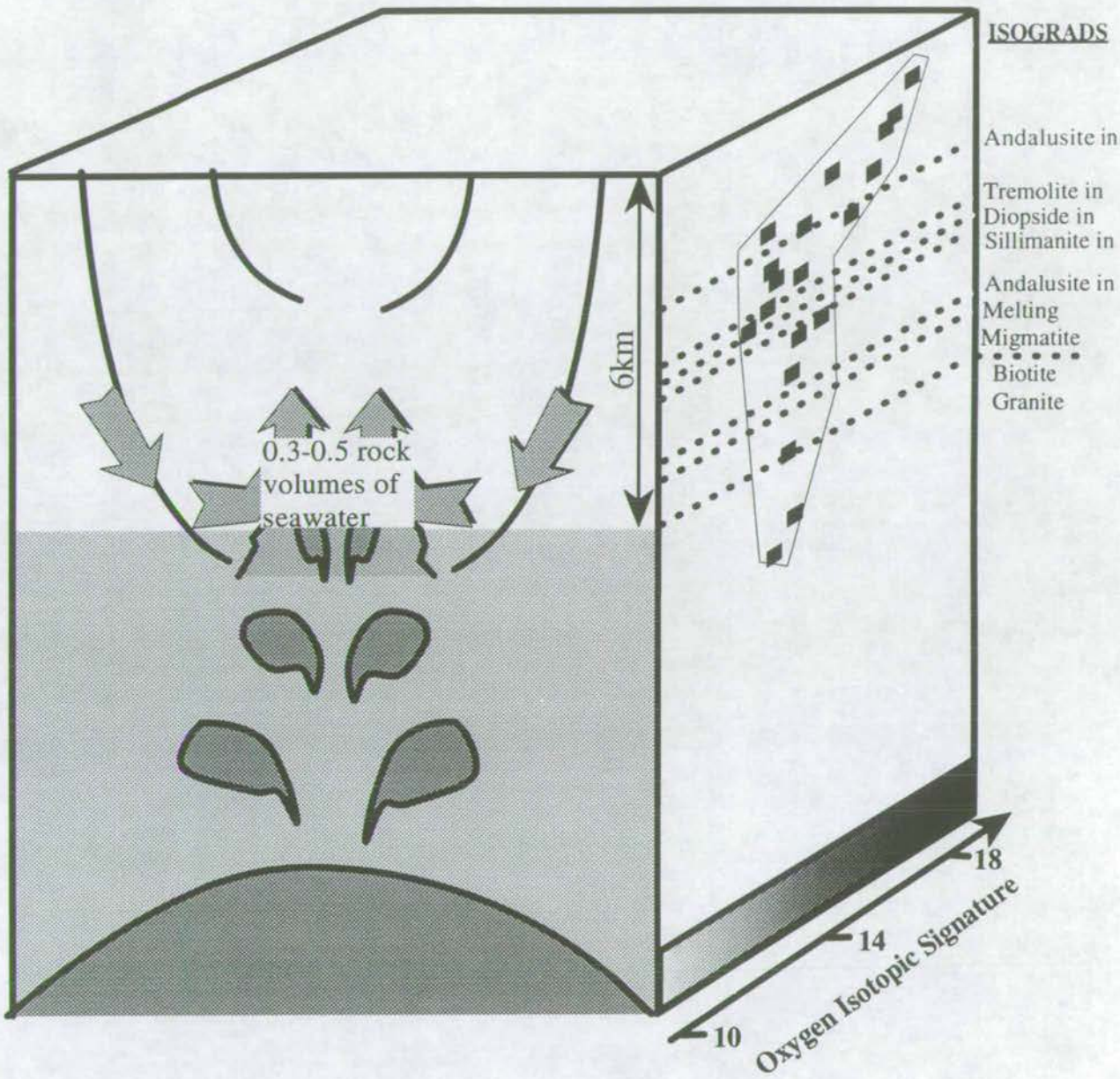

The side panel displays the plot of $\delta^{18}O$ against depth which was obtained by Wickham & Taylor (1985) for whole rock pelites. The isotopic signature is homogenised to $\delta^{18}O = 11$ to 13. The front panel illustrates the interpretation of fluid infiltration described by Wickham & Taylor (1985, 1987). Large scale convection of surface waters along fractures generates fluid:rock ratios of 0.3 to 0.5 and is responsible for the observed isotopic shift.

result of infiltration, (ii) the progress of each reaction, (iii) the composition of fluid with which the rock was in equilibrium during infiltration and (iv) the composition of the infiltrating fluid. For simplicity the infiltrating fluid is assumed to be pure H_2O.

The minimum number of moles of pure H_2O required to drive reactions i to extent, ξ, from the equation:

$$X_{CO_2,i} = \frac{R_{CO_2,i}\xi_i}{(R_{CO_2,i} + R_{H_2O,i})\xi_i + N_{H_2O}} \qquad (2.3)$$

where $X_{CO_2,i}$ is the composition of fluid in equilibrium with the rock during progress, ξ of reaction i; $R_{CO_2,i}$ and $R_{H_2O,i}$ are the stoichiometric coefficients of CO_2 and H_2O respectively, in reaction i. N_{H_2O} is the minimum number of moles of H_2O required to drive reaction i to extent, ξ. The reaction is expressed diagramatically in figure 2.4. The volumetric water:rock ratio, V_{H_2O} is quantified by rearrangement of equation 2.3 to give:

$$V_{H2O} = \overline{V}_{H2O} . N_{H2O} = \overline{V}_{H2O} . \frac{R_{CO2,i}\xi_i - X_{CO2,i}(R_{CO2,i} + R_{H2O,i})\xi_i}{X_{CO2,i}} \qquad (2.4)$$

where $\overline{V}_{H_2O}$ is the molar volume of H_2O at the physical conditions of the reaction. Volumetric water:rock ratios are by necessity a minimum for two reasons. Firstly, fluid which passes through the rock in equilibrium is not recorded. Secondly, the addition of CO_2 to the infiltrating fluid will increase the fluid:rock ratio.

Applications of the Fluid:Rock Ratio Model (Ferry 1980)

On the basis of this model, Ferry (1983) constructed a map of fluid:rock ratios and associated thermal variation calculated for metacarbonate rocks from the Vassalboro Formation of South Central Maine (figure 2.5). The Vassalboro Formation consists of shales, sandstones and argillaceous carbonates, which have been metamorphosed from chlorite through sillimanite grades, isoclinally folded, and

Figure 2.4: Zero-dimensional Mass Balance Model (Ferry 1980)

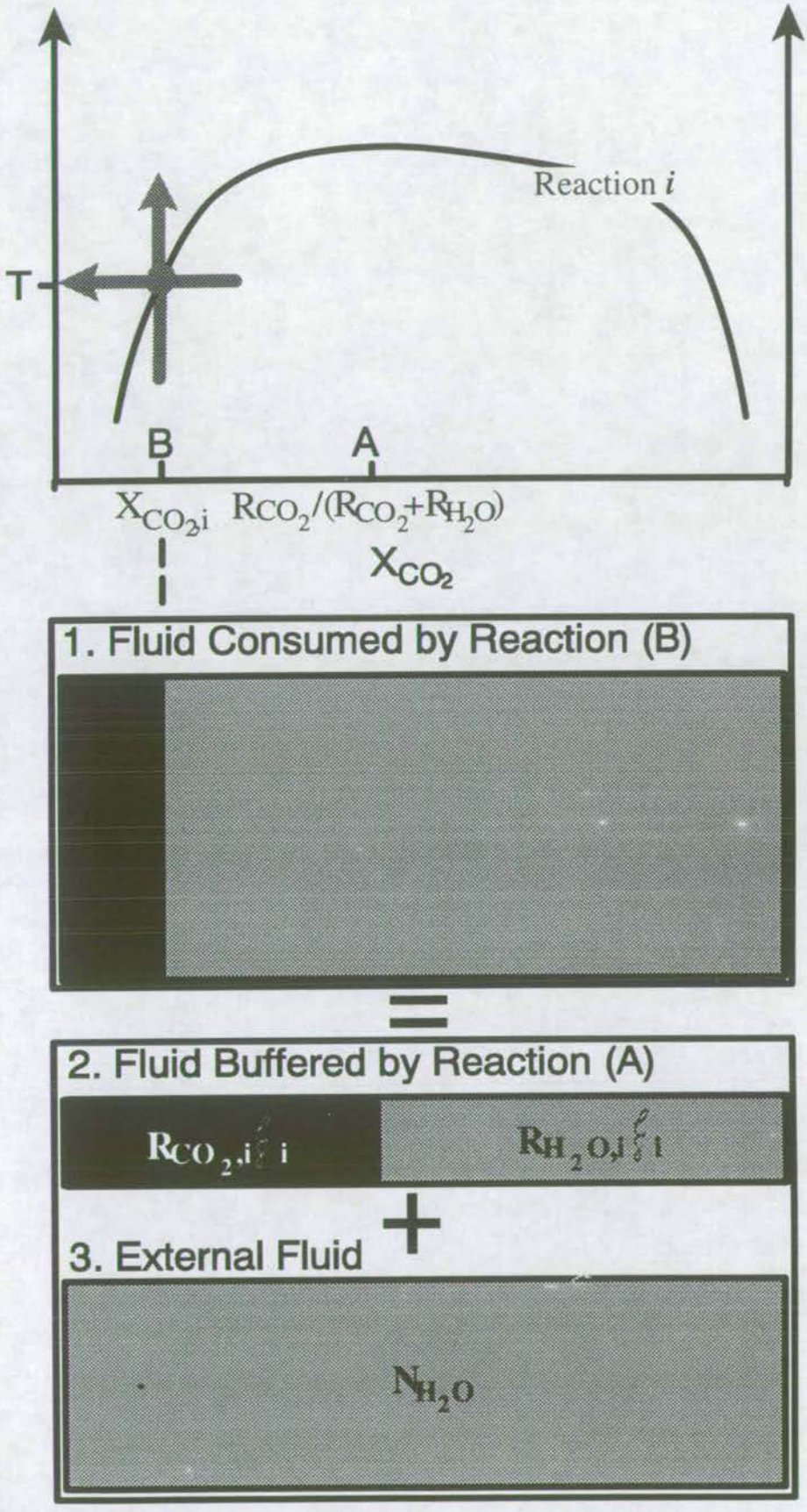

This figure illustrates the box-model of Ferry 1980. The volume of H2O-CO2 fluid required to externally buffer reaction i at X(CO2) = B (1), is expressed as the sum of H2O-CO2 fluid buffered by reaction i (2) and externally derived H2O (3). Equation variables are explained in the text. Dark shading represents CO2 and light shading represents H2O. Areas are proprotional to volumes of the respective fluid species.

Figure 2.5: Applications of the Fluid:Rock Ratio Model (1) Fluid:Rock Ratio Mapping of the Vassalboro Formation, Maine (Ferry 1983)

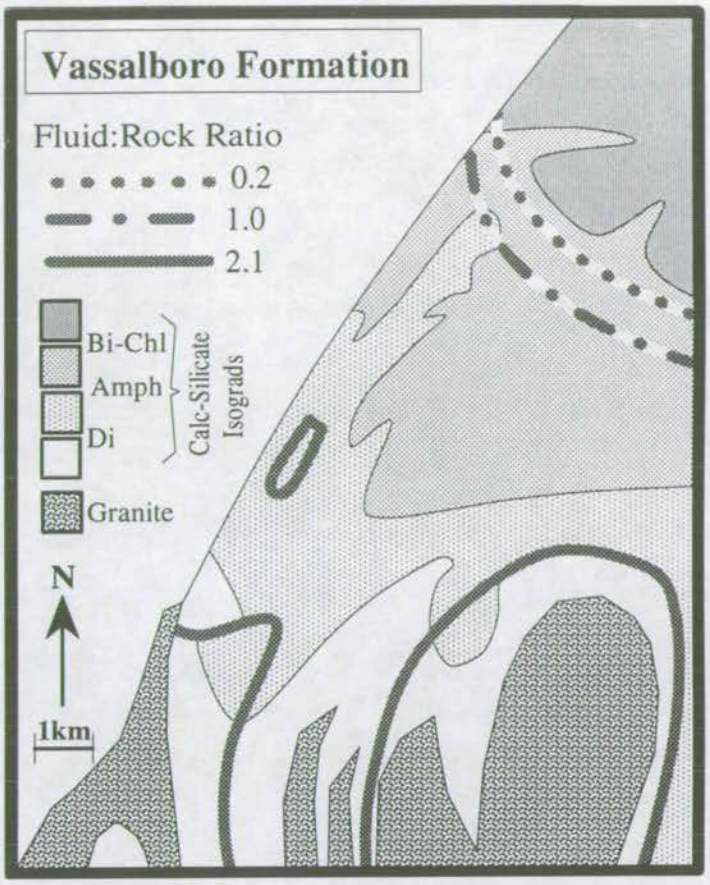

The fluid:rock ratio map of the Vassalboro Formation, South-central Maine, constructed by Ferry (1983) is shown above. Fluid:rock ratios are observed to increase markedly near the Bi-Chl calc-silicate isograd, from 0.2 to 1.0. Fluid:Rock ratios are generally increased near the granitic stocks. Zones of increased fluid:rock ratio are elongate in a NW-SE direction (parallel to regional bedding.

intruded by three syn-metamorphic granitic stocks. A total lack of appreciable reaction textures is taken to suggest that the rocks were subjected to a single phase of metamorphism. Ferry (1983) measured fluid:rock ratios which increased from 0.2 in the lower biotite zone to 1.0 in the upper biotite zone and 2.1 in the sillimanite zone adjacent to a granitic stock. In general, high fluid:rock ratios were correlated with positive thermal variations. Fluid:rock ratio contours predicted channelisation of fluids associated with granitic plutons and elongation of these channels parallel to the lithological bedding.

In a more detailed study undertaken in the adjacent Waterville Formation, Ferry (1987) measured outcrop-scale variation of fluid:rock ratios perpendicular to lithological bedding (figure 2.6). In the chlorite zone, fluid:rock ratios were found to vary from 0.0 to 0.4 between adjacent beds; in the garnet zone, fluid:rock ratios varied from 0.0 to 1.5 in adjacent beds; in the staurolite-andalusite zone, fluid:rock ratios varied from 0.4 to 1.0 in adjacent beds, and in the sillimanite zone, fluid:rock ratios were more or less constant at about 1.0. Ferry (1987) interpreted this data to represent a change from lithologically channelled fluid flow at lower grades towards more generally pervasive fluid flow at higher grades.

A similar study was undertaken by Ferry (1988) in which he drew a comparison between fluid:rock ratio profiles constructed across bedding in micaceous, carbonate-bearing metasandstones of the Vassalboro Formation with similar profiles constructed across bedding in argillaceous metacarbonates of the Waterville formation (figure 2.7). He identified pervasive fluid flow at all grades through micaceous, carbonate-bearing metasandstones of the Vassalboro Formation, whereas fluid flow was channelled at lower grades and pervasive at higher grades through argillaceous metacarbonates of the Waterville Formation. Ferry (1988) attributes these contrasting fluid flow patterns to lithological variation. He inferred that micaceous, carbonate-bearing metasandstones were more permeable than argillaceous metacarbonates.

Figure 2.6: Applications of the Fluid:Rock Ratio Model (2) Construction of Fluid:Rock Ratio Profiles Perpendicular to Layering, Waterville Formation, Maine (Ferry 1987)

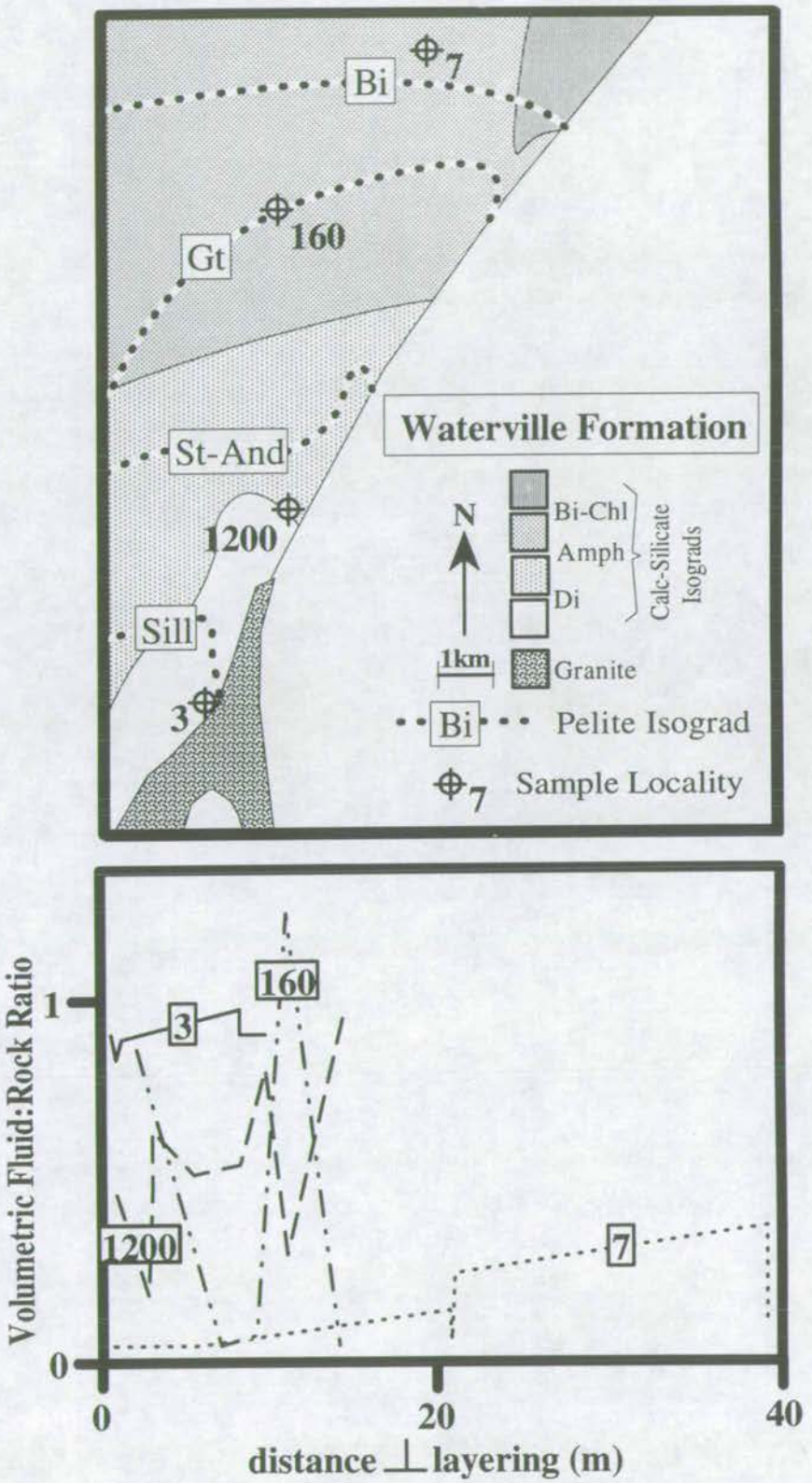

Fluid:rock ratio traverses, constructed across layering, are shown in the above plot. Locality 7 is in the chlorite zone and records channelised fluid:rock ratios from 0.0-0.4. Locality 160 is in the garnet zone and records channelised fluid:rock ratios from 0.1-1.3. Locality 1200 is in the staurolite-andalusite zone and records a pervasive fluid:rock ratio of 0.3-0.5 with channeilsed fluid:rock ratios from 0.3-1.0. Locality 3 is in the sillimanite zone and records a pervasive fluid:rock ratio of 0.9.

Figure 2.7: Applications of the Fluid:Rock Ratio Model (3) A Comparison of Fluid Flow Patterns between Micaceous, Carbonate-bearing Sandstones of the Vassalboro Formation and Argillaceous Carbonates of the Waterville Formation, Maine (Ferry 1988)

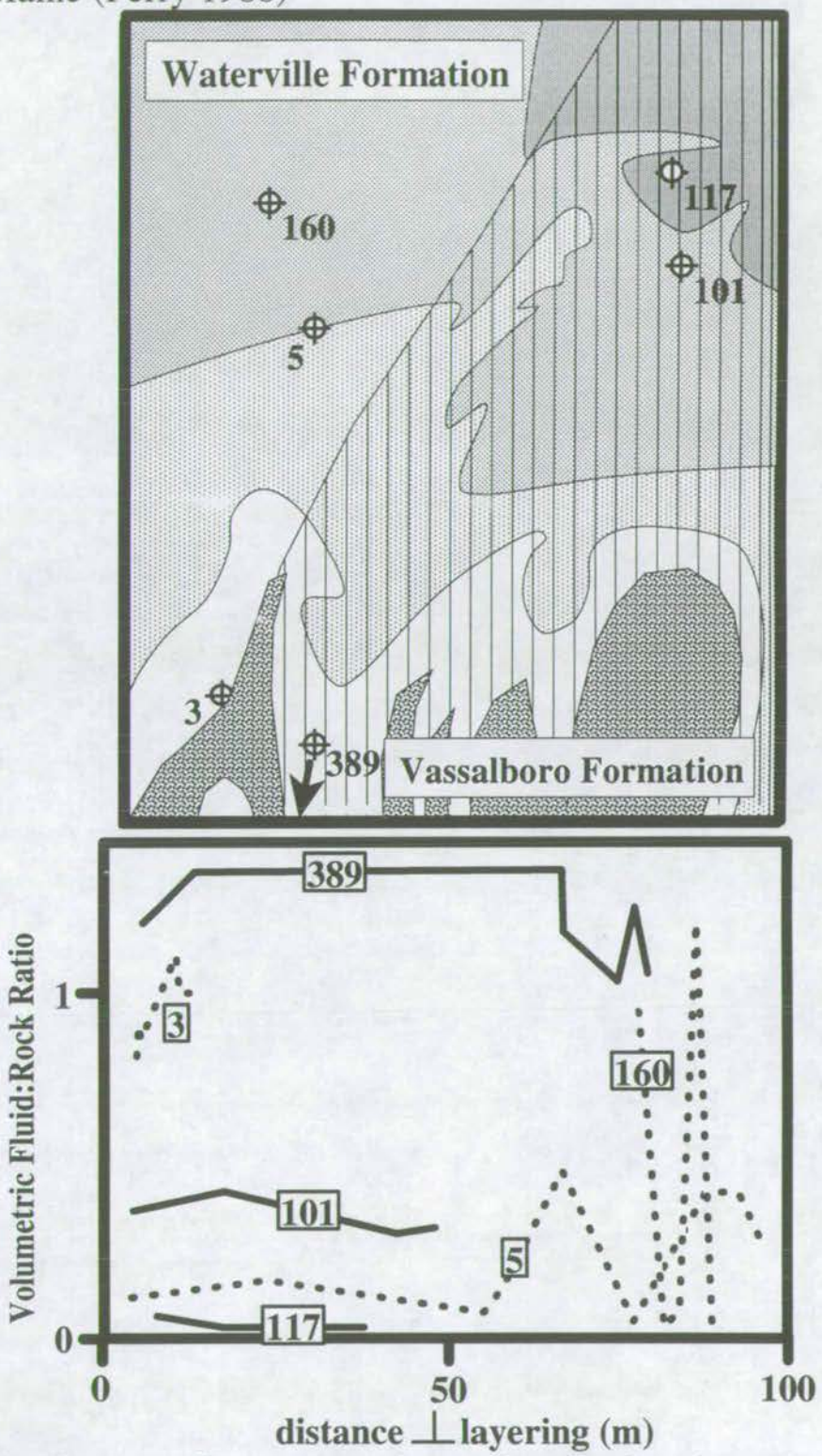

Fluid:rock ratio profiles, constructed across layering, for micaceous, carbonate -bearing sandstones of the Vassalboro Formation (localities 117, 101, 389) and argillaceous marbles of the Waterville Formation (localities 5, 150, 3) are compared in the above plot. Fluid flow is generally pervasive at all grades in the Vassalboro Formation and at high grades in the Waterville Formation. Fluid flow is channellised at low grades in the Waterville Formation. Fluid:rock ratios generally increase with increasing grade.

In summary, Ferry (1980, 1983, 1987 and 1988), measured minimum volumetric fluid:rock ratios between 0.2 and 2.1. He inferred that such large fluid volumes would significantly affect the distribution of heat in the crust and may therefore form an integral driving force for regional metamorphism. By constructing fluid:rock ratio maps he was able to make the following interpretations:

(1) The largest increase in the fluid:rock ratio is observed in the biotite zone.

(2) Fluid is generally focused around granitic stocks.

(3) Fluid is channelled along specific lithologies, particularly at lower metamorphic grades.

(4) Fluid flow is generally pervasive at higher metamorphic grades.

Assumptions and Problems of the Fluid:Rock Ratio Model of Ferry (1980)

Unfortunately the model assumptions on which these interpretations are based, are both simplistic and probably quite unrealistic. Equation 2.4 makes the flawed assumptions that fluid passes through rock undergoing active metamorphism without reacting with rocks along its flow path, and that the fluid composition is ***pure*** H_2O. Although Ferry overcame the latter problem in later studies by expanding the model to account for a CO_2-bearing fluid, the composition of the external fluid was still assumed.

Furthermore, the input parameters: (1) $X_{CO2,i}$ and (2) ξ_i are poorly constrained.

(1) $X_{CO2,i}$, the composition of fluid in equilibrium with reaction i, is critically dependent on poorly constrained geothermal temperature estimates. A built in error of at least ±30°C may be expected from many common geothermometers. In the regime of a T-X_{CO_2} section where $\partial T/\partial X_{CO_2}$ is small, a minor difference in temperature can induce a large difference in estimated X_{CO_2} and therefore a large difference in the calculated fluid:rock ratio.

For this reason, Wood & Graham (1986) challenged the fluid:rock ratio calculations of Ferry (1983,1984). Ferry (1984) calculated that mineral reactions at the biotite isograd in the Waterville Formation of South Central Maine required infiltration of a minimum of 0.9-2.2 rock volumes of fluid. Such large quantities of fluid are problematic as detailed later in this chapter. Ferry (1984) based fluid:rock calculations on a temperature, estimated by calcite-dolomite geothermometry, of 408°C. Wood & Graham (1986) suggested that this figure was about 40°C too low, on the basis that Ferry failed to account for Fe in carbonates. They recalculated the fluid:rock ratio at the biotite isograd in the Waterville Formation at T=448°C and obtained much lower and, as will be explained later in this chapter, more realistic fluid:rock ratios of 0.1-0.2. Wood & Graham (1986) concluded their assault on the fluid:rock ratio calculations by constructing a plot of fluid:rock ratio as a function of temperature and X_{CO_2} (figure 2.8) to demonstrate the extreme susceptibility of calculated fluid:rock ratios to temperature estimation.

(2) The extents of reactions (ξ_i) is quantified from inferred changes in the mineralogical mode of the rock during infiltration. A further source of inaccuracy arises because the actual protolith is not observed. Instead, high grade rocks are assumed to have evolved from adjacent low grade assemblages. However, no textural evidence is documented to justify the inferred reaction pathways. The assumption that high grade rocks evolved from adjacent low grade assemblages, on which estimates of the extent of reaction(ξ_i) are based, may therefore be essentially flawed.

Even if fluid:rock ratio predictions are reliable, the model lacks dimensions and therefore offers absolutely ***no*** constraint on fluid flow direction and minimal information is offered regarding fluid transport or the whereabouts of the fluid source. It is not therefore a viable or particularly meaningful technique for regional mapping of fluid flow.

Despite the fatal draw-backs of the fluid:rock ratio model, the work of Ferry (1983, 1987 and 1988) was not all wasted. Although fluid:rock ratios are inaccurate

Figure 2.8: Dependence of Fluid:Rock Ratios on X(CO2) and Temperature (Wood & Graham 1986)

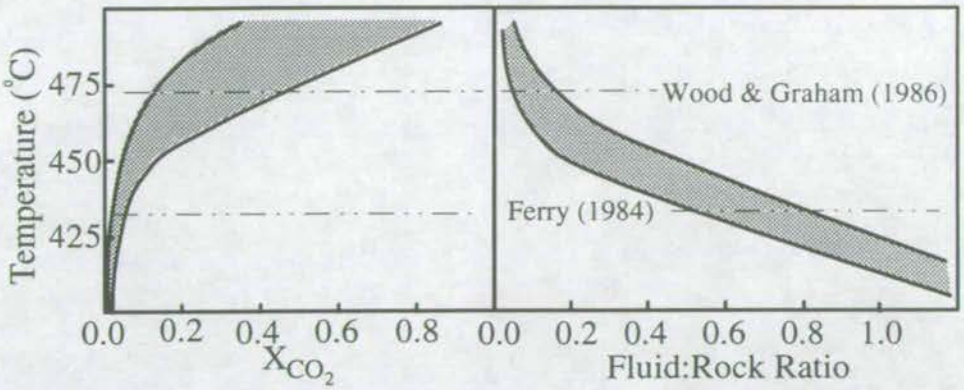

The above plots have been modified from Wood & Graham (1986), and describe the critical dependence of fluid:rock ratio on X(CO2) and temperature.
The temperature estimates and predicted fluid:rock ratios at the biotite isograd of the Waterville Formation of Ferry (1984) and Wood & Graham (1986) are compared.

Figure 2.9: Diagramatic Comparison of Single Pass and Convective Fluid Flow

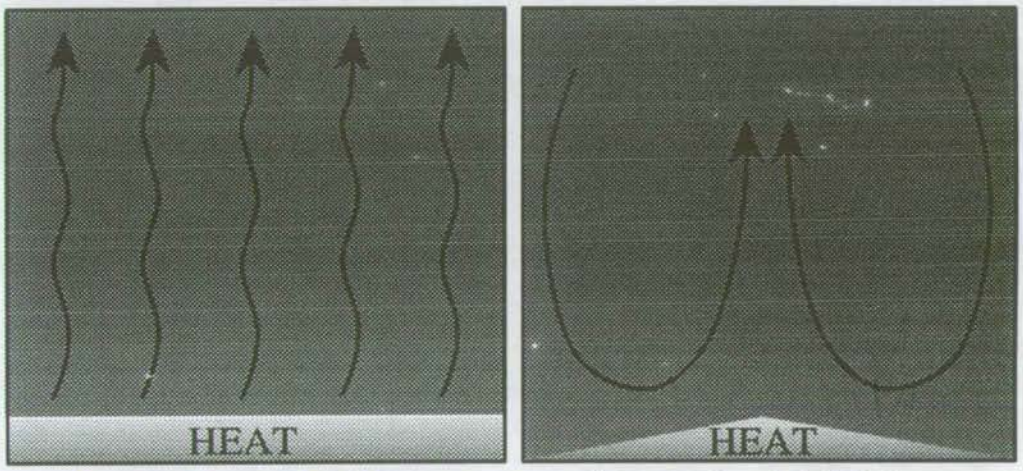

Single Pass Fluid Flow Convective Fluid Flow

Figure 2.10: Fluid Pressure as a function of Depth (after Gregory & Backus 1980)

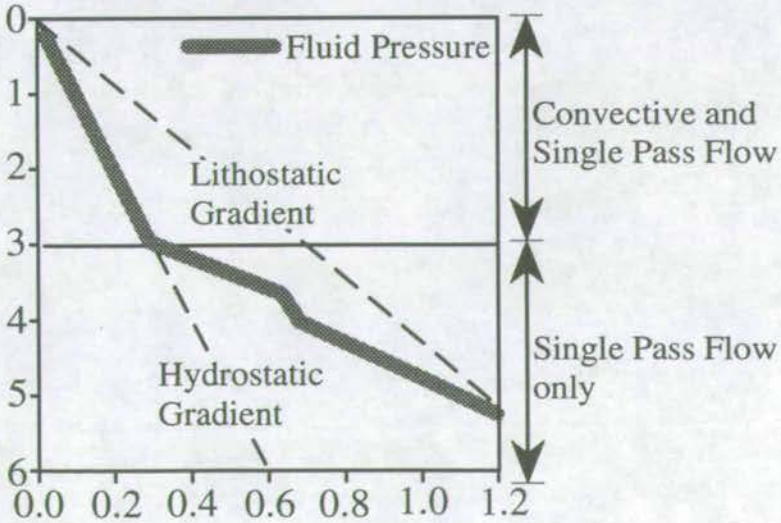

and misleading for quantification of fluid flow, they do provide useful indicators of the presence of fluid in the crust. In these studies, Ferry presented convincing evidence for the importance of plutonism, lithologies and structure in governing crustal fluid flow paths.

2.2.3 The Significance of High Fluid:Rock Ratios

If the high fluid:rock ratios predicted by Wickham & Taylor (1985, 1987) and Ferry (1984) of 0.3-0.5 and 0.2-2.1 respectively are real, the implications for geological processes are of major importance. Walther & Orville (1982) calculated that the maximum amount of fluid which an average pelite may liberate during complete metamorphic devolatilisation is ≈5 wt.%. At 500°C, 5kb, this is approximately equivalent to 12 vol.% or a fluid:rock ratio of 0.12, which is therefore the maximum fluid:rock ratio which may be generated by metamorphic devolatilisation reactions. The larger fluid:rock ratios predicted by Wickham & Taylor (1985, 1987) and Ferry (1984) require either (i) a large external source reservoir, or (ii) a mechanism by which fluid may be effectively re-used.
Several cases are considered:

1) Fluid is derived from the mantle; the presence of fluid in the mantle has been inferred in a number of studies many of which have shown that in many examples mantle fluids will be CO_2-rich and are therefore unlikely to be responsible for observed mineral reactions (e.g. Greenwood 1967). The mantle is not therefore a viable source for the bulk of deep-crustal fluids.

2) Fluid is derived from surface reservoirs; surface waters may have acted as a source reservoir for large volumes of H_2O-rich fluid. For such fluid to reach great depths, convective circulation must have occurred. This is physically implausible as is discussed below.

The Problems of Convection

Wood & Walther (1986) had already cast well-founded doubt on the physical plausibility of convection of fluids in the deep-crust. In a convective system, hot, low-density fluids rise towards the surface. As they rise, they cool and their density increases, causing them to sink back into the crust (figure 2.9). The resulting downwards movement of fluid is only possible if the fluid pressure is equal to hydrostatic pressure, that is, if the host rock is sufficiently strong to maintain a fluid-filled interconnected porosity against the lithostatic pressure of the rock overburden. If the rock fails, the fluid pressure becomes greater than hydrostatic pressure and can approach lithostatic pressure. In this case. convection is no longer possible. Instead, fluids are driven upwards through the rock by density contrast, once only (single pass flow, figure 2.9). The average lithostatic pressure gradient of continental crust is given by:

$$\frac{\partial P_l}{\partial z} = \rho_{rock} g = 280 \text{bars} / \text{km} \qquad (2.5)$$

assuming ρ_{rock}= 2.8g/cc and the hydrostatic pressure gradient is given by:

$$\frac{\partial P_h}{\partial z} = \rho_{H_2O} g = 100 \text{bars} / \text{km} \qquad (2.6)$$

Therefore at a depth, z (km), the rock strength must be greater than 180z (bars) to support an interconnected porosity which is open to the surface and therefore able to support fluid convection. In the deep-crust, rock strengths are poorly constrained, but values on the order of tens of bars at 500°C are thought to be appropriate (Fyfe *et al.* 1978; Etheridge *et al.* 1984). It is therefore unlikely that fluid convection can be supported in the deep-crust. At shallow crustal levels the strengths of quartz-rich rocks at 200°C are thought to be approximately 300 bars (Fyfe *et al.* 1978). This

could support convection to maximum depths of a few kilometres. Gregory & Backus (1980) measured near-surface fluid pressures near the U.S. Gulf coast. They observed fluid pressure to follow the hydrostatic gradient to approximately 3km depth. At greater depth, fluid pressure increases more rapidly with depth, departing the hydrostatic pressure gradient and gradually approaching the lithostatic pressure gradient (figure 2.10). It is therefore most likely that 3km is about the maximum depth at which convection of fluids is physically plausible. Below this depth, fluid flow must be single pass (figure 2.9).

3) Fluid is derived from metamorphic devolatilsation reactions *and* re-used by 'dilatancy pumping'; in the Mary Kathleen Fold Belt of Northern Australia, Oliver *et al.* (1990) describe fracture-controlled fluid infiltration structures, ***developed under amphibolite facies conditions***. Such features occur in zones of extremely low mean shear stress, developed in metasediments which are adjacent to (structurally) strong metabasite lenses. Elsewhere metasediments show only ductile deformation. Yardley & Bottrell (1992) record similar features in pelites of the Ballynakill Formation in Connemara, Ireland. These observations are of fundamental importance as fluid may be driven into zones of low mean shear stress, even if ***downwards*** fluid flow is entailed. This provides a mechanism where convective re-circulation of fluids, and hence increase of the apparent time-integrated fluid flux, can occur at depth in the crust, if only on a localised scale.

Summary

In summary, large fluid:rock ratios are problematic for the following reasons: 1) Fluid:rock ratios of 0.3-0.5 and 1-2 (predicted by Wickham & Taylor (1985, 1987) and Ferry (1980)) are too great to have been derived by devolatilisation reactions during metamorphism and therefore must originate from a larger external source reservoir.

2) The mantle is ineffective as a source because it provides fluid of the wrong composition.

3) The surface is ineffective as a source because it relies on physically implausible convective transport of fluid to great crustal depths.

4) Fluid focusing by means of dilatency pumping may arise but is probably only effective on a localised scale.

Regional-Scale Focusing of Fluids: A Viable Alternative?

One remaining solution is that both the Trois Seigneurs Massif and the Waterville-Vassalboro Formation represent zones of intense focusing of fluid from a laterally extensive volume of underlying rocks. This situation is modelled in figure 2.11, in which the total volume of pelites undergoing complete devolatilisation at 500°C, 5kb is given, as expressed by Walther & Orville (1982) as 12 vol.% (fluid:rock ratio = 0.12). The predicted volume is described in terms of its horizontal area with respect to an assumed crustal thickness. In the example of the Trois Seigneurs Massif, the required volume would encompass some 1.7-2.0 times the horizontal area of the Massif itself assuming a maximum reasonable crustal thickness of 30km. In the example of the Waterville-Vassalboro Formation, the required volume of pelite would encompass some six times the horizontal area of the Formation, assuming a maximum reasonable crustal thickness of 30km. These conclusions are worrying because they assume all pelites surrounding the Trois Seigneurs Massif and the Waterville-Vassalboro Formation to be unaffected by fluid. Such a conclusion is clearly unsatisfactory.

It was this dilemma that brought the validity of the zero-dimensional mass-balance models into question. It was only then, with fluid:rock ratio calculations cast firmly into doubt, that the need for a new dimensionalised approach to modelling deep-crustal fluids was fully realised.

Figure 2.11: Illustration Depicting Volume of Pelite required to undergo Metamorphic Devolatilisation to Generate Calculated Fluid:Rock Ratios

1. Trois Seigneurs Massif

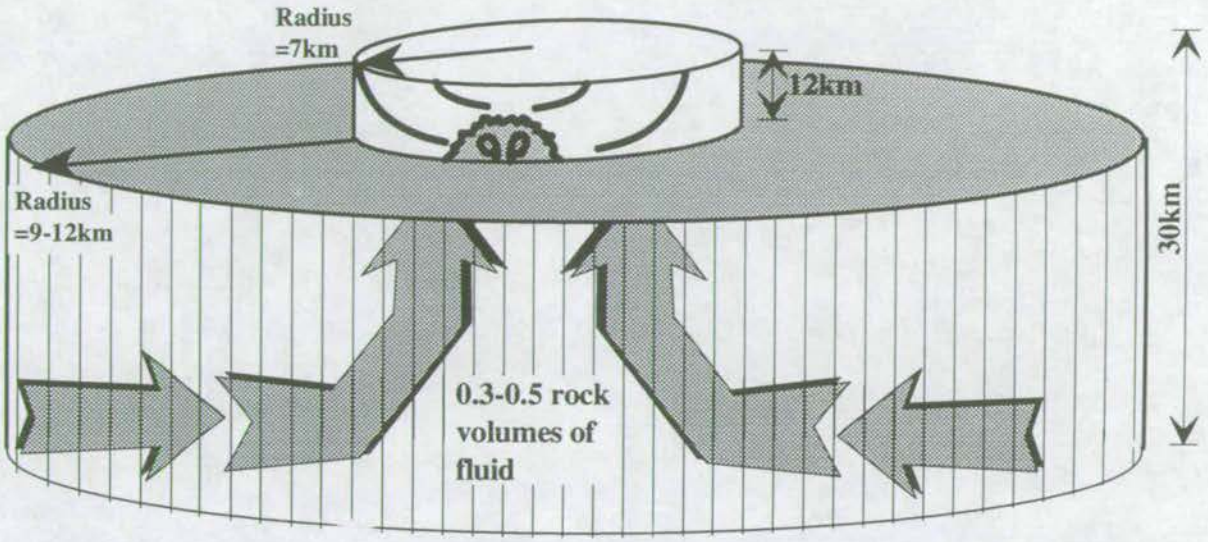

The above diagram depicts the volume of pelites which would be required to undergo complete metamorphic devolatilisation to generate a fluid:rock ratio of 0.3-0.5, as predicted by Wickham & Taylor (1985, 1987). The radius of the Trois Seigneurs massif is assumed to be 7km and the crustal thickness is assumed to be 30km. The required volume of pelites is 2.5-4.2 times the volume of the Trois Seigneurs massif. This is represented by a cylinder of pelites 9-12km in radius.

2. Waterville-Vassalboro Formations

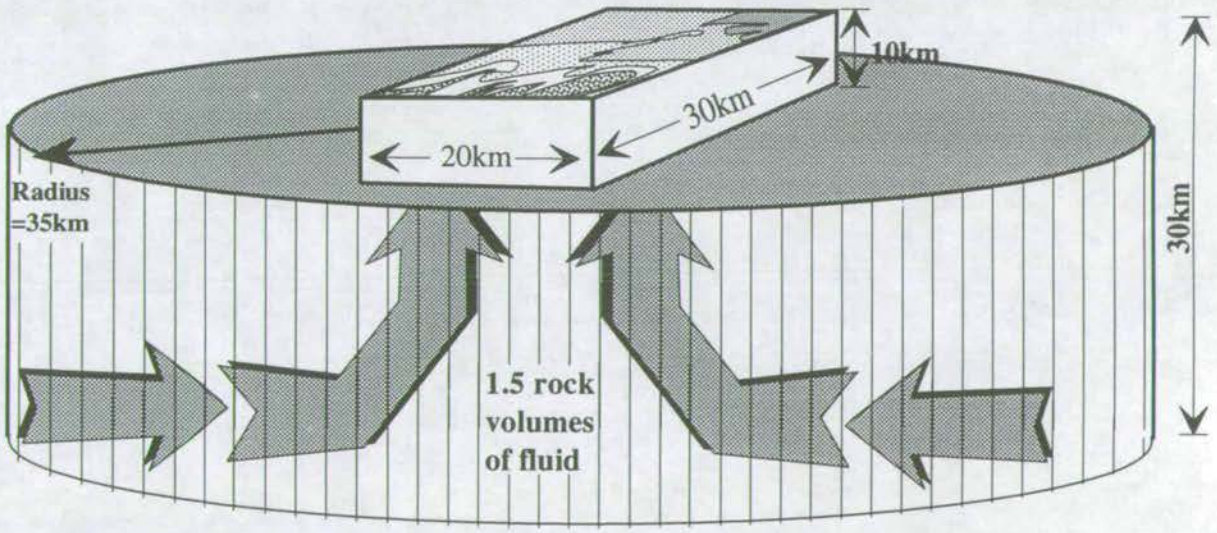

The above diagram depicts the volume of pelites which would be required to undergo complete metamorphic devolatilisation to generate an average fluid:rock ratio of 1.5 (see figure 2.5), as predicted by Ferry (1983). The dimensions of the Waterville-Vassalboro Formation are assumed to be 20km, 30km and 10km, as shown. The crustal thickness is assumed to be 30km.The required volume of pelites is 12.5 times the volume of the Waterville-Vassalboro Formation. This is represented by a cylinder of pelites 35km in radius.

2.3 One-dimensional Models for Quantification of Fluid Flow

The development of a dimensionalised approach to the quantification of fluid flow was along two quite different paths. Ferry (1989) developed a one-dimensional model which calculated the time-integrated flux of fluid flowing along a temperature and/or pressure gradient and internally buffered by the reacting mineral assemblages. Bickle & McKenzie (1987) and Bickle & Baker (1990b) devised one-dimensional models which calculated the time-integrated fluid flux, from advection of isotope or (externally-buffered) reaction fronts. It is probably fair to say that Ferry's model is based loosely on his own earlier zero-dimensional model, whereas Bickle & McKenzie (1987) and Bickle & Baker (1990b) adopt a new approach based on chromatographic theory as described by Hoffman (1972), which was founded on the pioneering works of Korzhinskii (1951, 1952).

2.3.1 One dimensional Modelling of Fluid Flow along a Temperature and/or Pressure Gradient under Conditions of Internal Buffering

Ferry (1989) devised a new approach to the quantification of fluid flow. In this paper, he outlined the crucial weaknesses of the fluid:rock ratio box model (section 2.2.2) and presented a one-dimensional model for the measurement of time-integrated fluid fluxes along a specified temperature gradient.

One-Dimensional Gradient Flow Model (Ferry 1989)

Ferry (1989) presented a model which calculates the time-integrated fluid flux as the sum of incremental volumes of fluid evolved along a unit column oriented parallel to a specified temperature and/or pressure gradient along which local fluid-rock equilibrium is always maintained. The model is illustrated in figure 2.12 and expressed as follows:

Figure 2.12: Model for Calculation of Time-integrated Fluid Flux
(Assumes Internal Buffering, after Ferry 1989)

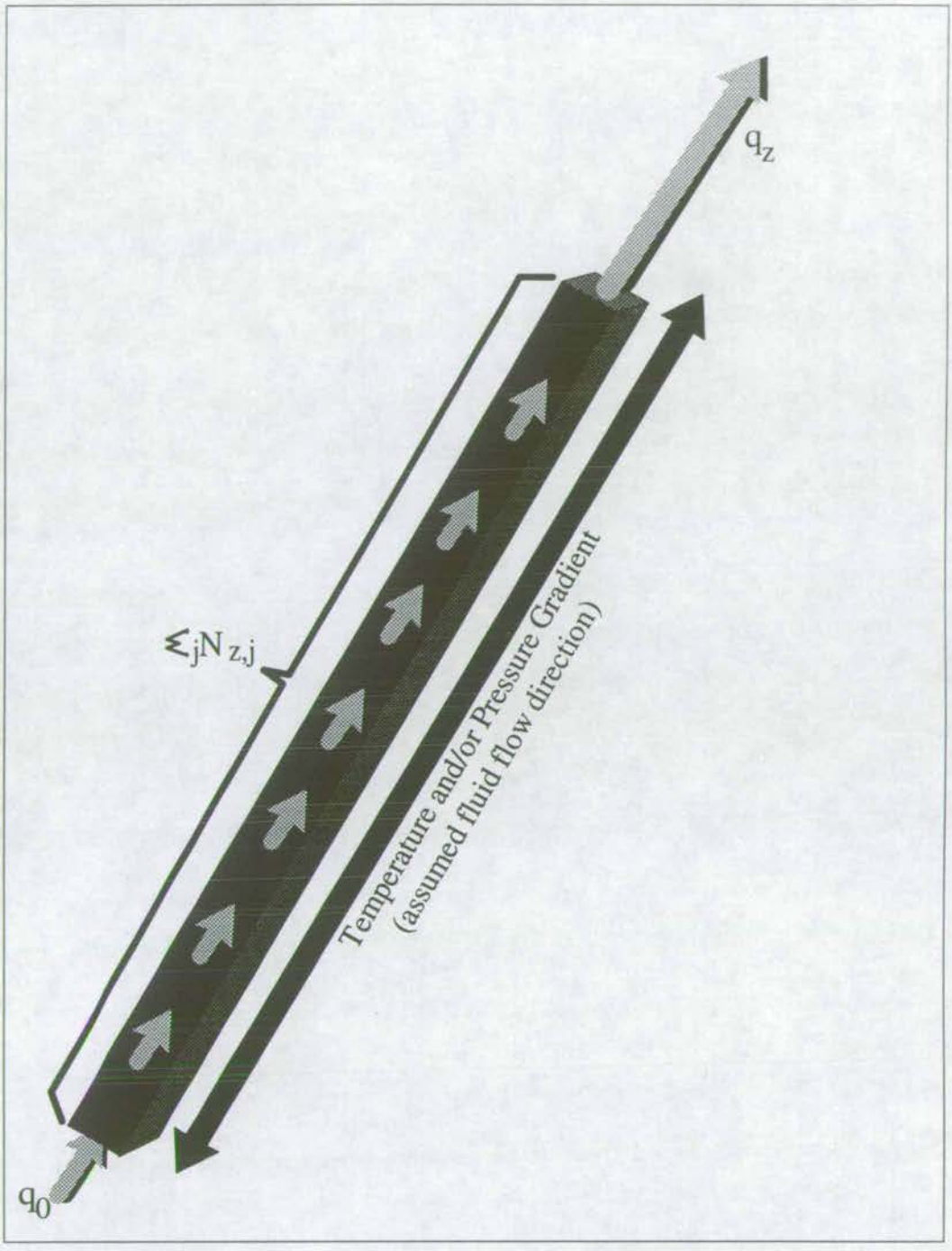

The above diagram shows a column of unit area oriented along a pre-specified temperature and/or pressure gradient. The time-integrated fluid flux, q_z is measured along this column. q_0 is the flux of fluid entering the base of the column, $\Sigma_j N_{z,j}$ is the total volume of fluid generated by reactions along the column and q_z is the fluid flux exiting the top of the column.

Consider a column of rock of unit area with long dimension, z, oriented parallel to the direction of fluid flow, by definition. The value of z increases in the direction of fluid flow. A fluid flux, q_0(moles/cm^2) enters the column at z=0 and is in chemical equilibrium with the rock (at z=0). If, and only if, a temperature or pressure gradient is imposed ***along*** the column, the fluid will continuously react with the rock along its flow path consuming or liberating fluid species such as H_2O and CO_2. The fluid composition will therefore change systematically with increasing z. By mass-balance of the entire column between z=0 and z>0:

$$X_{z,i} = \frac{(q_0 X_{0,i} + N_{z,i})}{(q_0 + \sum_j N_{z,j})} \tag{2.7}$$

where $X_{0,i}$ and $X_{z,i}$ are the respective molar fractions of fluid species i at position z=0 and z=z in the column. $N_{z,i}$ (moles/cm^2) is the cumulative number of moles of species i produced or consumed by reaction between z=0 and z=z, and $N_{z,j}$ (moles/cm^2) is the cumulative number of moles of all fluid species produced or consumed by mineral reaction between z=0 and z=z. Differentiation of equation 2.7 with respect to z gives:

$$(q_0 X_{0,i} + \sum_j N_{z,j})\left(\frac{\partial X_{z,i}}{\partial z}\right) = n_{z,i} - X_{z,i} \sum_j n_{z,j} \tag{2.8}$$

where $n_{z,i} = \partial N_{z,i}/\partial z$ and $n_{z,j} = \partial N_{z,j}/\partial z$ are the change in cumulative number of moles of species i and j, respectively produced or consumed per increment distance, ∂z at position z along the column. $n_{z,i}$ (moles/cm^3) and $n_{z,j}$ (moles/cm^3) are equivalent to the number of moles of species i and j produced or consumed per unit volume of rock at z.

The molar time-integrated fluid flux is given by;

$$q_z = q_0 + \sum_j N_{z,j} \tag{2.9}$$

and includes both the input flux, q_0 and the production of volatiles along the column $\sum_j N_{z,j}$. Combining equations 2.8 and 2.9 gives;

$$q_z = \frac{n_{z,i} - X_{z,i} \sum_j n_{z,j}}{\left[\left(\frac{\partial X_{z,i}}{\partial T} \cdot \frac{\partial T}{\partial z}\right) + \left(\frac{\partial X_{z,i}}{\partial P} \cdot \frac{\partial P}{\partial z}\right)\right]} \qquad (2.10)$$

where $\partial T/\partial z$ and $\partial P/\partial z$ are the temperature and pressure gradients along the column. $\partial X_{z,i}/\partial T$ and $\partial X_{z,i}/\partial P$ are the dependencies of fluid composition on temperature and pressure at point z, and are simply the slopes of the appropriate univariant equilibrium curves on an isobaric T-X_i section and an isothermal P-X_i section, respectively. In the simplest and most general case, where i=CO_2, $X_{z,CO_2}<0.1$ and $\partial T/\partial z >> \partial P/\partial z$, equation 2.10 can be grossly simplified to give:

$$q_z = \frac{n_{z,CO_2}}{\left(\frac{\partial X_{z,CO_2}}{\partial T} \cdot \frac{\partial T}{\partial z}\right)} \qquad (2.11)$$

The number of moles of CO_2 produced or consumed at z, n_{z,CO_2} are estimated by evaluation of the extent of reaction, $\partial X_{z,CO_2}/\partial T$ is estimated from the appropriate univariant equilibrium curves on an isobaric T-X_{CO_2} section, and $\partial T/\partial z$ is taken from geothermometric estimates at either end of the column. Henceforth, the time integrated fluid flux at any point, z, in the crust can be estimated, assuming internal buffering of the fluid composition by the reacting mineral assemblages along the flow path.

Applications of the Gradient Flow Model

Ferry applied the gradient flow model to a contact metamorphic terrain at Hope Valley, California (Ferry 1989), and to regional metamorphism of the Waits River Formation, Eastern Vermont (Ferry 1992).

Application of the Gradient Flow Model to Roof Pendants at Hope Valley, California (Ferry 1989)

Ferry (1989) first applied the gradient flow model to quantify time-integrated fluid fluxes during contact metamorphism of roof pendants at Hope Valley in California (figure 2.13). Time-integrated fluid fluxes were calculated for calcareous hornfelses and marbles containing the assemblages cc + K-fsp + qz + sph ± amph ± bi ± mu ± di ± plag ± scap ± cz which record P=2kb and T=440-540°C. The calculation assumes that $\partial T/\partial z$ = 67 and 90°C/km, $\partial P/\partial z$ is negligible, $\partial X_{z,CO_2}/\partial T$ is given by the average of the slopes of the reaction curves:

$mu + cc + 2qz = K\text{-}fsp + an + CO_2 + H_2O$

and:

$5bi + 6cc + 24qz = 5K\text{-}fsp + 3chl + 6CO_2 + 2H_2O$

and n_{z,CO_2} is given by the number of moles of CO_2 produced per litre of rock divided by 1000. Time-integrated fluid fluxes were estimated as 0.0-0.1×10^5 cm^3/cm^2 in marbles, 0.8-1.3×10^5 cm^3/cm^2 in amphibole-bearing hornfelses and 1.2-2.5×10^5 cm^3/cm^2 in garnet-bearing hornfelses (figure 2.13). On the basis of these fluxes, Ferry (1989) makes the following interpretations:

(1) Contact metamorphism is driven by absorption of heat by rocks and chemical reaction with infiltrating fluid.

(2) The variability in calculated fluxes is due to channelisation of fluid along specific lithologies (figure 2.13).

Application of the Gradient Flow Model to the Waits River Formation, E. Vermont (Ferry 1992)

Ferry (1992) applied the gradient flow model to regional metamorphism of the Waits River Formation, E. Vermont (figure 2.14). Time-integrated fluid fluxes were calculated from impure carbonates which are abundant throughout the Waits River Formation. Metamorphic zones defined by the development of ankerite +

Figure 2.13: Application of the Gradient Flow Model to Roof Pendants at Hope Valley, California (Ferry 1989)

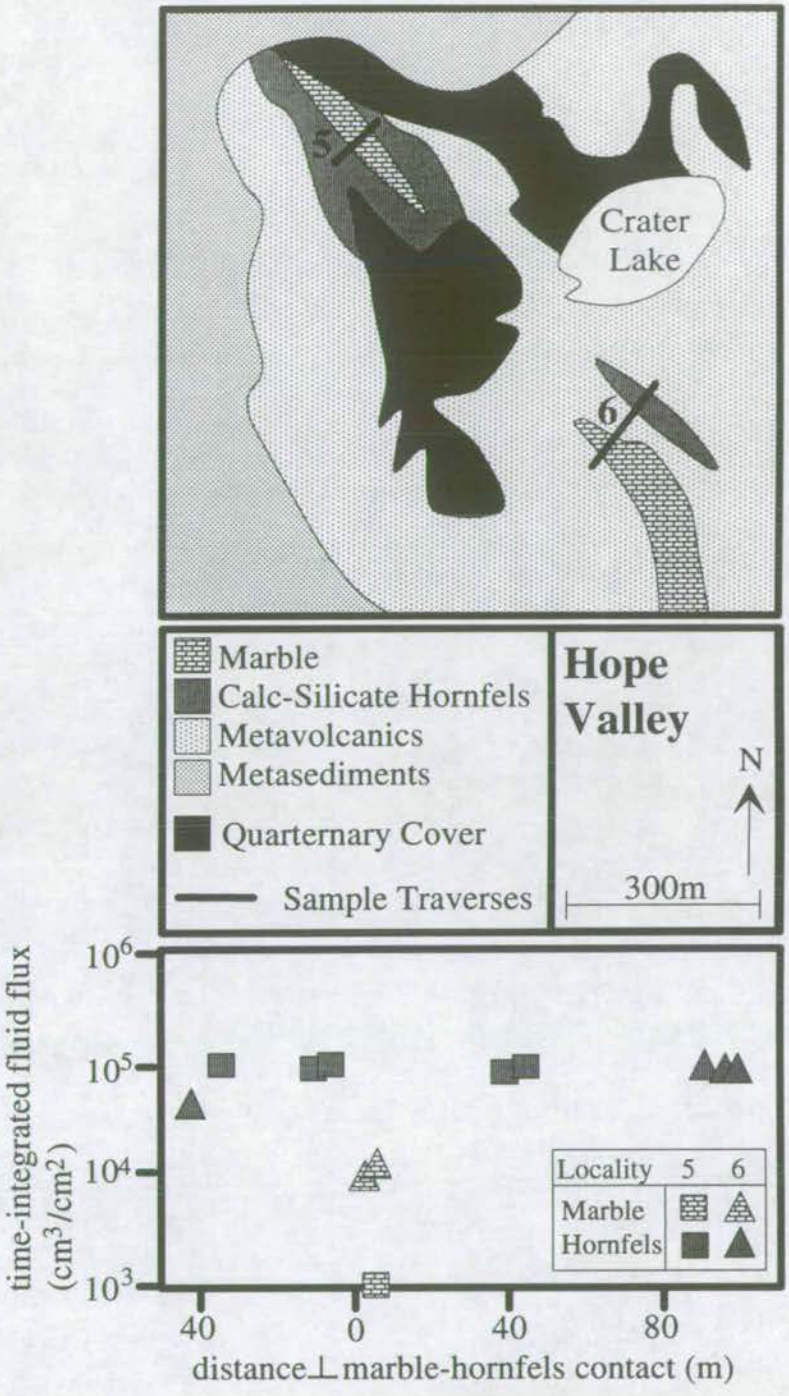

The above map shows the outcrop of roof-pendants at Hope Valley and sample localities 5 and 6 (Ferry 1989). The calculated time-integrated fluid fluxes are shown on the above plot as a function of distance from the hornfels-marble contacts. Time-integrated fluid fluxes within the Hornfels are consistently around 10^5 cm^3/cm^2 and time-integrated fluid fluxes are considerably lower; 10^3-10^4 cm^3/cm^2.

Figure 2.14: Application of the Gradiant Flow Model to the North Waits River Formation (Ferry 1991)

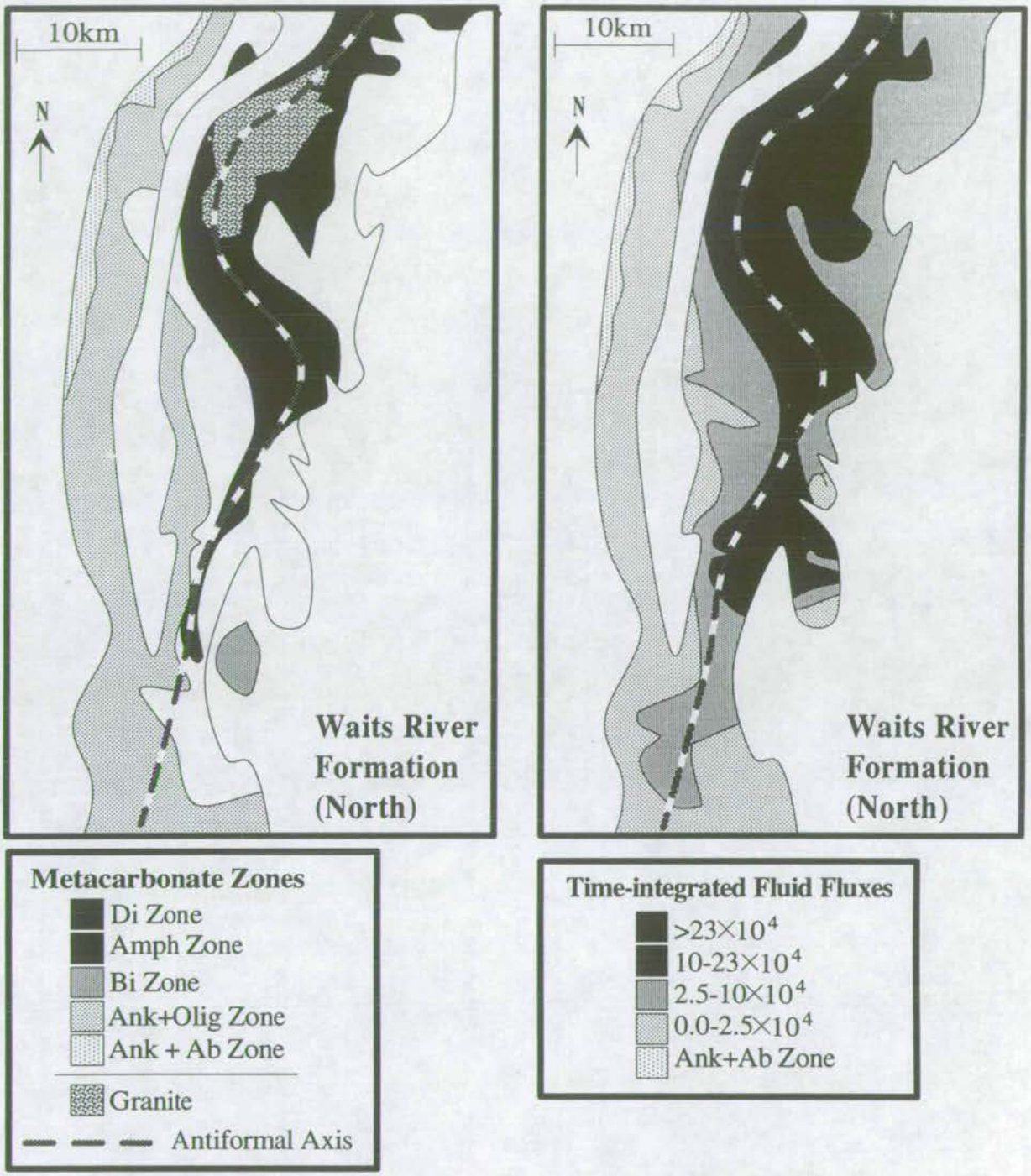

The above maps compare metacarbonate metamorphic zonation with calculated time-integrated fluid fluxes in the northern Waits River Formation, E. Vermont, adapted from Ferry (1991). An elongate metamorphic high is developed along the antiformal axis which coincides with the maximum time-integrated fluid flux. Rocks within the ankerite+albite zone are assumed to represent the protoliths of rocks within the ankerite+oligoclase, biotite, amphibole and diopside zones and therefore record a time-integrated fluid flux of zero.

Figure 2.14: Application of the Gradiant Flow Model to the South Waits River Formation (Ferry 1991)

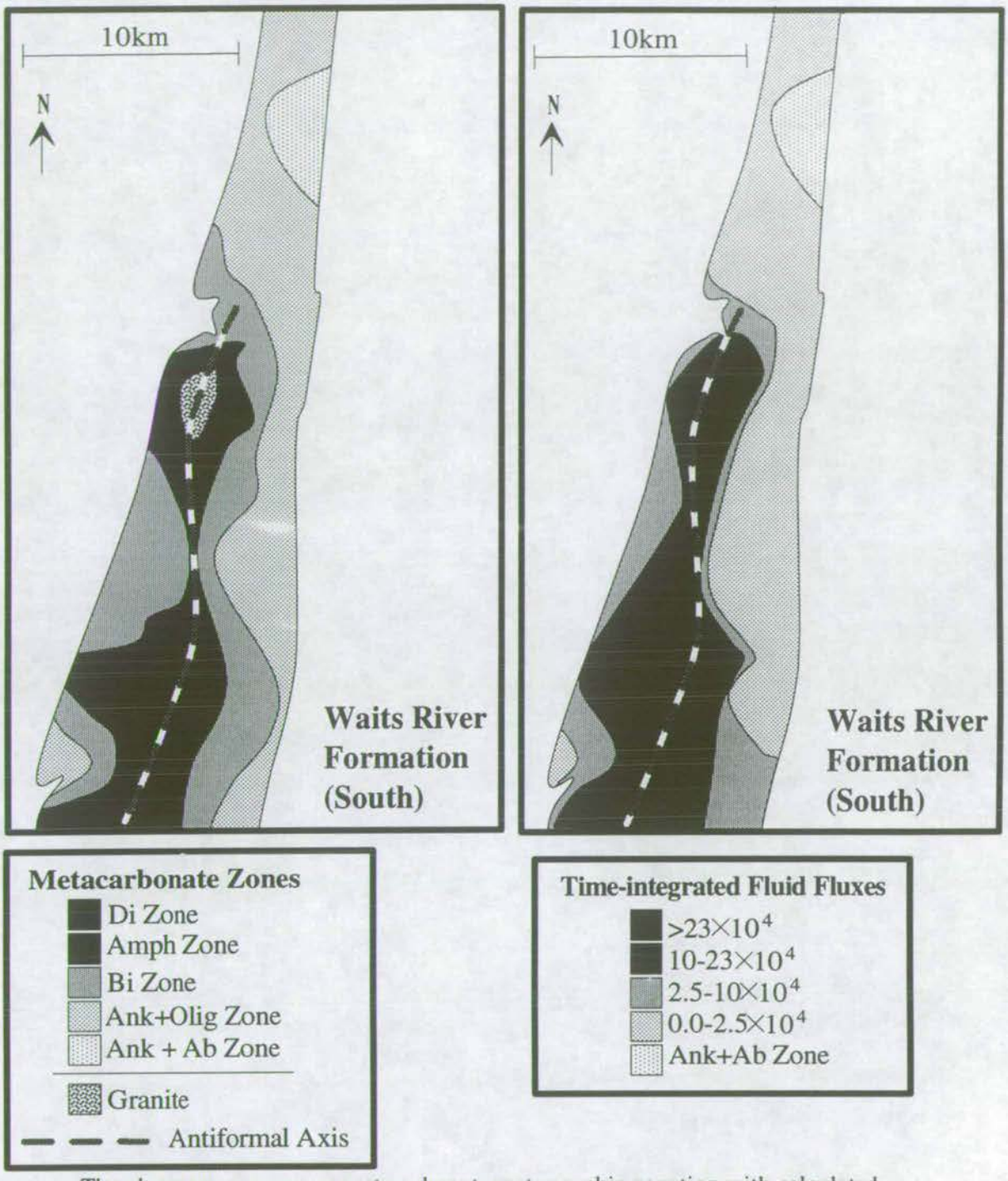

The above maps compare metacarbonate metamorphic zonation with calculated time-integrated fluid fluxes in the southern Waits River Formation, E. Vermont, adapted from Ferry (1991). An elongate metamorphic high is developed along the antiformal axis which coincides with the maximum time-integrated fluid flux. Rocks within the ankerite+albite zone are assumed to represent the protoliths of rocks within the ankerite+oligoclase, biotite, amphibole and diopside zones and therefore record a time-integrated fluid flux of zero.

Figure 2.14: Giant Hydrothermal System described by Ferry (1991).

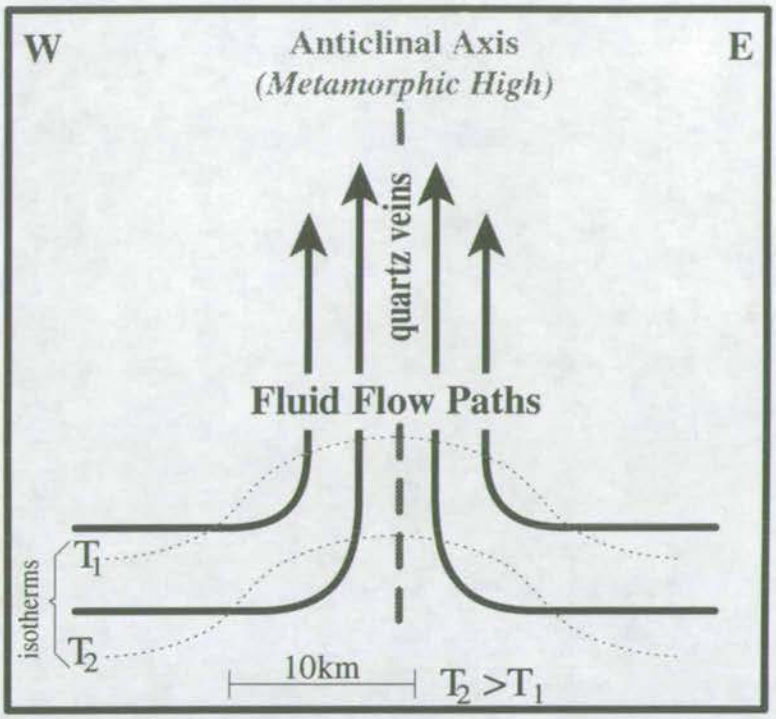

The giant hydrothermal system delineated by Ferry (1991) is described in the above diagram. Fluid flow is sub-horizontal and up-temperature, towards the hot core of the antiform. In the core of the antiform, fluid flow was, generally upwards, down-temperature and focussed along-side syn-metamorphic plutons. Upwards fluid flow in the axial region of the antiform was responsible for extensive quartz veining.

albite, ankerite + oligoclase, biotite, amphibole and diopside in metacarbonates define elongate metamorphic highs centred on the axes of two regional-scale antiforms and closely associated with syn-metamorphic plutons (figure 2.14). Pressures calculated from mineral equilibria are uniformly 7±1.5kb and temperatures increase from ≈480° C in the ankerite zones to ≈575°C in the diopside zone. n_{z,CO_2} may be calculated by assuming that the protoliths of rocks presently in the ankerite + oligoclase, biotite, amphibole and diopside zones are similar to rocks presently in the lowest grade, ankerite + albite zone. Ferry (1992) states that:

(1) $\partial T/\partial z.\partial X_{z,CO_2}/\partial T >> \partial P/\partial z.\partial X_{z,CO_2}/\partial P$,

(2) $n_{z,CO_2} - X_{z,CO_2}\Sigma_j n_{z,j} > 0$ because (i) prograde reactions generate CO_2 and therefore $n_{z,CO_2}>0$ and (ii) fluids are dominantly hydrous and therefore X_{z,CO_2} is small,

and (3) $q_z>0$, by definition.

On the basis of the above criteria and assuming an average value of $\partial X_{z,CO_2}/\partial T$, the gradient flow model is shown to predict that $\partial T/\partial z>0$. Therefore, by default, Ferry (1992) states that fluid flow must have been sub-horizontal, on the basis that (i) near-vertical, upwards fluid flow is generally characterised by $\partial T/\partial z<0$ and (ii) downwards fluid flow has been shown to be physically implausible (Walther & Wood 1984).

Calculated time-integrated fluid fluxes increase with metamorphic grade and are given by $0.0\text{-}2.4\times10^4$ in the ankerite-oligoclase zone, $2.5\text{-}10 \times 10^4$ in the biotite zone, $10\text{-}23\times10^4$ in the amphibole zone, and $>23\times10^4$ in the diopside zone (figure 2.14).

On the basis of (i) the above time-integrated fluid flux measurements, (ii) the directional constraint imposed by the gradient flow model, that fluid flow is sub-horizontal and up temperature, and (iii) an increased abundance of quartz veins near the centre of the regional antiforms, Ferry (1992) describes a new type of giant hydrothermal system (figure 2.14), in which (i) fluid flow is sub-horizontal towards

the hot centres of the regional antiforms and (ii) fluid flow is upwards, near-vertical and focused along-side syn-metamorphic plutons in the centres of the antiforms.

This model requires large-scale sub-horizontal fluid flow, where fluid is effectively "sucked" out of cubic kilometres of surrounding metasediments into the giant hydrothermal system. In the light of work undertaken in this thesis, it is perhaps more likely that structural channelisation of fluid along the axes of the regional antiforms is responsible for the measured increase of calculated time-integrated fluxes with increasing metamorphic grade (and decreasing distance from the antiformal axes, figure 2.14) and increased generation of quartz-veins in the axial zones of the antiforms.

As with Ferry's previous interpretations, this "giant hydrothermal system" would impose a major strain on the regional fluid budget. This repeated requirement of excessive fluid volumes remains problematic even with the new dimensionalised modelling approach. The problem cannot be solely linked to suspect geothermometry because the model is a function of $\partial X_{z,CO_2}/\partial T$ not X_{CO_2} and cannot therefore fall foul, to the same extent as his previous box model, to poor geothermal constraints. This is because $\partial X_{z,CO_2}/\partial T$, the slope of the appropriate univariant equilibrium curve, is not nearly so dependent on temperature estimates as X_{CO_2}, at all values of X_{CO_2} (figure 1.2). One potentially suspect assumption which is applied consistently in both Ferry's older box model (1980) and his later gradient flow model (1989) is that reactions are buffered along univariant reaction curves. Many studies, including Greenwood (1967), have shown that the majority of reactions occur when a univariant curve is crossed, that is where fluids are externally buffered. It is also possible that the problem lies in Ferry's interpretation of the model calculations. It is of critical importance, and has perhaps been over-looked, that the model only calculates the vector component of the true time integrated fluid flux which is parallel to the geological temperature and pressure gradients. It fails to account for any other component of flux and therefore makes predictive modelling of the true fluid flow

paths somewhat ill-founded. Furthermore, as with Ferry's earlier fluid:rock ratio calculations, the mineralogy of the protoliths to the higher-grade (ankerite-oligoclase - diopside zone) rocks is assumed to be that of the lowest grade (ankerite-albite zone) rocks. Mineralogical modes of the protoliths are, again calculated by a series of mass-balance equations from which reaction progress is quantified. However, as with Ferry's earlier fluid:rock ratio calculations, reaction pathways with time are again unsupported by textural evidence.

Most of these assumptions were overcome by Bickle & McKenzie (1987) and Bickle & Baker (1990b) who developed one-dimensional approaches based on chromatographic theory, as discussed by Hoffman (1972), originating from the pioneering work of Korzhinskii (1951, 1952), which models the advective transport distance of a reaction front by externally buffered fluid perpendicular to the reaction front. As reaction fronts may develop in a variety of different orientations, application of vector mathematics will enable the true fluid flux to be calculated in the absence of localised fluid focusing.

2.3.2 One dimensional Modelling of Fluid Flow, from Advection of an Isotopic Front

A new approach to the modelling of deep-crustal fluid flow, based on chromatographic theory, as discussed by Hoffman (1972), was presented by Bickle & McKenzie (1987). They considered a fluid phase moving relative to a solid framework within an interconnected pore or fracture network, and advecting a step in isotopic composition (an isotope front), as an example of two-phase flow. Different lithologies inherit different pre-metamorphic isotopic signatures and therefore a lithological contact marks a shift in isotopic composition (an isotopic front). An isotope front may be advected a distance which is a function of the rock and fluid densities, porosity and the distribution co-efficient of oxygen between rocks and

fluids. This approach is of particular value because unlike the models of Taylor (1977), the time-integrated fluid flux is ***not*** a function of the magnitude of the isotopic shift. The model is expressed as follows:

From a frame of reference moving with an isotope front, mass-balance of the isotopic species across the front gives (figure 2.15):

$$(1-\varphi).V_f.(\rho_s C_{f2} K_d - \rho_s C_{f1} K_d) = \varphi.(\omega - V_f).(\rho_f C_{f2} - \rho_f C_{f1}) \qquad (2.12)$$

where φ is the porosity and therefore (1-φ) is the volume of rock; V_f is the velocity of the rock relative to the front (figure 2.15) and therefore (1-φ).V_f is the flux rate of the front relative to the rock; ρ_s is the rock density; C_{f2} and C_{f1} are the relative concentrations of the isotopic species upstream and downstream of the front (figure 2.15) and K_d is the volumetric distribution coefficient of the isotopic species between the solid and fluid phases. Therefore ($\rho_s C_{f2} K_d$ - $\rho_s C_{f1} K_d$) is the change in volumetric concentration of the isotopic species in the rock, and (1-φ).V_f.($\rho_s C_{f2} K_d$ - $\rho_s C_{f1} K_d$) is the volume flux of the isotopic species in the rock relative to the front (i.e. ***downstream*** of the front). Similarly, the porosity, φ, is the volume of fluid; ω is the fluid velocity and therefore (ω-V_f) is the fluid velocity relative to the front and φ.(ω-V_f) is the flux of fluid relative to the front; ρ_f is the density of the fluid, and therefore ($\rho_f C_{f2}$-$\rho_f C_{f1}$) is the change in volumetric concentration of the isotopic species in the fluid, and φ.(ω-V_f).($\rho_f C_{f2}$-$\rho_f C_{f1}$) is the volume flux of the isotopic species in the fluid relative to the front (i.e. ***upstream*** of the front). Equation 2.12 may be rearranged algebraically to give:

$$V_f = \frac{\omega\varphi}{\left(\frac{\rho_s \cdot K_d}{\rho_f}\right)\cdot(1-\varphi)+\varphi} \qquad (2.13)$$

which can be further simplified if φ is small (approx. 10^{-3}) and $\varphi << K_d$ to give;

Figure 2.15: Model for Calculation of Time-integrated Fluid Flux (Assumes External Buffering, after Bickle & MacKenzie 1987)

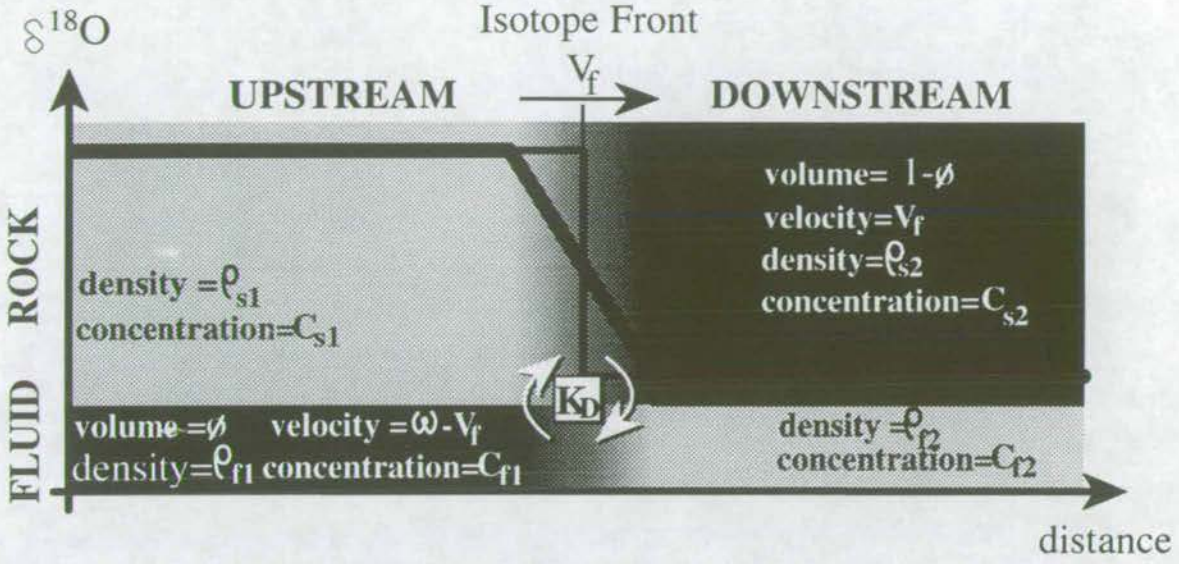

The one-dimensional model of Bickle & McKenzie is illustrated in the above plot of $\delta^{18}O$ against distance. ρ_{s1} and ρ_{s2} are the densities of the solid upstream and downstream of the front, respectively. ρ_{f1} and ρ_{f2} are the densities of the fluid upstream and downstream of the front, respectively. C_{s1} and C_{s2} are the concentrations of the isotopic species in the solid upstream and downstream of the front, respectively. C_{f1} and C_{f2} are the concentrations of the isotopic species in the fluid upstream and downstream of the front respectively. ø is the porosity. K_D is the distribution coefficient of the isotopic species between the solid and fluid phases. ω is the fluid velocity. V_f is the velocity of the isotopic front.
In essence, the model equation describes mass-balance of the tracer across an isotopic front which is advected at velocity V_f by an infiltrating fluid moving at velocity ω. An advective profile is developed, defining a step function in isotopic composition which is smoothed by diffusion.

$$V_f = \frac{\omega\varphi}{\left(\frac{\rho_s . K_d}{\rho_f}\right)} \qquad (2.14)$$

Multiplying through by time, t, gives;

$$V_f . t = \frac{\omega\varphi t}{\left(\frac{\rho_s K_d}{\rho_f}\right)} \qquad (2.15)$$

Equation 2.15 relates the advection distance of the isotope front (V_f.t), to the time-integrated fluid flux ($\omega.\varphi.t$) by the densities of the solid and fluid phases, and the distribution coefficient of the isotopic species between the rock and fluid phases. Densities of rocks and fluids have been determined experimentally for many rock and at various crustal depths (Deer, Howie & Zussmann 1992, Todheide 1972 and Bottinga & Richet 1981). The distribution coefficient may be calculated from the concentrations of the isotopic species in the rock and fluid phases.

Boundary Conditions and Assumptions of the Isotope Front Advection Model

Successful application of the isotope front advection model is subject to satisfaction of the following boundary conditions:

(1) The partition coefficient of oxygen between the rock and the fluid phases must be known (figure 2.15),

(2) The densities of the rock and fluid phases must be known (figure 2.15),

and (3) The initial and final loci of the isotope front must be known (figure 2.15).

Furthermore, the isotope front advection model assumes that fluid infiltration is pervasive and that grain-scale fluid-rock equilibrium will be attained. However, Lassey & Blattner (1988) and Bickle (1992) state that ***only*** the morphology of an isotope front profile will be affected by such kinetic hindrance. Therefore, provided that an isotope front may be distinguished, it should be possible to calculate the time-integrated fluid flux. This conclusion is tested in chapter 7.

Applications of the Isotope Front Advection Model (Baker et al. 1989)

The model has been applied in several studies. Most notably in a comprehensive study of fluid infiltration of inter-bedded marbles and schists on Naxos, Greece undertaken by Baker *et al.* (1989).

Inter-bedded marbles and schists exposed on Naxos structurally overlie a migmatitic-gneissic complex, and have undergone two phases of metamorphism. An early Tertiary high-pressure glaucophane-schist facies metamorphism (M1) is over-printed by Miocene regional greenschist facies metamorphism (M2). Buick (1988) documents two phases of folding. An earlier syn-M2 phase of isoclinal folding associated with development of a penetrative extensional fabric precedes gentle doming which exposes higher grade rocks in the centre of Naxos (figure 2.16a).

Detailed petrological work identified two generations of calc-silicate growth. The first generation of calc-silicates developed during prograde M2 metamorphism. The common occurrence of invariant assemblages implied that fluid compositions were internally buffered. The second generation of calc-silicates developed during retrogression and define well-developed lineations or infill pull-apart fractures of first generation minerals. Detailed mineralogical and textural analysis implied that second generation calc-silicates developed in response to vein-controlled infiltration of H_2O-rich fluids.

Carbonate stable isotopic profiles, shown in figure 2.16(b), were constructed across the five marble layers (A-E) which are located in figure 2.16(a), from which

Figure 2.16(a): Geological Map of Naxos, showing Isograds/Isotherms, Structural Doming, and Locations of Isotope Traverses A-E.

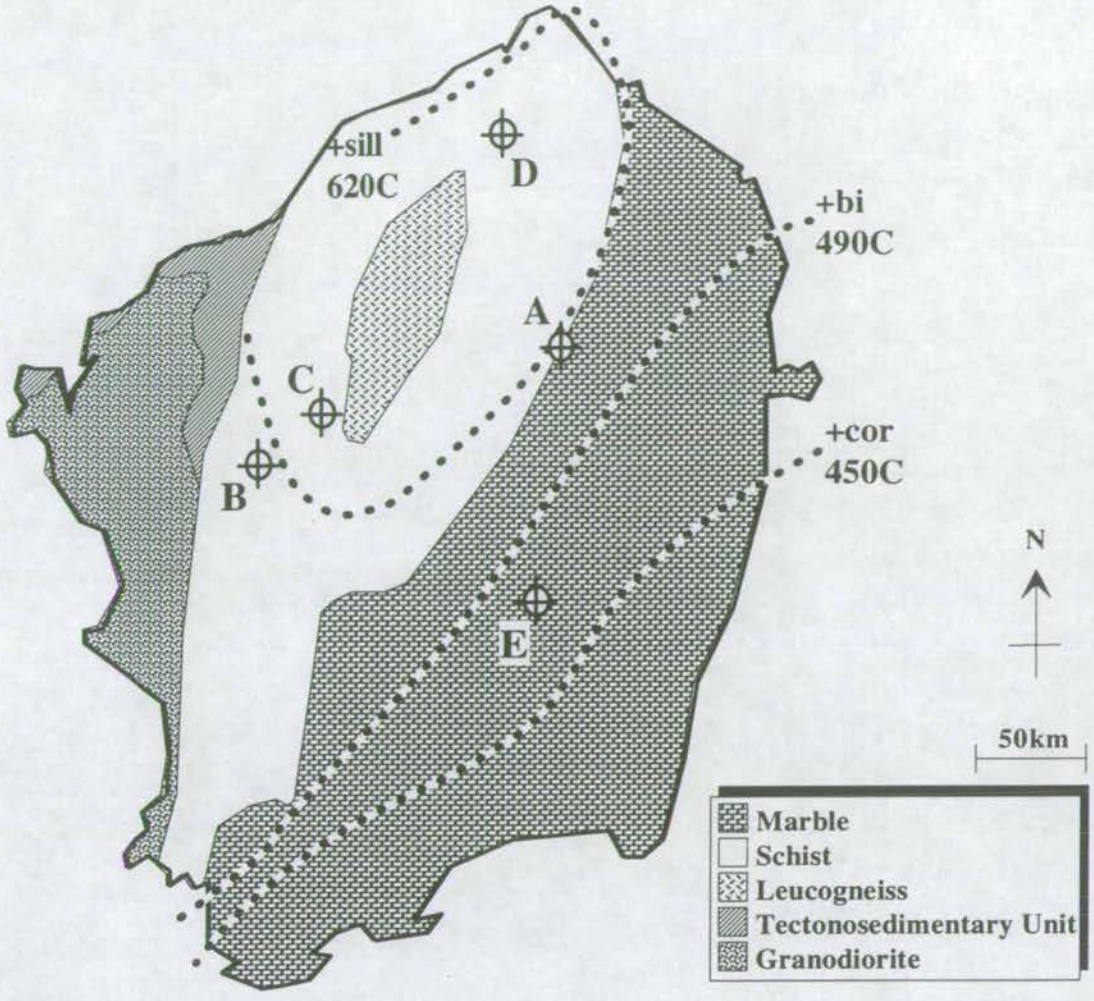

Figure 2.16(b): Carbonate Oxygen Isotope Profiles of Marbles A-E

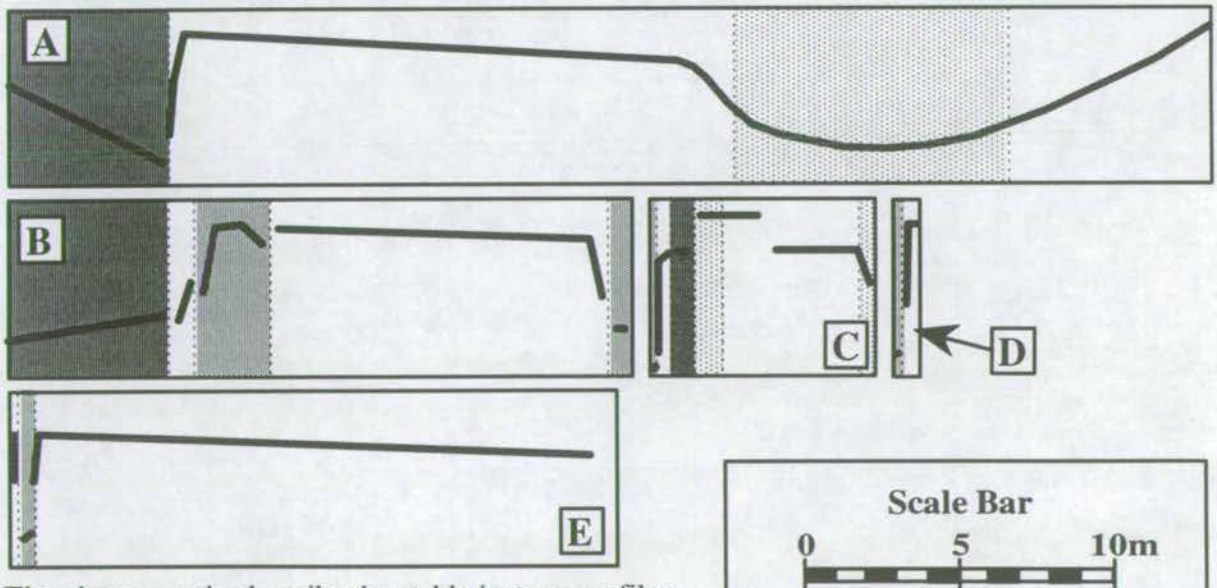

The above graphs describe the stable isotope profiles constructed across individual marble layers which are located in figure 2.16(a). Advection distances were estimated from these graphs. Retrograde veining is associated with lower isotopic signatures.
*Isotopic modification of yellow dolomite records an earlier phase of infiltration.

the two phases of fluid infiltration may be distinguished. Prograde infiltration resulted in the isotopic homogenisation of marginal boundary layers with adjacent schists, to lower $\delta^{18}O$ (12-16‰), which are progressively broader with increasing grade (figure 2.16b). Retrograde calc-silicates record interaction with a very low $\delta^{18}O$-fluid (<10‰) which is inferred to have evolved during crystallisation of migmatites (figure 2.16a). Isotopic homogenisation of marginal boundary layers is laterally-extensive and therefore prograde fluid infiltration is inferred to have been pervasive. Isotopic alteration of retrograde calc-silicates is limited to the veins in which they develop and therefore retrograde infiltration is inferred to have been fracture controlled.

One-dimensional time-integrated fluid fluxes were calculated using the isotope front advection model of Bickle & McKenzie (1987). Advective displacements of the infiltrating $\delta^{18}O$ signature of the fluid into the marble layers are in the range 0.1-1.0m (figure 2.16a). $(\rho_s K_d/\rho_f)$ is approximately 1.7 for marble at the P-T conditions of M2 metamorphism (6±1kb, 450-700°C). Therefore time-integrated fluid fluxes are between 0.2 and 1.7 m^3/m^2. The fluid flow direction perpendicular to the schist-marble contacts, is constrained from the asymmetry of profiles A-D, to be upwards.

Walther & Orville estimated that an average pelite may liberate 5wt.% (≡12vol.% at P=5kb, T=450°C) fluid as a result of total metamorphic devolatilisation. A mere 2-14m of underlying pelites are required to generate the above determined time-integrated fluid fluxes. Marbles are separated by tens to hundreds of metres of phyllites. It is therefore clear that the recorded fluxes are only a part of the flow. The majority of fluid flow must therefore be lithology-parallel. Quantification of this larger and consequently more important component of fluid flow in terms of its advective potential proved problematic in their study due to lack of any identifiable fluid flow "markers". It is therefore an essential aim of this thesis to devise a method

by which the lithology-parallel component of the time-integrated fluid flux may be constrained.

2.3.3 One dimensional Modelling of Fluid Flow from Advection of an (Externally Buffered) Reaction Front

Bickle & Baker (1990b) advanced this theoretical approach to the modelling of deep-crustal fluid flow in one dimension by considering a mobile H_2O-CO_2 fluid exchanging H_2O or CO_2 with the rock and hence advecting a mineral reaction front. Again, they considered a fluid phase moving relative to a solid framework within an interconnected pore network, but in this case, advecting a mineral reaction front. This is of particular value, because, in contrast to the models of Ferry (1980, 1989), the initial and final mineralogies and the reaction textures which relate them, may be observed. Furthermore, this approach considers the more common situation, in which the composition of the infiltrating fluid is externally-buffered and therefore drives mineral reactions ***across*** univariant reaction curves rather than along them.

From a frame of reference moving with the reaction front, mass-balance of CO_2 across the front (figure 2.17) gives the equation:

$$(\omega_1 - V_f).\varphi_1.X_{CO2,1} + R_{CO2} = (\omega_2 - V_f).\varphi_2.X_{CO2,2} \qquad (2.17)$$

where ω_1 and ω_2 are the respective fluid velocities upstream and downstream of the reaction front; V_f is the velocity of the reaction front, and therefore $(\omega_1\text{-}V_f)$ and $(\omega_2\text{-}V_f)$ are the respective fluid velocities upstream and downstream of the reaction front relative to the moving frame of reference of the front; φ_1 and φ_2 are the respective porosities, and therefore fluid volumes, upstream and downstream of the front, and therefore $(\omega_1\text{-}V_f)\varphi_1$ and $(\omega_2\text{-}V_f)\varphi_2$ are the respective fluid fluxes upstream and

Figure 2.17: Model for Calculation of Time-integrated Fluid Flux (Assumes External Buffering, after Bickle & Baker 1990b)

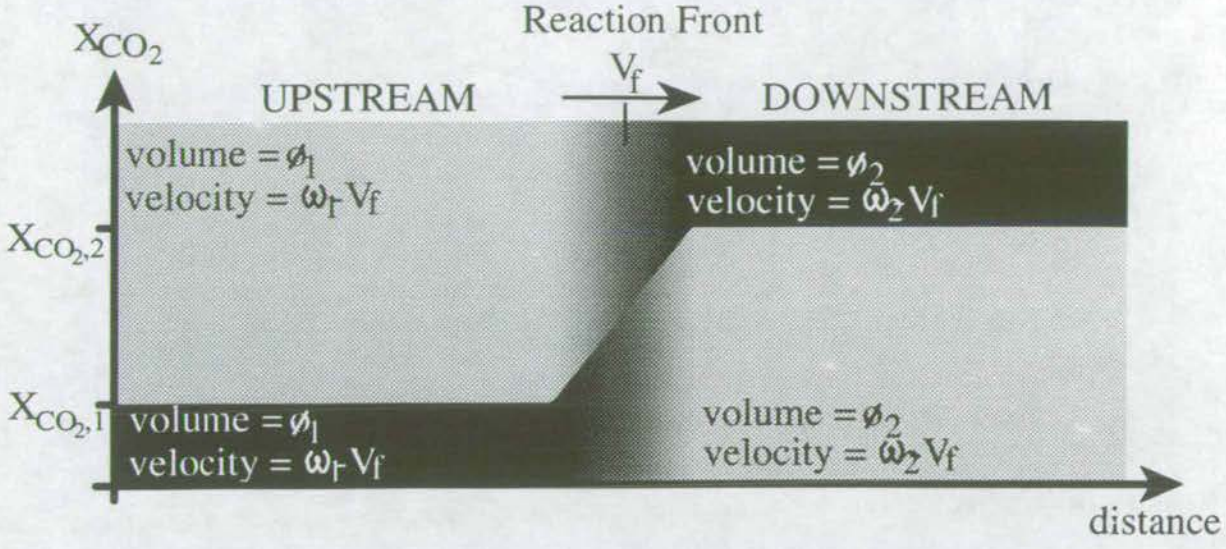

The one dimensional model of Bickle & Baker (1990) is illustrated in the above plot of X(CO2) against distance. ϕ_1 and ϕ_2 are the porosities of the rock upstream and downstream of the front, respectively. ω_1 and ω_2 are the respective velocities of the fluid upstream and downstream of the front. V_f is the velocity of the reaction front.
In essence, the model describes mass-balance of the fluid species downstream of a reaction front, which is advected at velocity V_f by an infiltrating fluid moving at velocity ω_1, with fluid species upstream of, and generated at the reaction front. An advective profile is developed, defining a step in fluid composition (reaction front) which is smoothed by diffusion of fluid species.

downstream of the reaction front relative to the front; $X_{CO_2,1}$ and $X_{CO_2,2}$ are the volumetric fractions of CO_2 in the respective fluids, upstream and downstream of the front, and therefore, $(\omega_1-V_f)\varphi_1.X_{CO_2,1}$ and $(\omega_2-V_f)\varphi_2.X_{CO_2,2}$ are the respective volumetric fluxes of CO_2 upstream and downstream of the front; R_{CO_2} is the volume of CO_2 produced or consumed by reaction of a unit volume of rock. A similar mass-balance of H_2O across the reaction front is given by;

$$(\omega_1 - V_f).\varphi_1.(1-X_{CO_2,1}) + R_{CO_2} = (\omega_2 - V_f).\varphi_2.(1-X_{CO_2,2}) \tag{2.18}$$

Equations 2.17 and 2.18 can be combined to give:

$$V_f = \frac{\omega_1.\varphi_1.(X_{CO2,2} - X_{CO2,1})}{R_{CO2}.(1-X_{CO2,2}) - R_{H2O}.X_{CO2,2} + \varphi_1.(X_{CO2,2} - X_{CO2,1})} \tag{2.19}$$

Where φ_1 is small, equation 2.18 can be simplified to give:

$$V_f = \frac{\omega_1.\varphi_1.(X_{CO2,2} - X_{CO2,1})}{R_{CO2}.(1-X_{CO2,2}) - R_{H2O}.X_{CO2,2}} \tag{2.20}$$

dividing through by time, t, gives:

$$V_f t = \frac{\omega_1.\varphi_1.t.(X_{CO2,2} - X_{CO2,1})}{R_{CO2}.(1-X_{CO2,2}) - R_{H2O}.X_{CO2,2}} \tag{2.21}$$

which relates the advection distance of the reaction front ($V_f t$), to the time-integrated fluid flux ($\omega_1\varphi_1 t$) by $X_{CO_2,1}$, $X_{CO_2,2}$, R_{CO_2} and R_{H_2O}. Provided that the reaction has gone to completion upstream of the front, R_{CO_2} and R_{H_2O} are given by the volumetric

stoichiometric coefficients of the reaction. $X_{CO_2,2}$ is the composition of fluid which is buffered by the reaction and can be taken directly from an appropriate isobaric T-X_{CO_2} diagram. $X_{CO_2,1}$ is the composition of the infiltrating (upstream) fluid and is the most difficult variable to constrain, usually requiring additional independent evidence.

In addition to satisfying the boundary conditions of the isotope advection model (Bickle & McKenzie 1987), if the reaction front advection model of Bickle & Baker (1990b) is to be used to calculate time-integrated fluid fluxes from measured advection distances, two further requirements must be satisfied:

(1) Firstly, the reaction must be well constrained in terms of both its stoichiometry and its T-X_{CO_2} relations.

(2) Secondly, additional reliable and independent evidence must be present constraining the composition of the infiltrating fluid, $X_{CO_2,1}$.

To my knowledge, other than a study undertaken by Harris & Bickle (1989) to investigate the process of charnockitisation, the work in this thesis represents the first major application of this, the latest, and potentially most powerful approach to the quantification of deep-crustal fluid flow.

2.3.4 Comparison of the Gradient Flow and Front Advection Models

A paradox is evident regarding the predicted magnitudes of the time-integrated fluid fluxes estimated by application of the gradient flow model to the Waits River Formation (e.g. Ferry 1992) and application of the front advection model to Naxos, Greece (e.g. Bickle & Baker 1990a). The gradient flow model assumes ***internal-buffering*** of the (chemical) composition of pore-fluids along the entire fluid flow path but predicts ***relatively high*** time-integrated fluid fluxes (2.5×10^3 m^3/m^2), whereas the front advection models assumes dominant ***external-***

buffering of the (isotopic and chemical) composition of pore-fluids but predicts ***relatively low*** time-integrated fluid fluxes (≈0.2-1.7 m^3/m^2).

Time-integrated fluid fluxes predicted by application of the reaction front advection model (Bickle & Baker 1990a) are consistent with fluid having been derived from devolatilisation of rocks along the (one-dimensional component of the) flow path. By contrast, time-integrated fluid fluxes predicted by application of the gradient flow model (Ferry 1992) imply regional-scale horizontal fluid flow to account for the large fluid volumes, but the fluid source and large fluxes remain unexplained.

2.3.5 Historical evolution of the one-dimensional advection models from the early works of Hoffman and Korzhinskii

It is of interest to view the recent one-dimensional advection models of Bickle & McKenzie (1987) and Bickle & Baker (1990b) in the historical perspective of their evolution from the chromatographic approach of Hoffman (1972) and ultimately from the transport equations of Korzhinskii (1951, 1952).

Korzhinskii (1951) devised mass balance equations of the form:

$$-\frac{\partial C_{i,s}}{\partial V} = \Phi \frac{\partial C_{i,f}}{\partial z} \qquad (2.22)$$

where $C_{i,s}$ and $C_{i,f}$ are the concentrations of component i in solid and fluid phases respectively, V is the time-integrated fluid flux (per unit area), z is distance in the direction of transport, and Φ is termed the filtration coefficient and describes the 'differential mobility' of components within a complex fluid phase. Equation 2.22 may be re-arranged to give transport equations of the form:

$$\left(\frac{dz}{dV}\right)_{C_{i,f}} = \Phi \frac{dC_{i,f}}{dC_{i,s}} \qquad (2.23)$$

where dz/dV describes the advective displacement of a concentration discontinuity, per unit flux of fluid which has passed through a column of unit area in direction z.

Hoffman (1972) challenged the purpose of the filtration coefficient (Φ) stating that it violated mass-balance where $\Phi \neq 1$. Indeed, the filtration coefficient seems merely a repetition of the term $C_{i,f}/C_{i,s}$ and therefore unnecessary. Hoffman therefore re-wrote mass-balance equation 2.22 as:

$$-\frac{\partial C_{i,s}}{\partial V} = \frac{\partial C_{i,f}}{\partial z} \tag{2.24}$$

and subsequently re-wrote transport equation 2.23 as:

$$\left(\frac{dz}{dV}\right)_{C_{i,f}} = \frac{dC_{i,f}}{dC_{i,s}} \tag{2.25}$$

Equation 2.25 forms the basis for transport equations 2.14 and 2.20. This becomes more immediately apparent by considering that z is essentially equivalent to the term $V_f t$ (transport distance of a step in concentration) and V is essentially equivalent to the term $\omega\varphi t$ (time-integrated fluid flux).

2.4 Grain-Scale Mechanisms of Fluid Flow

In a discussion about fluid transport it is important to consider the grain-scale mechanisms by which fluids move. Watson & Brenan (1987) discussed the importance of developing an understanding of grain-scale fluid flow mechanisms to meaningful quantitative interpretation of crustal fluid flow. If rocks are deformed, fluid flow ***may*** be through an interconnected fracture network. If rocks are not fractured, fluid flow is only possible (i.e. a rock is ***permeable*** to fluid) if either (i) the ***instantaneous*** porosity (φ) is sufficiently large so as to permit the existence of an ***interconnected pore-network***, or (ii) physical conditions are such as to permit the existence of an ***interconnected grain-edge porosity*** at all φ.

Watson (1982), Watson & Brenan (1987), Holness & Graham (1991), Holness (*in prep.*), Holness (*in press*) and Holness (*pers. comm.*) have experimentally determined the P-T-X_{CO_2} conditions at which an interconnected grain-edge porosity will exist in quartzites and marbles at all φ.

Theoretical Modelling of the Dihedral Angle

Smith (1948), and later, Watson (1982) demonstrated theoretically that the ability of a rock to develop an interconnected grain edge porosity, under conditions of chemical and textural equilibrium, depends solely on the solid-fluid-solid dihedral angle (θ) which is developed at a triple junction (figure 2.18). Watson (1982) modelled the surface energies of a solid-solid interface, $\gamma_{s\text{-}s}$ (figure 2.18a) and a solid-fluid interface $\gamma_{s\text{-}f}$ (figure 2.18b). He developed a geometric relationship between the ratio of the surface energy of a dry grain-edge ($\gamma_{s\text{-}s}$) to the surface energy of a fluid triple junction ($2\gamma_{s\text{-}f}$) and the dihedral angle (θ) which is illustrated in figure 2.18c and given by:

$$\frac{\gamma_{s-s}}{2\gamma_{s-f}} = \cos\frac{\theta}{2} \qquad (2.26)$$

It may be shown by a graphical representation of equation 2.26 (figure 2.18d) that $\gamma_{s\text{-}f}>\gamma_{s\text{-}s}$ for all $\theta<60°$ and $\gamma_{s\text{-}f}<\gamma_{s\text{-}s}$ for all $\theta>60°$. Therefore an interconnected grain-edge porosity is energetically favoured at $\theta<60°$ for all φ.

Experimental Determination of the Dihedral Angle

Watson & Brenan (1987), Holness (*in press*) and Holness (*in prep.*) have constrained the dependence of the quartz-fluid-quartz dihedral angle (θ) on pressure, temperature and fluid composition. The data from all of these studies are compiled in the P-T diagrams shown in figure 2.19, which are constructed at X_{CO_2}=0.0, 0.5 and 1.0 and contoured in θ. The P-T-θ plots, shown in figure 2.19, predict that an

Figure 2.18: Dihedral Angle Constraints on the Occurrence of an Interconnected Porosity (Watson 1982)

Figure 2.18a: Dry Grain-edge (Solid-Solid Interfacial Energy)

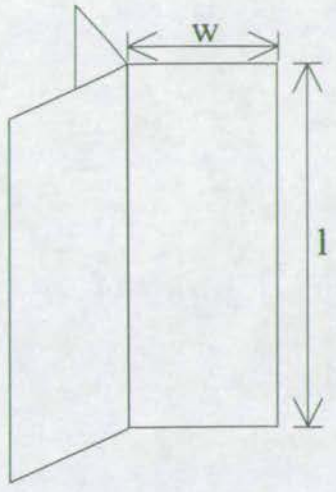

$\gamma_{s\text{-}s} = 3wl$

Figure 2.18b: Wet Grain-edge (Solid-Liquid Interfacial Energy)

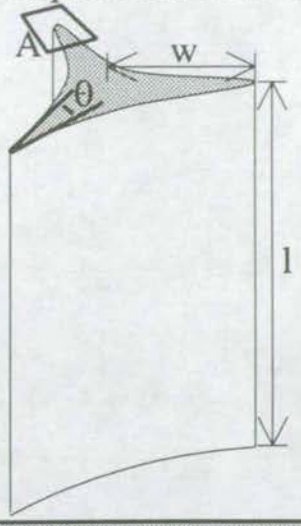

$$\gamma_{s\text{-}f} = \frac{\sqrt{3}[(\pi/6) - (\theta/2)]}{\sin[(\pi/6) - (\theta/2)]} 3wl$$

Figure 2.18c:Area A (flgure 2.18b)

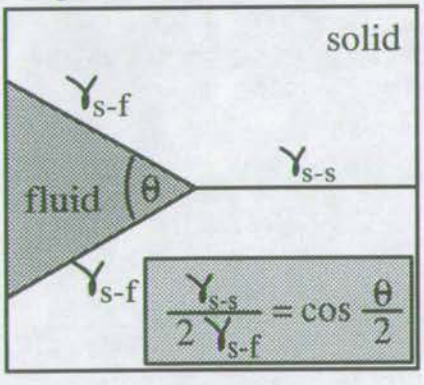

$\gamma_{s\text{-}s}$ = Total surface energy of solid-solid interface
$\gamma_{s\text{-}f}$ = Total surface energy of solid-fluid interface

Figure 2.18d: Plot of $\frac{\gamma_{s\text{-}s}}{2\gamma_{s\text{-}f}} = \cos\frac{\theta}{2}$

$\gamma_{s\text{-}s} = 3wl$

$$\gamma_{s\text{-}f} = \frac{\sqrt{3}[(\pi/6) - (\theta/2)]}{\sin[(\pi/6) - (\theta/2)]} 3wl$$

$$\frac{\gamma_{s\text{-}s}}{2\gamma_{s\text{-}f}} = \cos\frac{\theta}{2}$$

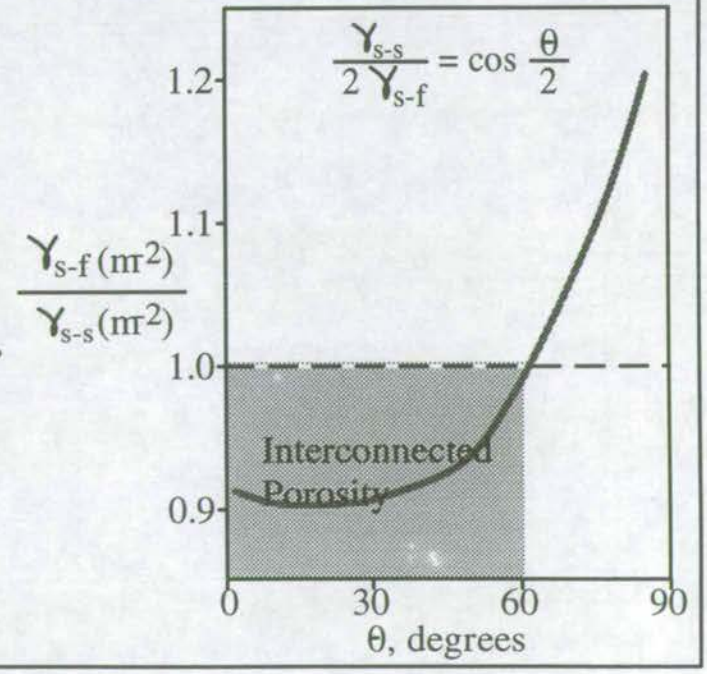

Figure 2.19: Dependence of the Dihedral Angle on Temperature and Pressure (Watson & Brenan 1987, Holness *in press*, Holness *in prep.*)

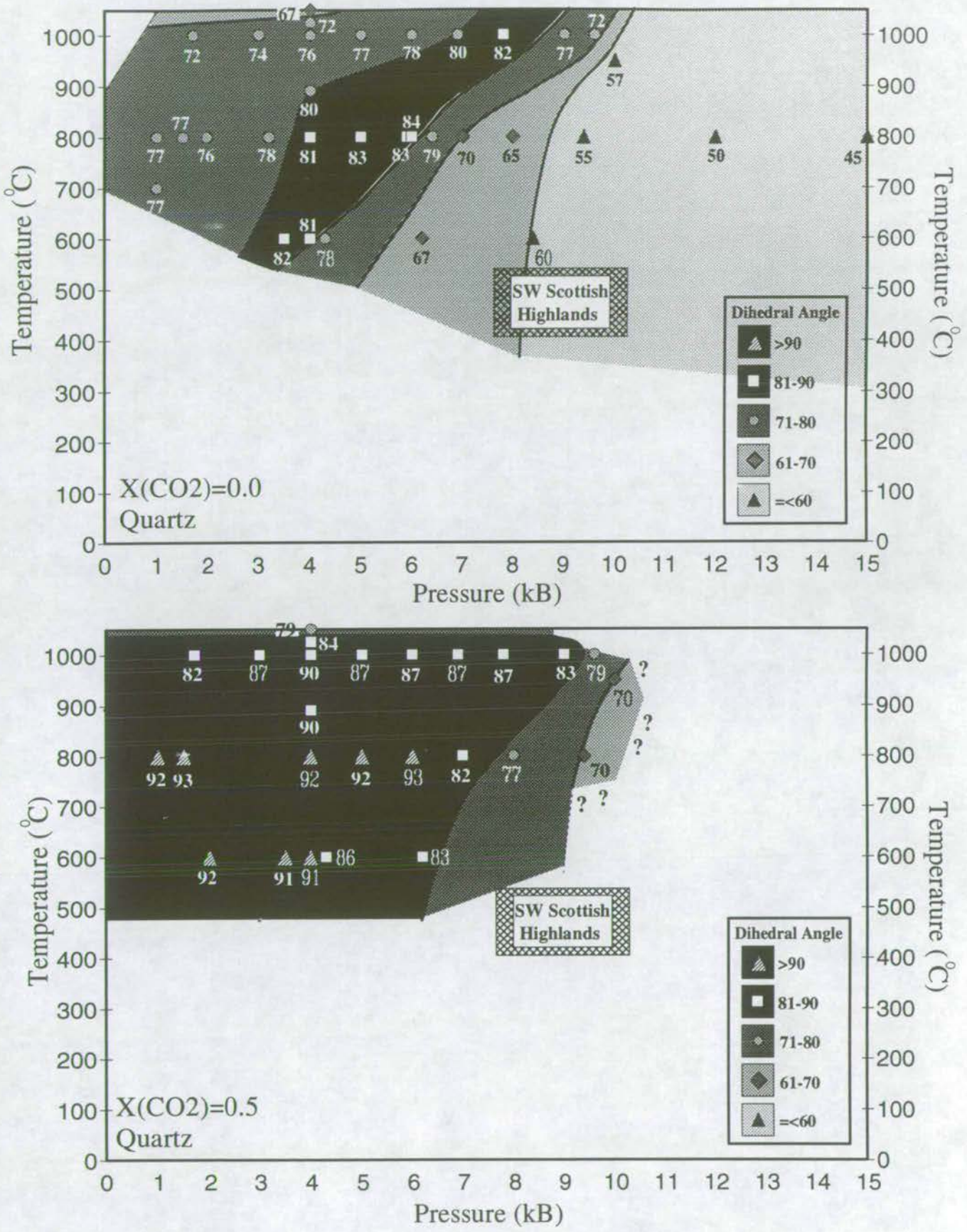

Figure 2.19: Dependence of the Dihedral Angle on Temperature and Pressure (*continued*)

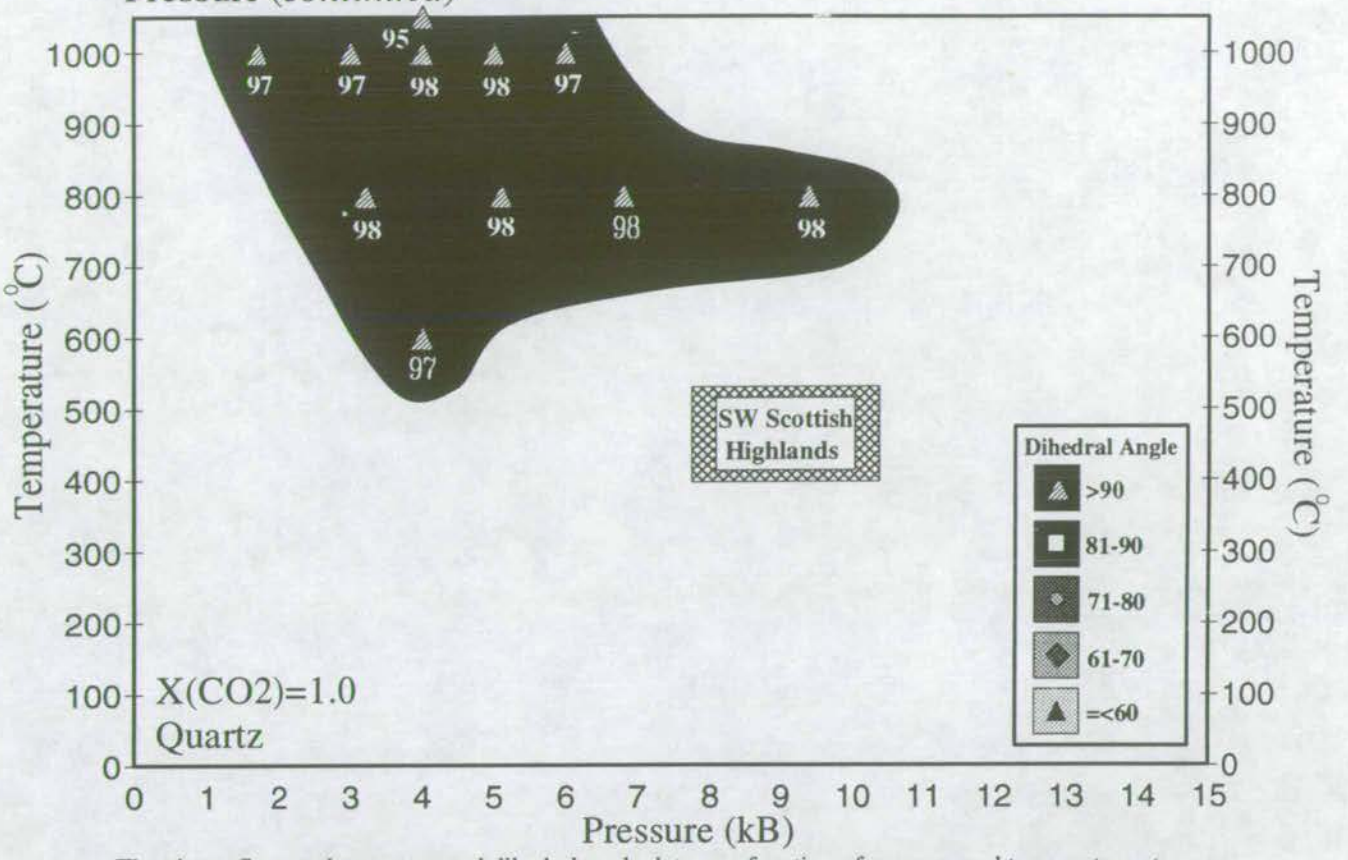

The above figures show contoured dihedral angle data as a function of pressure and temperature at X(CO2)=0.0, 0.5 and 1.0, for pure quartz. Average SW Highland P-T conditions are included on each plot. It is clear, from this data that grain-edge fluid flow through quartzites of the SW Highlands may have been possible for low X(CO2) fluids but was not likely to have been possible for high X(CO2) fluids. Data was compiled from Holness (in press), Holness (in prep) and Brenan & Watson (1987).

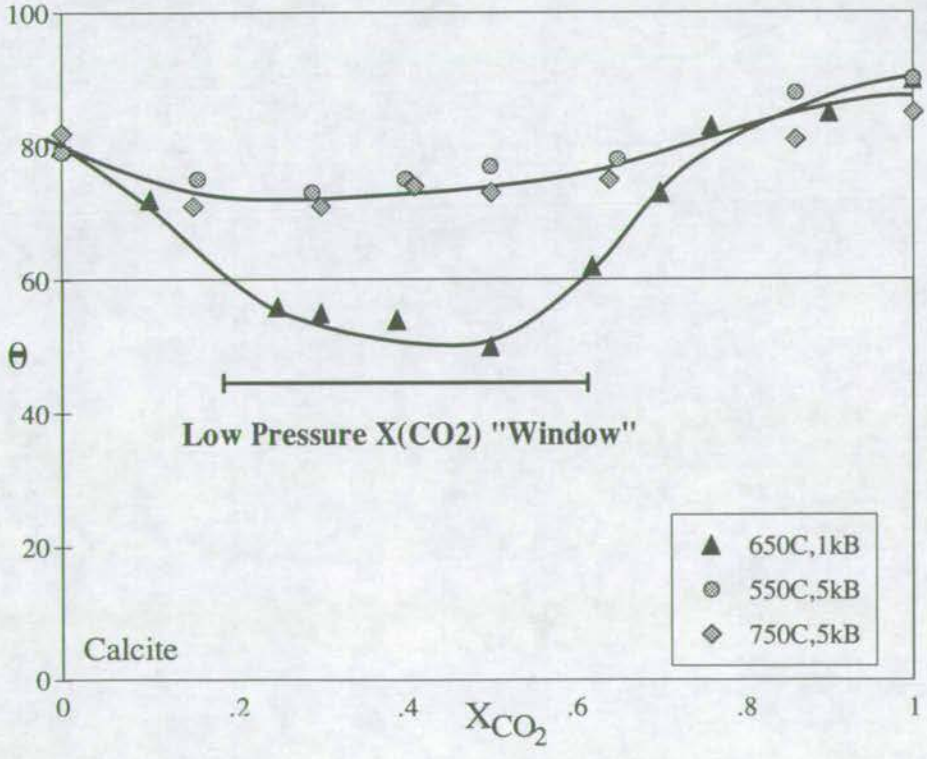

The adjacent plot shows the dependence of the calcite-fluid-calcite dihedral angle on fluid composition at P= 1kB & T=650C, P=5kB & T= 550C and P=5kB & T=750C. At low pressures an X(CO2) "window" exists from X(CO2)=0.2-0.6, across which the dihedral ange is less than 60 degrees and therefore an interconnected grain-edge porosity will exist. This window disappears at higher pressures. Therefore at the P-T conditions of peak regional metamorphism in the SW Highlands, it was unlikely that an interconnected grain-edge porosity existed, irrespective of the fluid composition.

Figure 2.19: Computer-generated 3-D representations of the Dependence of the Dihedral Angle on Temperature and Pressure

Pressure-Temperature-Dihedral Angle (X_{CO_2}=0.0)

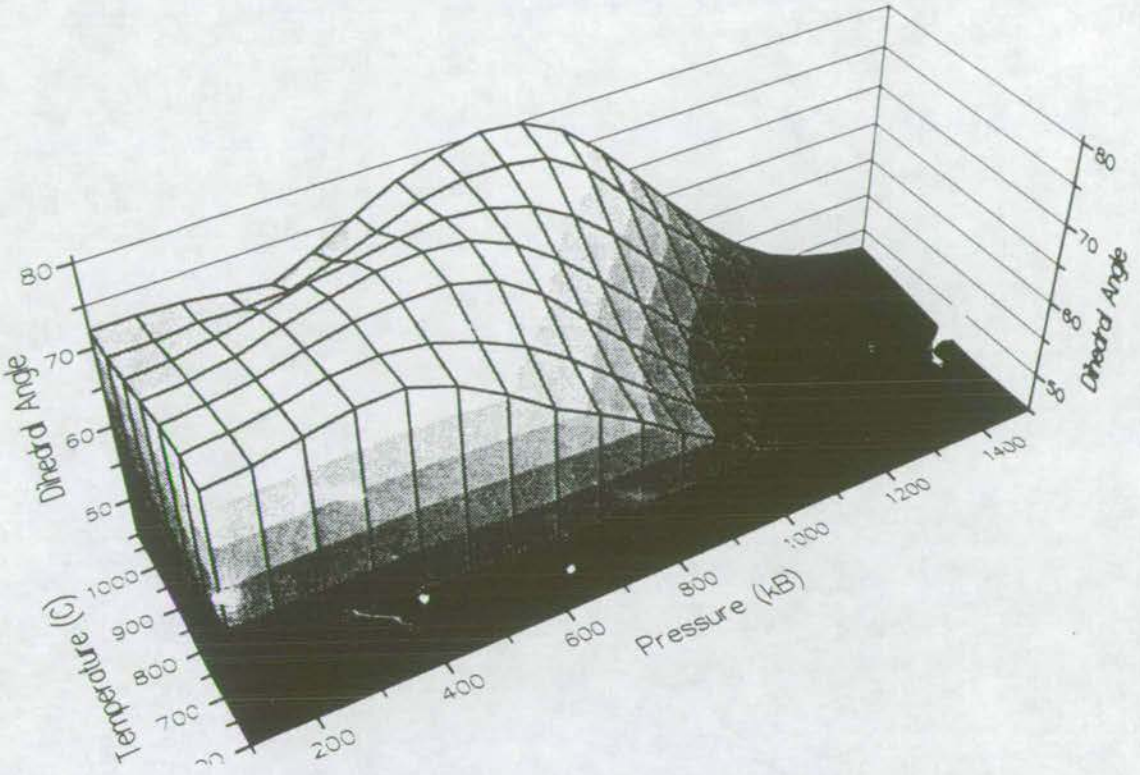

Pressure-Temperature-Dihedral Angle (X_{CO_2}=0.5)

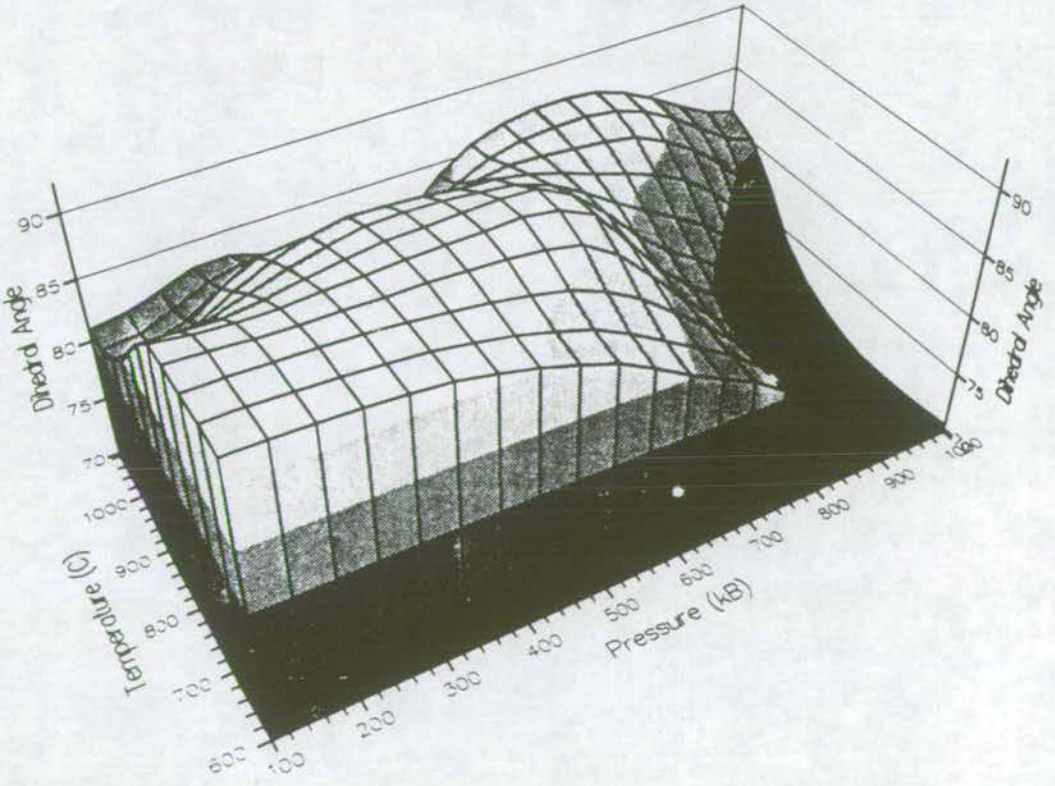

interconnected grain-edge porosity (for all porosities) will have existed in pure quartzites at the P-T conditions of regional metamorphism in the SW Scottish Highlands. This conclusion will be re-addressed in chapter 8, in the context of the regional fluid flow geometry.

Holness & Graham (1991) and Holness (*pers. comm.*) undertook similar experiments to constrain the dependence of the calcite-fluid-calcite dihedral angle (θ) on pressure, temperature and fluid composition. Calcite-fluid-calcite dihedral angles were estimated at P=1kb & T=650°C, P=5kb & T=550°C and P=5kb & T=750°C and plotted as a function of X_{CO_2}. The data which they obtained is plotted in figure 2.19. Holness & Graham (1991) recognised a low-pressure (P=1kb) "window" at $0.2<X_{CO_2}<0.6$ where $\theta<60°$. Under these conditions (P=1kb, T=650°C), the plot predicts that an interconnected grain-edge porosity will exist in pure marble. Holness (*pers.comm.*) has demonstrated experimentally that this "window" progressively disappears at higher pressures. At 5kb, an interconnected grain-edge porosity may not be sustained in a pure marble.

In summary, it is energetically favourable for an interconnected grain-edge porosity to develop if the mineral-fluid-mineral dihedral angle is less than 60°. Under the prevailing pressure-temperature conditions of regional metamorphism in the SW Scottish Highlands, experimental determination of the dihedral angle predicts that (i) it is possible for an interconnected grain-edge porosity network to develop in pure quartzite in equilibrium with very low X_{CO_2}-fluids (for all φ), and (ii) fluid flow will only be possible in marbles as a result of brittle failure or sufficiently high φ as to permit the development of an interconnected pore-network. In chapter 8, the viability of these predictions is assessed by contrasting them with the regional fluid flow geometry. Hence, the importance of an interconnected micro-fracture network as a viable alternative fluid flow geometry is considered.

2.5 Conclusion

In this chapter, modelling techniques for the quantification of fluid flow have been examined critically. The one-dimensional fluid flux models of Bickle & McKenzie (1987) and Bickle & Baker (1990b) have been discussed in the context of their historical development.

The earliest approaches to quantification of fluid flow were the zero-dimensional fluid:rock ratio models of Taylor (1977) and Ferry (1980). Zero-dimensional box-models consistently predicted high fluid:rock ratios, the generation of which could not be explained physically. Such models were discarded on the basis of their inherent assumptions and largely replaced by one-dimensional models of Ferry (1989), Bickle & McKenzie (1987) and Bickle & Baker (1990b). The model of Ferry (1989) is limited to constraining the component of the fluid flux parallel to the geothermal gradient and therefore does not constrain the true flux. Secondly, his calculation makes the assumption that fluid is internally buffered which is not likely to be generally applicable. Where Ferry's model may be applied, the mineralogy of the precursor rock is not constrained and must therefore be assumed.

Only the models of Bickle & McKenzie (1987) and Bickle & Baker (1990b) will enable measurement of the fluid flux at different orientations in the crust and therefore permit the true flux to be calculated. The models of Bickle & McKenzie (1987) and Bickle & Baker (1990b) assume external buffering of the chemical and isotopic fluid composition. They may only be applied where the initial and final loci of the isotopic or mineral reaction fronts may be identified. Subsequently, these later models are applied in this study to enable qualitative mapping of fluid flow on a regional scale.

In the following chapter the study area is presented and described with particular reference to the applicability of these modelling techniques.

CHAPTERS 3, 4 & 5

THE STUDY AREA

PRELUDE TO CHAPTERS 3, 4 & 5

The Study Area

In chapters 3, 4 and 5, the Dalradian of the SW Scottish Highlands is presented, in the context of its depositional, lithostratigraphic, structural and metamorphic evolution, as an ideal "natural laboratory" for detailed quantitative modelling of fluid flow and the construction of regional-scale fluid flux maps.

In chapter 2, the models which have been used in previous studies to quantify fluid flow were reviewed, and the one-dimensional models of Bickle & McKenzie (1987) and Bickle & Baker (1990), which quantify fluid flow as a time-integrated flux from the advection distances of isotopic and reaction fronts, were shown to offer the most reliable and generally applicable quantitative solutions. Therefore, these models have been applied in this study. For their successful application, the requirements detailed in sections 2.3.2 and 2.3.3 and outlined below must be satisfied:

(1) The initial and final loci of the isotopic and/or reaction front(s) must be identifiable so that the advection distance(s) can be measured;

(2) The rock mineralogy must permit pervasive fluid flow, either along an interconnected grain-edge porosity (Watson & Brenan 1987) or a micro-fracture network. If the former is true, and fluid flow is along grain-edges, the dihedral angle (θ) must be less than 60° (section 2.3.2);

(3) The isotopic shifts must be quantified and/or the mineral reactions involved must be well characterised both stoichiometrically and in P-T-X_{CO_2} space;

(4) Grain-scale mineral-fluid equilibrium must be achieved;

(5) The composition of the infiltrating fluid must be reliably constrained.

For the former three requirements to be satisfied, the study area must host clearly defined, relatively permeable, marker lithologies which may be isotopically distinguished from their host rock and/or contain at least one well characterised mineral reaction, and the associated isotopic and/or reaction front(s) must be ***measurably*** advected. The fourth requirement is likely to be satisfied where fluid infiltration occurs at high temperatures, at or near the peak of regional metamorphism. The fifth, and final requirement may only be satisfied if the fluid composition is independently constrained or may be calculated.

If a study area is to be suitable for extensive, regional-scale fluid flux mapping, then in addition to satisfying the five model requirements listed above, the following criteria are also important:

(6) An abundance of suitable marker lithologies, cropping out throughout the entire area is critical;

(7) Interpretation of the regional and local structure should be unambiguous and thorough;

(8) The timing of fluid infiltration relative to regional metamorphism and deformation should be well constrained.

In chapters 3, 4 and 5, the Dalradian of the Southwest Scottish Highlands is shown to satisfy all the above requirements. Chapter 3 reviews the depositional, lithostratigraphic, structural and metamorphic evolution of the Dalradian supergroup of the SW Scottish Highlands in the context of the model requirements discussed above. Chapter 4 discusses the fluid infiltration history affecting the SW Scottish Highlands. Chapter 5 presents general field observations and detailed mineralogical interpretation of the individual lithologies which are directly affected by fluid infiltration. Chapters 3, 4 and 5 are concluded by summarising the reasons for which the Dalradian of the SW Scottish Highlands were selected for this study.

3. THE STUDY AREA:

The Dalradian of the SW Scottish Highlands

3.1 Introduction

In this chapter, the depositional, lithostratigraphic, metamorphic and deformational histories of the Dalradian of the SW Scottish Highlands is discussed, integrating a comprehensive review of the literature with observations and results obtained in this study.

3.2 Location of Study Area

The Dalradian Supergroup forms a NE-SW trending regional metamorphic belt straddling the northeast, central and Southwest Scottish Highlands, and north and Northwest Ireland (figure 3.1). The study area is located to the Southwest of the Scottish Dalradian belt, encompassing Knapdale, Islay, Jura and Scarba (figure 3.1).

3.3 Lithostratigraphy and Depositional Facies

The lithological sequence of the Dalradian Supergroup, exposed in the SW Scottish Highlands, described in figure 3.2, can be readily sub-divided into three major groups (Roberts & Treagus 1977); the Lower (Appin), Middle (Argyll) and Upper (Southern Highland) Dalradian, by the laterally continuous horizons of the Port Askaig Boulder Bed (forming the base of the Argyll group) and the Tayvallich - Loch Tay limestone (forming the top of the Argyll group). The Appin, Argyll and lowermost Southern Highland Groups are exposed in the study area.

Figure 3.1: Geographical Location Map

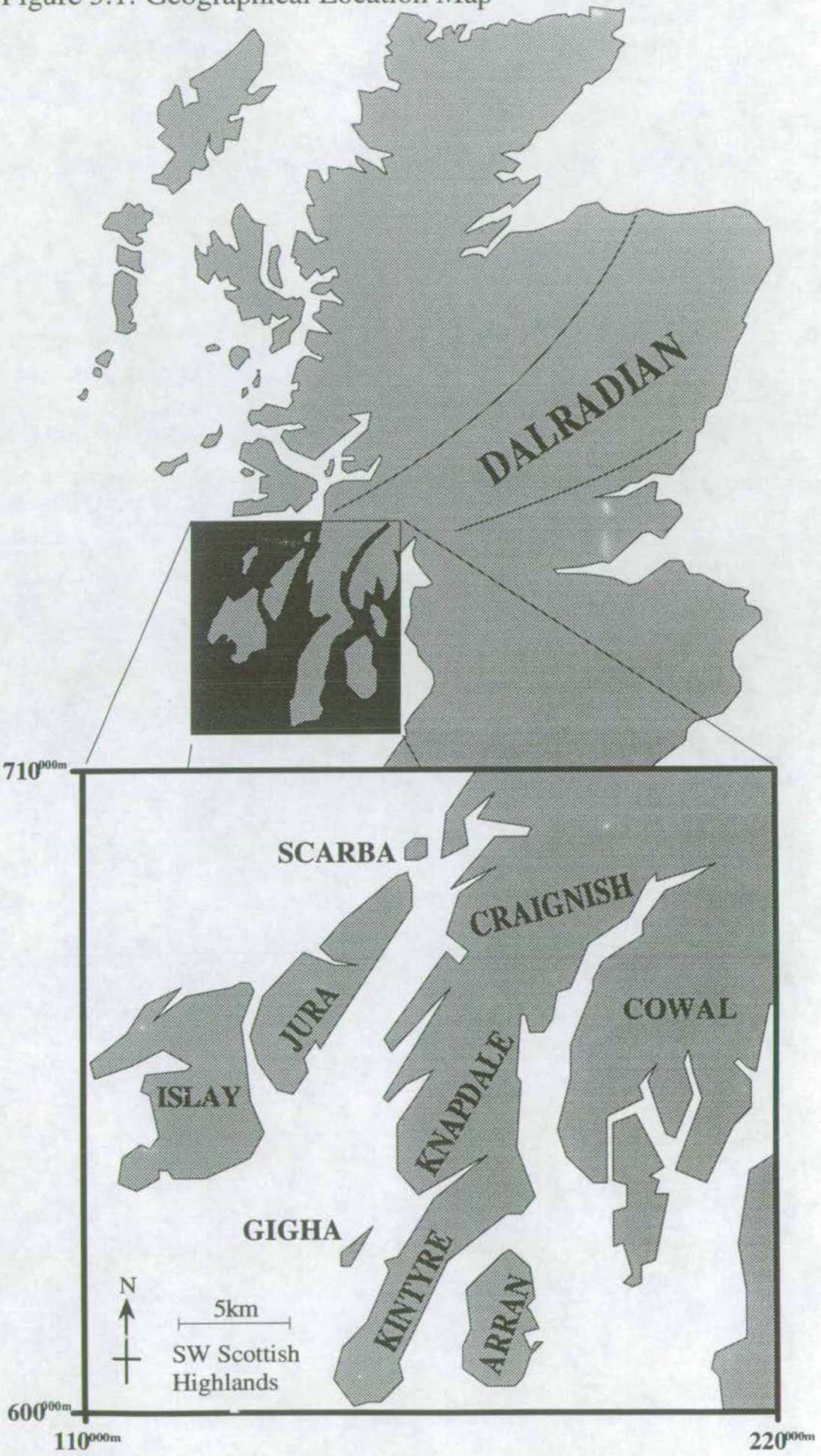

Figure 3.2: Lithological Map of the SW Scottish Highlands

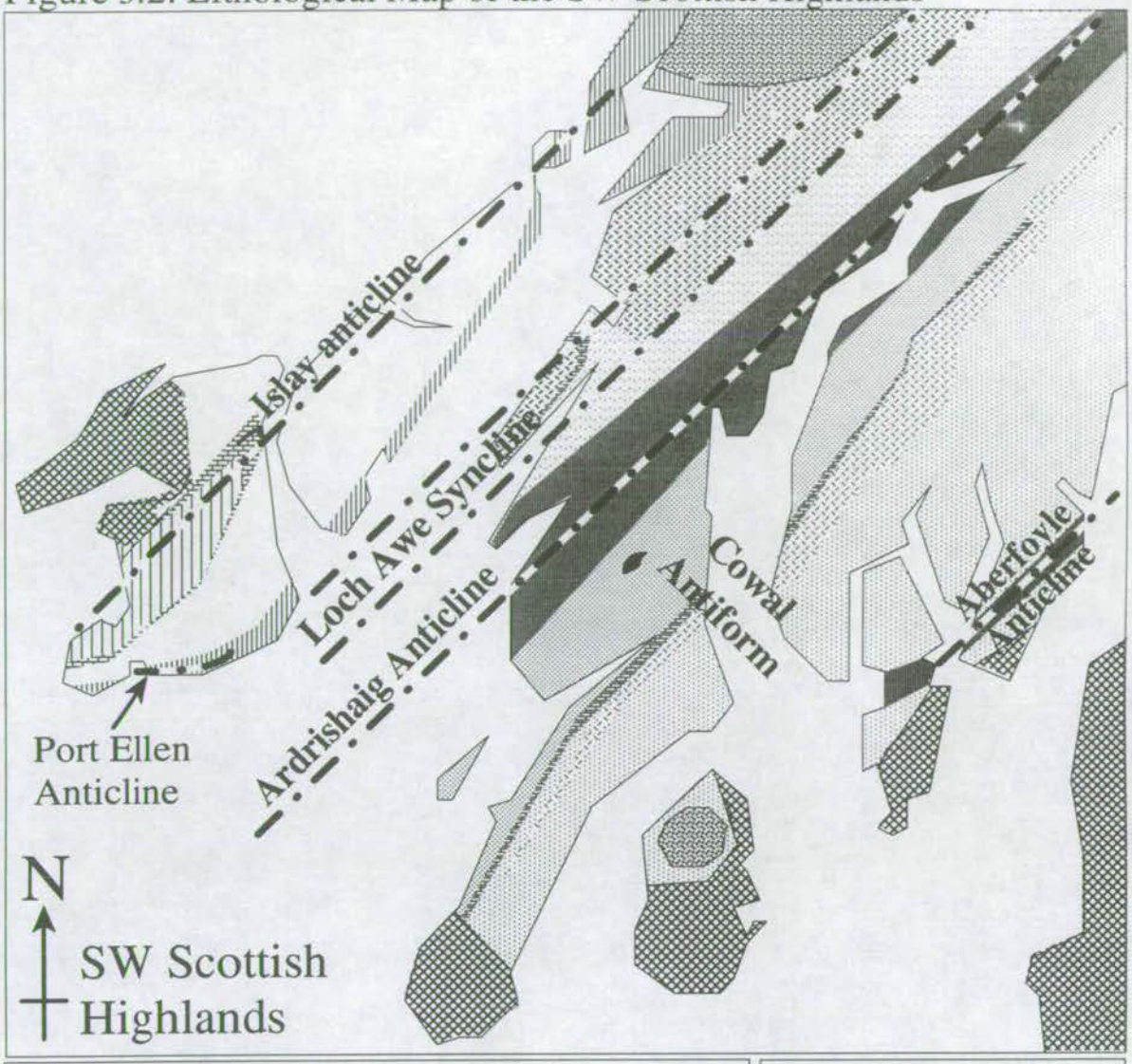

Schematic Lithological Column

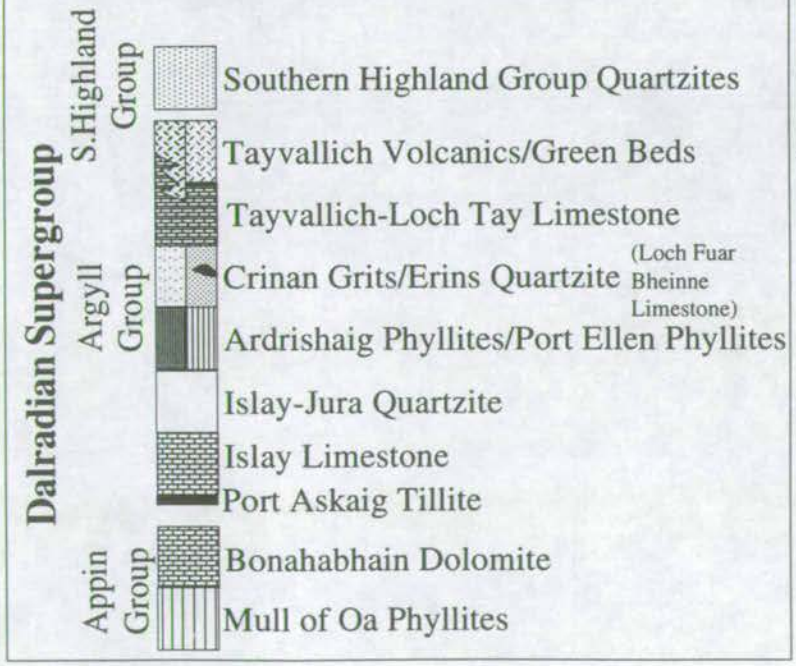

Other Rocks

- Other Metamorphic and sedimentary rocks
- Other Igneous Rocks

3.3.1 The Appin Group

The oldest Dalradian rocks in the SW Scottish Highlands are the Mull of Oa Phyllites which are exposed on SW Islay (figure 3.2). This subgroup is dominated by a sequence of fine-grained phyllites which become progressively darker and more carbonaceous upwards through the sequence and are host to dark fine-grained marbles. Roberts & Treagus (1977) interpret this to represent marine deposition in progressively shallower water and under conditions of increasingly restricted circulation.

The upper unit of the Appin group is the Islay limestone, which is typically represented by marble with oolites, algal stromatolites and mud-flake breccias (Roberts & Treagus 1977). The top of this unit is dolomitic with stellar structures which may be pseudomorphs of an evaporite mineral (Spencer 1971). These varied sedimentary features indicate laterally or temporally diverse depositional facies. Oolites are formed in shallow water under conditions of high energy current activity, algal stromatolites represent an intertidal environment, mud-flake-breccias are likely to be the product of desiccation and erosion in a sub-aerial environment, and evaporite pseudomorphs could only develop in a terrestrial, arid environment.

The Appin group indicates an unstable shelf environment, the lithological succession being representative of an either lateral or temporal marine regression towards shallow-water, tidal and even terrestrial conditions.

3.3.2 The Argyll Group

The base of the Argyll group is defined by the Port Askaig Boulder Bed, a laterally continuous horizon, described as a glacial tillite (Thomson 1875 and Kilburn *et al.* 1965), mysteriously sandwiched between two quite similar, shallow-water to sub-aerial carbonates, the Islay Limestone, and the Bunahabhain Dolomite (figure 3.2). The presence of a glacial tillite between two carbonates, both of which appear to

have been derived in warm semi-arid conditions, is problematic. One possible explanation is that deposition in late Appin - early Argyll times was, indeed at low latitudes and the Port Askaig Tillite was deposited during a brief world-wide episode of glaciation. Eyles & Eyles (1983) preferred to consider the tillite as being deposited from floating ice, reducing the severity of the otherwise implied climatic fluctuation.

The boulder bed crops out on NE Islay (figure 3.2) and is directly overlain by the Bunahabhain Dolomite. In terms of depositional facies, as is mentioned above, there is little difference between this latter horizon and the Islay Limestone below the Port Askaig Tillite. The dolomite is sandy with ripple bedding, algal stromatolites and possible evaporite pseudomorphs and can probably be attributed to shallow-water and inter-tidal depositional facies.

The Bunahabhain Dolomite is overlain by the lens-shaped mass of the Islay-Jura Quartzite. Following the predominant palaeocurrent direction towards the NNE, the quartzite succession progresses laterally from a several kilometre thick sequence of cross-bedded sands on Islay and SW Jura, through a 5km thick sequence with increasingly predominant laminated and rippled sands and silts on central and NE Jura, until the sequence thins and disappears underneath the Scarba conglomerate to the NNE. The Islay-Jura Quartzite is thought to represent deposition on a tidal-current dominated marine shelf (Anderton 1977). The cross-bedded sands are interpreted as shallow marine tidal dunes (Anderton 1976). Large-scale flat and channel surfaces are interpreted as the result of storm currents (Anderton 1976). The finer sands and silts are laminated, ripple-bedded and exhibit linear channel structures. They are interpreted by Anderton (1976) as shallow marine storm deposits.

Rapid subsidence due to fault-block movement north of Jura is thought to be responsible for the deposition of the Scarba conglomerate (Anderton 1977) as rock falls, mass-flows and turbidity currents on Scarba (figure 3.2). The conglomerates fine upwards into the Easdale Slates, a thick, pelitic sequence, derived from dilute

turbidity currents, which were deposited in, and rapidly infilled, the newly formed basin (Anderton 1985).

The Islay-Jura Quartzite, Scarba Conglomerate and Easdale Slates are conformably overlain by the Port Ellen (or Craignish) and Ardrishaig Phyllites, a sequence of finely inter-bedded calc-phyllites and fine-grained quartzites. These are thought to represent the return of the whole of the SW Scottish Highlands to shallow marine conditions after the infilling of the Easdale basin to the north (Anderton 1987, 1985).

Deposition of the Crinan Grit (or Erins Quartzite) marks the development of a new fault-bounded basin. The Crinan Grits crop out in NW Knapdale and are poorly sorted, often feldspathic, course-grained, pebbly-quartzites or conglomerates (Roberts & Treagus 1977). The Erins quartzite was probably deposited in a separate basin to the SE, and is a finer-grained quartzite (Anderton 1985). Beds are crudely graded throughout the Crinan grits. However both sorting and sediment maturity increase markedly towards the NW where the sequence thins. The sequence is therefore likely to represent turbidity-current controlled sedimentation on the NW margin of a rapidly deepening basin, where conditions of open circulation are likely (Roberts & Treagus 1977).

The Tayvallich (Loch Tay) Limestone marks the top of the Argyll group and lies directly above the Crinan grits, marking a sudden cessation of clastic input to the newly-developed Crinan basin (Anderton 1975). This laterally continuous horizon is dark and often gritty, with occasional ooids, slump breccias, laminar bedding, ripple-drift bedding and detrital quartz and feldspar (Roberts & Treagus 1977). These sedimentary features are indicative of considerable syn-depositional re-working of the carbonate as would be expected in an unstable marine slope environment.

In the SW Highlands, the Tayvallich (Loch Tay) Limestone is intercalated with the Tayvallich Volcanics which must therefore also belong to the Argyll group (Anderton 1985). The Tayvallich Volcanics consist of a suite of lava flows, with

pillows, pipe amygdales (Gower 1977) and widespread spilitic alteration (Graham 1976) and were, therefore, extruded on the sea-floor. The volcanics represent the final surface extrusion of an otherwise extensive episode of basic igneous intrusion which is responsible for some 3km of basic sills cropping out throughout the Ardrishaig Phyllites, Port Ellen (Craignish) Phyllites, Easdale Phyllites, Erins Quartzite, Crinan Grits and the upper Islay-Jura Quartzite, and a much smaller suite of basic dykes which are confined to the Islay-Jura Quartzite. These basic rocks were intruded at progressively higher levels in decreasingly consolidated sediments from Islay-Jura Quartzite and Easdale Slate times until the sea-floor extrusion of the Tayvallich Volcanics (Anderton 1985). Graham (1976) has shown that the major element characteristics of most of these sills differ from MORB only in that they are enriched in Fe, Ti and P, and depleted in Ni and Cr and are therefore likely to represent highly evolved MORB-basalts. Graham & Borrodaile (1984) further demonstrated that the extrusive volcanics and intrusive sills are more evolved than the dykes. Graham (1976) demonstrated by detailed geochemical analysis that the igneous suite straddles the fields of oceanic and continental tholeiites and Graham (*unpublished data*) establishes that some metabasites have an isotopic signature of $\delta^{18}O \approx 6^{o}/_{oo}$, which is characteristic of MORB basalts (Taylor 1968). By analogy with the present-day Gulf of California, Graham & Borrodaile (1984) suggest that the basic igneous event occurred during the early stages of continental extension.

The Argyll group appears to describe the progression from the unstable shelf environment which dominates the lower, Appin Group, towards cyclic fault-controlled basin development, rapid infilling and shallow marine sedimentation (McKenzie 1978). The first cycle was initiated by the rapid, fault-controlled development and subsequent infilling of the deep Easdale basin to the north. This was followed by a return to widespread shallow marine conditions and deposition of the Port Ellen (Craignish) and Ardrishaig Phyllites. The second cycle began with the fault-controlled development of two new deep basins to the SE and rapid deposition

of the Crinan Grits and Erins Quartzite. An unexplained, but sudden, cessation of sediment input resulted in the deposition of the Tayvallich (Loch Tay) Limestone. Finally, extension associated with the fault-block tectonics was responsible for the intrusion of some 3km of basic sills and dykes and the extrusion of the Tayvallich Volcanics.

3.3.3 General Interpretation of Depositional Facies

The combined strengths of sedimentological and geochemical evidence enabled Anderton (1985) to interpret the Appin and Argyll Groups as having been deposited in an ensialic rift zone, precursor to the late Precambrian - early Cambrian break-up of the Proterozoic super-continent (Piper 1983) into the Laurentian and Baltic continents, and the development of the Iapetus Ocean.

3.3.4 Implications of Lithostratigraphy to Modelling of Fluid Flow

The lithostratigraphic sequence of the SW Scottish Highlands includes a variety of compositionally and isotopically distinct units which crop out extensively throughout the study area. Individual basic dykes, sills and lava flows occur in abundance throughout the entire area and have a characteristic MORB-like isotopic signature of $\delta^{18}O \geq 6^{o}/_{oo}$ (Taylor 1968). Marble units are less abundant but have a similarly distinct isotopic signature of $\delta^{18}O = 22\text{-}26^{o}/_{oo}$ (Veizer & Hoefs 1976). The most abundant lithologies are pelites and psammites which are typically characterised by an isotopic signature of $\delta^{18}O = 11\text{-}14^{o}/_{oo}$. Metabasites and marbles are ideal marker lithologies for modelling of fluid flow for the following reasons:

(1) Metabasites and marbles are abundant as individual, mappable units throughout the study area.

(2) Metabasites and marbles are generally better exposed than host phyllites.

(3) Metabasites and marbles are compositionally, mineralogically and isotopically distinct and therefore their boundaries define measurable compositional, mineralogical and isotopic discontinuities. The potential of ***measurable*** chemical, mineralogical and isotopic modification of such boundaries as a result of fluid infiltration is immediately evident.

3.4 Deformation and Metamorphism

The Dalradian Supergroup has undergone orogenic polyphase deformation and regional metamorphism resulting from the closure of the Iapetus Ocean (Johnson 1983). The timing of the orogenic event and therefore its nomenclature is at present uncertain. Until recently deformation and metamorphism were linked to the Grampian Orogeny of late Cambrian to early Ordovician times (Johnson 1983). This interpretation is in agreement with a U-Pb Zircon date of 595±4Ma obtained from a keratophyre associated with the Tayvallich Volcanics by Halliday *et al.* (1989), and Rb-Sr and K-Ar cooling ages of muscovites and biotites of about 440-460Ma obtained from Perthshire by Dempster (1985). This interpretation was thrown into serious doubt by Rogers *et al.* (1989) who obtained a high precision U-Pb zircon date of 590±2Ma, using state-of-the-art analytical techniques, for the Ben Vuirich granite in Perthshire. The implications of this date are of major consequence to the interpretation of Dalradian orogenesis because the Ben Vuirich granite has been clearly shown to post-date D_1-D_2 deformation (section 3.4.1) and therefore to post-date major orogenesis and nappe formation. Arbitrarily ignoring the Rb-Sr and K-Ar cooling dates of Dempster (1985), Dalradian orogenesis and nappe formation appears therefore to be constrained to having occurred ***after*** 595±4Ma from the Tayvallich Volcanics (Halliday *et al.* 1989) and ***before*** 590±2Ma from the Ben Vuirich granite. Although the 595±4Ma zircon date from the Tayvallich Volcanics (Halliday *et al.* 1989) is not quite concordant, a maximum duration of about 10Ma is implied for the

entire Dalradian orogenic event. This is clearly not possible, yet a late Cambrian to early Ordovician timing of orogenesis also seems unlikely. It is beyond the scope of this study to unravel this paradox, as it is only the ***relative*** timings of metamorphism and deformation which concern modelling and interpretation of fluid flow.

3.4.1 Deformation History

Harte *et al.* (1984) describe the following four deformational phases which affected the Dalradian Supergroup as a result of orogenesis:

D_1: In the SW Highlands, the earliest deformational phase resulted in the development of major regional fold-structures (f_1) which are, from NW to SE; the Islay Anticline, a partly recumbent antiform facing NW adjacent to the Loch Skerrols Thrust; the Loch Awe Syncline, an upright synform; and the Ardrishaig Anticline, a partly recumbent antiform facing SE and forming the root of the Tay Nappe (figure 3.3). The entire structure is best described as a "mushroom" centred on the Loch Awe Syncline which is "pinned-down" by the relatively dense and voluminous Tayvallich Volcanic suite and associated sill complex. D_1 is represented by a strong upright axial planar cleavage which fans through the Loch Awe syncline (s_1) (figure 3.4). s_1 defines a penetrative fabric, developed through most phyllitic and some metabasic lithologies.

D_2: The second deformational phase has been described as a symmetry-constant continuation of D_1 (Voll 1960). D_2 is characterised by localised minor folding (f_2) and associated with pressure-solution cleavage in psammites (s_2). s_1 and s_2 may form a composite cleavage or where they are developed at a high angle they may result in "herring-bone" patterns. s_2 cannot usually be distinguished in the SW Scottish Highlands.

Figure 3.3: Structural Map and Schematic Cross-section of the SW Scottish Highlands

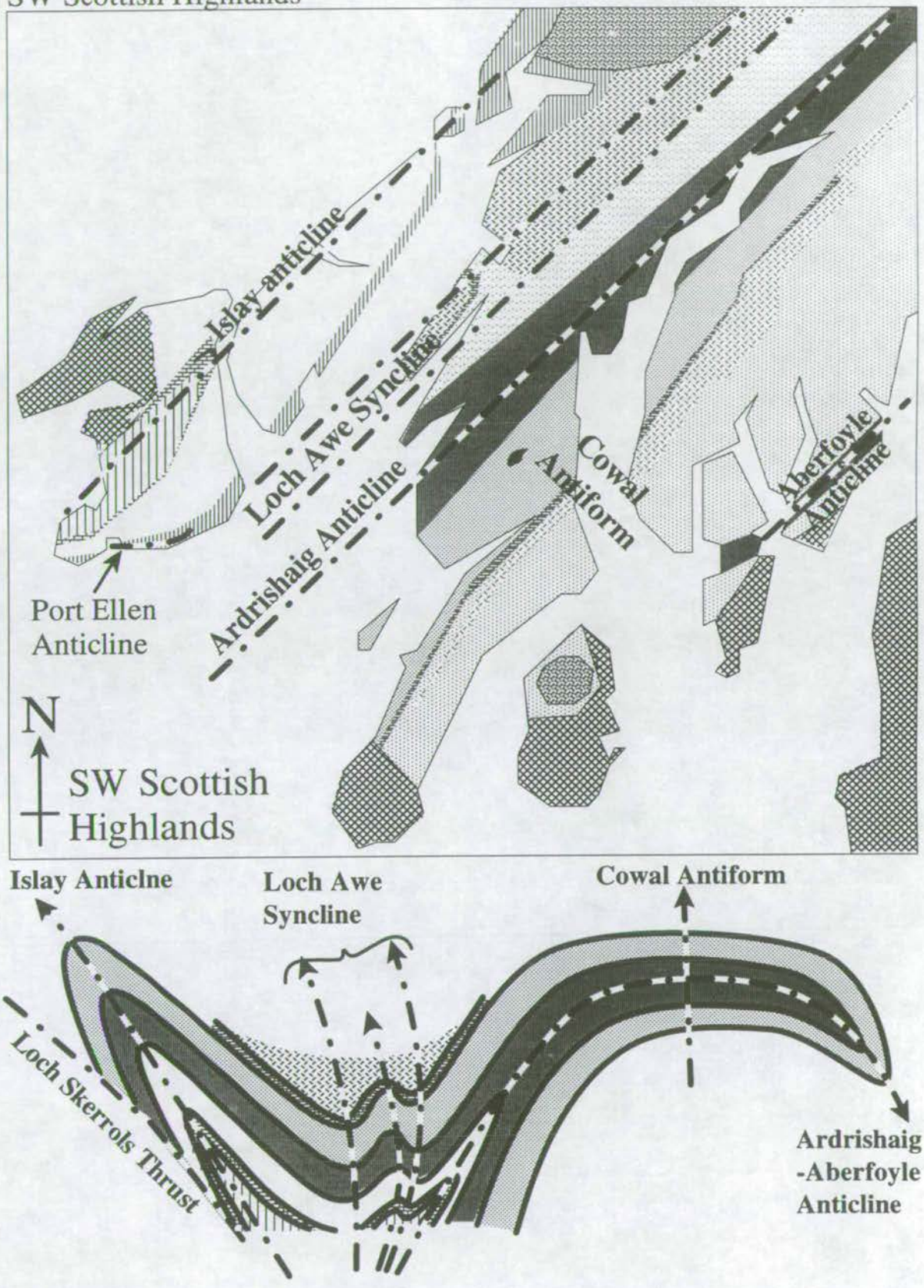

Figure 3.4(a): Photograph showing refraction of a D1 penetrative fabric at a Phyllite-Metabasite Contact

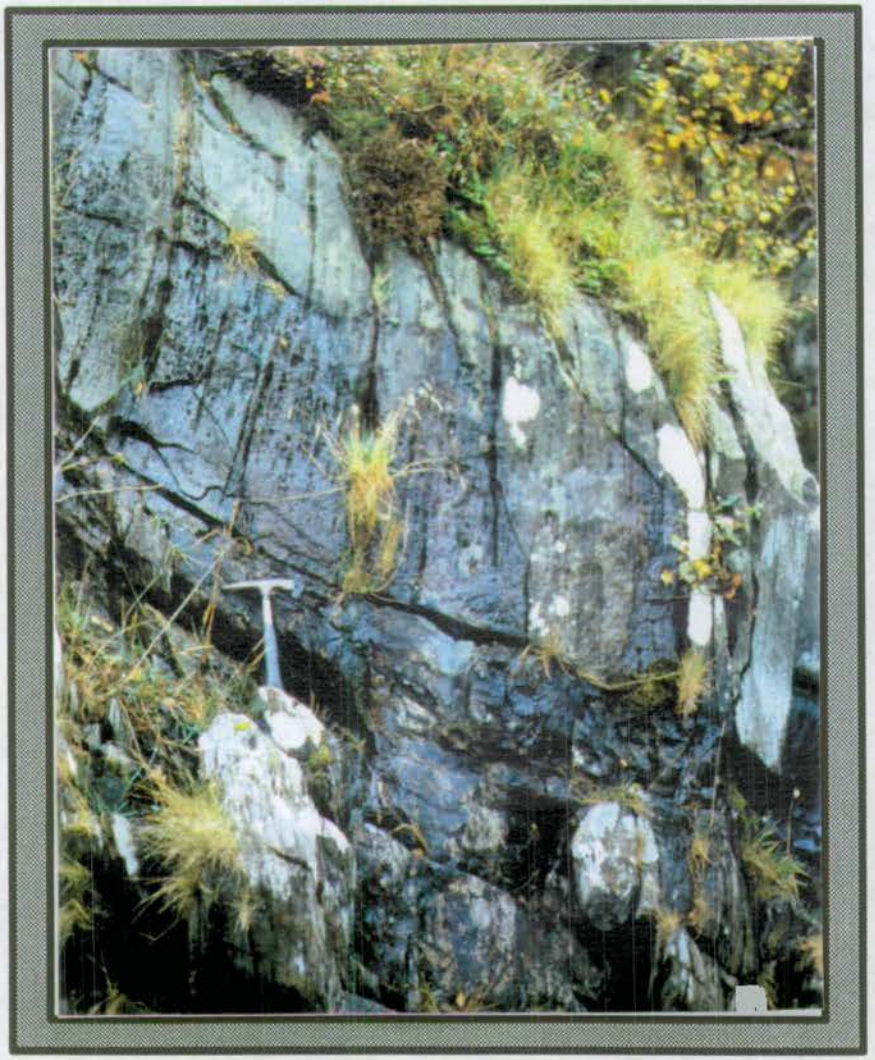

Locality:
Carsaig, Knapdale
(GR729 878)

Scale:
Hammer (30cm)

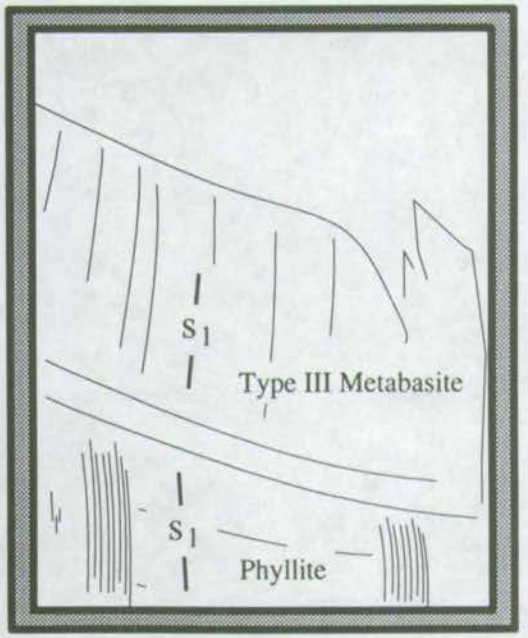

Figure 3.4(b): Photograph showing D1-D2 folding of Port Ellen Calc-Phyllites with associated S1-S2 Axial Planar Cleavage

Location: Port Ellen, Islay GR367 451 **Scale:** 20p piece

Figure 3.4(c): Photograph Showing F4 Box Folds

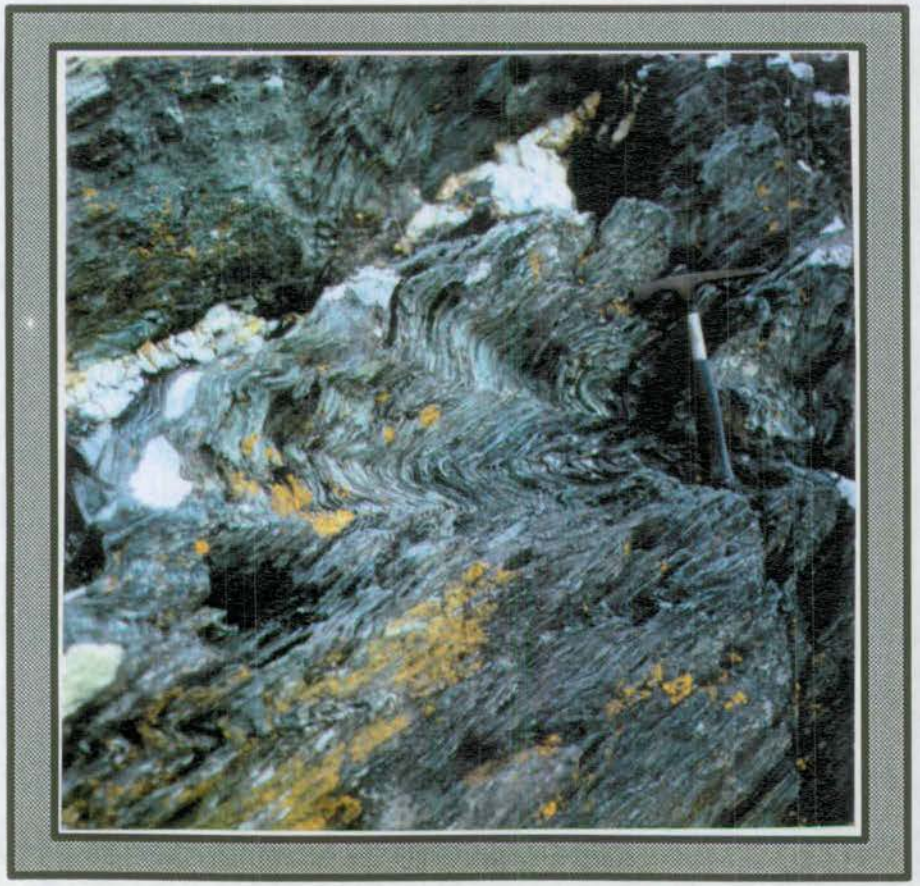

Locality:
Rubha Garbh, Knapdale GR753 766
Scale:
Hammer (30cm)

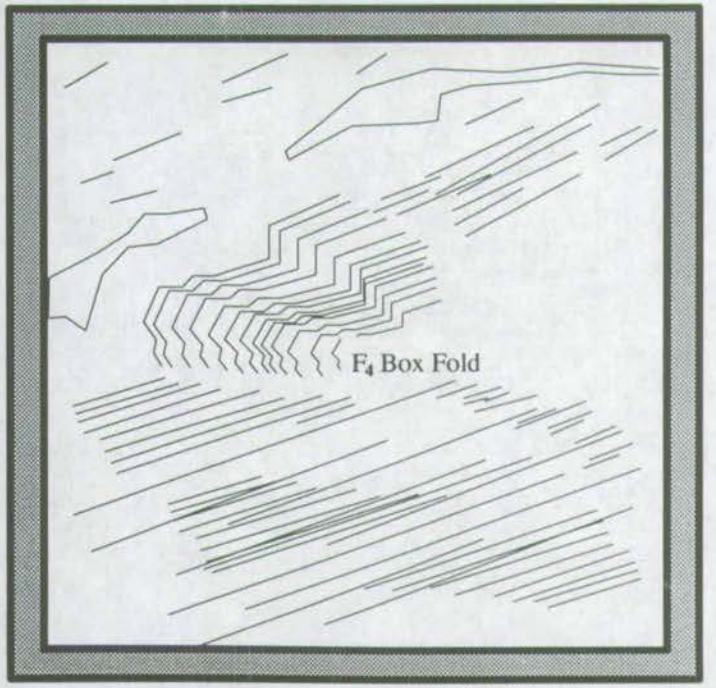

Figure 3.4(d): Photograph Showing S4 Crenulation Cleavage

Locality:
Port Ellen, Islay GR367 452
Scale:
50p piece

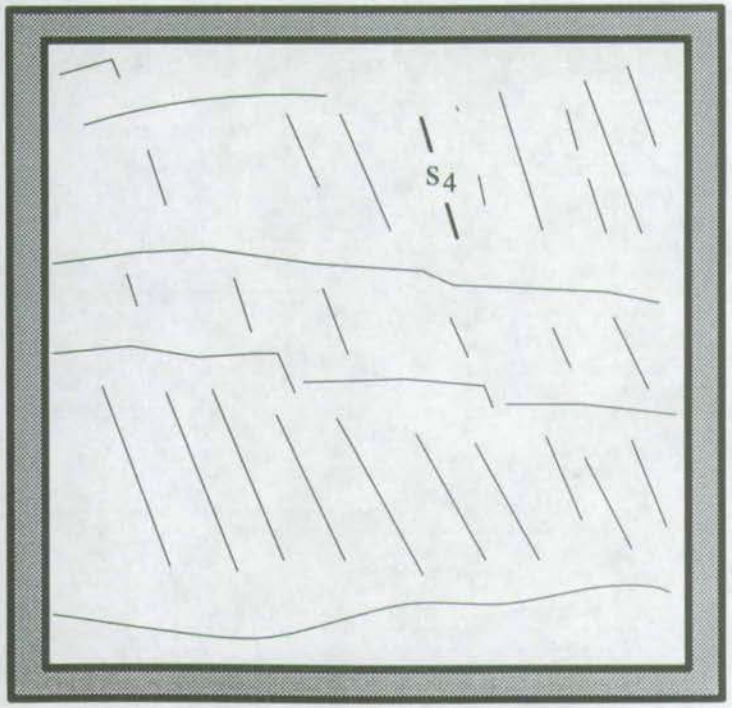

D_3: The third deformational phase is developed locally with associated minor folding and the development of pressure-solution cleavage in psammites and crenulation cleavage and penetrative schistosity in pelites (s_3). D_3 is not generally evident throughout the SW Scottish Highlands other than in association with narrow zones of albite schist along the Tarbert Monoform (Dymoke 1988).

D_4: The final deformational phase resulted in the general uplift and subsequent tightening of the Tay Nappe. This was associated with the development of the major f_4 fold structures: the Tarbert and Ben Ledi Monoforms and the Cowal Antiform (figure 3.5). The Aberfoyle Anticline is the downwards facing closure of the Ardrishaig Anticline and Tay Nappe which is developed in response to f_4 folding (figure 3.5). D_4 deformation is generally widespread throughout the SW Highlands and is associated with the development of box-folds and crenulation cleavage (figure 3.4).

For the purposes of this study, the deformational history of the SW Highlands can be considered, quite simply, as two major deformational phases:

(1) A primary deformational phase (D_1-D_2) which involved major recumbent folding and the development of the Islay Anticline, Loch Awe Syncline and Ardrishaig Anticline - Tay Nappe, and was associated with the development of a penetrative, axial planar foliation which fans through the Loch Awe syncline.

(2) A secondary deformational phase (D_4) which involved the uplift of the Tay Nappe and the subsequent development of the Cowal Antiform, Tarbert and Ben Ledi Monoforms and tightening of the Loch Awe Syncline, and was associated with the development of minor box-folding and crenulation fabrics.

The practical simplicity of this deformation sequence makes the area ideal for modelling fluid flow in relation to structural development.

Figure 3.5: D_4-deformation: Development of the Tarbert & Ben Ledi Monoforms and Tightening of the Loch Awe Syncline

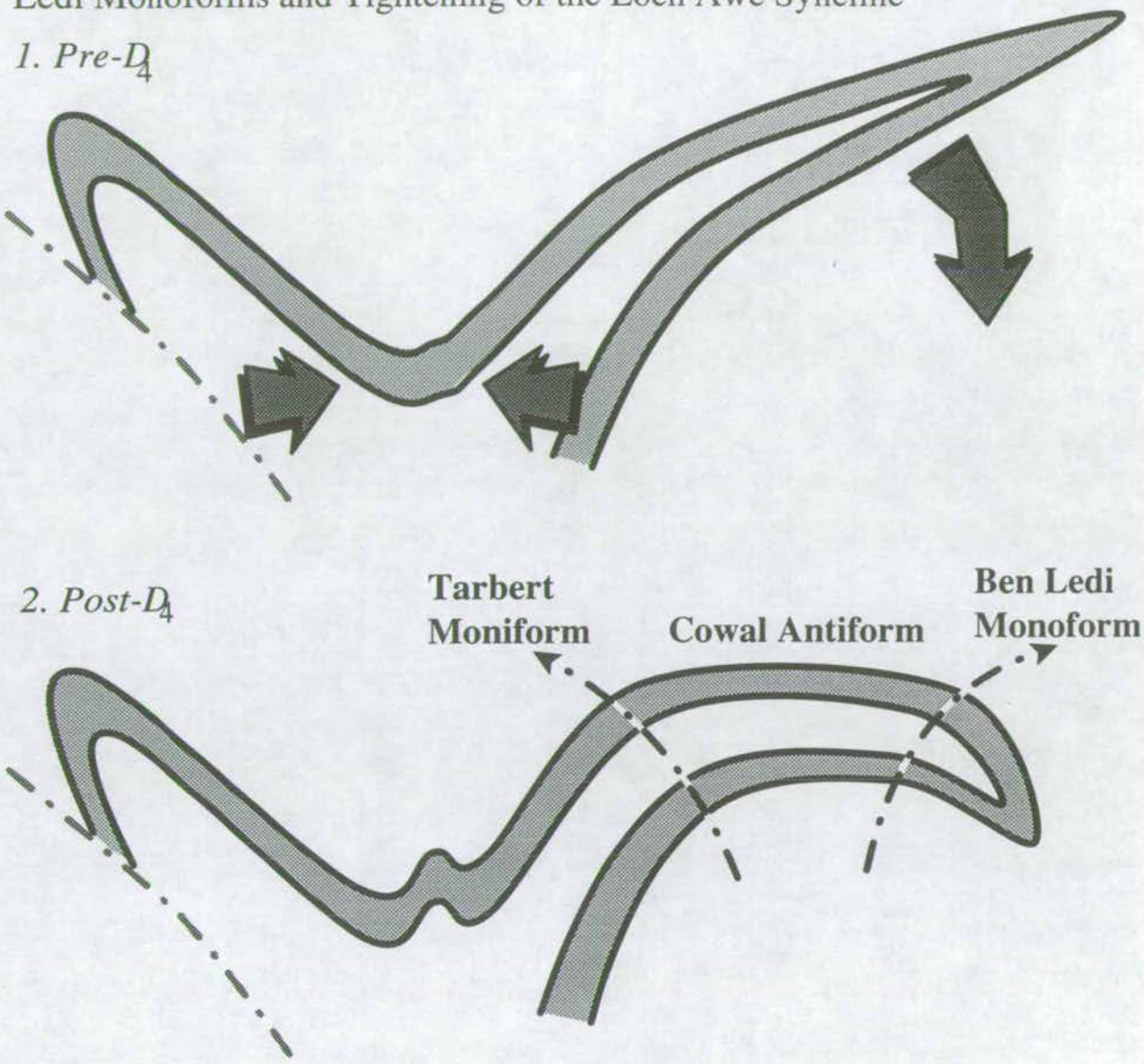

3.4.2 Regional Metamorphic History

Much of the Dalradian Supergroup has undergone regional metamorphism of the Barrovian facies series.

The SW Scottish Highland terrain lies to the SW of the Cruachan Lineament, a trans-Caledonoid (NW-SE) trending feature which separates relatively high density SW Highland rocks which are rich in mafics from lower density rocks to the NW which are poor in mafics. Graham (1986) proposed that basic volcanism and sedimentation in the SW Highlands occurred in a pull-apart basin, bounded to the NE by a major fault zone which is now represented by the Cruachan Lineament. The Cruachan Lineament was identified by geophysical evidence, including gravity data, magnetic data and seismic profiling (Hall 1985), and geological evidence, including a major increase in the abundance of mafics and a general decrease of metamorphic grade to the SW. Consequently the majority of the lowest grade rocks in the Dalradian occur in the SW Highlands.

Metamorphic zonation of the SW Highlands was initially described by Elles & Tilley (1930) who recorded the occurrence chlorite-zone metasediments centred on the axis of the Loch Awe Syncline, biotite-zone metasediments from the Ardrishaig Anticline to the Tarbert Monoform boundary and garnet-zone metasediments SE of the Tarbert Monoform. Zonal distributions within metabasic rocks (Wiseman 1934 and Philips 1930) roughly coincide with the metasediment zonation described by Elles & Tilley (1930). More recently detailed petrological studies (e.g. Harte & Graham 1976, Graham et al. 1983, Dymoke 1988) have described the rare but widespread occurrence of biotite throughout the entire SW Highlands hence removing the chlorite zone alleged by Elles & Tilley (1930). Furthermore Harte & Graham (1976) described the occurrence of garnet throughout the entire Erins Quartzite. They therefore re-located the garnet-isograd as near coincident with the lithological boundary between the Ardrishaig Phyllites and the Erins Quartzite. SW

Highlands are assemblages. The metamorphic zonation of the SW Highlands is illustrated in figure 3.6.

It is apparent from figures 3.6 and that metamorphic zonation is unaffected by and must therefore post-date D_1 nappe formation. Furthermore, it is evident that the garnet-zone rocks symmetrically span the Cowal Antiform. For the development of the Cowal Antiform to bring garnet-zone rocks to the surface it is imperative that D_4 folding must post-date the peak of regional metamorphism (figure 3.7).

The coexistence of stilpnomelane and actinolitic amphibole, in the absence of hornblende, in metabasites at the core of the Loch Awe Syncline defines the lowest grade. The isograd which is defined by this assemblage is folded during D_4-tightening of the Loch Awe Syncline (figure 3.7), re-inforcing the interpretation that D_4 folding must post-date the peak of regional metamorphism.

The garnet-zone rocks which span the Cowal Antiform represent the highest grade attained within the SW Highlands. However, Watkins (1983) describes albite-porphyroblast schists developed locally along the crest of the Cowal Antiform. Albite is found to co-exist with more pyrope-rich garnets than occur in other garnet-zone rocks indicating that they may have developed at slightly higher temperatures than adjacent garnet-zone rocks. However, Dymoke (1988) describes albite porphyroblast schists developed near the Tarbert Monoform. From detailed analysis of these albite porphyroblasts and associated inclusion trails, he proposed that their development was associated with a localised and intense deformational phase (D_3?) which post-dates D_1-D_2 and pre-dates D_4. From the conclusions of this thesis, it would therefore seem likely that porphyroblast development may therefore be associated with fluid infiltration.

For the purposes of this study, peak metamorphism can be considered as a single event during which greenschist and epidote-amphibolite facies conditions were attained. It is probable that peak metamorphism occurred between the primary (D_1-D_2) and secondary (D_4) phases of deformation.

Figure 3.6: Metamorphic Map of the SW Scottish Highlands

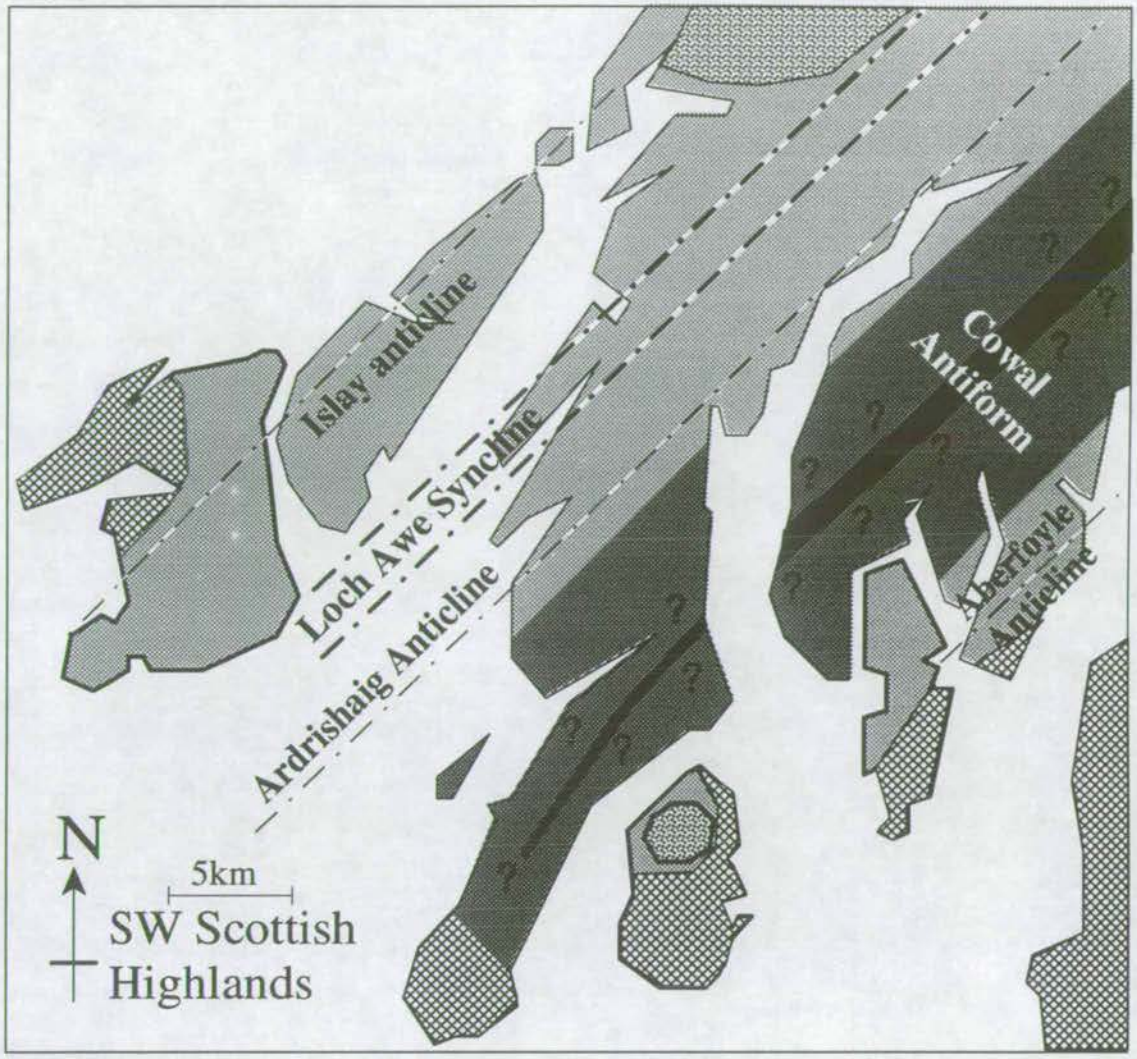

Biotite Zone

Garnet Zone

? Albite-Porphyroblast zone ?

Ornamentations are explained in figure 3.2.

Figure 3.7: D_4-folding of Regional Metamorphic Isograds

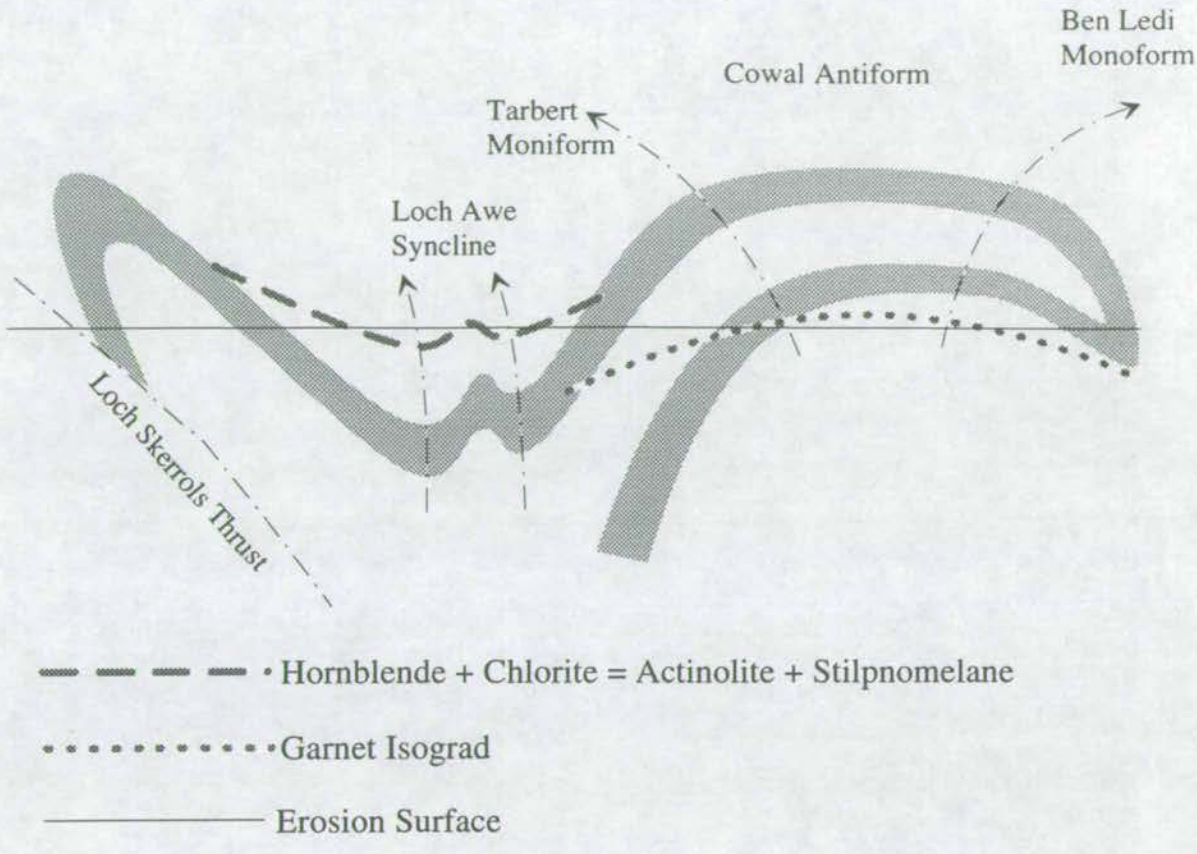

The inherent simplicity of the metamorphic history makes the area ideal for modelling fluid flow in relation to regional metamorphism.

3.4.3 Pressure-Temperature Conditions Metamorphism

Although recent one-dimensional models of fluid flow are less critically dependent on pressure and temperature estimates than the earlier zero-dimensional models (section 2.2), accurate geothermometry and geobarometry is still valuable.

Dymoke (1988) presented experimentally-constrained P-T data for Dalradian metamorphism in the SW Scottish Highlands. This data-set is reinforced with new data derived both experimentally and using THERMOCALC, a spaghetti Fortran program developed by Holland & Powell (1988) which constrains temperature from the loci of intersection of two or more independent univariant reactions (appendices 1 and 2).

Geothermometry

Dymoke (1988) presented geothermometric data constraining the temperatures of metamorphism in the SW Highlands, obtained using calcite-dolomite geothermometry (Powell & Evans 1984), calcite-dolomite-ferrodolomite geothermometry (Annovitz & Essene 1987), garnet-biotite geothermometry (Hodges & Spear 1982) and garnet-hornblende geothermometry (Graham & Powell 1984). Relevant geothermometers are listed in table 3.1. The sample localities are shown in figure A2.1 (appendix 2) and the results are tabulated in figure A2.9 (appendix 2), and are summarised below.

Table 3.1 Traditional Geothermometers applied in the SW Highlands

Geothermometer	Authors	Calibration
Calcite (Fe-Mg) & Caclite-Dolomite	Powell *et al.* (1984)	Calibration curves are plotted in Figures A2.2 and A2.3 in Appendix 2
Calcite-Dolomite	Annovitz & Essene (1987)	$T^{CaMg} = A.X_{Cc}^{MgCO_3} + \frac{B}{\left(X_{Cc}^{MgCO_3}\right)^2} + C.\left(X_{Cc}^{MgCO_3}\right)^2 + D\sqrt{X_{Cc}^{MgCO_3}} + E$ $A = -2360.0, B = -0.01345, C = 2620.0, D = 2608.0, E = 334.0$
Calcite-Dolomite-Ferrodolomite	Annovitz & Essene (1987)	$T^{CaMgFe} = T^{CaMg} + a.X_{Cc}^{FeCO_3} + b.\left(X_{Cc}^{FeCO_3}\right)^2 + c.\frac{X_{Cc}^{FeCO_3}}{X_{Cc}^{MgCO_3}}$ $+d\left(X_{Cc}^{FeCO_3}.X_{Cc}^{MgCO_3}\right) + e.\left(\frac{X_{Cc}^{FeCO_3}}{X_{Cc}^{MgCO_3}}\right) + f.\left(X_{Cc}^{FeCO_3}.X_{Cc}^{MgCO_3}\right)^2$ $a = 1718.0, b = -10610.0, c = 22.49, d = -26260.0,$ $e = 1.333, f = 0.32837 \times 10^7$
Garnet-Biotite	Hodges & Spear (1982)	$0 = 12454 - 4.662T + 0.057P + RT\ln K$ $K = \frac{\left(X_{gt}^{alm}\right)^3.\left(X_{bi}^{phl}\right)^3}{\left(X_{gt}^{py}\right)^3.\left(X_{bi}^{ann}\right)^3} + \frac{\left(\gamma_{alm}\right)^3}{\left(\gamma_{py}\right)^3}$
Garnet-Hornblende	Graham & Powell (1982)	$T = \frac{2880 - 3280 \cdot X_{Ca}^{gt}}{\ln K + 2.426}$ $K = \left(\frac{a_{alm}^{gt}}{a_{py}^{gt}}\right)^{1/3} \cdot \left(\frac{a_{mg-parg}^{hb}}{a_{fe-parg}^{hb}}\right)^{1/4}$

(1) Temperatures obtained at SW Jura and Tayvallich using calcite-dolomite geothermometry (Powell & Evans 1984) and calcite-dolomite-ferrodolomite

geothermometry (Annovitz & Essene 1987) are in the average ranges 470-480°C and 410-430°C, respectively.

(2) Temperatures obtained at East Loch Tarbert and Clachbreac using garnet-biotite geothermometry (Hodges & Spear 1982) are in the average ranges 480-510°C and 480-530°C, respectively.

(3) Temperatures obtained at Stronachullin, East Loch Tarbert and West Loch Tarbert using garnet-hornblende geothermometry (Graham & Powell 1984) are in the average ranges 530-560°C, 500-520°C and 500-540°C, respectively.

Furthermore, Burgess et al. (1982) identified kyanite porphyroblasts rimmed in pyrophyllite in aluminous phyllites developed as intercalations within the Islay-Jura Quartzite at Carraig Fhada, Port Ellen, SE Islay. Temperature is constrained to be greater than 430°C by the reaction:

$$Pyhl = Ky + 3Qz + H_2O$$

This data-set has been re-inforced and expanded in this study, again using calcite-dolomite and calcite (Fe-Mg) geothermometry (Powell & Evans 1984), calcite-dolomite-ferrodolomite geothermometry (Annovitz & Essene 1987) and garnet-biotite geothermometry (Ferry & Spear 1977 and Hodges & Spear 1982). In addition to these conventional geothermometers, temperatures were estimated using THERMOCALC (Holland & Powell 1988) which calculates temperature from the intersections of all the possible univariant reactions for a specific mineral assemblage at a pre-determined pressure. THERMOCALC method may in fact represent a major advance from more traditional geothermometers because it employs ***all potential reactions*** within an assemblage whereas traditional geothermometers employ ***only one such reaction***. In addition, THERMOCALC enables anomalous mineral data to be identified and removed from the calculation thus reducing the inevitable errors brought about by un-detected mineral zonation or chemical dis-equilibrium. The

calculation details and the results of traditional geothermometry and application of THERMOCALC are presented in appendix 2 and are summarised as follows:

(1) Temperatures obtained at Traigh Gheighsgeir, Stronefield, Keppoch Point and Loch Fuar Bheinne using calcite-dolomite geothermometry (Powell & Evans 1984) are in the average ranges 330-430°C, ≈230°C, <200°C and 400-450°C, respectively.

(2) Temperatures obtained at Traigh Gheighsgeir, Stronefield, Keppoch Point and Loch Fuar Bheinne using calcite (Fe-Mg) geothermometry (Powell & Evans 1984) are in the ranges 320-420°C, ≈280°C, <200°C and 400-450°C, respectively.

(3) Temperatures obtained at Traigh Gheighsgeir, Stronefield and Loch Fuar Bheinne using calcite-dolomite-ferrodolomite geothermometry (Annovitz & Essene 1987) are in the average ranges 290-480°C, ≈50°C and 430-470°C, respectively. At Keppoch Point the result was un-obtainable. The interpretation of this and the huge variance of results obtained at Traigh Gheighsgeir can probably be explained by variable extents of retrograde alteration of dolomites and/or calcite. This retrogression will be discussed in depth in chapter 7.

(4) Temperatures obtained at Gigha and Loch Stornoway using garnet-biotite geothermometry (Hodges & Spear 1982) are both approximately 500°C.

(5) Temperatures obtained at Scarba, Port Cill Maluaig, Traigh Gheighsgeir and Stronefield using THERMOCALC are as follows:

(i) The temperature estimated for a phyllitic intercalation in the Islay-Jura quartzite at Scarba (SCARBA, figure A2.8, appendix 2) is 529±32°C. This value was calculated from the following four independent reactions and the fit is good.

$2clin + 3mu += ames + 3east + 7qz + 4H_2O$

$clin + phl + 3mu = 4east + 7qz + 4H_2O$

$6clin + 4daph + 15mu = 5fames = 15east + 35qz + 20H_2O$

$10clin + 4ann + 21mu = 3fames + 25east + 49qz + 28H_2O$

(ii) The temperature estimated from chlorite-calcite-quartz schists (type III metabasite assemblage, section 3.3.3) at the margin of a metabasite exposed at Port Cill Maluaig (PCM1, figure A2.8, appendix 2) is 446±19°C. This value was calculated from the following two independent reactions and the fit is good.

5ames + 8cc + 14qz = 4clin + 4cz + $2H_2O$ + $8CO_2$

5fames + 8cc + 14qz = 4daph + 4cz + $2H_2O$ + $8CO_2$

(iii) The temperature estimated from chlorite-calcite-quartz-amphibole-epidote-albite rock (type II metabasite assemblage, section 3.3.3) near the margin of a metabasite exposed at Port Cill Maluaig (PCM2, figure A2.8, appendix 2) is 474±15°C. This value was calculated from ten independent reactions and the fit is poor.

20ames + 3tr + 22cc + 35qz = 19clin + 14cz + $22CO_2$

10clin + 12cc + 28qz = 5ames + 6tr + $12CO_2$ + $14H_2O$

17ames + 3hb + 22cc + 35qz = 16clin + 14cz + $22CO_2$

10daph + 12cc + 28qz = 5fame + 6ftr + 12 + $14H_2O$

17fames + 3fhb + 22cc + 35qz = 16daph + 14cz + $22CO_2$

4daph + fame + 12cc + 28qz = 6fhb + $12CO_2$ + $14H_2O$

10clin = tr + 7ab + 12cc = 5ames +7ed + $12CO_2$ + $14H_2O$

5clin + 5phl + 12cc + 28qz = 5east + 6tr + $12CO_2$ + $14H_2O$

3clin + 2ames + tr + 7ab + 12cc = 7parg + $12CO_2$ + $14H_2O$

52clin + 68ann + 72cz + 21ab = 10ames + 68east + 21parg + 51fhb +$132H_2O$

(iv) The temperature estimated from amphibole-epidote-albite rock (type I metabasite assemblage, section 3.3.3) at the centre of a metabasite exposed at Port Cill Maluaig (PCM3, figure A2.8, appendix 2) is 477±16°C. This value was calculated from eight independent reactions and the fit is poor.

20ames + 3tr + 22cc + 35qz = 19clin + 14cz + $22CO_2$

$10clin + 12cc + 28qz = 5ames + 6tr + 12CO_2 + 14H_2O$

$17ames + 3hb + 22cc + 35qz = 16clin + 14cz + 22CO_2$

$10daph + 12cc + 28qz = 5fame + 6ftr + 12 + 14H_2O$

$17fames + 3fhb + 22cc + 35qz = 16daph + 14cz + 22CO_2$

$4daph + fame + 12cc + 28qz = 6fhb + 12CO_2 + 14H_2O$

$10clin = tr + 7ab + 12cc = 5ames + 7ed + 12CO_2 + 14H_2O$

$3clin + 2ames + tr + 7ab + 12cc = 7parg + 12CO_2 + 14H_2O$

(v) The temperature estimated from a phyllitic intercalation within a metabasite exposed at Port Cill Maluaig (PCM4, figure A2.8, appendix 2) is 469±27°C. This value was calculated from eight independent reactions and the fit is very poor.

$15ames + 64cc + 126qz = 12tr + 20cz + 64CO_2 + 38H_2O$

$3fame + 10cc + 21qz = 3hb + 2cz + 10CO_2 + 8H_2O$

$fame + 19fhb + 22cc + 35qz = 16ftr + 14cz + 22CO_2$

$10ames + 4ftr + 12cc + 28qz = 5fame + 10hb + 12CO_2 + 14H_2O$

$5ames + tr + 3ed + 7ab + 12cc = 10parg + 12CO_2 + 14H_2O$

$27ames + 12tr + 42ab + 76cc = 42parg + 8cz + 76CO_2 + 74H_2O$

$3fame + 4fgl + 12cc + 28qz = 6fhb + 8ab + 12CO_2 + 10H_2O$

$7ames + 145fhb + 4gl + 170cc + 241qz = 116ftr + 8ed + 106cz + 170CO_2$

(vi) The temperatures estimated from ankerite-paragonite-quartz-chlorite-calcite-albite metabasite at Traigh Gheighsgeir (TGS1 and TGS2, figure A2.8, appendix 2) are 493±47°C and 490±28°C. The values were calculated from four independent reactions and the fit is better for the latter value.

$ames + 6dol + 4qz + 4H_2O = 2clin + 6cc + 6CO_2$

$fame + 6fdol + 4q + 4H_2O = 2daph + 6cc + 6CO_2$

$5ames + 3fdol + 20qz + 20H_2O = 4clin + 6daph + 30cc + 30CO_2$

$5dol + 3q + pa + 3H_2O = clin + 5cc + ab + 5CO_2$

(vii) The temperature estimated from a chlorite-muscovite-dolomite-calcite-quartz metabasite at Stronefield (STF1, figure A2.8, appendix 2) is 483±28°C. The value is calculated from four independent reactions and the fit is poor.

$ames + 6dol + 4qz + 4H_2O = 2clin + 6cc + 6CO_2$

$fame + 6fdol + 4q + 4H_2O = 2daph + 6cc + 6CO_2$

$5ames + 3fdol + 20qz + 20H_2O = 4clin + 6daph + 30cc + 30CO_2$

$mu + 4qz + 6dol + 4H_2O = clin + cel + 6cc + 6CO_2$

(viii) The temperature estimated from phyllites at Stronefield (STF2 and STF3, figure A2.8, appendix 2) are 538±63°C and 488±33°C. The values are calculated from four independent reactions and the fit is better for the latter value.

$ames + 6dol + 4qz + 4H_2O = 2clin + 6cc + 6CO_2$

$fame + 6fdol + 4q + 4H_2O = 2daph + 6cc + 6CO_2$

$5ames + 3fdol + 20qz + 20H_2O = 4clin + 6daph + 30cc + 30CO_2$

$mu + 4qz + 6dol + 4H_2O = clin + cel + 6cc + 6CO_2$

The fits of the calculated values were in general poor. However, where two or more values were calculated for adjacent assemblages, consistent temperatures were obtained. In general therefore, the temperatures calculated at Scarba, Traigh Gheighsgeir, Stronefield and Port Cill Maluaig are 500-560°C, 460-520°C, 450-520°C and 440-470°C, respectively. Temperatures generated using THERMOCALC are generally higher than temperatures estimated using traditional geothermometers. Although geothermometric predictions based on THERMOCALC are advantaged by the large number of independent reactions upon which they are based, they are disadvantaged because the reactions are not necessarily as well

constrained, in terms of activity-composition relationships and P-T-X_{CO_2} phase relations as the single reactions which are utilised in traditional geothermometry. Therefore, more confidence is held in the temperatures estimated using traditional geothermometers.

In conclusion, temperature estimates are based on a variety of traditional geothermometers and strengthened by slightly (20-30°C) higher temperatures calculated using THERMOCALC (Holland & Powell 1988). The geothermometric data-set is tabulated in figure A2.8 (appendix 2) and data is compiled and presented in the form of a temperature map in figure 3.8. Isotherms are constructed tentatively across this map which form the basis for temperature estimates which will be input in to the fluid flux calculations in chapter 10.

Geobarometry

Geobarometry in the SW Scottish Highlands is problematic. Dymoke (1988) found that only one geobarometer could be successfully applied to estimate peak metamorphic pressures. This is the "phengite" barometer of Powell & Evans (1983) which is based on calibration of the reaction:

$3cel + clin = mu + 3phl + qz + 4H_2O$

Initially, Dymoke (1988) estimated pressure using the following calibrations of the phengite barometer:

(1) Ideal site mixing models of Powell & Evans (1983) and Bucher-Nurminen (1987);

and (2) Models based on the assumption that a_{phl} = Mg/(Fe+Mg) of Powell & Evans (1983) and Bucher-Nurminen (1987).

Dymoke (1988) estimated ***minimum*** pressures by application of the phengite barometer of Massonne & Schreyer (1987) which is based on a rigorous experimental

Figure 3.8: Temperature Map of the SW Scottish Highlands

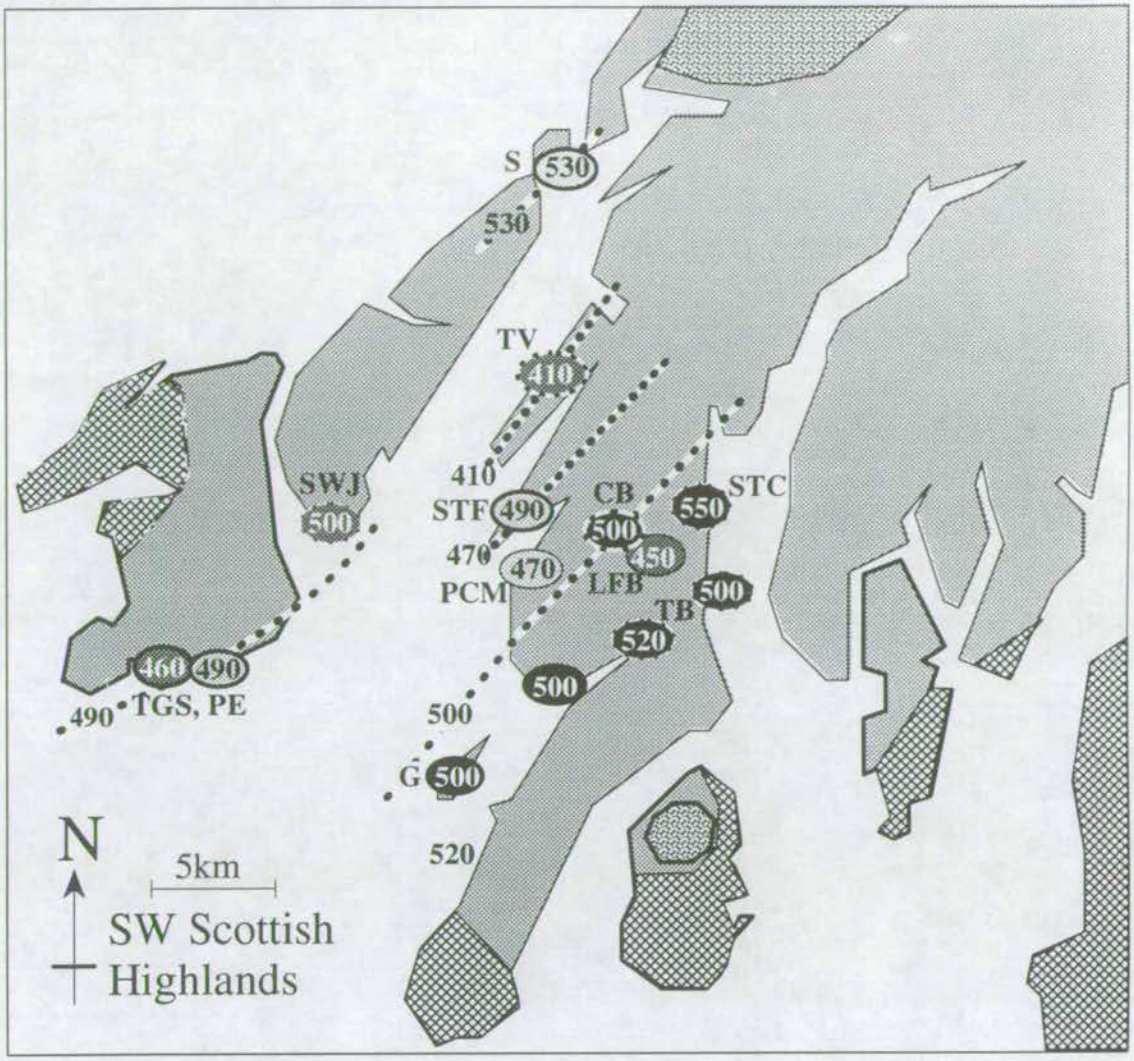

S=Scarba, TV=Tayvallich, SWJ=SW Jura,
STF=Stonefield, CB=Clachbreac,
LFB=Loch Fuar Bheinne, STC=Stronachullin,
PCM=Port Cill Maluaig, TB=Tarbert,
TGS=Traigh Gheighsgeir, PE=Port Ellen,
LS=Loch Stornoway, G=Gigha

T	**Temperature estimate (THERMOCALC, this study)**
T / T	**Average temperature estimate (Cc-Dol-Fdol geothermometry, this study/Dymoke 1988)**
T / T	**Average temperature estimate (Gt-Bi and Gt-Hb geothermometry, this study/Dymoke 1988)**
T	**Approximated temperature contours**

Ornamentations are explained in figure 3.2.

calibration of the reaction:

$3cel = phl + 3Kfsp + 3qz + 2H_2O$

On the basis of this calibration, pressures may be constrained in natural rocks where phengite co-exists with the limiting assemblage biotite + feldspar + quartz. Furthermore, where phengites are developed together with another Mg-Fe silicate, in the absence of the limiting assemblage, ***minimum*** pressures may be constrained on the basis of this calibration from the Si-content of the ***most Si-rich*** phengite (Massone & Schreyer 1987). By this approach, Dymoke (1988) obtained minimum pressures of 7-10Kb across the SW Highlands.

Dymoke compared pressure estimates from the SW Highlands, based on the phengite barometers of Powell & Evans (1983) and Bucher-Nurminen (1987), with minimum pressure estimates based on the experimental calibration of the phengite barometer of Massone & Schreyer (1987). Only the ideal site mixing model calibration of Powell & Evans (1983) gave pressures which were consistent with the minimum of 7-10Kb and are therefore taken to best represent the pressures during Dalradian metamorphism of the SW Highland. The pressures obtained by Dymoke (1988) are tabulated in figure A1.5 (appendix 1) and are summarised as follows:

(1) at Tayvallich, the minimum pressure was estimated to be 9-10Kb and actual pressures were estimated to be 9-10Kb;

(2) at Clachbreac, the minimum pressure was estimated to be 7-8Kb and actual pressures were estimated to be 11-12Kb;

and (3) at Stronachullin the minimum pressure was estimated to be 7-9Kb and actual pressures were estimated to be 10.5-12Kb.

Further pressure estimates were obtained in the present study, again using the phengite barometer and the ideal site mixing model of Powell & Evans (1983). The

calculation details and data are presented in appendix 1 and are summarised as follows:

(1) at Clachbreac, pressure was estimated to be ≈11Kb;

(2) at Port Ellen, pressure was estimated to be ≈10Kb;

and (3) on Scarba, pressure was estimated to be ≈11Kb.

These pressure estimates are consistent with those of Dymoke (1988). However, pressures of around ≈11Kb are somewhat problematic as the development of jadeite within the metabasites would be expected but is not observed. However, Graham (*pers.comm.*) suggests that higher grade phengites tend to develop zonation which could result in anomalous pressure estimates.

The use of THERMOCALC (Holland & Powell 1988) to constrain pressure in the SW Highlands was unsuccessful. This was presumably because $\partial P/\partial T$ of most available reaction curves was very high and the location of intersections was therefore highly inaccurate.

Constraints on metamorphic pressures are in general unsatisfactory. The mineral assemblages are so restrictive that only the phengite barometer may be applied. Although the phengite barometer is reputed to be reliable, calculated pressures are highly vulnerable to zonation within analysed phengites. Although this is an important consideration in the higher grade (garnet-zone) rocks, lower grade phengites are reputed to be generally homogeneous (Graham *pers. comm.*). Nevertheless, the skeletal nature of the pressure dataset (figure A1.5, appendix 1) prohibits construction of a metamorphic pressure map, similar to figure 3.8. Therefore, for lack of better constraints, pressure throughout the SW Highlands has been approximated at 10Kb for the purposes of this study.

Summary

In summary, SW Highland Dalradian metamorphism occurred at pressures of about 10Kb and temperatures increasing from 410-430°C, in the lowest grade rocks

at the core of the Loch Awe Syncline to 510-530°C at the garnet isograd (figure 3.7) and 440-460°C at Port Ellen on Islay.

3.4.4 Relative Timing of Deformation and Metamorphism

The significance of the spatial distribution of metamorphic zones in the SW Highlands in relation to the relative timing of deformation and metamorphism has already been addressed. The symmetrical occurrence of garnet-zone assemblages across the Cowal Antiform and the folding of the isograd defining the reaction:

chlorite + hornblende = stilpnomelane + actinolite

at the core of the Loch Awe Syncline provide unequivocal evidence that peak metamorphism post-dated D_1 and pre-dated D_4-deformation.

Dymoke (1988) presents textural evidence from the SW Highlands which re-inforces the above interpretation. These are summarised as follows:

(1) the peak metamorphic minerals (hornblende, phengite. biotite, chlorite) grow in fabrics which are planar, and axial planar to the major D_1 structures.;

(2) these fabrics are deformed by later microfolding and crenulation;

(3) inclusion trails within garnet porphyroblasts, growing in a crenulated matrix, mimic the uncrenulated D_1 fabrics.

An essential question arising from the first of these observations, which will be investigated later in the thesis, is whether the development of these minerals was syn-D_1 or if they mimic an earlier D_1-fabric.

In addition to the above criteria, Burgess *et al.* (1982) identified peak metamorphic kyanites which are developed in highly aluminous phyllites at Port Ellen on Islay and have been rotated by D_4 deformation.

3.4.5 Implications of Deformation and Metamorphism to Modelling of Fluid Flow

For meaningful modelling of fluid flow during orogenesis to be achieved a well-founded understanding of the inter-relationship of deformation and metamorphism is essential. For the purposes of this study, the orogenic evolution of the SW Highlands can be considered to be relatively simple. Although the specific timing of Dalradian orogenesis is not firmly established, the relative timing of deformational and metamorphic events is well constrained and may be summarised by the following sequence:

(1) D_1-D_2 (primary) deformation, involving development of the Islay Anticline, Loch Awe Syncline and Ardrishaig Anticline - Tay Nappe ("mushroom"-structure) and associated axial planar s_1-s_2 fabrics which fan through the Loch Awe Syncline.

(2) Peak metamorphism, associated with the development of greenschist facies mineral assemblages, during which pressures of around 10Kb and temperatures between 410 and 530°C were attained.

(3) D_4 (secondary) metamorphism, involving tightening of the Loch Awe Syncline and Tay Nappe and resulting in the development of the Cowal Antiform and Tarbert and Ben Ledi Monoforms and associated minor box-folds and crenulation cleavage. This later deformation folds peak metamorphic isograds.

Conclusions from this study are generally consistent with peak metamorphism occurring during extended D_1-D_2 penetrative deformation, rather than the simple chronology detailed above.

3.5 Summary

In this chapter, the depositional, lithostratigraphic, metamorphic and deformational history of the Dalradian of the SW Scottish Highlands has been

discussed. The essential points, pertaining to the modelling of fluid flow and arising from this discussion are:

(1) The lithostratigraphic sequence of the SW Highlands includes abundant metabasite horizons. Metabasites are compositionally, mineralogically and isotopically distinct from their host-rocks (phyllites and psammites) and therefore their boundaries define measurable compositional, mineralogical and isotopic discontinuities. The potential of ***measurable*** chemical, mineralogical and isotopic modification of such boundaries as a result of fluid infiltration is immediately evident.

(2) The relative timing of regional metamorphism and deformation in the SW Highlands is well constrained and summarised in table 3.2.

Table 3.2 Relative Timing of Metamorphism and Deformation of the SW Highlands

Event	Characteristics
D_1-D_2	Development of major fold-structures: Islay Anticline, Loch Awe Syncline and Ardrishaig Anticline (Tay Nappe). Associated penetrative s_1 fabric.
Peak Metamorphism	P≈10Kb, T=410-530°C, biotite-garnet grades. Alignment of phyllo-silicates //D_1: phyllosilicates developed syn-D_1 or post-D_1 but mimic pre-existing D_1 fabric.
D_3	Localised intense deformation associated with growth of albite porphyroblasts near the Tarbert Monoform.
D_4	Uplift and tightening of the Tay Nappe and Loch Awe Syncline and resultant development of the Tarbert and Ben Ledi Monoforms and the Cowal Antiform. Associate crenulation cleavage and minor box-folds.

(3) A large geothermometric data-set exists which constrain the temperatures of Dalradian metamorphism to range from about 410°C in the lowest grade rocks in the centre of the Loch Awe syncline to about 530°C above the garnet isograd.

(4) A skeletal geobarometric data-set enables an average pressure of 10±2Kb to be estimated for Dalradian metamorphism.

In chapter 4, the fluid infiltration history of the Dalradian of the SW Scottish Highlands will be discussed in the context of the metamorphism and deformation sequence outlined in table 3.2.

4. THE STUDY AREA:

Fluid Infiltration History

4.1 Rationale

This chapter serves to outline our qualitative understanding of the fluid infiltration history of the Dalradian rocks in the SW Highlands. Field observations pertaining to the infiltration history are presented in the framework of the qualitative model of fluid infiltration in the SW Highland Dalradian proposed by Graham *et al.* (1983).

4.2 Qualitative Model of Fluid Infiltration in the SW Highland Dalradian (Graham *et al.* 1983)

Graham *et al.* (1983) described three major fluid infiltration events involving hydrous fluids in the Dalradian rocks of the SW Highlands. In chronological order, these are:

(1) Pre-metamorphic spilitisation involving convective circulation of heated sea-water in the shallow crust;

(2) Syn-metamorphic infiltration involving pervasive movement of a CO_2-bearing hydrous fluid in the deep-crust, comparable to the present day Gulf of California (Graham & Borradaile 1984 and Graham 1986);

(3) Post-metamorphic fracture-controlled fluid infiltration producing assemblages containing ankerite + K-feldspar + chlorite during uplift.

Although their interpretation of these fluid infiltration events was essentially qualitative, they presented one of the first models which did not require the presence of large volumes of fluid (e.g. Ferry (1983, 1988, 1991) and Wickham & Taylor (1985, 1987)). Instead required fluid volumes were well within the limits defined by Walther & Orville (1982) who calculated that total devolatilisation ofof an average pelite during metamorphism could generate a ***maximum*** of 5wt.% volatiles (≡ 12 vol.% at 5kb, 500°C).

This thesis presents a quantitative re-appraisal of the fluid-infiltration history of the Dalradian of the SW Scottish Highlands in the light of the recently developed theoretical models of Bickle & McKenzie (1987) and Bickle & Baker (1990). It is fundamental to the structuring of the thesis to outline our qualitative understanding of fluid flow in the SW Highlands based on field observations, phase relations and stable isotope data and the model proposed by Graham *et al.* (1983), which essentially defines the starting point of the project. Therefore, qualitative observations and interpretations pertaining to the three successive fluid infiltration events, which they describe, are presented in the following sub-sections.

4.2.1 Pre-metamorphic Spilitisation

Graham (1976) recognised pre-metamorphic spilitic alteration of basic sills and flows of the Argyll Group of the SW Scottish Highlands.

Field Observations of Spilitisation

In the field, Graham (1976) noted an increased abundance of albite in a number of metabasite sills and flows cropping out throughout the SW Highlands. The distribution of albitic phenocrysts is patchy and the size of individual phenocrysts is extremely variable (figure 4.1). Albite enrichment is often associated with the development of 10-50cm elongate epidote-rich pods or segregations (figure 4.2).

Figure 4.1: Photographs illustrating Albite enrichment developed as a result of Spilitisation

Locality: Rubha Garbh GR753 766 **Scales**: Pencil (15cm), 20p piece

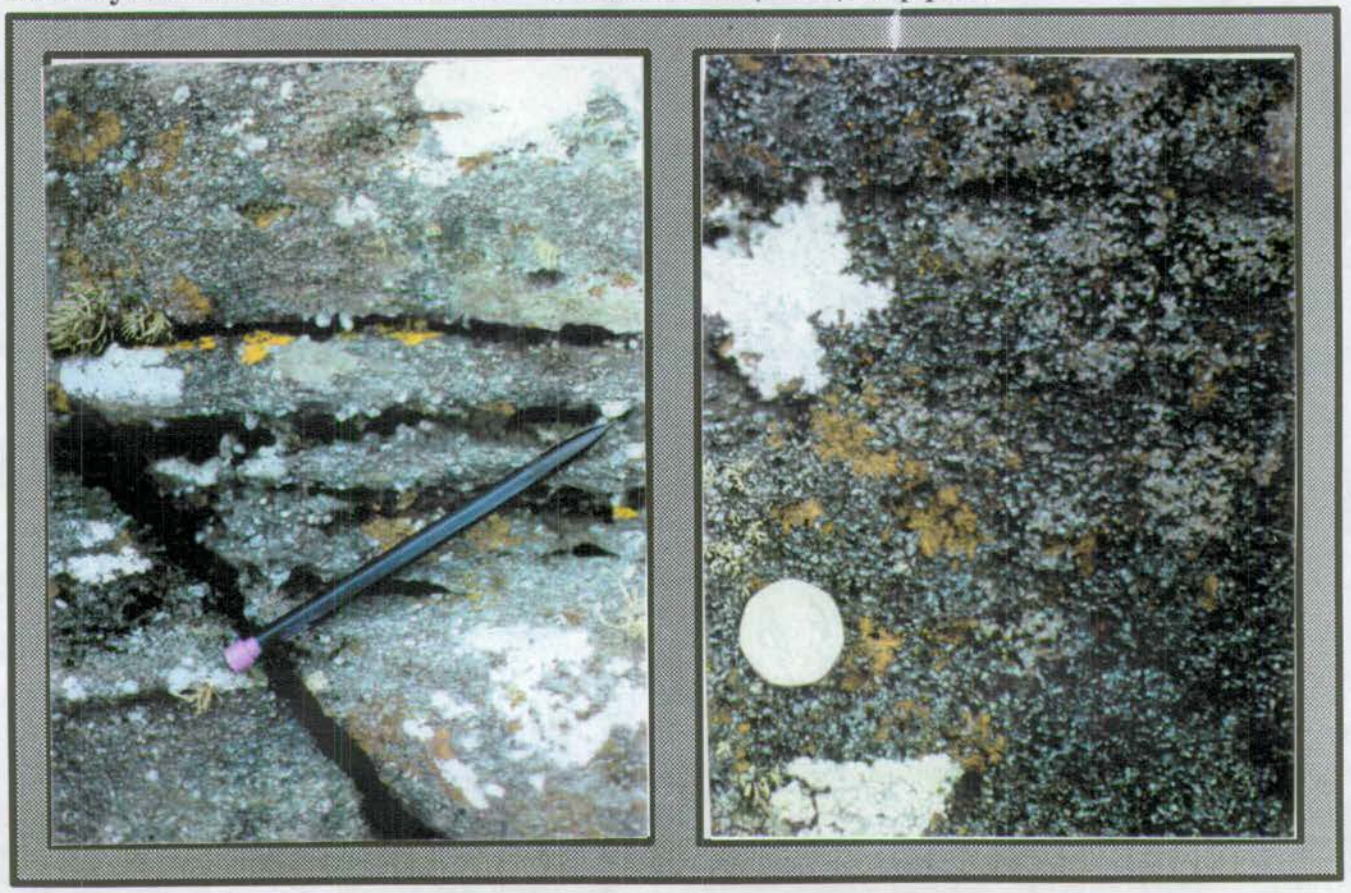

Figure 4.2: Photograph showing a large Epidotite Segregation developed as a result of Spilitisation

Locality:
Rubha Garbh
GR753 766

Scales:
Hammer (30cm)

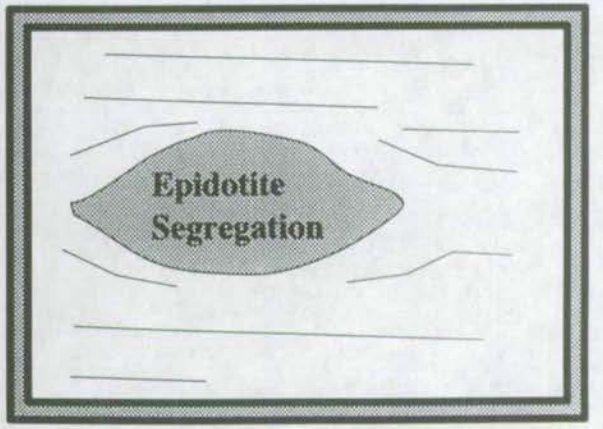

Geochemical Observations of Spilitisation

Graham (1976) constructed a plot of wt.% Na_2O against wt.% CaO for 93 SW Highland metabasites. He found that the metabasite distribution was clearly bimodal (figure 4.3). A relatively low Na_2O, high CaO group is distinguished from a relatively high Na_2O, low CaO group. The former group corresponds to an average of 282 oceanic tholeiites (Manson 1967) and an average 946 continental tholeiites (Manson 1967), whereas the latter group corresponds to an average of 225 spilites (Vallance 1967). The latter group consists largely of those metabasites which are enriched in albite and/or contain epidote-rich segregations. Epidote segregations plot in a third, low Na_2O - high CaO field such that they may represent a chemical bi-product of spilitisation.

There is a strong spatial association of spilitic albite enriched zones and epidote segregations. However a qualitative assessment of the relative volumes of albite-enriched metabasite and associated epidote segregations implies the volume of epidote segregations is insufficient. It is therefore inferred that spilitisation and associated fluid infiltration was spatially extensive, at least in the vicinity of an individual sill and resulted in a bulk loss of CaO.

Model of SW Highland Spilitisation

Extrusion of the Tayvallich Volcanics and intrusion of some 3km of basic sills and dykes, as a result of continental extension and rifting, acted as a "heat engine" driving circulation of sea-water in the upper crust and subsequent re-distribution of Na and Ca. This resulted in constant volume transformation of calcic plagioclase to albite, by diffusive replacement of CaAl with NaSi, within the newly intruded basic lavas and higher level sills. This phenomena is termed "spilitisation" and was recognised in the SW Highland metabasites by Graham (1976).

Figure 4.3: Plot of wt.% Na2O vs. wt.% CaO for SW Highland Metabasites

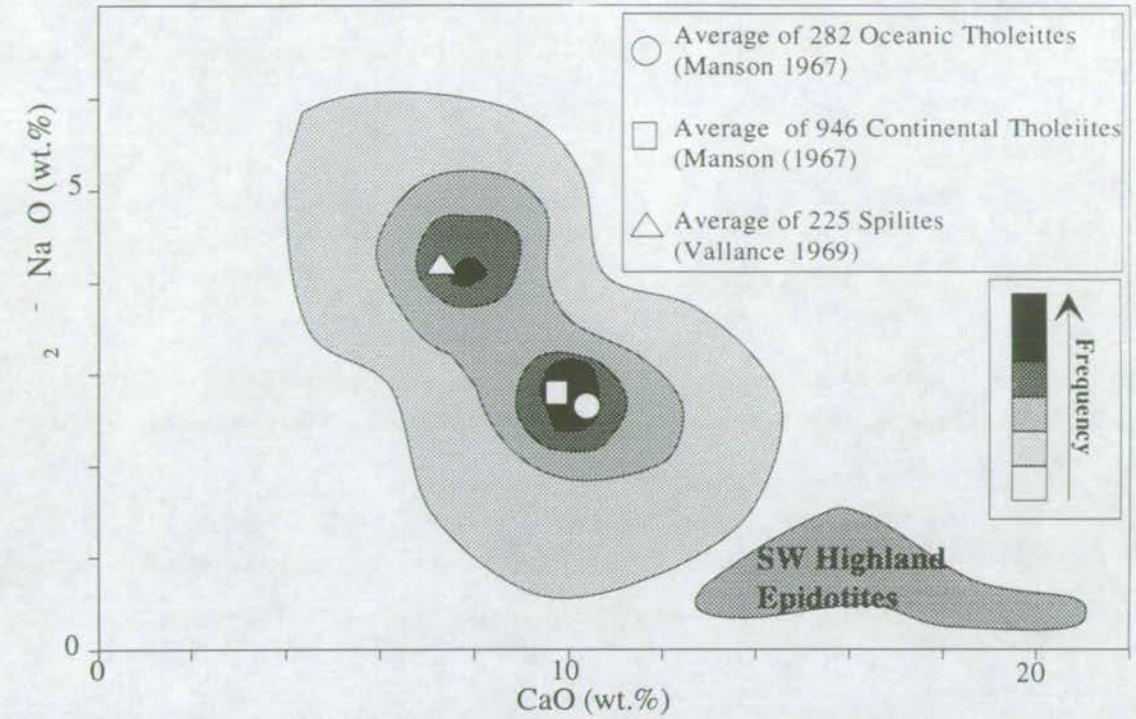

The above plot contours compositional data from 93 metabasites from the SW Highlands, compiled by Graham (1976). A bimodal distribution is evident. A high Na2O, low CaO group which corresponds an average of 225 spilites, compiled by Vallance (1969), is distinct from a low Na2O, high CaO group which corresponds to an average of 282 oceanic tholeiites and an average of 946 continental tholeiites, both of which were compiled by Manson (1967). Epidotite segregations from the SW Highlands form a third distinct. It is clear from the above plot that derivation of spilites from oceanic or continental tholeiites is likely to generate a chemical by-broduct of equivalent composition to the epidotites.

Figure 4.4: Plot of wt.% Na2O vs. modal Plag. for SW Highland Metabasites

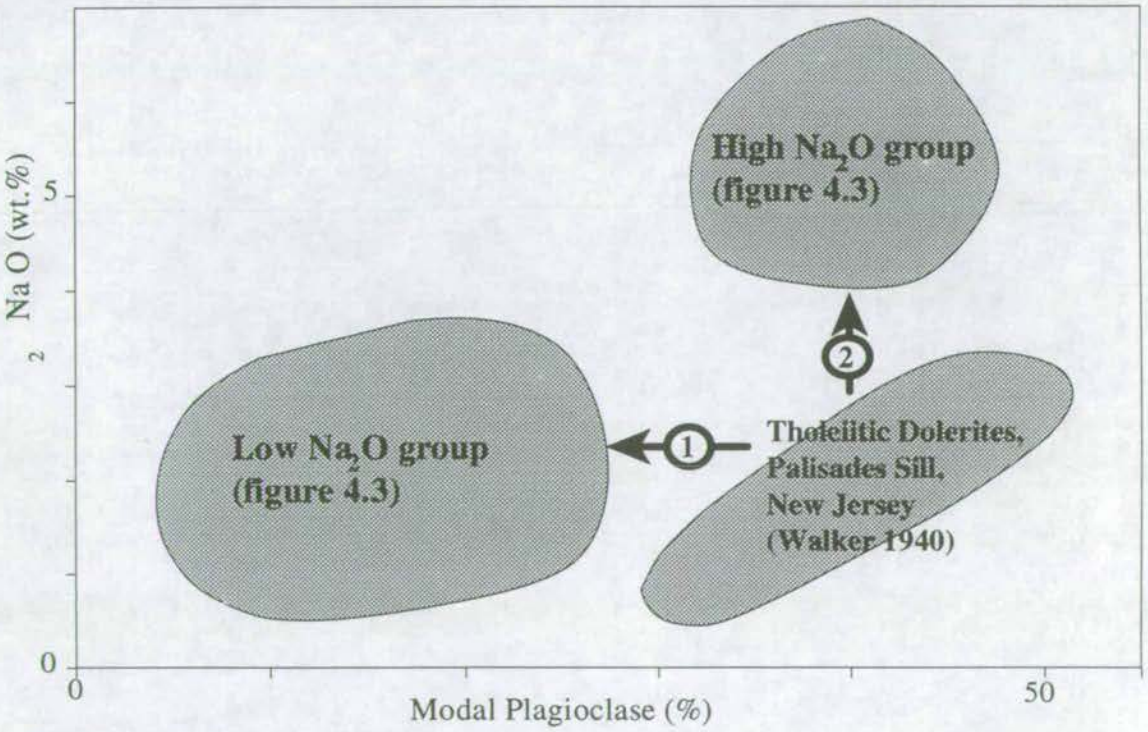

The above plot identifies two chemical evolution paths by which the high Na2O and low Na2O groups, which are distinguished in figure 4.3, may develop:
(1) Isochemical Metamorphism without Spilitisation
(2) Isochemical Metamorphism subsequent to Spilitisation

Graham (1976) proposed that subsequent isochemical metamorphism of the SW Highland basic sills and lavas emphasised the effects of spilitisation (Graham 1976) by modifying the two compositional groups, depicted in figure 4.3, with respect to modal plagioclase and wt.% Na_2O (figure 4.4). Two modification paths are distinguished:

(1) Isochemical greenschist facies metamorphism of the low Na_2O, non-spilitic group led to reduction of modal plagioclase by replacement of calcic plagioclase with albite and epidote. The result is a typical greenschist facies metabasite.

(2) Isochemical greenschist facies metamorphism of the high Na_2O, spilitic group did not affect modal plagioclase as calcic plagioclase had ***already*** been replaced with albite. The result is a greenschist facies metabasite enriched in albite.

Isotopic Modification

Gregory & Taylor (1981) describe isotopic modification of pillow lavas and sheeted dykes of the Samail Ophiolite, Oman. Pillow lavas record $\delta^{18}O$ = 10.7 to 12.7, sheeted dykes record $\delta^{18}O$ = 4.9 to 11.3, and gabbros record $\delta^{18}O$ = 3.7 to 5.9. The sequence describes a progressive increase of $\delta^{18}O$ towards the seafloor from the magmatic values recorded in gabbros ($\approx 6^{o}/_{oo}$, Taylor 1968). They infer that the observed isotopic modification is developed in response to hydrothermal isotopic exchange, associated with shallow-crustal convection of seawater. An analogous situation may have developed in the Tayvallich Volcanics and associated sill complex, at the time of extrusion and emplacement. However, although similar isotopic modification is observed in SW Highland metabasites, it is possible to unambiguously "tag" this modification to have developed in response to syn-metamorphic fluid infiltration, by spatial correlation of reaction and isotope fronts (chapter 8). Therefore if isotopic modification is developed in response to pre-metamorphic hydrothermal circulation it is subsequently obscured.

4.2.2 Syn-metamorphic Fluid Infiltration

Graham et al. (1983) recognised pervasive infiltration of CO2-bearing hydrous fluids into the margins of metabasite dykes, sills and flows cropping out throughout the SW Highlands. Fluid infiltration resulted in the zonal development of the type I-III metabasite assemblages described in section 3.3.3 and outlined below.

Metabasite Mineral Assemblage Zones

Harte & Graham (1975) and Graham *et al.* (1983) recognised and defined three types of metabasite assemblage (types I to III, Graham *et al.* 1983). These assemblages will be discussed in detail in section 5.3. Briefly, the type I metabasite assemblage is characterised by the equilibrium assemblage; **amph + epid**, the type II metabasite assemblage is characterised by the equilbrium assemblage; **amph + epid + chl + cc + qz**, which buffers the divariant $CFMASHCO_2$ reaction (1):

$3amph + 2epid + 10CO_2 + 8H_2O = 3chl + 10cc + 21qz$ **(1)**[1]

and the type III metabasite assemblage is characterised by the equilibrium assemblage; **chl + cc + qz**.

Spatial Distributions of Type I-III Metabasite Zones

Graham *et al.* (1983) describes the zonation sequence illustrated in figure 4.5, in which the type I assemblage is developed in the centre of a metabasite and the type III assemblage is developed in asymmetric layer-parallel zones at the margins of the metabasite. The type II assemblage is developed in narrow zones seperating type I and type III assemblage zones, within which reaction (1) is buffered.

Petrology of Type I-III Metabasite Assemblages

The petrology of type I-III metabasite assemblages is described in detail in section 5.3, therefore it is sufficient at this stage to summarise those petrological

[1] Reaction (1) is included in a reference card at the back of the thesis.

Figure 4.5: Metabasite Zonal Patterns
(adapted from Graham *et al.* 1983)

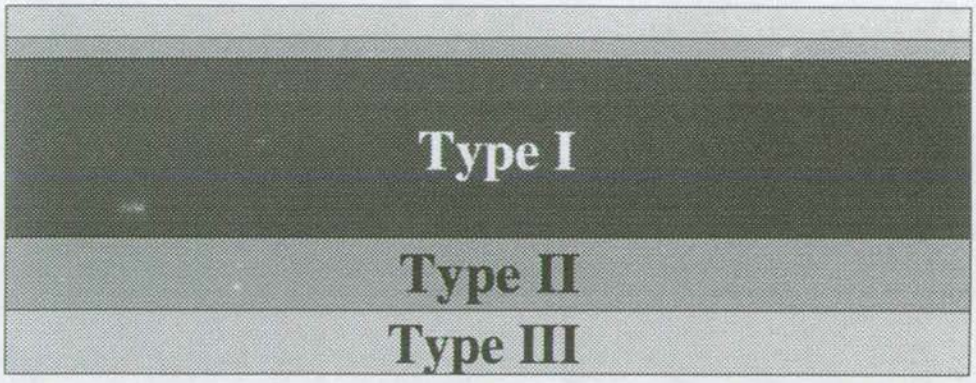

features which are critical to the interpretation of fluid infiltration by Graham *et al.* (1983) as outlined below:

The type I assemblage include **amph + epid + ab + sphene ± chl ± qz ± bi, in the absence of cc** and are largely undeformed preserving many of their original igneous textural characteristics.

The type II assemblage buffers reaction (1) and includes **amph + epid + chl + cc + qz + ab + sphene ± bi**. Reaction textures, defining the progress direction of reaction (1) are preserved within some type II assemblages. For example, chlorite + calcite are observed to replace, and in some instances pseudomorph amphibole (figure 5.11). Also, calcite is observed to rim epidote grains (figure 5.11). Type II assemblages are seldom deformed.

The type III assemblage includes **chl + cc + qz + ab ± sph ± ru ± ep ± bi, in the absence of amph**. Type III assemblages develop a strong penetrative s_1-s_2 fabric which is defined by alignment of phyllosilicates.

Furthermore, Graham et al. (1983) describe the occurrence of the reaction:

Sph + CO_2 = Ru + Cc + Qz **(2)**[2]

Reaction (2) is developed in type III assemblages only. This is consistent with P-T-X_{CO_2} phase relations discussed below.

T-X_{CO_2} Phase Relations of Metabasite Assemblages

Figure 4.6 is an isobaric T-X_{CO_2} section calculated at 10Kb constructed using the computer prgram THERMOCALC (Holland & Powell 1988) which is distilled from the comprehensive T-X_{CO_2} dataset presented in appendix 3. The T-X_{CO_2} phase relations of reactions (1) and (2) are shown. Type I and III metabasite assemblages define specific fields in T-X_{CO_2} space. Reaction (1) may be driven, such that type I assemblages are replaced by type III assemblages, either by decreasing temperature

[2] Reaction (2) is included in a reference card at the back of the thesis.

Figure 4.6: Isobaric T-X(CO2) Section: Reactions (1) and (2): 10kb

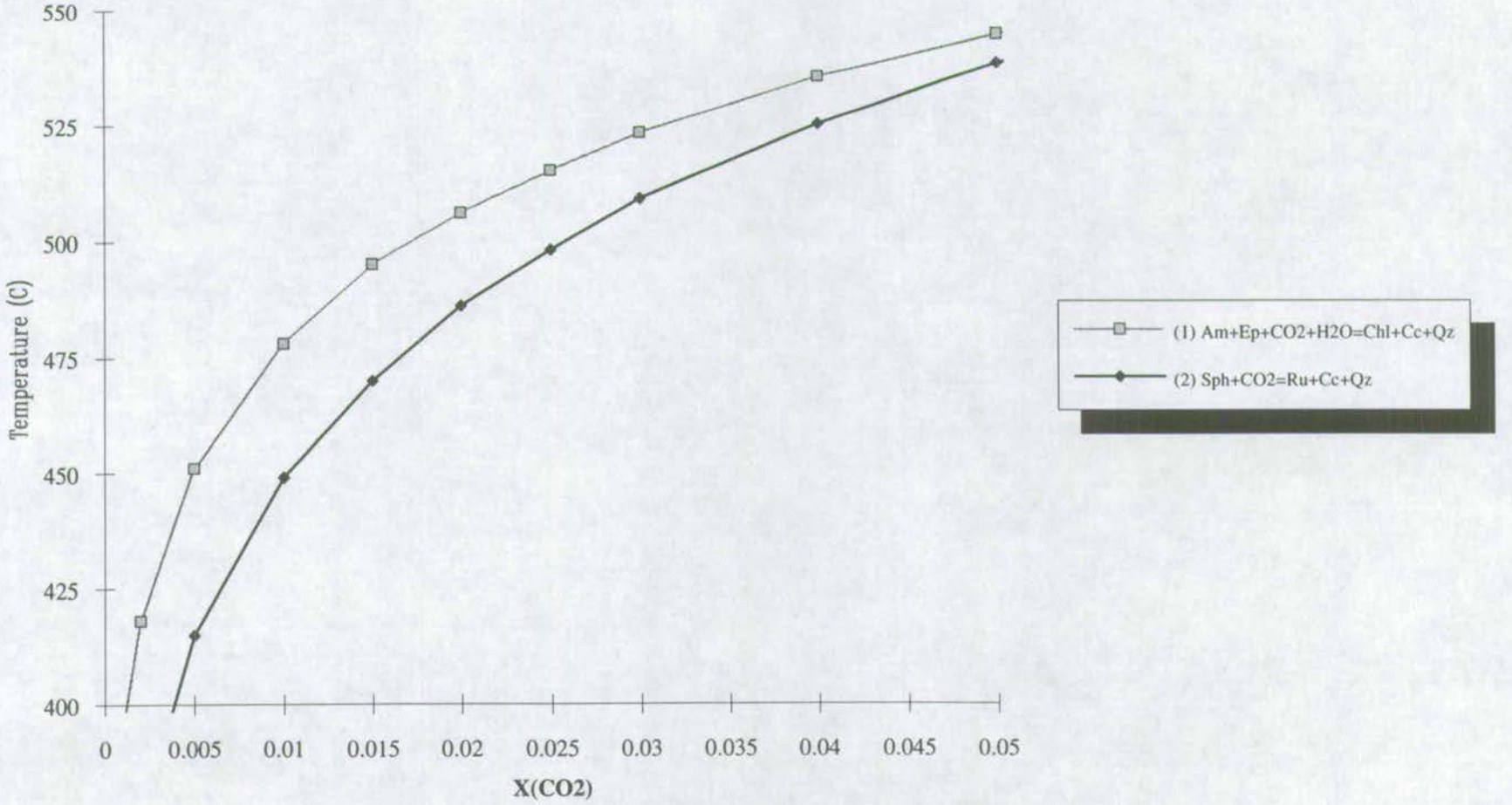

(retrogression) or increasing X_{CO_2} (fluid infiltration). The relatively small width of the individual metabasites precludes local temperature fluctuations to be responsible for the observed zonal distribution of mineral assemblages. Graham *et al.* (1983) therefore concluded that reaction (1) was driven into the margins of metabasites by infiltration of a CO_2-bearing hydrous fluid.

Furthermore, reaction (2) is developed in the type III assemblage field, at higher X_{CO_2} than reaction (1). This is consistent with the field observations mentioned above.

Metabasites as Potential Marker Horizons for Quantitative Modelling of Fluid Flow

In the light of recent theoretical advances in modelling techniques pertaining to the quantification of fluid flow (Bickle & McKenzie 1987 and Bickle & Baker 1990b), which are described in section 2.3.2 and 2.3.3, the potential of zoned metabasites as marker horizons for quantification of fluid flow has been realised. The fluid flow direction is constrained, in one dimension from the asymmetric distribution of type I-III assemblage zones throughout individual metabasites. Furthermore, the time-integrated fluid flux is constrained from the advection distance of reaction (1) (i.e. the width of marginal type III zones).

Qualitative model of Fluid Flow in the SW Highlands of Graham et al, (1983)

Graham *et al.* (1983) attribute the spatial distribution of type I-III metabasite assemblages to influx of CO_2-bearing hydrous fluids driving reaction (1) into the margins of individual metabasite sills or dykes.

Graham *et al.* (1983) propose that hydrous fluid is generated by devolatilisation at the garnet isograd (which is approximately coincident with the lithological boundary between the Erins Quartzite (garnet-zone) and the Ardrishaig Phyllites (biotite-zone)). Hydrous fluid permeates the Ardrishaig Phyllites and immediately takes up CO_2 by oxidation of graphite within the phyllites. The CO_2-

bearing hydrous fluid reacts with type I metabasites to generate the type III assemblage by progress of reaction (1). The former presence of graphite is implied from a predominance of low $\delta^{13}C$ carbonates (-11 to -15‰) within SW Highland phyllites. Unmetamorphosed organic matter typically has $\delta^{13}C$ between -15 and -30‰. It is therefore inferred that low $\delta^{13}C$ carbonates are a product of the relevant oxidation reaction.

Timing of Fluid Infiltration

Graham et al. (1983) constrained the timing of fluid infiltration to be during D_1-D_2 penetrative deformation, on the basis of textural evidence outlined above and described in detail in section 5.3, specifically, that type III phyllosilicates are aligned parallel to D_1-D_2. Furthermore, a strong spatial correlation between infiltration-driven reaction and deformation of metabasite margins is observed (section 5.3.6), hence further re-inforces the conclusion of Graham et al. (1983) that fluid infiltration was syn D_1-D_2.

Isotopic Alteration

A considerable wealth of isotopic data has been compiled for the SW Highland metabasites (Graham *unpublished data*) since publication of Graham et al. (1983). Relevant data is summarised in table 4.1. SW Highland metabasites which contain only type I assemblages retain their original, MORB-like, isotopic signature ($\delta^{18}O$ = 5 to 7‰), whereas metabasites which develop type III assemblages, even at their margins are largely homogenised in $\delta^{18}O$ with the host phyllites or psammites ($\delta^{18}O$ = 10 to 12‰) or marbles ($\delta^{18}O$ = 22 to 26‰).

Table 4.1: $\delta^{18}O$ Data from SW Highland Metabasites Compiled from Graham (*unpublished data*) and Skelton (*unpublished data*)

Sill / Sample Number	Grid Ref.	Sample Location	Sill Width	M3-Zone Width	$\delta^{18}O$
Clachbreac / 69CMG06	767 755	M1-type Interior	100m	<3m	**6.27**
Clachbreac / 69CMG03	767 755	M2-type Margin	100m	<3m	**7.80**
Clachbreac / 69CMG04	767 755	M3-type Margin	100m	<3m	**8.2**
Port Ellen / 89PE28	365 448	M1-type Interior	5.1m	2m	**9.75**
Port Ellen / 89PE28	365 448	M3-type Margin	5.1m	2m	**11.4**
Stronefield	720 742	M1-type Interior	100m	<<10cm	**6.85**

A chronological correlation of mineral reactions and isotopic homogenisation is implied, qualitatively, from their observed association. A spatial correlation was also initially assumed. However, in the light of the recent advances in theoretical modelling of fluid flow from the advection distances of isotope and reaction fronts (Bickle & McKenzie 1987, Bickle & Baker 1990b) the intuitive assumption that isotope and reaction fronts must correlate spatially is challenged. This is addressed in chapter 8, where an isotope and reaction front which were advected by the same phase of fluid infiltration into the same metabasite sill are found to be spatially separated by an order of magnitude, yet they consistently predict identical time-integrated fluid fluxes.

4.2.3 Post-metamorphic Dolomite + K-feldspar + Chlorite + Quartz Veining and Ankerite Porphyroblast Growth

Ankerite + K-feldspar + Chlorite + Quartz Veining

Graham *et al.* (1983) identify a third stage of fluid infiltration which affected the Dalradian of the SW Scottish Highlands during retrogression. Fracture-controlled development of K-fsp + dol + chl + qz was identified in a number of localities throughout the SW Scottish Highlands. The equilibrium coexistence of K-fsp + dol and K-fsp + chl define low temperature stability (figure 4.7). K-fsp + dol + chl + qz

Figure 4.7: T-X(CO2) Section Showing Retrograde Assemblages: 6kb

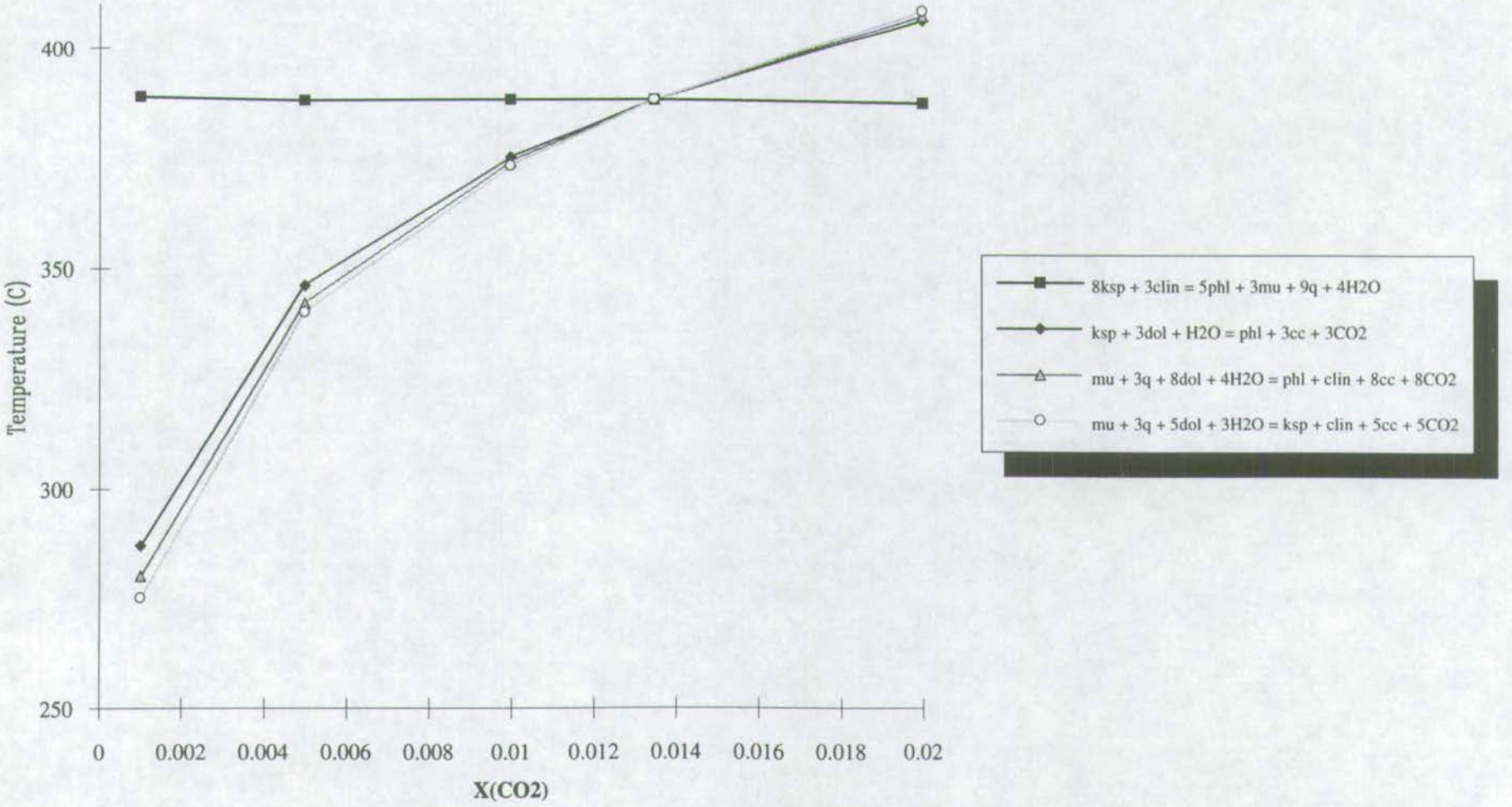

filled fractures which transect bedding and acted as feeders for laterally extensive, dolomitisation of individual beds (figure 4.7). Graham (*unpublished data*) and Greig (1984) has shown that the development of K-fsp + dol + chl + qz is associated with retrograde high-$\delta^{18}O$ fluids (table 3.2). Fein et al. (1993) have shown that isotopic alteration fronts correlate spatially with mineralogical alteration fronts (defined by the development of dolomite).

Fein *et al.* (1993) undertook a comprehensive study of retrograde fluid infiltration of the Loch Tay Limestone, at Stonefield Castle, near Tarbert, Loch Fyne. They implemented fluid inclusion studies, back-scattered electron imaging and the recently developed isotope front advection model of Bickle & McKenzie (1987) to establish the composition and grain-scale flow mechanisms of the causitive retrograde fluid, and the temperature at which infiltration occurred.

(i) The Composition of the Causitive Retrograde Fluid

Fein *et al.* (1993) determined the composition of the causitive retrograde fluid by analysis of fluid inclusions trapped within vein quartz and found that the fluid was CO_2-poor but rich in dissolved salts.

(ii) Grain-scale Flow Mechanisms of the Causitive Retrograde Fluid

Fein *et al.* (1993) recognised the pervasive development of dolomite at grain edges and triple junctions between calcite grains, near the termination of individual layer parallel dolomitic veins. They attributed this observation to grain-edge fluid flow. Furthermore, Fein et al. (1993) noted that the lateral extent of dolomite development in individual beds was extremely variable. They identified a positive correlation between the distance which the mineral alteration front was advected and the vol.% calcite in the bed (figure 4.9). They inferred that this correlation was in response to a mineralogical control of fluid flow. A calcite-rich rock was clearly more permeable than a quartz-rich rock. Two possibilities arise:

Figure 4.8: Photograph showing Layer Parallel Ankeritic Veining of the Loch Tay LImestone

Locality:
Stonefield Castle, Tarbert, Loch Fyne
GR869 710

Scales:
Hammer (30cm)

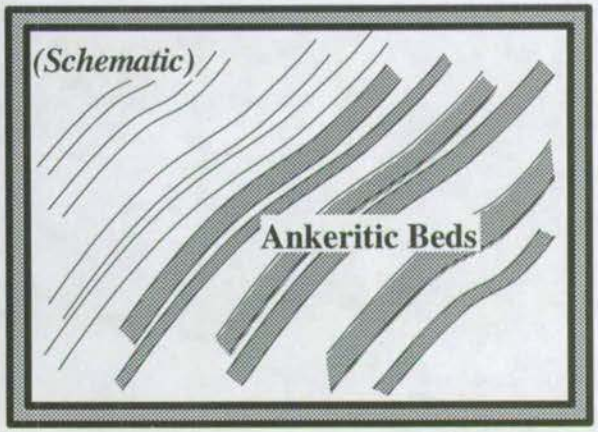

Figure 4.9: Plot of Advection Distance of Ankeritisation Front vs. Vol.% Calcite of Host

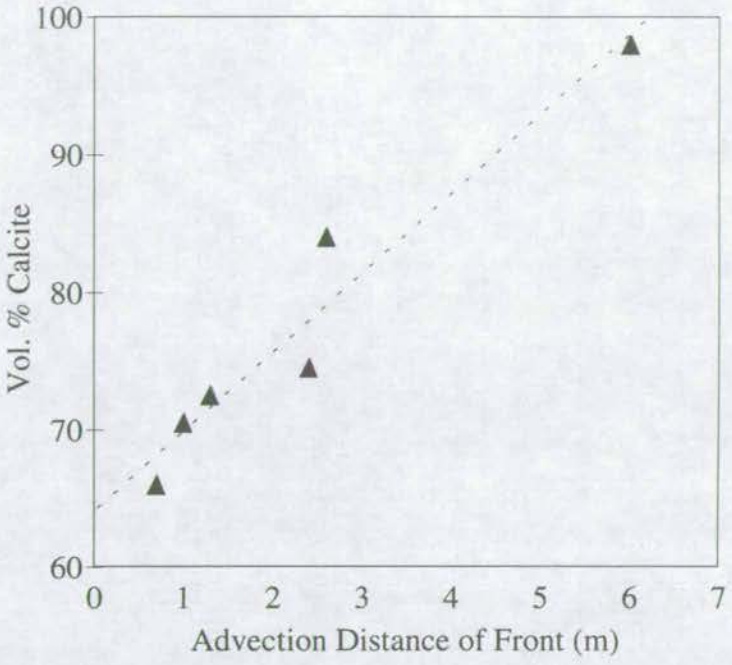

The above graph is a plot of the measured advection distance of the retrograde ankeritisation front against vol.% calcite estimated by modal point-counting. A strong positive correlation is visible, inferring that fluid flow is a function of rock mineralogy. From Fein *et al.* (1993).

(1) Firstly, retrograde fluid was clearly saturated with respect to dolomite and quartz because these phases are percipitated within veins. However fluid may have been undersaturated in calcite. Therefore where the retrograde fluid encountered calcite dissolution would occur enabling fluid flow, whereas quartz would behave as an impermeable barrier to fluid flow.

(2) An alternative model is that the calcite-fluid-calcite dihedral angle was less than 60° whereas the quartz-fluid-quartz dihedral angle was greater than 60°. This would result in fluid infiltration along calcite-calcite grain-edges only. Unfortunately, insufficient data is presently available to quantitatively substantiate this interpretation.

A second line of evidence which confirms the importance of rock-mineralogy in controlling the grain-scale mechanism of fluid flow is evident from the field observation that the above described pervasive infiltration is ***only*** developed in marbles, whereas carbonate-filled micro-cracks, record fracture-controlled fluid flow in adjacent metabasites.

(iii) Temperature of Retrograde Infiltration

The temperature at which retrograde infiltration occurred was constrained on the basis of fluid inclusion studies and closure temepratures to isotopic exchange. Fluid inclusion studies predicted temperatures in the range 200-400°C for retrograde infiltration. The isotopic shift measured in carbonates was not reflected in adjacent quartz grains and therefore retrograde infiltration occurred at temperatures below the closure temperature of quartz (300-400°C). Therefore temperatures of around 400°C for retrograde infiltration are consistent with both fluid inclusion studies and isotopic closure temperatures.

Ankerite Porphyroblast Growth

Disseminated growth of ankerite porphyroblasts in calc-phyllites and metabasites has been recognised in this study. Their petrogenesis is discussed in detail in sections 5.2.5 and 5.3.7, where it is concluded that they developed as a result of the same phase of retrograde fluid mobility which was responsible for the development of dol + Kfsp + chl + qz veins.

4.2.4 Relative Timing of Phases of Isotopic Modification

Isotopic modifications may not be independently correlated with specific phases of fluid infiltration. However, in the SW Scottish Highlands, isotopic modifications has been "tagged" to specific mineral and chemical alterations. The timing of such changes are unambiguously constrained by textural relations. Therefore, the relative timing of isotopic modifications has been constrained by correlation with mineral or chemical alterations, in the SW Highlands, as is summarised in table 4.2.

Table 4.2: Chronological Correlation of Isotopic Modification with Mineral and Chemical Alterations

InfiltrationPhase (Graham *et al.* (1983)	**Mineral or Chemical Alteration**	**Isotopic Modification**	**Isotopic Shift**	**Relative Timing**
Pre-Metamorphic	Spilitisation	Obscured by later isotopic modification		Pre-D_1
Syn-Metamorphic	Type I-III Mineral Zonation of Metabasites	Isotopic homogenisation of Metabasite Margins	5-7 → 10-12 ‰	Syn-D_1-D_2
Post-Metamorphic	K-fsp + Ank Veins Ank Porphyroblasts (section 5.2.5 & 5.3.7)	Isotopic modification spatially correlating with mineral alteration	10-12 → 16-20 ‰	Post-D_4

4.3 Conclusion

In this chapter qualitative observations pertaining to the fluid infiltration history of the Dalradian of the SW Scottish Highlands have been presented together with recent isotopic data (Graham *unpublished data*) in the framework of the qualitative model of SW Highland fluid infiltration history presented by Graham et al. (1983). A three stage fluid infiltration history emerges which is described as follows:

(1) Pre-metamorphic (pre-D_1) spilitisation of basic lithologies, associated with re-distribution of CaO and Na_2O and resulting in patchy enrichment in albite phenocrysts which are closely associated to epidote-rich segregations. Any associated isotopic modification has been obscured by syn-metamorphic isotopic modification;

(2) Syn-metamorphic (syn-D_1-D_2) infiltration of a CO_2-bearing hydrous fluid resulting in mineralogical (types I-III) and isotopic ($\delta^{18}O$ = 5 to 7‰ $\rightarrow$ $\delta^{18}O$ = 10 to 12‰) zonation of metabasites. Reaction and isotope fronts are advected simultaneously, however the isotopic front is advected an order of magnitude further than the reaction front.

(3) Post-metamorphic (post-D_4) fracture-controlled K-fsp + ank veining and more pervasive ank-porphyroblast development. Isotopic modification ($\delta^{18}O$ = 10 to 12‰ $\rightarrow$ $\delta^{18}O$ = 16 to 20‰) is spatially correlated with the development of ankerite.

This qualitative interpretation forms the framework for quantification of fluid fluxes and regional mapping of fluid flow in chapters 9, 10 and 11.

5. THE STUDY AREA

Lithological Descriptions

5.1 Introduction

In this chapter the major lithologies of the SW Scottish Highlands are described. Field descriptions, mineral descriptions and mineral analyses of the major lithologies will be reviewed in the context of their lithostratigraphic, deformational and metamorphic histories, so as to develop a lithological data-base for modelling of fluid flow in chapters 9, 10 and 11. The analytical techniques assumed in this chapter are described in detail in chapter 6.

5.2 Calc-Phyllites

5.2.1 Distribution of Calc Phyllites

Calc-phyllites are widespread throughout the SW Highlands. They form the predominant rock types of the Ardrishaig, Port Ellen (Craignish) and Mull of Oa Phyllite Groups (figure 3.2).

5.2.2 Field Relations of Calc-Phyllites

In the Port Ellen Phyllite Group, two types of calc-phyllite are developed. In the axial region of a minor antiform (the Port Ellen Anticline, figure 3.3), which is parasitic to the SE limb of the recumbent Islay Anticline, calc-phyllites are fine-grained, relatively psammitic and develop pronounced red/green banding, on a 1-2cm

scale, defined by the relative proportions of hematite and chlorite (figure 5.1a). Outwith the axial region of the minor antiform, calc-phyllites are fine-grained, variably psammitic, and pale grey-green in colour. The more psammitic layers are studded with 1-3mm diameter rusty ankeritic porphyroblasts (figure 5.1b). The more phyllitic layers are rich in ankeritic porphyroblasts, blebs and lenses. Ankeritic veinlets cross cut D_1-D_2 fabrics at Port Ellen.

In the Ardrishaig Phyllite Group, similar calc-phyllite types are developed. In the axial regions of the recumbent Ardrishaig Anticline, calc-phyllites are variably psammitic and generally a homogeneous grey-green in colour (figure 5.2). Calc-phyllites are interlayered with calc-psammites on scales varying from a few centimetres to several metres. The abundance and width of psammitic layers is highly variable, but generally increases with proximity to the Erins Quartzite. Calc-phyllites outwith the axial zone of the Ardrishaig Anticline, adjacent to the Erins Quartzite in the SE and the Crinan Grits in the NW, are generally ankeritic. Ankerites develop as large (1-5mm) rusty, porphyroblastic masses.

5.2.3 Mineralogy of Calc-Phyllites

Calc-phyllites of the SW Highlands are mineralogically homogeneous and characterised by the peak metamorphic mineral assemblage:

white mica + chlorite + quartz + calcite ± albite ± biotite

Typical accessory phases are:

rutile + ilmenite + hematite ± tourmaline

Retrograde phases are:

ankerite ± K-feldspar ± paragonite

Calc-phyllites commonly contain the equilibrium assemblages: **biotite + chlorite + calcite**, **albite + chlorite + calcite**, and **rutile + calcite + quartz** which define a very narrow field in P-T-X_{CO_2} space (figure 5.3). Calc-phyllites also contain

Figure 5.1(a): Photograph showing Port Ellen Calc-Phyllites with Red/Green banding. S1-S2 foliation is near parallel to bedding.

Locality: Port Ellen, Islay GR367 452 **Scale:** 50p piece

Figure 5.1(b): Photograph showing the development of Ankerite Porphyroblasts in Port Ellen Calc-Phyllites

Locality: Port Ellen, Islay GR367 452 **Scale:** 20p piece

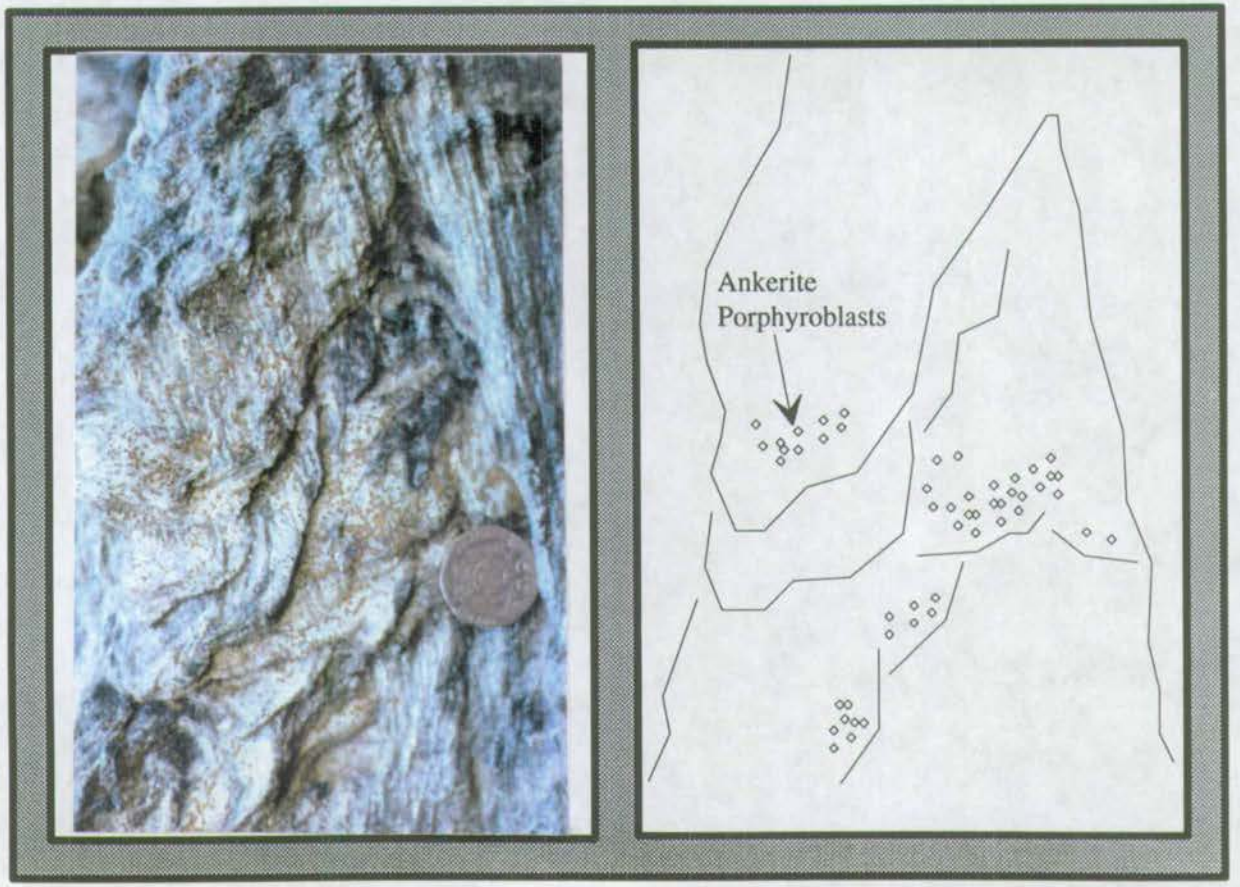

Figure 5.2: Photograph Showing Ardrishaig Calc-Phyllites with Inter-layered Psammites and Phyllites. S1-S2 Foliation is near parallel to Bedding.

Locality: Port Ban, Knapdale GR706 656 **Scale:** Hammer (30cm)

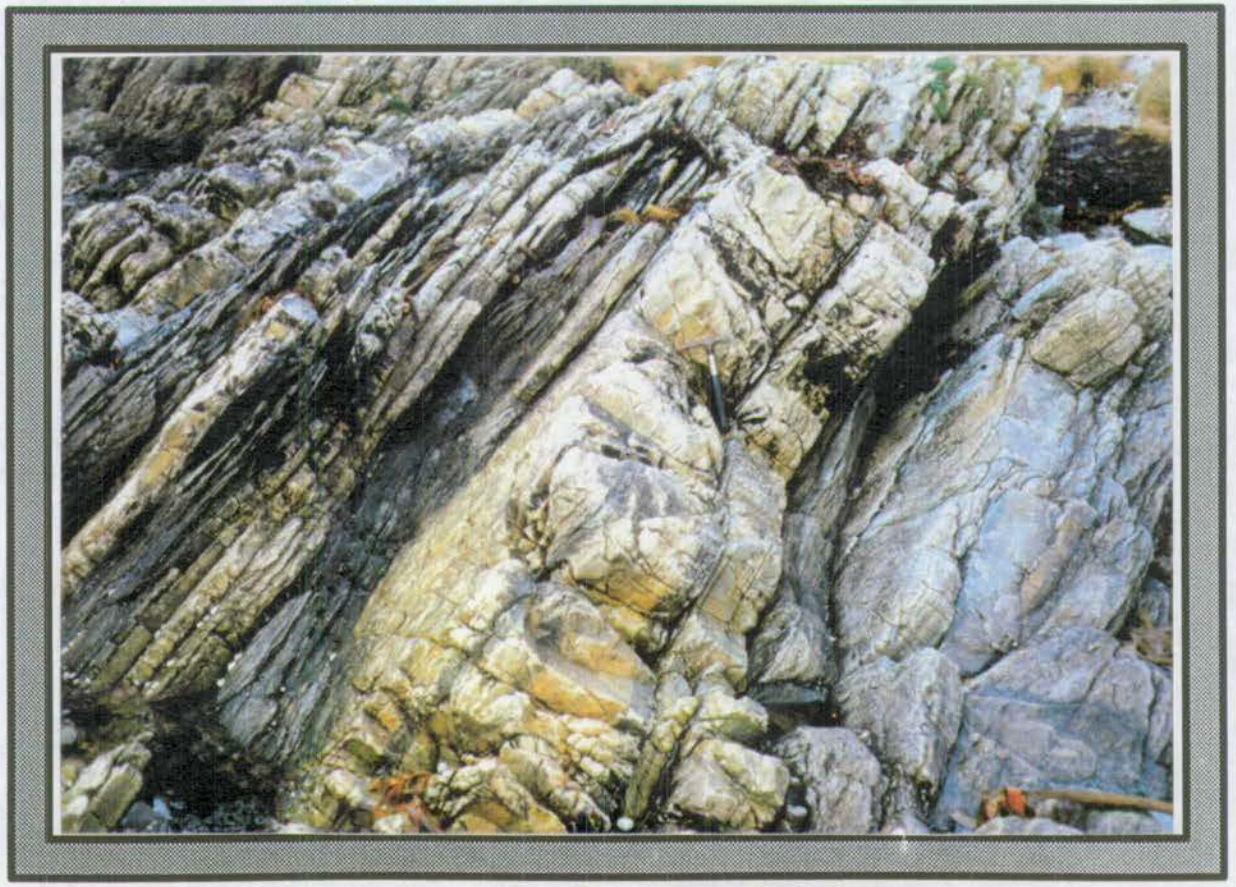

Figure 5.3(a): T-X(CO2) Section : NKCMASH+CO2 : P=10kb: THERMOCALC

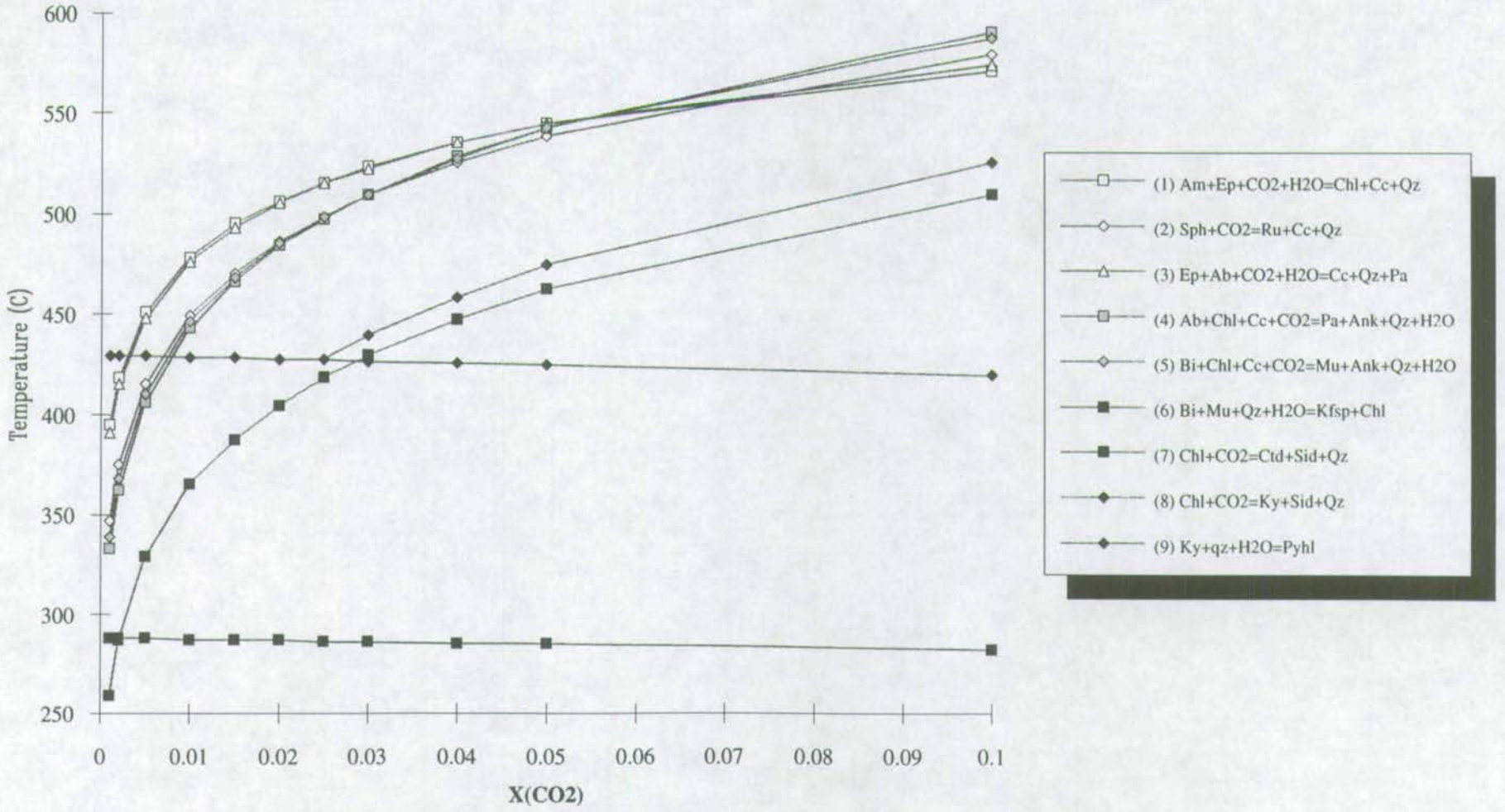

Figure 5.3(a): T-X(CO2) Section : NKCMASH+CO2 : P=10kb: THERMOCALC

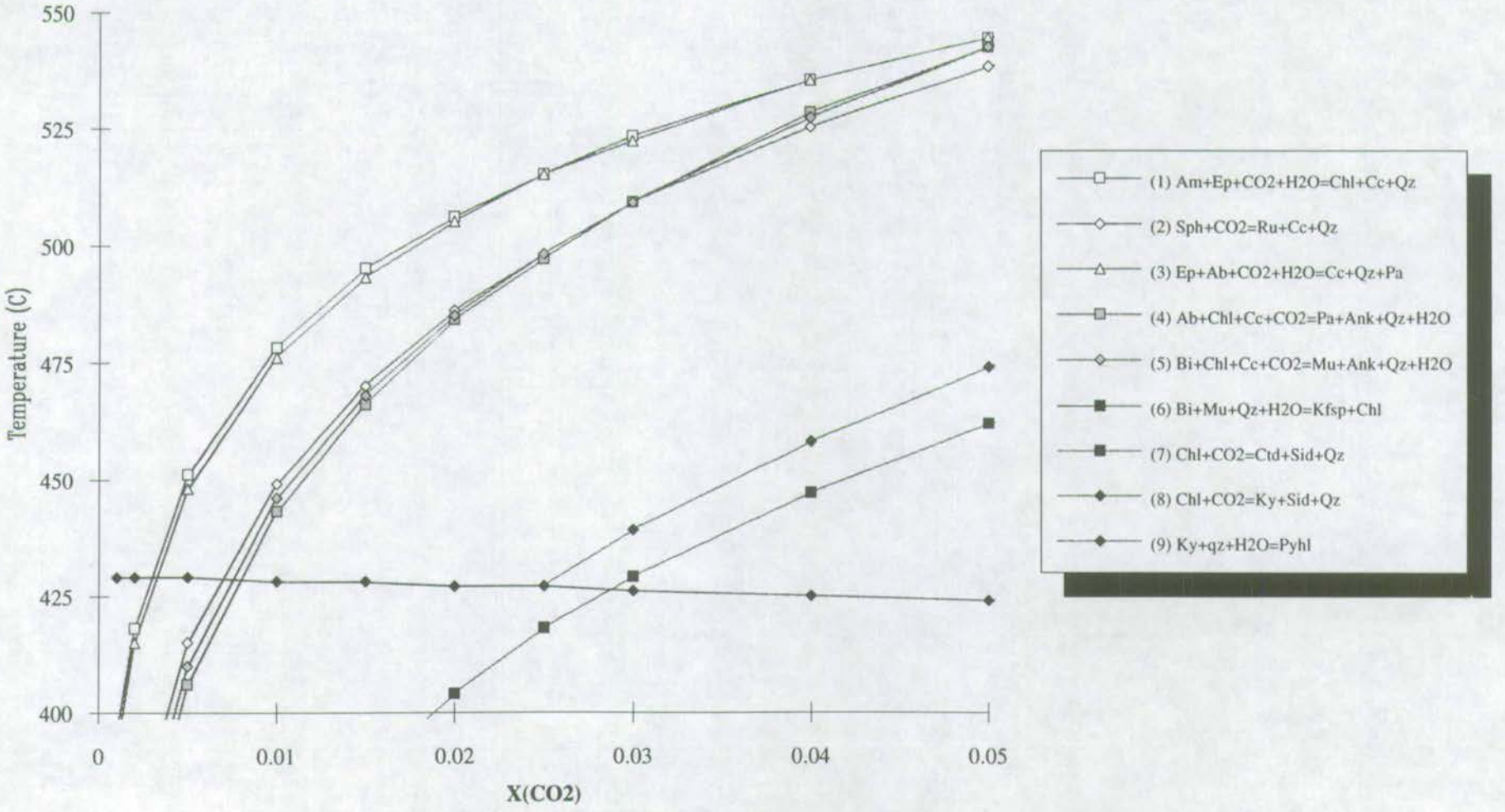

Figure 5.3(a): T-X(CO2) Section : NKCMASH+CO2 : P=10kb: THERMOCALC

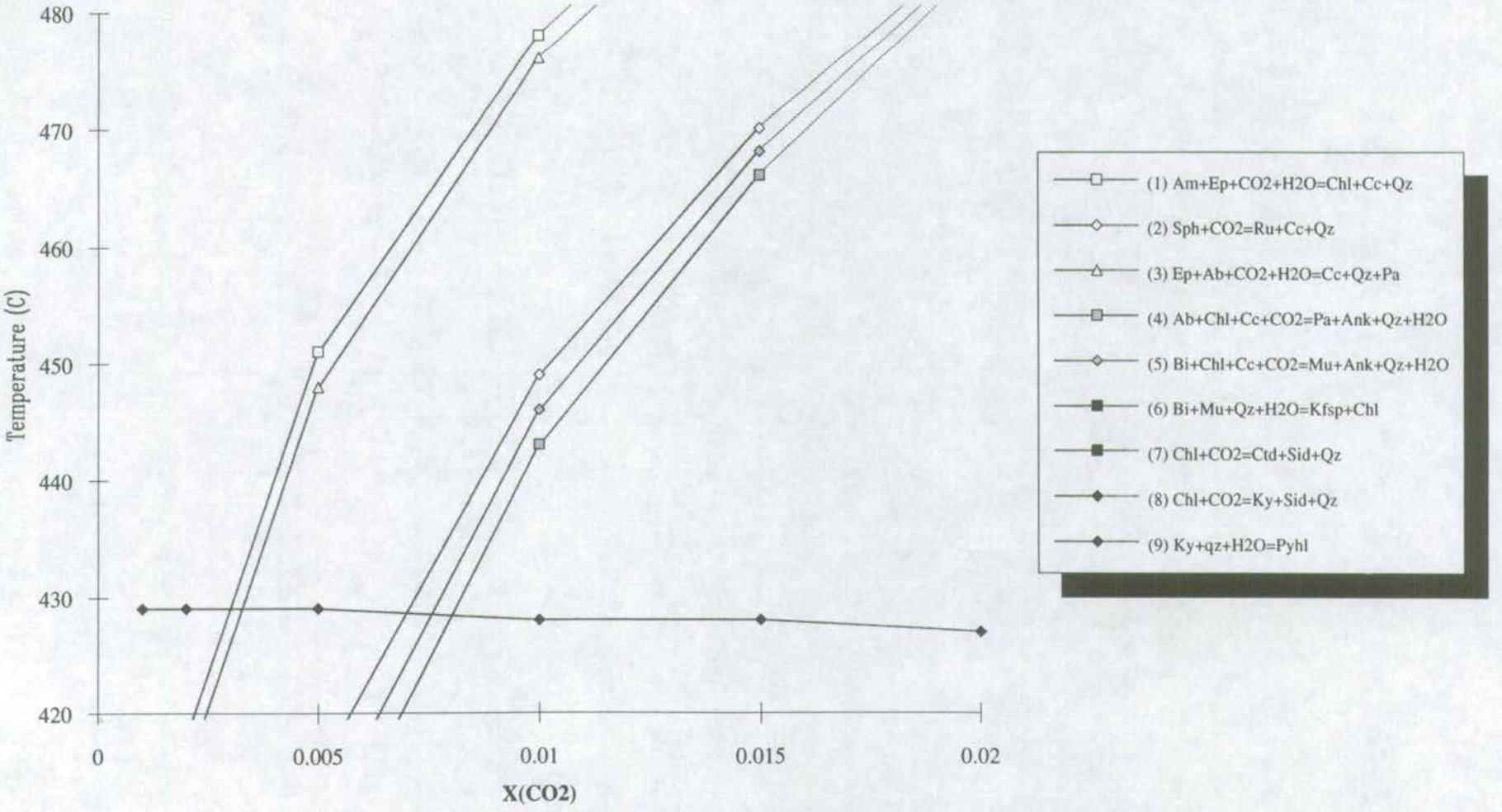

Figure 5.3(b): Divariance of Reaction (1): P=10kb

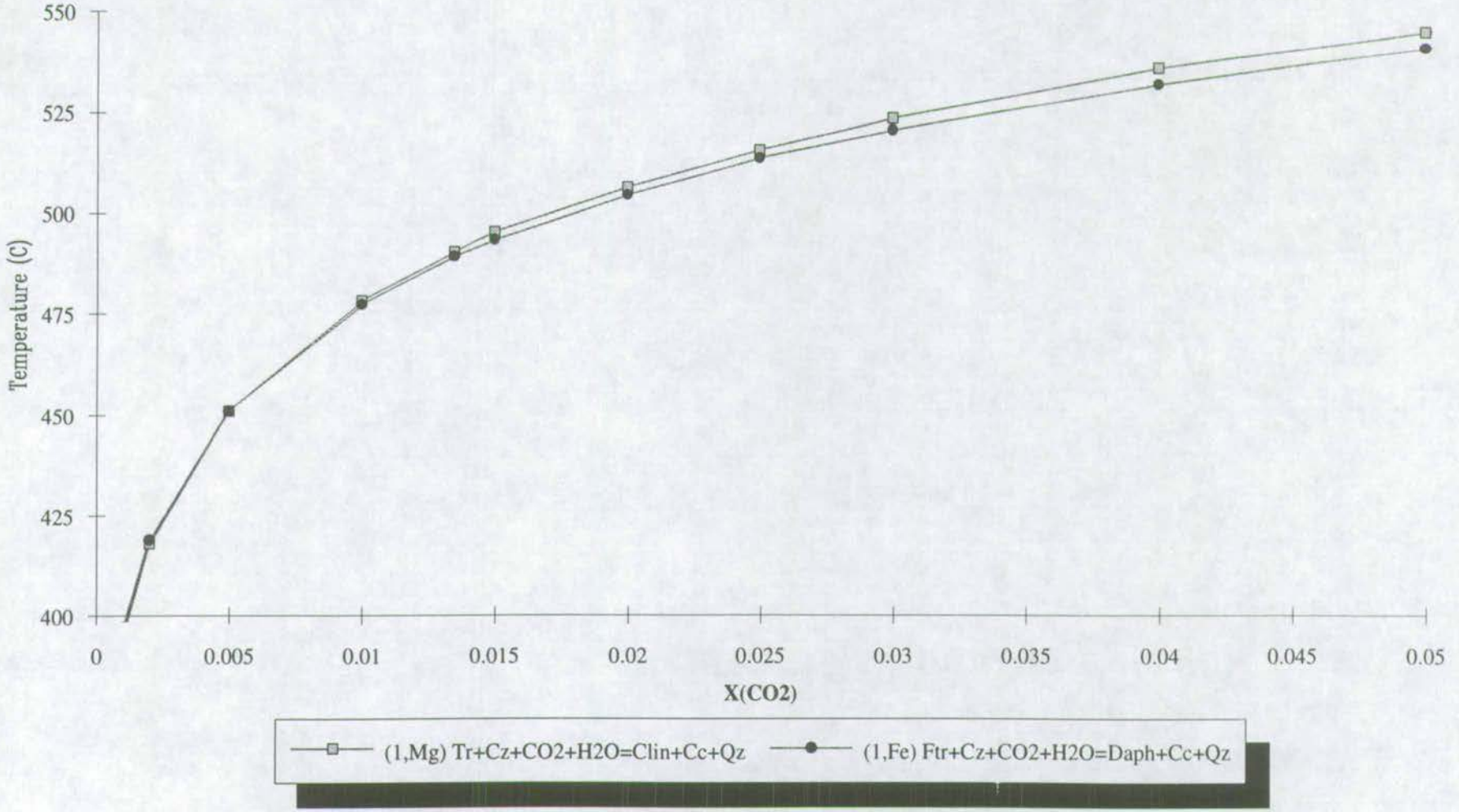

Figure 5.3(c): Divariance of Reaction (4): P=10kb

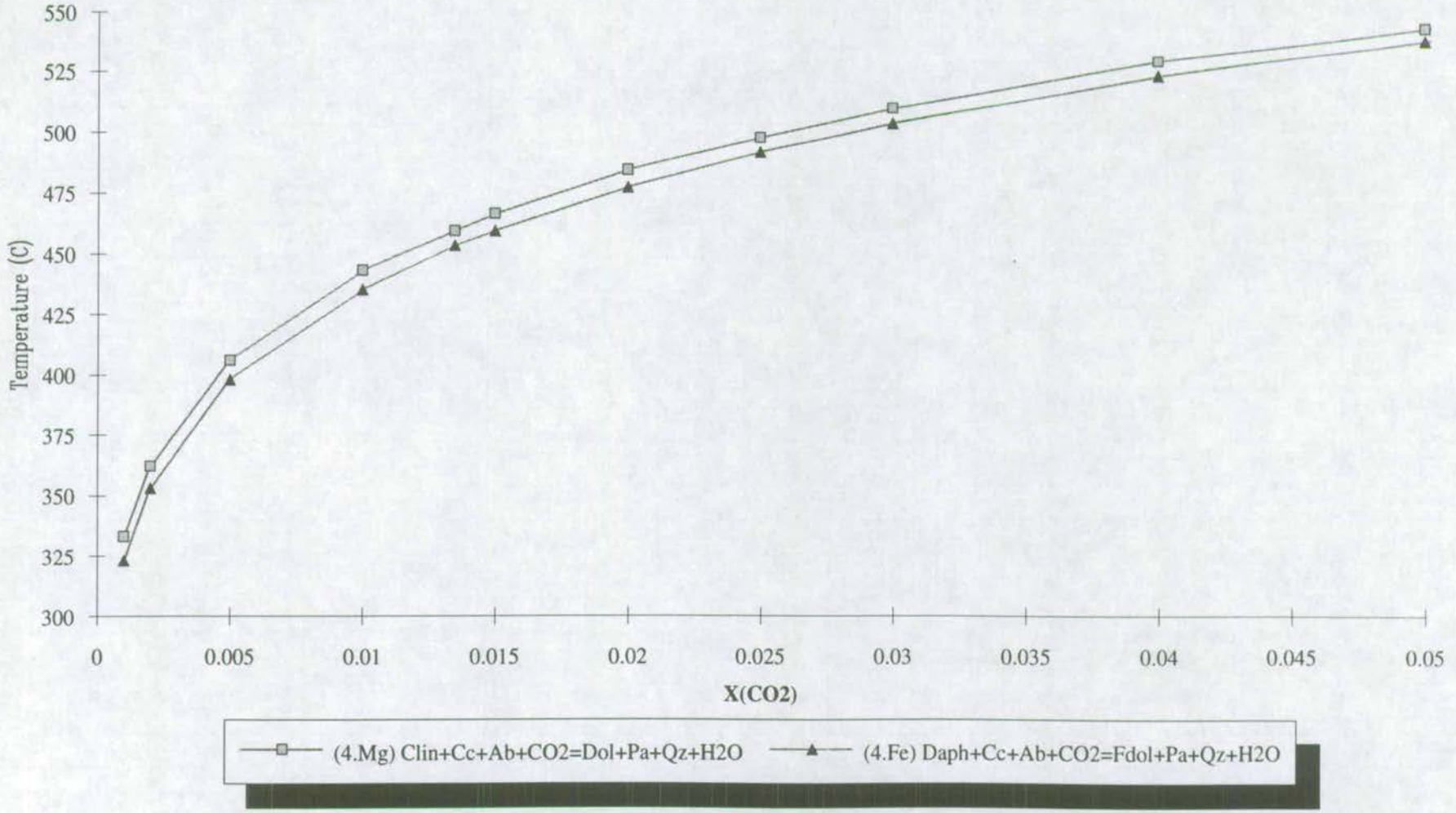

Figure 5.3(d): Divariance of Reaction (5): P=10kb

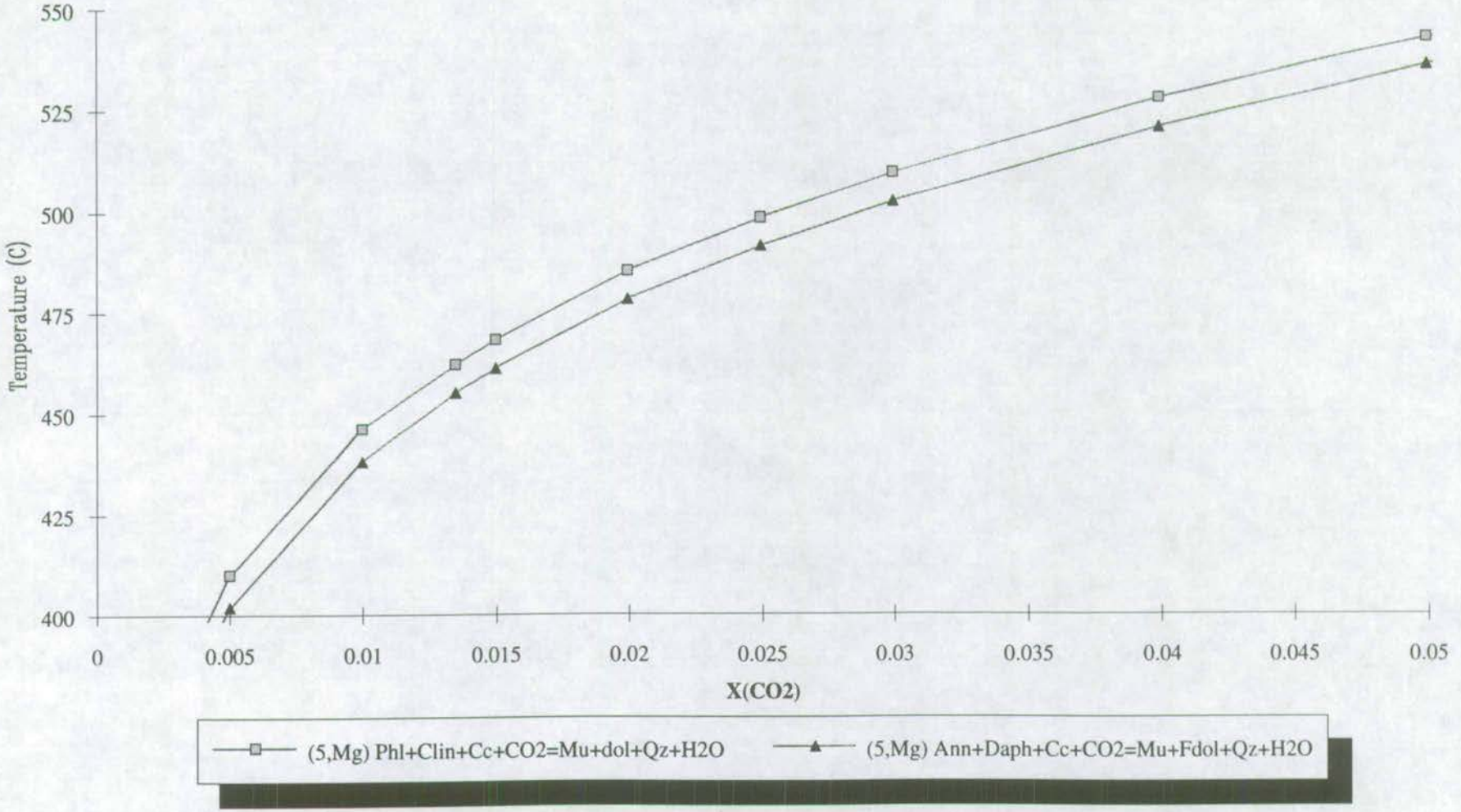

Figure 5.3(e): Divariance of Reaction (7):P=10kb

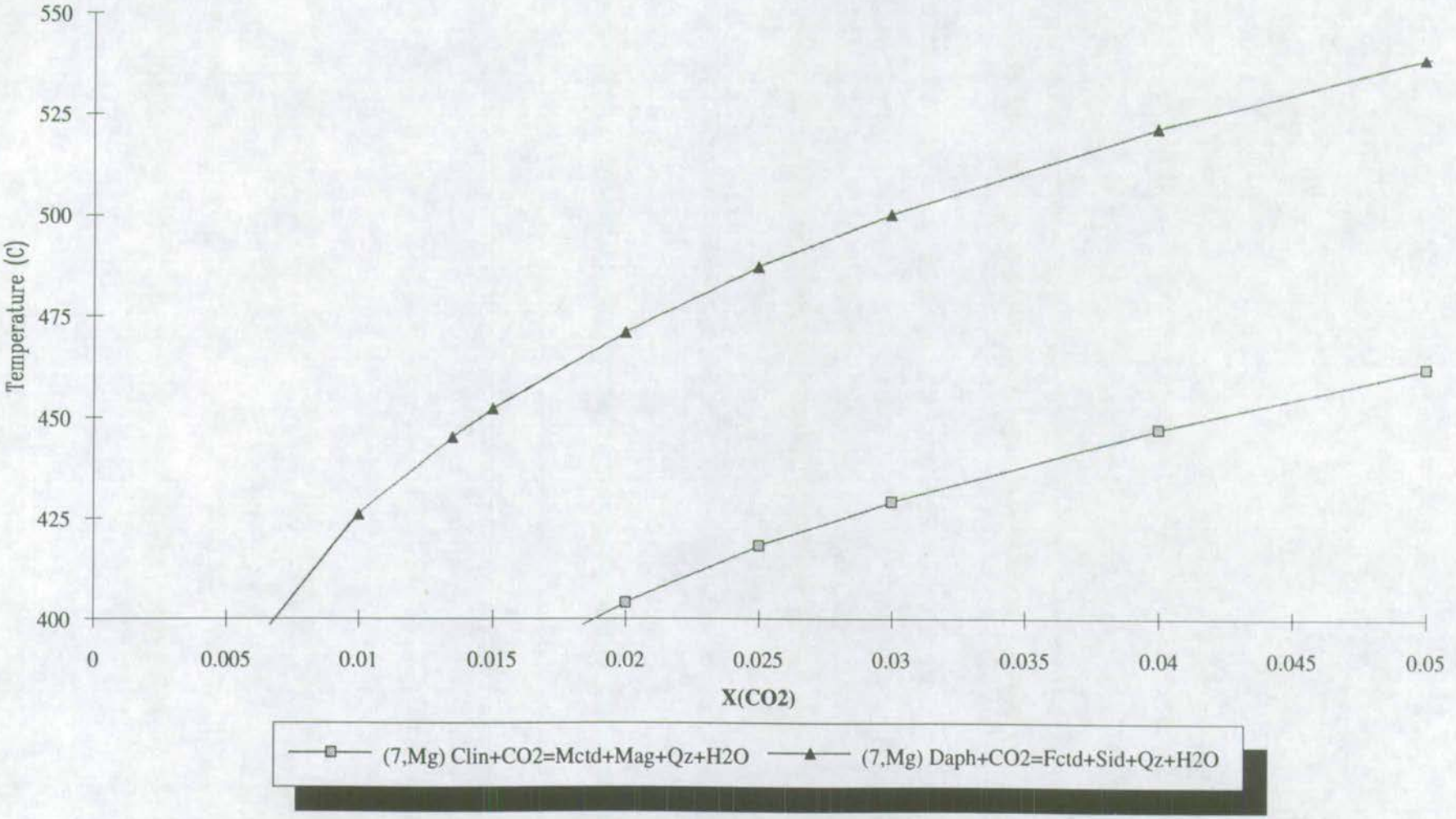

Figure 5.3(f): Divariance of Reaction (8): P=10kb

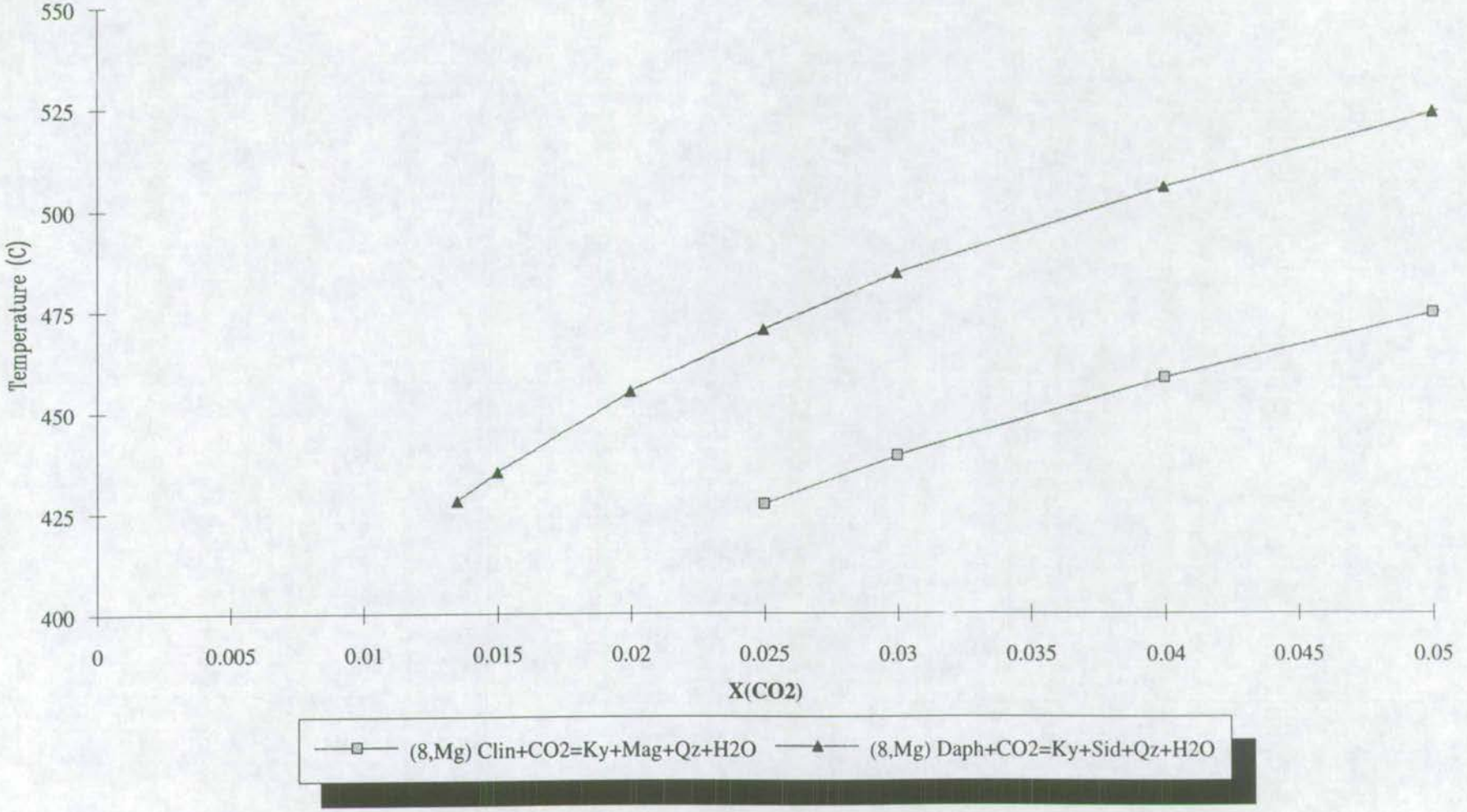

muscovite and, as described above, ankerite. Typical calc-phyllite mineral assemblages are listed in table 5.1.

Table 5.1: Representative Mineral Assemblages of P1-Type Calc-phyllites

	Port Ellen Phyllites			*Ardrishaig Phyllites*		
Sample	**89PE21**	**91CMG05**	**91PE120**	**91KB25**	**92CMG03**	**91KB55**
Mineral						
Muscovite	+	+	+	+	+	+
Chlorite	+	+	+	+	+	+
Calcite	+	+	-	+	+	+
Quartz	+	+	+	+	+	+
Albite	+	+	+	+	-	+
Biotite	-	+	-	-	+	-
Rutile	-	+	*	-	*	*
Ilm/Hem	+	-	-	-	-	*
Tourmaline	-	-	-	-	*	-
Ankerite	-	-	+	-	-	+
K-feldspar	-	-	-	-	-	+
Paragonite	-	-	*	-	-	-

(+) = present, (*) = traces and (-) = absent

89-PE-21 was collected at the core of the Port Ellen Anticline (GR366 448). CMG-91-05 was collected from close proximity to the Port Ellen Anticline (GR366 450). 91-PE-120 was collected about 100m NNW of the Caledonian Macbrayne ferry terminal within the Port Ellen phyllites. GR364 453). 91-KB-25, CMG-92-03 and 91-KB-55 were collected from the SE limb of the Ardrishaig Anticline (GR707 660, GR708 672 and GR702 639, respectively).

5.2.4 Petrogenesis and Deformation of Calc-phyllites: Phyllosilicates

Alignment of phyllosilicates defines a strong penetrative s_1-s_2 schistosity which is axial planar to the regional D_1-D_2 fold structures (section 3.4.1). This fabric is later refolded resulting in the development of f_4 box-folds (figure 3.4) which are approximately 0.5-1.0m in wavelength and are parasitic to the regional D_4 fold structures (section 3.4.1). Later refolding of the s_1-s_2 fabrics also resulted in the development of an s_4 crenulation fabric (figure 3.4). It is therefore apparent that phyllo-silicates grew before or during D_1-D_2 deformation.

5.2.5 Petrogenesis and Deformation of Calc-Phyllites: Porphyroblast Phases

The only porphyroblastic phases which generally develop in the calc-phyllite lithologies, described above, are ankerite and, more rarely, albite. Garnet is observed in higher grade (epidote-amphibolite facies) lithologies in SE Knapdale and kyanite is locally developed in peraluminous phyllitic intercalations in the Islay-Jura Quartzite (section 5.5).

Albite Porphyroblasts

Albite porphyroblasts are developed in a few samples in the Port Ellen phyllites (figure 5.4) in association with muscovite + chlorite + calcite + quartz ± rutile (table 5.1). Where present, albite porphyroblasts contain inclusion trails of phyllosilicates which are aligned parallel to the s_1-s_2 fabric outwith the porphyroblasts. Porphyroblasts are rarely rotated, however they are quite clearly deformed by folding and crenulation associated with D_4-deformation.

Ankerite Porphyroblasts

The petrogenesis of the more abundant ankerite porphyroblasts is not immediately obvious. Ankerite porphyroblasts and porphyroblastic masses are developed extensively in the Port Ellen Phyllites, outwith the axial zone of the Port Ellen Anticline, and in the Ardrishaig Phyllites, outwith the axial zone of the Ardrishaig Anticline.

A clearer appreciation of the petrogenetic evolution and timing of ankerite growth was developed by a combination of field, optical, geochemical, thermodynamic, geothermometric and stable isotopic data. Resultant observations, measurements and data, together with pertinent interpretations are listed as follows:

Figure 5.4: Photomicrograph of Deformed Albite Porphyroblasts in the Port Ellen Phyllites

Locality: Port Ellen, Islay GR364 452 **Magnification:** X100

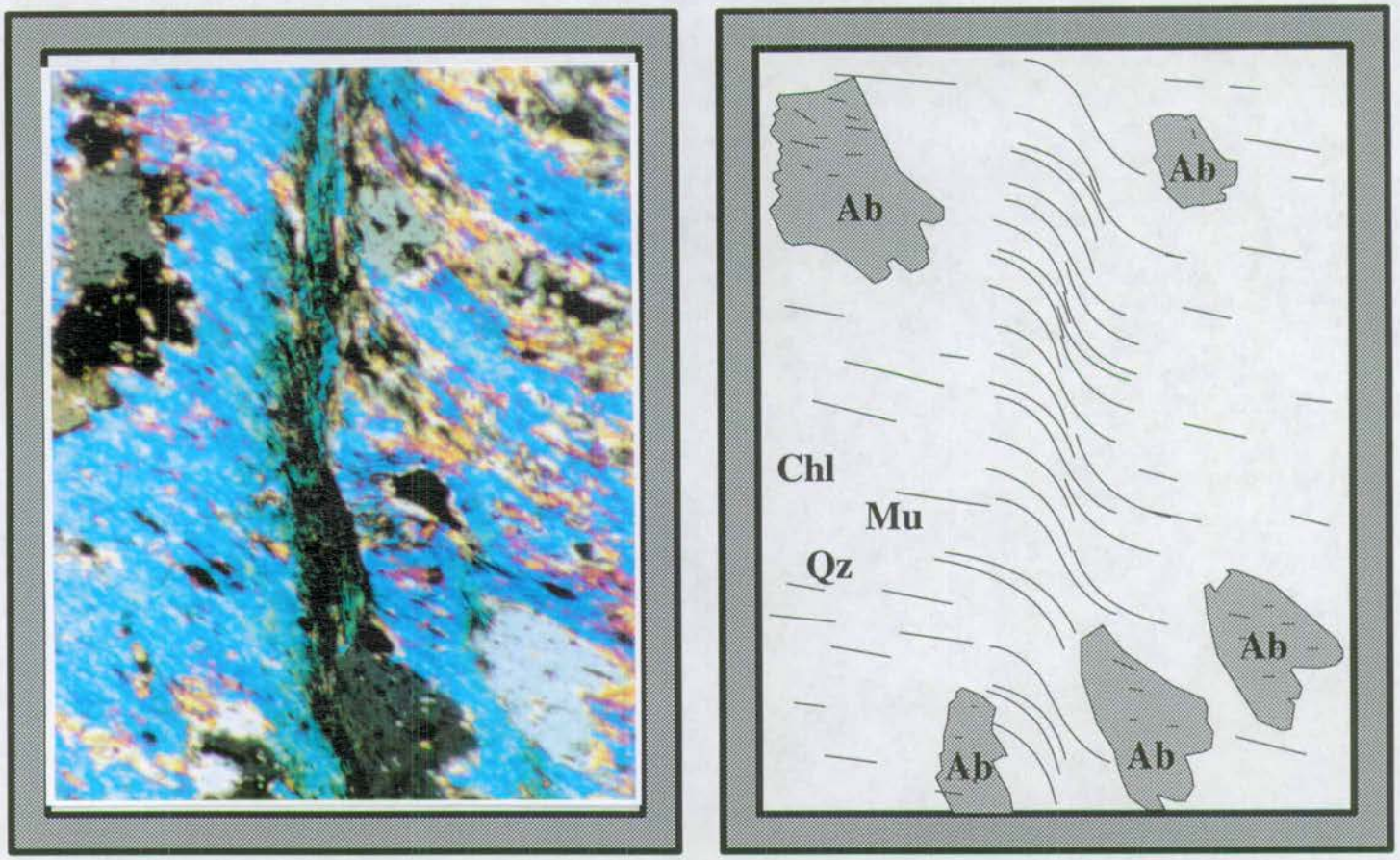

(i) Field Observations and Interpretations

- Extensive ankerite porphyroblast development is often spatially coincident with ankerite + K-feldspar + chlorite + quartz veins which unequivocally cross cut D_1-D_4 fabrics (figure 5.5), implying that porphyroblasts developed after D_1-D_4 deformation.
- On a regional-scale ankerite porphyroblast development is most extensive outwith the axial-zones of the regional recumbent Ardrishaig Anticline and the local Port Ellen Anticline, implying that there is some structural or lithological control affecting their petrogenesis.

(ii) Optical and Back-scattered Electron Image Observations and Interpretations

- Aggregates of ankerite porphyroblasts are observed to originate in veinlets which cross cut D_1-D_4 fabrics.
- Inclusion trails within individual ankerite porphyroblasts consistently mimic the D_1-D_4 fabrics outwith the porphyroblasts (figure 5.6a-f).
- Ankerite porphyroblasts are not deformed by D_1-D_4 folding or shearing (figure 5.6d-f).

These observations are consistent with ankerite growth having post-dated D_1-D_4 deformation.

- Individual ankerite porphyroblasts develop as large skeletal grains where ankerite growth is largely along grain-edges (figure 5.6a, c and d). Such textures imply that kinetic impedance of growth and nucleation were important controlling factors during ankerite development.

(iii) Geochemical Data and Interpretations

- The composition of SW Highland ankerites is extremely variable. Ankerites define a broad, scattered compositional field on a Ca-Mg-Fe plot (figure 5.7a). Compositions range from Mg-rich dolomite to Fe-rich ankerite. Selected ankerites from calc-phyllites which are intercalated within the Islay-Jura quartzite at Carraig

Figure 5.5: Photograph of an Ankerite vein transecting phyllite bedding and D1-D2 fabric. S1-S2 is near parallel to bedding.

Locality: Port Ellen, Islay GR364 447 **Scale:** 50p piece

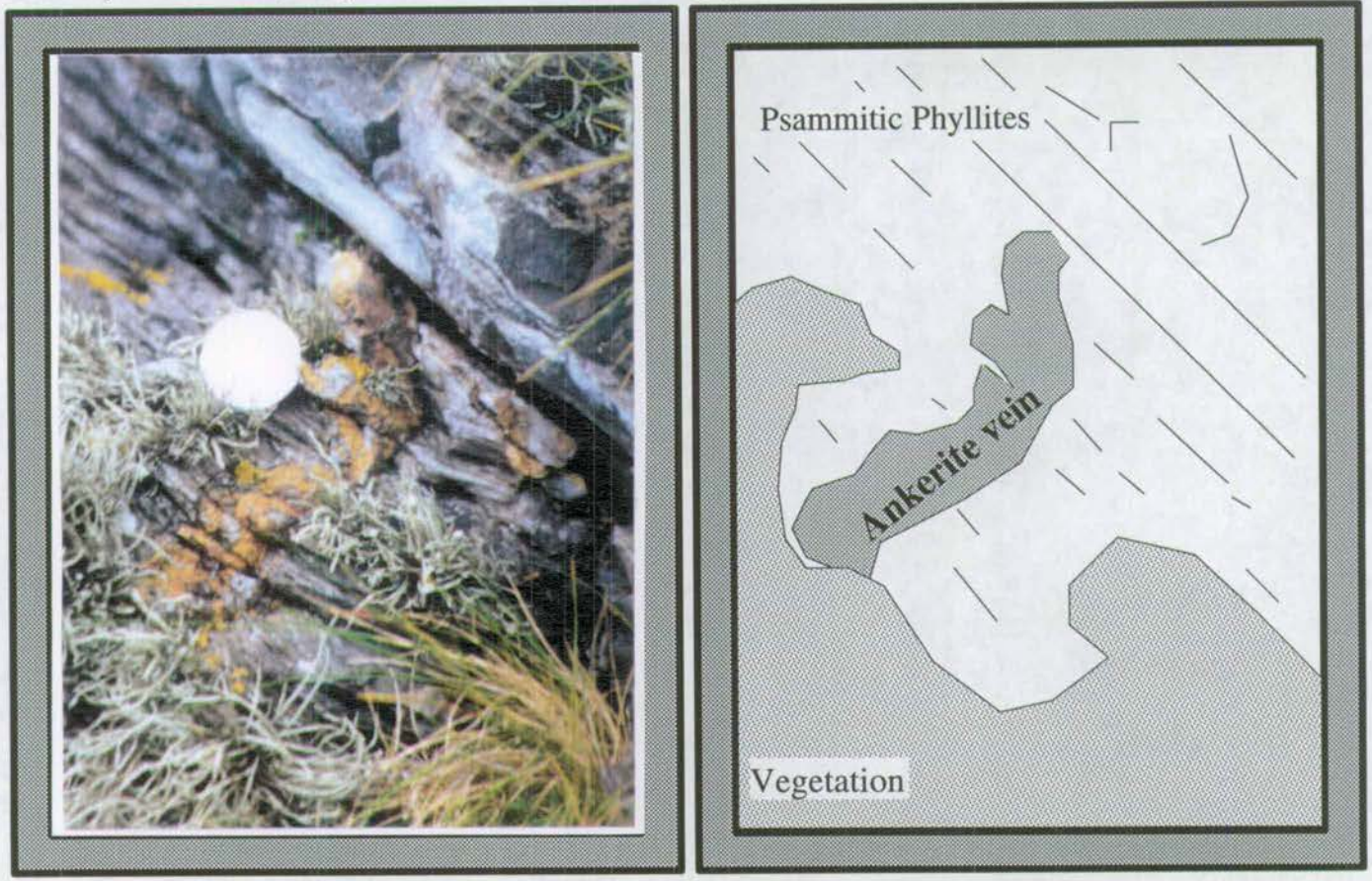

Figure 5.6(b): Back-Scattered electron image of Ankerite (1) in figure 5.6(a).

Locality:
Port Ellen, Islay GR364 452

Magnification:
x2000

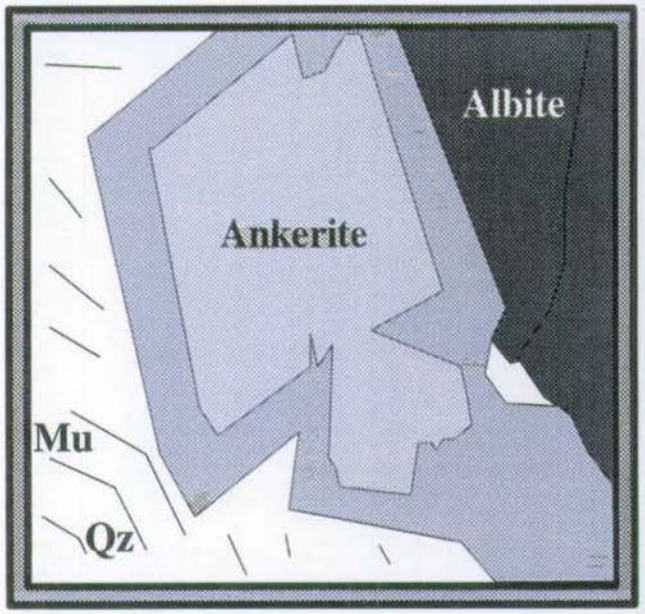

A crenulated S1-S2 fabric is continuous through the euhedral ankerite porphyroblast.

Figure 5.6(c): Back-Scattered electron image of Ankerite (2) in figure 5.6(a).

Locality:
Port Ellen, Islay GR364 452

Magnification:
x1000

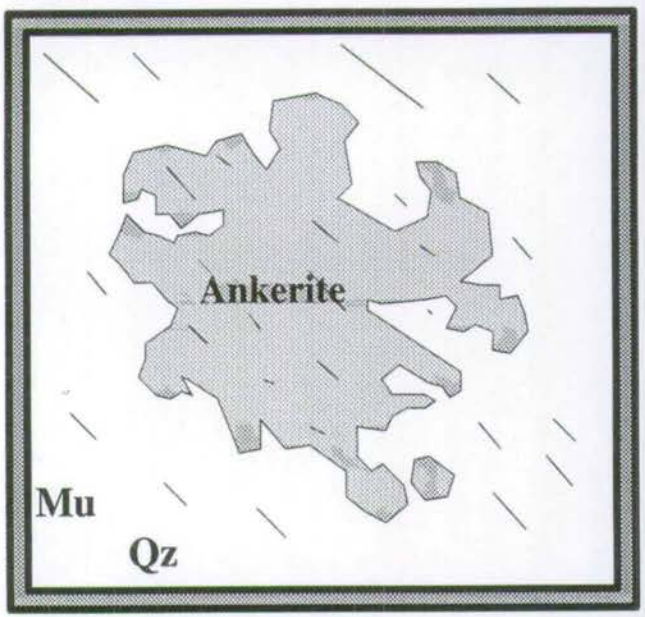

A crenulated S1-S2 fabric is continuous through the skeletal ankerite porphyroblast.

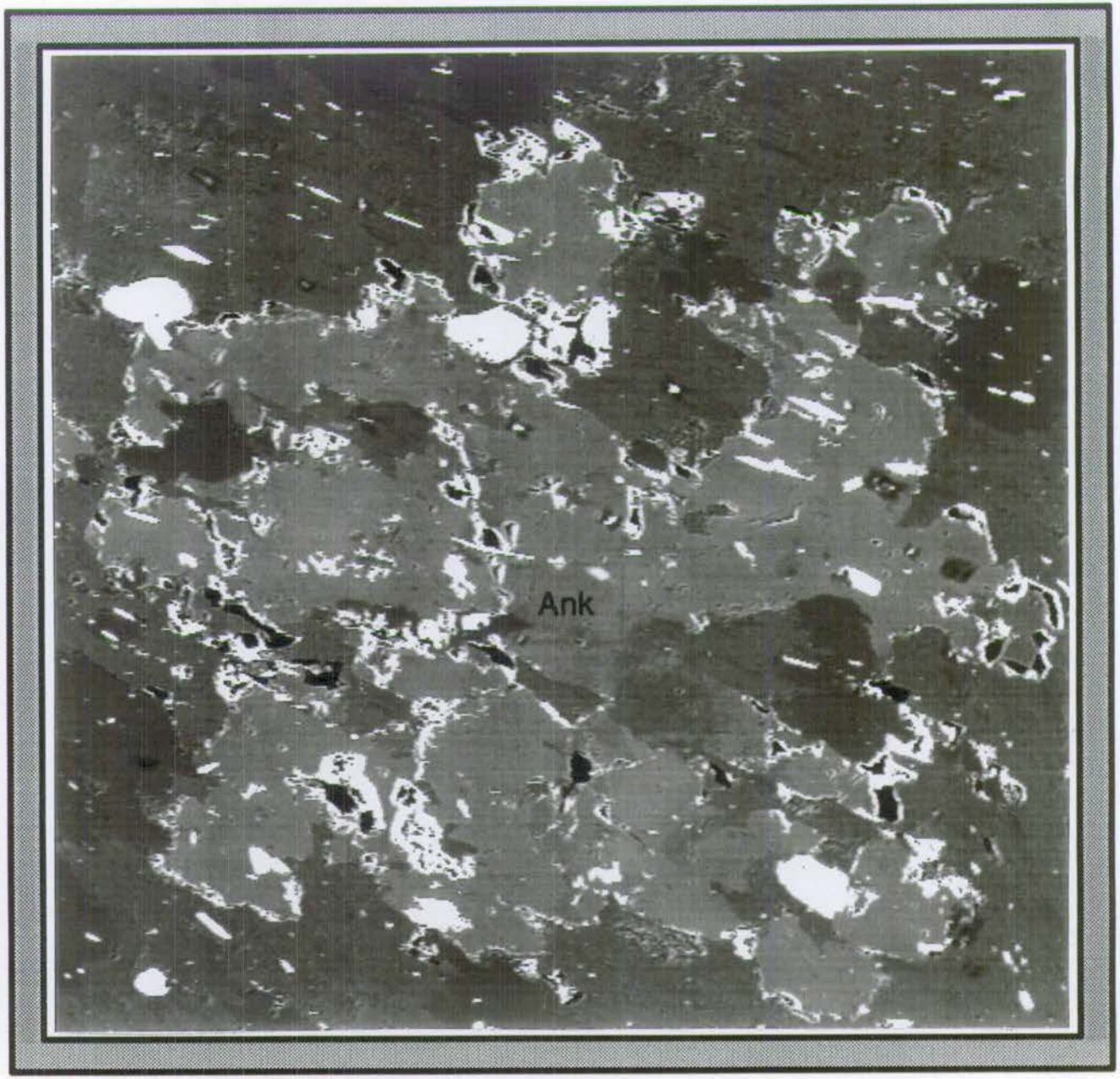

Figure 5.6(d): Photomicrograph of Euhedral and Skeletal Ankerite Porphyroblasts which over-grow a crenulated S1-S2 fabric.

Locality: Port Ellen, Islay GR364 452 **Magnification:** x100

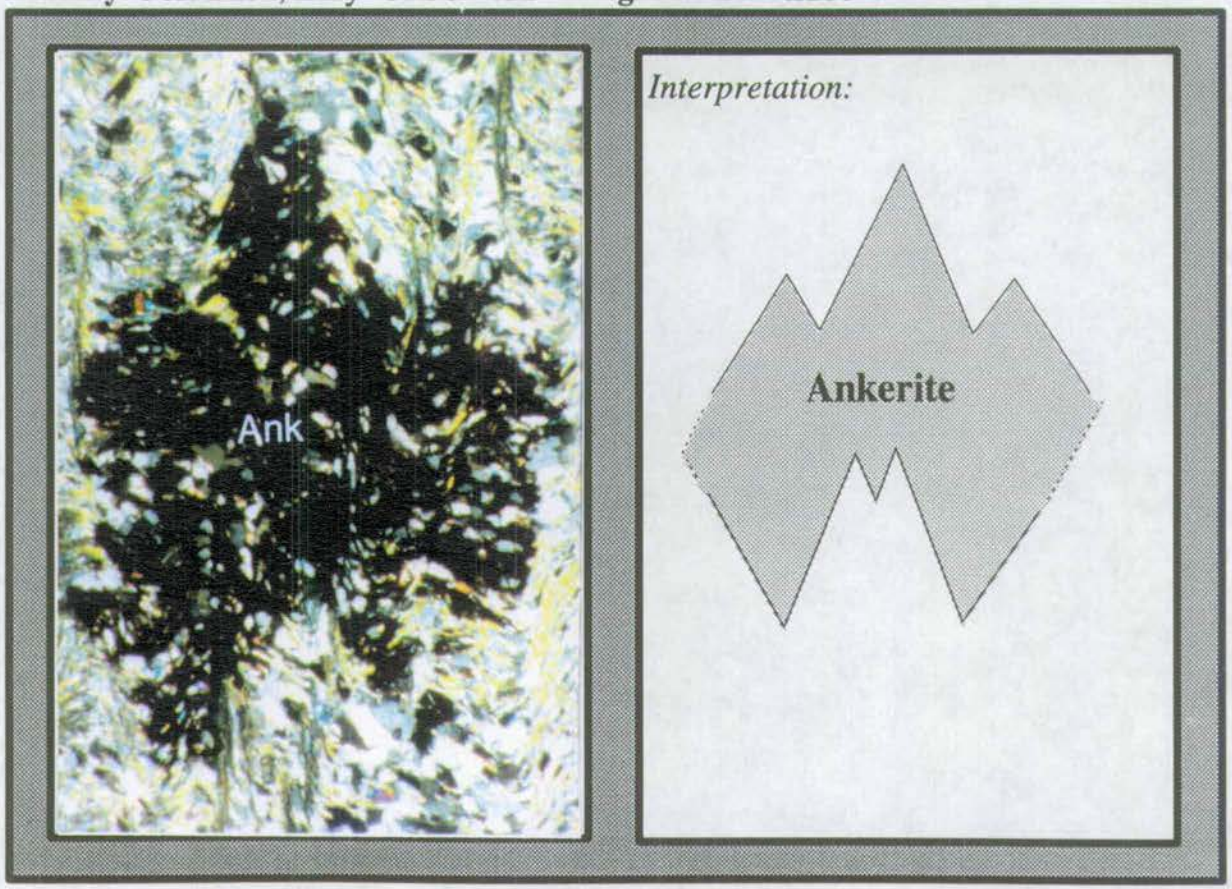

Figure 5.6(e): Photomicrograph of Euhedral Ankerite Porphyroblasts which over-grow a crenulated S1-S2 fabric.

Locality: Port Ellen, Islay GR364 452 **Magnification:** x100

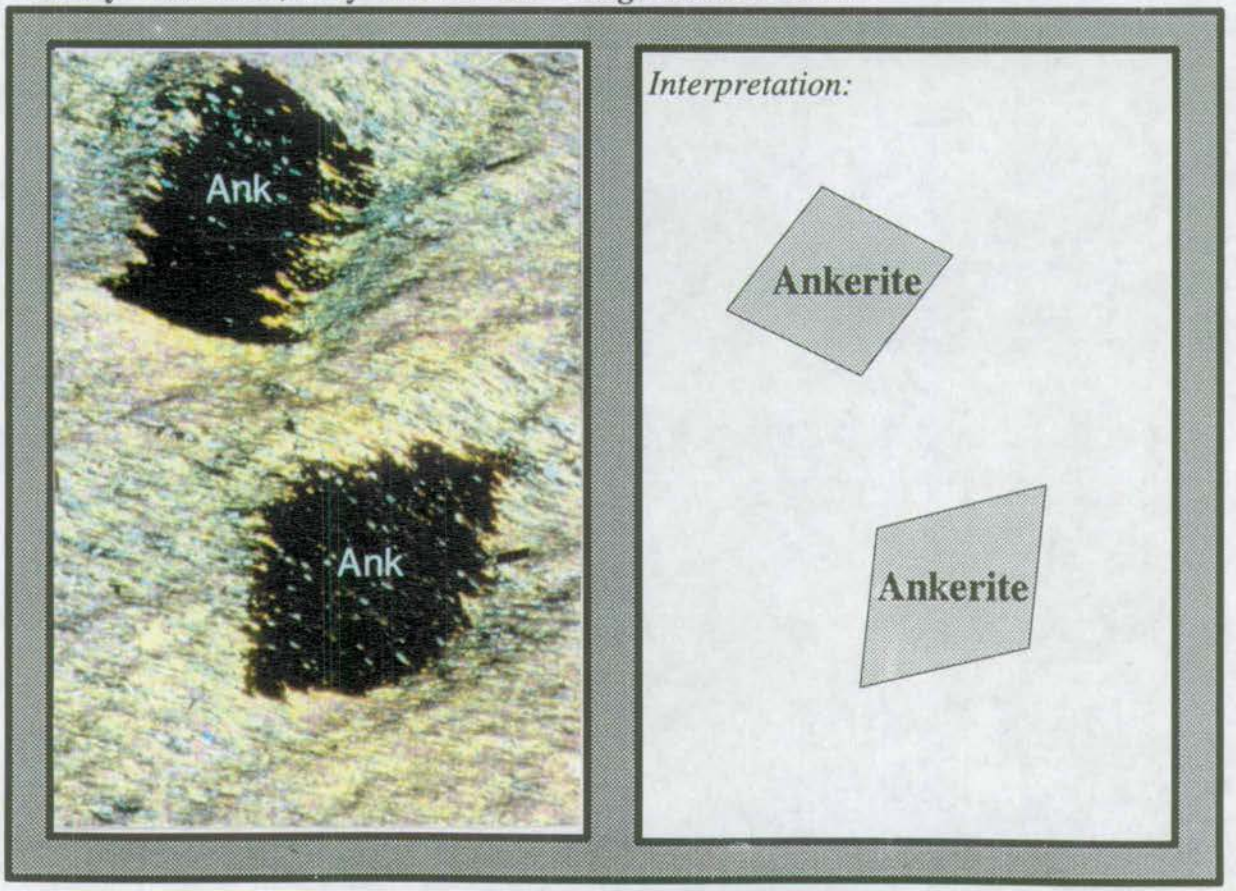

Figure 5.6(f): Photomicrograph of Euhedral Ankerite Porphyroblasts which over-grow a crenulated S1-S2 fabric.

Locality: Carraig Fhada, Islay GR349 443 **Magnification:** x100

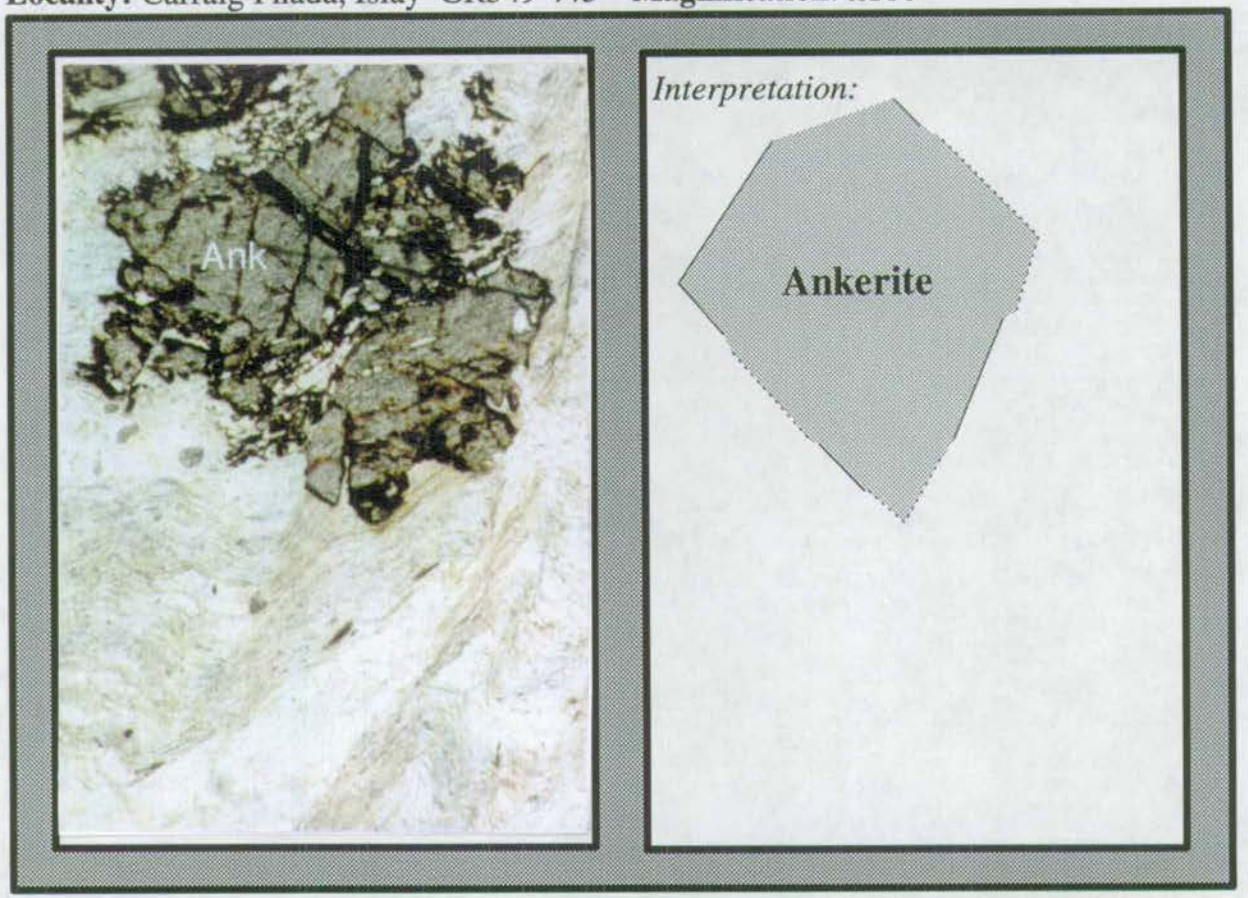

Figure 5.7(a): Ca-Mg-Fe Plot of SW Highland Carbonates

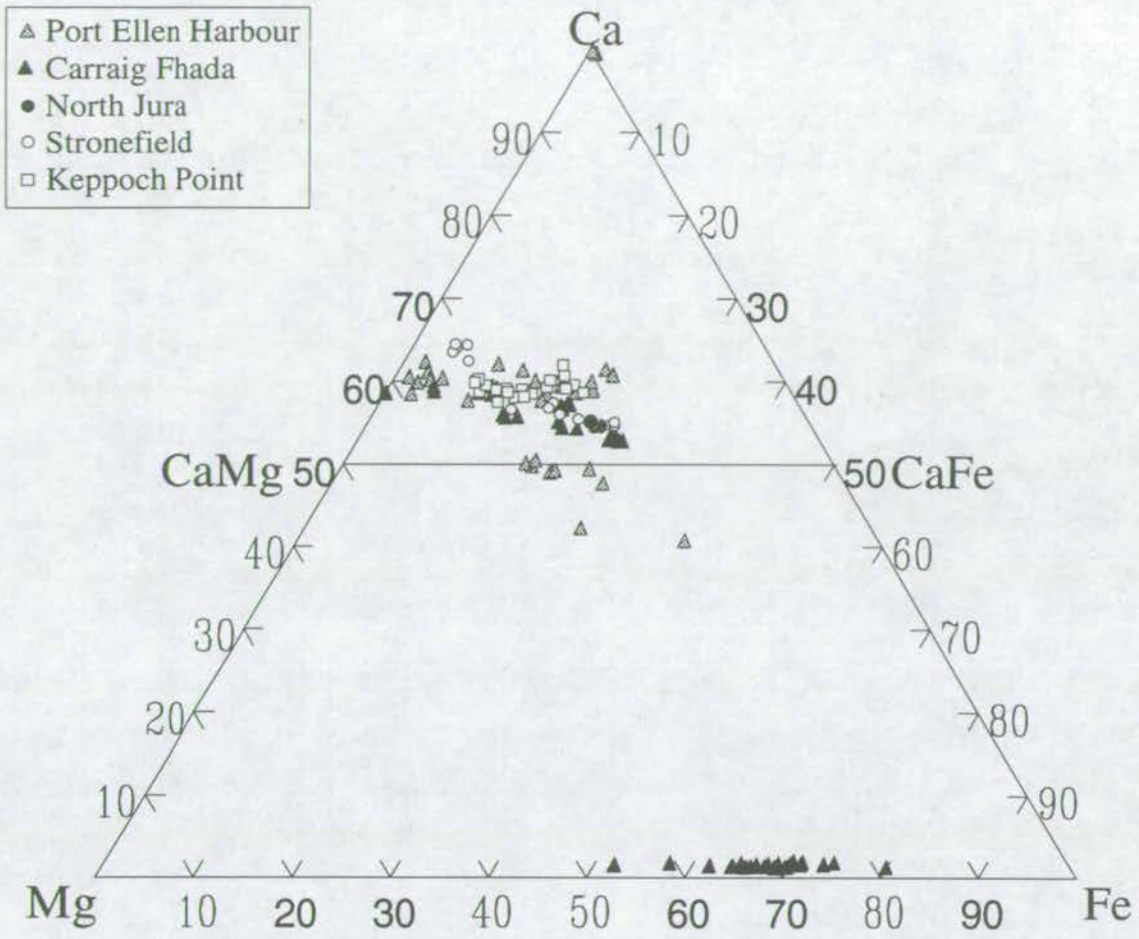

The above plot shows carbonates from different localities in the SW Highlands. In particular the above plot emphasises the broad scattered composition field which is occupied by ankerites.

Figure 5.7(b): Ca-Mg-Fe Plot of SW Highland Carbonates

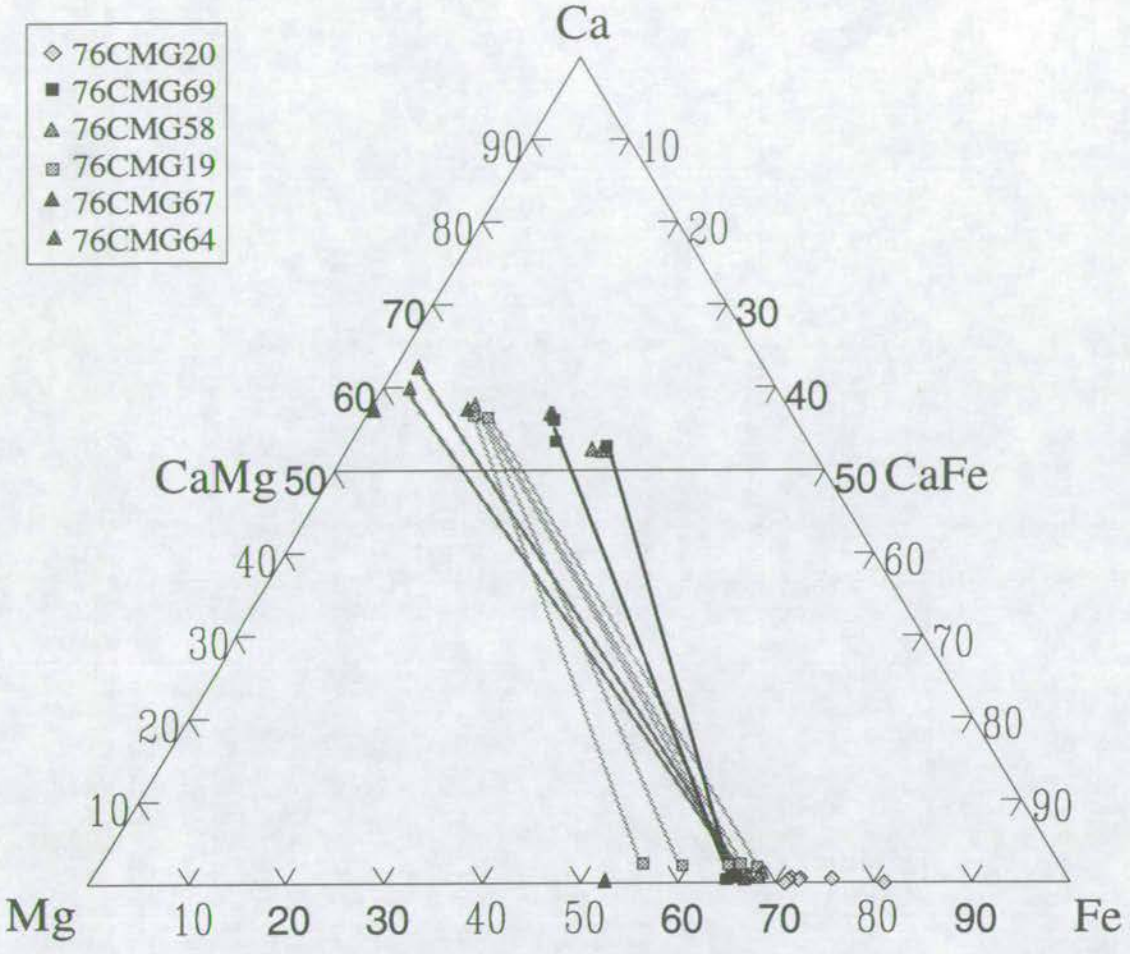

The above plot shows ankerites and siderites developed in phyllitic intercalations within the Islay-Jura Quartzite cropping out at Carraig Fhada (GR 349 443) on SE Islay. Tie-lines are constructed for each sample to emphasise the general lack of chemical equilibrium.

Fhada, which co-exist with siderite are shown with appropriate tie-lines in figure 5.7b. Crossing tie-lines are evident implying that ankerite growth was essentially out of equilibrium with siderites. Siderites belong to the peak metamorphic assemblages: ky + sid + qz and ctd + sid + qz which are discussed in section 5.5. Therefore, it is inferred that ankerite growth was at a later stage than siderite growth at lower temperatures at which re-equilibration was not achieved.

These observations are consistent with a retrograde origin for the ankerite porphyroblasts.

(iv) Thermodynamic Data and Interpretations

- K-feldspar is found to coexist stably with chlorite in ankerite bearing calc-phyllites from Keppoch Point (table 5.1). It is clear from the T-X_{CO_2} section in figure 5.3 that the assemblage K-feldspar + chlorite defines temperatures below about 300°C. This is significantly lower than those predicted by garnet-hornblende and garnet-biotite geothermometry for nearby assemblages (section 3.4.3).

(v) Geotherometric Data and Interpretations

- Geothermometric estimates, obtained using the calcite-dolomite geothermometer of Annovitz & Essene (1987), for ankeritic calc-phyllites from the Ardrishaig and Port Ellen phyllites are in the respective ranges <200°C and 300-450°C (section 3.4.3). Such values are low relative to temperatures, estimated from the garnet-biotite and garnet-hornblende geothermometers and THERMOCALC (Holland & Powell 1988) (500°C, section 3.4.3), and probably imply a retrograde origin for the ankerites. The large range of temperatures calculated for the Port Ellen phyllites probably records kinetic hindrance to equilibration as may be expected under retrograde conditions.

(vi) Stable Isotopic Data and Interpretation

- Graham (*unpublished data*) has obtained stable isotope data from a number of ankeritic phyllites from the Port Ellen Phyllites. This data is presented in table 5.2

and compared with stable isotopic data from unequivocally retrogressive ankerite + K-feldsar + Chlorite veins and stable isotopic data from ankerite-absent calc-phyllites.

Table 5.2: Stable Isotopic Data Analysis of Carbonates from Ankeritic and Ankerite-absent Calc-phyllites and Ank + Kfsp + Chl Veins.

Sample	Locality	Lithology	Mineral Assemblage	$\delta^{18}O$
CA57	Tarbert	Vein	**Ank**+Qz+Kfsp+Mu	25.45
CA47	Tarbert	Vein	**Ank**+Qz+Kfsp+Mu	25.24
Ag-7-4	Rubha Garbh	Calc-phyllite	Cc+Qz+Mu+Chl+Ab	11.94
Ag-7-6	Rubha Garbh	Calc-phyllite	Cc+Qz+Mu+Chl+Ab	11.56
76CMG58	Carraig Fhada	Calc-phyllite	**Ank**+Sid+Qz+Mu+Ru	14.86
76CMG60	Carraig Fhada	Calc-phyllite	**Ank**+Qz+Mu+Ru	17.82
80CMG07	Port Ellen	Calc-phyllite	**Ank**+Qz+Mu+Chl+Ab	22.76
80CMG08	Port Ellen	Calc-phyllite	**Ank**+Qz+Mu+Pa+Chl+Ab	25.88
91KB28	Kilberry	Calc-phyllite	**Ank**+Qz+Mu+Chl+Ab+Kfsp	31.86
91KB27	Kilberry	Calc-phyllite	**Ank**+Qz+Mu+Chl+Ab+Kfsp	26.38

Samples CA57 and CA47 were collected from ankerite + K-feldspar veins approximately 3km north of Tarbert (GR869 710) (K.M.Greig, *unpublished*). Samples Ag-7-4 and Ag-7-6 were collected at Rubha Garbh (GR752 765) located near the axial zone of the Ardrishaig Anticline (Graham *et al.* 1983). Samples 79CMG58 and 79CMG60 were collected from calc-phyllites developed as intercalations in the Islay-Jura Quartzite near Carraig Fhada lighthouse (GR349 443) (Graham & Fallick,*unpublished*). Samples 80CMG07 and 80CMG08 were collected from calc-phyllites outwith the Port Ellen Anticline near Port Ellen harbour (GR367 451) (Graham & Fallick,*unpublished*). Samples 91KB27 and 91KB28 were collected from calc-phyllites of the Ardrishaig Phyllites Group at Kilberry (GR701 639).

The isotopic signatures of ankerite-absent calc-phyllites are in the range $\delta^{18}O$ = 11-13‰. The isotopic signatures of ankerite-bearing calc-phyllites are in the range $\delta^{18}O$ = 14-26‰ and the isotopic signatures of ankerite + K-feldspar veins are in the range $\delta^{18}O$ = 25-26‰. The elevated $\delta^{18}O$ values obtained for ankerite-bearing calc-phyllites, relative to ankerite-absent calc-phyllites, is consistent with there being an association between the growth of ankerite porphyroblasts and an increase in $\delta^{18}O$.

The broad range of isotopic values obtained for the ankerite-bearing calc-phyllites is consistent with their having originated (at peak metamorphism) as ankerite-free, isotopically homogeneous calc-phyllites (similar to those observed at Rubha Garbh) and having been subsequently isotopically modified to varying extents by retrograde fluid infiltration responsible for the development of ankerite porphyroblasts and dolomite + K-feldspar + chlorite + quartz veining.

(vii) Summary

In summary, field, optical, geochemical, thermodynamic, geothermometric and stable isotopic data are consistent with ankerite porphyroblasts having grown during the later stages of D_4 deformation as a result of relatively high-temperature (300-400°C) retrograde fluid infiltration and associated with dolomite + K-feldspar + chlorite + quartz veining (Fein *et al.* 1993). However, it is evident that the mechanisms of fluid infiltration inferred as responsible for porphyroblast growth and veining must be different. Porphyroblast growth implies pervasive infiltration along grain-edges or micro-fractures, whereas veining implies fracture-controlled infiltration.

5.3 Metabasites

5.3.1 Distribution of Metabasites

The occurrence of metabasites is widespread throughout the SW Highlands. Metabasic dykes intrude the Islay-Jura Quartzite exposed on North Jura and Scarba. Metabasic sills are abundant throughout the majority of SW Highland lithologies. Metabasic lava flows are extruded above the Tayvallich limestone and crop out in the centre of the Loch Awe Syncline. The field and stratigraphical relations, and the

geochemistry of this comagmatic suite of basaltic rocks were described in section 3.3.2.

5.3.2 Mineral Assemblages and Petrogenesis of Metabasites

Harte & Graham (1975) and Graham *et al.* (1983) describe three types of metabasite assemblage (types I, II and III) which are typically characterised as follows:

Type I: Am + Ep + Chl + Ab + Sph + Ilm ± Qz ± Bi ± Ap

Type II: Am + Ep + Chl + Cc + Qz + Ab + Sph + Ilm ± Bi ± Ap

Type III: Chl + Cc + Qz + Ab + Sph ± Ep ± Ilm ± Bi ± Ap

or: Chl + Cc + Qz + Ab + Ab + Ru ± Ep ± Ilm ± Bi ± Ap

These assemblages are defined by the following equilibrium assemblages:

Type I: **amphibole + epidote, in the absence of calcite**

Type II: **amphibole + epidote + chlorite + calcite + quartz**

Type III: **chlorite + calcite + quartz, in the absence of amphibole**

Type I-III assemblages can be related by the $CMFASHCO_2$ reaction, mentioned in section 4.2.2:

$3am + 2ep + 8H_2O + 10CO_2 = 3chl + 10cc + 21qz$ **(1)**[1]

where the type II assemblage buffers the above reaction.

This reaction is at least divariant in real multicomponent rocks and defines a narrow field in T-X_{CO_2} space (figures 5.3a and 5.3b) which is bounded by the univariant Fe and Mg end-member reactions listed below:

(1) The univariant $CMASHCO_2$ reaction:

$3tr + 2cz + 8H_2O + 10CO_2 = 3clin + 10cc + 21qz$ **(1,Mg)**

(2) The univariant $CFASHCO_2$ reaction:

[1]Reactions (1) and (2) are included on a reference card at the back of the thesis.

$3ftr + 2cz + 8H_2O + 10CO_2 = 3daph + 10cc + 21qz$ **(1,Fe)**

The spatial separation of the Mg and Fe end-members of reaction (1), over the P-T range of interest, is much less than the error of their predicted T-X_{CO_2} locations. Therefore, for the purposes of this study, the T-X_{CO_2} phase relations of reaction (1) will be assumed to be that of the Mg end-member reaction.

A second reaction, mentioned in section 4.2.2 and observed by Graham *et al.* (1983) to have occurred in the metabasites, is given by:

$sph + CO_2 = ru + cc + qz$ **(2)**[1]

Type I-III metabasite mineral assemblages typically developed in parallel zones symmetrically or more commonly asymmetrically about the centre of sills or dykes. Typical zonal patterns, illustrated in figure 5.8, are:

(1) Type I, throughout,

(2) Type I interior, Type II-III margin (see also figure 4.5),

(3) Type III, throughout.

Two critical observations emerge from comparison of the above zonal patterns with the T-X_{CO_2} phase relations depicted in figures 5.3a and 5.3b:

(1) All of the above zonal patterns could be generated by decreasing temperature or increasing X_{CO_2} towards the metabasite margin. As metabasites are in general only tens of metres in width, yet two or even three zones are regularly developed in metabasite margins on a metre scale, it is physically implausible that this could be induced merely by temperature perturbations. The zonal patterns must therefore result from infiltration of a higher X_{CO_2} fluid, from outwith the sill, towards the metabasite interior.

(2) The sequence of zonal patterns (1→3, above) describes an increasing influence of CO_2 as a result of either (i) increasing X_{CO_2} of the infiltrating fluid, or (ii) increasing time-integrated fluid flux.

Figure 5.8· Metabasite Zonal Patterns

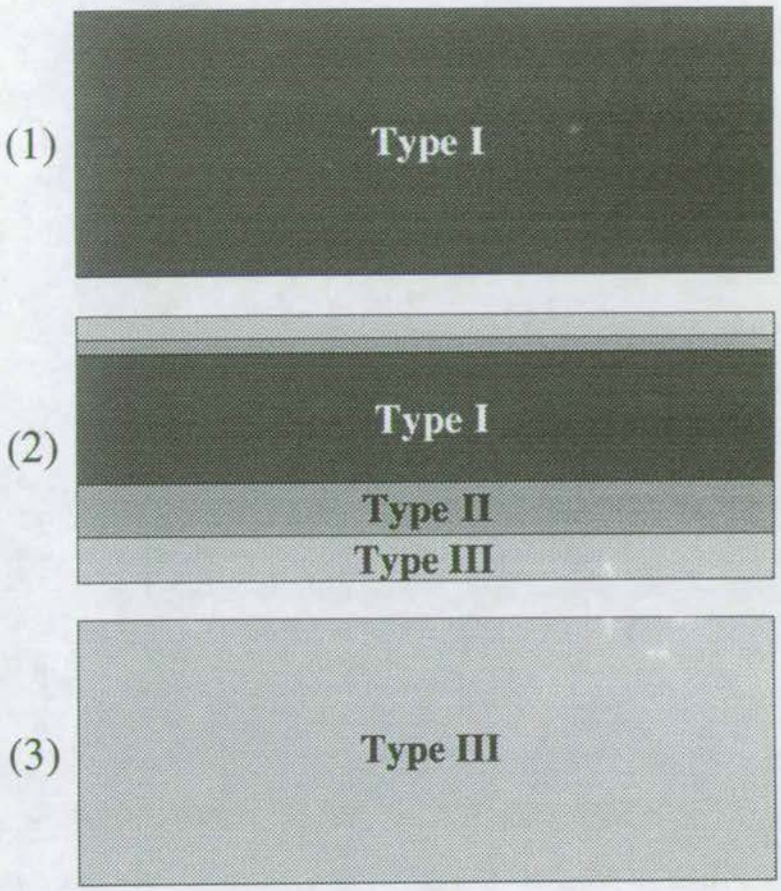

5.3.3 Type I Metabasites

Greenschist facies type I metabasite assemblages typically preserve their original igneous texture (figure 5.9a and b). In some instances large albites are preserved (figure 5.9b). Although the sills and dykes themselves are often isoclinally folded during D_1, the minerals within type I zones rarely preserve any deformation features (figure 5.9a and b).

Representative mineral modes are presented in table 5.3 and discussed below.

Table 5.3: Representative Mineral Modes of Type I Metabasites

Sample	**90NJ61**	**89PE18**	**CARS21**	**90PCM11**	**91LS7**	**89CB13**
Mineral						
Amphibole	33.8	14.0	8.5	39.6	60.5	34.0
Clinozoisite	29.0	56.8	4.0	28.4	7.0	22.0
Chlorite	12.6	7.0	9.5	9.2	-	16.0
Albite	12.2	16.6	32.0	16.6	3.0	12.0
Quartz	1.6	1.4	-	2.4	15.7	1.0
Biotite	1.2	*	*	0.2	5.5	-
White Mica	-	1.4	-	-	-	12.0
Garnet	-	-	-	-	0.5	-
Calcite	-	1.4	-	0.6	-	*
Sphene	5.0	1.4	8.5	3.0	7.7	3.0
Ilmenite	4.0	-	0.5	*	*	-
Pyrite	*	-	-	*	*	-
Apatite	-	-	*	-		-
Stilpnomelane	-	-	37.0	-	-	-

(+) = present, (*) = traces and (-) = absent

90NJ61 was collected from the interior of an 8m wide dyke on North Jura (GR679 006). 89PE18 was collected from the interior of a 30m wide sill near the core of the Port Ellen Anticline (GR366 448). CARS21 was collected by C.M.Graham from the interior of a 40m wide, folded sill at Carsaig, near the core of the Loch Awe Syncline (GR726 878). 90PCM11 was collected from the interior of a 13.4m wide sill on the SE limb of the Ardrishaig Anticline at Port Cill Maluaig (GR722 671). 91LS7 was collected from the interior of a 25m wide sill in the garnet zone at Loch Stornoway (GR730 612). 89CB13 was collected from the interior of a 50m wide sill cropping out just below the garnet isograd at Clachbreac (GR767 755).

The type I assemblage develop most frequently in the interiors of metabasite sills at all grades. A typical type I assemblage is given by:

am + ep + chl + ab + sph ± qz ± bi ± mu ± ap ± pyr ± ilm

Figure 5.9(a): Photograph of Type I Metabasite

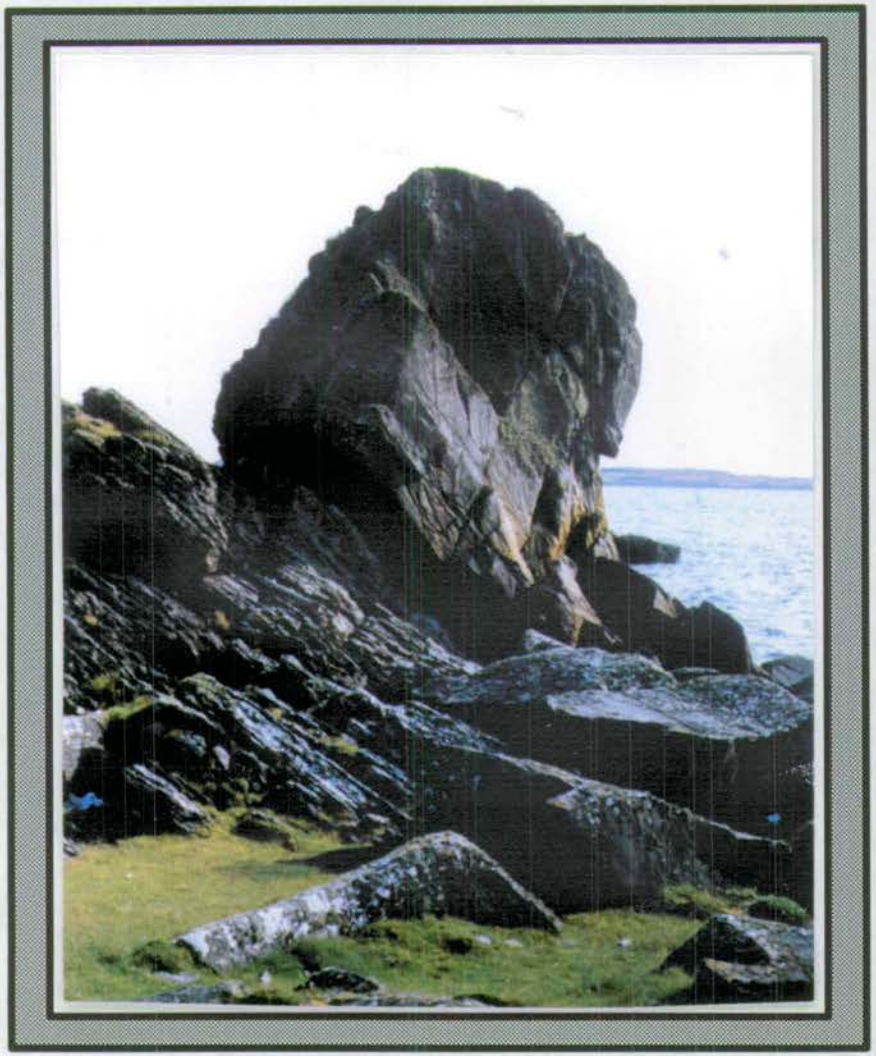

Locality:
Port Ellen, Islay GR367 446

Scale:

1m

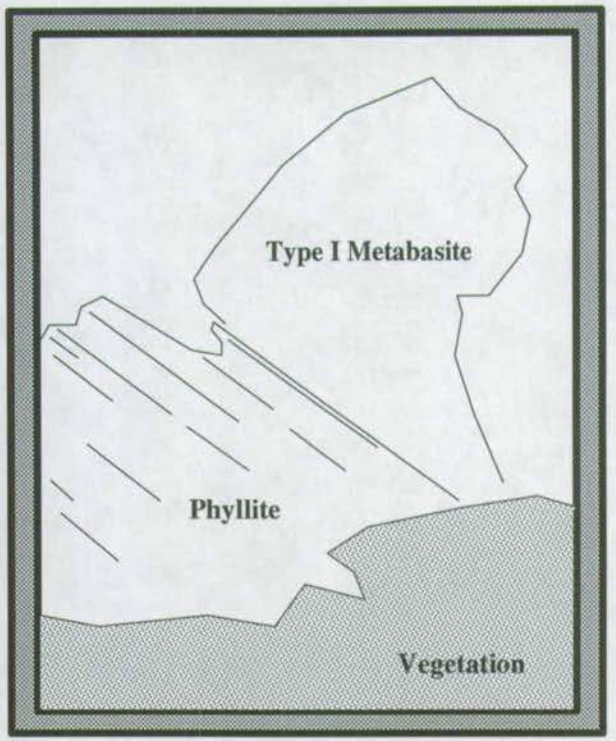

Figure 5.9(b): Photomicrograph of Type I Metabasite

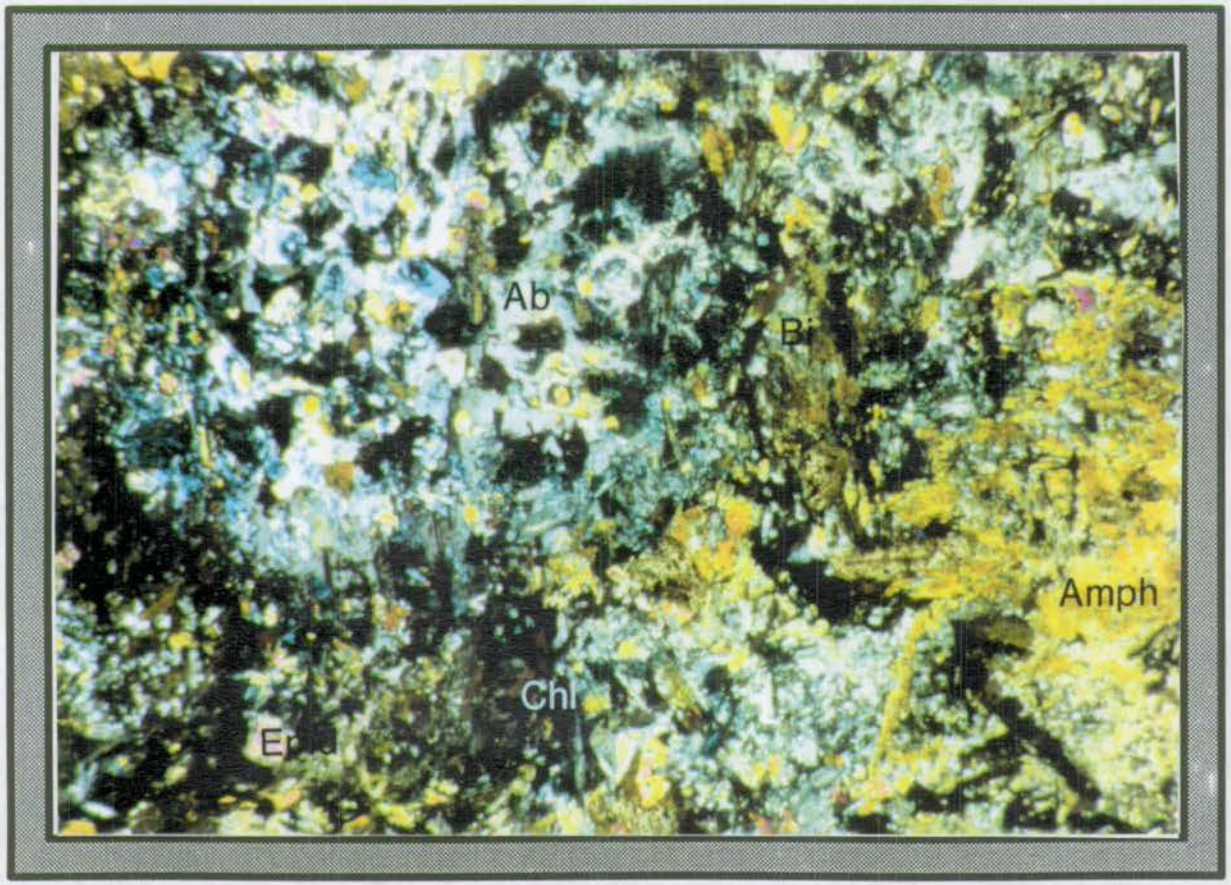

Locality:
Port Ellen, Islay GR365 448

Magnification:
x40

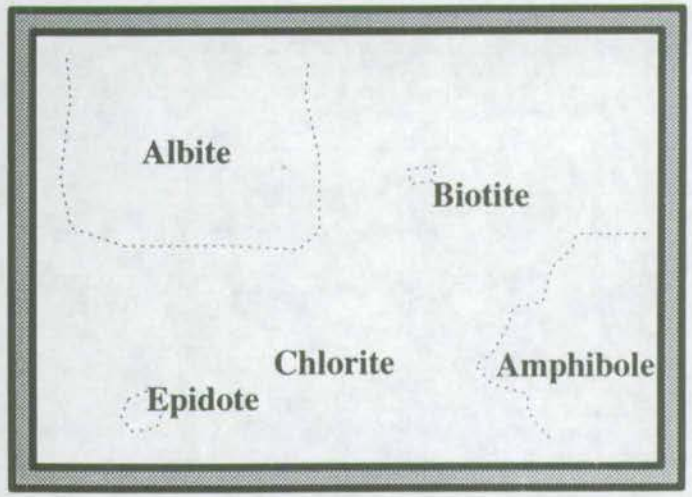

Note: Large amphiboles and albites show no evidence of D1-D4 deformation. Instead, they preserve their original igneous texture.

The common presence of biotite in type I metabasite assemblages is diagnostic of biotite-grade conditions having been attained. As biotite is rare in the surrounding phyllites the diagnostic properties of the metabasites are invaluable in establishing the metamorphic grade.

In the garnet-zone, the assemblage lacks chlorite which is presumably partly destabilised relative to garnet by the isograd reaction (Harte & Graham 1975):

Mg-chlorite + Mg-amphibole = Fe-chlorite + Fe-amphibole + Fe-garnet

and in the lowest biotite-zone, below the isograd (Graham 1973):

hornblende + chlorite = actinolite + stilpnomelane

the assemblage is rich in stilpnomelane but deficient in chlorite and amphibole.

As is predicted by the phase relations in the T-X_{CO_2} section shown in figure 5.3a, sphene is stable relative to rutile, calcite and quartz in type I assemblages at all grades in the SW Highlands.

5.3.4 Type III Metabasites

Type III metabasite assemblages appear strongly foliated and extensively pitted, in the field, due to the abundance of chlorite and calcite (figure 5.10a&b). Foliation is developed parallel to s_1 (figure 5.10b). Although type III metabasites are also of igneous origin, all textural evidence is obliterated. In several examples, however, albites are pseudomorphed by chlorite and/or calcite while retaining their original shape, if elongated and aligned parallel to the s_1 fabric (figure 5.10b).

Representative mineral modes are presented in table 5.4, and discussed below.

Figure 5.10(a): Photograph of Type III Metabasite

Locality:
Port Ellen, Islay GR365 448

Scale:
Hammer (1m)

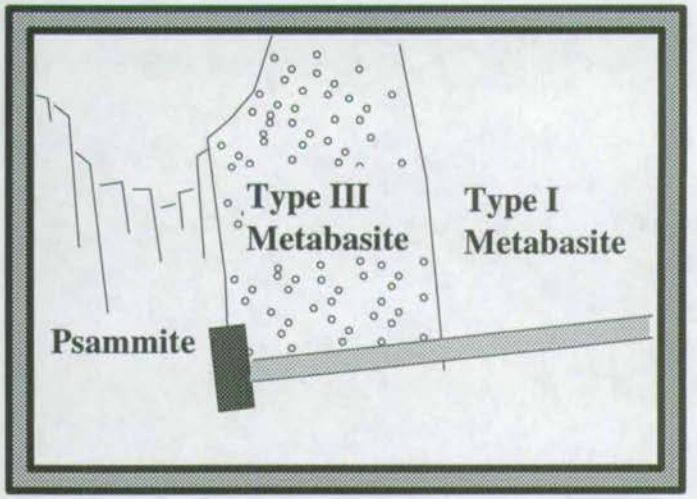

Figure 5.10(b): Photomicrograph of Type III Metabasite

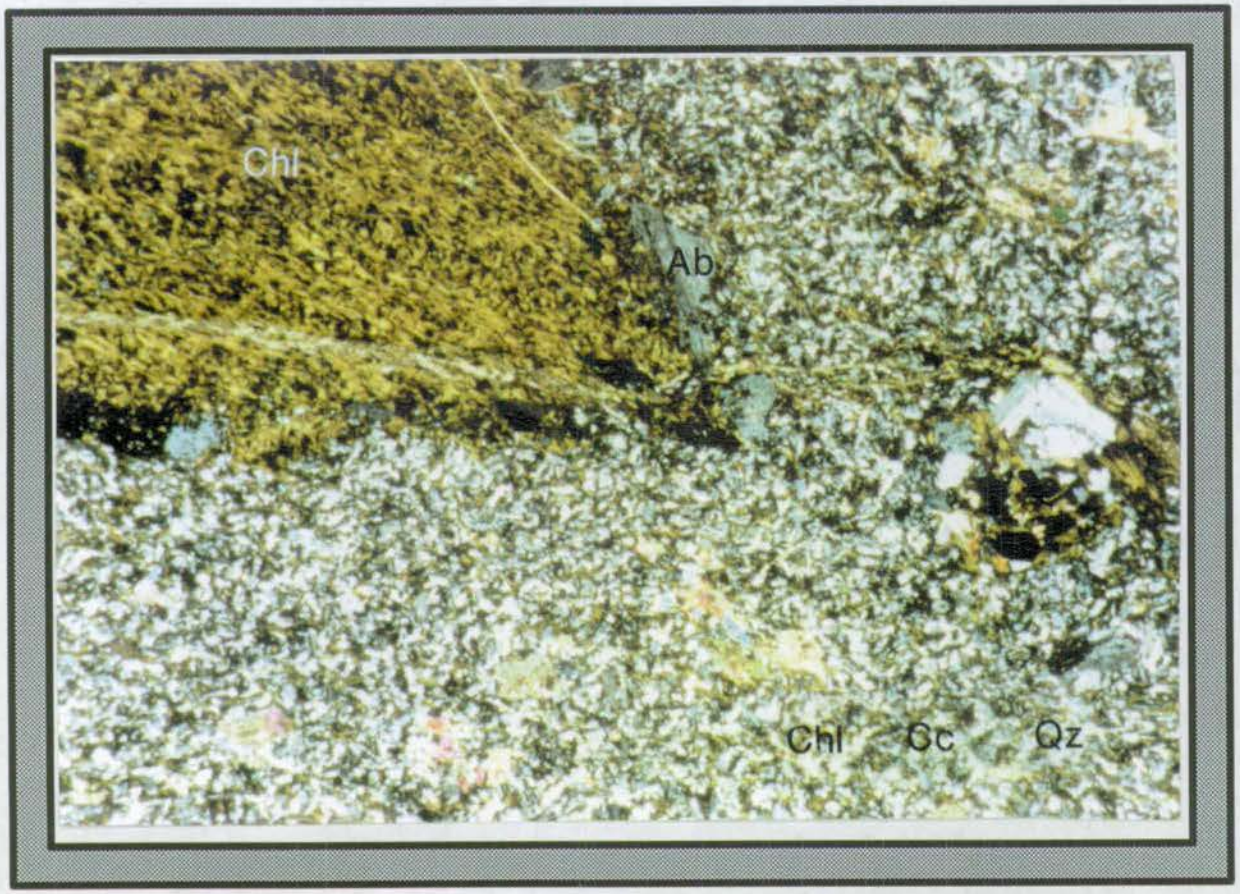

Locality:
Port Ellen, Islay GR365 448

Magnification:
x40

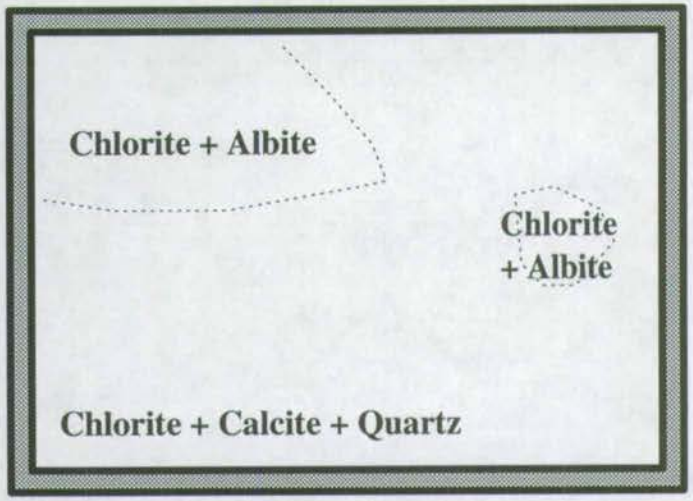

Note: Albite phenocrysts are replaced by chlorite, and matrix amphiboles + epidotes are replaced by chlorite + calcite + quartz.

Table 5.4: Representative Mineral Modes of Type III Metabasites

Sample	90NJ56	89PE30	90PE130	CARS3	90PCM36	91LS10
Mineral						
Chlorite	33.2	41.0	40.7	26.0	41.6	33.5
Calcite	5.6	20.0	6.5	12.0	21.8	26.5
Quartz	18.0	14.0	22.7	17.0	22.2	25.2
Clinozoisite	0.6	-	-	-	2.6	0.2
Albite	29.4	23.0	15.2	18.0	7.6	4.2
Biotite	6.6	-	-	-	-	4.7
White Mica	0.6	-	6.5	-	-	-
Sph/Rut	5.6	2.0	*	6.0	4.2	-
Ilm/Hem	0.2	-	8.2	1.0	-	5.5
Apatite	-	-	-	1.0	-	-
Stilpnomelane	-	-	-	19.0	-	-

(+) = present, (*) = traces and (-) = absent

90NJ56 was collected from the margin of an 8m wide dyke on North Jura (GR679 006). 89PE30 was collected from the margin of a 30m wide sill near the core of the Port Ellen Anticline (GR366 448). 90PE130 was collected from the interior of a 20m wide sill which is hosted by ankerite-bearing phyllites at Traigh Gheighsgeir near Port Ellen (GR364 453). CARS3 was collected by C.M. Graham from the margin of a 40m wide, folded sill at Carsaig, near the core of the Loch Awe Syncline (GR726 878). 90PCM36 was collected from the margin of a 13.4m wide sill on the SE limb of the Ardrishaig Anticline at Port Cill Maluaig (GR722 671). 91LS10 was collected from the margin of a 25m wide sill in the garnet zone at Loch Stornoway (GR730 612).

The type III assemblage occurs most frequently at the margins of metabasite sills at all grades. However in a few metabasic sills, such as Traigh Gheighsgeir (sample 90PE130), type III assemblages persist throughout the entire width of the sill. This is an example of the third zonal pattern depicted in figure 5.8. A typical type III assemblage is given by:

chl + cc + qz + ab ± sph ± ru ± mica ± bi ± ap ± ilm ± hem

As is predicted by the phase relations in the T-X_{CO_2} section shown in figure 5.3a, either sphene or rutile can stably co-exist with the type III assemblage.

5.3.5 Type II Metabasites

Type II assemblages buffer reaction (1). They therefore occur, in relatively narrow zones, sandwiched between zones of type I and type III metabasite.

They are similar in appearance to type I assemblages although they tend to develop weak foliation and a fine pitted weathering texture. A typical mineral assemblage is given by:

am + ep + chl + cc + qz + ab ± bi ± sph ± ilm ± hem ± ap

Mineral reaction textures which develop include the replacement of amphibole by calcite and/or chlorite (figure 5.11a) and rimming of epidote by calcite (figure 5.11b). This is a critically important observation as it indicates the direction of the reaction to be towards higher X_{CO_2} conditions. This observation strengthens the interpretation posed earlier in this chapter that reaction is driven by infiltration of ***relatively*** CO_2-rich fluid towards the interior of the metabasite. On the basis of this conclusion, a third reaction which is described by the P-T-X_{CO_2} phase relations (figure 5.3a) must be included as having a potentially important role in controlling types I-III metabasite assemblages.

$2cz + 3ab + 4CO_2 + 2H_2O = 3pa + 4cc + 6qz$ **(3)**[2]

Progress of this reaction may have been limited because it will have been preceded by reaction (1) which consumes clinozoisite.

5.3.6 Deformation of Metabasites and Timing of Fluid Infiltration

Throughout the SW Highlands, metabasite sills are generally observed as laterally extensive, undulous sheets. Sill interiors are seldom deformed whereas sill margins are regularly sheared and foliated. A correlation is evident between the spatial extent of marginal deformation and the spatial extent and progress of marginal type I → type III reaction. Foliation of type III assemblages is defined by chlorites which are aligned parallel to s_1 fabrics. The widths of the sheared/reacted zones vary from several centimetres to several metres. Although broad, largely type I, metabasite synformal fold hinges are evident at a number of localities, **no antiformal hinges**

[2]Reaction (3) is included on a reference card at the back of the thesis.

Figure 5.11a: Type II Metabasite: Reaction Texture: Amphipole → Calcite + Chlorite

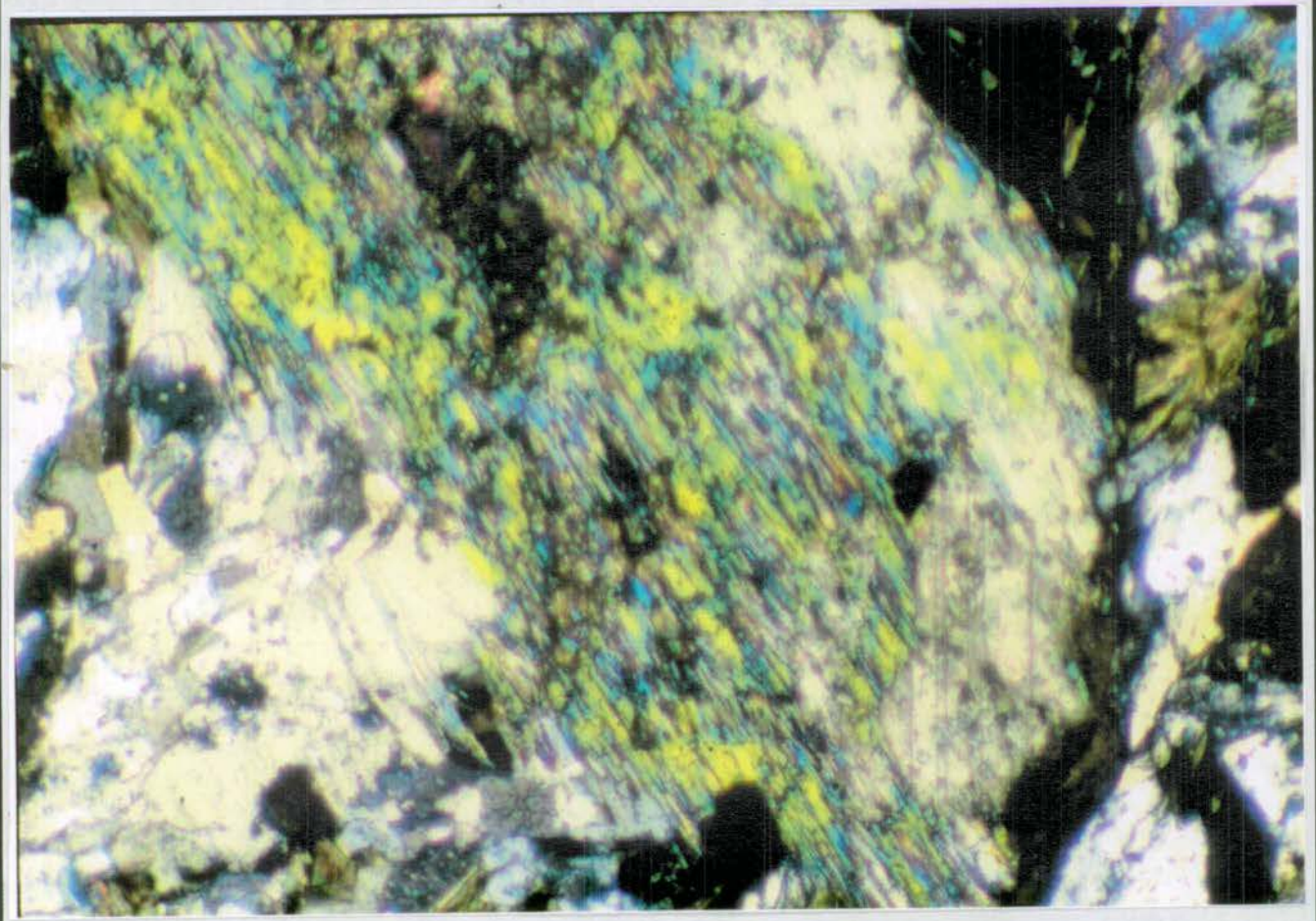

Locality:
Port Cill Maluaig, Knapdale
GR723 702

Magnification:
x100

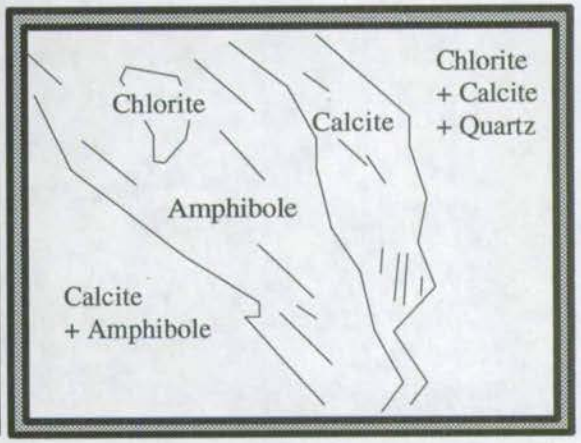

Figure 5.11b: Type II Metabasite: Reaction Texture: Epidote → Calcite

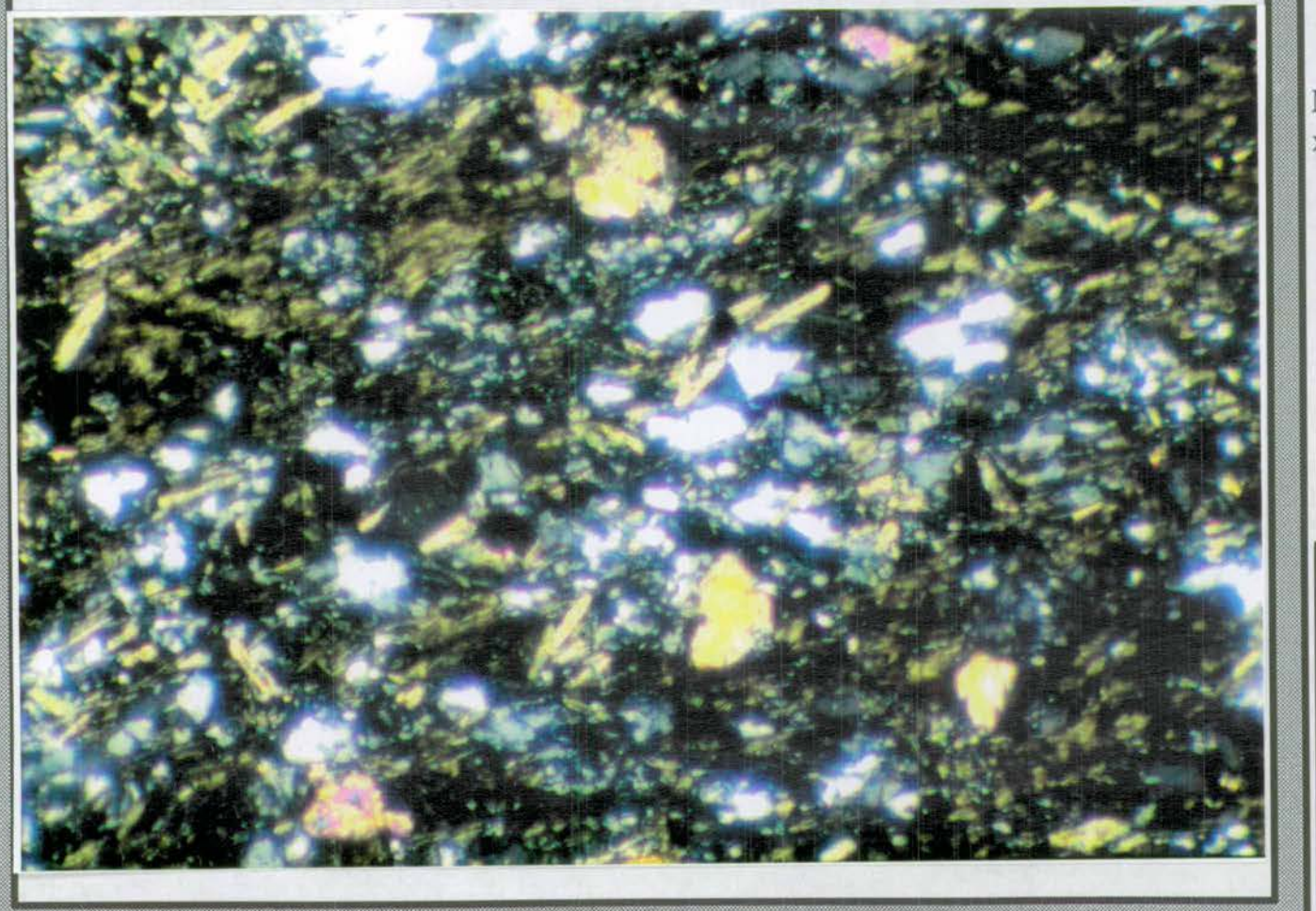

Locality:
North Jura

Magnification:
x100

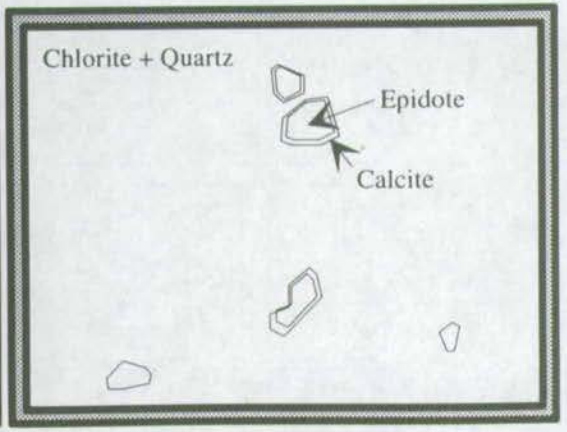

have been observed throughout the entire SW Highland terrain (figure 5.12). Furthermore, on a regional scale, metabasite units become progressively thinner and less abundant with increasing proximity to the axial zone of the Ardrishaig Anticline, in which no metabasites crop out (figure 5.12).

The spatial correlation of deformation with type I → type III reaction implies that type I metabasites are more competent than type III assemblages. Furthermore, the observed refraction of s_1 foliation across a phyllite-type III metabasite boundary at Carsaig, NW Knapdale (figure 3.4a) implies that type III metabasites are more competent than the host phyllites. It is therefore predicted that phyllites will shear more readily than type III metabasites which, in turn, will shear more readily than type I metabasites.

Furthermore, the widespread occurrence of broad synformal fold hinges implies that metabasites are generally more competent that the host phyllites which are extensively sheared and develop tight isoclinal folding.

The absence of antiformal fold hinges is more problematic. One possible explanation is that development of type III assemblages was more extensive along antiformal fold axes resulting in intensified shearing and deformation and the subsequent obliteration of antiformal fold closures. The distribution of type III assemblages is controlled by the flow patterns of the causative fluid. Two possible mechanisms arise:

(1) One possible mechanism is that fluid flow may have been focused along ***already*** deformed zones at the margins of metabasite sills. If marginal deformation were most intense in the axial zones of antiformal folds, excessive development of type III assemblages would be incurred. Type III minerals (particularly chlorites) would therefore mimic a pre-existing D_1-D_2 fabric. However there is little apparent structural reason for assuming that deformation should be more intense in the axial zone of an antiformal fold as opposed to a synformal fold (Ramsay 1967).

Figure 5.12: Geological Map of West Knapdale showing the distribution of Metabasite Lithologies and the relative abundances of Anticlines and Synclines

KEY

Metabasite

S Synclines (Total=28)

A Anticlines (Total=6)

The above map shows the distribution of metabasite lithologies throughout West Knapdale together with the relative abundances of anticlines and synclines. Some 28 synclines were identified, whereas a mere 6 anticines were identified. Furthermore where anticinal folds were investigated the fold closure was consistently found to have been obliterated. Also, the abundance of metabasites decreases towards the axis of the Ardrishaig Anticline, such that no metabasites are observed in the axial region.

(2) A second possible mechanism is that fluid is structurally channellised along the axial zone of the antiform. Therefore, wider type III metabasite margins would develop on the inner limbs of the antiform and, because type III assemblages are less competent than type I assemblages, shearing and deformation would be more intensive in the axial zone of the antiform. Intensified shearing and deformation in the axial zone of the antiform would obliterate the fold closure.

The implications of the above discussion on the timing of the causative fluid infiltration are paramount. The former mechanism requires that fluid infiltration should post-date D_1-D_2 deformation whereas the latter mechanism requires the causative fluid infiltration to pre-date or coincide with D_1-D_2 deformation.

Quantitative modelling and regional-scale mapping of fluid flow, undertaken in this study, unequivocally demonstrates that fluid is structurally channellised along antiformal fold axes. On the basis of this conclusion, it is most likely that fluid infiltration and resultant reaction occurred in the presence of a D_1-D_2 stress field (i.e. fluid infiltration was probably syn-D_1-D_2)

In addition to the above arguments, temperatures calculated using THERMOCALC (Holland & Powell 1988) for all independent reactions from type I and all independent reactions from type III assemblages from a sill at Port Cill Maluaig, Knapdale (GR722 701), are equivalent within error and are realistic estimates of the temperature of syn-D_1-D_2 peak metamorphism. The temperature estimated from the type I assemblage is 474±15°C and the temperature estimated from the type III assemblage is 446±19°C. The calculation details are given in appendix 2. Furthermore these temperatures are consistent with the isotherm map shown in figure 3.8 which is constructed from temperatures estimated using traditional geothermometers (e.g calcite-dolomite-ferrodolomite, Annovitz & Essene 1987 and garnet-biotite, Hodges & Spear 1982).

5.3.7 Ankerite-bearing Metabasite Assemblages

In several metabasite sills, which crop out at Keppoch Point and Traigh Gheighsgeir and in several metabasite dykes which crop out on North Jura and Scarba, type III assemblages are found to include ankerite.

Field Description of Ankeritic Metabasites

At Keppoch Point and Traigh Gheighsgeir, ankeritic metabasites are generally hosted by ankeritic calc-phyllites (section 5.2). On North Jura and Scarba, ankerite-bearing metabasites are hosted by quartzites (section 5.5). Ankerite-bearing metabasites are highly micaceous, fissile, weakly pitted, and generally rusty in appearance (figure 5.13), and may be confused with ankeritic calc-phyllites, in the field. Individual, rusty ankerite porphyroblasts, up to 3-4mm in diameter may be recognised (figure 5.13).

Mineralogy of Ankeritic Metabasites

Ankerite porphyroblasts develop in type III metabasites only, where they are observed to replace calcite, often as pristine rhombs (figure 5.14a and b). Ankerite growth is locally associated with the development of paragonite or K-feldspar. Both paragonite and K-feldspar are developed as fine grains which may only be distinguished by electron microprobe analysis. The assemblage ankerite + paragonite + quartz defines higher X_{CO_2} or lower temperatures than types I-III metabasites (figure 5.3a). The assemblages ankerite + K-feldspar and K-feldspar + chlorite constrain lower temperatures (figure 4.7). Representative mineral modes are presented below, in table 5.5.

Figure 5.13: Ankerite-bearing Metabasite intruding the Islay-Jura Quartzite

Locality:
Gulf of Corryvreckan, North Jura
GR705 005

Scale:
Pencil (15cm)

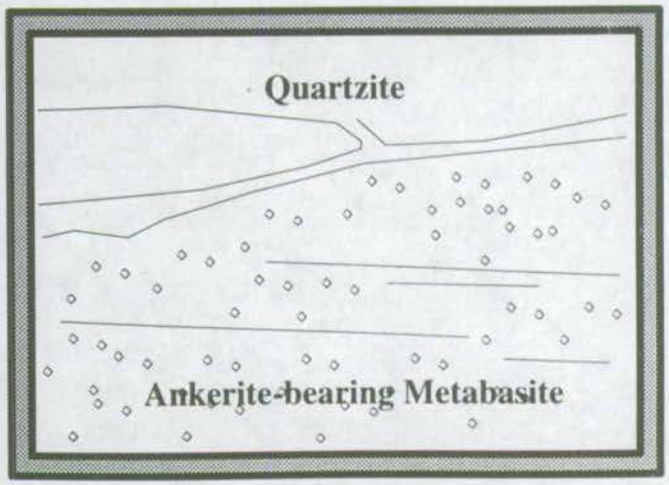

Figure 5.14a: Ankeritic Metabasites: Reaction Texture: Replacement of Calcite with Retrograde Ankerite

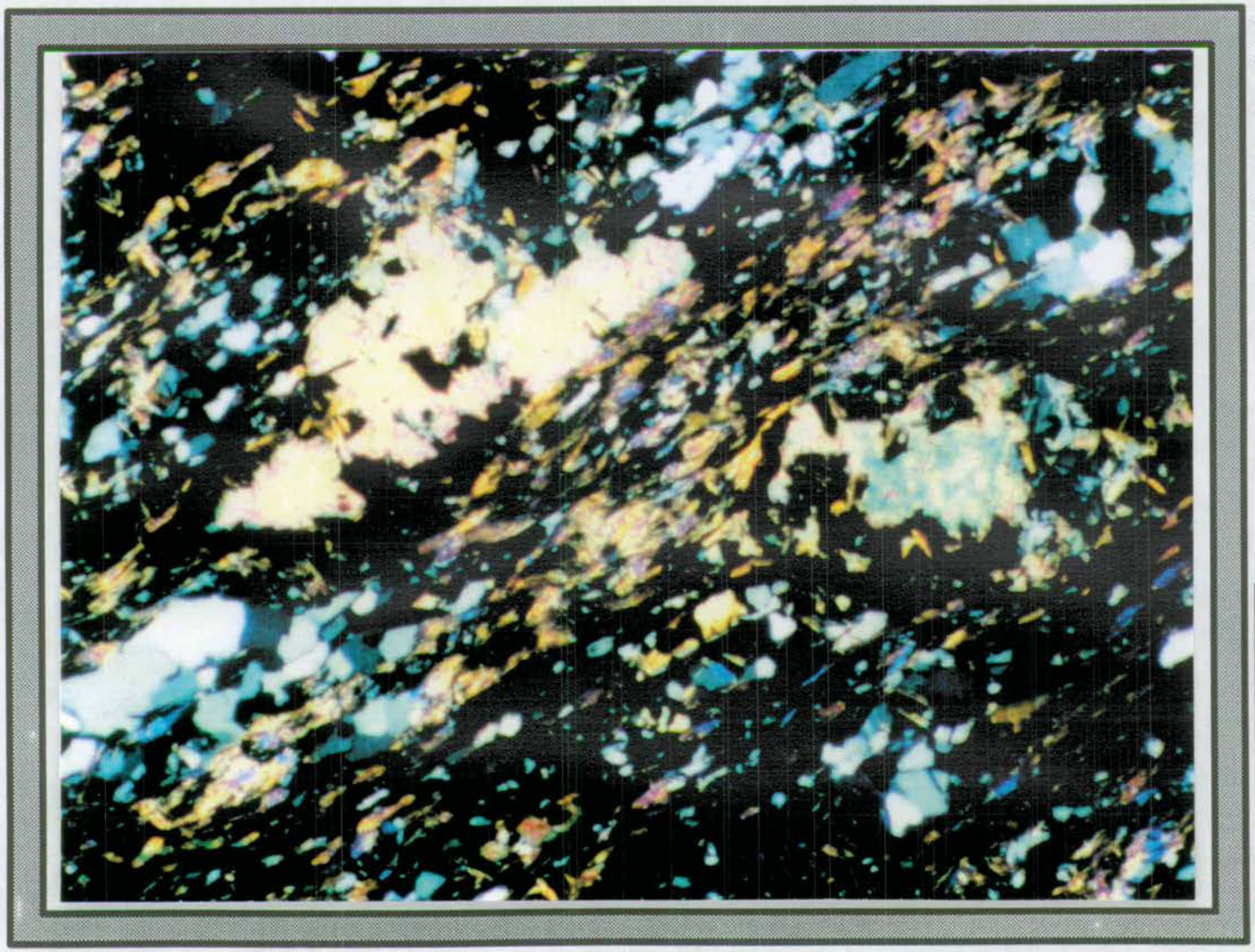

Locality:
Traigh Gheighsgeir, Port Ellen, Islay
GR363 452

Magnification:
x40

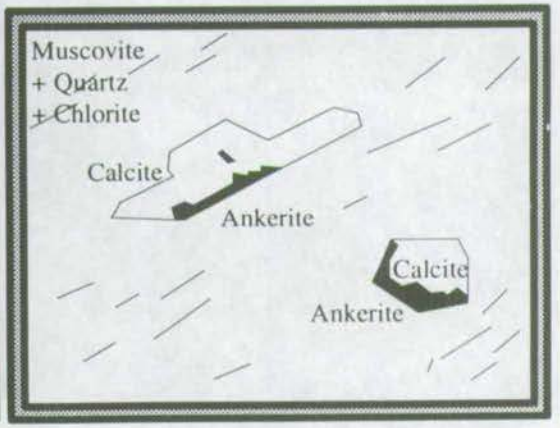

Figure 5.14(b): Back-Scattered electron image of Ankerite replacing calcite in Ardrishaig Calc-Phyllites.

Locality:
Kilberry Head, Knapdale GR701 639

Magnification:
x8000

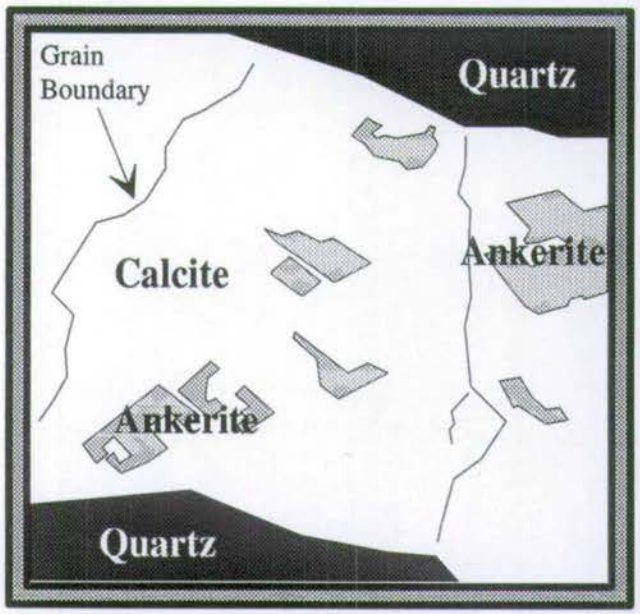

Euhedral ankerites replace large irregular calcite grains. **Note:** Ankerites ***do not*** grow at grain boundaries inferring that they may have developed as a result of (retrograde) fracture-controlled fluid infiltration.

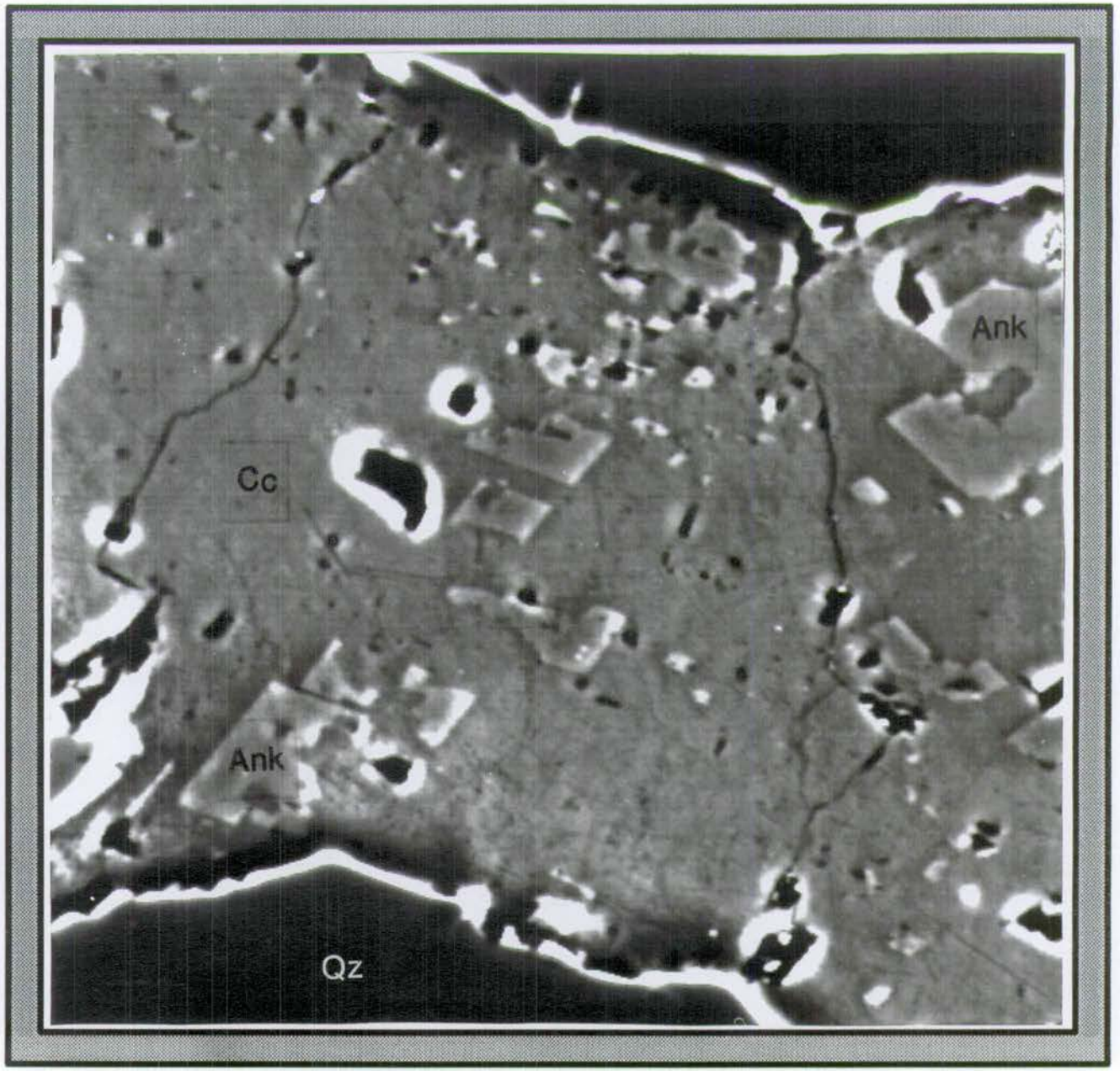

Table 5.5: Representative Mineral Modes of Ankerite-bearing Metabasites

Sample	**90NJ1**	**90PE125**
Mineral		
Ankerite	6.4	40.0
Quartz	34.7	20.2
Chlorite	-	18.0
Muscovite	48.3	17.5
Paragonite	-	*
Albite	-	2.7
Biotite	8.1	-
Calcite	-	0.5
Rutile	-	*
Ilm/Hem	1.9	1.0

(+) = present, (*) = traces and (-) = absent

90NJ1 was collected from a 1m wide sill on North Jura hosted by quartzite (GR705 004) and 90PE125 was collected from the margin of a 20m wide sill which is hosted by ankeritic calc-phyllites at Traigh Gheighsgeir (GR364 453).

The assemblages **ankerite + paragonite + quartz** and **ankerite + muscovite + quartz** define higher X_{CO_2} conditions, and the assemblage **K-feldspar + chlorite** defines lower temperature conditions than the generalised type III assemblage **chlorite + calcite + quartz ± biotite ± albite** (figure 5.3a).

The assemblages **ankerite + paragonite + quartz** and **ankerite + muscovite + quartz** are related to the type III assemblage by the divariant NCMFASHCO2 reaction:

ab + chl + 5cc + 5CO_2 = pa + 5ank + 3qz + 3H_2O **(4)**

and the divariant KCMFASHCO2 reaction:

bi + chl + 8cc + 8CO_2 = mu + 8ank + 3qz + 4H_2O **(5)**

respectively, and the assemblage **K-feldspar + chlorite** is related to the type III assemblage by the divariant reaction:

5bi + 3mu + 9qz + 4H_2O = 8Kfsp + 3chl **(6)**

Reactions (4) and (5) are bounded in T-X_{CO_2} space (figures 5.3c and 5.3d) by the univariant Fe and Mg end-member reactions listed below:

(1) the univariant NCMASHCO2 reaction:

ab + clin + 5cc + $5CO_2$ = pa + 5dol + 3qz + $3H_2O$ (4,Mg)

(2) the univariant NCFASHCO2 reaction:

ab + daph + 5cc + $5CO_2$ = pa + 5fdol + 3qz + $3H_2O$ (4,Fe)

(3) the univariant KCMASHCO2 reaction:

phl + clin + 8cc + $8CO_2$ = mu + 8dol + 3qz + $4H_2O$ (5,Mg)

(4) the univariant KCFASHCO2 reaction:

ann + daph + 8cc + $8CO_2$ = mu + 8fdol + 3qz + $4H_2O$ (5,Fe)

Within reasonable error the Mg and Fe end-members of reactions (4) and (5) are coincident in T-X_{CO_2} space and therefore, for the purposes of this study, the Mg end-member reaction curve is used to constrain relevant fluid compositions in chapters 7 through 11.

Deformation of Ankeritic Metabasites

Ankeritic metabasites develop a strong penetrative fabric, defined by alignment of phyllosilicates parallel to s_1-s_2. This fabric is crenulated parallel to s_4. Ankerite porphyroblasts are large and often skeletal in habit. Porphyroblasts are undeformed and over-grow the s_1-s_4 fabric.

Summary

The mineralogical and deformational characteristics of ankeritic metabasites and their spatial association with ankeritic calc-phyllites are consistent with ankerites having grown as a result of the retrograde fluid infiltration held responsible for ankerite growth in the calc-phyllites.

5.3.8 Summary

In summary, metabasites develop three distinct assemblages. Type I metabasites contain amphibole + epidote, in the absence of calcite. Type iII metabasites contain chlorite + calcite + quartz, in the absence of amphibole. Type II

metabasites contain the assemblage amphibole + epidote + chlorite + calcite + quartz and buffer the reaction:

$3am + 2ep + 8H_2O + 10CO_2 = 3chl + 10cc + 21qz$ **(1)**

Infiltration of externally-derived CO_2-bearing fluids generates type III assemblages, by progress of reaction (1) at the margins of type I metabasites.

Type III assemblages are spatially coincident with deformation of the sill margins. This is attributed to the incompetence of the type III assemblage relative to the type I assemblage. Although metabasites develop broad D_1-D_2 synformal folds, no antiformal fold closures are observed. On the basis of fluid flux modelling and fluid flow mapping, presented later in this thesis, the total obliteration of antiformal fold closures is attributed to focusing of fluid along antiformal fold axes resulting in extensive development of type III assemblages which are easily deformed during D_1-D_2. This interpretation constrains the timing of fluid infiltration to have been pre- or syn- D_1-D_2. Furthermore temperature estimates from type I and type III assemblages in the same metabasite sill record similar and consistent, ***peak metamorphic*** temperatures. Late-stage ankerite porphyroblasts over-grew pre-existing type III assemblages during syn- or post-D_4 retrograde fluid infiltration at lower temperatures.

5.4 Marbles

Marbles are not abundant in the SW Highlands. They represent a mere 1-2% of the entire sequence. Where marbles do occur, they are usually impure and interlayered with psammites or phyllites, often a 10cm-1m scale. Nevertheless, several marble units may be distinguished, notably the Tayvallich/Loch Tay Limestones, the Islay Limestone, the Bunahabhain Dolomite, and the Loch Fuar Bheinne Limestone (figure 3.2).

Biotite Zone Marbles

The Tayvallich Limestone, Islay Limestone and Bunahabhain Dolomite crop out in the biotite zone.

The Tayvallich Limestone crops out at Tayvallich on West Knapdale and is weakly deformed, coarse-grained, conglomeritic and rich in clastic and metabasite debris. Typical mineral assemblages are given by:

qz + mu ± cc ± dol ± chl ± bi ± ab ± graphite

Such an assemblage is shown in figure 5.15.

Deformation of the Islay Limestone and Bunahabhain Dolomite is extremely variable. In some localities marbles are intensely folded and deformed (e.g. Mull of Oa) whereas in other localities marbles still preserve diagenetic textures (Fairchild 1985). They are mineralogically heterogeneous on a 10cm-1m scale and are host to abundant phyllitic intercalations. Typical mineral assemblages are given by:

qz + mu ± cc ± dol ± chl ± bi

Such an assemblage is shown in figure 5.15.

Neither of these assemblages are uniformly diagnostic of the fluid composition. Marbles containing the diagnostic assemblages dol + mu + qz and bi + chl + cc are both observed. The spatial distribution of these assemblages has not been investigated for these rocks. It is, therefore, only possible to state that fluid compositions tend to fluctuate around the divariant field of reaction (5) (figure 5.3d).

Garnet Zone Marbles

The Loch Tay and Loch Fuar Bheinne Limestones crop out in the garnet zone.

The Loch Tay Limestone crops out near Stonefield Castle, about 4km NNE of Tarbert. It is the lateral continuation of the Tayvallich Limestone. The limestone is mineralogically heterogeneous and interlayered with phyllites and metabasites, often on a 10cm-1m scale. Typical mineral assemblages are:

Figure 5.15: Photomicrographs of the Tayvallich Limestone, Islay Limestone and Loch Fuar Bheinne Limestone

Tayvallich Limestone
Locality: Tayvallich GR711 850
Assemblage: Cc+Qz+Gph
Magnification: x40

Islay Limestone
Locality: Mull of Oa GR285 413
Assemblage: Cc+Bi+Chl+Mu+Qz
Magnification: x40

Loch Fuar Bheinne Limestone
Locality: Loch Fuar Bheinne GR810 789
Assemblage: Cc+Dol+Mu+Qz
Magnification: x40

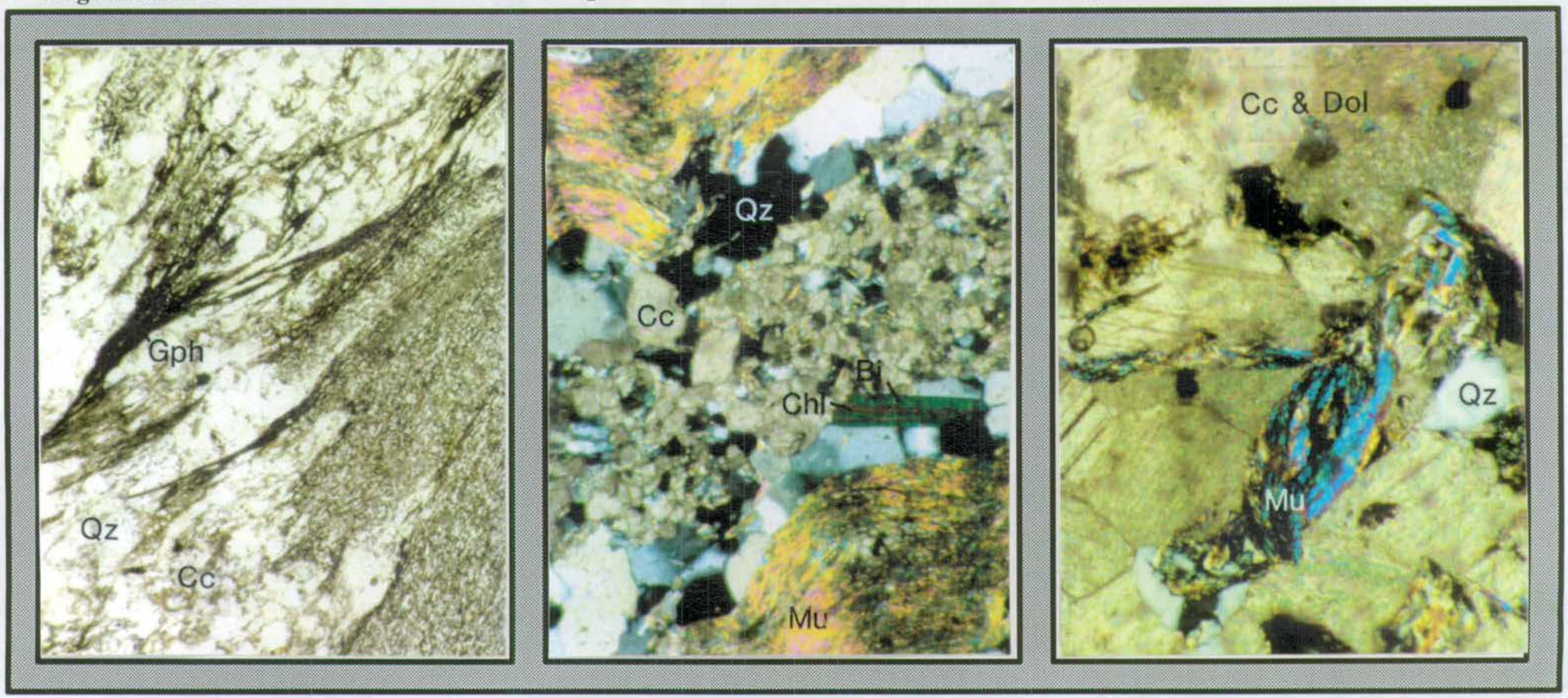

(1) qz + ab + Kfsp + mu + bi + cz + am + sph

(2) qz + ab + Kfsp + cc + di + cz + gross + sph

The development of diopside and grossular from the assemblage amphibole + calcite + quartz (assemblage 1 → assemblage 2) records influx of H_2O (figure 5.16). These mineral assemblages are described in detail in Graham *et al.* (1983) and Fein *et al.* (1993). The calc-silicate phases; amphibole, epidote, diopside and hydrogrossular are typically developed in cm-scale layer-parallel zones within calc-mica schists and siliceous marbles. Graham et al. (1983) invoke devolatilisation reactions in adjacent amphibolites, involving the break-down of chlorite to generate garnet + amphibole, as a source for H_2O-rich fluids.

The Loch Fuar Bheinne Limestone is hosted by the Erins Quartzite and is intensely folded. It is mineralogically homogeneous and relatively pure. It does, however, contain small amounts of dolomite, muscovite and quartz. This assemblage is diagnostic of relatively high X_{CO_2} conditions (figure 5.3a), in contrast to the low X_{CO_2} conditions observed at Stonefield. It is of particular interest to consider the reason for this difference. Both the Loch Fuar Bheinne Limestone and the Loch Tay Limestone crop out in the garnet zone. Probably the only major difference lies in the nature of the host rock. The Loch Fuar Bheinne Limestone is hosted by quartzite and the Loch Tay Limestone is hosted by amphibolites, and psammitic and micaceous schists. It is evident therefore that the host rock lithology may be exerting a control on the development of mineral assemblages in the marbles and therefore the composition of the fluid phase. This is a fundamentally important conclusion because it emphasises the potential of host-rock lithology permeability in controlling fluid transport and fluid-rock interaction.

For reference, representative mineral assemblages of SW Highland marbles are listed in table 5.6.

Figure 5.16: Isobaric T-X(CO2) Section: 6kb
Low X(CO2) Assemblages at Southbay, Tarbert, Loch Fyne

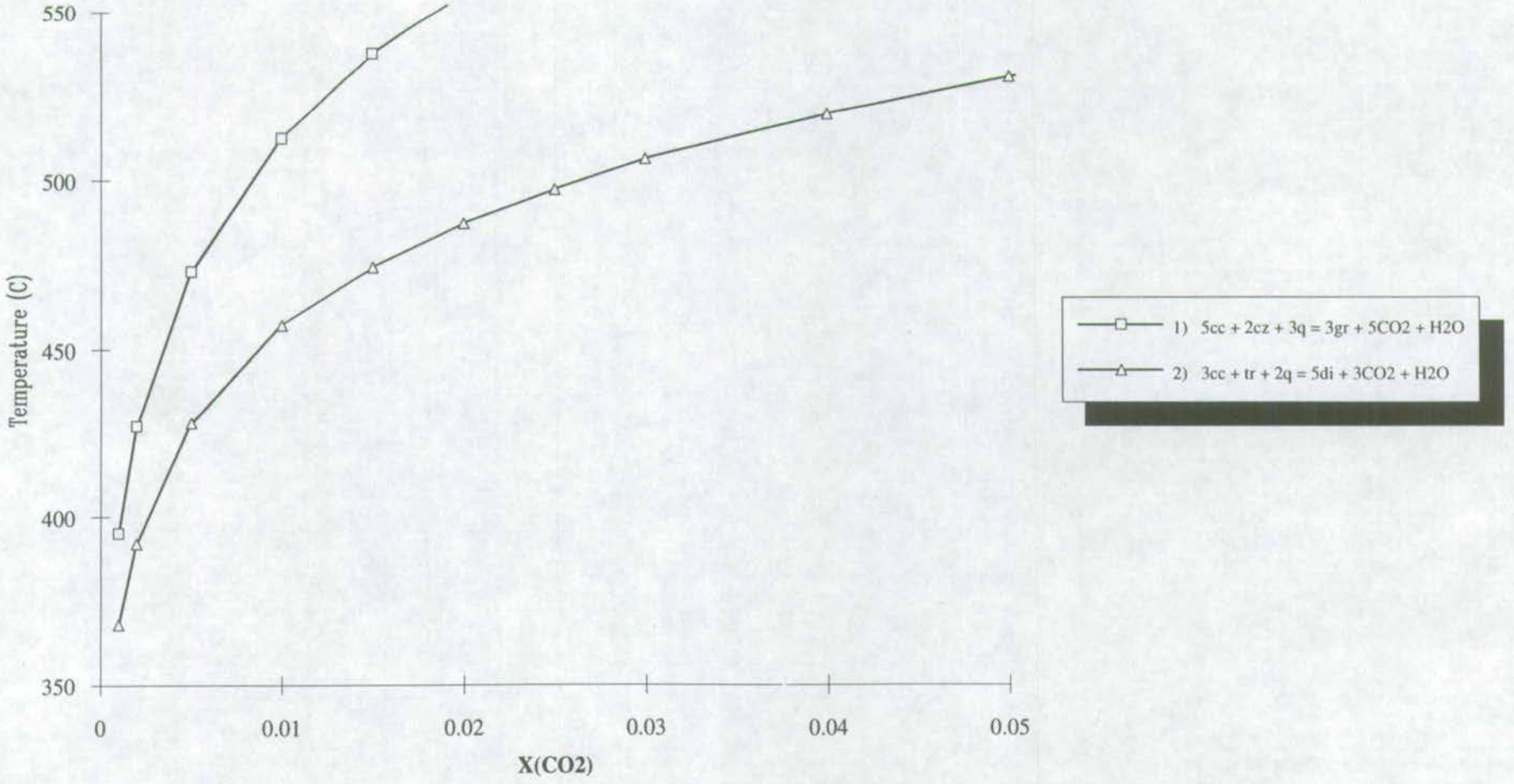

Table 5.6: Representative Assemblages of SW Highland Marbles

Sample	**90OA10**	**CMG *et al.*(1983)**			**86CMG02**
Mineral					
Calcite	*	-	+	-	+
Dol/Ank	+	-	-	+	-
Quartz	+	+	+	+	+
Albite	+	+	+	+	-
K-feldspar	-	+	+	+	-
Biotite	*	+	-	+	-
White Mica	+	+	-	+	+
Chlorite	*	*	-	+	-
Amphibole	-	+	-	-	-
Clinozoisite	-	+	+	-	-
Diopside	-	-	+	-	-
Grossular	-	-	+	-	-
Apatite	*	-	-	-	-
Tourmaline	*	-	-	-	-
Sphene	-	+	+	-	-
Rutile	-	-	-	+	-

(+) = present, (*) = traces and (-) = absent

90OA10 was collected from the Islay Limestone exposed at the Mull of Oa (GR285 413), CMG *et al.* (1983) is compiled from the assemblage data presented in Graham et al. (1983) for the Loch Tay Limestone exposed at South Bay (GR869 710) and 86CMG02 was collected from the Loch Fuar Bheinne Limestone exposed near Loch Fuar Bheinne (GR811 779).

5.5 Psammites

The major psammitic lithologies are the Islay-Jura Quartzite, the Crinan Grits and the Erins Quartzite. These are all dominated by quartz, although the Erins Quartzite has a larger proportion of feldspathic and micaceous material. Other than in the Erins Quartzite, evidence of deformation is minimal. The Islay-Jura Quartzite, in particular, has been sufficiently resilient to deformation as to preserve pristine sedimentary structures, including cross-bedding and channelling (figure 5.17).

The Islay-Jura quartzite is host to intercalations of graphite-rich phyllites and chlorite-absent, kyanite or chloritoid schists (figure 5.18a-e). Typical assemblage data for phyllitic intercalations within the Islay-Jura Quartzite are listed below in table 5.7.

Figure 5.17: Well Preserved Cross-bedding and Channel Structure in the Islay-Jura Quartzite demonstrating the lack of appreciable deformation (scale: hammer=35cm) exposed on the Corryvreckan coast of North Jura

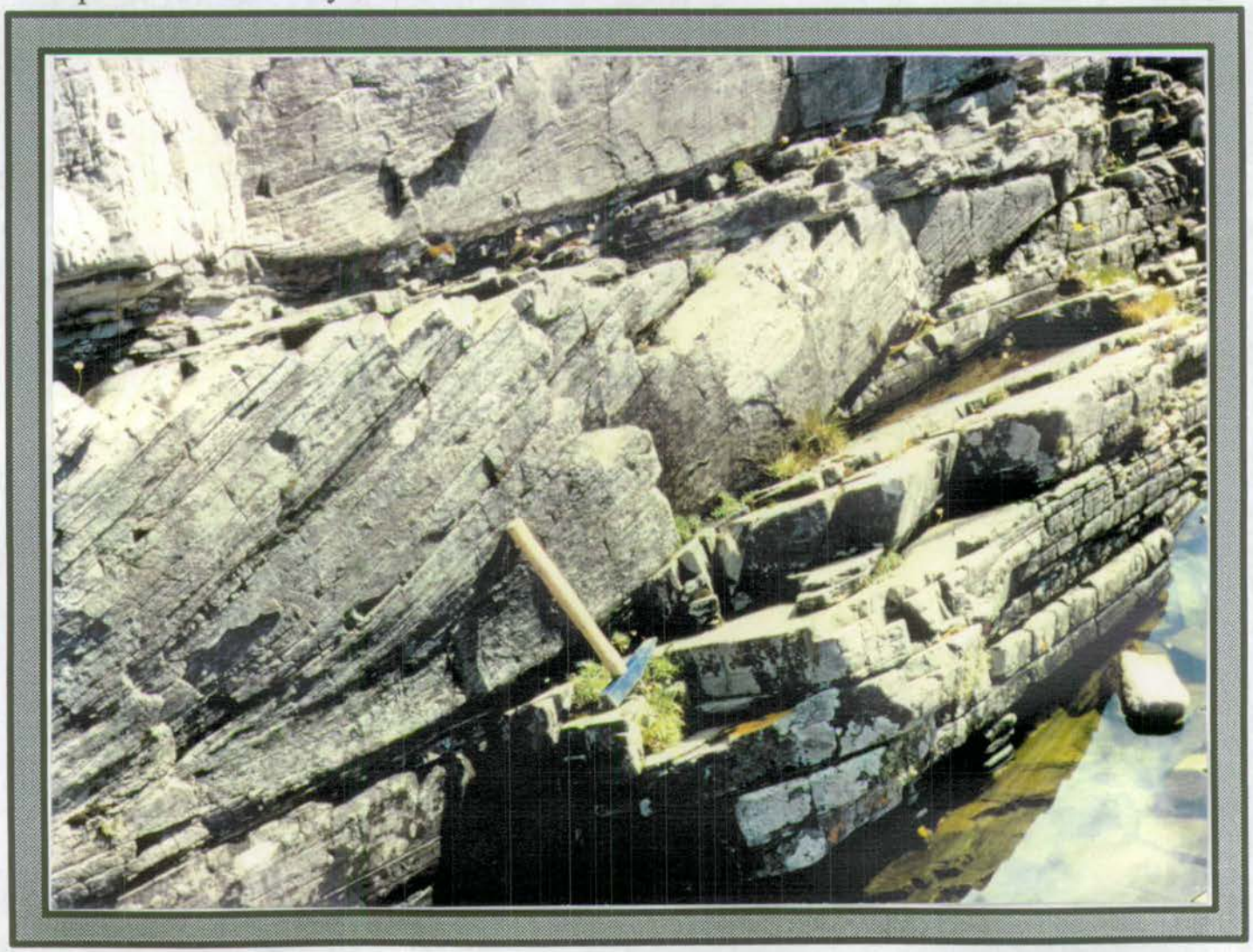

Figure 5.18(a): Photograph showing Chlorite-absent Whiteschist developed as an intercalation in the Islay-Jura Quartzite

Locality:
Carraig Fhada
GR349 443

Scale:
20p piece

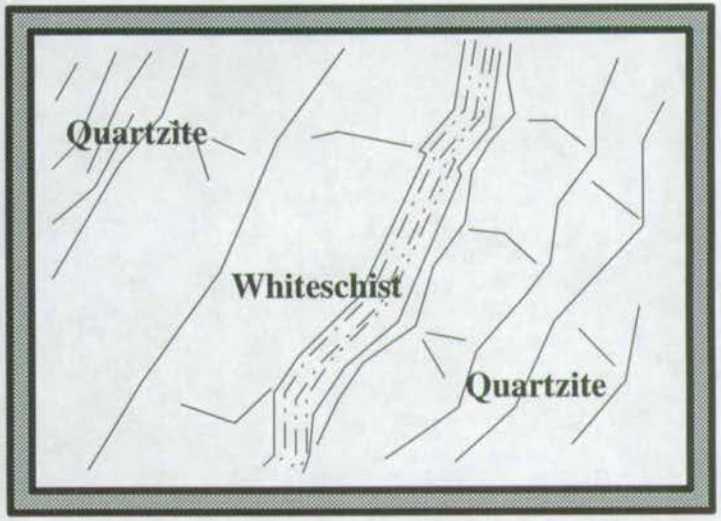

Figure 5.18(b):
Photograph showing Radiating Kyanite Needles developed in phyllitc intercalation s in the Islay-Jura Quartzite

Locality:
Carraig Fhada
GR349 443

Scale:
20p piece

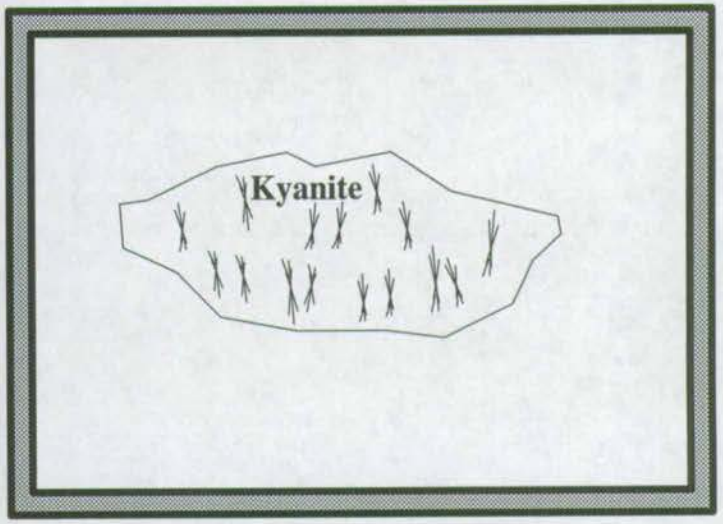

Figure 5.18c: Kyanite-bearing Phyllites

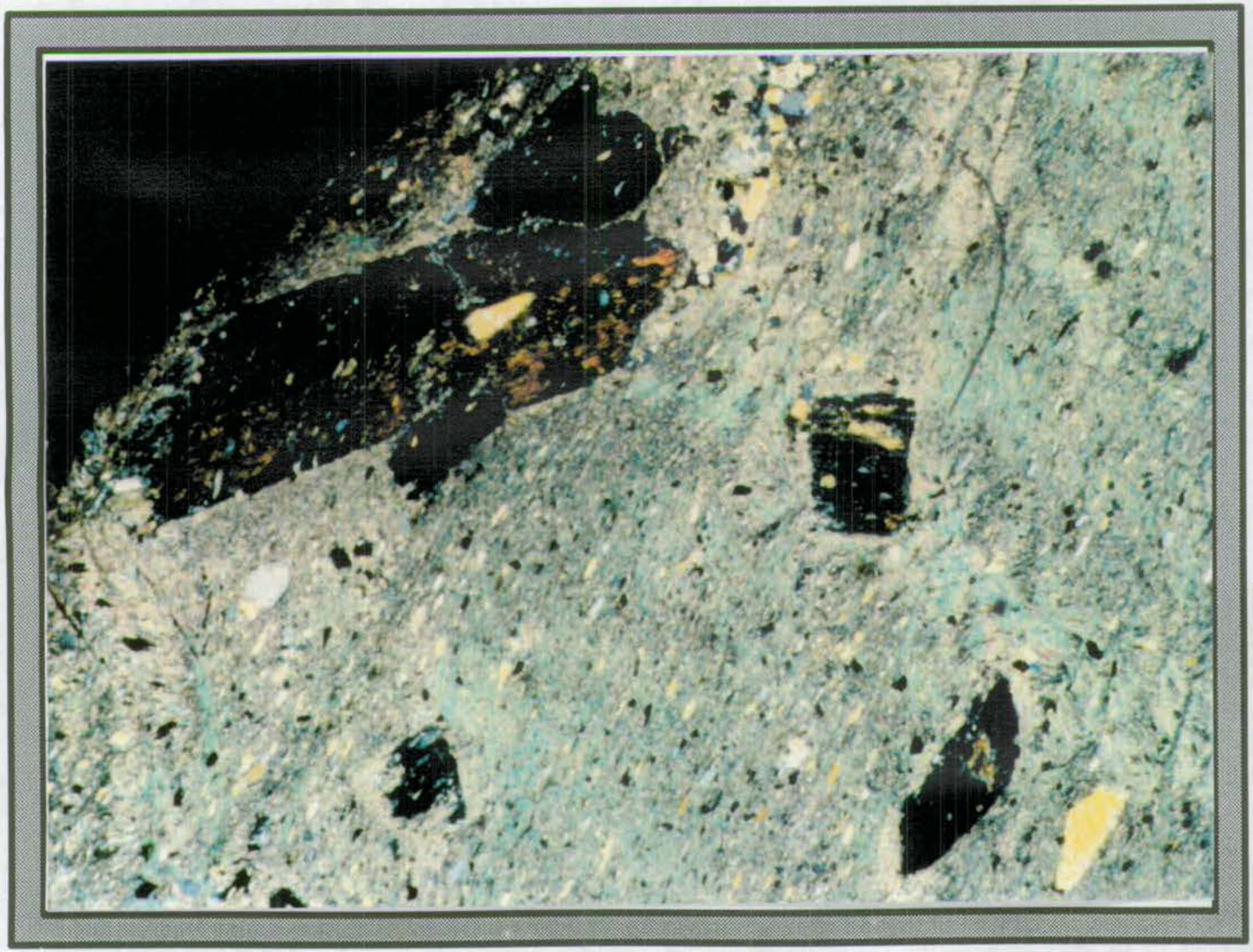

Locality:
Carraig Fhada, Port Ellen, Islay
GR347 445

Magnification:
x40

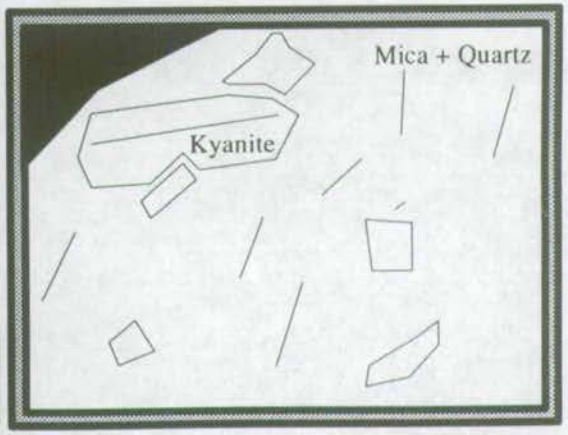

Figure 5.18d: Chloritoid-bearing Phyllites

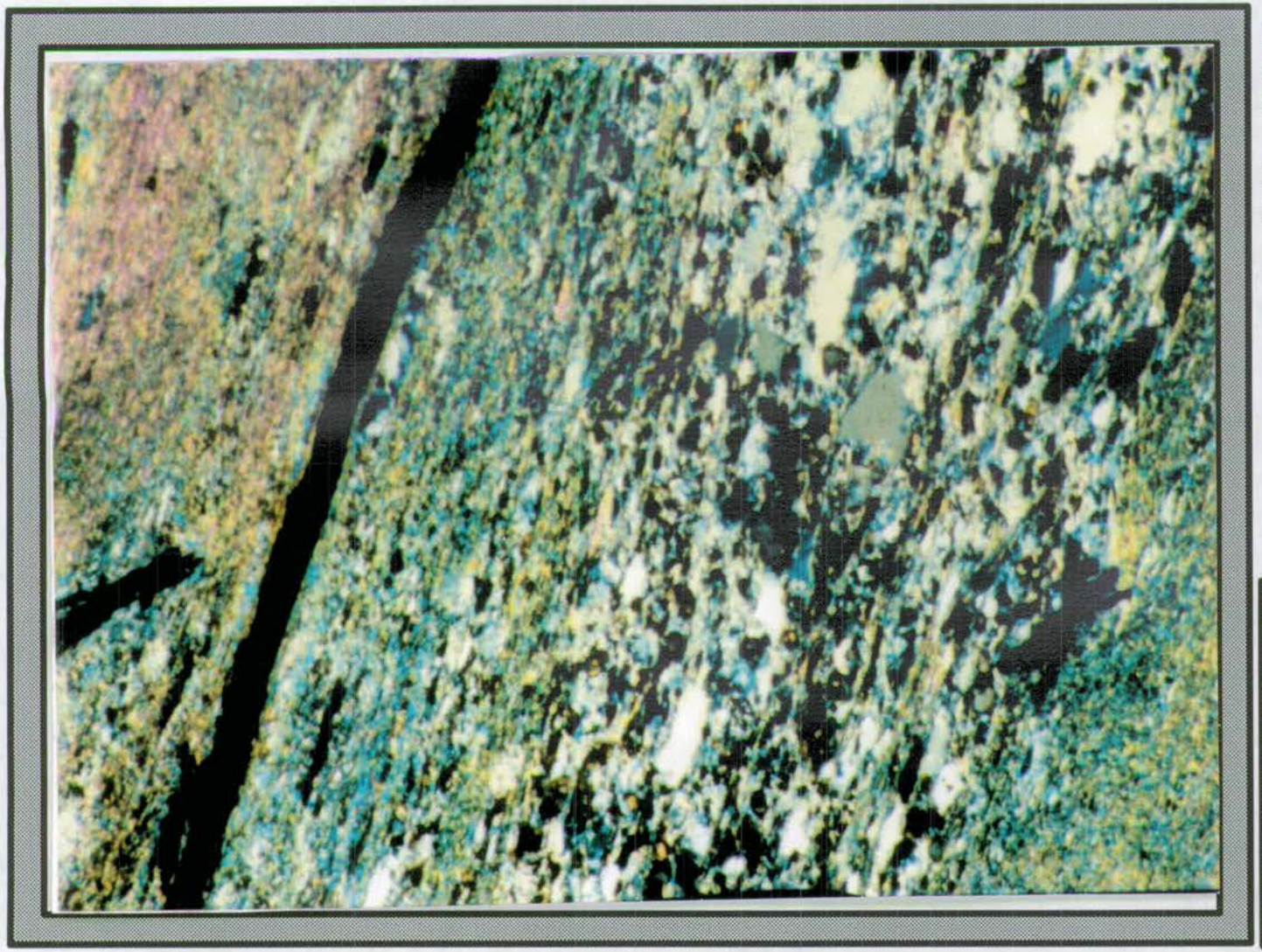

Locality:
Carraig Fhada, Port Ellen, Islay
GR347 445

Magnification:
x40

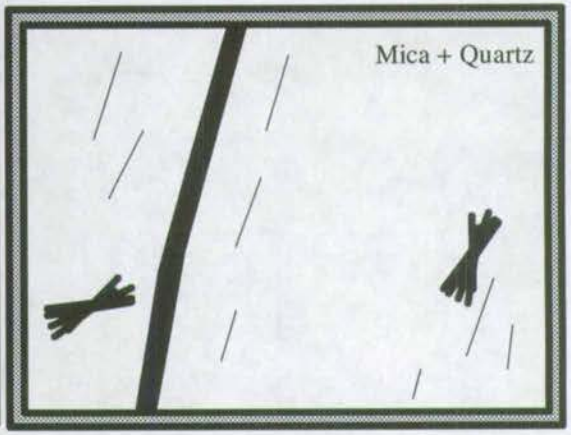

Figure 5.18(e): Photomicrograph of Graphitic phyllite developed as an intercalation in the Islay-Jura Quartzite

Locality: Carraig Fhada GR349 443 **Magnification:** x100
Assemblage: Graphite + Quartz

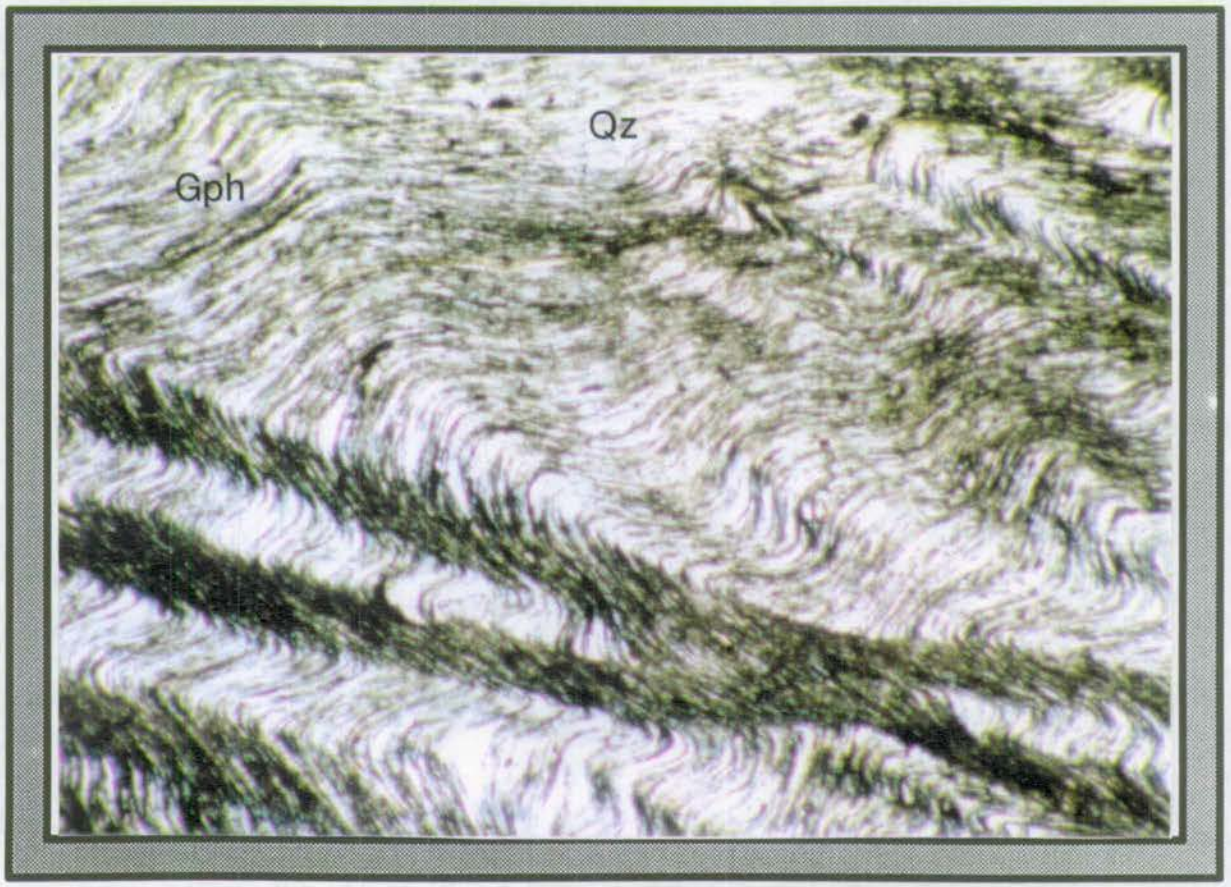

Table 5.7: Representative Assemblages of Phyllitic Intercalations within the Islay-Jura Quartzite

Sample	90CMG03	90CMG04	90CMG01	76CMG05
Mineral				
Chlorite	+	-	-	-
Ankerite	-	-	+	+
Siderite	*	*	+	+
Quartz	+	+	+	+
Mu/Pa	+	+	+	+
Kyanite	-	-	+	-
Pyrophyllite	-	-	+	-
Chloritoid	-	-	-	+
Graphite	*	+	-	-
Pyrite	+	-	-	-

(+) = present, (*) = traces and (-) = absent

All the above samples were collected in the vicinity of Carraig Fhada lighthouse (figure 5.19), near Port Ellen (GR349 443). 90CMG03 is a dark, pyritic phyllite, 90CMG04 is a graphitic phyllite, 90CMG1 is a kyanite-bearing schist and 76CMG05 is as chloritoid-bearing schist collected by Dr.C.M.Graham in 1976.

White micas define a strong, penetrative s_1-s_2 fabric which is axial planar to the regional D_1-D_2 fold structures. Kyanite and chloritoid grew as radiating needles, up to 1-2cm in length (figure 5.18b, c and d) and were clearly rotated by s_4 crenulation (figure 5.18c). Kyanites are also commonly rimmed by pyrophyllite. Ankerites grew as large euhedral porphyroblasts up to 1-2mm in diameter. They grew in a state of chemical disequilibrium with co-existing siderites. Individual ankerite porphyroblasts contain inclusion trails which mimic D_1-D_4 fabrics which are developed outwith the porphyroblasts (figure 5.6f). There is no conclusive evidence that ankerite porphyroblasts are deformed or significantly rotated.

The presence of chloritoid or kyanite, in the absence of chlorite constrains these assemblages to relatively high X_{CO_2} conditions (figure 5.3a) by the divariant $MFASHCO_2$ reaction:

$chl + 4CO_2 = ctd + 4sid + 2qz + 3H_2O$ (7)[3]

and the divariant $MFASHCO_2$ reaction:

[3]Reactions (7) is included in a reference card at the back of the thesis.

chl + $5CO_2$ = ky + 5sid + 2qz + H_2O **(8)**[4]

which describe fields in T-X_{CO_2} space (figures 5.3e and 5.3f) which are bounded by the univariant reactions listed below:

(1) The $MASHCO_2$ reaction:

clin + $4CO_2$ = mctd + 4mag + 2qz + $3H_2O$ **(7,Mg)**

(2) The $FASHCO_2$ reaction:

daph + $4CO_2$ = fctd + 4sid + 2qz + $3H_2O$ **(7,Fe)**

(3) The $MASHCO_2$ reaction:

clin + $5CO_2$ = ky + 5mag + 2qz + H_2O **(8,Mg)**

(4) The $FASHCO_2$ reaction:

fctd + $5CO_2$ = ky + 5sid + 2qz + H_2O **(8,Fe)**

The Mg and Fe end-member reactions are spatially distinct in T-X_{CO_2} space. However, neither reaction is used for quantitative modelling of fluid flow and therefore, for the purposes of this study, it is sufficient to note that both Mg and Fe end-member curves plot down temperature and up X_{CO_2} from reactions 1-5.

Similar high X_{CO_2} conditions are indicated by the presence of graphite.

The rimming of kyanite by pyrophyllite records the progress of the univariant reaction:

ky + 3qz +H_2O = pyhl **(9)**[4]

during retrogression. The existence of this reaction constrains the temperature at which kyanite grew as having been in excess of 429±25°C.

5.6 High X_{CO_2} Assemblages

It has become apparent throughout this section that relatively high X_{CO_2} conditions are generally attained where phyllites or marbles are hosted by psammites

[4]Reactions (8) and (9) is included in a reference card at the back of the thesis.

(c.f. Loch Fuar Bheinne Limestone, section 5.4 and phyllitic intercalations, Carraig Fhada, section 5.5).

Phyllitic Intercalations at Carraig Fhada

Phyllitic intercalations, observed within the Islay-Jura Quartzite, near Carraig Fhada Lighthouse, Port Ellen, Islay (figure 5.19), are chlorite-absent and (1) kyanite-bearing, (2) chloritoid-bearing or (3) graphite-bearing (table 5.7). The T-X_{CO_2} section shown in figure 5.3a restricts these assemblages to having developed under higher X_{CO_2} conditions than fluids in equilibrium with adjacent Port Ellen Phyllites outwith the Islay-Jura Quartzite. Therefore the phyllitic intercalations hosted by the Islay-Jura Quartzite are effectively isolated fluid reservoirs where higher X_{CO_2} conditions are attained and preserved. That is to say the fluid composition within the phyllitic intercalation is internally buffered in partial or complete isolation from fluid present within the Port Ellen Phyllites.

For psammites to be able to isolate individual fluid reservoirs from one another, they must be impermeable to fluid escape. As discussed in section 2.4, rock-permeability depends on (i) porosity (φ) and (ii) the solid-fluid-solid dihedral angle (θ). However if $\theta<60°$, fluid flow is possible for ***all*** φ (section 2.4). It is therefore uncertain as to whether the observed impermeability of the quartzite may be reconciled with the experimental work of Holness (*in prep.*), Holness (*in press*) and Watson & Brenan (1982) (section 2.4 and figure 2.18). They predict that the quartz-fluid-quartz dihedral angle (θ) is likely be less than the critical value of 60° (55-60° at 9±1kB, 430-490°C) for a pure-H_2O fluid. However compositions relevant to reactions (7) and (8)[5] at 450°C record a fluid composition of $X_{CO_2}>0.05$ (figure 5.3a). Holness (*pers.comm.*) suggests that 5% CO_2 may be sufficient to increase the dihedral angle to values in excess of 60°. Also, the presence of graphite may indicate significant CH_4 which would also significantly increase the dihedral angle (Holness

[5]Reactions (1) to (5), (7) and (8) are included in a reference card at the back of the thesis.

Figure 5.19: Location Map of Phyllitic Intercalations at Carraig Fhada

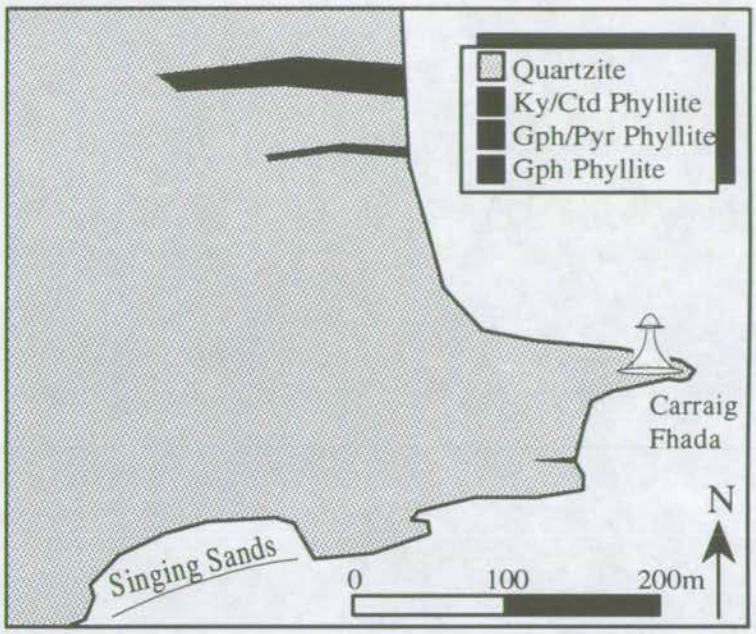

pers.comm.). Furthermore the Islay-Jura Quartzites are underlain by a thin, laterally continuous marble horizon which if we assume upwards fluid flow, driven solely by buoyancy forces, will be encountered by fluids ***before*** reaching the base of the quartzite. Experiments of Holness & Graham (1991) and Holness (*pers. comm.*) have shown that the calcite-fluid-calcite dihedral angle is in excess of 60° at all X_{CO_2} at P=5kb, T=450°C (section 2.3.2 and figure 2.18) and that the calcite-fluid-calcite dihedral angle ***increases*** with pressure. It is therefore reasonable to conclude that at 9kb and 450°C, marble will behave as an impermeable barrier to grain-edge flow and may effectively isolate the overlying quartzite from upwards migrating fluids. This interpretation is consistent with carbonate stable isotope data obtained from marbles from the Mull of Oa, Islay which are presented in full in figure A6.2 (appendix 6) and summarised in table 5.8.

Table 5.8: Carbonate Stable Isotopic Data from the Mull of Oa Marbles

Sample	Distance from Base of Quartzite	Lithology	$\delta^{18}O$
90-OA-23	3.0m	Phyllitic Marble	21.6
90-OA-22	10.0m	Marble	29.8
90-OA-19	28.2m	Marble	26.7
90-OA-15	40.0m	Phyllitic Marble	23.8
90-OA-8	66.5m	Marble	20.4
90-OA-1	85.0m	Phyllitic Marble	16.9

Samples were collected from a traverse of three narrow, intensely deformed marble units interlayered with more phyllitic marble at Port nan Gallan, Mull of Oa, Islay (GR285 413). The complete dataset is included in figure A6.2, appendix 6 and the analytical procedure is described in section 6.5.2.

It is apparent from the data in table 5.8, that the marbles which underlie the Islay-Jura Quartzite record isotopic signatures similar to those of sedimentary limestones ($\delta^{18}O$=22-26‰, Veizer & Hoefs 1976) and therefore record minimal modification as a result of fluid infiltration. It is likely, therefore that marbles were essentially impermeable.

A Marble Intercalation at Loch Fuar Bheinne

A marble at Loch Fuar Bheinne which is hosted by the Erins Quartzite contains the stable assemblage; dolomite + muscovite + quartz. This assemblage records higher X_{CO_2} fluids than in either the adjacent Ardrishaig Phyllites or garnet-zone marbles hosted by calc-mica schists (Stonefield Schists) and amphibolites (e.g. Tarbert, section 5.4). It is therefore inferred that the Loch Fuar Bheinne Limestone was essentially isolated from the more H_2O-rich fluids in the Ardrishaig Phyllites and Stonefield Schists.

Carbonate stable isotope data were obtained by Graham (*unpublished*) from several samples of marble from Loch Fuar Bheinne and are listed in table 5.9.

Table 5.9: Carbonate Stable Isotopic Data from the Loch Fuar Bheinne Limestone

Sample	Distance from Base of Limestone	Mineral Assemblage	$\delta^{18}O$
86-CMG-02A	4.0m	Cc-Dol-Qz-Mu-Chl	12.93
86-CMG-02B	4.0m	Cc-Dol-Qz-Mu-Chl	13.22
86-CMG-03	6.0m	Cc-Dol-Qz-Mu	14.64
86-CMG-04A	>10.0m	Cc-Dol-Qz-Mu-Ab	16.11
86-CMG-04B	>10.0m	Cc-Dol-Qz-Mu	16.01
86-CMG-05	>10.0m	Cc-Dol-Qz-Mu-Ab	15.79

Samples were collected by C.M. Graham from the Loch Fuar Bheinne Limestone (GR811 779). Exposure was too limited to permit confident location of samples 86-CMG-04A, 86-CMG-04B and 86-CMG-05.

The interior of the marble records $\delta^{18}O \approx 16‰$. This value may record limited isotopic depletion from the pre-cursor sedimentary signature of $\delta^{18}O=22\text{-}26‰$ ascribed by Veizer & Hoefs (1976). Significantly depleted values in the range $\delta^{18}O=12\text{-}15‰$ are recorded at the basal margin of the marble unit. Isotopic depletion at the basal margin of the Loch Fuar Bheinne Limestone is spatially limited and may developed wholly in response to diffusive exchange with the adjacent quartzite. Therefore it is inferred that only small quantities of fluid infiltrated the marble. Therefore, the marble must have been relatively impermeable resulting in preservation of high X_{CO_2} assemblages. This interpretation is again consistent with the

prediction that marbles are impermeable to fluid at the elevated pressures and temperatures of Dalradian metamorphism. Furthermore, this interpretation is consistent with quartzites also being impermeable to syn-metamorphic fluid infiltration.

Summary

In summary, quartzites are observed to behave as impermeable barriers to fluid movement under the P-T conditions of Dalradian metamorphism, despite the experimental predictions of $\theta<60°$ of Holness (*in prep.*) ,Holness (*in press*) and Watson & Brenan (1982), probably as a result of the affect of a small percentage of CO_2, or small uncertainties in constraining pressure and temperature, on the dihedral angle. Quartzites are observed to separate and isolate individual fluid reservoirs enabling internal buffering of phyllite or marble intercalations to higher X_{CO_2} conditions than are evident in adjacent phyllitic lithologies. Furthermore marbles have been shown to be nearly impermeable to fluid infiltration under the P-T conditions of Dalradian metamorphism, consistent with the experimental predictions of Holness & Graham (1991) and Holness (*pers. comm.*).

5.7 Implications arising from Lithological Descriptions to Modelling of Fluid Flow

The following general implications arise from the lithological descriptions which are presented in this section:

(1) Calc-phyllites and metabasites are predominantly permeable to fluid whereas quartzites and marbles are predominantly impermeable.

(2) Metabasites develop zonal distributions of type I to III mineral assemblages as a result of infiltration of a CO_2-bearing fluid. They are ideally suited as "marker" lithologies for the quantitative modelling of fluid flow on the following basis:

(i) Type I and III metabasite assemblages can easily be distinguished on the basis of their radically different mineral modes.

(ii) Type I and III metabasite assemblages are spatially separated by a narrow zone of type II metabasite in which reaction (1) is buffered. The reaction front is developed in this zone.

(iii) Reaction (1) originated at the metabasite margin and was propagated inwards towards the metabasite interior.

(iv) Metabasites are abundant and widespread throughout the SW Highlands.

(3) It is assumed that composition of the fluid which infiltrates metabasites and drives mineral reaction is controlled by, and buffered within the host rock.

CONCLUSIONS TO CHAPTERS 3, 4 & 5

The Study Area

The essential requirements which a suitable study area should adhere to if quantitative modelling of fluid flow and regional fluid flux mapping are to be achieved were set down in the prelude to chapters 3, 4 and 5 and are re-iterated, in brief, below:

(1) The initial and final positions of isotope and reaction fronts must be identifiable in a suitable marker lithology;

(2) The rock must permit pervasive fluid flow;

(3) Isotopic shifts and mineral reactions must be well constrained and measurable;

(4) Grain-scale mineral-fluid equilibrium must be achieved;

(5) The composition of the fluid infiltrating the marker lithologies must be constrained;

(6) Marker lithologies must be abundant and widespread;

(7) Regional and local structure should be varied and its unambiguous interpretation must be possible;

(8) The timing of fluid infiltration relative to regional metamorphism and deformation must be known.

The Dalradian of the SW Scottish Highlands was selected for this study, the reasons for which have been addressed in chapters 3, 4 and 5 and are summarised below:

(1) Mineral reaction (1)[1] is driven by infiltration of CO_2-bearing hydrous fluids into the margins of individual metabasite units. The modal changes associated with these

[1] Reaction (1) is included in a reference card at the back of the thesis.

reactions are large and therefore the reaction fronts may easily be located. The reactions originated at the margin of the metabasite and therefore the advection distance of the reaction front may be measured as the distance between the reaction front and the margin of the metabasite unit.

(2) Merely because pervasive mineral reaction has occurred, it can be assumed that, at the time of fluid infiltration, either an interconnected grain-edge porosity ($\theta<60$) or an interconnected and closely-spaced fracture network must have existed within the metabasites.

(3) The stoichiometry of reaction (1) is known, and the reaction is well characterised in P-T-X_{CO_2} space (figures 5.3a and 5.3b). The original isotopic signatures of the metabasites are well-constrained and differ significantly from those of the different host rocks.

(4) The timing of the causative fluid infiltration is constrained on the basis of the integral relation between deformation and infiltration-driven mineral reaction (section 5.3.6), to have occurred at or near peak metamorphism and during D_1-D_2 deformation. This is the most likely time at which grain-scale mineral-fluid equilibrium should be attained.

(5) The infiltrating fluid composition may be assumed to be in equilibrium with the host phyllites.

(6) The obvious "marker" lithologies for fluid flux mapping are the metabasite sills and dykes which are especially well-exposed and outcrop in abundance throughout the SW Scottish Highlands.

(7) D_1 deformation of the Dalradian of the SW Scottish Highlands resulted in the development of the three regional-scale fold structures: the Islay Anticline, the Loch Awe Syncline and the Ardrishaig Anticline. Although uplift and tightening of the Tay Nappe probably post-dates fluid infiltration the attitude of the structures within the study areas are only minorly affected (Roberts 1974).

(8) The timing of fluid infiltration is constrained to be around peak metamorphism (syn-D_1-D_2) on the basis of the following criteria:

(i) Temperatures estimated using THERMOCALC (Holland & Powell 1988) are similar for type I and III assemblages in the same metabasite unit, and comparable to independent geothermometers specifically relating to peak metamorphic minerals.

(ii) Type III assemblages develop D_1-D_2 fabrics.

(iii) Deformation and reaction front advection are integrally inter-dependent (section 5.3.6).

CHAPTER 6

TECHNIQUES

6.TECHNIQUES

6.1 Rationale

The aim of this chapter is to describe and justify the techniques employed in this study to identify and quantify infiltration-driven mineralogical, isotopic and chemical alteration with a view towards regional-scale quantitative modelling of deep-crustal fluid flow. The chapter is divided into eight further sections. The first seven of these describe, individually, the field and laboratory techniques implemented in this study, concentrating, not only on their practical usage, but also on the problems which were encountered and how these were tackled. The last section draws upon these descriptions to present the field and laboratory strategy adopted in this project.

6.2 Geological Mapping

Detailed geological mapping of selected coastal exposure was undertaken, at scales between 1:6000 and 1:10000, to establish the local lithostructural successions at various key localities of the SW Scottish Highlands where quantification of fluid-rock interaction processes was feasible. Well-exposed metabasites and carbonates were located as potential marker horizons for quantitative one-dimensional modelling of deep-crustal fluid flow. Particular attention was directed towards their structural, lithological and metamorphic setting. Fair copies of relevant field slips are enclosed with this thesis.

6.3 Petrography

Mineral assemblage data were obtained by combined optical microscopy and X-ray diffraction techniques. That is, where optical mineral identification was uncertain (particularly differentiating between calcite, ankerite and dolomite), interpretations were reinforced with X-ray diffraction analysis. Optical microscopy was carried out on a James Swift MP3502 binocular microscope at magnifications of ×40, ×100 and ×400. X-ray diffraction analyses were obtained using an automated Philips PW1800 X-ray diffractometer.

Textural analysis was achieved largely by optical microscopy, again using a James Swift MP3502 binocular microscope at magnifications of ×40, ×100 and ×400, and photomicrographs (chapter 5) were taken with a "Wild" photomicroscope M400.

Mineral modes used for estimation of reaction progress were estimated by a standard point-counting technique and are based on a minimum of 400-500 points per slide. Spacing between points was greater than the diameter of the largest grain in a sample. Mineral modes are either presented for individual samples (chapters 5 and 10) or used as measures of reaction progress. In the later case, reaction progress estimates were used to locate mineral reaction fronts within metabasite horizons and are plotted as a function of distance from the structural base. Standard modal profiles were calculated from the volumetric stoichiometric coefficients of reaction 1[1] and are illustrated in figure 6.1. Real modal profiles are presented in appendix 4 and discussed in chapter 10.

Point-counting is indisputably both time-consuming and tedious. Depending on the individual sample, 400-500 points can be counted in about 1 hour. Metabasite horizons are typically 5 to 20 metres in width, and if a mineral reaction front is to be located with reasonable accuracy, the sampling interval cannot usually exceed 0.3 to 0.5 metres. Therefore, for the accurate location of a mineral reaction front, up to

[1]Reactions 1 is included on the reference card at the back of the thesis.

Figure 6.1; Standard Modile Profiles of Reaction 1:
Am + Ep + CO2 + H2O = Chl +Cc + Qz

Reaction 1(Mg): Tr + Cz + CO2 + H2O = Clin + Cc + Qz

Reaction 1(Mg)	Clin	Cc	Qz	Cz	Tr	CO2	H2O	Unit
Mol.Stoich.Coeff.	3	10	21	-2	-3	-10	-8	mol.
Molar Wt.	555	100	60	454	811	44	18	g/mol.
Density	3.02	2.71	2.65	3.12	3.02	1.32	0.98	g/cc.
Vol.Stoich.Coeff.	0.50	0.34	0.43	-0.27	-0.73	-0.30	-0.13	cc.

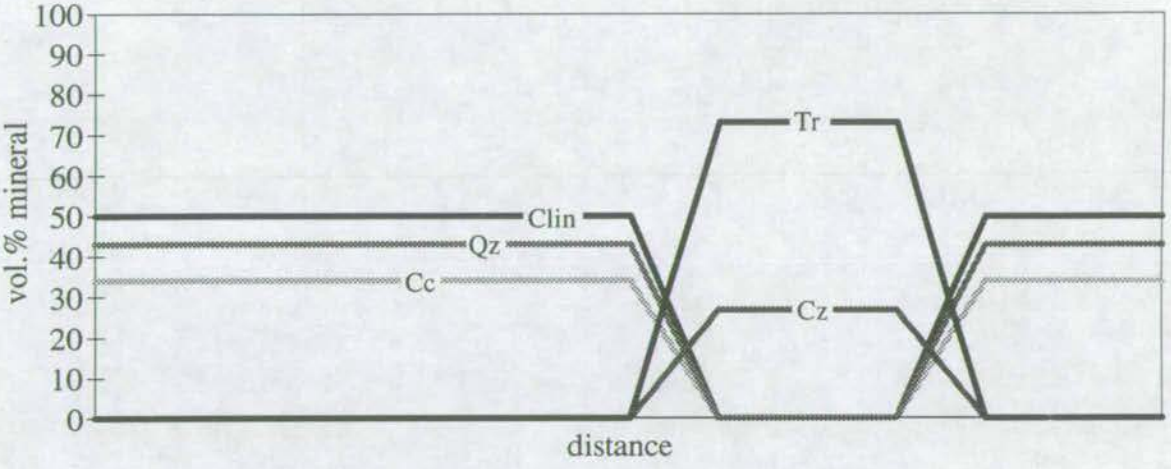

Reaction 1(Fe): Ftr + Cz + CO2 + H2O =Daph + Cc + Qz

Reaction 1(Fe)	Daph	Cc	Qz	Cz	Ftr	CO2	H2O	Unit
Mol.Stoich.Coeff.	3	10	21	-2	-3	-10	-8	mol.
Molar Wt.	714	100	60	454	906	44	18	g/mol.
Density	3.20	2.71	2.65	3.12	3.44	1.32	0.98	g/cc.
Vol.Stoich.Coeff.	0.62	0.34	0.44	-0.27	-0.73	-0.31	-0.14	cc.

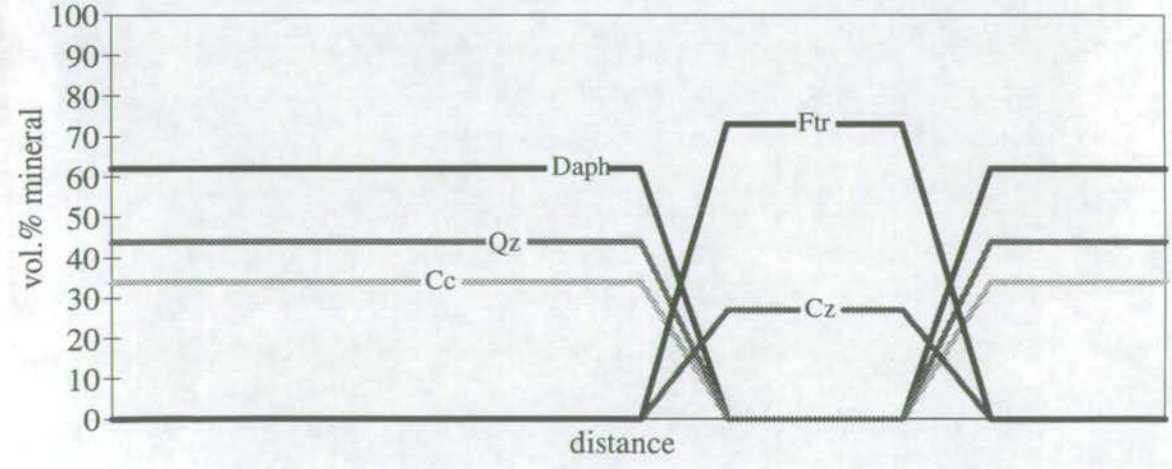

about 50 samples must be taken. Including sampling, cutting, sectioning and point-counting, this can easily represent 2 to 3 weeks work, not to mention the excessive expense of the thin-section preparation involved. This is clearly impractical for regional fluid flux mapping, where some 40 to 50 such metabasites should ideally be analysed.

6.4 Field Geochemistry

The practical problems of point-counting as a technique for measuring reaction progress were overcome, with the adaptation and application of a simple, quantitative geochemical field technique which exploited the fact that reactions (1), (2) and (3) all involve marked changes in the modal percentages of calcite and dolomite. Calcite reacts rapidly with dilute hydrochloric acid generating gaseous CO_2, and dolomite undergoes a similar reaction, but much more slowly. The technique is illustrated in figure 6.2 and outlined below:

(1) A lump of fresh rock is crushed with a geological hammer, and ground in a portable steel mortar and pestle;

(2) An aliquot of finely-ground sample, of known volume, is placed in a perspex reaction vessel with a built-in pressure-gauge, over-which a bucket of excess 10% HCl acid is suspended carefully, avoiding spillage and premature reaction;

(3) The vessel is sealed and shaken to bring the acid into contact with the sample and initiate the reaction.

(4) Arbitrarily, the vessel is shaken for 40 seconds in every 60 seconds, allowing 20 seconds to write down readings. The pressure of evolved CO_2 is measured on the built -in pressure-gauge every 60 seconds for ten minutes.

Where a rock contains neither calcite nor dolomite, no pressure increase is observed; where a rock contains only calcite, the maximum pressure, which corresponds to the modal % calcite, is usually attained after approximately 3 minutes; where a rock contains only dolomite, the pressure increases gradually throughout the

Figure 6.2; Field apparatus for measurement of whole rock calcite content.

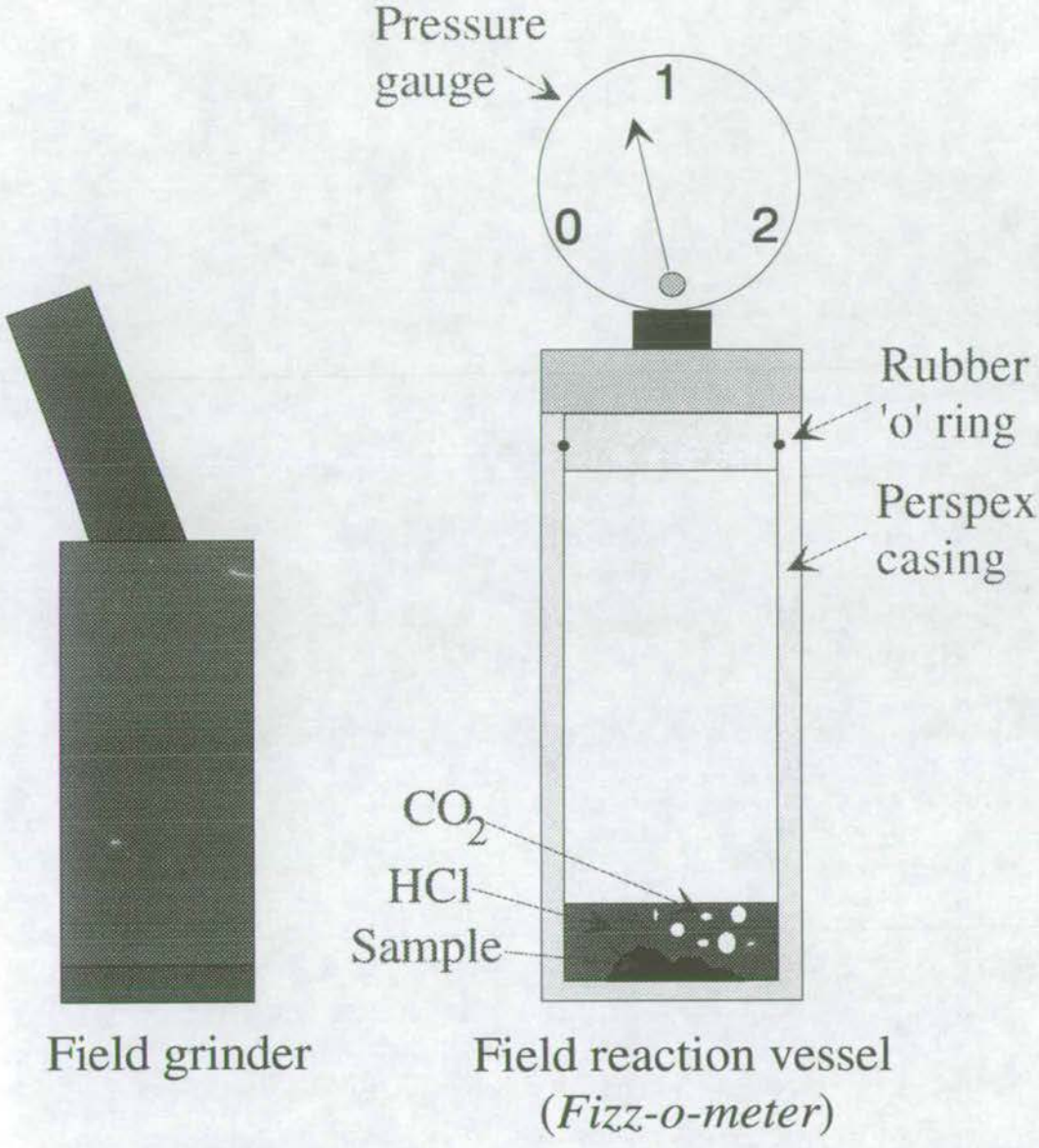

entire period of the reaction; and where a rock contains both calcite and dolomite, all the calcite reacts first, within about 3 minutes, and the dolomite reacts more slowly throughout the duration of the reaction. The relative quantities of calcite and dolomite may be obtained by calibration with standards in the laboratory.

To minimise the errors brought about by impurities, calcite and dolomite standards were taken directly from metabasite rocks within the study area. The resultant standard calibrations are presented in figure 6.3, and their use is inferred in chapter 10.

Finally, the stoichiometric coefficients of the relevant reaction may be used to calculate reaction progress. Field geochemical data are presented in appendix 5 and discussed in chapter 10.

This new field geochemical technique offers several advantages over the more traditional point-counting approach:

(1) The technique itself is rapid; an analysis only takes about 15 minutes to complete;

(2) The results obtained constrain reaction progress ***at least*** as accurately as counting 500 points;

(3) Because the technique is implemented in the field, waste sampling is minimised and the position of the reaction front is more accurately constrained by "bracketing" the reaction front from both sides.

The rapidity and relative accuracy of this technique has made its application invaluable towards constructing a regional-scale map of syn-metamorphic deep-crustal fluid flow. Nevertheless, as this is the first-ever large-scale application of reaction front advection modelling (Bickle & Baker 1990b) to quantify fluid flow, it was essential that comparative recourse to the better established technique of isotope front advection modelling (Bickle & McKenzie 1987 and Bickle & Baker 1990b) was attempted.

Figure 6.3: Calibration of "Fizz-o-meter"

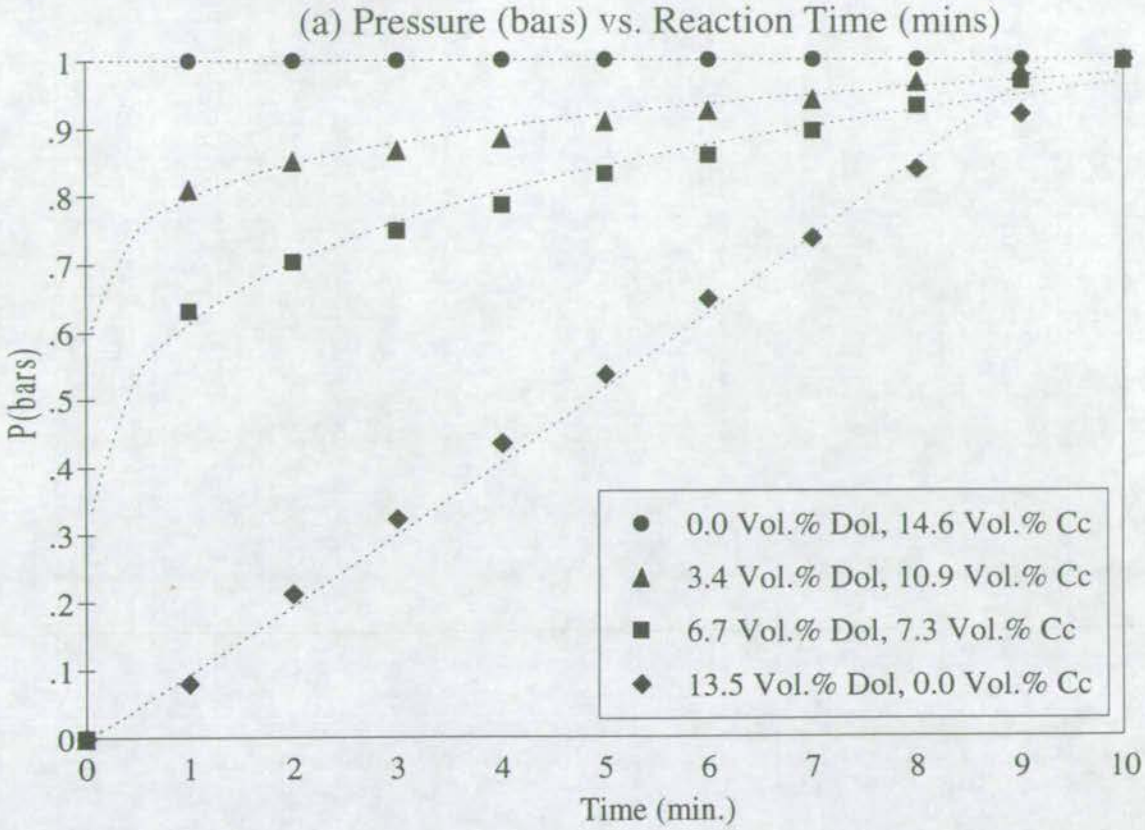

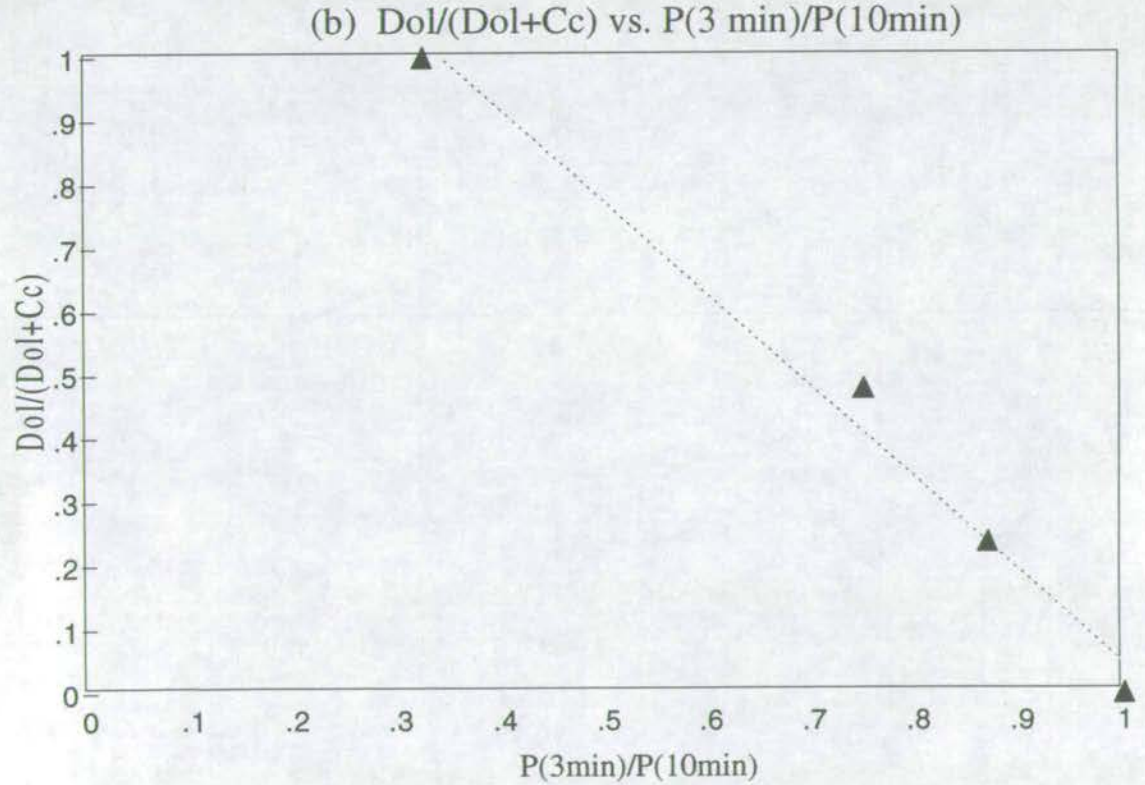

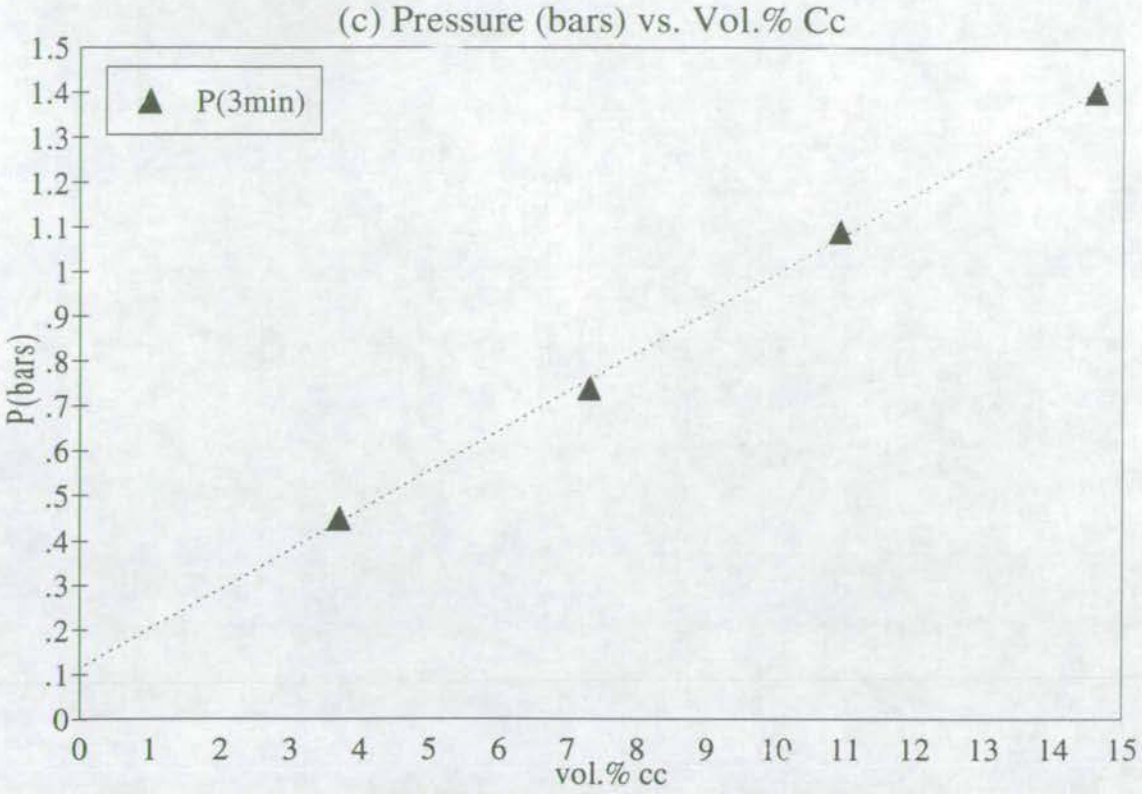

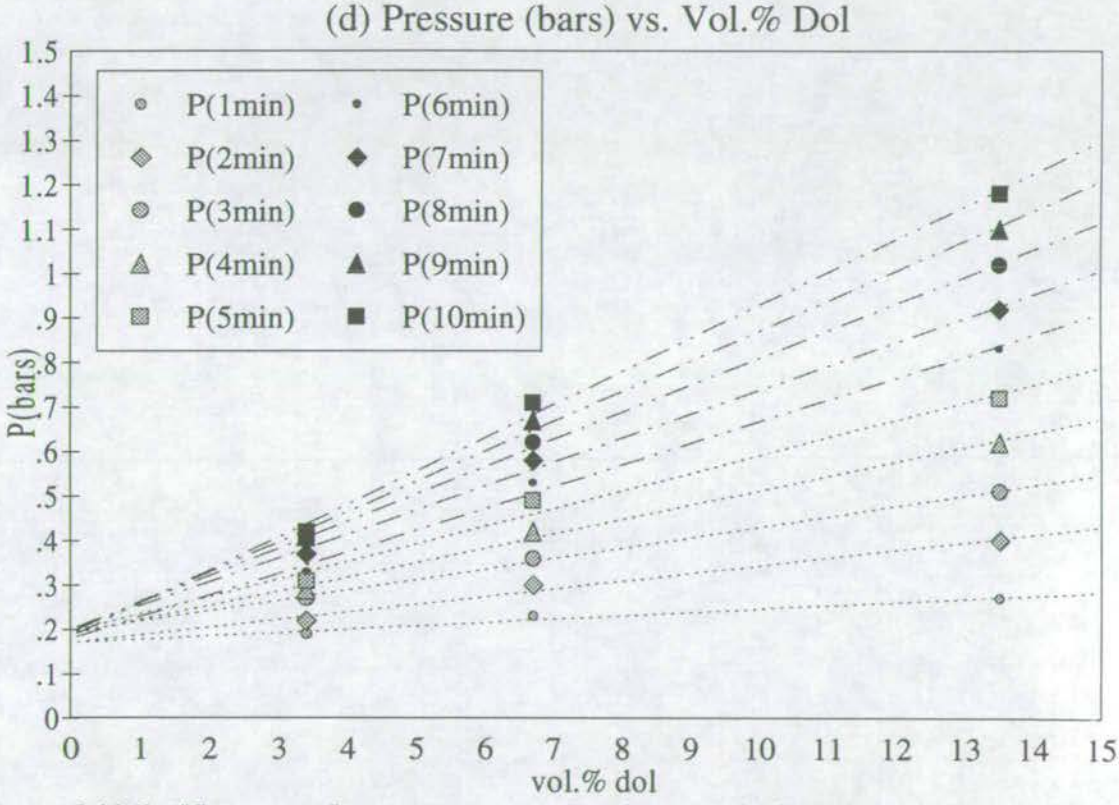

Initially, "fizz-o-meter" measurements are plotted on a graph of pressure (of evolved CO2) vs. reaction time. Graph (a) shows calibration curves for known volumetric percentages of dolomite and calcite. The relative proportions of calcite and dolomite are then evaluated on the graph (b). The vol.% calcite and vol.% dolomite may subsequently measured from the calibration curves shown in figures in graphs (c) and (d), which were constructed from samples containing known volumes of pure calcite and dolomite.

Logarithmic regression curves are fitted to graph (a) and linear regression curves are fitted to graphs (b), (c) and (d). Regression curves are computed using the IBM PC computer program CHARISMA.

6.5 Stable Isotope Geochemistry

Stable isotope work was carried out at the Scottish Universities Research and Reactor Centre (SURRC) at the National Engineering Laboratory (NEL) in East Kilbride. Both silicates and carbonates were analysed, and because their analytical procedures differ radically, they will be dealt with separately.

6.5.1 Stable Isotope Analysis of Whole Rock Silicates

Stable isotope analysis of sample traverses across two metabasite sills at the Ard of Port Ellen on Islay was undertaken in a comparative study of reaction front and isotope front advection, in an attempt to test the one-dimensional quantitative fluid flow models of Bickle & McKenzie (1987) and Bickle & Baker (1990b). The interpretations and conclusions of this study are presented in chapter 8.

Because of the extent of the mineral reactions affecting the metabasite sills, few minerals are common to all mineral assemblages (types I-III) throughout the entire width of the sills. Stable isotope analyses of mineral separates would therefore be of limited value towards constraining the position of an isotopic front. The next best approach, of analysing whole rock samples, was therefore adopted. This has the added advantage that direct comparison with the average δ18O-signature of MORB $\approx$ 6‰, Taylor 1968) is made possible, from which the extent of isotopic alteration may be quantified.

Fresh samples, which were free from weathering, late-stage veins and spilitic alteration, were crushed using a jaw-crusher, and ground using a Glen Creston "Gy-Ro Mill" grinder. A relatively coarse (200-mesh) fraction was taken. Care was exercised to minimise preferential mineral loss as fines, notably by grinding the sample for minimal time and, where necessary, re-grinding the coarse fraction. The sample was subsequently reacted with warmed 10% HCl for about 1 hour to remove all possible traces of calcite and dolomite. The remaining acid was removed by

Buchner filtration, accompanied by several washings with acetone and then distilled water.

Under the direction of Dr. A. E. Fallick, the sample was weighed and reacted with ClF_3 for 2 days to liberate oxygen. O_2 was then converted to CO_2 by reaction with a hot carbon-rod and analysed on a V.G. Osogas SIRA 10 mass spectrometer. Raw data was converted to give $\delta^{18}O_{SMOW}$.

All samples were run in duplicate. Replication of the initial results, which were run without acid washing on the mistaken belief that samples were carbonate free, proved problematic. All the samples were therefore re-run after careful acid washing, again in duplicate, as described above. A number of analyses were again lost, in this case, due to contamination and insufficient conversion of the sample from O_2 to CO_2, associated with disintegration of the carbon-rod. Only on the third run, were the first reasonable duplicable results obtained. Whole rock silicate stable isotope data are presented in appendix 6 where all the collected data, plotted against distance from the structural basal margin of the metabasite sill, is compared with a similar plot showing those only results which are both duplicable and have reasonable yields. Similar trends are observed in both cases, although the former trend shows considerable scatter.

6.5.2 Stable Isotope Analysis of Carbonates

Stable isotope analysis of sample traverses across three carbonate units belonging to the Islay Limestone, exposed at the Mull of Oa, was undertaken to identify fluid flow at the base of the Islay-Jura quartzite, for reasons which have been discussed in chapter 5.

Carbonate preparation and analysis was altogether more simple and results were, in general, easily reproducible.

Fresh samples, free from weathering or late-stage veining, were crushed and ground by a similar procedure to that which was adopted for silicates. Under the

direction of Dr. A. E. Fallick, samples were weighed and reacted with warm phosphoric acid for a minimum of 3 hours. CO_2 was liberated and analysed on a V.G. Isogas SIRA 10 mass spectrometer. Raw data were converted to give $\delta^{18}O_{SMOW}$, $\delta^{18}O_{PDB}$ and $\delta^{13}C_{PDB}$.

Good, reproducible data were obtained on the first run. These were plotted against distance from the tectonic basal margin of the marble units. Data are presented in appendix 6 and were interpreted in chapter 5.

6.6 Electron Microprobe Analysis

Electron microprobe analyses were undertaken to develop a mineral composition data-set for comparison of individual phases and for geothermometry and geobarometry calculations.

Electron microprobe analyses were carried out using a Cambridge Instruments "Microscan 5" electron microprobe, running at 20kV, with a beam current of 30nA. A ZAF correction procedure (described by Sweatman & Long 1969) was applied. Although occasional analytical problems were encountered, due to large beam diameter, unstable beam currents and spectrometer drift, results were in general excellent. A minimum of 3 grains of each mineral were analysed in each sample, and considerably more analyses were made where replication was poor. In general, a representation of the rock as a whole was required and therefore analyses were taken in the centres of large, clean grains and imperfections were avoided.

Resultant mineral analyses were employed in state-of-the-art geothermometers and geobarometers, and were found to give reasonable estimates of metamorphic pressures and temperatures (section 3.4.3 and appendices 1 and 2), consistent with previous studies.

General electron microprobe data are presented in appendix 7. Data which are relevant to geobarometry and geothermometry are listed with the relevant geobarometer or geothermometer in appendices 1 and 2 respectively.

In addition, the back-scattered electron imaging capabilities of the CAMEBAX electron microprobe were utilised to facilitate detailed examination of retrograde ankerite growth textures (figures 5.6(b) & (c) and 5.14(b)).

6.7 Applications of THERMOCALC and AX (Powell & Holland 1988)

Mineral compositions were converted to thermodynamic activities using the computer program AX (Powell & Holland 1988). The program THERMOCALC (Powell & Holland 1988) was used to calculate metamorphic temperatures from estimated activities. The data and the calculation procedure are presented and discussed in appendices 1 and 2. A pure-end member T-X_{CO_2} section was calculated for reactions 1-9[2] at 10kb (figure 5.3) and is presented, together with the input data and calculation details in appendix 3. Reactions 1, 2, 4, 5, 7 and 8 are divariant, but they generally describe narrow fields in T-X_{CO_2} space. It is not therefore necessary to construct T-X_{CO_2} sections using real mineral compositions. Instead modelling of time-integrated fluid fluxes is achieved using pure end-member univariant curves. The Mg end-member curves are used in preference to Fe end-member curves as they are better constrained by experiment (Holland *pers. comm.*). The reasons for this interpretation are explained in more detail in appendix 3. The T-X_{CO_2} section is included on the reference card at the back of the thesis.

6.8 X-Ray Fluorescence Analysis

Major element chemistry of sample traverses across several metabasite horizons, determined using X-ray fluorescence techniques, served two purposes:

[2]Reactions 1-9 are listed in the refe.ence card at the back of the thesis.

(1) major element chemical analyses of sample traverses were used to confirm that mineral reactions were in fact a result of fluid infiltration and did not merely reflect variation in bulk composition of the rock;

(2) major element chemical analyses of sample traverses enabled the spatial extent of pre-metamorphic spilitic alteration, manifested as variations in bulk Na_2O and CaO contents, to be assessed (chapter 9).

Fresh samples, free from weathering and late-stage veining, were crushed, using a steel jaw crusher, and fine ground, using a Glen Creston "Gy-Ro Mill" grinder. The sample was weighed and heated in a furnace at 1100°C together with a borate flux. The melts were cast as discs and analysed on a Philips PW1480 automatic X-ray fluorescence generator operating at 100kV and 30mA.

Resultant analyses were generally of a fairly high standard. However, a number of analyses gave low totals (<99%). Several of these were re-run and higher totals were obtained. Normalisation of first and second run analyses of the same sample gave identical major element chemistries. Therefore all data, including those with low totals, are presented in appendix 8. Selected data are interpreted in chapters 9 and 10.

6.9 Analytical Strategy

In summary, the analytical strategy developed in this project, in a view towards regional scale quantitative modelling of deep-crustal fluid flow, is detailed, as follows:

(1) Detailed geological mapping of coastal exposure was undertaken to establish the whereabouts, dimensions, and the structural, lithological and metamorphic settings of well-exposed metabasites and carbonates.

(2) The morphology of mineral reaction fronts was investigated from a detailed modal traverse across a 13.4m wide metabasite sill at Port Cill Maluaig, West

Knapdale. Modal data was obtained by point-counting 400-500 points in 42, evenly spaced samples (chapter 7).

(3) Both mineral reaction and isotope fronts were identified in a 94.5 metre wide metabasite sill at the Ard of Port Ellen on Islay, using the techniques described in sections 6.4 and 6.5.1, respectively. Lithology-perpendicular time-integrated fluid fluxes were calculated independently from the reaction and isotope fronts, making the initial assumption that the infiltrating fluid composition was buffered by reactions 2, 4 and 5 in the host phyllites. Predicted time-integrated fluid fluxes were found to be identical within error, implying that (i) application of the reaction and isotope front advection models was successful, and (ii) the assumption that the composition of the infiltrating fluid was buffered by the host phyllite was reasonable.

(4) The spatial extent of pre-metamorphic spilitisation was deduced in a semi-quantitative manner by identifying affected sills and quantifying the associated chemical alteration by X-ray fluorescence analysis of bulk rock Na_2O and CaO concentrations (chapter 9).

(5) The field geochemical technique, described in section 6.4, was implemented to identify mineral reaction fronts within the majority of well exposed metabasite sills and dykes throughout the SW Scottish Highlands. Results were reinforced, in a number of examples, by traditional point-counting techniques (chapter 10). Time-integrated fluid fluxes were calculated and a regional syn-metamorphic fluid flow map was constructed from which the lithological and structural controls of syn-metamorphic fluid flow were constrained and the fluid source reservoir was identified (chapter 10);

(6) The spatial extent of post-metamorphic fluid infiltration was evaluated by field mapping, petrographical and isotopic techniques (chapter 11).

CHAPTER 7

THE MORPHOLOGY OF REACTION FRONTS

7. INTERPRETATION OF REACTION FRONT PROFILES

7.1 Rationale

Quantitative modelling of deep-crustal fluid flow using the one-dimensional model of Bickle & Baker (1990b) is undertaken in chapter 10 of this thesis. Using this model, time-integrated fluid fluxes are calculated from the advection distances of reaction fronts. For this to be achieved successfully, we must develop a clear understanding of the morphology and interpretation of reaction front profiles.

In this chapter, detailed modal and reaction progress profiles, constructed across a 13.4m wide metabasite sill which is exposed at Port Cill Maluaig on the west coast of Knapdale (figure 7.1), are presented. The morphologies of these profiles are discussed and compared, with a view towards quantitative interpretation.

7.2 Geological Setting

The geological history of the SW Scottish Highlands is discussed in detail in chapter 3. It is therefore sufficient at this stage to briefly summarise the lithological, structural and metamorphic development relevant to West Knapdale.

In West Knapdale, variably calcareous phyllites belonging to the Ardrishaig Phyllite Group, which lie on the lower (SE) limb of the recumbent, NE-plunging Ardrishaig Anticline, are intruded by numerous metabasic sills. At Port Cill Maluaig which is situated just below the garnet isograd, one such sill, which is 13.4m wide and well-exposed at low tide, was selected for this study. The sill is folded into an outcrop scale "z"-type fold structure (figure 7.1). The sill is sheared into two segments along the axial surface of the "z"-type fold (figure 7.1). The "z"-type fold is

Figure 7.1: Port Cill Maluaig: Outcrop Map

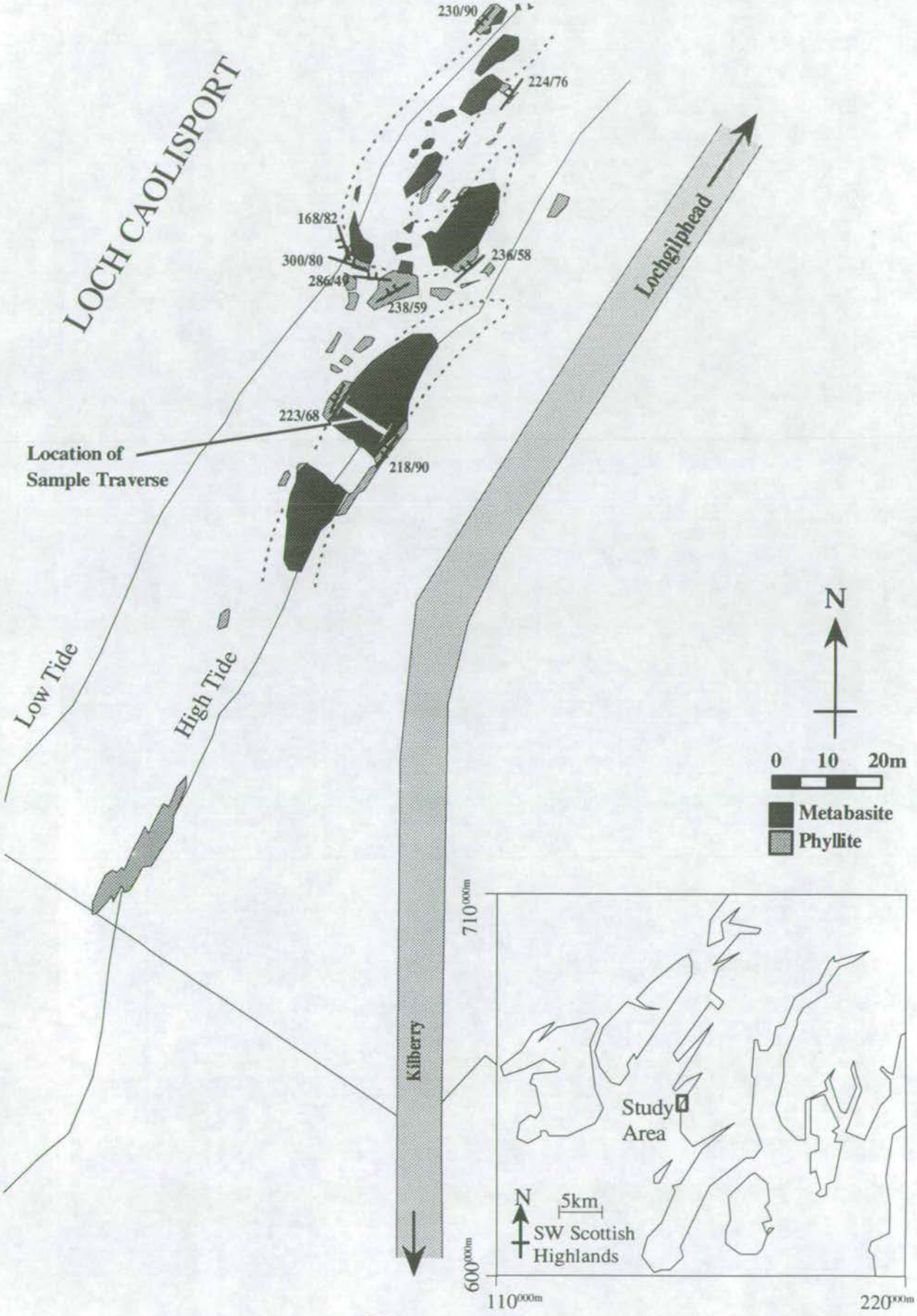

parasitic to the overturned SE limb of the recumbent Ardrishaig Anticline and must therefore plunge (along with the Ardrishaig Anticline) to the NE (Roberts 1974). Axial planar foliation is parallel to D_1-D_2 and it is therefore likely that this structure was present during syn-metamorphic fluid infiltration. As will be discussed in chapter 8, shearing is only likely to be responsible for increased fluid fluxes and the reaction front morphology will not be affected.

Pressure-temperature conditions of greenschist facies metamorphism in the Port Cill Maluaig area are determined on the basis of conventional geothermobarometry and using THERMOCALC (Powell & Holland 1988). The techniques employed and their interpretation were discussed in section 3.4.3 and calculation details are outlined in appendices 1 and 2. From these calculations, pressure is 10±2kb and temperature is 470±20°C.

The metabasite sill at Port Cill Maluaig is hosted by calc-phyllites which contain the equilibrium assemblages: biotite + chlorite + calcite, albite + chlorite + calcite and/or rutile + calcite + quartz. The metabasite itself develops a typical zonation pattern from a type I interior containing the equilibrium assemblage: amphibole + epidote, to a type III margin containing the equilibrium assemblage: chlorite + calcite + quartz. Typical mineral assemblages are listed in table 7.1 and for reference typical metabasite mineral analyses are presented in table 7.2.

Table 7.1: Mineral Assemblage Data from Port Cill Maluaig

Mineral	**Metabasite**		**Calc-Phyllite**
	Type I	*Type III*	
Amphibole	+	-	-
Epidote	+	+	-
Chlorite	+	+	+
Calcite	*	+	+
Quartz	*	+	+
Albite	+	+	+
Biotite	*	*	+
White Mica	*	*	+
Sphene	+	*	-
Rutile	-	*	+

+ = present, - = absent, * = traces

Table 7.2: Representative Metabasite Mineral Analyses from Port Cill Maluaig

	Am	*Ep*	*Chl*
SiO_2	51.4	37.3	25.1
TiO_2	0.16	0.09	0.04
Al_2O_3	3.49	23.2	19.7
FeO	14.9	11.5	25.4
MnO	0.29	0.20	0.33
MgO	13.1	0.04	15.0
CaO	12.0	23.2	0.04
Na_2O	0.59	0.02	0.07
K_2O	0.06	0.00	0.02
TOTAL	96.0	95.6	85.8

An isobaric T-X_{CO_2} section was constructed using THERMOCALC (Powell & Holland 1988) for the assemblages listed in table 7.1 (figure 5.3a).

7.3 Reaction Front Modelling

42 evenly spaced samples were taken across the 13.4m wide sill at Port Cill Maluaig. These samples were cut and sectioned, and a minimum of 400 points were counted on each slide. Resulting mineral modes were used to construct the modal profile presented in figure 7.2.

By comparison of figure 7.2 with theoretical modal profiles[1], it is evident that the observed modal changes fairly precisely replicate reaction 1[2].

It is further apparent from figure 7.2 that reaction fronts have been asymmetrically transported towards the sill interior from both upper and lower margins. Advection of fronts from both upper and lower margins is non-intuitive when we consider that the sill is most likely to have been subjected to unidirectional fluid flow originating from a specific source reservoir. This problem may be resolved by considering the combined influences of advection and diffusion on the

[1]Theoretical modal profiles are included in the reference card at the back of the thesis.
[2]Reaction (1) is included in the reference card at the back of the thesis.

development of different modal profile morphologies. This is achieved by comparing the real reaction front profile morphology with theoretical reaction front profile morphologies which are developed in a unidirectional (upwards) fluid flux, for different advective and diffusive regimes. Theoretical modal profile morphologies are shown in figure 7.3 and discussed below.

Theoretical Modal Profile Morphologies

Figure 7.3(a) describes the development of a reaction front profile under conditions of pure advection. In the case of a univariant reaction, a single sharp front is advected in the direction of flow only. In the case of a divariant reaction, a single broadened front is advected in the direction of flow only. Broadening results from spatial separation of the Mg and Fe end-member reactions, as a result of their different relative T-X_{CO_2} stabilities.

Figure 7.3(b) describes the development of a reaction front profile under conditions of combined advection and diffusion, making the assumption that the diffusion rate greatly exceeds the rate of reaction. In the case of a univariant reaction a single front is advected into the sill in the direction of fluid flow. The profile is symmetrically tapered downstream of the front and upstream of the upper margin. This is in response to diffusion of CO_2 across the front and upper margin, to smooth what are effectively discontinuities in X_{CO_2}. Subsequently, Type I assemblages consume CO_2 causing the modes of product species to effectively mimic the diffusive X_{CO_2} profile. Tapering of the profile is only observed downstream of the front and upstream of the upper margin (i.e. where Type I metabasite assemblages are present). Tapering of the reaction front profiles upstream of the reaction front or downstream of the upper margin is not observed because the Type III metabasite and calc-phyllite assemblages can accommodate a limited loss of CO_2 before destabilising chlorite + calcite + quartz relative to amphibole + epidote. In the case of a divariant reaction, a similar profile is observed except that the front is broadened as in 7.3(a), above.

Figure 7.3: Model Reaction Front Profiles

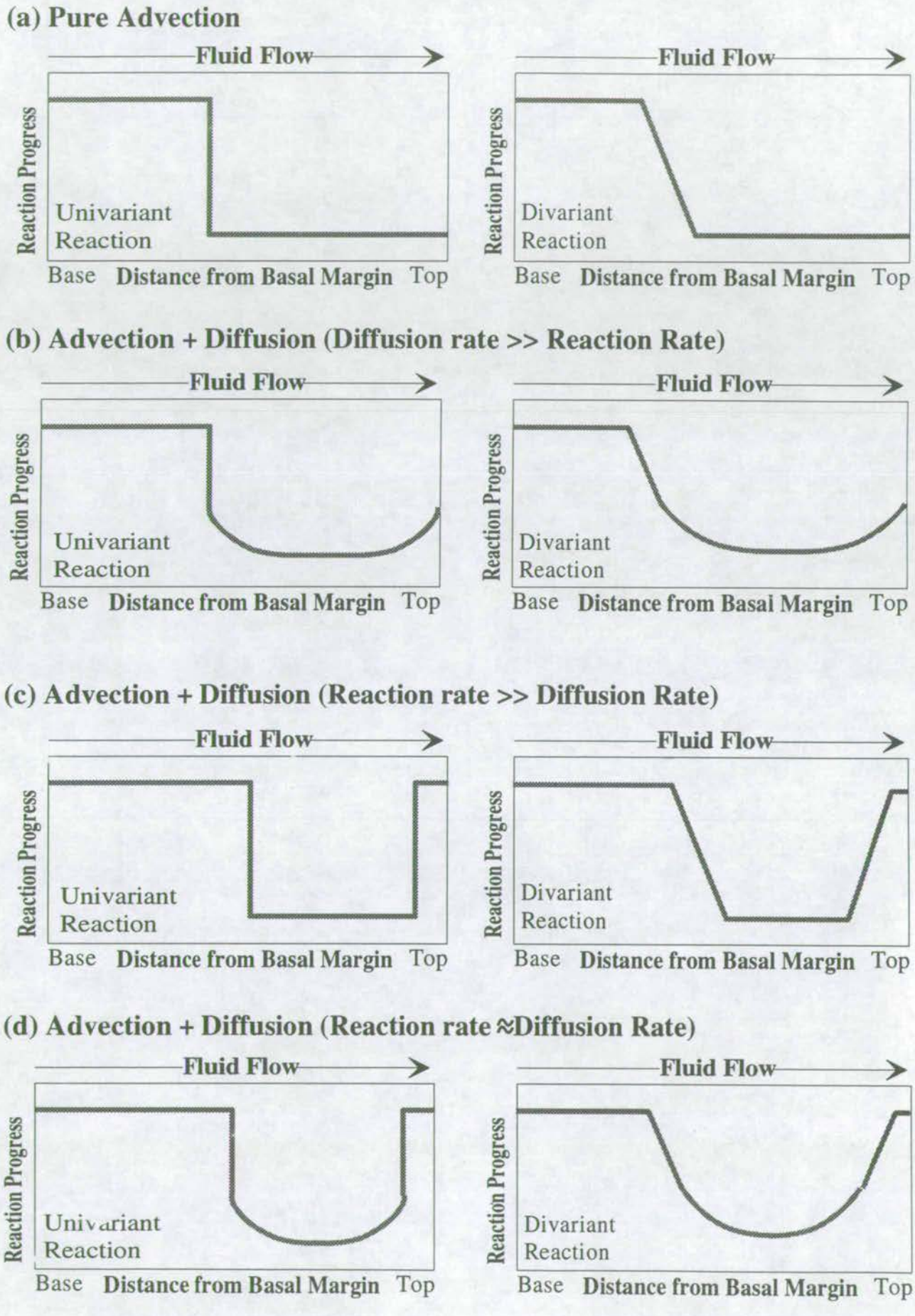

Figure 7.3(c) describes the development of a reaction front profile, again under conditions of combined advection and diffusion, but making the alternative assumption that the rate of reaction greatly exceeds the diffusion rate. In the case of a univariant reaction, unidirectional advective transport of the reaction front (in the direction of fluid flow), is superimposed upon symmetrical diffusive transport of the reaction front into the sill from ***both*** upper ***and*** lower margins. This is in response to relatively slow diffusion of CO_2 across the advective front and the upper margin, where all CO_2 diffusing downstream of the front or upstream of the upper margin is rapidly consumed by the type I metabasite assemblage to drive reaction (1) to completion and generate the type III metabasite assemblage. In the case of a divariant reaction, a similar profile is observed except that the front is broadened as in 7.3(a), above. The scenario presented in figure 7.3(c) is crucially important as it explains the non-intuitive observation of apparent advection from both sides of a sill in what is assumed to be uni-directional fluid flow.

Figure 7.3(d) describes the reaction front profile generated where the relative rates of reaction and rates of CO_2 diffusion are intermediate between 7.3(b) and 7.3(c)

Real Modal Profile Morphology

The morphology of the real reaction front profile at Port Cill Maluaig is well constrained (figure 7.2) and, by inspection, is best described by the theoretical modal profile shown in figure 7.3(d), constructed for a divariant reaction.

Diffusion versus Advection

It is possible to distinguish between ***apparent*** advection resulting from ***true*** advection and ***apparent*** advection resulting from diffusion on the basis of the following criteria:

(1) Diffusion is ***solely responsible*** for apparent advection ***upstream***, the mechanism for which is back-diffusion of CO_2 through the mobile fluid phase;

(2) Diffusion is ***symmetrical*** across the metabasite sill.

At Port Cill Maluaig, two reaction fronts are evident (**A** and **B**, figure 7.2). The apparent advection distances were estimated as the distance from the sill margin to the mid-point of the reaction front. The apparent advection distance of reaction front (**A**) is 4.6m on the downstream side and the apparent advection distance of reaction front (**B**) is 1.0m on the upstream side (figure 7.2). These distances result from the combined symmetrical diffusion distance of 1.0m and asymmetric advection distance of 3.6m downstream.

Reaction Front Broadening

Reaction fronts (**A**) and (**B**) are broadened by approximately 0.8-1.0m in response to the divariance of reaction 1 in T-X_{CO_2} space. The reaction fronts are further broadened, downstream of reaction front (**A**) and upstream of reaction front (**B**) as a result of symmetrical diffusion of CO_2 through the mobile fluid phase.

Reaction front broadening may also develop in response to kinetics (Bickle 1992). It is mathematically-complex to model this for a multi-phase reaction. Therefore, for simplicity, kinetic effects have been ignored in this study, but will be subject of future work.

7.4 Reaction Progress Profiles

Construction of modal profiles, such as that which is shown in figure 7.2, is highly time-consuming. The sampling, sectioning and point-counting required to accurately measure the true advection distance of reaction 1 in a single metabasite takes, on average, 3-4 weeks with the possibility of further recourse between the laboratory and the field if initial sampling failed to adequately constrain the locations of the reaction fronts. Therefore, if detailed regional-scale mapping of fluid fluxes was to be achieved, a much more rapid and more robust approach was essential.

A simple geochemical technique was adapted and employed to measure the vol.% calcite of a sample in the field. The analytical procedure was described in detail in section 6.4. In essence, a sample of known volume is reacted with excess 10% HCl in a sealed reaction vessel and the pressure of evolved CO_2 is measured and calibrated with vol.% calcite which is calibrated with reaction progress. This technique is rapid and accurate and because it can be implemented in the field the location of a reaction front may be "bracketed" with increasing accuracy, without repeated recourse between the field and the laboratory. The result is that the true advection distance may be measured in a single metabasite in 2-3 hours enabling detailed regional-scale fluid flux mapping to be realistically undertaken.

A profile of reaction progress is constructed at Port Cill Maluaig and presented in figure 7.4, from which the advection distance of the reaction front is found to be 4.0±0.5m. This is effectively identical to the value which is predicted by the modal profile (3.6m), yet the result was obtained in 2-3 hours instead of 3-4 weeks.

7.5 Interpretation and Conclusion

A modal profile was constructed across a 13.4m wide metabasite sill which is exposed at Port Cill Maluaig, West Knapdale. Reaction 1 is transported towards the centre of the sill from both margins. This is the combined effects of symmetrical diffusion and asymmetrical advection in the downstream direction. Reaction fronts were found to develop morphologically-distinct broadening as a result of the divariance of reaction 1 and symmetrical diffusion of CO_2 through the mobile fluid phase.

Figure 7.4: Wt.% Calcite (Reaction Progress) Profile at Port Cill Maluaig

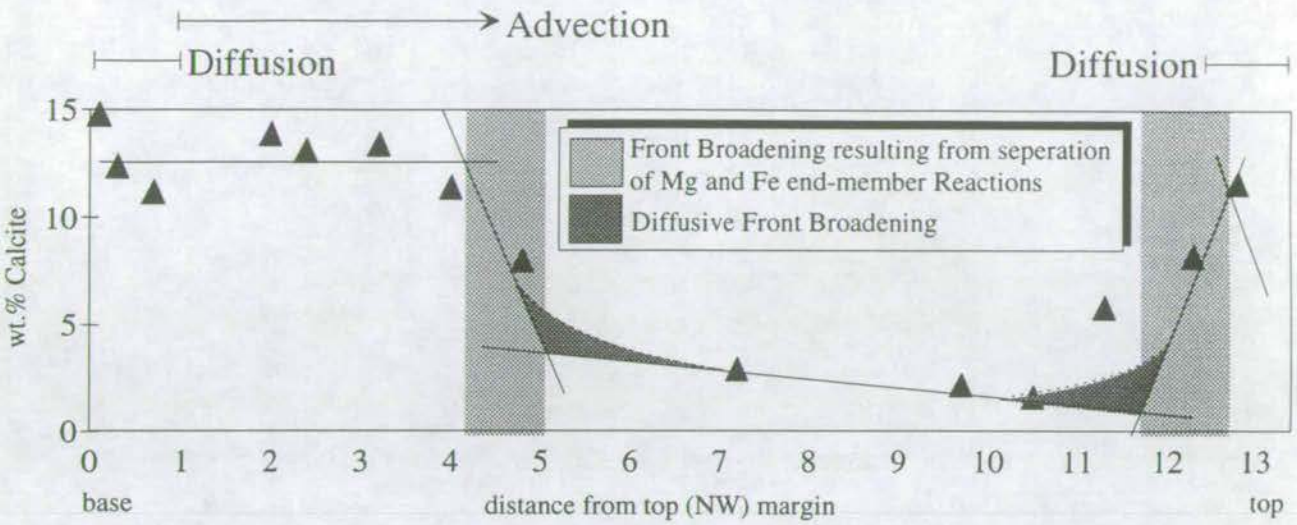

Reaction progress (wt.% calcite) data obtained from the metabasite sill at Port Cill Mauaig is shown above. The interpretation of the modal profile (figure 7.2) is super-imosed to emphasise the excellent agreement of the two techniques.

CHAPTER 8

CORRELATION OF REACTION AND ISOTOPE FRONTS

8.CORRELATION OF REACTION AND ISOTOPE FRONTS

8.1 Rationale

The quantitative interpretation of syn-metamorphic fluid flow in chapter 10 of this thesis depends largely on the validity of the one-dimensional modelling technique of Bickle & Baker (1990b), by which time-integrated fluid fluxes were calculated from measured advection distances of mineral reaction fronts. This model critically depends on the fundamental assumption that perfect local chemical fluid-rock equilibrium is attained. The assumption is only satisfied if mineral grains were never sufficiently isolated from the fluid as to preclude complete equilibration. Effective fluid-mineral isolation would occur if fluid were channelled along fracture zones or if fluid flow was too rapid to allow sufficient time for equilibration.

Hence, the validity of this assumption, and therefore, the viability of the model of Bickle & Baker (1990b) is tested in this chapter by independent calculation of time-integrated fluid flux from (i) the advection distance of mineral reaction 1[1], using this model, and (ii) the advection distance of an oxygen isotope front, using the model of Bickle & McKenzie (1987), into the basal margin of a 95 metre wide metabasite sill at the Ard of Port Ellen on SE Islay (figure 8.1). The latter model is also limited by the same fundamental assumption described above, yet by testing the consistency of the independent predictions of both models, their validity may be tested.

[1]Reaction 1 is included in the reference card at the back of the thesis.

Figure 8.1: Port Ellen: Outcrop Map

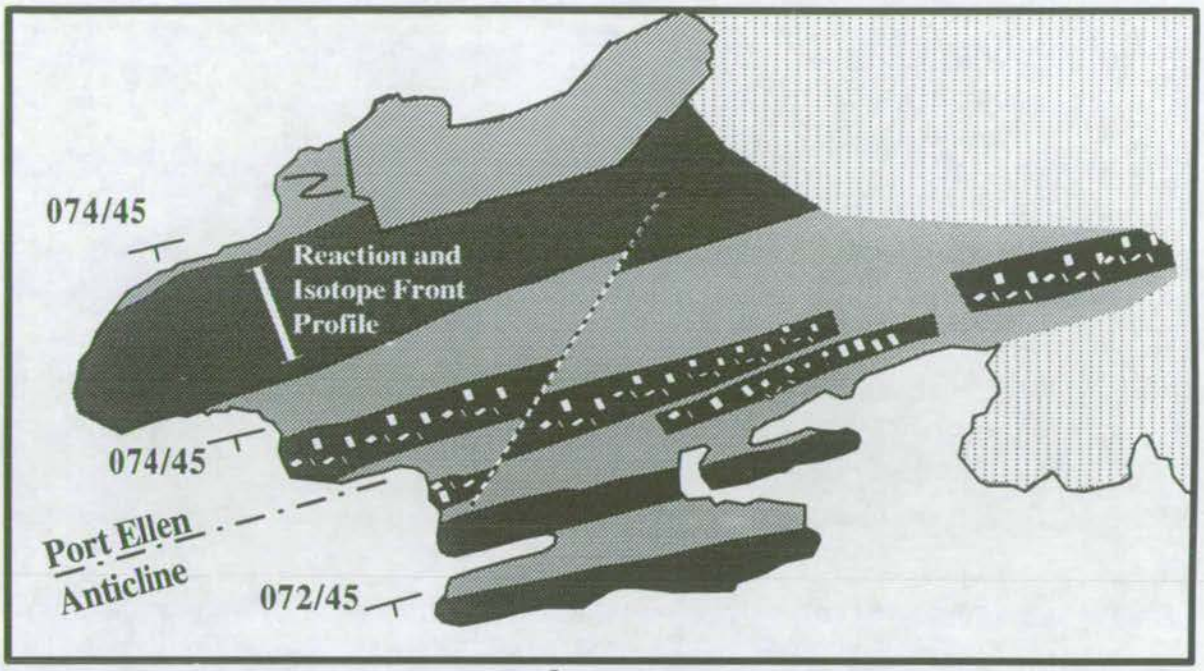

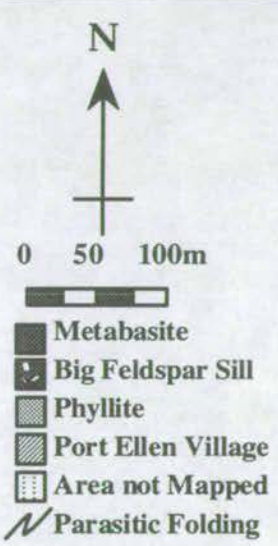

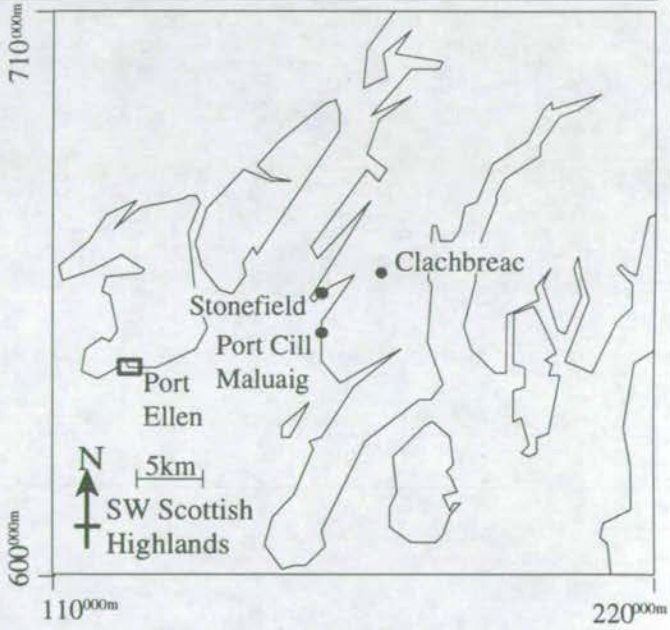

8.2 Theory

The theoretical basis for the one-dimensional models of Bickle & Baker (1990b) and Bickle & McKenzie (1987) have been described in chapter 2 and therefore it is sufficient at this stage to set down the relevant equations:

(1) The model of Bickle & Baker (1990b) which calculates the time-integrated fluid flux from the advection distance of an isotopic front is described by equation 8.1:

$$V_f t = \frac{\{\omega\varphi t(X_{CO2,2} - X_{CO2,1})\}}{\{R_{CO2}.(1-X_{CO2,2}) - R_{H2O}.X_{CO2,2}\}} \qquad (8.1)^2$$

where V_f = velocity of the reaction front, t = time and therefore $V_f t$ = advection distance of the reaction front, ω = fluid velocity, φ = porosity (or fluid volume) and therefore $\omega\varphi$ = fluid flux rate and $\omega\varphi t$ = time-integrated fluid flux. $X_{CO2,1}$ = volumetric composition of the infiltrating fluid (upstream fluid), $X_{CO2,2}$ = volumetric composition of fluid in equilibrium with the reaction at the reaction front (downstream fluid). R_{CO2} and R_{H2O} are the volumetric stoichiometric coefficients of CO_2 and H_2O, respectively, in the reaction.

(2) The model of Bickle & McKenzie (1987) which calculates the time-integrated fluid flux from the advection distance of an isotopic front is given by equation 8.2:

$$V_f t = \frac{\rho_s}{\rho_f . K_d} . \omega\varphi t \qquad (8.2)^3$$

where $V_f t$ = advection distance of the isotope front, $\omega\varphi t$ = time-integrated fluid flux, ρ_s and ρ_f are the densities of the solid and fluid phases respectively and K_d = distribution coefficient of the isotopic species between solid and fluid phases.

Provided that the variables; $X_{CO2,1}$, $X_{CO2,2}$, R_{CO2}, R_{H2O}, ρ_s, ρ_f and K_d, may be estimated, and that $V_f t$ can be measured for both reaction and isotope fronts, within

---

[2]Equation 8.1 is included in the reference card at the end of the thesis.
[3]Equation 8.2 is included in the reference card at the back of the thesis.

the same metabasite unit, the time-integrated fluid flux, $\omega\varphi t$, can be calculated independently from the models of Bickle & Baker (1990b) ***and*** Bickle & McKenzie (1987).

8.3 Geological Setting

The geological history of the SW Scottish Highlands is discussed in detail in chapter 3. It is therefore sufficient at this stage to briefly summarise the lithological, structural and metamorphic development specific toPort Ellen, Islay.

Lithostratigraphy and Structure

In the Port Ellen area, variably calcareous phyllites belonging to the Port Ellen Phyllite Group, which lie on the upper (SE) limb of the recumbent Islay Anticline, are intruded by numerous metabasic sills. The sequence of metabasites and calc-phyllites is folded into an isoclinal anticline (the Port Ellen Anticline) parasitic to the Islay anticline and centred about the Ard peninsula, to the south of Port Ellen (figure 8.1).

Pressure and Temperature of Metamorphism

Pressure-temperature conditions of greenschist facies metamorphism in the Port Ellen area have been determined, using mineral assemblages and analyses similar to those listed in tables 8.1 and 8.2, to be about 10kbars and about 470°C, based on the celadonite content of phengite in equilibrium with chlorite, biotite and quartz (appendix 1), calcite-dolomite geothermometry (appendix 2) and the stability of kyanite relative to pyrophyllite in nearby phyllites (Burgess *et al.* 1982).

Metabasite Assemblages and Fluid Composition

The metabasic sills within the Port Ellen Anticline are hosted by calc-phyllites (figure 8.1) and develop a typical zonation pattern from type I interiors to type III margins (figure 4.5). Type I assemblages, by definition (section 4.2.2) contain the

assemblage: **amphibole + epidote + sphene, in the absence of calcite**, which buffers the equilibrium fluid composition to $\mathbf{X_{CO2} \leq 0.0086}$ by reactions 1 (figure 5.3a). Type III assemblages, by definition (section 4.2.2) contain the equilibrium assemblage: **chlorite + calcite + quartz + sphene ± albite ± biotite, in the absence of amphibole**, which buffers the equilibrium fluid composition to $\mathbf{0.0086 \leq X_{CO2} \leq 0.0150\text{-}0.0156}$ by reactions 2, 4 and 5 (figure 5.3a).

Phyllite Assemblages and Fluid Composition

Calc-phyllites within and proximal to the Port Ellen Anticline (figure 8.1) develop the mineral assemblages; **biotite + chlorite + calcite**, **albite + chlorite + calcite**, **rutile + calcite + quartz**, which constrain the equilibrium fluid composition to $\mathbf{0.0150 \leq X_{CO2} \leq 0.0156}$ by reactions 2, 4 and 5 (figure 5.3a).

Representative Mineral Assemblages and Mineral Analyses

Representative mineral assemblages of the metabasite and host phyllites, relevant to this study, are listed in table 8.1 and representative mineral analyses are listed in table 8.2.

Table 8.1: Mineral Assemblage Data from the Ard of Port Ellen

Mineral	**Metabasite**		**Calc-Phyllite**
	Type III	*Type II*	
Quartz	+	*	+
Albite	+	+	*
Biotite	-	-	*
Chlorite	+	+	+
White Mica	+	+	+
Amphibole	-	+	-
Epidote	+	+	-
Calcite	+	*	*
Sphene	*	*	-
Rutile	*	-	*

+ = present, - = absent, * = traces

Table 8.2: Representative Mineral Analyses from the Ard of Port Ellen

	Metabasite				Calc-Phyllite				
	Chl	*Am*	*Ep*	*Cc*	*Bi*	*Fsp*	*Chl*	*Cc*	*Mica*
SiO2	27.6	48.7	38.8	0.00	45.5	70.3	26.6	0.04	48.6
TiO2	0.06	0.48	0.00	0.00	0.18	0.02	0.04	0.01	0.03
Al2O3	18.4	3.15	31.8	0.00	30.3	19.8	19.7	0.02	30.8
FeO	18.9	15.2	2.69	1.00	4.47	0.09	22.7	0.44	2.46
MnO	0.27	0.33	0.05	0.83	0.01	0.00	0.30	0.58	0.00
MgO	20.6	12.8	0.06	0.00	1.45	0.01	17.0	0.20	2.40
CaO	0.01	11.8	23.6	57.7	0.05	0.05	0.17	59.6	0.00
Na2O	0.02	1.21	0.41	0.00	0.64	9.27	0.05	0.00	0.18
K2O	0.05	0.10	0.00	0.00	8.86	0.07	0.01	0.01	11.1
TOTAL	85.9	96.6	97.4	59.5	91.4	99.6	86.4	60.9	93.9

Syn-metamorphic Fluid Infiltration History

During D_1-D_2 deformation and peak metamorphism, phyllites and metabasites were infiltrated by a CO_2-bearing hydrous fluid (section 4.2.2).

Field evidence discussed in section 3.3.3 is consistent with the infiltrating fluid having equilibrated with the phyllite. Furthermore phyllites are generally isotopically homogenised such that $\delta^{18}O$ = 11-13‰ (Graham *unpublished data*). The chemical and isotopic composition of the fluid are therefore likely to be "pinned" within the phyllites.

Prior to infiltration the metabasite contained the type I assemblage and retained its pre-metamorphic MORB-like isotopic signature of $\delta^{18}O \approx 6‰$. Infiltration of CO_2-bearing, high-$\delta^{18}O$ fluids into the margins of metabasite sills induced progress of reaction 1 and isotopic modification at the sill margins. Reaction and isotope fronts were advected into the sills by distances which are predicted by equations 8.1 and 8.2.

Selection of an Appropriate Metabasite Sill for Correlation of Reaction and Isotope Fronts

As is discussed below, equations 8.1 and 8.2 predict that reaction 1 will be advected an order of magnitude less distance than the associated oxygen isotope

front. Therefore in selecting a suitable sill for this study, it was necessary to select the largest available sill with the smallest reacted (type III) margin. The northernmost sill of the Ard peninsula, immediately to the south of the town of Port Ellen (figure 8.1) is some 95m wide, with a type III margin merely 0.2m wide, making this sill ideal for the purposes of this study.

8.4 Calculation of the Time-integrated Fluid Flux from the Advection Distance of a Mineral Reaction Front

A reaction progress profile was constructed across the NNW metabasite sill at the Ard of Port Ellen (figure 8.2), using the field geochemical technique described in section 4.4. The advection distance of reaction 1 was measured from this profile to be ≈0.2m towards the NNW (figure 8.2). R_{CO2} and R_{H2O} are calculated from the molar reaction stoichiometry to be -0.306 and -0.133 (section 10.8.1), respectively. $X_{CO2,2}$ is estimated from the T-X_{CO2} shown in figure 5.3a at 470°C to be 0.0086. It has been established in chapter 6 that $X_{CO2,1}$ was buffered by upstream reactions in the host phyllite assemblage. At Port Ellen, the stable coexistence of rutile + calcite + quartz and biotite + chlorite + calcite in the absence of sphene buffers $X_{CO2,1}$ to values between 0.0150 and 0.0156. From equation 8.1, taking these limiting values of $X_{CO2,1}$ the time-integrated fluid flux is calculated to be 8.6-9.4 m^3/m^2.

8.5 Calculation of the Time-integrated Fluid Flux from the Advection Distance of an Oxygen Isotope Front

A $\delta^{18}O$ profile was constructed across the NNW metabasite sill at the Ard of Port Ellen (figure 8.3), using the sampling and laboratory techniques described in section 4.5. Dr. M.J. Bickle fitted the data to a "pinned"-boundary solution, which mathematically describes the situation, which is applicable to the Port Ellen area (section 8.3), where the isotopic composition of the fluid is fixed in the host phyllites

Figure 8.2: Reaction Progress Profile at The Ard of Port Ellen

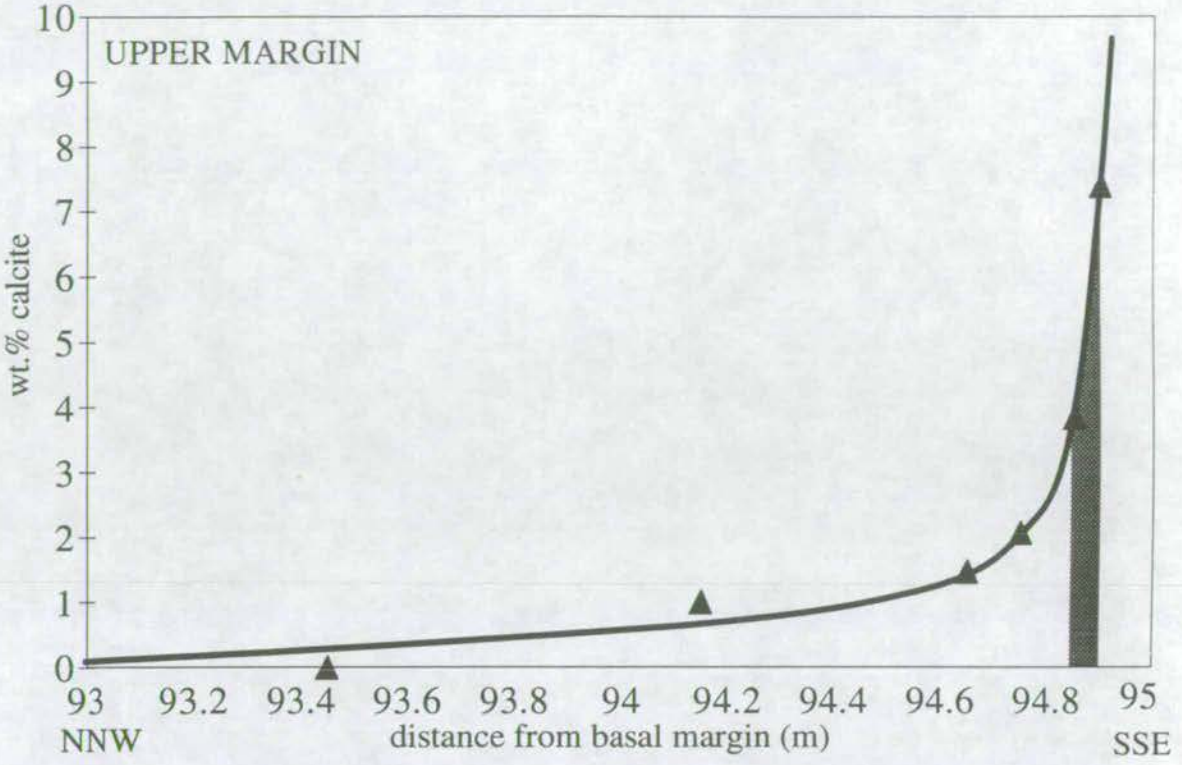

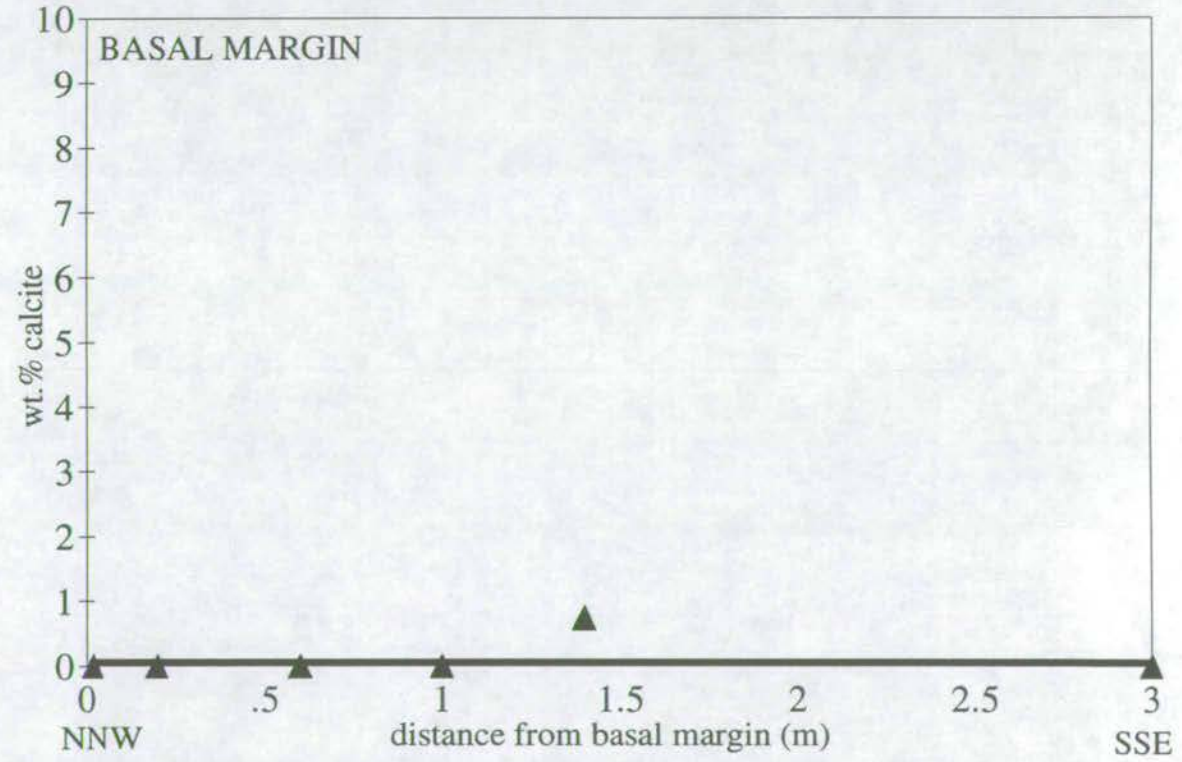

In this figure profiles of wt.% calcite are constructed across the upper and lower margins of the Northernmost sill at the Ard of Port Ellen.
The shaded area represents the approximate location of the reaction front on the upper margin assuming that the locus of the reaction front is at the point of inflection of the reaction progress profile.

Figure 8.3: Oxygen Isotope Profile at the Ard of Port Ellen

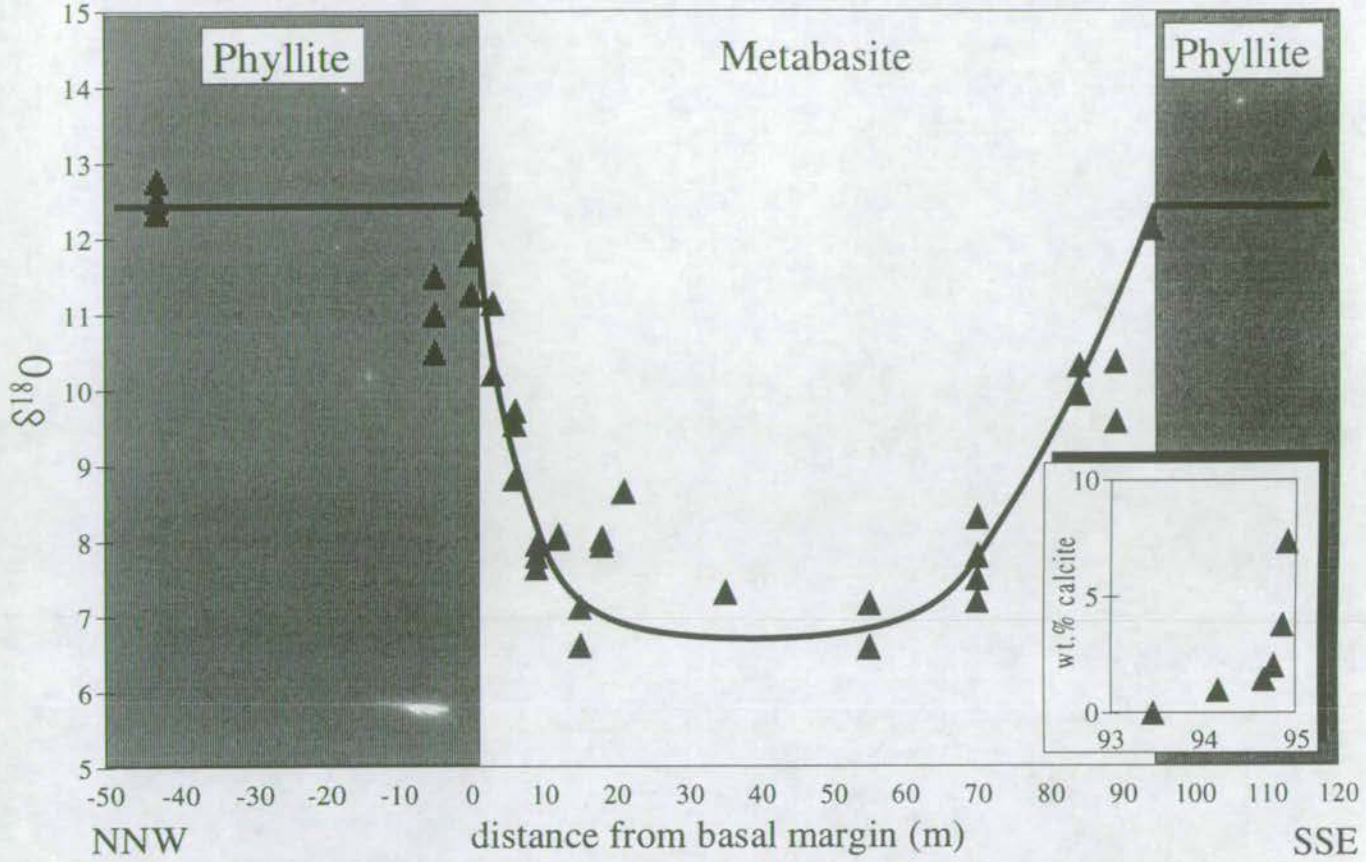

An oxygen isotope profile, contstructed across a 94.5m wide metabasite at the Ard of Port Ellen, Islay is shown above. The fit is a "pinned" boundary approximation and was constructed by Dr. M.J. Bickle (Cambridge). The reaction progress profile (figure 8.2) for the upper margin is shown as an inset.

(Bickle & McKenzie 1987). The calculations are included in appendix 6. At Port Ellen, assuming that $X_{CO2} \approx 0.01$ and mixing of H_2O and CO_2 is ideal, ρ_f is estimated from the tabulated data of Bottinga and Richet (1981) to be 0.98g/cc, and ρ_s is assumed to be equivalent to the density of an average unreacted greenschist facies metabasite, estimated from the data of Deer, Howie & Zussman (1992) to be approximately 3.1g/cc. The weight fraction of oxygen in the rock is estimated for a typical reactant metabasite assemblage to be 0.46, the weight fraction of oxygen in the fluid is estimated to be 0.89, therefore K_d is given by 0.46/0.89 = 0.52 and $\rho_s/\rho_f.K_d=1.64$. Therefore, by fitting averaged isotopic data from figure 8.4 to a "pinned"-boundary solution, assuming $(\rho_s/\rho_f).K_d \approx 1.6$, the time-integrated fluid flux was calculated to be 7.7±2.2 m^3/m^2.

8.6 The Correlation of Reaction and Isotope Fronts

The consistency of the two independent modelling approaches described in sections 8.4 and 8.5 is quite remarkable. Independently calculated time-integrated fluid fluxes are consistent with one another. The correlation is further consistent with the following assumptions:

(1) The composition of the infiltrating (upstream) fluid is buffered by the adjacent host phyllites. This is of importance in this study because it provides a general basis for estimation of the infiltrating (upstream) fluid composition in the SW Highlands.

(2) Both reaction and isotope fronts were advected by the same fluid, therefore the observed isotopic modification may be unambiguously attributed with syn-metamorphic fluid infiltration. This is of widespread general importance because the tagging of isotopic fronts to mineralogical or chemical alterations, the relative timing of which may be un-ambiguously determined on the basis of textural constraints, provides a unique opportunity to constrain the timing of isotopic modification, which is not otherwise temporally constrainable.

The model is internally consistent and is therefore proven to accurately predict the time-integrated fluid fluxes relevant to fluid-infiltration during greenschist facies metamorphism of the SW Highland Dalradian.

The correlation, and therefore the above conclusions, are strengthened by comparing further isotopic data from SW Scottish Highland metabasic sills with measured widths of Type III reacted sill margins to demonstrate their consistency with the above correlation. Tabulated data from this study, and Graham (*unpublished data*) are presented in table 8.3.

Table 8.3: Further Oxygen Isotope Data from SW Highland Metabasic Sills

Metabasite Locality	**Sill Width**	**Advection Distances**		**$\delta^{18}O$ (Interior)**
		Reaction Front *(measured)*	**Isotope Front** *(predicted)*	
Port Ellen	30m	1.0m	14.7-16.6m	9-10‰
Port Cill Maluaig	13.2m	3.6m	53-59m	9-10‰
Clachbreac	100m	<3.0m	<44-49m	6-7‰
Stronefield	100m	<<0.1m	<<1.4-1.6m	6-7‰

Metabasites are located in figure 8.1.

The more general implication of this correlation, that the one-dimensional reaction and isotope front advection models successfully constrain one-dimensional time-integrated fluid fluxes, may be generally applicable. Nevertheless, its application must be treated with considerable caution because the degree of grain-scale fluid-rock equilibrium will probably vary from one metamorphic terrain to another, presumably as a function of pressure and temperature.

CHAPTERS 9, 10 & 11

QUANTITATIVE MODELLING AND REGIONAL MAPPING OF FLUID FLOW

PRELUDE TO CHAPTERS 9, 10 & 11

Quantitative Modelling and Regional Mapping of Fluid Flow in the Dalradian of the SW Scottish Highlands

Chapters 9, 10 & 11 present the results and subsequent interpretation of the quantitative modelling and regional mapping of fluid flow in the Dalradian of the SW Scottish Highlands, which forms the basis of this thesis. Chapters 2-8 presented the necessary background information for this to be achieved.

In chapter 2, a variety of quantitative modelling techniques were presented and discussed, in the context of their historical development. The isotope and reaction front advection models of Bickle & McKenzie (1987) and Bickle & Baker (1990b) which quantify fluid flow as a directional time-integrated flux (constrained in one dimension) were selected for the majority of quantitative modelling undertaken in this study for the following reasons:

(1) Fluid flow is quantified as a flux and therefore offers a directional constraint, thus providing meaningful information regarding the fluid flow path and the location of the fluid source.

(2) The isotope front advection model (Bickle & McKenzie 1987) describes advection of an isotopic front. Unlike other fluid flow models, the essential model boundary conditions (i.e. the initial and final isotopic signatures) may be unambiguously determined.

(3) The reaction front advection model (Bickle & Baker 1990b) assumes that the infiltrating fluid composition is externally-buffered. Therefore, in P-T-X_{CO_2} space, a mineral reaction will be driven to completion by ***crossing*** a univariant reaction curve. A reaction front will be generated which describes the spatial location of the univariant P-T-X_{CO_2} curve and separates reactants and products. Thus, unlike all other quantitative fluid flow models, the essential boundary conditions (*i.e.* the initial and final mineralogical modes) may be unambiguously determined, together with textural control on the nature and direction of reaction.

(4) The equation variables of the former model (the rock and fluid densities and the distribution coefficient of the isotopic species between solid and fluid phases) and the latter model (the upstream and downstream fluid compositions and the volumetric stoichiometric reaction coefficients) may be determined independently.

In chapters 3, 4 and 5, the general lithostratigraphic, metamorphic and fluid infiltration history of the Dalradian of the SW Scottish Highlands was outlined and lithological descriptions were presented and discussed. Three phases of fluid infiltration were described:

(1) pre-metamorphic spilitisation,

(2) syn-metamorphic pervasive fluid infiltration,

(3) post-metamorphic ankeritic veining and porphyroblast growth.

All three phases are associated with measurable chemical, mineralogical and/or isotopic alteration. Pre-metamorphic spilitisation is associated with a spatial re-distribution of Na and Ca. Syn-metamorphic fluid infiltration is associated with the advective transport of reaction and isotope fronts into the margins of metabasic sills, dykes and flows. Post-metamorphic ankeritic veining and porphyroblast growth is associated with bulk chemical and mineralogical changes which are spatially correlated with isotopic modification.

In chapter 6, the techniques employed in this study were outlined and a comprehensive analytical strategy was devised. Wherever possible, measurements were taken in the field, minimising recourse to the laboratory and therefore maximising the size of the study area.

Chapters 7 and 8 refer specifically to syn-metamorphic infiltration and will therefore be referred to in chapter 10.

Chapters 9, 10 and 11 draw upon the foundations laid down in these previous chapters to develop a comprehensive, quantitative and regional interpretation of pre-, syn- and post- metamorphic fluid infiltration, in the framework of regional-scale fluid flow mapping.

9. QUANTITATIVE MODELLING AND REGIONAL MAPPING OF FLUID FLOW:

Pre-metamorphic Spilitisation

9.1 Introduction

In this chapter, alteration associated with pre-metamorphic spilitisation will be investigated. Isotopic alteration, if present, has been wholly or partly obscured by later syn-metamorphic and retrograde episodes of fluid infiltration (chapter 10). Spilitisation involved chemical re-distribution of Na and Ca, whereas syn-metamorphic infiltration was isochemical and post-metamorphic infiltration may have involved chemical re-distribution of Fe. Therefore, on the basis of the bulk chemistry, it may be possible to measure the spatial extent of spilitisation.

Therefore, bulk rock composition traverses, constructed across spilitised metabasic sills throughout the SW Highlands, will be used to impose semi-quantitative constraints on the mechanisms of pre-metamorphic spilitisation.

Bulk composition data was obtained by XRF analysis. The analytical techniques are discussed in section 6.8 and the complete data-set is presented in appendix 8.

9.2 Background Rationale

Ensialic rifting in the late stages of Dalradian deposition, resulted in extrusion of the Tayvallich Volcanics and emplacement of some 3km of basic sills and dykes into sub-seafloor sediments. Associated heat drove convection of sea-water to shallow crustal levels resulting in extensive spilitic alteration, manifested as a bulk re-distribution of Na and Ca in shallow level basic sills and flows (section 4.2.1). Chemical re-distribution in basic lithologies resulted in constant volume

transformation of calcic plagioclase to albitic plagioclase. During metamorphism this mineralogical modification was emphasised. Modal plagioclase is generally reduced as a result of isochemical metamorphism by the generalised reaction:

anorthite → albite + epidote

Spilites contain only albitic plagioclase and therefore modal plagioclase remains constant during isochemical metamorphism. The metamorphosed spilite is therefore effectively enriched in albite.

Epidotite segregations are developed extensively in spilitic metabasites in close spatial association with zones of albite enrichment.

9.3 Quantification of Pre-Metamorphic Spilitisation

Enrichment of albite or bulk redistribution of Na and Ca should provide effective monitors of the spatial extent of spilitic alteration and should therefore enable semi-quantitative modelling of pre-metamorphic fluid flow. Albite-enrichment is difficult to quantify because of extensive centimetre-scale modal variation. Bulk Na_2O and CaO contents therefore provide a more meaningful estimate of the "extent" of spilitisation. Error associated with centimetre-scale modal variation could be minimised by analysis of large (>10cm samples). Bulk rock Na_2O and CaO was estimated for sample traverses constructed across 7 metabasite units, using standard X-ray fluorescence (XRF) techniques (section 5.8). XRF data are presented in entirety in appendix 8. Selected, relevant data are presented and interpreted in this section.

9.4 XRF Data

Plots of Na_2O against CaO and $Na_2O/(Na_2O+CaO)$ against distance were constructed, using XRF data retrieved from appendix 8, for sample traverses of metabasite sills at Carsaig, Bagh an Doide, Rubha Garbh, Lochead and Port Cill

Maluaig. The metabasite sills are located in figure 9.1 and the data are presented in figure 9.2.

9.4.1 Na_2O-CaO Compositional Plots

All samples from the metabasites at Lochead and Port Cill Maluaig plot in the low Na_2O, high CaO field of Graham (1976) on an Na_2O-CaO plot, and are not, therefore, altered by spilitisation (compare figures 9.2 and figure 4.3). All samples from the metabasite at Rubha Garbh plot in the high Na_2O, low CaO field of Graham (1976) on an Na_2O-CaO plot, and are, therefore, altered by spilitisation (compare figures 9.2 and figure 4.3). Samples from the metabasites at Carsaig and Bagh an Doide are distributed across the high Na_2O, low CaO and the low Na_2O, high CaO fields on an Na_2O-CaO plot, and are, therefore, at least partially altered by spilitisation (compare figures 9.2 and 4.3).

9.4.2 $Na_2O/(Na_2O+CaO)$-Distance Profiles

$Na_2O/(Na_2O+CaO)$ is consistently low (0.1-0.3) throughout sample traverses of the metabasite sills, which plot in the non-spilitic field of Graham (1976), from Lochead and Port Cill Maluaig (figure 9.2). Relatively systematic $Na_2O/(Na_2O+CaO)$-distance profiles are developed for those metabasite sills, which plot, at least partly, in the spilitic field of Graham (1976), from Carsaig, Bagh an Doide, and Rubha Garbh (figure 9.2). The profile shapes generally describe increased $Na_2O/(Na_2O+CaO)$ in the ***interiors*** of the sills. Furthermore, at Bagh an Doide, smaller increases of $Na_2O/(Na_2O+CaO)$ are evident at the sill margins. It is probable that this merely reflects compositional variation due to development of an alkali-enriched glassy chilled margin during sill emplacement. Graham (1973) describes a metabasite sill exposed NW of Loch Arail, Knapdale (GR805 799,

Figure 9.1: Location Map of XRF Sample Traverses

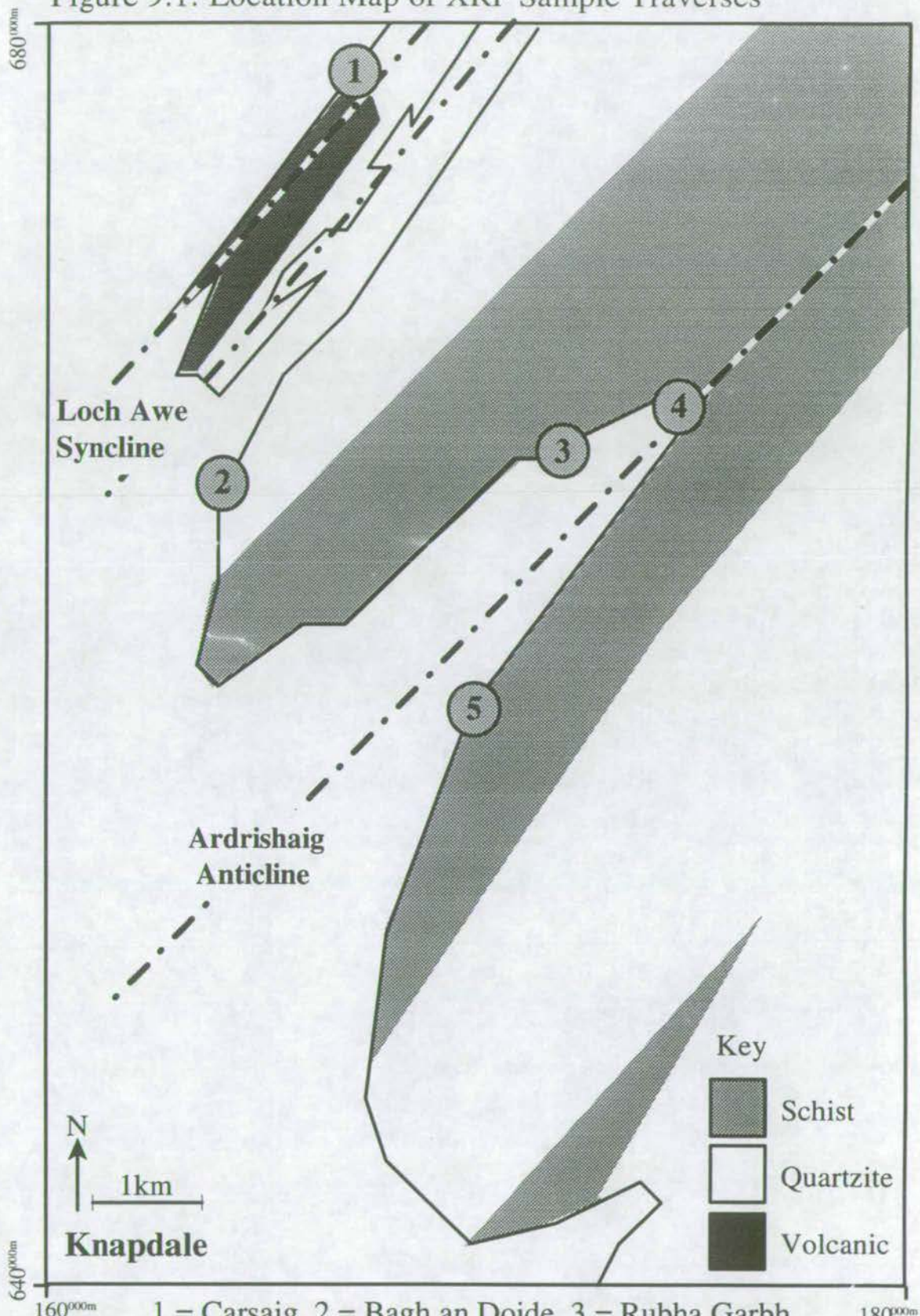

1 = Carsaig, 2 = Bagh an Doide, 3 = Rubha Garbh
4 = Lochead and 5 = Port Cill Maluaig

Figure 9.2: Na2O-CaO and Na2O/(CaO+Na2O)-distance Plots

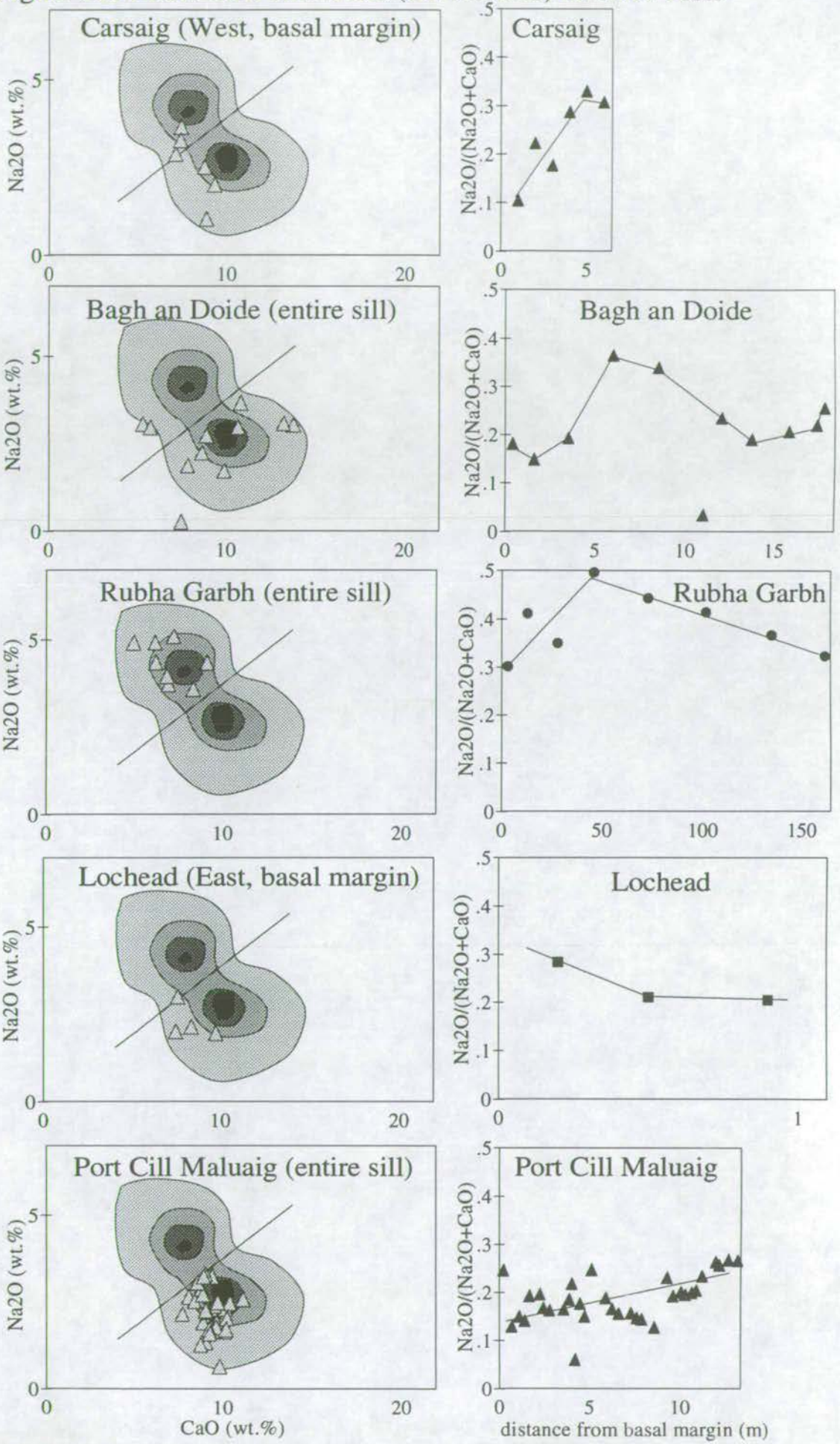

Na2O-CaO and Na2O/(Na2O+CaO) plots, constructed from XRF data obtained from samples collected across five SW Highland basic sills are presented above. Na2O-CaO plots are superimposed on contoured data of Graham (1976) for 93 SW Highland metabasites (*c.f.* figure 4.3).

approx.) which develops the reverse of the above described profiles (i.e. $Na_2O/(Na_2O+CaO)$ is highest at the sill margins).

9.5 Qualitative Interpretations of XRF Data

Assuming that $Na_2O/(Na_2O+CaO)$ is an effective monitor of the extent of spilitisation, the observed profiles may be interpreted to describe zones of enhanced spilitisation in the interiors of some metabasite sills. Possible mechanisms by which the observed profiles could be generated are outlined below.

Basic sills were emplaced into cold, consolidating sub-seafloor sediments and therefore the sill margins will have cooled more rapidly than the relatively well-insulated sill interiors. Three possible mechanisms for enhanced spilitisation of the sill interiors arise from this fundamental statement:

(1) Sill margins and sill interiors may have experienced similar time-integrated fluid fluxes and the higher temperature of the sill interior may have induced more rapid exchange of Na and Ca between fluid and rock. **Enhanced spilitisation of sill interiors would therefore result from thermally-enhanced rate of reaction**.

(2) Convecting fluids may have been thermally-focused along the hot sill interiors. **Enhanced spilitisation of sill interiors would therefore result from thermally-enhanced time-integrated fluid fluxes**.

(3) Slower cooling rates of sill interiors may have resulted in more intense fracturing and therefore convecting fluids may have been structurally-focused through sill interiors. **Enhanced spilitisation of sill interiors would therefore result from structurally-enhanced time-integrated fluid fluxes**.

A modern analogue of Dalradian spilitisation is found in the Guaymas Basin, Gulf of California, which represents a newly evolving oceanic basin. A number of investigations were undertaken following leg 64 of the DSDP of which sites 477, 478 and 481 provided cores of unconsolidated sediments and the upper part of a major basic sill complex underlying the rift-zone. Hydrothermal activity was implied from the development of hydrothermal minerals such as dolomite, anhydrite, pyrite,

epidote, quartz and albite in sediments surrounding basic sills. Porosity-depth profiles display a decrease in porosity adjacent to the sills which is attributed to expulsion of sediment pore fluid in response to sill emplacement. Unfortunately, minimal information has arisen from the DSDP report regarding the nature of fluid flow ***within*** the sills.

With the lack of better or independent constraints, it is probably reasonable to assume that all the above mechanisms may play contributory roles towards generating the observed Na_2O-enrichment within the sill interiors. In conclusion, it must be emphasised that the above discussion assumes that the studied sills are representative of the general pattern. For this to be confirmed, a more extensive study is clearly essential.

9.6 Spatial Distribution of Spilitic Metabasites

Spilitic alteration is most extensive in basic rocks emplaced in sediments which immediately underlie the Tayvallich Volcanics. This is consistent with spilitisation having occurred as a result of sub-seafloor hydrothermal circulation for the following reasons:

(1) These sediments are at a high stratigraphic level and were near the surface prior to metamorphism;

(ii) The above interpretation assumes that the Tayvallich Volcanics were the predominant heat source driving hydrothermal circulation.

However, spilitised metabasites are observed, in isolation, elsewhere throughout the SW Highlands. For example, spilitic metabasites have been observed on the Loch Fyne coast, on the SE (inverted) limb of the Ardrishaig Anticline (Graham *pers.comm.*). Their structural location demands that they were at some distance from the Tayvallich Volcanics. Therefore it is probable, that emplacement of these sills induced localised hydrothermal circulation.

9.7 Summary

In summary, Na_2O-CaO and $Na_2O/(Na_2O+CaO)$-distance plots were constructed from bulk composition data obtained by standard XRF analytical techniques.

Na_2O-CaO plots were implemented to identify spilitic alteration of basic sills by comparison with the compositional data-set of Graham (1976). Sills at Carsaig, Bagh an Doide and Rubha Garbh were found to be spilitic (figures 9.1 and 9.2).

$Na_2O/(Na_2O+CaO)$-distance plots were implemented to constrain the geometries of spilitic alteration. Increased spilitisation (i.e. higher $Na_2O/(Na_2O+CaO)$) was observed at the interiors of sills at Carsaig, Bagh an Doide and Rubha Garbh. Thermally-enhanced spilitisation reaction rates, thermal or structural focusing of causative fluids along sill interiors were inferred to be responsible.

Spilitisation is most extensive in basic rocks cropping out in close proximity to the Tayvallich Volcanics, affirming the assumed correlation of spilitic alteration with magmatically-driven shallow-crustal convection of sea-water. Spilitic metabasites are observed in a few localities at greater distances from the Tayvallich Volcanics and it is assumed that their emplacement resulted in localised hydrothermal circulation.

10. QUANTITATIVE MODELLING AND REGIONAL MAPPING OF FLUID FLOW:

Syn-Metamorphic Fluid Infiltration

10.1 Introduction

In this chapter, the reaction front advection model (Bickle & Baker 1990b) is used to calculate one-dimensional time-integrated fluid fluxes from measured advection of mineral reaction fronts into the margins of greenschist facies metabasites which are abundant throughout the SW Scottish Highlands.

One-dimensional time-integrated fluid fluxes are compiled to produce a regional map of fluid fluxes, from which it is possible to identify fluid flow patterns and deduce the predominant controls of fluid infiltration.

The theoretical background to the quantitative modelling of one-dimensional time-integrated fluid fluxes in this chapter is discussed in chapter 2, and lithological and mineralogical evidence describing the advection of mineral reactions into the margins of greenschist facies metabasites were presented in chapter 5.

Three-dimensional time-integrated fluid fluxes are constrained within limits from one-dimensional time-integrated fluid flux vector components. A three-dimensional time-integrated fluid flux profile is constructed across the SW Highlands from which the predominant controls of syn-metamorphic fluid infiltration may be unambiguously deduced. From the mean regional three-dimensional fluid flux it is possible to constrain the total volume of syn-metamorphic fluid infiltrating the Dalradian of the SW Scottish Highlands. It is therefore possible to identify a realistic source reservoir.

10.2 Rationale

At the peak of greenschist facies regional metamorphism, metabasite sills and dykes developed the equilibrium type I mineral assemblage (section 5.3.2):

amphibole + epidote + chlorite ± albite ± sphene ± quartz ± biotite

Type I metabasites were subsequently infiltrated by a CO_2-bearing hydrous fluid phase, which was in chemical and isotopic equilibrium with host phyllites or psammites. Fluid infiltration drove the CO_2-consuming mineral reaction:

$3Am + 2Ep + 10CO_2 + 8H_2O = 3Chl + 10Cc + 21Qz$ **(1)**[1]

which was buffered by the equilibrium type II mineral assemblage (section 5.3.2):

amphibole + epidote + chlorite + calcite + quartz ± albite ± sphene

and generated the equilibrium type III mineral assemblage (section 5.3.2):

chlorite + calcite + quartz ± sphene ± rutile ± biotite

at the margins of metabasite sills and dykes. The type II mineral assemblage coincides with a mineral reaction front which is defined by a change in the modal mineralogy of the metabasite corresponding to progress of reaction 1. The mineral reaction front was transported by advection (and diffusion, see chapter 7) towards the interior of the metabasite sill or dyke. The advection distance, which corresponds to the width of the type III zone developed at the sill margin, is quantitatively related to the time-integrated fluid flux perpendicular to the sill margin by the model equation of Bickle & Baker (1990b) as described in section 2.3.3.

10.3 Quantification of Syn-Metamorphic Fluid Infiltration

Syn-metamorphic fluid infiltration was quantified by application of the one-dimensional model of Bickle & Baker (1990b) to calculate one-dimensional time-integrated fluid fluxes from the advection distances of reaction 1 into the margins of metabasites.

[1]Reaction (1) is included on a reference card at the back of the thesis.

10.3.1 Identification of Mineral Reaction Fronts

Initially reaction fronts have been identified from modal profiles, constructed from point-counting data (section 6.4). These profiles were compared with reaction progress profiles, constructed from volumetric carbonate data measured in the field (section 6.5). Reaction fronts identified on modal and reaction progress profiles were found to be consistent. The reaction progress approach has been adopted in the majority of this study, for the following reasons:

(1) Firstly, provided that every effort is made to minimise inaccuracies inherent from geochemical analysis undertaken in the field, more accurate constraint of the position of the reaction front may be achieved from volumetric carbonate data than modal point-counting of up to 2000 points (section 6.5).

(2) Secondly, the inherent simplicity of the field geochemical technique enables its efficient application in the field without repeated recourse to the laboratory (section 6.5).

The morphology and quantitative interpretation of modal and reaction progress profiles were discussed in chapter 7.

10.3.2 Calculation of Time-integrated Fluid Fluxes

The advection distances were measured as the distances between the reaction fronts and the metabasite margins. Time-integrated fluid fluxes were then calculated from the measured advection distances using the reaction front advection model equation of Bickle & Baker (1990b) which is discussed in section 2.3.3 and given by:

$$V_f t = \frac{\omega_1 . \varphi_1 . t . \left(X_{CO2,2} - X_{CO2,1}\right)}{R_{CO2} . \left(1 - X_{CO2,2}\right) - R_{H2O} . X_{CO2,2}} \qquad (10.1)^2$$

where V_f is the velocity of the reaction front, t is time, and therefore $V_f t$ is the advection distance of the reaction front; ω_1 is the fluid velocity upstream of the

[2]Equation 9.1 is included on a reference card at the back of the thesis.

reaction front, φ_1 is the porosity upstream of the reaction front, and therefore $\omega_1\varphi_1$ is the fluid flux and $\omega_1\varphi_1 t$ is the time-integrated fluid flux; $X_{CO_2,1}$ and $X_{CO_2,2}$ are the respective volumetric fractions of CO_2 in the fluid, upstream and downstream of the front; R_{CO_2} and R_{H_2O} are the respective volumetric stoichiometric coefficients of CO_2 and H_2O produced or consumed by reaction (1). Calculation of the time-integrated fluid flux ($\omega_1\varphi_1 t$) requires knowledge of the parameters $V_f t$, $X_{CO_2,1}$, $X_{CO_2,2}$, R_{CO_2} and R_{H_2O}. $V_f t$ is measured from modal and reaction progress profiles which are discussed in section 10.3.1. $X_{CO_2,2}$ is constrained at the appropriate P-T conditions for each metabasite from the P-T-X_{CO_2} stability curve of reaction (1) which is shown in figure 10.1 and detailed in section 5.3.2, figures 5.3(a) and (b) and appendix 3.

$X_{CO_2,1}$ is constrained by the mineral assemblages of the host metasediments. Calc-phyllites are the most widespread host lithology and generally contain the equilibrium assemblages:

biotite + chlorite + calcite, albite + chlorite + calcite and rutile + calcite + quartz

which constrain the fluid composition to a very narrow P-T-X_{CO_2} stability field (figure 10.1). The fluid composition is assumed to be maintained within this narrow P-T-X_{CO_2} stability field in other phyllitic host lithologies because no other buffering assemblages are developed and isotopic homogenisation (discussed later) implies that fluids within the phyllites were thoroughly mixed.

Pressure is assumed to be a constant 10kb throughout the SW Highlands, for lack of better constraints (section 3.4.3). Temperatures are generally better constrained (section 3.4.3) and are therefore estimated for each metabasite from the geothermometric map which is presented in figure 3.8. R_{CO_2} and R_{H_2O} are estimated from the volumetric stoichiometry of reaction 1 which is detailed below and discussed in section 6.3 and figure 6.1.

The reaction front advection model is based on the assumptions that fluid infiltration is pervasive (section 2.3.3) and that the infiltrating fluid composition is

Figuure 10.1: Isobaric T-X(CO2) Section calculated at 10kb showing the stability of reaction (1) and the calc-phyllite assemblage: Bi+Ab+Ru+Chl+Cc+Qz

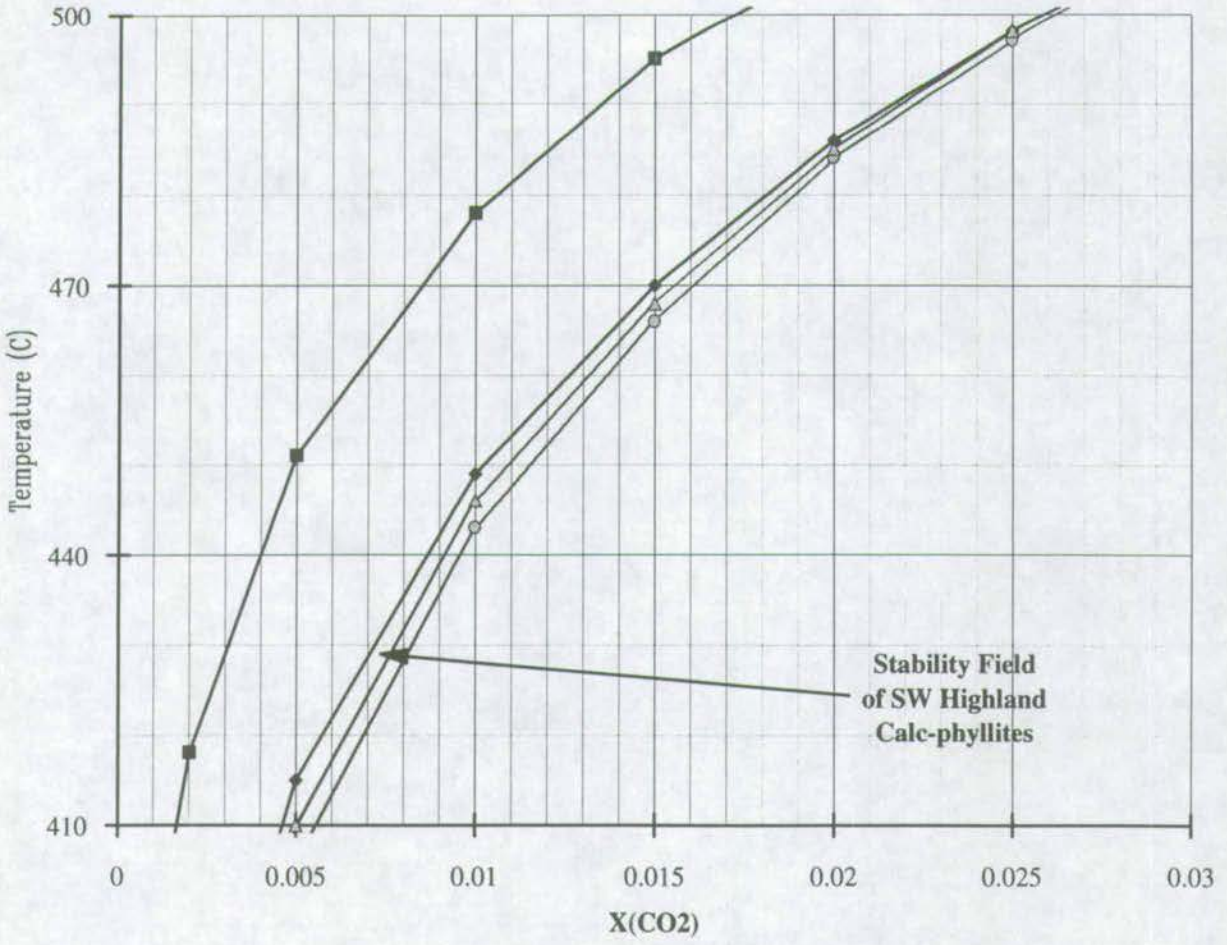

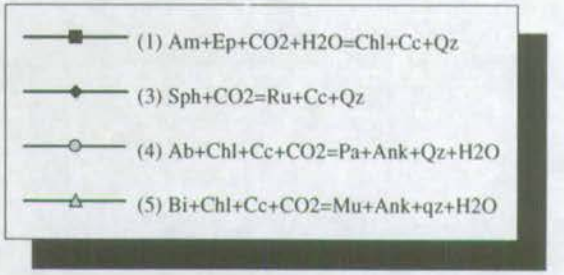

X(CO2), the infiltrating fluid composition is assumed to be in equilibrium with the predominant host phyllite assemblage: Bi+Ab+Ru+Chl+Cc+Qz, which defines a very narrow T-X(CO2) stability field at 10kb, as is shown on the adjacent plot.

X(CO2,2), the fluid composition buffered by reaction (1) is constrained from the adjacent plot.

consistently buffered by the predominant host phyllite assemblage. These assumptions were tested in chapter 8. The time-integrated fluid flux was predicted from the advection distance of reaction 1 using the reaction front advection model, outlined above, and found to be consistent with the time-integrated fluid flux predicted from the advection distance of a front in $\delta^{18}O$ using the isotope front advection model of Bickle & McKenzie (1987) which is based on similar assumptions to those described above (section 2.3.2). It is likely, therefore, that the above assumptions and therefore the reaction front advection model are applicable to the metabasites which crop out in the Dalradian of the SW Highlands.

10.3.3 Regional Fluid Flux Mapping

Reaction progress profiles and/or modal profiles have been constructed for some 66 metabasite sills and dykes which crop out throughout the Dalradian of the SW Highlands. Time-integrated fluid fluxes have been calculated from most of these profiles and have been compiled in the form of a regional fluid flux map. It is possible form such a map to predict syn-metamorphic fluid flow paths, to identify the predominant structural, lithological and micro-textural controls on fluid infiltration, to quantify the true, three-dimensional time-integrated fluid flux and to constrain the physical nature of the fluid source reservoir.

10.4 Modal Profile Data

Modal profiles were constructed using modal assemblage data, estimated by classical point-counting techniques, across metabasites from several key localities. In this section, these profiles are presented, discussed and compared with the standard modal profiles which were constructed in figure 5.1[3], in conjunction with field descriptions and available compositional data.

[3]A standard modal profile describing modal changes as a result of progress of reaction (1) is included on a reference card at the back of the thesis.

Figure 10.2: Location Map of Modal Traverses

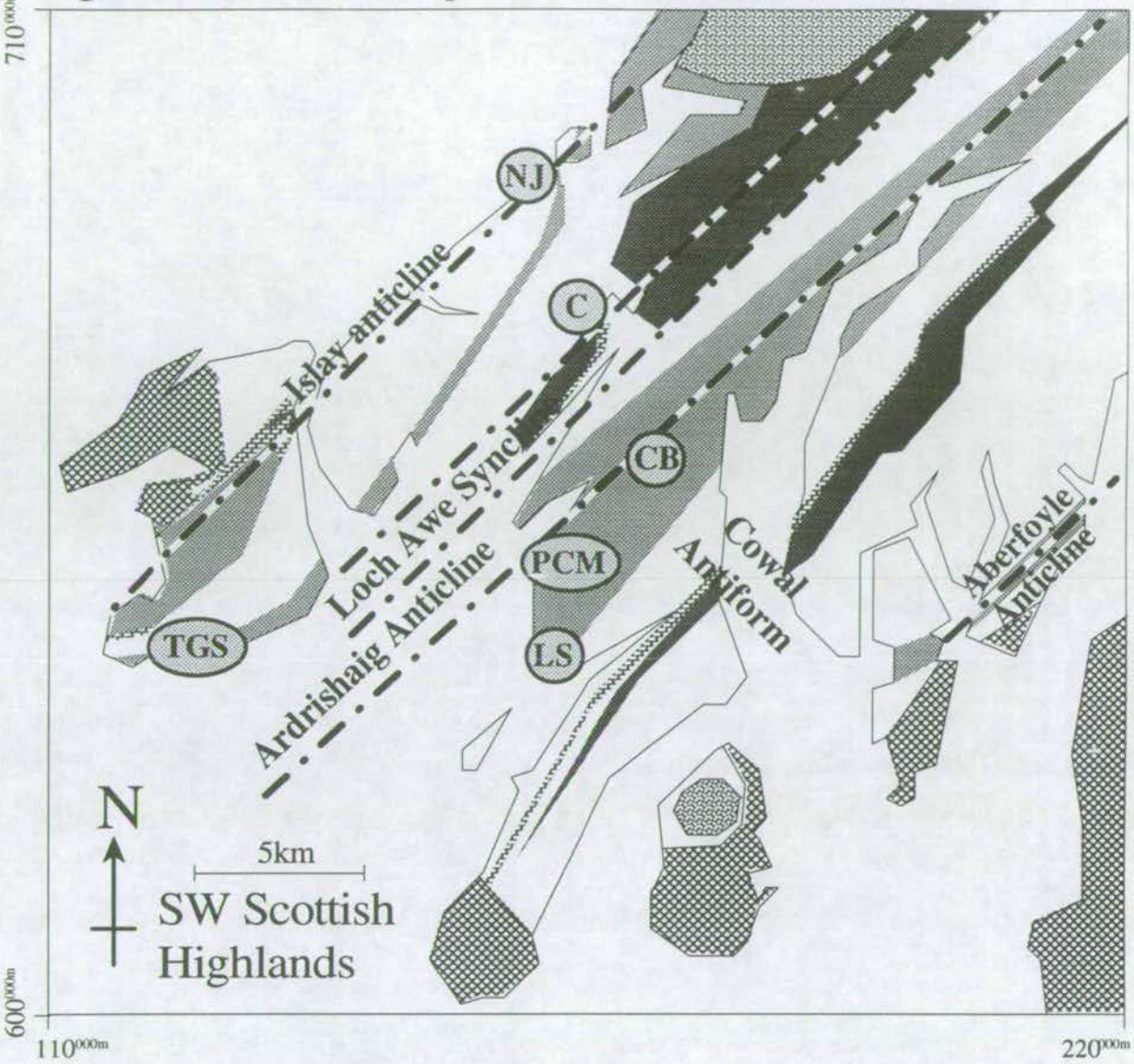

Phyllite

Psammites

Volcanics and Related Rocks

Marble and calc-schists

Other Metamorphic and sedimentary rocks

Other Igneous Rocks

PCM = Port Cill Maluaig
NJ = North Jura
CB = Clachbrac
C = Carsaig
LS = Loch Stornoway
TGS = Traigh Gheighsgeir

Figure 10.3(a) Port Cill Maluaig: Outcrop Map

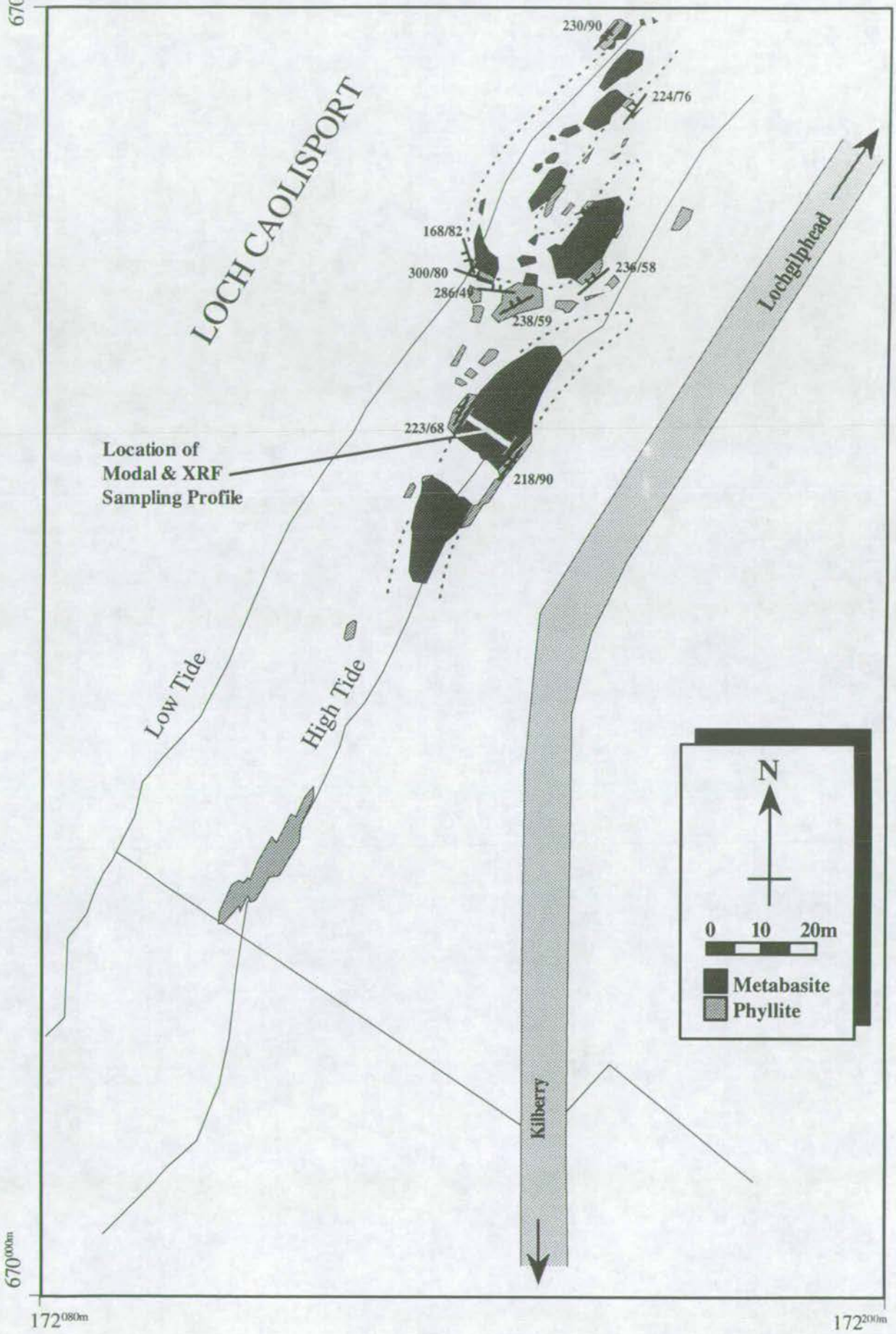

Figure 10.3(b): Port Cill Maluaig: Modal Profile
(showing the reaction:
Am+Ep+CO2+H2O=Chl+Cc+Qz)

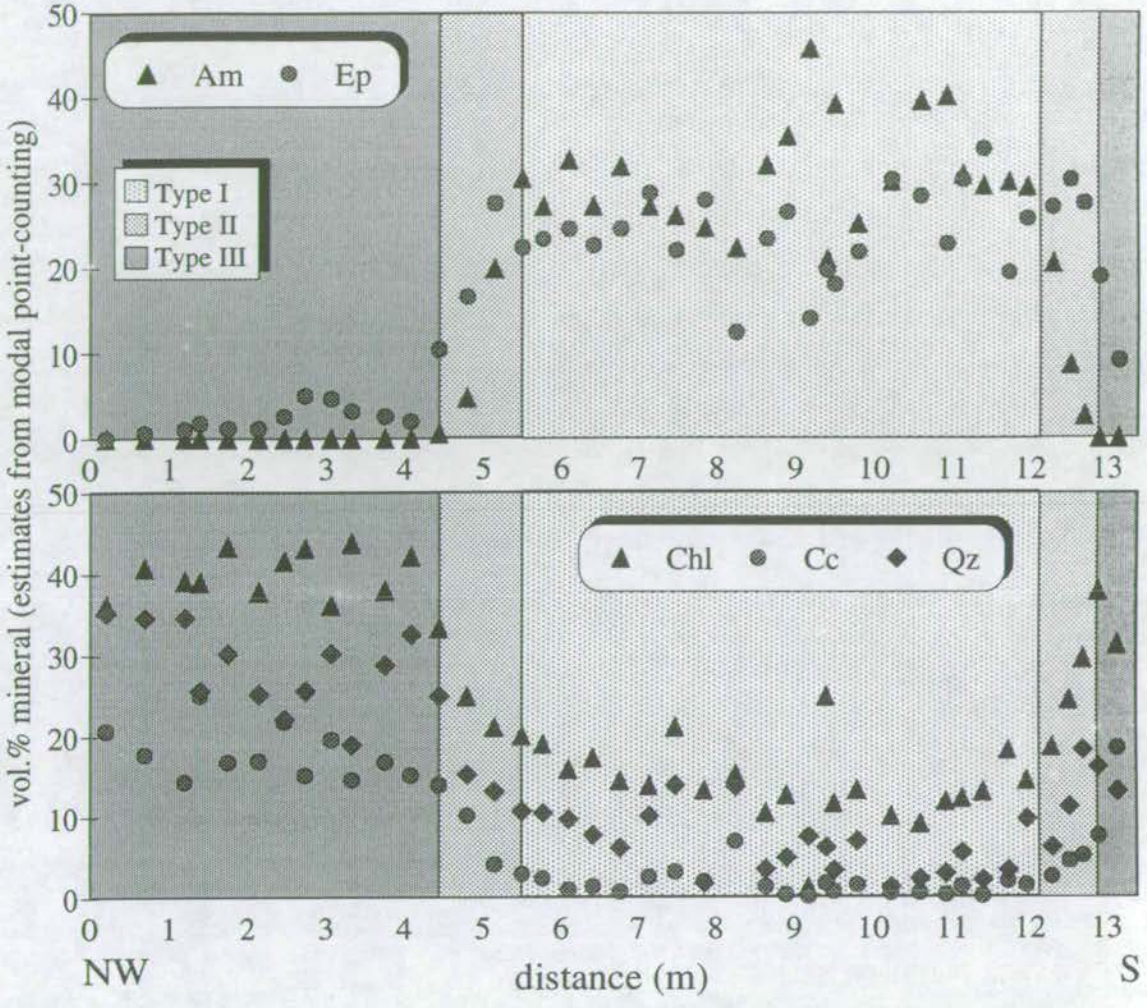

Figure 10.3(c) Port Cill Maluaig: XRF Profile

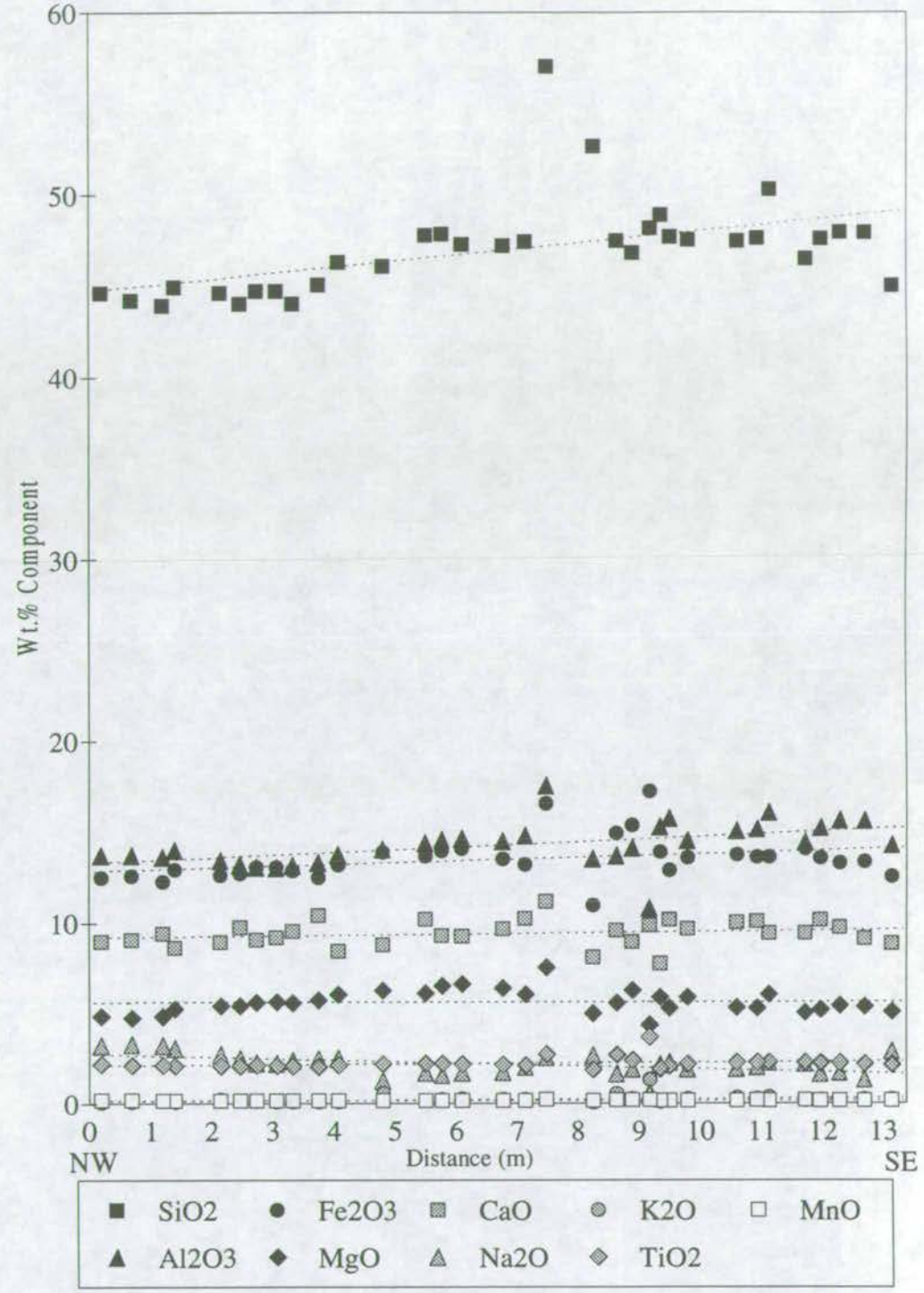

The above XRF profile shows the general lack of compositional variation (w.r.t.spatial distribution of type I-III metabasite zones). Dashed lines are linear regression curves. The profile below shows variation in wt.% volatiles which correlates precisely with the distribution of type I-III metabasites (figure 10.3a).

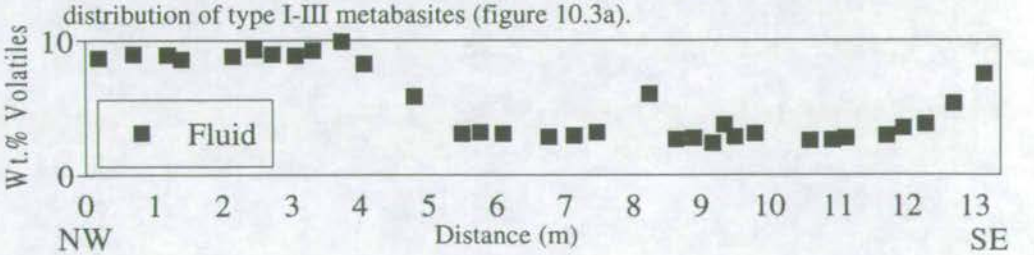

constructed from 42 evenly spaced mineralogical modes, estimated by counting 400-500 points per thin section. The compositional profile was constructed from 32 evenly spaced bulk rock XRF analyses.

A sheared "z"-type fold is identified from the outcrop map shown in figure 10.3(a). The sense of shearing is sinistral. The axial surface of the fold is oriented parallel to the axial surface of the recumbent D_1-D_2 Ardrishaig Anticline. It is therefore probable that the sheared "z" fold is parasitic to the Ardrishaig Anticline and will therefore plunge (along with the Ardrishaig Anticline, Roberts 1974) to the NE. It is may thus be inferred that shearing and folding either pre-dated or was synchronous with syn-metamorphic fluid infiltration (section 3.4.4). In close proximity to the sill, the fabric in the host phyllites is re-oriented such that it parallels the sill margins, in response to marginal shearing at the sill-phyllite contact due to their contrasting competencies. Modal and compositional profiles were constructed as far from the shear-zone as exposure permitted as to avoid any unnecessary additional complications.

Zones of the type I assemblage: amphibole + epidote, the type II assemblage: amphibole + epidote + chlorite + calcite + quartz, and the type III assemblage: chlorite + calcite + quartz, may be distinguished from the modal profile (figure 10.3b). The type I assemblage is preserved in the sill interior and contains, on average 31-38 vol.% amphibole, 24-29 vol.% epidote, 11-18 vol.% chlorite, 3-8 vol.% quartz and 0-1 vol.% calcite. The type III assemblage is developed, asymmetrically, in the sill margins and contains, on average, 0-3 vol.% epidote, 42 vol.% chlorite, 14-17 vol.% calcite, 29-33 vol.% quartz and no amphibole. Types I and III assemblages are separated by narrow zones of type II metabasite across which 31-38 vol.% amphibole and 21-29 vol.% epidote are consumed, and approximately 24 vol.% chlorite, 14-17 vol.% calcite and 21 vol.% quartz are produced by mineral reaction. Quantitative correlation of these volumetric modal changes with the standard modal profile of reaction 1[4] implies that progress of reaction was limited by

[4]The standard modal profile of reaction (1) is included on a reference card at the back of the thesis.

the amount of calcite in the rock. The remaining excess of chlorite + quartz, together with non-reacting phases (e.g. albite), constitutes approximately 50% of the reactant assemblage. Otherwise, the standard modal changes of reaction 1 are almost perfectly replicated at Port Cill Maluaig.

The bulk compositional profile shows minimal variation (figure 10.3c), particularly between type I and type III assemblages, indicated that reaction 1 is isochemical. However the volatile content of the type I assemblage, developed in the sill interior, is considerably less than that of the type III assemblage, developed in the sill margins (figure 10.3c). Type I metabasite contains 2-4 wt.% volatiles, whereas the type III metabasite contains 8-10 wt.% volatiles. This reflects fluid absorption induced by progress of reaction 1.

Whole rock stable isotopic analysis by Graham & Fallick (*unpublished*) gives $\delta^{18}O = 9.72$ for the type I metabasite from the interior of the sill at Port Cill Maluaig. Adjacent psammites record $\delta^{18}O = 12.55$. Noting that some unreacted SW Highland metabasites record pre-metamorphic MORB-like isotopic signatures, given by $\delta^{18}O_{\text{whole rock}} \approx 6^{o}/_{oo}$, and allowing for the effects of isotopic fractionation, it appears reasonable to infer that the Port Cill Maluaig sill has been homogenised in $\delta^{18}O$ by advection of the $\delta^{18}O$ front.

10.4.2 North Jura (figure 10.4)

A series of metabasic dykes intrude the Islay-Jura Quartzite on the Corryvreckan coast of North Jura. Outcrop maps of a 5.0m wide, N-S trending dyke, exposed at GR694 013, are presented in figure 10.4(a), together with modal data in figure 10.4(b). A modal profile was constructed for the dyke, from 10 regularly spaced mineralogical modes, estimated by counting 400-500 points per thin section. The dyke margin is sheared and intensely deformed, yet the dyke is hosted by undeformed meta-psammites. This contrast reflects the inherent differences in competency which are intensified by modification of the dyke assemblage to type III.

Figure 10.4(a) North Jura: Outcrop Map

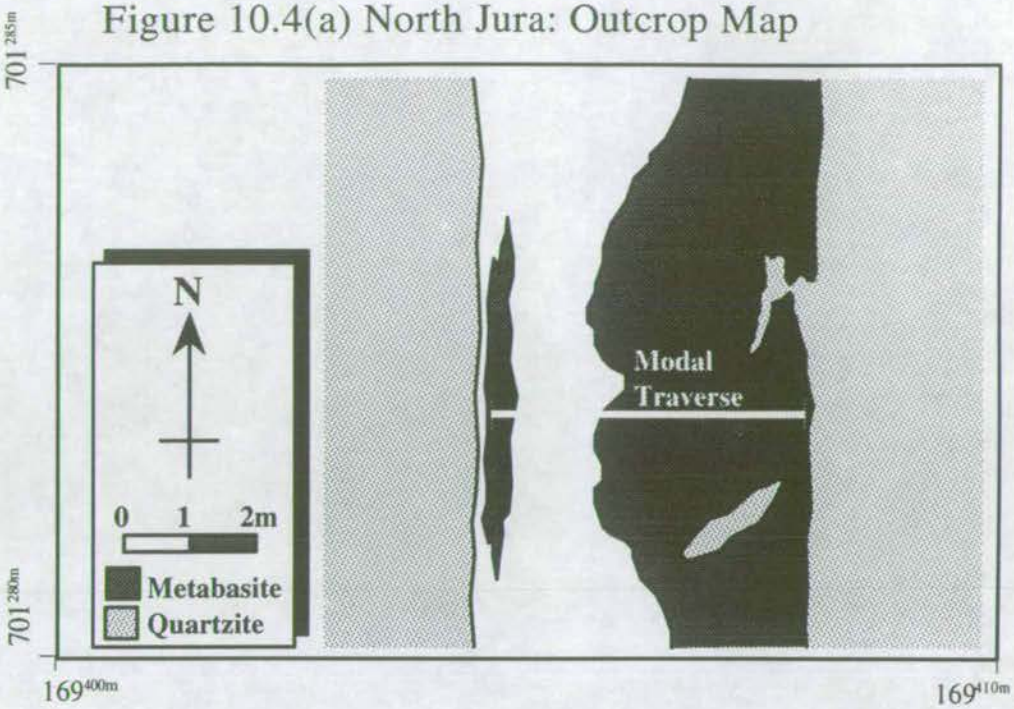

Figure 10.4(b): North Jura: Modal Profile
(showing the reaction: Am+Ep+CO2+H2O=Chl+Cc+Qz)

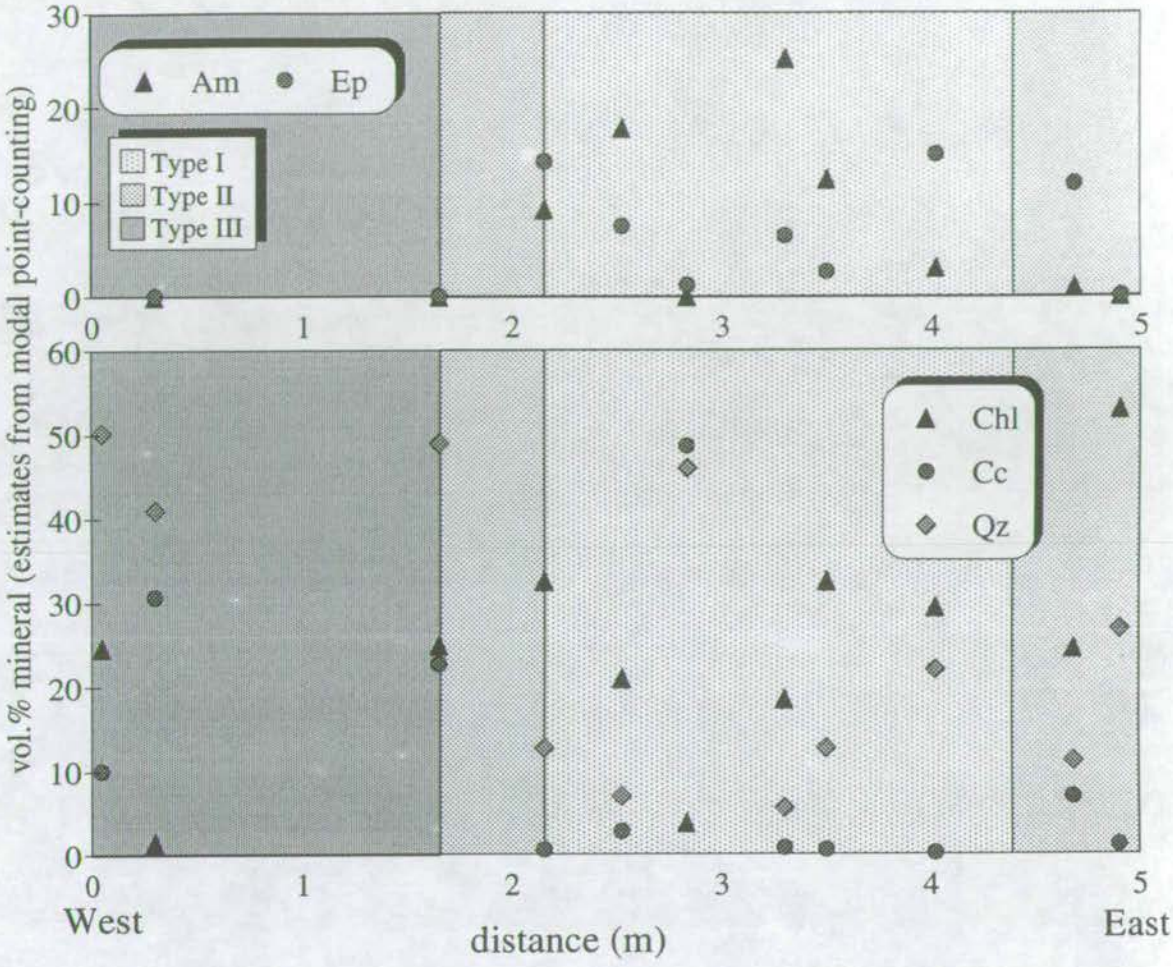

Zones of the type I assemblage: amphibole + epidote, the type II assemblage: amphibole + epidote + chlorite + calcite + quartz, and the type III assemblage: chlorite + calcite + quartz, may again be distinguished from the modal profile (figure 10.4). The type I assemblage is predominant in the dyke interior and contains, on average, 15-25 vol.% amphibole, 10-15 vol.% epidote, 25-35 vol.% chlorite, 5-15 vol.% quartz and minimal calcite. The type III assemblage is predominant in the dyke margins and contains, on average, 25-35 vol.% chlorite, 20-45 vol.% quartz, 20-30 vol.% calcite, minimal epidote and minimal amphibole. Types I and III assemblages are separated by narrow zones of type II metabasite across which 15-20 vol.% amphibole and 10-15 vol.% epidote are consumed, and 20-30 vol.% calcite and 10-35 vol.% quartz are produced by mineral reaction. The mode of chlorite is fairly constant throughout the reaction. Quantitative correlation of these volumetric modal changes with the standard modal profile of reaction (1)[5] predicts that excess chlorite and insufficient amphibole are present in the interior of the dyke to satisfy the stoichiometry of reaction (1). One possible explanation of this modal imbalance is that amphibole is replaced by chlorite in subsequent retrogression. Furthermore, anomalously high vol.% calcite is recorded from one sample from the sill interior. The sample was collected adjacent to the break in outcrop illustrated in figure 10.4(a) and may therefore identify infiltration-driven development of type III assemblages resulting from internal shearing of the sill. Nevertheless, if reaction 1 does in fact describe the modal changes observed in the dyke, progress of reaction 1 was limited by the amount of calcite in the rock. The remaining excess of chlorite + quartz, together with non-reacting phases (e.g. albite) constitutes approximately 50% of the reactant assemblage.

10.4.3 Clachbreac (figure 10.5)

A 40m wide, possibly folded sill is exposed at Clachbreac, Knapdale (GR771 756) which is hosted by relatively psammitic Ardrishaig Phyllites and is located

[5]The standard modal profile of reaction (1) is included on a reference card at the back of the thesis.

Figure 10.5(a) Clachbreac: Outcrop Map

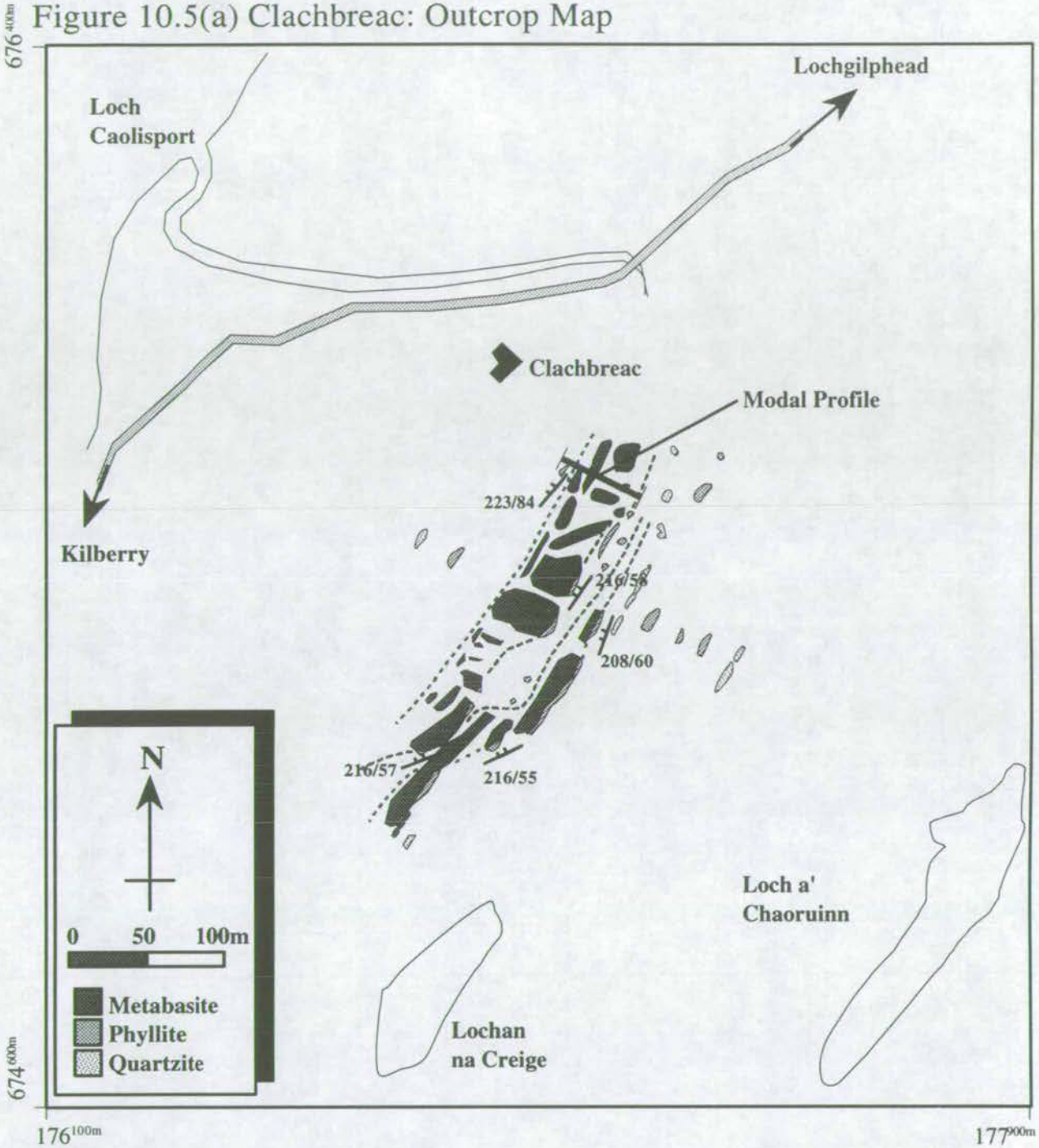

Figure 10.5(b): Clachbreac: Modal Profile
(showing the reaction: Am+Ep+CO2+H2O=Chl+Cc+Qz)

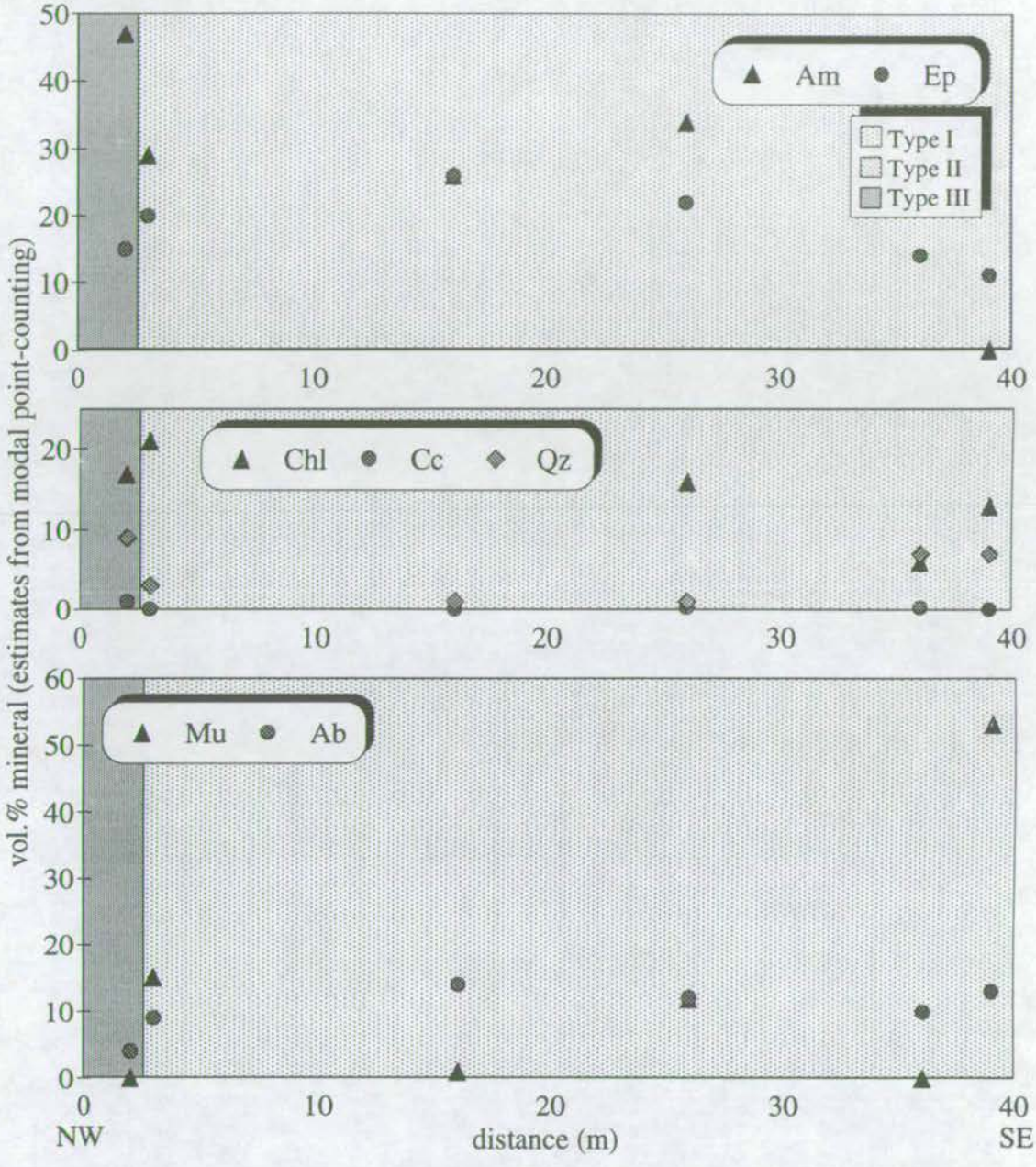

approximately 0.5km NW of the garnet isograd and Erins Quartzite-Ardrishaig Phyllite contact. An outcrop map of the metabasic sill is presented in figure 10.5(a), together with modal data in figure 10.5(b). A modal profile was constructed for the sill from 6 evenly spaced mineralogical modes, estimated by counting 400-500 points per thin section.

The metabasic sill at Clachbreac forms a broad, precipitous ridge, which rises 170m above the head of Loch Caolisport. The name Clach Breac may be translated from the gaelic to "speckled stone". The name is well chosen as it aptly describes the igneous appearance of this coarse-grained amphibole + epidote-bearing type I metabasite which is "speckled" with coarse albites. Indeed almost the entire 40m wide sill consists of type I metabasite. The outcrop pattern of the sill predicts the existence of a fold hinge or two near-parallel metabasic sheets. Insufficient information is available to prove the existence of this fold or if the fold exists, to determine whether the fold is antiformal or synformal.

A muscovite-bearing type I assemblage with accessory muscovite is developed throughout the majority of the sill. The type I assemblage contains, on average, 30-35 vol.% amphibole, 20-25 vol.% epidote, 10-20 vol.% chlorite, 2-7 vol.% quartz, 0-15 vol.% muscovite, 10-12 vol.% albite and occasional traces of calcite. The NW (structurally) upper margin is enriched in amphibole, calcite and quartz, and depleted in chlorite and epidote. Reaction 1 may have occurred at the upper margin, facing the Ardrishaig Anticline. White mica is abundant as an accessory phase and probably records a bulk compositional effect.

10.4.4 Carsaig (figure 10.6)

A broad, antiformally folded metabasite sill is exposed on Eilean Traighe, an island which is connected to the mainland by a tidal strand, at Carsaig, West Knapdale (GR726 879). The sill is hosted by Crinan Grits near the core of the Loch Awe Syncline, on the low-grade side of the isograd defined by the prograde reaction: actinolite + stilpnomelane → hornblende + chlorite (Graham 1973). An outcrop map

Figure 10.6(a): Carsaig: Outcrop Map

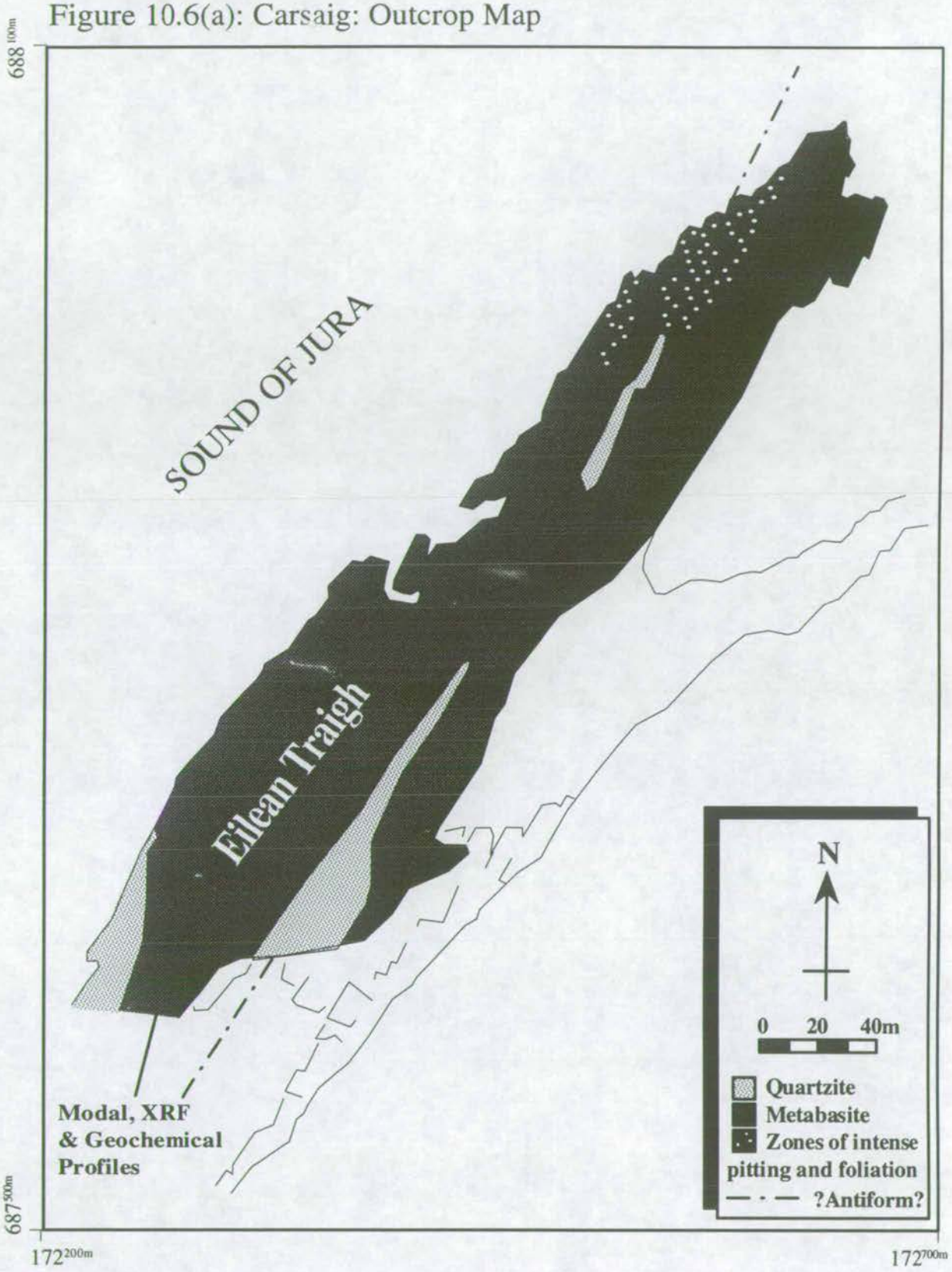

Figure 10.6(b): Carsaig: Modal Profile
(showing the reaction:Am+Ep+H20+CO2=Chl+Cc+Qz)

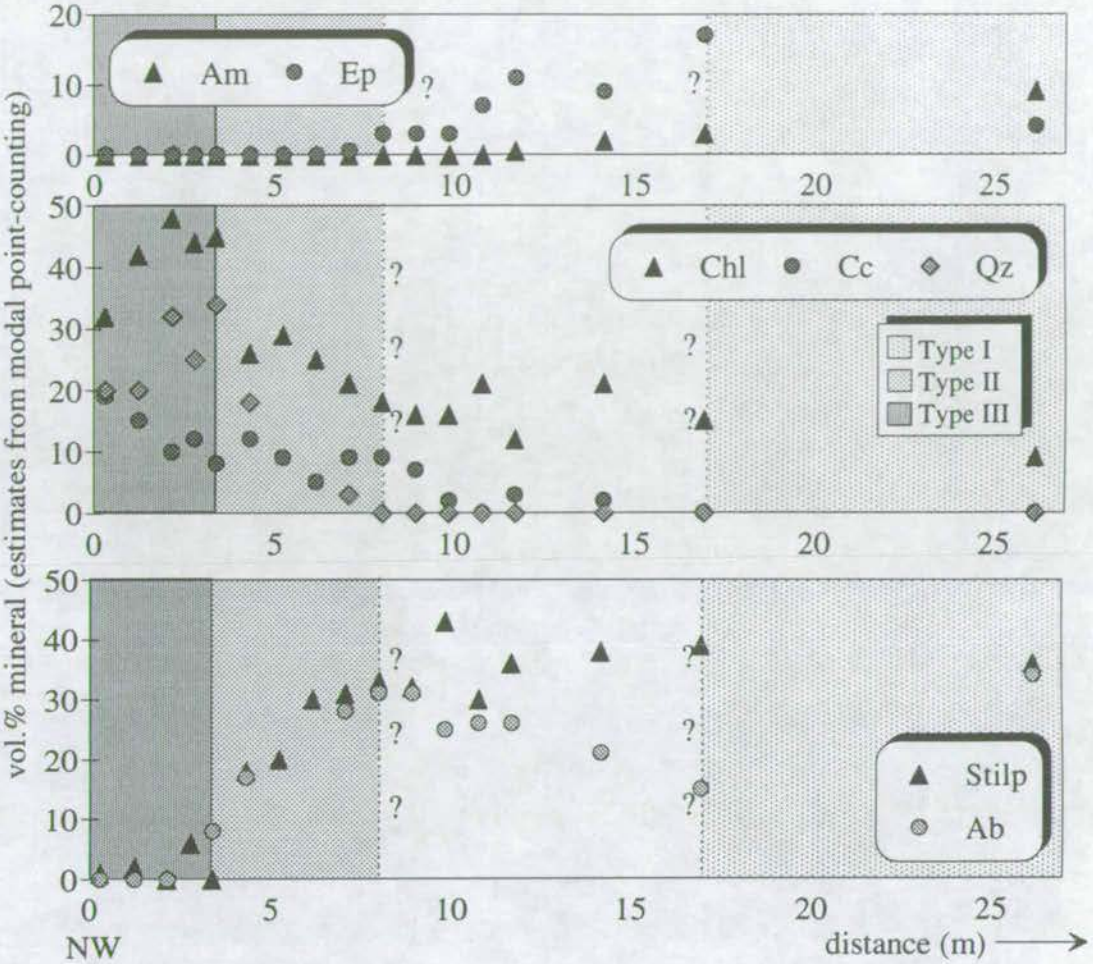

Figure 10.6(c): Carsaig: XRF Data

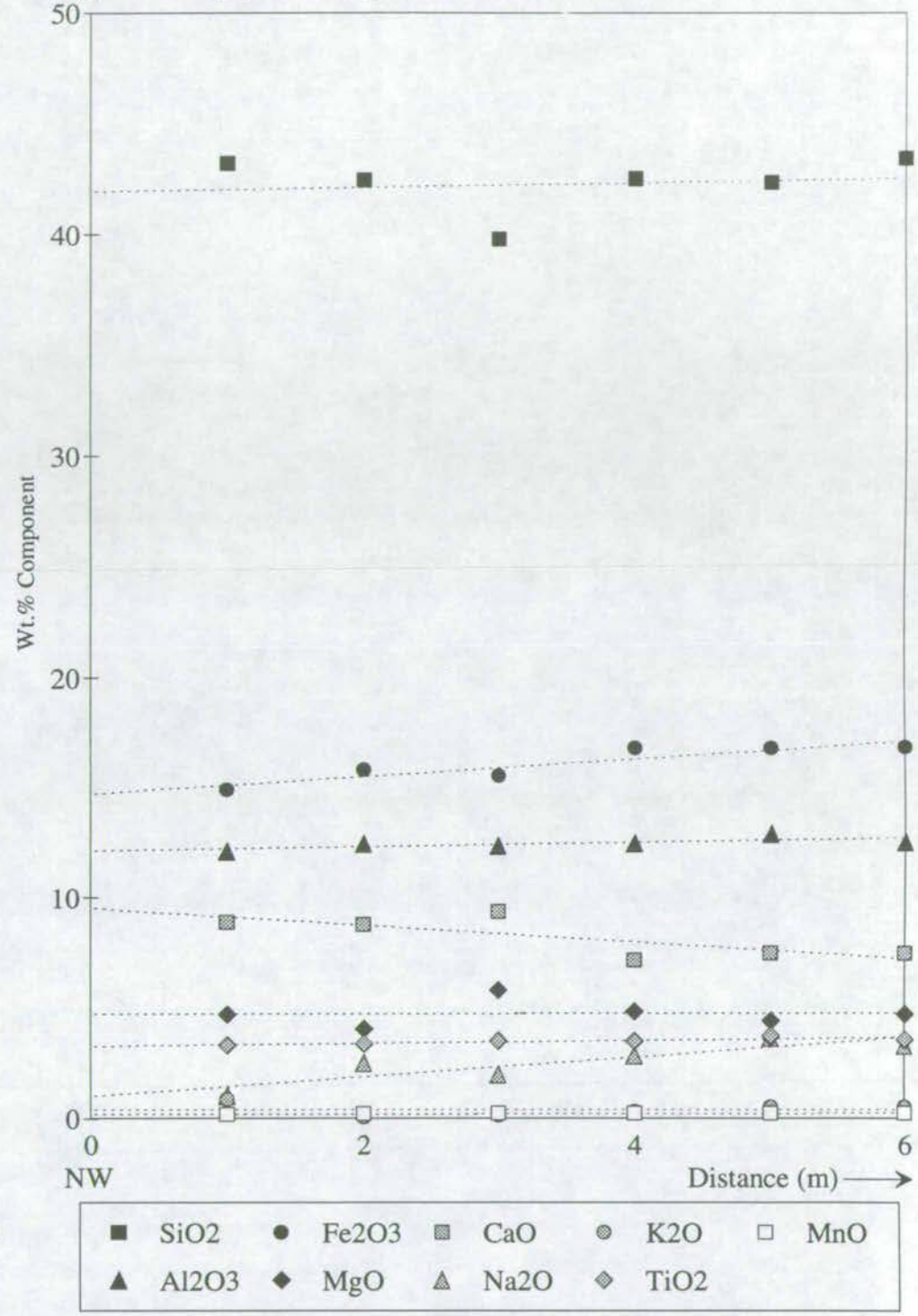

The above XRF profile shows the general lack of compositional variation (w.r.t. spatial distribution of type I-III metabasite zones). Dashed lines are linear regression curves. The profile below shows variation in wt.% volatiles.

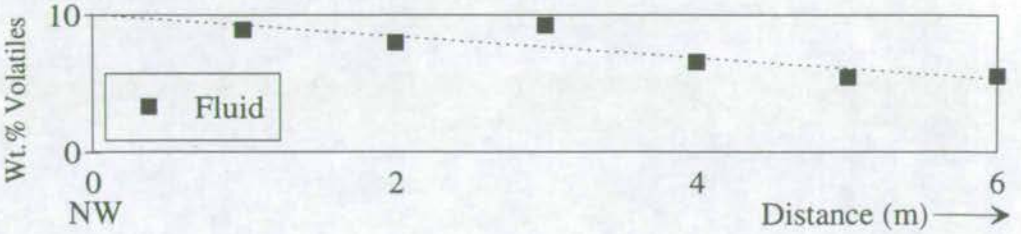

Figure 10.6(d): Fluid:Rock ratio estimated by Reaction Prgoress technique by I. Roberts

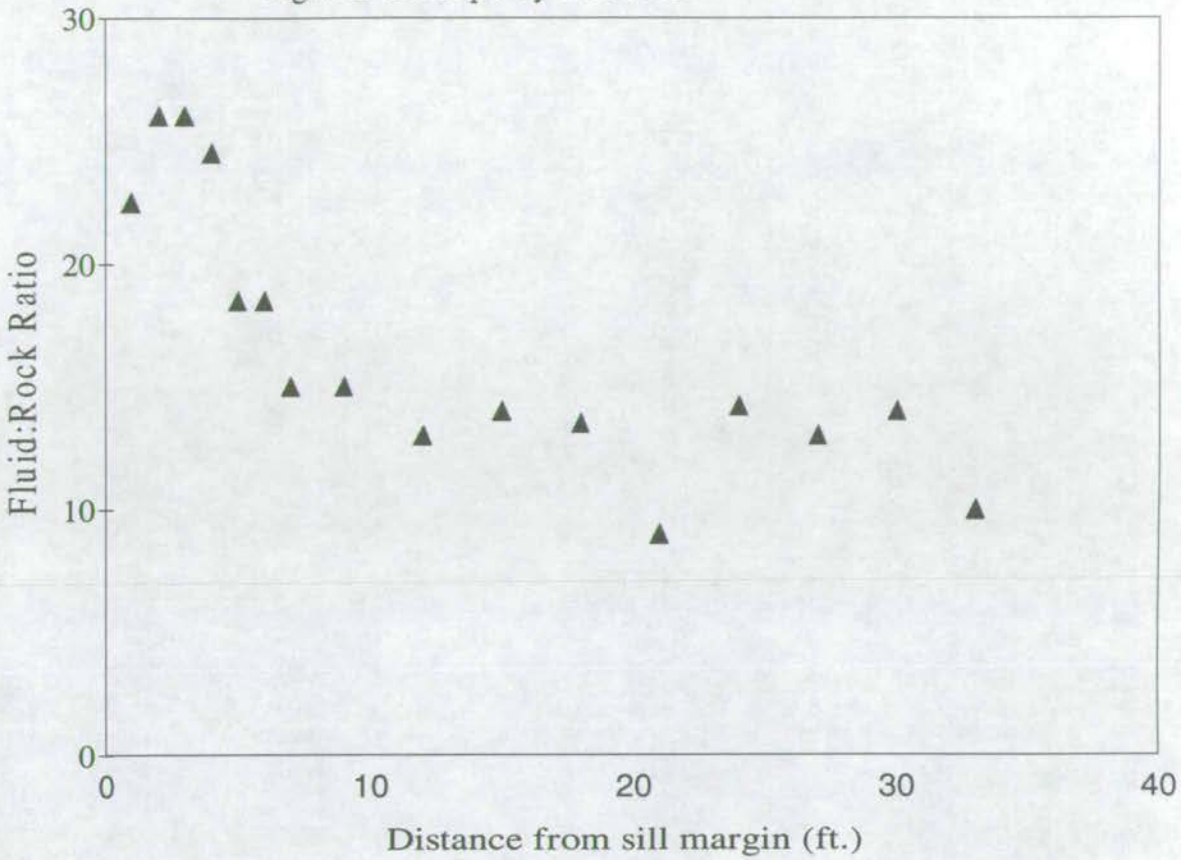

of the metabasic sill is presented in figure 10.6(a), together with modal, compositional and geochemical data (figures 10.6(b), (c) and (d), respectively). A modal profile was constructed for the well-exposed NW margin of the sill, from 17 regularly spaced mineralogical modes, estimated by counting 400-500 points per thin section.

The metabasic sill at Carsaig has undergone spilitic alteration, and is antiformally-folded. The sill consists largely of type III metabasite. Where type I metabasites are preserved they are reddish brown and dusty in appearance, which is characteristic of excessive stilpnomelane.

The modal profile (figure 10.6b) can be described by three parallel mineral assemblage zones which are analogous to the type I-III metabasite zones. The mineral assemblage of the sill margin is not atypical of the classic type III assemblage, consisting of 42-48 vol.% chlorite, 25-34 vol.% quartz and 8-12 vol.% calcite. However, the mineral assemblage of the sill interior differs considerably from the classic type I assemblage, instead consisting of 0-8 vol.% amphibole, 3-17 vol.% epidote, 10-20 vol.% chlorite, 0-2 vol.% calcite, 15-30 vol.% albite and 30-40 vol.% stilpnomelane. The type III and pseudo-type I assemblage zones are separated by a narrow zone of pseudo-type II metabasite in which 0-8 vol.% amphibole, 3-17 vol.% epidote, 30-40 vol.% stilpnomelane and about 30 vol.% albite are consumed, and 24-30 vol.% chlorite, 25-34 vol.% chlorite and 7-17 vol.% calcite are produced.

The bulk compositional profile shows minimal variation (figure 10.6(c)), the lack of which, particularly between the pseudo-type I and type III assemblages, implies that mineral reaction is isochemical. It is not possible to constrain the stoichiometry of the observed reaction because of the inherent uncertainties in defining the formula and constraining the P-T-X_{CO_2} stabilities of stilpnomelane.

Geochemical analysis of bulk-rock CO_2 content for the NW margin of the Carsaig metabasite was undertaken by Graham *et al.* 1987. Data were found to mimic the modal profile precisely (figure 10.6d).

10.4.5 Loch Stornoway (figure 10.7)

A group of metabasic sills is exposed within garnet grade phyllites and mica-schists of the Erins Quartzite Group at Loch Stornoway, Knapdale (GR731 612). An outcrop map of the westernmost metabasic sill is presented in figure 10.7(a), together with modal data in figure 10.7(b). A modal profile was constructed across the sill, from 7 strategically placed mineralogical modes, estimated by counting 400-500 points per thin section.

The metabasite is largely massive, garnetiferous amphibolite, with a narrow garnetiferous schistose (structurally) upper margin. Type I and type III assemblages may be identified from the modal profile (figure 10.7(b)). Type I assemblages are developed within the massive sill interior and contain 58-65 vol.% blue-green hornblende, 6-8 vol.% epidote, 13-16 vol.% quartz, 0.5-1.0 vol.% garnet, minimal chlorite and minimal calcite. Type III assemblages are developed within the schistose upper sill margin and contain approximately 32 vol.% chlorite, 35 vol.% quartz, 25 vol.% calcite, minimal amphibole, minimal epidote and minimal garnet. Type I and III assemblage zones are separated by an extremely narrow zone containing the type II assemblage in which 58-65 vol.% amphibole, 6-8 vol.% epidote and 0.5-1.0 vol.% garnet are consumed and about 32 vol.% chlorite, 35 vol.% quartz and 25 vol.% calcite are generated. Quantitative correlation of these volumetric modal changes with the standard modal profile of reaction 1[6] implies that progress of reaction was limited by the amount of calcite and chlorite in the rock. The remaining excess of quartz, together with non-reacting phases (e.g. albite) constitutes approximately 50% of the reactant assemblage. The role if garnet is uncertain. However, due to its low abundance, it is unlikely to be an important contributory phase.

10.4.6 Traigh Gheighsgeir (figure 10.8)

A 10m wide, sheared metabasite sill is exposed at the south end of Traigh

[6]The standard modal profile of reaction (1) is included on a reference card at the back of the thesis.

Figure 10.7(a) Loch Stornoway: Outcrop Map

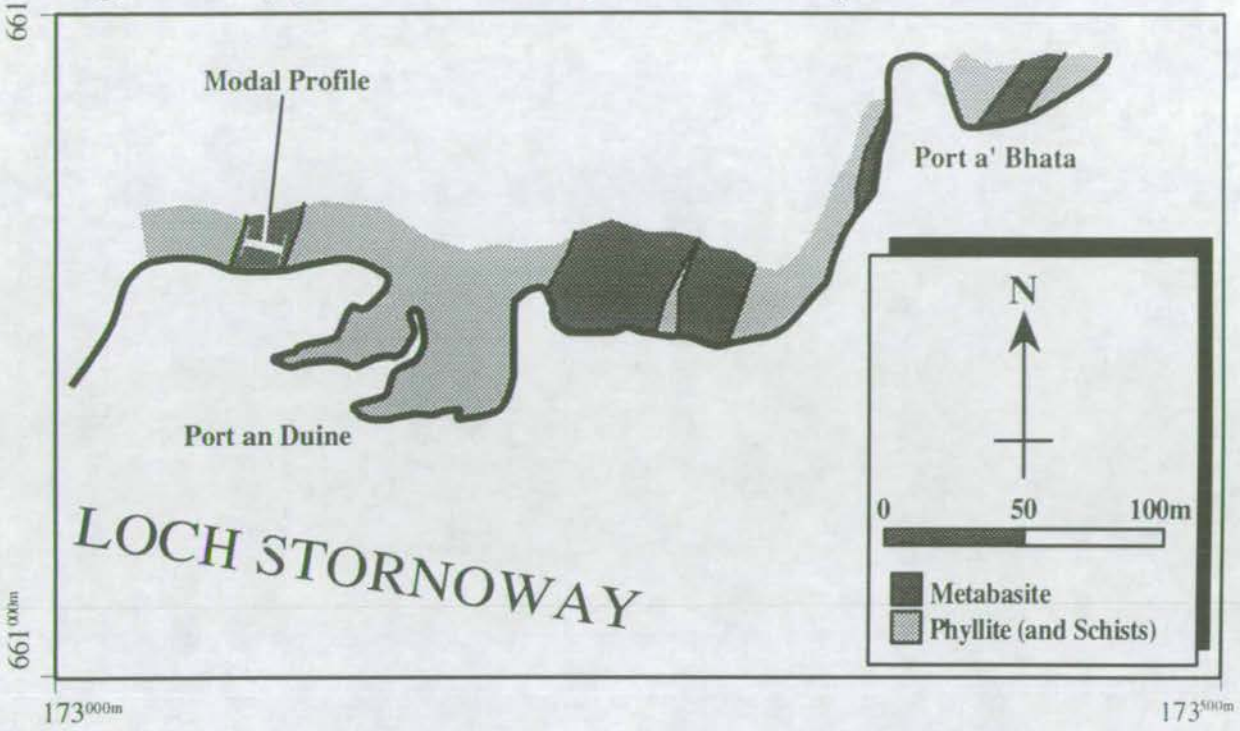

Figure 10.7(b): Loch Stornoway: Modal Profile
(showing the reaction: Am+Ep+CO2+H2O=Chl+Cc+Qz)

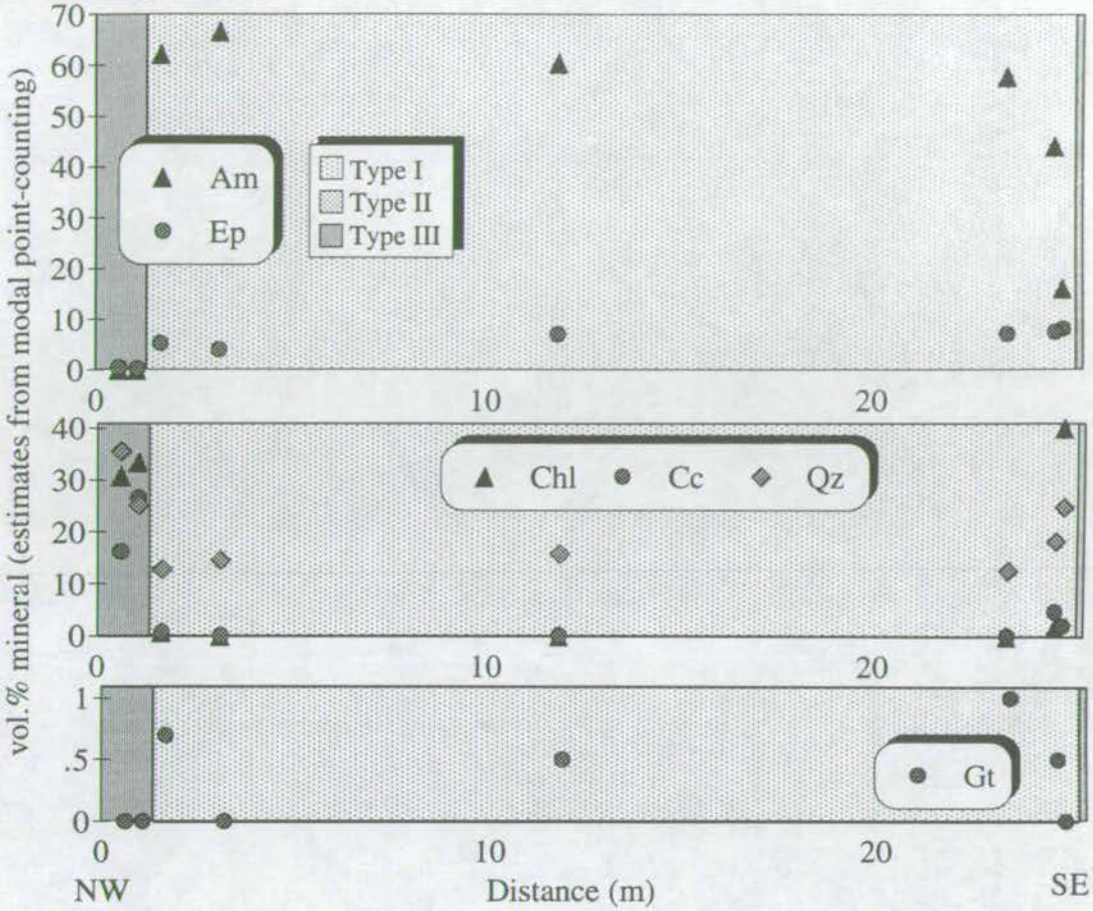

Figure 10.8(a) Traigh Gheighsgeir: Outcrop Map

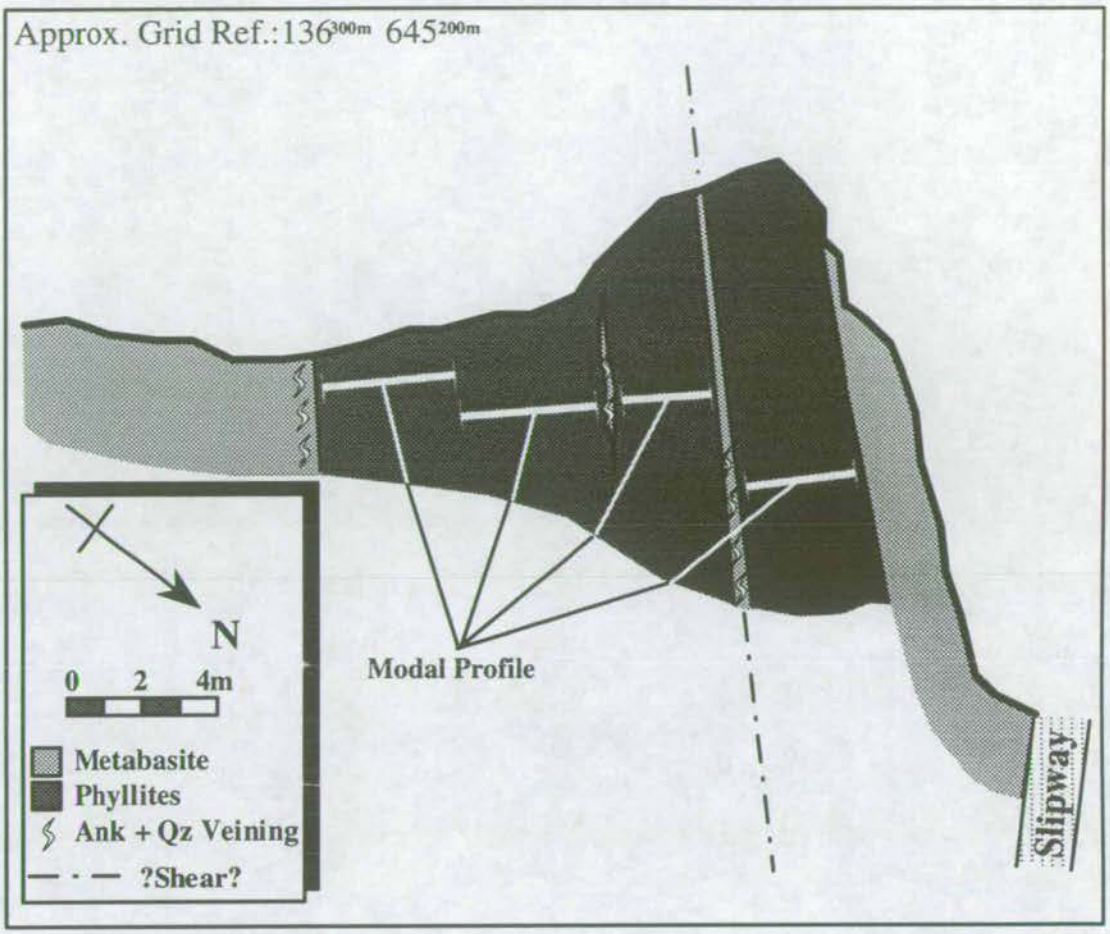

Figure 10.8(b): Traigh Gheighsgeir: Modal Profile

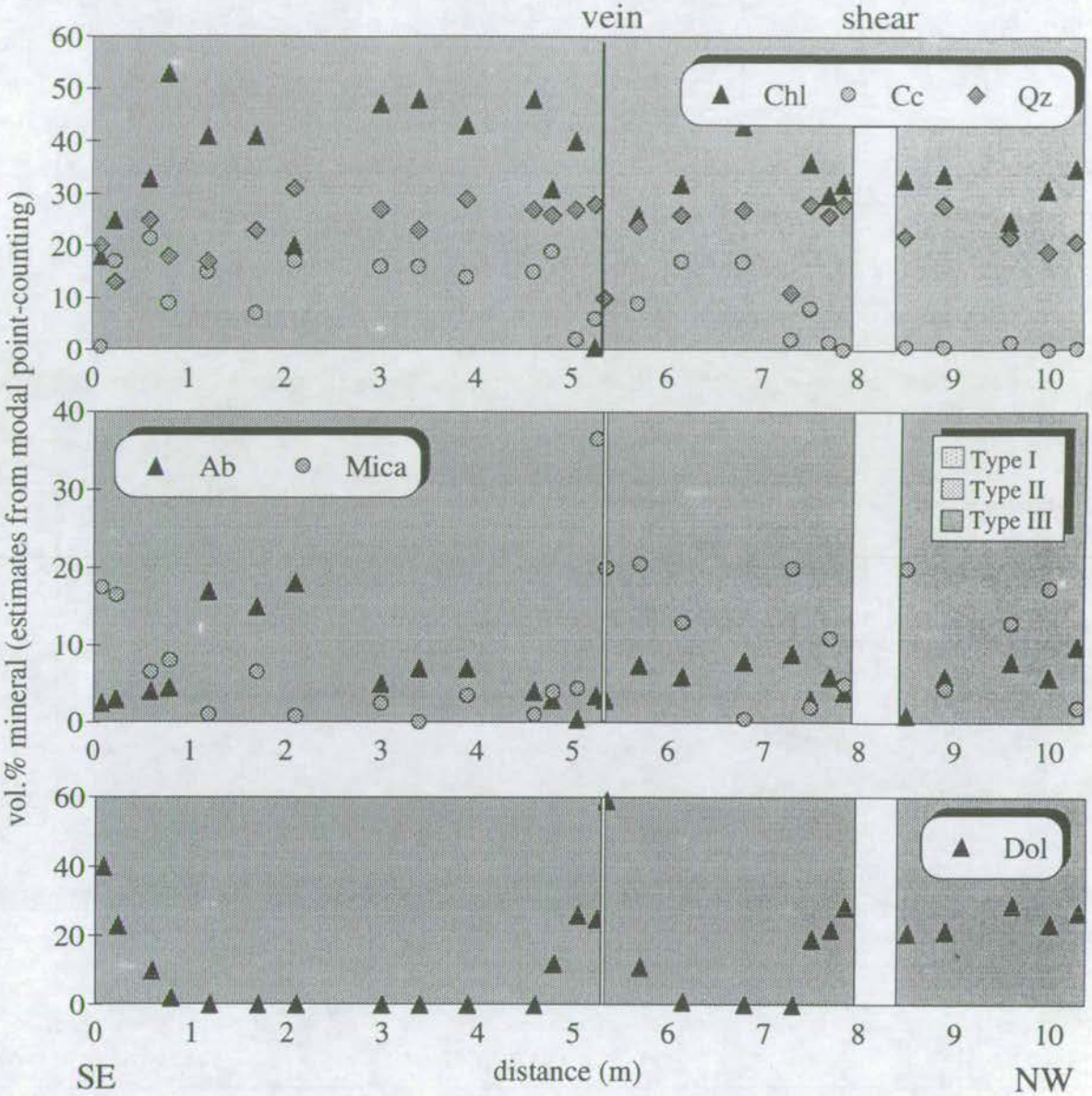

Gheighsgeir, near Port Ellen, Islay (GR363 453). Retrograde ankerite is developed. An outcrop map of the sill is presented in figure 10.8(a). A modal profile was constructed across the sill, from 26 evenly spaced mineralogical modes, estimated by counting 400-500 points per thin section (figure 10.8b).

In outcrop, the metabasic sill is intensely foliated. A 50cm wide shear-zone containing intensely deformed phyllite divides the sill into two parts. Large, rusty ankerite porphyroblasts are developed extensively throughout the sill margins. Their spatial distribution is apparently unaffected by the narrow shear zone.

A predominance of the type III assemblage is apparent from the modal profile shown in figure 10.8(b), with zonal distribution of ankeritic metabasite. The non-ankeritic type III assemblage contains, on average, 40-50 vol.% chlorite, 14-16 vol.% calcite, 25-30 vol.% quartz, 8-18 vol.% albite and 2-5 vol.% white mica (largely muscovite). The ankeritic type III assemblage contains, on average, 20-30 vol.% ankerite, 30-35 vol.% chlorite, 20-30 vol.% quartz, 5-10 vol.% albite, 5-20 vol.% white mica and minimal calcite. Growth of 20-30 vol.% ankerite is spatially associated with the growth of 5-15 vol.% white mica and the replacement of 10-20 vol.% chlorite and 10-15 vol.% calcite. The modal changes may be associated with the combined influences of reactions (4), (5) and (6)[7], but generally result from the addition of ankerite. Therefore, growth of ankerites may not be isochemical, which is consistent with their implied retrograde origin (sections 4.2.3, 5.2.5 and 5.3.7). The modal changes define distinct ankeritisation "fronts" (figure 10.8b).

10.4.7 Summary of Modal Profile Data

Essentially, modal profiles of six SW Highland metabasites record two phases of mineral reaction, both of which result in pronounced layer-parallel zonation of the mineral assemblages.

The early phase involves the advection of reaction 1 into the margins of type I metabasite sills and dykes and the subsequent development of layer-parallel

[7]Reactions (4), (5) and (6) are included in a reference card at the back of the thesis.

marginal zones of type III metabasite. The model reaction stoichiometry is best replicated by the Port Cill Maluaig metabasite. Other sills develop subtle variations of the model reaction stoichiometry as a function of differences in metamorphic grade and/or later retrograde overprinting. Reaction 1 is isochemical.

The later phase involves the development of layer-parallel ankerite-rich zones at the margins of metabasites. This is well developed at Traigh Gheighsgeir, where an original type III assemblage is over-printed by late-stage ankerite. The distribution of ankeritic zones bears no relation to structure (e.g. shear-zone at Traigh Gheighsgeir, figure 10.8). Furthermore, textural constraints, discussed in sections 4.2.3, 5.2.5 and 5.3.7 imply retrograde timing for ankerite development.

10.5 Quantification of Fluid Flow from Modal Profile Data

Modal profile data present unequivocal evidence for the progress of reaction 1[8] at the margins of sills and dykes throughout the SW Scottish Highlands. Textural evidence, discussed in section 5.3.5, predicts that reaction 1 is driven by infiltration of a CO_2-bearing hydrous fluid, the composition of which is buffered by the host phyllites, into the margins of individual metabasites.

Modal profile data further identify a pronounced asymmetry in the distribution of reactant and product mineral assemblages within metabasic dykes and sills. The asymmetry results from advection of the mineral reaction front by ***uni-directional*** fluid infiltration. It is therefore possible to constrain the direction of fluid flow in one-dimension from the observed asymmetry of the modal profile, as is discussed in section 6.3.

The advection distance ($V_f t$, equation 10.1) can be measured, and used to quantify fluid flow, by applying the one-dimensional model of Bickle & Baker (1990b). Prior to measurement of the advection distance it is essential to be able to distinguish between advective and diffusive transport of the reaction front, as is discussed in section 6.3. In general, symmetric transport may be attributed to

[8]Reaction (1) is included in a reference card at the back of the thesis.

diffusion, whereas ***additional*** asymmetric transport may be attributed to advection (section 7.3. Advection and diffusion distances are illustrated in figures 10.3 to 10.8 and listed in table 10.1.

Table 10.1: Measured advection & diffusion distances from Modal Profile Data

Metabasite	Diffusion	Advection	1-D Fluid Flow Direction *(constrained by asymmetry)*
Port Cill Maluaig	1.0m	3.6m	SE
North Jura	0.1m	1.6m	East
Clachbreac	0.5m	3.0m	SE
Carsaig	???	?9.0m?*[1]	???
Loch Stornoway	0.1m	1.5m	SE
Traigh Gheighsgeir	???	>5.2m	???

*[1] No information is available regarding the asymmetry of the Carsaig profile because the modal traverse was constructed for the NW margin ***only***. However, much of the sill is schistose and pitted in appearance and therefore the observed advection distance is probably fairly representative of the general scale of infiltration.

10.6 Comparison of the Modal and Reaction Progress Approaches to Identification of Mineral Reaction Fronts

Identification of reaction fronts and subsequent measurement of advection distances from modal profiles have proved successful. However, the analytical process was found to be extremely time-consuming and therefore prohibited the regional-scale mapping of fluid flow which is the aim of this thesis. It is therefore essential to consider the more practical alternative of identification of reaction fronts by constructing profiles of reaction progress, estimated from field measurement of the volumetric percentage of calcite in the sample, as described in section 6.4. Vol.% calcite is clearly an efficient and effective monitor of the progress of reaction 1, as progress of reaction (1) may generate as much as 35 vol.% calcite. In chapter 7, reaction progress and modal profiles were found to offer identical predictions.

10.7 Reaction Progress Profile Data

Reaction progress was estimated for some 63 metabasite sills and dykes, exposed throughout the SW Scottish Highlands. The metabasite sills and dykes are located on figure 10.9 and reaction progress data are presented in appendix 5 and discussed below.

Using this technique, ankerite-bearing metabasites may be readily identified by laboratory calibration of reaction rates with standards (figure 5.3). It is therefore possible to unambiguously and accurately locate the fronts of reaction 1 even where retrograde ankerite is developed. Advection and diffusion distances of reaction 1 were measured from the reaction progress profiles (appendix 5), in a similar fashion to that detailed above, and are presented in tables 10.2(a) and (b).

Table 10.2: Measured advection and diffusion distances from Reaction Progress Profile Data: Constrained from Progress of Reaction (1)

(a) Scarba, Islay and Jura

Metabasite	Host Rock	Diffusion	Advection	1-D Fluid Flow Direction *(constrained by asymmetry)*	Ank?
Scarba(1)	Q‖Q	???	>2.0m	???	Yes
Scarba(2)	Q‖Q	???	>0.4m	???	Yes
Scarba(3)	Q‖Q	???	>0.6m	???	No
Scarba(4)	Q‖Q	0.5m	0.5m	West	No
Scarba(5)	Q‖Q	???	>1.5m	???	No
Scarba(6)	Q‖Q	0.0m	0.2m	East	No
North Jura (1)	Q‖Q	1.2m	0.0m	N/A	No
North Jura (2)	Q‖Q	0.7m	0.3m	East	No
North Jura (3)	Q‖Q	0.7m	0.2m	East	No
North Jura (4)	Q‖Q	0.0m	0.0m	N/A	No
North Jura (5)	Q‖Q	0.0m	0.9m	East	No
Port Ellen (A.B/C)	P‖P	0.0m	0.2m	NW	No
Port Ellen (F,G,H/J)	P‖P	0.8-1.0m	0.2-0.4m	NW	No
Port Ellen (E/I)	P‖*[1]	1.0m	3.5m	NW	No
Port Ellen (D/I)	P‖P	2.4m	2.6m	NW	No
Port Ellen (K/M)	*[1]‖P	2.0m	>6.0m	SE	No
Port Ellen (N/O)	P‖P	0.2m	3.0m	SE	No
Port Ellen (Q,P/R)	P‖P	0.5m	0.2-1.0m	SE	No
Traigh Gheighsgeir	P‖P	???	>5.2m	???	Yes

(b) Knapdale

Metabasite	Host Rock	Diffusion	Advection	1-D Fluid Flow Direction *(constrained by asymmetry)*	Ank?
Island of Danna	Q‖Q	0.0m	0.25m	NW	No
Castle Sween	|QPM|	0.0m	0.4m	NW	No
Bagh an Doide (1)	Q‖Q	0.0m	0.8m	NW	No
Bagh an Doide (2)	Q‖Q	2.5m	4.5m	NW	No
Bagh an Doide (3)	Q‖Q	3.0m	0.5m	SE	No
Point of Knap (1)	Q‖Q	0.0m	0.0m	N/A	No
Point of Knap (2)	Q‖Q	0.0m	0.8m	SE	No
Point of Knap (3)	Q‖Q	0.4m	1.0m	SE	No
Point of Knap (4)	Q‖Q	1.0m	0.8m	SE	No
Point of Knap (5)	Q‖Q	0.0m	0.6m	SE	No
Stronefield, West	P‖P	0.0m	0.3m	NW	No
Stronefield, East (1)	P‖Q	???	>1.6m	???	No
Stronefield, East (2)	Q‖P	???	>1.8m	???	No
Rubha Garbh	|P|	0.8m	1.3m	???	No
Lochead	P‖P	???	>7.5m	?SE?*[2]	No
Ormsary	???‖Q	???	?0.2m?*[3]	???	No
Port Cill Maluaig (A/B,C)	P|P	0.7m	0.2-0.9m	NW	No
Port Cill Maluaig (D)	P‖P	0.7m	1.1m	SE	No
Port Cill Maluaig (E)	P‖P	1.2m	5.2m	SE	No
Rubha Cill Maluaig	P‖P	0.5m	3.5m	SE	No
Stotfield Bay (A)	P‖P	0.8m	1.8m	NW	No
Stotfield Bay (B)	P‖P	???	>5.5m	???	No
Stotfield Bay (C)	P‖P	???	>1.0m	???	No
Stotfield Bay (D)	P‖P	0.0m	0.5m	NNW	No
Stotfield Bay (E)	P‖P	0.0m	0.5m	SSE	No
Stotfield Bay (F)	P‖P	0.0m	0.3m	NNW	No
Stotfield Bay (G)	P‖P	???	>1.2m	???	No
Stotfield Bay (H)	P‖P	2.8m	0.0m	N/A	No
Stotfield Bay (I)	P‖P	???	0.8m	???	No
Stotfield Bay (J)	P‖P	0.3m	1.2m	SE	No
Cretshangen Bay (/A,B/)	|Q|	0.0m	0.2m	NW	No
Cretshangen Bay (/C.D/)	|Q|	0.0m	0.0m	N/A	No
Port Ban (1)	P‖P	3.6m	0.8m	NW	No
Port Ban (2)	P‖P	1.5m	0.2m	SE	No
Kilberry Head	P‖P	0.0m	0.4m	SE	No
Sgeir Figheadair	QP‖QP	???	>0.75m	???	Yes
Keppoch Point	P‖P	0.5m	0.9m	SE	Yes
Sgeir Maire	QP‖QP	0.0m	0.4m	SE	No
Loch Stornoway (1)	P‖P	0.0m	0.7m	NW	No
Loch Stornoway (2)	P‖P	0.3m	0.3m	SE	No
Loch Stornoway (3)	P‖P	0.2m	0.1m	NW	No
Rudha' Bharr Ruaidh	P‖P	0.2m	0.7m	NW	Yes

??? = Unknown

N/A = Not applicable

Q = Quartzite

P = Phyllite

M = Marble

| = Metabasite margin

(e.g. QP‖M = metabasite, hosted by interbedded quartzites and phyllites to the west and marble to the east, or |P| = phyllite between two metabasites)

*1 The metabasite at Port Ellen is folded and therefore bounded on the axial surface of the Port Ellen Anticline.

*2 The reaction progress profile is asymmetric and indicates a south-easterly component of the fluid flow direction.

*3 The sill at Ormsary is not entirely exposed. However its massive appearence implies that minimal advection occurred.

10.8 Quantification of Syn-metamorphic Fluid Flow

The measured advection distances of reaction 1 into metabasite margins, measured from modal profiles and reaction progress profiles, are listed above in tables 10.1 and 10.2(a) and (b), respectively. Time-integrated fluid fluxes may be constrained from measured advection distances, in one-dimension, perpendicular to the metabasite margin, by application of the reaction front advection model of Bickle & Baker (1990b), which is given by equation (10.1)[9]. The model requires knowledge of the infiltrating fluid composition ($X_{CO_2,1}$), the fluid composition buffered by reaction 1 ($X_{CO_2,2}$) and the volumetric stoichiometric coefficients of CO_2 and H_2O in reaction 1 (R_{CO_2} and R_{H_2O}, respectively), as discussed in section 10.3.2.

10.8.1 Constraint of R_{CO_2} and R_{H_2O}

R_{CO_2} and R_{H_2O}, the stoichiometric coefficients of CO_2 and H_2O, respectively, may be obtained from the volumetric stoichiometry of reaction (1). Calculated values for the pure end-members of reaction (1) are listed in table 10.3, and assumed densities and molar weights are shown in figure 6.1.

Table 10.3: R_{CO_2} and R_{H_2O} Data

Reaction	R_{CO_2}	R_{H_2O}
(1,Mg) $3Tr+2Cz+10CO_2+8H_2O=3Clin+10Cc+21Qz$	-0.30	-0.13
(1.Fe) $3Ftr+2Cz+10CO_2+8H_2O=3Daph+10Cc+21Qz$	-0.31	-0.14

Volumetric stoichiometric data is normalised to 1cc reactant minerals (figure 6.1).

[9]Equation (9.1), the reaction front advection model, is included in a reference card at the back of the thesis.

Figure 10.9: Location Maps of Reaction Progress and Modal Profiles

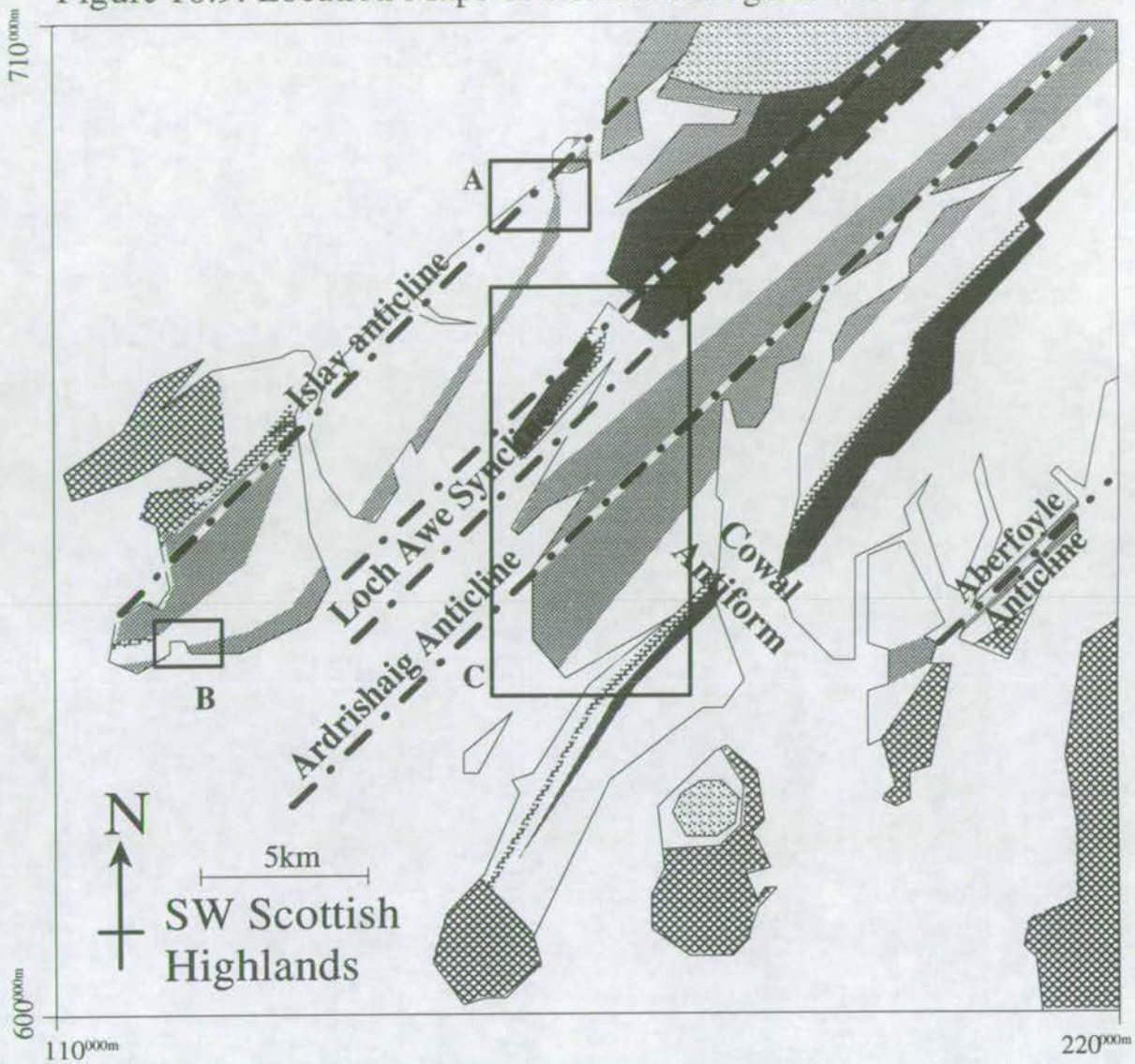

Phyllite
Quartzite
Volcanics
Marble
Other Metamorphic and sedimentary rocks
Other Igneous Rocks

A: Gulf of Corryvreckan
B: Port Ellen
C: Knapdale

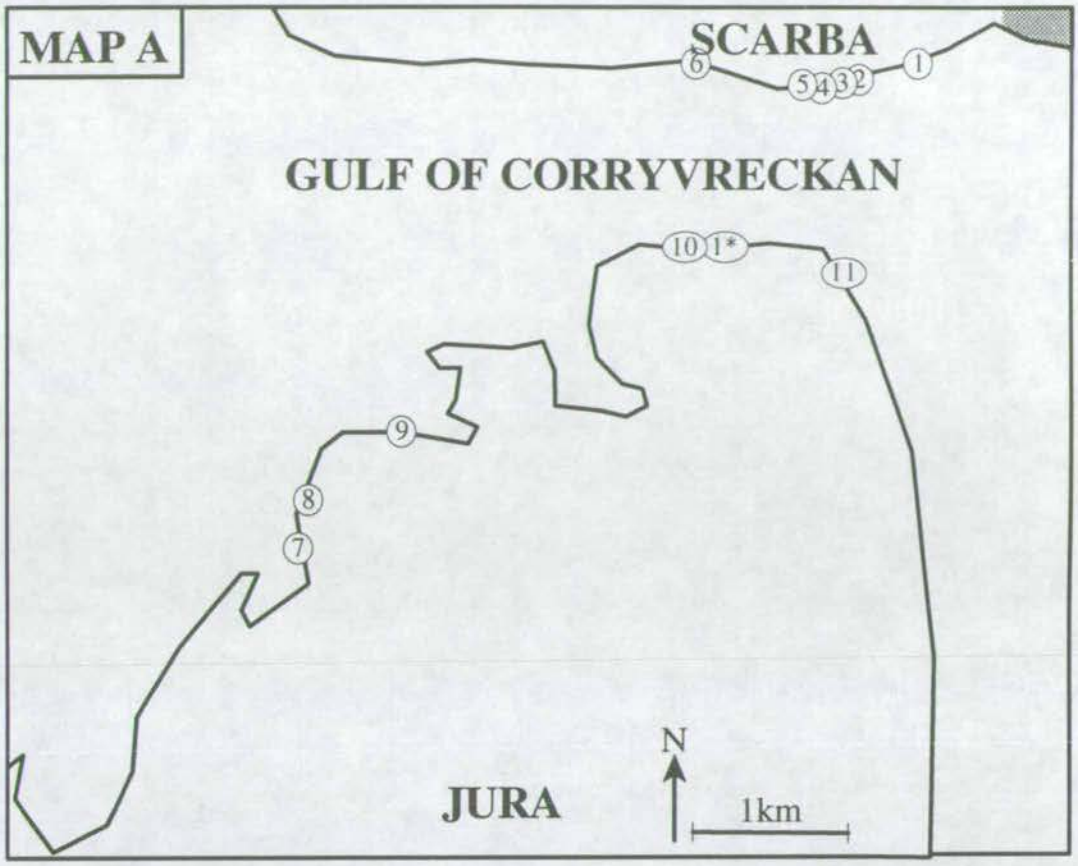

Reaction Progress Profiles
1-6 = Scarba(1-6)
7-11 = North Jura (1-5)

Modal Profile
1* = North Jura

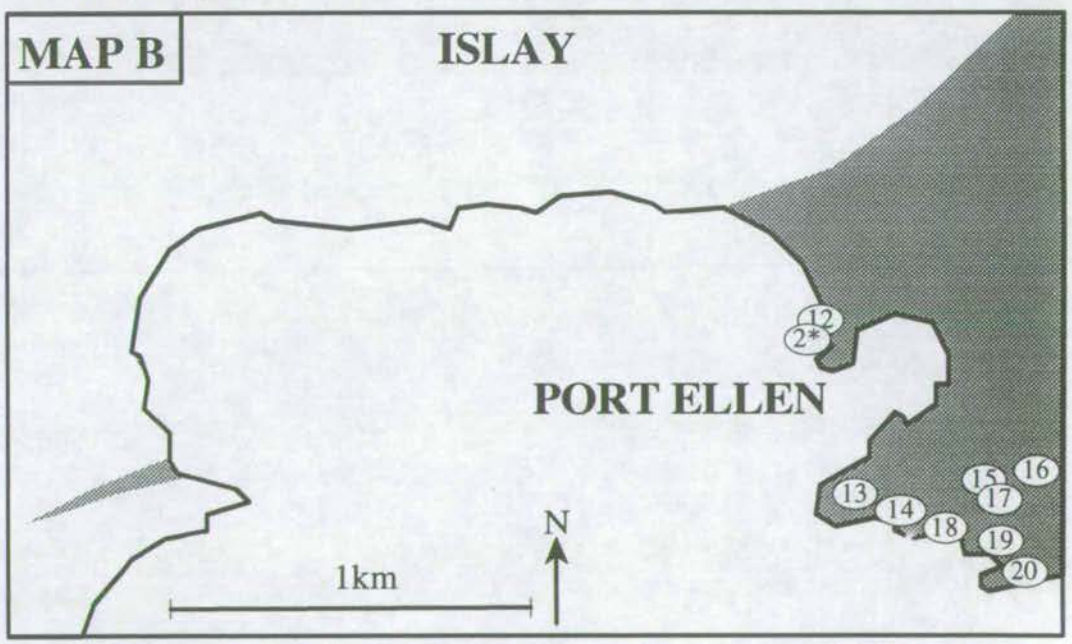

Reaction Progress Profiles
12 = Traigh Gheighsgeir (1-2)
13 = Port Ellen (A,B/C)
14 = Port Ellen (F-H/J)
15 = Port Ellen (E/I)
16 = Port Ellen (D/L)
17= Port Ellen (K/M)
18 = Port Ellen (extra)
19 = Port Ellen (N/O)
20 = Port Ellen (Q,P/R)

Modal Profile
2* = Traigh Gheighsgeir

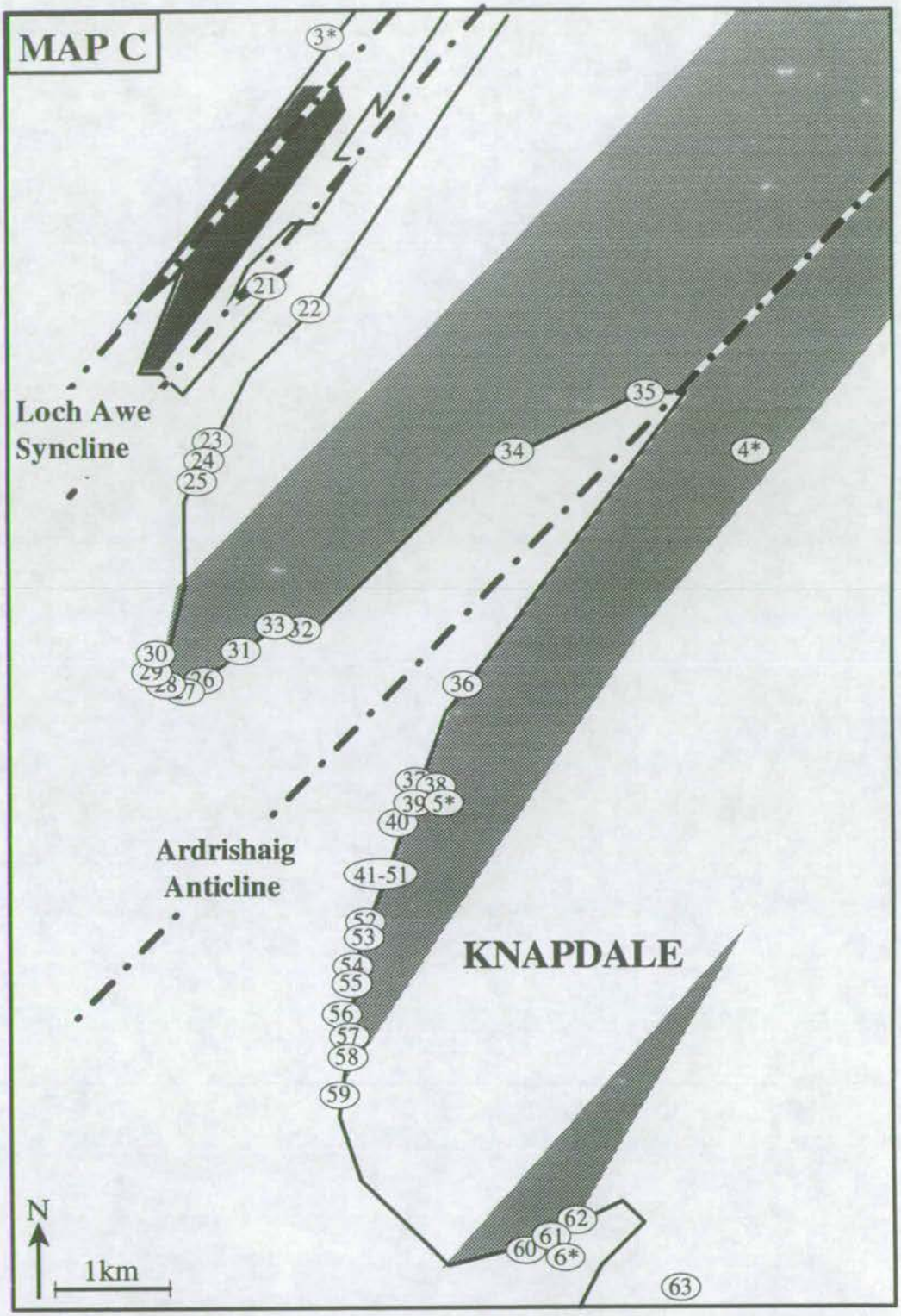

Reaction Progress Profiles

21 = Island of Danna
22 = Castle Sween
23-25 = Bagh an Doide (1-3)
26-30 = Point of Knap (1-5)
31 = Stronefield Bay, West
32-33 = Stronefield Bay, East (1-2)
34 = Rubha Garbh
35 = Lochead
36 = Ormsary
37 = Port Cill Maluaig (A/B,C)
38 = Port Cill Maluaig (D)
39 = Port Cill Maluaig (E)
40 = Rubha Cill Maluaig
41-51 = Stotfield Bay (A-J)
52-53 = Cretshangen Bay (A,B-C,D)
54-55 = Port Ban (1-2)
56 = Kilberry Head
57-58 = Keppoch Point
59 = Sgeir Maire
60-62 = Loch Stornoway (1-3)
63 = Rudha' Bharr Ruaidh

Modal Profiles

3* = Carsaig
4* = Clachbreac
5* = Port Cill Maluaig
6* = Loch Stornoway

The average ratios; tr:ftr and clin:daph are 4:6 and 7:3 respectively (from electron microprobe data from SW Highland amphiboles shown in appendix 7). **Therefore R_{CO_2} is best approximated as -0.306 and R_{H_2O} is best approximated as -0.133.**

10.8.2 Constraint of $X_{CO_2,1}$ and $X_{CO_2,2}$

$X_{CO_2,1}$ and $X_{CO_2,2}$, the upstream and downstream fluid compositions, respectively, were constrained from the appropriate isobaric T-X_{CO2} sections calculated at 10kb (section 4.3.4). $X_{CO_2,2}$ was simply read from the P-T-X_{CO_2} stability curve of reaction (1) at the appropriate temperature (figure 10.1). $X_{CO_2,1}$ is assumed to be in equilibrium with the predominant host phyllite assemblage, which includes the assemblage biotite + albite + rutile + chlorite + calcite + quartz and therefore constrains $X_{CO_2,1}$ to a narrow range in P-T-X_{CO_2} space (figure 10.1). Estimated values of $X_{CO_2,1}$ and $X_{CO_2,2}$ are listed in tables 10.4(a) and (b).

Table 10.4: Estimated Values of T, $X_{CO_2,1}$ and $X_{CO_2,2}$, assuming P=10kb

(a) Scarba, Islay and Jura

Metabasite	Profile	T(°C)*[1]	$X_{CO_2,1}$ Range	$X_{CO_2,2}$
Scarba(1)	Vol.%Cc	500	0.0258-0.0262	0.0173
Scarba(2)	Vol.%Cc	500	0.0258-0.0262	0.0173
Scarba(3)	Vol.%Cc	500	0.0258-0.0262	0.0173
Scarba(4)	Vol.%Cc	500	0.0258-0.0262	0.0173
Scarba(5)	Vol.%Cc	500	0.0258-0.0262	0.0173
Scarba(6)	Vol.%Cc	500	0.0258-0.0262	0.0173
North Jura (1)	Vol.%Cc	500	0.0258-0.0262	0.0173
North Jura (2)	Vol.%Cc	500	0.0258-0.0262	0.0173
North Jura (3)	Vol.%Cc	500	0.0258-0.0262	0.0173
North Jura (4)	Vol.%Cc	500	0.0258-0.0262	0.0173
North Jura (5)	Vol.%Cc	500	0.0258-0.0262	0.0173
North Jura	Modal	500	0.0258-0.0262	0.0173
Port Ellen (A.B/C)	Vol.%Cc	470	0.0150-0.0156	0.0086
Port Ellen (F,G,H/J)	Vol.%Cc	470	0.0150-0.0156	0.0086
Port Ellen (E/I)	Vol.%Cc	470	0.0150-0.0156	0.0086
Port Ellen (D/L)	Vol.%Cc	470	0.0150-0.0156	0.0086
Port Ellen (K/M)	Vol.%Cc	470	0.0150-0.0156	0.0086
Port Ellen (N/O)	Vol.%Cc	470	0.0150-0.0156	0.0086
Port Ellen (Q,P/R)	Vol.%Cc	470	0.0150-0.0156	0.0086
Traigh Gheighsgeir	Vol.%Cc	470	0.0150-0.0156	0.0086
Traigh Gheighsgeir	Modal	470	0.0150-0.0156	0.0086

(b) Knapdale

Metabasite	Profile	T(°C)*[1]	$X_{CO_2,1}$ Range	$X_{CO_2,2}$
Carsaig	Modal	410	0.0046-0.0050	0.0016
Island of Danna	Vol.%Cc	440	0.0086-0.0091	0.0040
Castle Sween	Vol.%Cc	440	0.0086-0.0091	0.0040
Bagh an Doide (1)	Vol.%Cc	440	0.0086-0.0091	0.0040
Bagh an Doide (2)	Vol.%Cc	440	0.0086-0.0091	0.0040
Bagh an Doide (3)	Vol.%Cc	440	0.0086-0.0091	0.0040
Point of Knap (1)	Vol.%Cc	470	0.0150-0.0156	0.0086
Point of Knap (2)	Vol.%Cc	470	0.0150-0.0156	0.0086
Point of Knap (3)	Vol.%Cc	470	0.0150-0.0156	0.0086
Point of Knap (4)	Vol.%Cc	470	0.0150-0.0156	0.0086
Point of Knap (5)	Vol.%Cc	470	0.0150-0.0156	0.0086
Stronefield, West	Vol.%Cc	470	0.0150-0.0156	0.0086
Stronefield, East (1)	Vol.%Cc	470	0.0150-0.0156	0.0086
Stronefield, East (2)	Vol.%Cc	470	0.0150-0.0156	0.0086
Rubha Garbh	Vol.%Cc	470	0.0150-0.0156	0.0086
Lochead	Vol.%Cc	470	0.0150-0.0156	0.0086
Calchbreac	Modal	500	0.0258-0.0262	0.0173
Ormsary	Vol.%Cc	470	0.0150-0.0156	0.0086
Port Cill Maluaig (A/B,C)	Vol.%Cc	470	0.0150-0.0156	0.0086
Port Cill Maluaig (D)	Vol.%Cc	470	0.0150-0.0156	0.0086
Port Cill Maluaig (E)	Vol.%Cc	470	0.0150-0.0156	0.0086
Port Cill Maluaig	Modal	470	0.0150-0.0156	0.0086
Rubha Cill Maluaig	Vol.%Cc	470	0.0150-0.0156	0.0086
Stotfield Bay (A)	Vol.%Cc	470	0.0150-0.0156	0.0086
Stotfield Bay (B)	Vol.%Cc	470	0.0150-0.0156	0.0086
Stotfield Bay (C)	Vol.%Cc	470	0.0150-0.0156	0.0086
Stotfield Bay (D)	Vol.%Cc	470	0.0150-0.0156	0.0086
Stotfield Bay (E)	Vol.%Cc	470	0.0150-0.0156	0.0086
Stotfield Bay (F)	Vol.%Cc	470	0.0150-0.0156	0.0086
Stotfield Bay (G)	Vol.%Cc	470	0.0150-0.0156	0.0086
Stotfield Bay (H)	Vol.%Cc	470	0.0150-0.0156	0.0086
Stotfield Bay (I)	Vol.%Cc	470	0.0150-0.0156	0.0086
Stotfield Bay (J)	Vol.%Cc	470	0.0150-0.0156	0.0086
Cretshangen Bay (/A,B/)	Vol.%Cc	470	0.0150-0.0156	0.0086
Cretshangen Bay (/C.D/)	Vol.%Cc	470	0.0150-0.0156	0.0086
Port Ban (1)	Vol.%Cc	470	0.0150-0.0156	0.0086
Port Ban (2)	Vol.%Cc	470	0.0150-0.0156	0.0086
Kilberry Head	Vol.%Cc	470	0.0150-0.0156	0.0086
Sgeir Figheadair	Vol.%Cc	470	0.0150-0.0156	0.0086
Keppoch Point	Vol.%Cc	470	0.0150-0.0156	0.0086
Sgeir Maire	Vol.%Cc	500	0.0258-0.0262	0.0173
Loch Stornoway (1)	Vol.%Cc	500	0.0258-0.0262	0.0173
Loch Stornoway (2)	Vol.%Cc	500	0.0258-0.0262	0.0173
Loch Stornoway (3)	Vol.%Cc	500	0.0258-0.0262	0.0173
Loch Stornoway	Modal	500	0.0258-0.0262	0.0173
Rudha' Bharr Ruaidh	Vol.%Cc	500	0.0258-0.0262	0.0173

*[1] Temperature is estimated from figure 3.8, to the nearest 30°C

10.8.3 Calculation of Time-integrated Fluid Fluxes

One-dimensional time-integrated fluid flux ($\omega_1\varphi_1 t$, equation 10.1) vectors have been calculated using the reaction front advection model of Bickle & Baker (1990b) (equation 10.1)[10], from the $V_f t$, R_{CO_2}, R_{H_2O}, $X_{CO_2,1}$ and $X_{CO_2,2}$ data presented above, in tables 10.2 to 10.5. Resultant time-integrated fluid fluxes and relevant calculation details are listed in tables 10.5(a) and (b). Calculated time-integrated fluid flux vectors have been compiled and presented on regional fluid flux maps in figure 10.10.

Table 10.5: Calculation of One-dimensional Time-integrated Fluid Flux Vectors

(a) Scarba, Islay and Jura

Metabasite	$X_{CO_2,1}$ Range	$X_{CO_2,2}$	Advection	Flow Dir^n	$\omega\varphi t$
Scarba(1)	0.0258-0.0262	0.0173	>2.0m	???	67.1m^3/m^2
Scarba(2)	0.0258-0.0262	0.0173	>0.4m	???	>13.4m^3/m^2
Scarba(3)	0.0258-0.0262	0.0173	>0.6m	???	>20.1m^3/m^2
Scarba(4)	0.0258-0.0262	0.0173	0.5m	West	16.8-17.6m^3/m^2
Scarba(5)	0.0258-0.0262	0.0173	>1.5m	???	>50.3m^3/m^2
Scarba(6)	0.0258-0.0262	0.0173	0.2m	East	6.7-7.0m^3/m^2
North Jura (1)	0.0258-0.0262	0.0173	0.0m	N/A	0.0m^3/m^2
North Jura (2)	0.0258-0.0262	0.0173	0.3m	East	10.1-10.5m^3/m^2
North Jura (3)	0.0258-0.0262	0.0173	0.2m	East	6.7-7.0m^3/m^2
North Jura (4)	0.0258-0.0262	0.0173	0.0m	N/A	0.0m^3/m^2
North Jura (5)	0.0258-0.0262	0.0173	0.9m	East	30.2-31.6m^3/m^2
North Jura	0.0258-0.0262	0.0173	0.6m	East	53.6-56.2m^3/m^2
Port Ellen (A.B/C)	0.0150-0.0156	0.0086	0.2m	NW	8.6-9.4m^3/m^2
Port Ellen (F,G,H/J)	0.0150-0.0156	0.0086	0.2-0.4m	NW	8.6-18.9m^3/m^2
Port Ellen (E/I)	0.0150-0.0156	0.0086	3.5m	NW	151-165m^3/m^2
Port Ellen (D/L)	0.0150-0.0156	0.0086	2.6m	NW	112-123m^3/m^2
Port Ellen (K/M)	0.0150-0.0156	0.0086	>6.0m	SE	>259m^3/m^2
Port Ellen (N/O)	0.0150-0.0156	0.0086	3.0m	SE	130-142m^3/m^2
Port Ellen (P,Q/R)	0.0150-0.0156	0.0086	0.2-1.0m	SE	8.6-47.2m^3/m^2
Traigh Gheighsgeir	0.0150-0.0156	0.0086	>5.2m	???	>225m^3/m^2
Traigh Gheighsgeir	0.0150-0.0156	0.0086	>5.2m	???	>225m^3/m^2

[10]Equation (9.1), the reaction front advection model, is included in a reference card at the back of the thesis.

(b) Knapdale

Metabasite	$X_{CO_2,1}$ Range	$X_{CO_2,2}$	Advection	Flow Dir[n]	$\omega\varphi t$
Carsaig	0.0046-0.0050	0.0016	?9.5m?	???	?808-916?m^3/m^2
Island of Danna	0.0086-0.0091	0.0040	0.25m	NW	14.9-16.5m^3/m^2
Castle Sween	0.0086-0.0091	0.0040	0.4m	NW	23.9-26.5m^3/m^2
Bagh an Doide (1)	0.0086-0.0091	0.0040	0.8m	NW	47.7-52.9m^3/m^2
Bagh an Doide (2)	0.0086-0.0091	0.0040	4.5m	NW	269-298m^3/m^2
Bagh an Doide (3)	0.0086-0.0091	0.0040	0.5m	SE	29.8-33.1m^3/m^2
Point of Knap (1)	0.0150-0.0156	0.0086	0.0m	N/A	0.0m^3/m^2
Point of Knap (2)	0.0150-0.0156	0.0086	0.8m	SE	34.5-37.8m^3/m^2
Point of Knap (3)	0.0150-0.0156	0.0086	1.0m	SE	43.2-47.2m^3/m^2
Point of Knap (4)	0.0150-0.0156	0.0086	0.8m	SE	34.5-37.8m^3/m^2
Point of Knap (5)	0.0150-0.0156	0.0086	0.6m	SE	25.9-28.3m^3/m^2
Stronefield, West	0.0150-0.0156	0.0086	0.3m	NW	13.0-14.2m^3/m^2
Stronefield, East (1)	0.0150-0.0156	0.0086	>1.6m	???	>69.1m^3/m^2
Stronefield, East (2)	0.0150-0.0156	0.0086	>1.8m	???	>77.7m^3/m^2
Rubha Garbh	0.0150-0.0156	0.0086	1.3m	???	56.1-61.4m^3/m^2
Lochead	0.0150-0.0156	0.0086	>7.5m	SE	>324m^3/m^2
Calchbreac	0.0258-0.0262	0.0173	3.0m	SE	101-105m^3/m^2
Ormsary	0.0150-0.0156	0.0086	0.2m	???	8.6-9.4m^3/m^2
Port Cill Maluaig (A/B,C)	0.0150-0.0156	0.0086	0.2-0.9m	NW	8.6-9.4m^3/m^2
Port Cill Maluaig (D)	0.0150-0.0156	0.0086	1.1m	SE	38.9-42.5m^3/m^2
Port Cill Maluaig (E)	0.0150-0.0156	0.0086	5.2m	SE	47.5-51.9m^3/m^2
Port Cill Maluaig	0.0150-0.0156	0.0086	3.6m	SE	225-246m^3/m^2
Rubha Cill Maluaig	0.0150-0.0156	0.0086	3.5m	SE	155-170m^3/m^2
Stotfield Bay (A)	0.0150-0.0156	0.0086	1.8m	NW	77.7-85.0m^3/m^2
Stotfield Bay (B)	0.0150-0.0156	0.0086	>5.5m	???	>238m^3/m^2
Stotfield Bay (C)	0.0150-0.0156	0.0086	>1.0m	???	>43.2m^3/m^2
Stotfield Bay (D)	0.0150-0.0156	0.0086	0.5m	NNW	21.6-23.6m^3/m^2
Stotfield Bay (E)	0.0150-0.0156	0.0086	0.5m	SSE	21.6-23.6m^3/m^2
Stotfield Bay (F)	0.0150-0.0156	0.0086	0.3m	NNW	13.0-14.2m^3/m^2
Stotfield Bay (G)	0.0150-0.0156	0.0086	>1.2m	???	>51.8m^3/m^2
Stotfield Bay (H)	0.0150-0.0156	0.0086	0.0m	N/A	0.0m^3/m^2
Stotfield Bay (I)	0.0150-0.0156	0.0086	0.8m	???	34.5-37.8m^3/m^2
Stotfield Bay (J)	0.0150-0.0156	0.0086	1.2m	SE	51.8-56.7m^3/m^2
Cretshangen Bay (/A,B/)	0.0150-0.0156	0.0086	0.2m	NW	8.6-9.4m^3/m^2
Cretshangen Bay (/C.D/)	0.0150-0.0156	0.0086	0.0m	N/A	0.0m^3/m^2
Port Ban (1)	0.0150-0.0156	0.0086	0.8m	NW	34.5-37.8m^3/m^2
Port Ban (2)	0.0150-0.0156	0.0086	0.2m	SE	8.6-9.4m^3/m^2
Kilberry Head	0.0150-0.0156	0.0086	0.4m	SE	17.3-18.9m^3/m^2
Sgeir Figheadair	0.0150-0.0156	0.0086	>0.75m	???	>32.4m^3/m^2
Keppoch Point	0.0150-0.0156	0.0086	0.9m	SE	38.9-42.5m^3/m^2
Sgeir Maire	0.0258-0.0262	0.0173	0.4m	SE	13.4-14.0m^3/m^2
Loch Stornoway (1)	0.0258-0.0262	0.0173	0.7m	NW	23.5-24.6m^3/m^2
Loch Stornoway (2)	0.0258-0.0262	0.0173	0.3m	SE	10.1-10.5m^3/m^2
Loch Stornoway (3)	0.0258-0.0262	0.0173	0.1m	NW	3.4-3.5m^3/m^2
Loch Stornoway	0.0258-0.0262	0.0173	1.5m	SE	50.3-52.7m^3/m^2
Rudha' Bharr Ruaidh	0.0258-0.0262	0.0173	0.7m	NW	23.5-24.6m^3/m^2

Figure 10.10(a): Regional Time Integrated Fluid Flux Maps

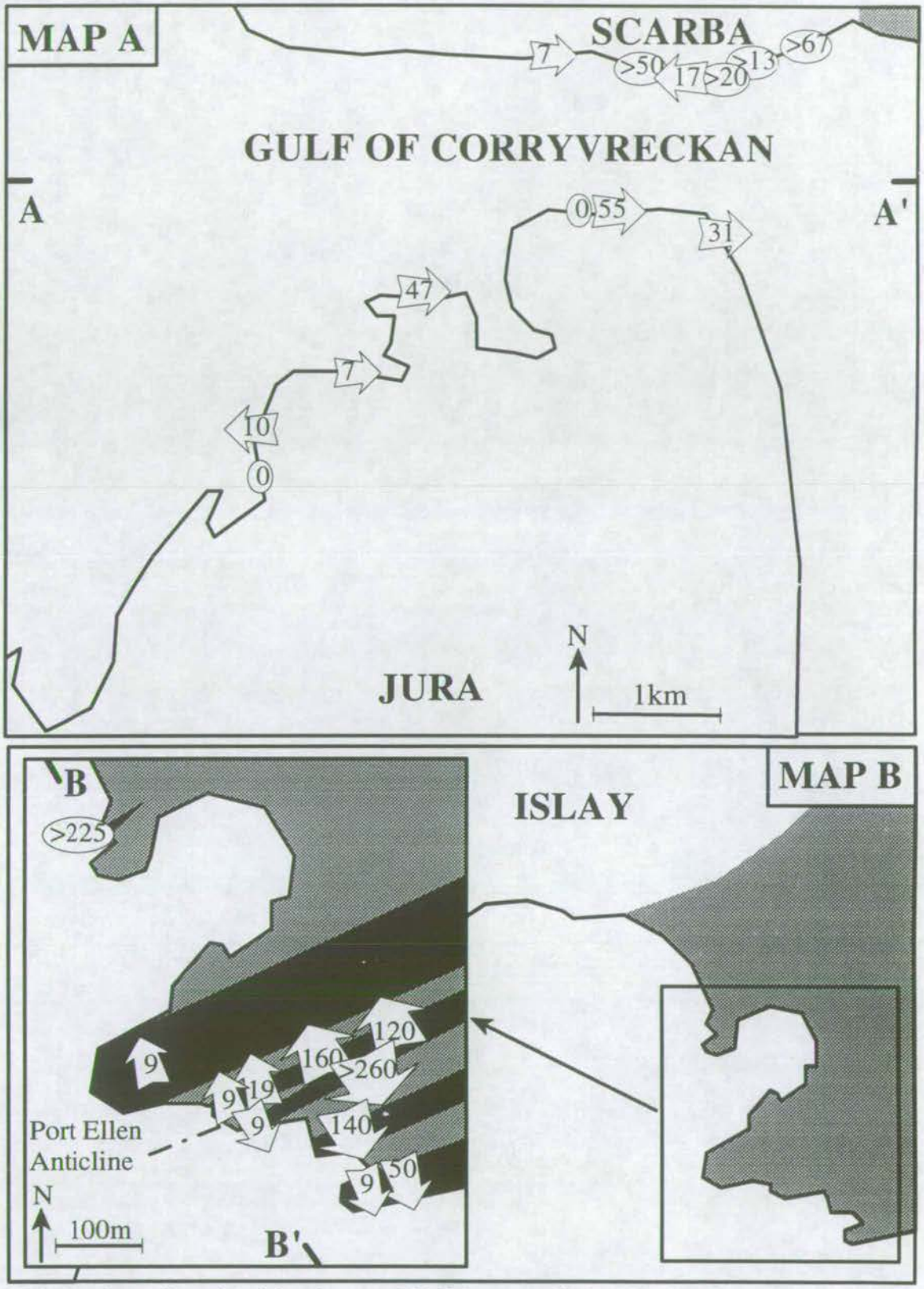

Calculated one-dimensional time-integrated fluid fluxes are displayed in the above maps. Arrows indicate the magnitude and direction of the component of flow ***perpendicular to the metabasite margin***. They do not, therefore, describe the component of flow which is parallel to the metabasite. A, A', B and B' locate cross-sections A-A' and B-B' which are presented in figure 10.10(b).
Sample localities and ornamentation are described in figure 10.9.

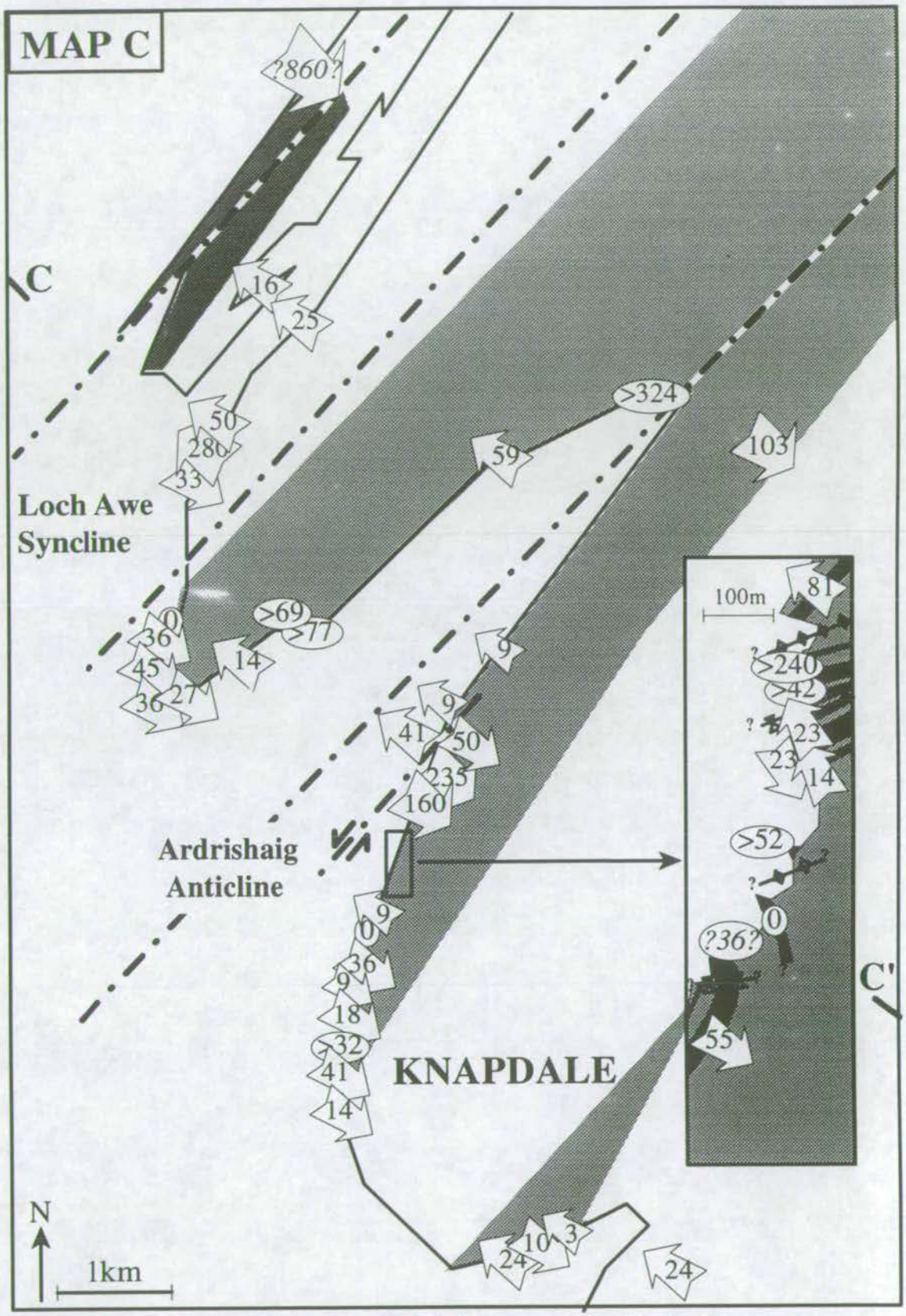

Calculated one-dimensional time-integrated fluid fluxes are displayed in the above map. Arrows indicate the magnitude and direction of the component of flow ***perpendicular to the metabasite margin***. They do not, therefore, describe the component of flow which is parallel to the metabasite. C and C' locate cross-section C-C' which is presented in figure 10.10(b). Sample localities and ornamentation are described in figure 10.9.

Figure 10.10(b): Regional Time Integrated Fluid Flux Cross-sections

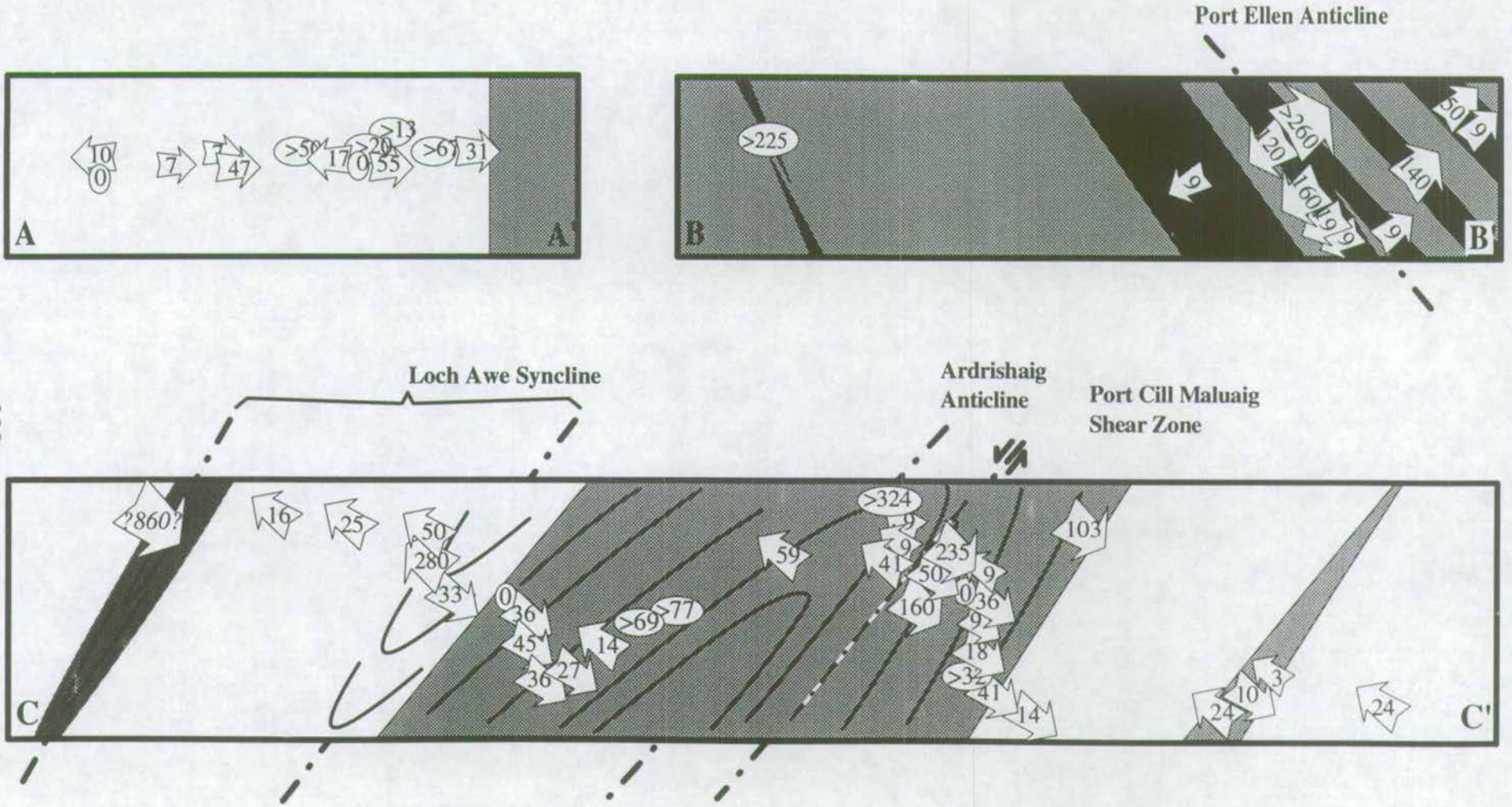

Sections are located in figure 10.10(a), sample localities and ornamentation are described in figure 10.9.

10.8.4 Errors in Calculation of Time-integrated Fluid Flux

If meaningful quantitative interpretation is to be based on the above time-integrated fluid flux estimates it is essential that the magnitude of the major sources of error are evaluated.

The stoichiometry and P-T-X_{CO_2} phase relations of reaction 1 are well-constrained. Furthermore the composition of the infiltrating fluid is well constrained by the buffering assemblages: rutile + calcite + quartz and biotite + chlorite + calcite and/or albite + chlorite + calcite. However, significant error in pressure and temperature estimates for metamorphism of the Dalradian of the SW Scottish Highlands is inevitable (section 4.3.4).

As a result of the restricted greenschist facies mineral assemblage of the SW Highlands, pressure could only be constrained, in a few localities, using the phengite geobarometer (appendix 1). Pressure was estimated at 10±2kb. The dataset was too limited to reliably describe variation in pressure across the SW Highlands.

Temperatures were essentially better constrained using both conventional geothermometry and THERMOCALC (Powell & Holland 1988). THERMOCALC calculates errors in predicted temperatures between of ±15°C and ±47°C (figure A2.8, appendix 2). Fe-Mg-Calcite (Powell *et al.* 1984), Calcite-dolomite (Powell *et al.* 1984) and Calcite-dolomite-ferrodolomite (Annovitz & Essene 1987) geothermometry predicts a range of temperatures for each locality most of which describe an error of about ±30°C (figures A2.2-A2.4, appendix 2). Garnet-hornblende (Graham & Powell 1984) and garnet-biotite (Hodges & Spear 1982) geothermometry predicts a narrower range of temperatures the majority of which describe errors of about ±20°C (figure A2.9, appendix 2).

In this section, the variation of time-integrated fluid flux as a function of pressure and temperature will be evaluated to enable quantification of the error in predicted time-integrated fluid fluxes estimated to arise from poor pressure and temperature constraints.

Figure 10.11 Variation of Calculated Time Integrated Fluid Flux as a function of Pressure and Temperature

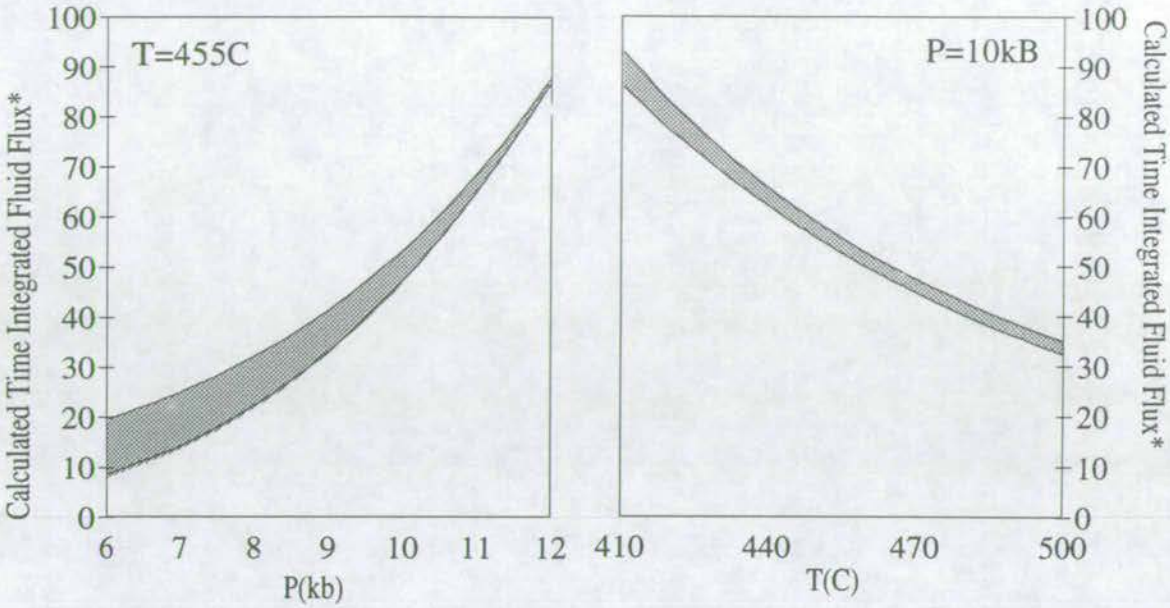

*Time-integrated fluid flux is calculated assuming advection of reaction (1) a distance of 1m by an infiltrating fluid, the composition of which is buffered by reactions (3), (4) and (5), as described in the text.
A range of time-integrated fluid fluxes are predicted at each pressure and temperature as a result of the range of possible infiltrating fluid compositions, as is discussed in the text.
The P-T-X(CO2) stabilities of reactions (1), (3), (4) and (5) are expressed in the adjoining P-X(CO2) and T-X(CO2) sections.

Temperature-X(CO2) Section calculated at P=10kb showing the stability of reaction (1) and the calc-phyllite assemblage: Bi+Ab+Ru+Chl+Cc+Qz

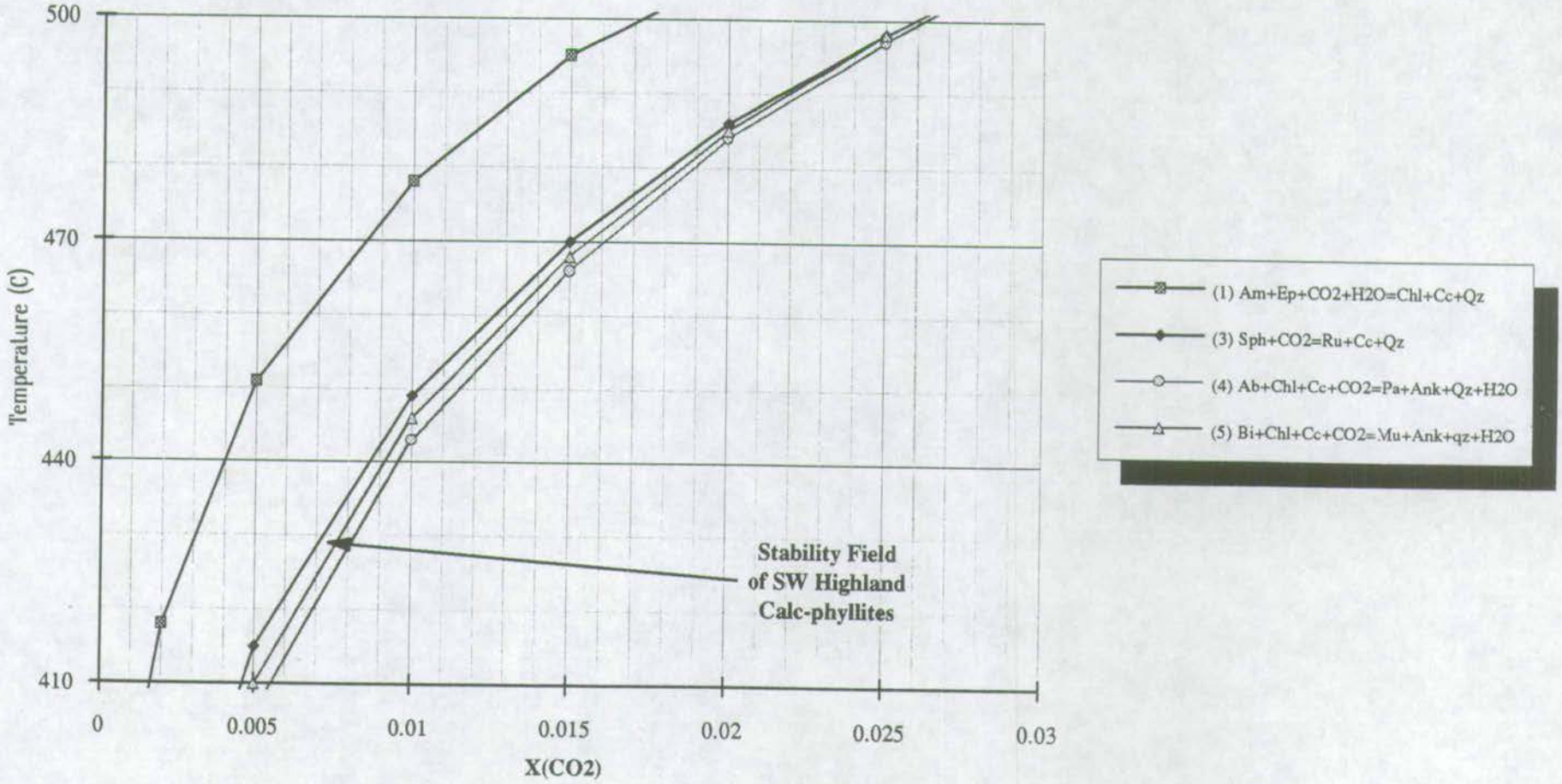

Pressure-X(CO2) Section calculated at T=455C showing the stabilities of reaction (1) and the calc-phyllite assemblage: Bi+Ab+Ru+Chl+Cc+Qz

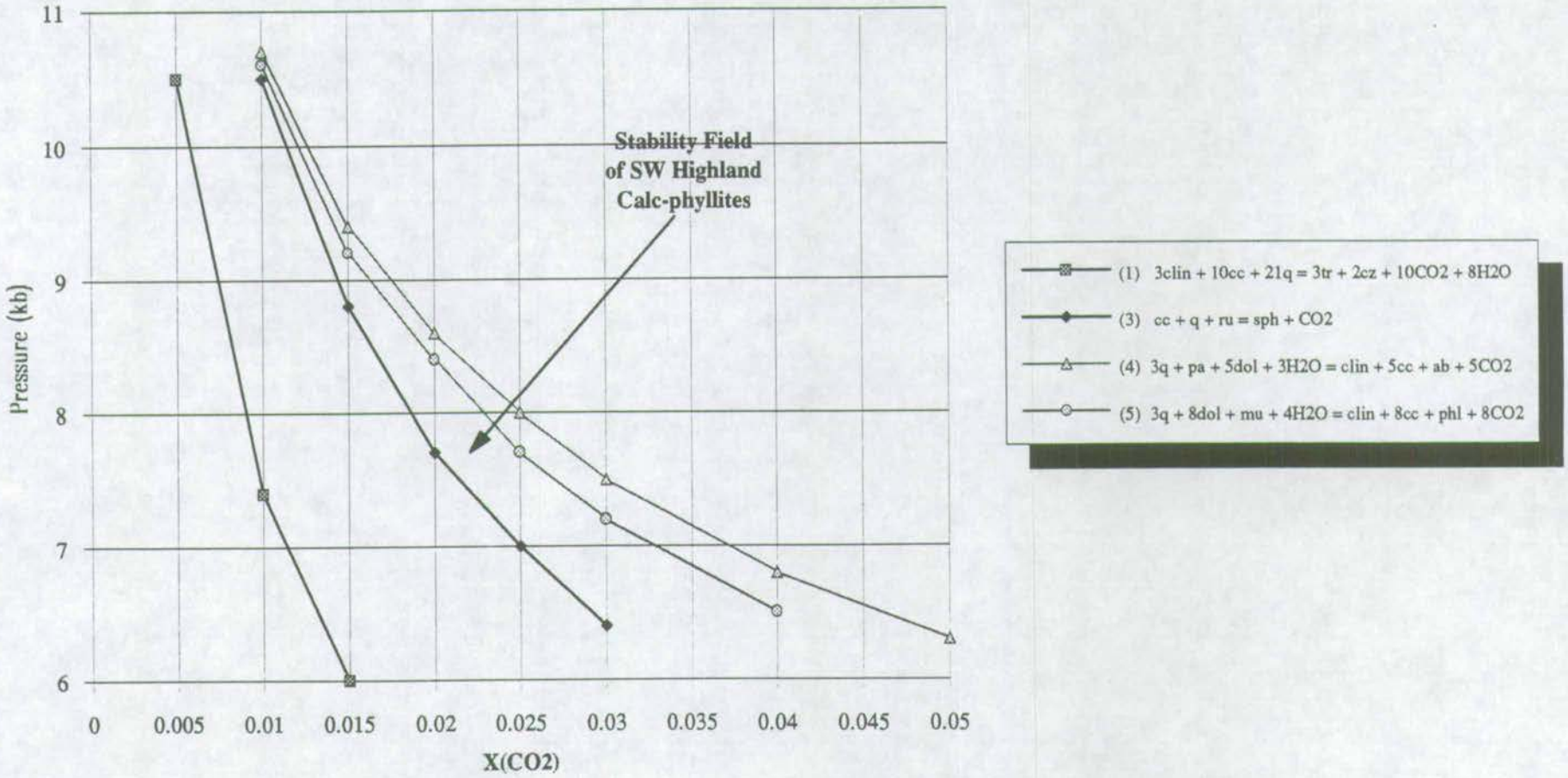

Figure 10.11 shows a plot of calculated time-integrated fluid flux as a function of pressure. A variation of ±1kb will result in a variation of calculated time-integrated fluid flux of about ±25% and a variation of ±2kb will result in a variation of calculated time-integrated fluid flux of about ±50%. Figure 10.11 also shows a plot of calculated time-integrated fluid flux as a function of temperature. A variation of ±30°C will result in a variation of calculated time-integrated fluid flux of about ± 30%.

10.9 Interpretation of Regional Time-integrated Fluid Flux Maps

In the preceding sections, one-dimensional time-integrated fluid flux vectors have been constrained from the advection of reaction 1[11] into the margins of greenschist facies metabasites, assuming advection to be driven by an infiltrating fluid, the composition of which was constrained by reactions 3, 4 and/or 5[12]. The resultant values have been used to construct the regional fluid flux maps which are presented in figure 10.10. In this section, the observed flow patterns are discussed, and the regional-scale structural and lithological controls of syn-metamorphic fluid infiltration, the grain-scale fluid flow mechanisms and the nature of the fluid source are evaluated.

General Statements

A general spatial relationship between the magnitude and direction of the calculated time-integrated fluid flux vectors and the D_1 deformational structures is immediately apparent from figure 10.10. The following general statements may be made:

(1) Fluid fluxes increase with proximity to the fold axes of the Ardrishaig and Port Ellen Anticlines and the Port Cill Maluaig Shear-zone.

[11]Reactions (1), (3), (4) and (5) are included in a reference card at the back of the thesis.

(2) Fluid fluxes decrease with proximity to the fold axes of the Loch Awe Syncline.

(3) One-dimensional fluid flow is generally ***outwards*** from anticlinal axes and the shear-zone and ***inwards*** towards synclinal axes.

10.9.1 Regional Fluid Flow Patterns: The Ardrishaig Anticline

The Ardrishaig Anticline is a major recumbent fold structure which forms the root of the Tay Nappe. The axis of the Ardrishaig Anticline trends SW-NE across central Knapdale. A 5km thick sequence of calc-phyllites and psammites, belonging to the Ardrishaig Phyllite Group is found in the core of the anticline. The Ardrishaig Phyllites are bounded to the NW by the coarse-grained, psammitic Crinan Grits, and to the SE by the finer-grained, psammitic Erins Quartzite. It is apparent from section 5.5 that the psammites are effectively impermeable whereas phyllites are permeable to syn-metamorphic fluid infiltration. Regional channelisation of syn-metamorphic fluid through the Ardrishaig Phyllites may therefore be anticipated.

One-dimensional time-integrated fluid flux vectors, calculated from measured advection of reaction 1 (section 10.3) into the margins of 39 metabasite sills, hosted by the Ardrishaig Phyllites and adjacent Crinan Grits and Erins Quartzite, are presented in map C (figure 10.10). The resultant fluid flow patterns not only confirm the occurrence of regional-scale channelisation of syn-metamorphic fluid through the Ardrishaig Phyllites but also identify regional-scale focusing of fluid along the axis of the Ardrishaig Anticline.

10.9.1.1 Interpretation of One-dimensional Time-integrated Fluid Flux Data

In figure 10.12, calculated time-integrated fluid fluxes are plotted as a function of distance from the axial surface of the Ardrishaig Anticline. Plots (a) and (b) show the entire one-dimensional time-integrated fluid flux data-set. Scatter is greatly reduced in plots (c) and (d) by restricting the dataset to include only those time-integrated fluid fluxes calculated where the fluid is constrained (by asymmetry of the reaction progress or modal profile) to flow ***outwards*** from the axial surface of

Figure 10.12: Regional Fluid Flow Patterns: The Ardrishaig Anticline

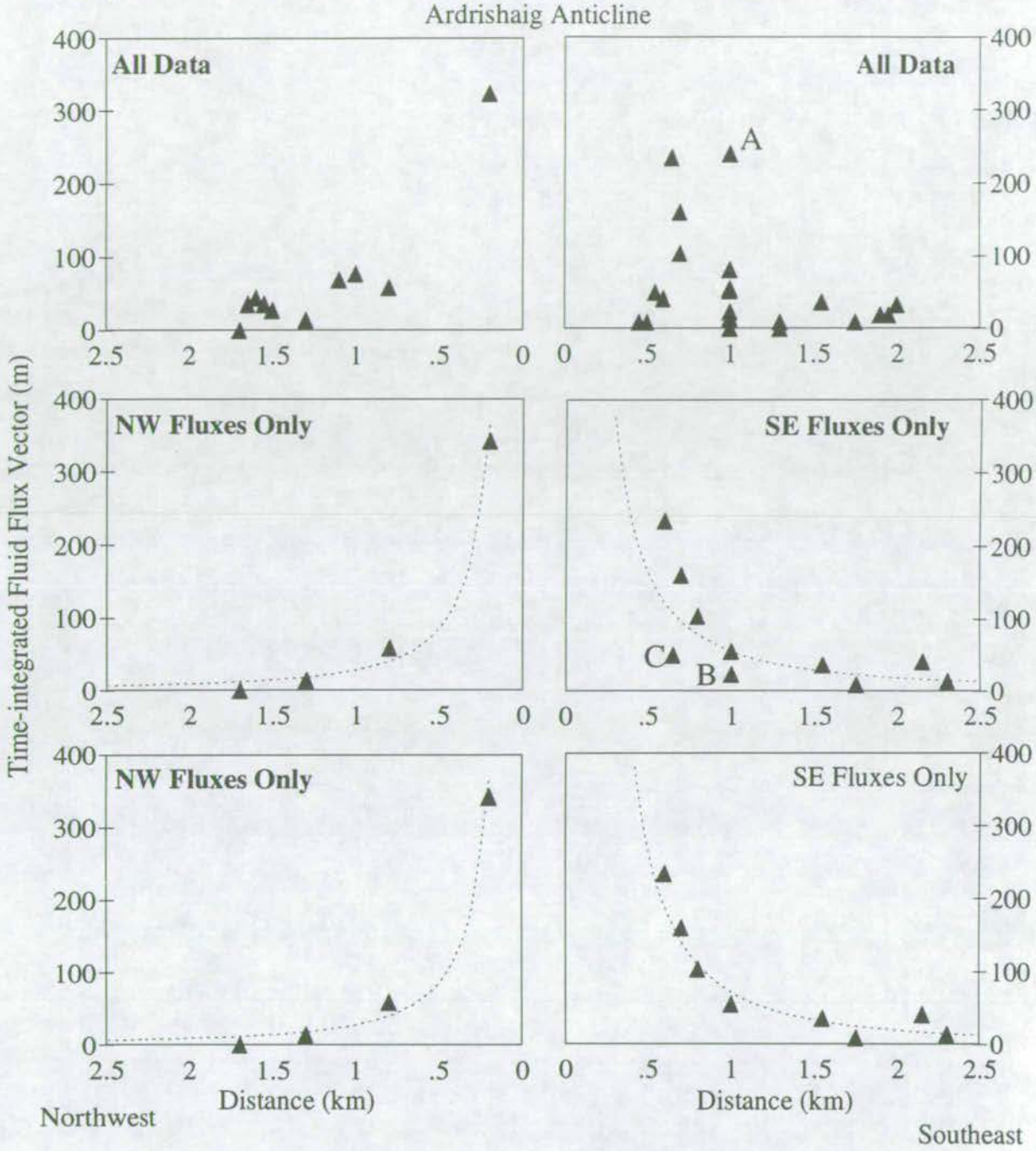

In the above graphs, calculated time-integrated fluid fluxes are plotted as a function of distance from the axial surface of the Ardrishaig Anticline. Graphs (a) and (b) show all calculated values, graphs (c) and (d) show only those values where the flow direction was outwards from the axial surface of the Ardrishaig Anticline (to minimise variation in response to local structure, as described in the text), and graphs (e) and (f) exclude points B & C which represent local structural anomalies (see below).

Dashed lines show best fit logarithmic regression curves (calculated using the IBM PC program CHARISMA).

Points A and B record anomalous fluxes from sills in atypical orientations at Stotfield Bay (see text). Point C describes an anomlaous low flux from a sill at Port Cill Maluaig, probably resulting from deflection of fluid as a result of combined shearing and folding (see text).

the Ardrishaig Anticline. Scatter is further reduced in plots (e) and (f) by eliminating data points B and C which are from Port Cill Maluaig (locality 38, map C, figure 10.9) and Stotfield Bay (locality 46, map C, figure 10.9), respectively. Both of these localities are subjected to localised folding and/or shearing and are discussed below. Logarithmic regression curves were calculated for data in figures 10.12(e) and (f) using the IBM PC program CHARISMA. Logarithmic fits were chosen because of their inherent mathematical simplicity. They are clearly not an ideal solution because they predict infinite fluxes along the axial surface of the Ardrishaig Anticline. However, on the basis of the available data any more complex fit would be arbitrary and may lead to conclusions which are essentially unjustified. Curves are illustrated in figures 10.12(e) and (f) and are given by:

NW limb: $\omega\varphi t_{1\text{-}D,\,NW} = 28.25(d_{NW})^{-1.61}$ (10.2)

and:

SE limb: $\omega\varphi t_{1\text{-}D,\,SE} = 71.62(d_{SE})^{-1.9}$ (10.3)

where d_{NW} and d_{SE} are the respective perpendicular distances from the axial surface of the Ardrishaig Anticline for the NW and SE limbs and $\omega\varphi t_{1\text{-}D,\,NW}$ and $\omega\varphi t_{1\text{-}D,\,SE}$ are the one-dimensional time-integrated fluid fluxes NW and SE of the axial surface of the Ardrishaig Anticline. The following observations pertain from the logarithmic fits which have been imposed on the data in figures 10.12(e) and (f):

(1) The magnitudes of one-dimensional time-integrated fluid fluxes, for which the flow directions are constrained to be ***outwards*** from the axial surface of the Ardrishaig Anticline, increase (pseudo-logarithmically) with increasing proximity to the axial surface of the Ardrishaig Anticline.

(2) One-dimensional time-integrated fluid flux vectors, for which the flow directions are constrained to be ***inwards*** towards the axial surface of the Ardrishaig Anticline, generally fall ***below*** the logarithmic fits (i.e. they predict lower time-integrated fluid fluxes).

These observations are consistent with the following interpretations:

(1) The general orientation of the fluid flow direction must lie within the narrow constraints of the limbs of the Ardrishaig Anticline.

(2) Fluid must flow ***towards*** the fold closure of the Ardrishaig Anticline. The direction of fluid flow must therefore have an ***upward*** component.

(3) The regional fluid flow pattern must be ***regular*** to account for the systematic distance-flux profile shown in figure 10.12.

(4) Structure ***must*** control fluid flow patterns on a local-scale, and ***may*** control fluid flow patterns on a regional-scale.

These interpretations are based on regional patterns of 1-D (lithology-perpendicular) time-integrated fluid flux vectors. Therefore no limits are posed on the magnitude of lithology-parallel flow. In chapter 8, it was shown that an isotopic profile constructed across a broad metabasic sill at Port Ellen ,Islay is best described by a "pinned-boundary" solution. The "pinned-boundary" solution requires the isotopic composition of the fluid to be fixed at the lithological boundary as a result of a ***major*** component of lithology-parallel fluid flow. It is therefore essential, to estimate the lithology-parallel component of fluid flow for a meaningful quantitative evaluation of syn-metamorphic fluid behaviour. This is essentially a three-dimensional geometric problem and may be solved by detailed vector analysis of one-dimensional fluid flow patterns.

10.9.1.2 Evaluation of the 3-D Geometry of Fluid Flow

Provided that the limbs of the Ardrishaig Anticline are not parallel, it is possible to impose quantitative limits on the direction and magnitude of the time-integrated fluid flux in three-dimensions. This represents a new and tentative development in the quantification of fluid flow, the basis of which is now discussed.

General Statement

For the observed systematic 1-D flux-distance relations (figure 10.12) to develop, the geometry of the general 3-D fluid flow pattern must be ***regular***. Exceptions to this statement arise from local structural and lithological controls and result in scatter on the 1-D flux-distance plot (figure 10.12).

Initial Assumption

For mathematical simplicity it is essential to make the initial assumption that fluid flow is uni-directional. This is essentially a geometric simplification, but it is soundly-based. The angle between the limbs of the Ardrishaig Anticline is small and therefore the orientation of the (3-D) fluid flow direction may only vary over a small angular range. The assumption of uni-directional flow may be formally tested as follows:

Test of the Uni-directional Flow Assumption

In general, metabasite sills exposed across the Ardrishaig Anticline show little variation in orientation. However, an exception to this is Stotfield Bay, West Knapdale (figure 10.13). At Stotfield Bay, 10 exposed metabasites are involved in intensive 500m-scale D_1-buckling and folding. The result of this that sills are found in a variety of different orientations. A detailed study was undertaken in this area to evaluate the validity of the assumption of uni-directional flow. 1-D time-integrated fluid fluxes were measured by the reaction progress technique detailed in chapter 6. The sill orientations were measured and apparent dips, viewed in a vertical plane perpendicular to the axial surface of the Ardrishaig Anticline, were calculated. Data are listed in table 10.6.

Figure 10.13: Stotfield Bay: Outcrop Map

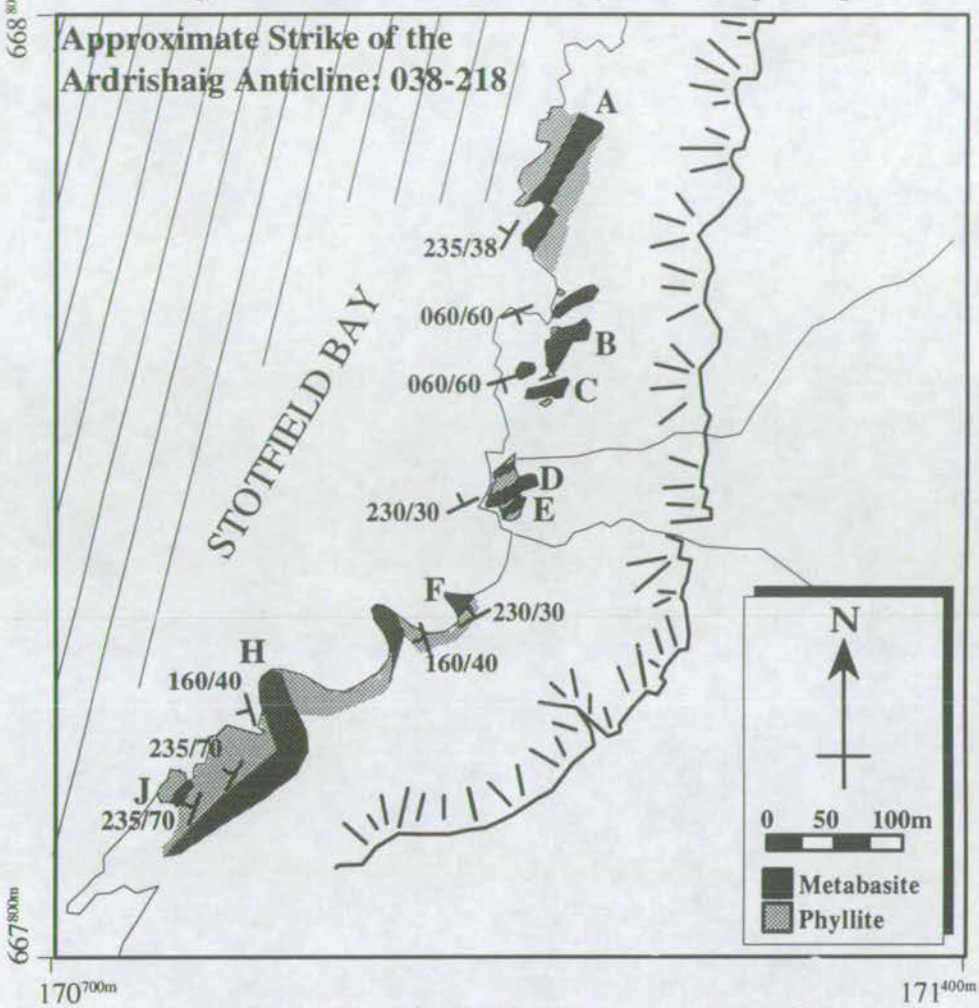

Figure 10.14: Plot of 1-D Time-integrated Fluid Flux vs. Apparent Dip of Sill to illustrate the dependence of the 1-D flux on Sill Orientation.

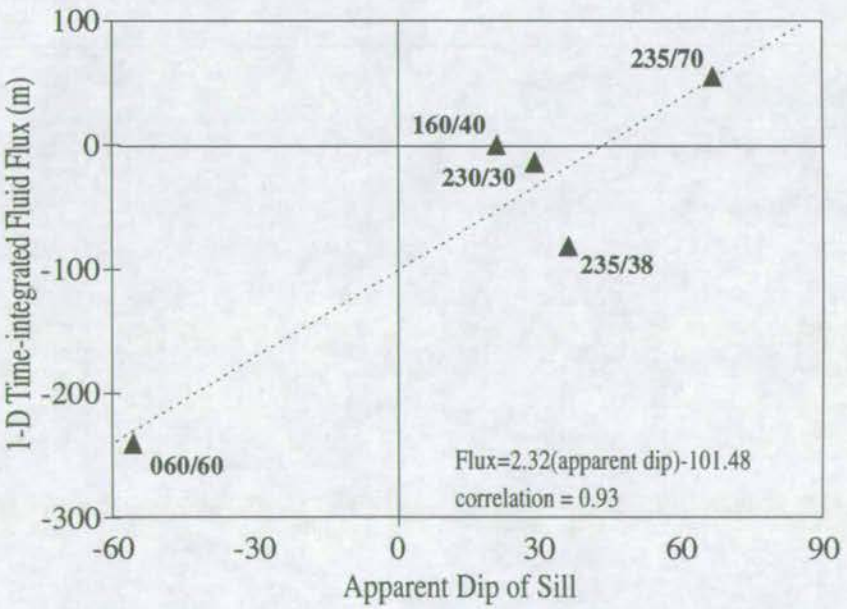

(equivalent strike to axial surface of Ardrishaig Anticline)

Note: The 1-D time-integrated fluid flux = 0 where the apparent dip in the equivalent strike to the Ardrishaig Anticline = 43.7 degrees. The dip of the axial surface of the Ardrishaig Anticline is about 45 degrees.

Table 10.6: 1-D Time-integrated Fluid Fluxes and Angles of Incidence of Fluid Syn-metamorphic Infiltration at Stotfield Bay

Sill	1-D Flux (m^3/m^2)	1-D Dir^n	Attitude	Apparent Dip (equivalent strike to the axial surface of the Ardrishaig Anticline
A	81	NW	235/38	36.3
B	>240	???	060/60	-55.6
C	>42	???	060/60	-55.6
D	23	NNW	230/30	29.3
E	23	SSE	230/30	29.3
F	14	NNW	230/30	29.3
H	0	N/A	160/40	21.2
J	55	SSE	235/70	66.9

??? = Unknown, N/A = Not applicable

Sills A-J correspond to localities 41-50 respectively on map C (figure 10.9). Sills G and I are ignored because that are too poorly constrained.

The data listed in table 10.6 is plotted in figure 10.14, from which a linear relationship between measured 1-D time-integrated fluid flux and sill orientation is immediately evident. Furthermore, the 1-D time-integrated fluid flux is predicted to be zero for an apparent dip of 45°. Based on data of Roberts (1974) and interpretation of the BGS 1" series sheet 55, the average dip of the axial surface of the Ardrishaig Anticline is ≈45°. These are remarkable conclusions. Not only is the assumption of uni-directional fluid flow shown to be viable, but also the fluid flow direction is constrained to be approximately parallel to the axial surface of the Ardrishaig Anticline. This interpretation is consistent with the conclusion, based on the 1-D flux profile (figure 10.12), that the orientation of the fluid flow direction is constrained within the limbs of the Ardrishaig Anticline.

The immediate interpretation arising from this study that the fluid flow direction is approximately parallel to the axial surface of the Ardrishaig Anticline is fundamentally important. Regional folding must offer a dominant control of syn-metamorphic fluid flow. Fluid flow must be approximately parallel to the axial planar fabric and may therefore be governed, at least in part, by rock anisotropy.

Constraint of the three-dimensional fluid flow direction has enabled quantification of the magnitude of the time-integrated fluid flux by an essentially simplistic vector mathematical approach. This is discussed in the following section.

10.9.1.3 Quantitative Constraint of 3-D Time-integrated Fluid Fluxes

1-D time-integrated fluid fluxes are measured within the pseudo-horizontal plane of surface exposure. The approach adopted for quantifying the magnitude of the 3-D time-integrated fluid flux involves (i) constraint of the 2-D time-integrated fluid flux by resolving measured 1-D time-integrated fluid flux vectors constrained on both limbs of the Ardrishaig Anticline with the inferred uni-directional fluid flow direction (parallel to the axial surface of the Ardrishaig Anticline); and (ii) geometric reconstruction to the vertical plane to calculate the 3-D time-integrated fluid flux // axial surface of the Ardrishaig Anticline.

(i) Quantitative Evaluation of 2-D Fluid Flux Vectors in the Horizontal Plane

The 2-D time-integrated fluid flux may be resolved into a lithology-parallel and a lithology-perpendicular vector component. The lithology-perpendicular vector component may be measured from the advection distance of reaction 1 into the margins of greenschist facies metabasites. This is the 1-D time-integrated fluid flux which is discussed above. The lithology-parallel vector component is unconstrained, as is the 2-D time-integrated fluid flux. However, the 2-D time-integrated fluid flux ($\omega\varphi t_{2\text{-}D}$) and the lithology-perpendicular 1-D fluid fluxes ($\omega\varphi t_{1\text{-}D}$) are related by the simple trigonometric expression:

$$(\omega\varphi t_{1\text{-}D})=(\omega\varphi t_{2\text{-}D}).\sin(\theta) \qquad (10.4)$$

where θ is the angle of incidence of the 2-D flux to the metabasite margin. Therefore, provided that $\theta>0$, the 2-D time-integrated fluid flux may be calculated, for ***a given fluid flow direction***, from two metabasites in ***different*** orientations.

The Geometric Relationship between Measured 1-D Fluid Flux Vectors and the 3-D Fluid Flux Vector

Before a quantitative interpretation of three-dimensional fluid flow may be presented, it is imperative that the spatial relationship between the 2-D flux vector which may be calculated within the horizontal surface and 3-D flux vector which lies within the vertical plane is established. In the unique example of the SW Highlands, the 2-D time-integrated fluid flux is equivalent to the 3-D time-integrated fluid flux because the primary D_1 fold structures (i.e. the Ardrishaig Anticline, Loch Awe Syncline and Islay Anticline) ***generally*** plunge at ≈45° (estimated from data of Roberts 1974, based on 731 fold hinges and cleavage-bedding intersections). The reasons for this are most simply envisaged geometrically (figure 10.15). Fluid flux vectors may be effectively "reflected" in the plane for which the fold axes of the major D_1-structures define the pole. The magnitude of flux vectors is conserved because this plane bisects the angle between the horizontal (observed) plane and the vertical plane within which the 3-D time-integrated fluid flux vector must lie (assuming that fluid flow is buoyancy driven). Therefore the dimensions of the fluid vectors are conserved.

Calculation of the magnitude of the 3-D Time-integrated Fluid Flux Vector // Axial Surface of the Ardrishaig Anticline

(1) Outline

The magnitude of the 3-D time-integrated fluid flux vector was calculated for fluid flow parallel to the axial surface of the Ardrishaig Anticline as follows. The 3-D geometry of the Ardrishaig Anticline is illustrated in figure 10.16 for clarity.

Figure 10.15: Geometric Relationship Between Horizontal (Map) Section and Vertical Section

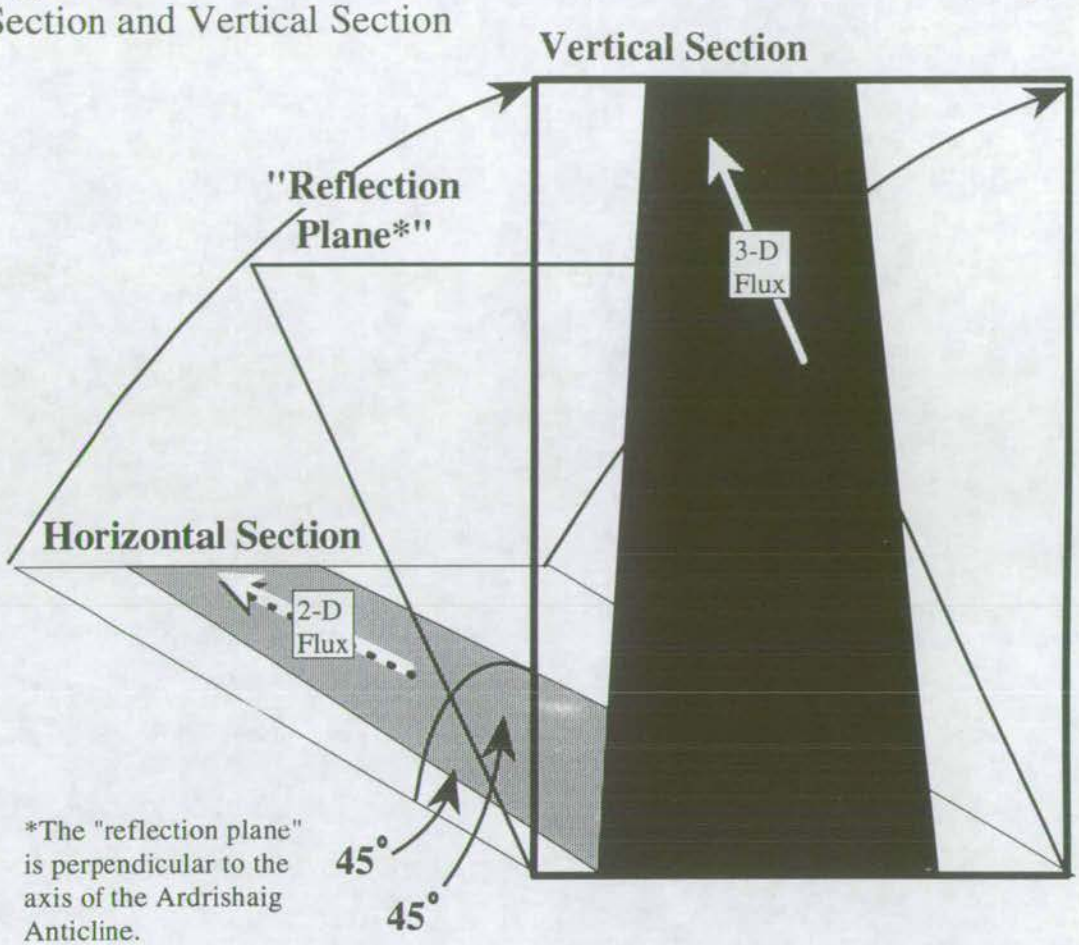

The above diagram shows the geometric relationship between the vertical section and the horizontal (map) section. The dimensions of the 2-D and 3-D fluxes are identical because they are "reflected" in the plane which bisects the angle between the horizontal section (in which measurements are made) and the vertical section (in which the 3-D flux lies).

10.16: The Ardrishaig Anticline

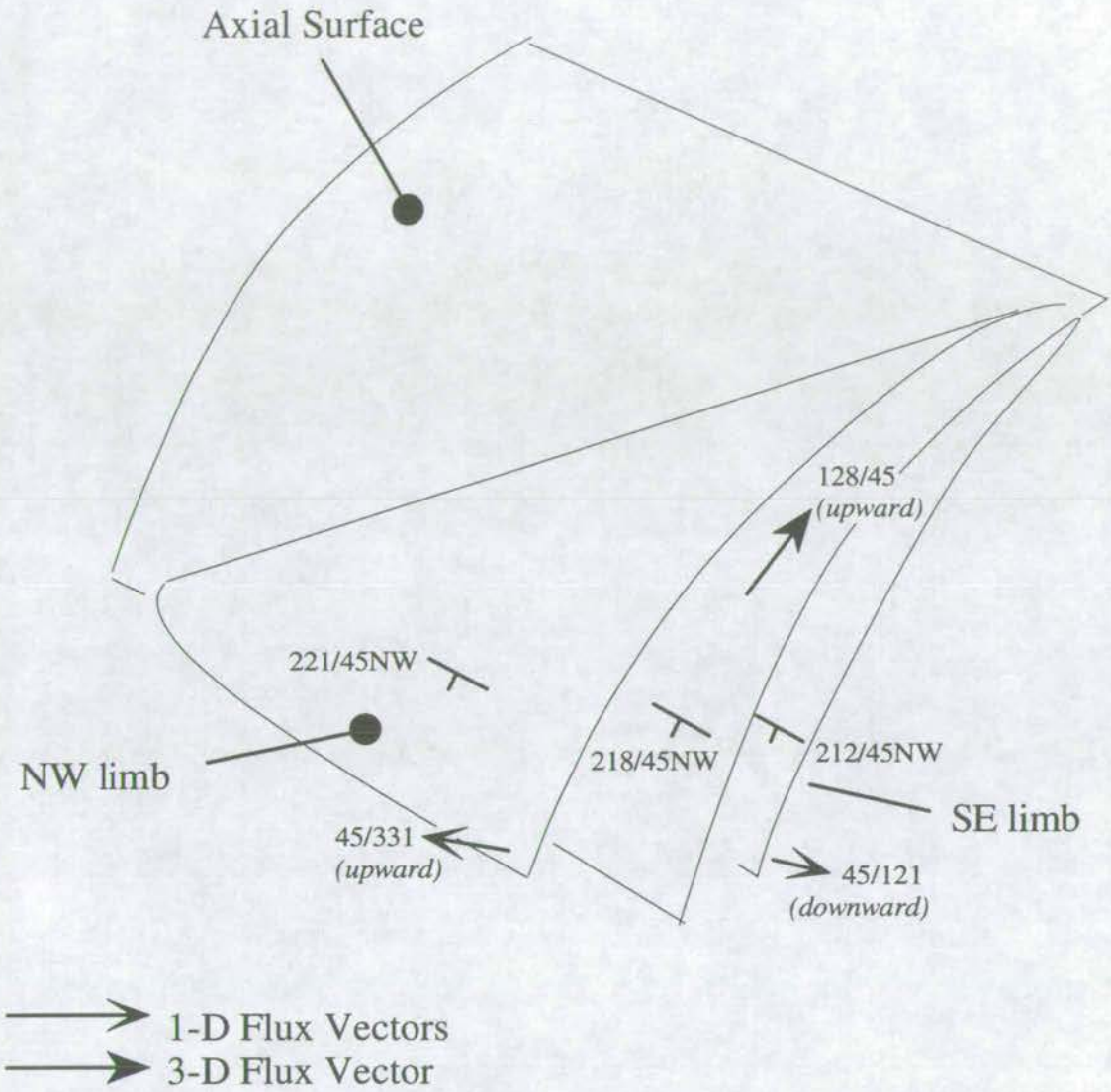

(1) The lithology-perpendicular vector component of the time-integrated fluid flux on each limb of the Ardrishaig Anticline is represented as a function of the lithology-perpendicular distance from the axial surface.

(2) The average orientations of one-dimensional time-integrated fluid flux vectors are estimated for each limb of the Ardrishaig Anticline.

(3) The magnitude of a ***single*** two-dimensional time-integrated fluid flux vector which is parallel to the axial surface of the Ardrishaig Anticline, and satisfies ***both*** of the one-dimensional time-integrated fluid flux - distance relationships, is determined mathematically. This two-dimensional flux vector is equated with the three-dimensional flux vector in the vertical plane.

(2) Quantification of 1-D (Lithology-perpendicular) Time-integrated Fluid Flux Vectors as a function of the Perpendicular Distance from the Axial Surface of the Ardrishaig Anticline

On the basis of the best fit logarithmic regression curves, shown in figure 10.12 and expressed by equations 10.2 and 10.3, the magnitudes of one-dimensional time-integrated fluid flux vectors (constrained perpendicular to sill margins) to the NW ($\omega\varphi t_{1\text{-}D,\ NW}$) and SE ($\omega\varphi t_{1\text{-}D,\ SE}$) of the axial surface of the Ardrishaig Anticline may be expressed as a function of distance from the axial surface of the Ardrishaig Anticline (d_{NW} and d_{SE}).

It is possible to predict the outward flux at any position within the Ardrishaig Phyllites using equations (10.2) and (10.3). Equations (10.2) and (10.3) describe one-dimensional, lithology-perpendicular, time-integrated fluid flux vectors.

(3) Orientation of the (Lithology-perpendicular) 1-D Time-integrated Fluid Flux Vectors

The orientations of the above one-dimensional time-integrated fluid flux vectors are constrained as follows (refer to figure 10.16):

(1) The average orientation of metabasite sills within the Ardrishaig Anticline is assumed to parallel the fold limbs. Local, structural exceptions to this (e.g. Stotfield Bay) are discussed above in section 10.9.1.2.

(2) The limbs of the Ardrishaig Anticline are assumed to parallel the Ardrishaig Phyllites - Crinan Grit contact in the NW, and the Ardrishaig Phyllites - Erins Quartzite contact in the SE.

(3) Therefore, the average strikes and dips of the NW and SE limbs of the Ardrishaig Anticline were estimated from the BGS 1 inch series geological map (sheet 28: Jura) by construction of structural contours along the Ardrishaig Phyllites - Crinan Grit and Ardrishaig Phyllite - Erins Quartzite contacts, averaged over a distance of 20km.

(4) Average strikes and dips of the NW and SE limbs of the Ardrishaig Anticline are approximated as 221/45NW and 212/45NW respectively. Estimated strikes were averaged over a distance of about 20km and are therefore likely to be accurate to ±1 or 2°. Estimated dips depend on construction of structural contours on an undulose surface and are therefore subject to large errors, probably in excess of ±10°.

(5) The orientations of the time-integrated fluid flux vectors are given as the poles to the respective limbs of the Ardrishaig Anticline. The flux vector direction is always outwards from the axial surface of the Ardrishaig Anticline. The resultant flux vector directions are 45/311 (*upwards*) to the NW, and 45/122 (*downwards*) to the SE of the Ardrishaig Anticline (figure 10.16).

(4) Orientation of the 3-D Time-integrated Fluid Flux Vector

The orientation of the three-dimensional time-integrated fluid flux vector is constrained as follows:

(1) As is justified in section 10.9.1.2, the three-dimensional time-integrated fluid flux vector is parallel to the axial surface of the Ardrishaig Anticline (218/45NW).

(3) Fluid flow is assumed to be buoyancy-driven and therefore adopts an upwards flow direction given by 128/45SE (figure 10.16).

(5) Calculation of 3-D Time-integrated Fluid Flux Vectors

The magnitude of the three-dimensional fluid flux was estimated such that it simultaneously satisfied both of the observed one-dimensional time-integrated fluid fluxes, as described by equations (10.2) and (10.3) for the NW and SE limbs of the Ardrishaig Anticline for $d_{NW}=d_{SE}$ as follows:

Figure 10.17 describes the trigonometric relationship between the measured 1-D lithology-perpendicular time-integrated fluid flux vector ($\omega\varphi t_{1\text{-}D,NW}$ and $\omega\varphi t_{1\text{-}D,SE}$), the 3-D time-integrated fluid flux vector ($\omega\varphi t_{3\text{-}D,NW}$ and $\omega\varphi t_{3\text{-}D,SE}$), the 1-D lithology-parallel time-integrated fluid flux vector, and the angle of incidence of the infiltrating fluid with the respective fold limb (θ_{NW} and θ_{SE}). The following trigonometric relationships may be derived from figure 10.17:

$$\omega\varphi t_{3-D,NW} = \frac{\omega\varphi t_{1-D,NW}}{\sin\theta_{NW}} \tag{10.5}$$

$$\omega\varphi t_{3-D,SE} = \frac{\omega\varphi t_{1-D,SE}}{\sin\theta_{SE}} \tag{10.6}$$

(3) For the predicted fluid infiltration direction of 128/45NW and the orientations of the NW and SE limbs of the Ardrishaig Anticline of 221/45NW and 212/45NW, respectively:

$$\theta_{NW}\approx 3° \tag{10.7}$$

and:

$$\theta_{SE}\approx 6° \tag{10.8}$$

The two-dimensional time-integrated fluid flux is calculated by substituting equations 10.2 and 10.7 in equation 10.5 to give:

$$\omega\varphi t_{3\text{-}D,NW} \approx 540(d_{NW})^{-1.61} \tag{10.9}$$

and substituting equations 10.3 and 10.8 in equation 10.6 gives:

Figure 10.17: Graphical Description of the "Angle of Incidence" of the Infiltrating Fluid (as described in text)

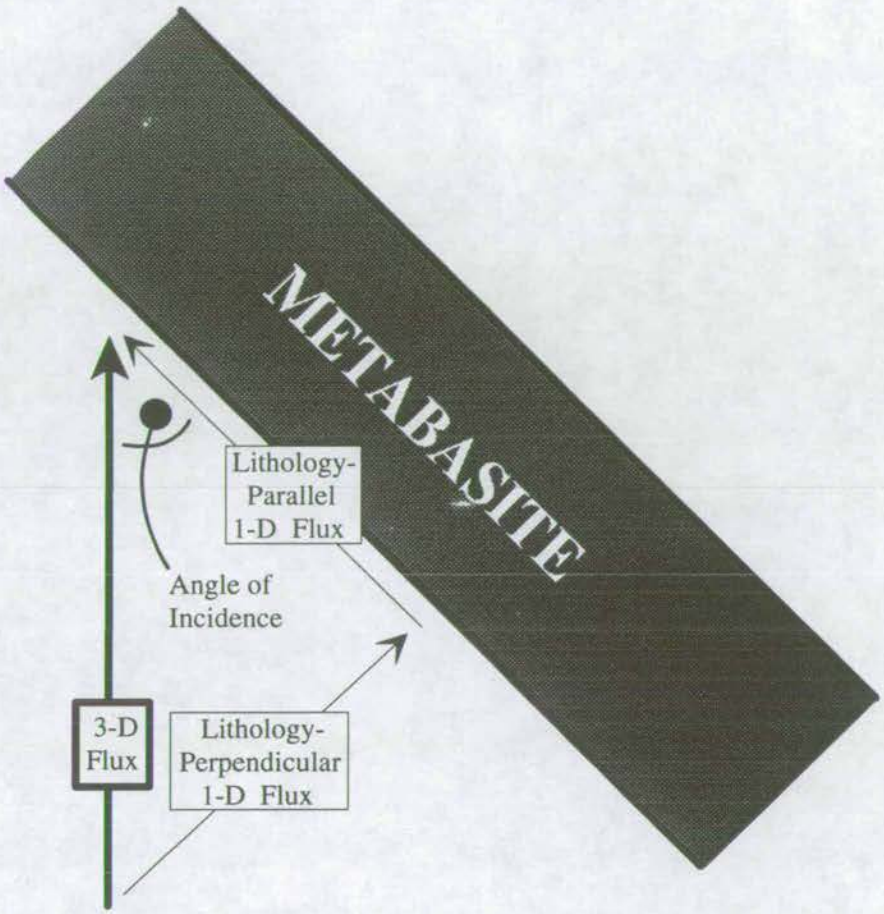

$$\omega\varphi t_{3\text{-}D,SE} \approx 685(d_{SE})^{-1.9} \quad (10.10)$$

Equations 10.9 and 10.10 are described graphically in figure 10.18, from which it is possible to estimate the 3-D time-integrated fluid flux, at any distance (d_{NW} or d_{SE}) from the axial surface of the Ardrishaig Anticline.

(6) Interpretations

A number of fundamentally important interpretations arise from 3-D flux distance plot shown in figure 10.18. These are discussed below.

(i) Focusing of Fluid Through the Axial Surface of The Ardrishaig Anticline

Figure 10.18 describes a logarithmic increase of the 3-D time-integrated fluid flux with increasing proximity to the axial surface of the Ardrishaig Anticline. The 3-D time-integrated fluid flux along the axial surface of the Ardrishaig Anticline is predicted to be infinite which is clearly not realistic and is merely an artefact from the simplification of describing the data by a logarithmic fit. A minimum limit may be fixed to the magnitude of the 3-D time-integrated fluid flux from the nearest 1-D time-integrated fluid flux measurement to the axial surface of the Ardrishaig Anticline. The metabasite at Lochead (locality 35, map C in figure 10.9) is 0.2km NW of the axial surface of the Ardrishaig Anticline and records a 1-D (lithology-perpendicular) time-integrated fluid flux in excess of $324 m^3/m^2$. From figure 10.18, the 3-D time-integrated fluid flux at 0.2km NW of the axial surface of the Ardrishaig Anticline is $\approx 10^4$ m^3/m^2. This is the minimum time-integrated fluid flux within ≈0.2km of the axial surface of the Ardrishaig Anticline. **Fluid is therefore focused along the axial surface of the Ardrishaig Anticline, along which fluxes in excess of $\approx 10^4$-10^5 m^3/m^2 may be attained.** It is interesting to recall that the axial zone of the Ardrishaig Anticline lacked visible metabasites. This may be explained if fluid fluxes were sufficiently high as to induce complete type I→type III reaction. Sills would

Figure 10.18: Variation in the Calculated Magnitude of the 3-D Time-integrated Fluid Flux Vector as a function of Distance from the Axial Surface of the Ardrishaig Anticline

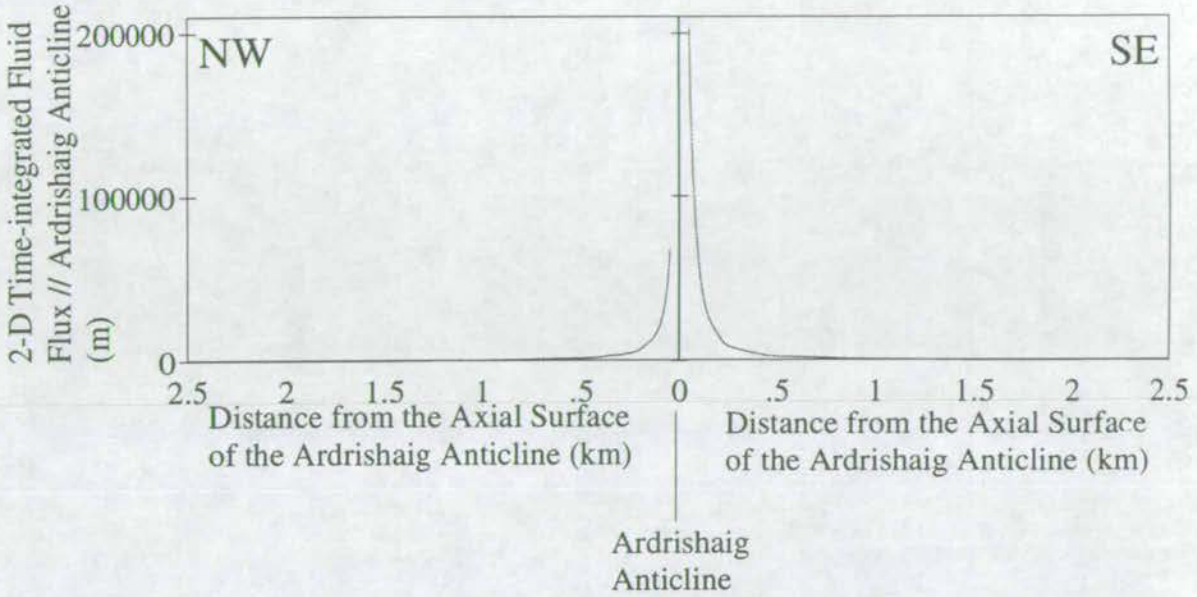

become less resilient to deformation and may have been sheared to sufficient extent as to be effectively obliterated.

(ii) Lithology-Parallel vs. Lithology-Perpendicular Fluid Flow

The 3-D time-integrated fluid fluxes expressed by equations 10.9 and 10.10 may be expressed as the vector sum of lithology-parallel and lithology-perpendicular 1-D time-integrated fluid flux vector components (figure 10.17). The 1-D lithology-perpendicular components of the 3-D time-integrated fluid flux are given by equations 10.5 and 10.6. The 1-D lithology-parallel components of the two-dimensional time-integrated fluid flux may be determined by trigonometry (figure 10.15) from equations 10.6, 10.7, 10.8 and 10.9 as follows:

$$\text{Lithology-parallel Flux (//NW limb)} = \omega\varphi t_{3\text{-D,NW}}.\cos(\theta_{NW}) = 539(d_{NW})^{-1.61} \qquad (10.11)$$

and:

$$\text{Lithology-parallel Flux (//SE limb)} = \omega\varphi t_{3\text{-D,SE}}.\cos(\theta_{SE}) = 681(d_{SE})^{-1.9} \qquad (10.12)$$

The ratios of lithology-parallel to lithology-perpendicular flow on the NW and SE limbs of the Ardrishaig Anticline may be estimated by combining equation 10.10 with equation 10.2 and by combining equation 10.11 with equation 10.3 to give:

NW limb: Lithology-parallel Flux : Lithology-perpendicular Flux $\approx$ 19 : 1 (10.12)

and:

SE limb: Lithology-parallel Flux : Lithology-perpendicular Flux $\approx$ 10 : 1 (10.13)

The immediate inference of equations 10.12 and 10.13 is that lithology-parallel flow predominates over lithology-perpendicular flow.

Summary of General Interpretations

The following general interpretations are immediately apparent from quantitative modelling of the magnitude and spatial variation of one- and three-dimensional time-integrated fluxes of syn-metamorphic fluid across the Ardrishaig Anticline (figure 10.18):

(1) Syn-metamorphic fluid flow in central Knapdale was channelled through the Ardrishaig Phyllites.

(2) Syn-metamorphic fluid was strongly focused through the axial zone of the Ardrishaig Anticline.

(3) Lithology-parallel fluid flow predominates over lithology-perpendicular fluid flow.

(4) **It is clearly evident from this section that both regional-folding and lithology are important in controlling syn-metamorphic fluid flow patterns.**

10.9.1.4 Misfitting Data

Logarithmic regression curves, fitted to the graphs of one-dimensional time-integrated fluid flux (constrained to flow outwards from the axial surface of the Ardrishaig Anticline) plotted against distance from the axial surface of the Ardrishaig Anticline, are intended to identify the predominant trends in the ***majority*** of one-dimensional time-integrated fluid flux data (figure 10.12). Clearly misfitting data (points A, B and C in figure 10.12) were excluded from the regression. The misfitting data are shown to identify areas of further structural complexity and are discussed below.

Points A and C respectively describes an anomalously high and an anomalously low calculated one-dimensional time-integrated fluid flux vector estimated from a sill in a structurally-complex area at Stotfield Bay (localities 42 and 45 in figure 10.9). The orientations of both sills are ***atypical*** as is discussed in section 10.9.1.2. Point B represents the time-integrated fluid flux calculated at the core of a minor synformal fold associated with a zone of shearing at Port Cill Maluaig (locality 38 in figure 10.9). The core of the synform is apparently structurally-isolated from

the prevailing fluid infiltration. A quantitative interpretation of fluid infiltration of the Port Cill Maluaig Shear-zone is presented below.

Port Cill Maluaig: A D_1 Shear Zone

At Port Cill Maluaig on the west coast of Knapdale a sheared "s"-type folded metabasic sill is hosted by calcareous phyllites and psammites of the Ardrishaig Phyllite Group. The outcrop is shown in figure 10.3 and discussed in section 10.4.1. Distribution of types I and III metabasite assemblage zones and one-dimensional time-integrated fluid flux data, compiled from figure A5.16 (appendix 5) are presented on a geological map of the Port Cill Maluaig coastal section in figure 10.19.

It is evident from the distribution of the types I and III metabasite assemblages and the direction and magnitude of one-dimensional time-integrated fluid flux vectors that infiltration was focused through the shear-zone, to a sufficient extent to violate the relationship between one-dimensional time-integrated fluid flux and the distance from the axial surface of the Ardrishaig Anticline. Equation 10.3 predicts a one-dimensional (lithology-perpendicular) time-integrated flux of $267 m^3/m^2$ towards the SE, at Port Cill Maluaig (0.5km SE of the Axial surface of the Ardrishaig Anticline). The violation is sufficient to induce a reversal of the prevailing unidirectional fluid flow direction downstream of the shear.

It is evident, in this example, that local deformation is imposing a greater control on fluid infiltration than that imposed by regional folding. This example emphasises the importance of deformational strain in focusing syn-metamorphic fluids.

Figure 10.19: 1-D Fluid Flux Map of Port Cill Maluaig

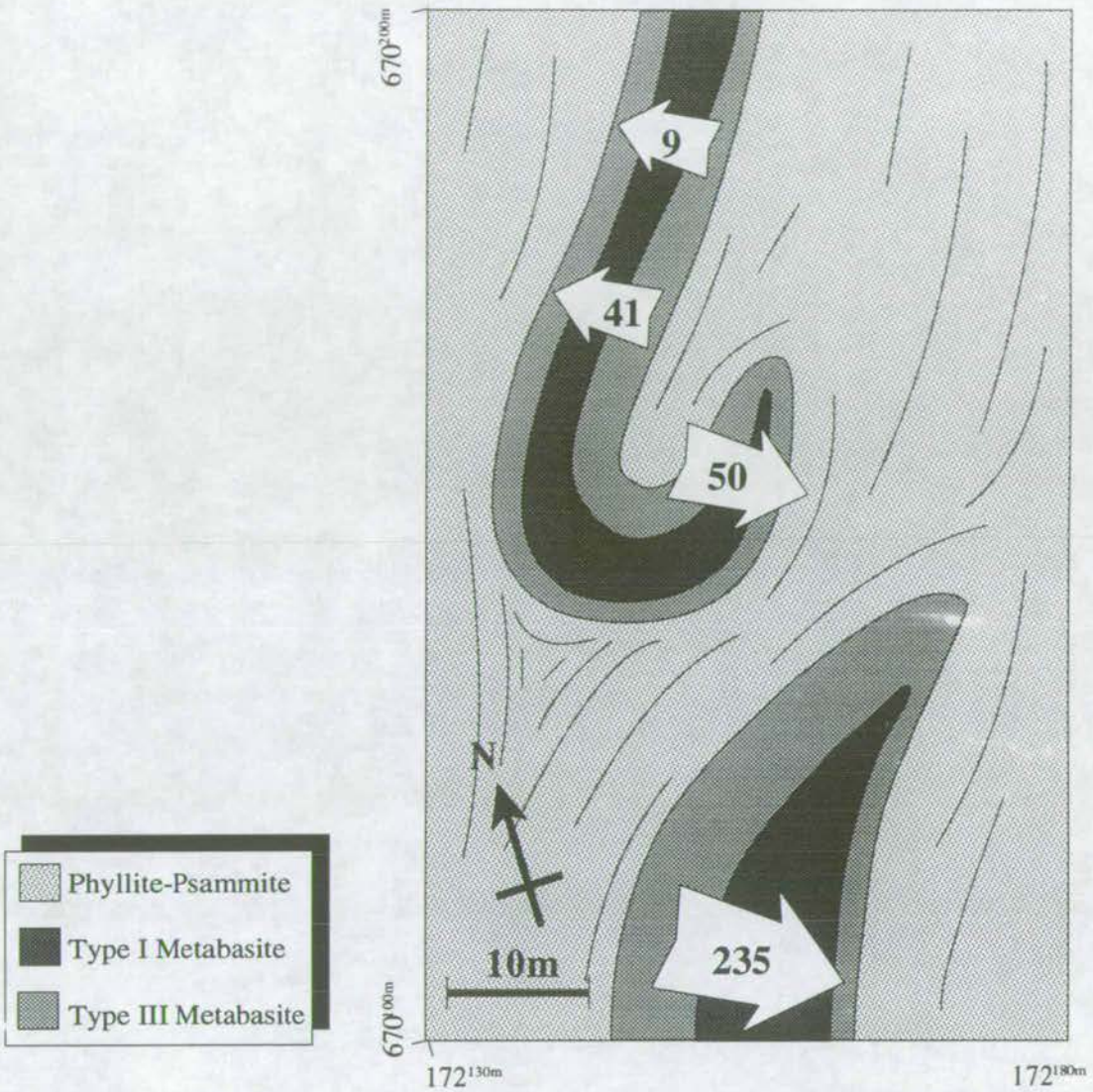

Figure 10.20: Port Ellen: Outcrop Map

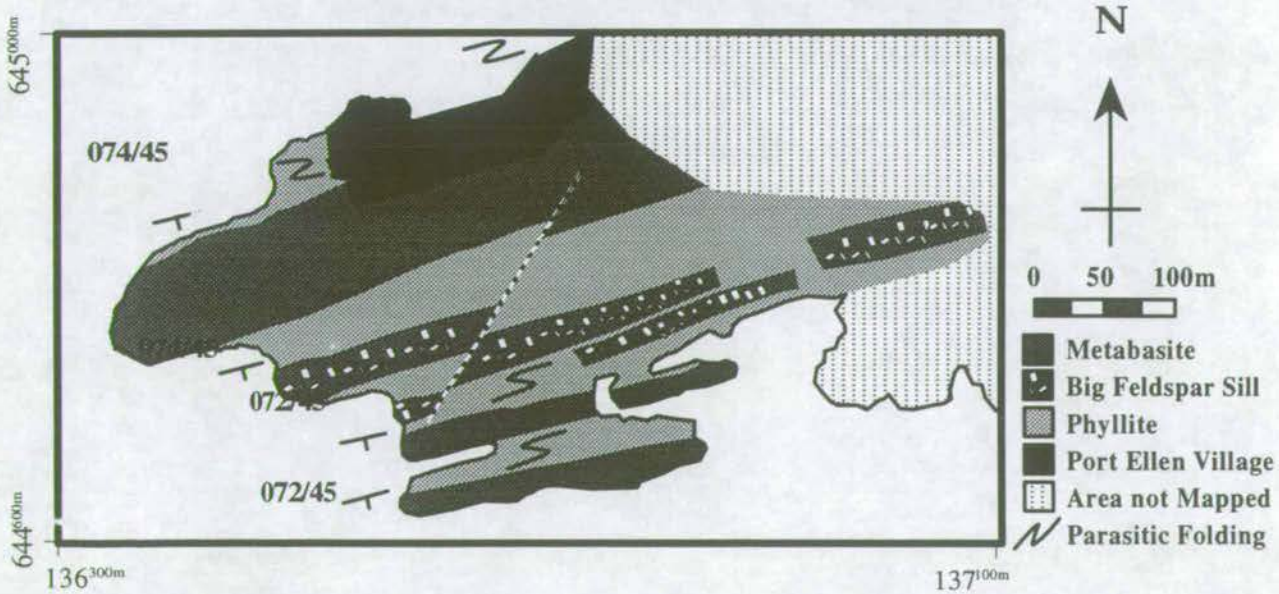

10.9.2 Local Fluid Flow Patterns: The Port Ellen Anticline

Anticlinal folding of metabasic sills, hosted by calcareous phyllites of the Port Ellen Phyllite Group, has been identified at the Ard of Port Ellen, SE Islay (figure 10.20). The fold structure is parasitic to the SE limb of the recumbent Islay Anticline (figure 10.20). The Port Ellen anticline was identified on the basis of the distribution of D1-D2 "s" and "z" folds (figure 3.4b) and the repetition of petrologically-distinct "big feldspar" sill (figure 10.20), a metabasite which is uniquely characterised by an abundance of large albites (figure 10.21).

One-dimensional time-integrated fluid flux vectors have been calculated from measured advection of reaction 1, as described in section 10.2. 11 measurements were made at strategic locations throughout the Port Ellen area and are presented in map B (figure 10.10). The resultant fluid flow pattern immediately identifies outcrop-scale focusing of syn-metamorphic fluid through the axial zone of the Port Ellen Anticline.

Interpretation of One-dimensional Time-integrated Fluid Flux Data

In figure 10.22, calculated time-integrated fluid fluxes are plotted as a function of distance from the axial surface of the Port Ellen Anticline. An inverse linear correlation between distance from the anticlinal axis and time-integrated fluid flux is immediately evident from figure 10.22. **It is therefore concluded that the majority of syn-metamorphic fluid was focused through the axial zone of the Port Ellen Anticline**. The complete lack of scatter exhibited in figure 10.22 implies that syn-metamorphic fluid flow is constant in direction and magnitude across the entire Port Ellen Anticline and is unaffected by any smaller-scale deformational features. The is an extremely important conclusion as it limits the scale at which structural channelisation of syn-metamorphic fluid may develop. **Structural channelisation of fluid is evident on a scale of ≈0.5-10km**.

Figure 10.21: Photograph of the Big Feldspar Sill, Ard of Port Ellen ,Islay (located on figure 10.23): Scale Hammer (35cm)

Constraint of Three Dimensional Time-integrated Fluid Flux at Port Ellen

Three dimensional time-integrated fluid fluxes may be constrained from the linear regression curves fitted to the one dimensional time-integrated fluid flux data in figure 10.22, in an identical manner to that adopted in section 10.9.1.3.

NNW of the axial surface of the Port Ellen Anticline, the one-dimensional time-integrated fluid flux ($\omega\varphi t_{1\text{-}D,NNW}$) can be described by the equations:

0.000-0.015km NNW of the axial surface of the Port Ellen Anticline:

$$\omega\varphi t_{1\text{-}D,NNW} = 178.9 - 9263.44d_{NNW} \quad (10.14)$$

0.020-0.300km NNW of the axial surface of the Port Ellen Anticline:

$$\omega\varphi t_{1\text{-}D,NNW} = 0 \quad (10.15)$$

in which flux is measured in metres (m^3/m^2) and distance is measured in kilometres. Likewise, from 0.0-0.3km SSE of the axial surface of the Port Ellen Anticline, the one-dimensional time-integrated fluid flux ($\omega\varphi t_{1\text{-}D,SSE}$) can be described by the equation:

$$\omega\varphi t_{1\text{-}D,SSE} = 265.28 - 810.39d_{SSE} \quad (10.16)$$

It should therefore be possible to predict the one-dimensional lithology-perpendicular time-integrated fluid flux at any position within 0.3km distance of the axial surface of the Port Ellen Anticline using equations 10.14, 10.15 and 10.16.

(2) Orientation of the 1-D (Lithology-perpendicular) Time-integrated Fluid Flux Vectors

The NNW and SSE limbs of the Port Ellen Anticline are sub-parallel within the error of field measurement (±1-2°). However, for the observed antiformal fold-closure to develop and for uni-directional fluid infiltration to result in one-dimensional (lithology-perpendicular) flow outwards from the axial surface of the antiform on ***both*** limbs, the fold limbs must not be parallel. It is therefore ***assumed*** for the purpose of this study that the angle between the fold limbs (α) is 2° (within

Figure 10.22: Regional Fluid Flow Patterns: The Port Ellen Anticline

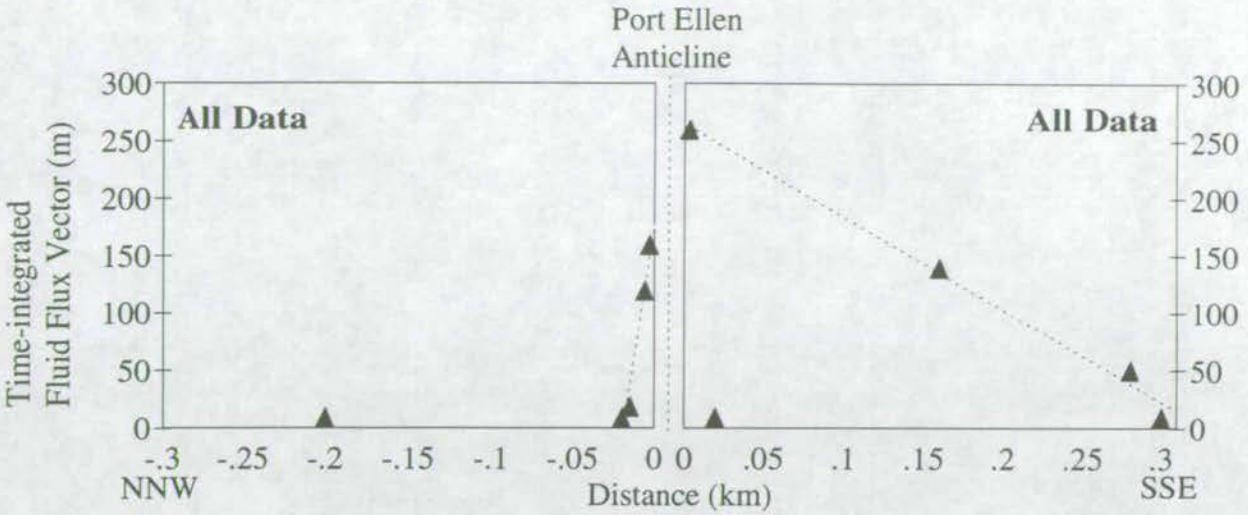

In the above graph, calculated 1-D time-integrated fluid fluxes are plotted as a function of distance from the axial surface of the Port Ellen Anticline.

the limits of error in field measurement). The average attitude of the sills at Port Ellen is 073/45SSE, and therefore the orientation of the fold limbs are given as:

NNW limb: 074/45SSE

SSE limb: 072/45SSE

The attitude of the Port Ellen Anticline is approximately 073/45 SSE and the plunge of the Port Ellen Anticline is assumed to be consistent with the Ardrishaig Anticline and is therefore taken as 45°. Therefore three-dimensional time-integrated fluxes are accurately represented on the horizontal surface (section 10.9.1.3).

(3) Calculation of Three-dimensional Time-integrated Fluid Flux Vectors

It is essential to make an initial assumption regarding the geometry of fluid infiltration detailed in section 10.9.1.3 to facilitate constraint of the two- and three-dimensional time-integrated fluid flux vectors. It is assumed that fluid flow is parallel to the axial surface of the Port Ellen Anticline, as is proven to be the case for the Ardrishaig Anticline (section 10.9.1.2).

Calculation of the 3-D Time-integrated Fluid Flux Vector at Port Ellen

The angles of incidence of the infiltrating fluid with the NNW and SSE limbs of the Port Ellen Anticline (θ_{NNW} and θ_{SSE} respectively) are given by:

$$\theta_{NNW} = \theta_{SSE} = 1° \tag{10.17}$$

By direct analogy with equations 10.7 and 10.8, the three-dimensional time-integrated fluid fluxes on the NNW and SSE limbs of the Port Ellen Anticline are given by:

$$\omega\varphi t_{3-D} = \frac{\omega\varphi t_{1-D,NNW}}{\sin\theta_{NNW}} \tag{10.18}$$

and:

$$\omega\varphi t_{3-D} = \frac{\omega\varphi t_{1-D,SSE}}{\sin\theta_{SSE}} \tag{10.19}$$

Substitution of equations 10.14, 10.15 and 10.17 in equation 10.18 and substitution of equations 10.16 and 10.17 in equation 10.19 gives:

0.000-0.015km NNW of the axial surface of the Port Ellen Anticline:

$$\omega\varphi t_{3\text{-}D,NNW} = 10250 - 5.308\times10^{5}.(d_{NNW}) \quad (10.20)$$

0.020-0.300km NNW of the axial surface of the Port Ellen Anticline:

$$\omega\varphi t_{3\text{-}D,NNW} = 0 \quad (10.21)$$

0.000-0.300km NNW of the axial surface of the Port Ellen Anticline:

$$\omega\varphi t_{3\text{-}D,SSE} = 15200 - 46434(d_{NNW}) \quad (10.22)$$

from which the magnitude of the three-dimensional time-integrated fluid flux may be estimated at any position within 0.3km of the axial surface of the Port Ellen Anticline.

Graphical representation of the 3-D time-integrated Fluid Flux across the Port Ellen Anticline

The resultant three dimensional time-integrated fluid flux profile is constructed on the basis of both of the above approximations in figure 10.23, from which it is evident that fluid is focused through the axial-zone of the Port Ellen Anticline.

10.9.3 Regional Fluid Flow Patterns: The Loch Awe Syncline

The Loch Awe syncline is a major upright D_1 synform. The axis of the Loch Awe Syncline trends SW-NE along the NW seaboard of Knapdale. A thick sequence of volcanics, belonging to the Tayvallich Volcanic Group, are found in the core of the Syncline. The Tayvallich Volcanics are underlain to the SE by a thin limestone unit (the Tayvallich Limestone) and a thick sequence of coarse, psammitic grits (the Crinan Grits). Petrological data from sections 5.5 and 5.6 suggests that the psammites are effectively impermeable to syn-metamorphic fluid infiltration. Therefore, it is

Figure 10.23: Variation in the Calculated Magnitude of the 3-D Time-integrated Fluid Flux Vector as a function of Distance from the Axial Surface of the Port Ellen Anticline.

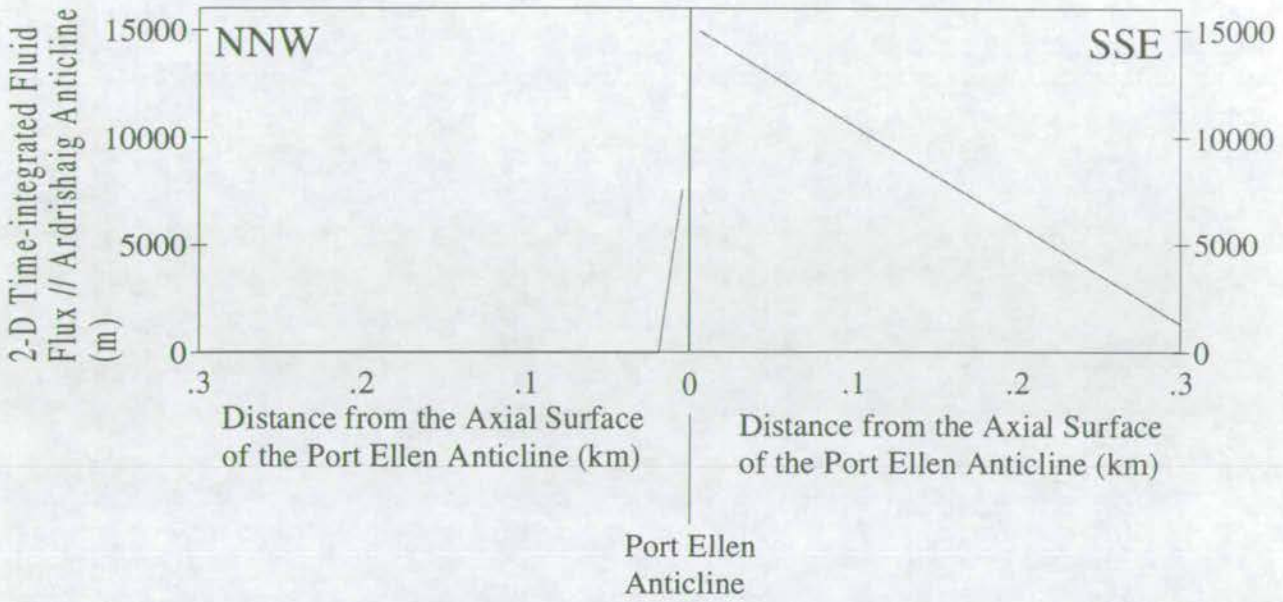

suggested that metabasites within the Loch Awe Syncline were effectively isolated from an upward-migrating fluid.

One-dimensional time-integrated fluid flux vectors, calculated from measured advection of reaction (1) (as described in section 10.3) into the margins of 6 metabasite sills within the Loch Awe Syncline (Carsaig-Bagh an Doide), 5 metabasite sills outwith the Loch Awe Syncline to the NW (Port Ellen), and 10 metabasite sills outwith the Loch Awe Syncline to the SE (Point of Knap-Lochead), are presented in maps B and C (figure 10.10).

Interpretation of One-dimensional Time-integrated Fluid Flux Data

In figure 10.24, calculated time-integrated fluid fluxes are plotted on a profile constructed from the Port Ellen Anticline (NW) to the Ardrishaig Anticline (SE), across the Loch Awe Syncline. The anticipated minimum in calculated time-integrated fluid flux is immediately obvious centred about the axial-zone of the Loch Awe Syncline. It is not possible to say whether this minimum is in response to the impermeability of the largely psammitic host-rock or preferential channelisation of fluid through the axial zone of the Ardrishaig and Port Ellen Phyllites.

Misfitting Data

Two data points clearly misfit this interpretation (A and B on figure 10.24), both of which predict anomalously high one-dimensional time-integrated fluid fluxes, and appear to have developed in response to structural complexities.

Point A describes a broad metabasite exposed on an island, connected to the mainland by a tidal strand at Carsaig (locality 3* in figure 10.9) at which a one-dimensional time-integrated fluid flux in excess of $800 m^3/m^2$ has been measured. This value is almost three times greater than any other one-dimensional time-integrated fluid flux recorded throughout the entire study area. Three potentially contributory complexities are evident at this locality:

Figure 10.24: Regional Fluid Flow Patterns: The Loch Awe Syncline

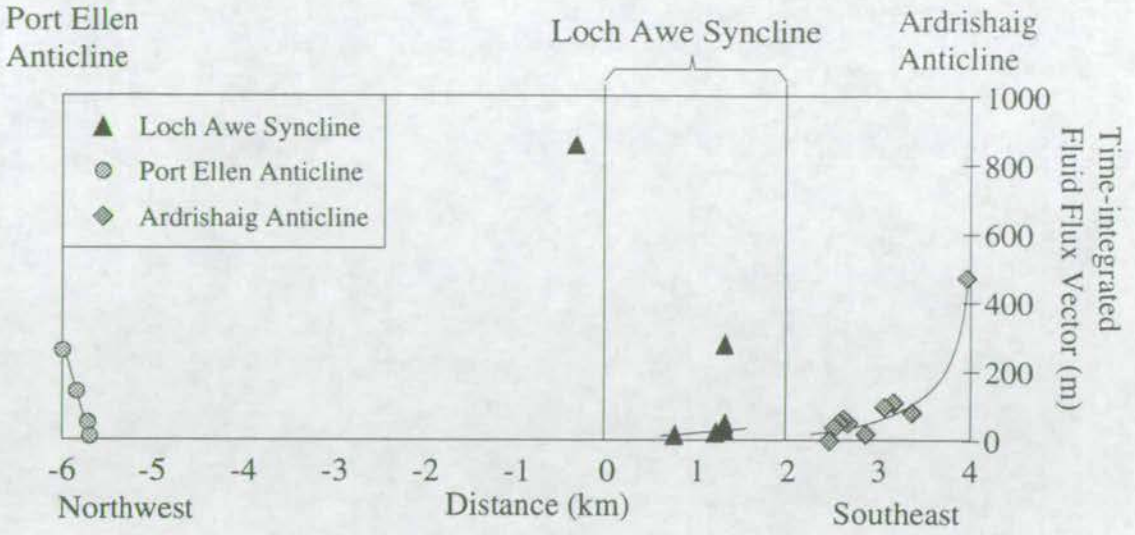

In the above graph, 1-D time-integrated fluid fluxes are plotted as a function of distance from the Loch Awe Synlcine.

Figure 10.25: Regional Fluid Flow Patterns: The Gulf of Corryvreckan

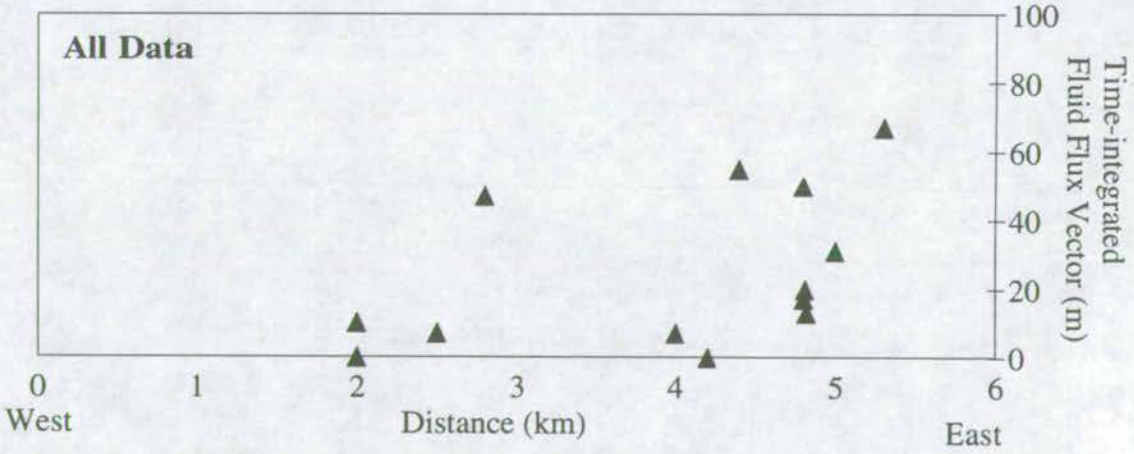

In the above graph, calculated 1-D time-integrated fluid fluxes are plotted as a function of distance from the projected location of the axial surface of the Islay Anticline (approx. 10km NW of Nort Jura)

(1) Reaction 1 is stoichiometrically imbalanced as a result of the major contributory roles of stilpnomelane and albite (figure 10.6 and section 10.4.4). It is therefore fairly probable that the estimated time-integrated fluid flux is incorrect.

(2) The observed outcrop pattern (figure 10.6) is consistent with the sill being isoclinally folded. Furthermore intense pitting and foliation of pseudo-type III metabasite is observed to propagate from the inferred fold hinge. Anomalously high time-integrated fluid fluxes, if applicable, may therefore be developed in response to structurally-induced fluid channelisation.

(3) The observed marginal carbonation is developed in response to retrograde fluid infiltration resulting in progress of a reaction similar to reaction 1 but involving stilpnomelane as a result of a decrease in temperature rather than just an increase in X_{CO_2}.

Point B describes one of a series of three metabasites which are exposed on a rocky headland at Bagh an Doide (localities 23-25 on figure 10.9) where an anomalously high one-dimensional time-integrated fluid flux in excess of $270m^3/m^2$ has been recorded. Metabasites intrude a phyllitic intercalation within the Crinan Grits. The anomalously high time-integrated fluid flux may be in response to focusing of syn-metamorphic fluids through the permeable phyllitic intercalation within otherwise impermeable Crinan Grits.

10.9.4 Regional Fluid Flow Patterns: The Gulf of Corryvreckan

The Gulf of Corryvreckan, reputed by West Highland legend to be the most dangerous stretch of water in Scotland, separates Scarba and Jura. As the tide begins to ebb, water escapes through the gulf at speeds in excess of 15 knots. A whirlpool is developed near to Scarba, but more ominous is the Dorus Mor, a wall of water which rises some 15 to 20 feet as the ebbing tide meets the Atlantic.

A series of metabasic dykes intrude the Islay-Jura Quartzite of Scarba and North Jura. Dykes are near vertical and seldom greater than 10-20m wide. Dykes are generally intensely deformed relative to the host quartzites which are observed to

preserve near-perfect sedimentary structures (figure 5.17). The dykes have been described as feeders for the SW Highland sill complex (Graham & Borradaile 1984). The potential of such dykes as through-going vertical channels for syn-metamorphic fluid to pass through the thick, impermeable Islay-Jura Quartzite is clear, depending, of course on their lateral and vertical continuity.

One-dimensional time-integrated fluid flux vectors, calculated from measured advection of reaction 1 (as described in section 10.3) into the margins of 12 metabasite dykes on the Corryvreckan coasts of Jura and Scarba, are presented in map A (figure 10.10).

Interpretation of One-dimensional Time-integrated Fluid Flux Data

In figure 10.25 , calculated time-integrated fluid fluxes derived from modal and reaction progress data are plotted on a profile constructed across the Islay-Jura Quartzite as a function of distance from the projected location of the Islay Anticline.

In general time-integrated fluid fluxes calculated from the metabasic dykes on Jura and Scarba are both low and variable. However, this does ***not*** reflect narrow type III margins. Instead the contrary is the case. Broad (≈1-2m) type III margins are commonly developed. However these are largely ***symmetrical*** about the sill. Furthermore, layer-parallel type III zones are developed within the dykes. An immediate implication of these observations is that the development of type III assemblages does not result from (layer-perpendicular) advection of reaction 1. Instead the width of the margins merely reflects zones of marginal deformation and shearing through which upward moving fluids are channelled. ***Layer-parallel*** advection of reaction 1 must therefore result in generation of type III assemblages.

Summary of Fluid Infiltration of the Jura-Scarba Dykes

Metabasites define planes of structural weakness within the rigid undeformed Islay-Jura Quartzite. They are subsequently highly deformed, particularly at their margins as a result of marginal shearing (Graham & Borradaile 1984). Therefore upward migrating fluids pass through the largely impermeable Islay-Jura Quartzite

structurally-focused along the highly deformed metabasite margins which would therefore act as fluid *"pipes"*. Increased time-integrated fluid fluxes along sheared sill margins result in the generation of type III assemblages. This is consistent with the width of the margins resulting from deformation ***not*** lithology-perpendicular advection.

10.10 Syn-metamorphic Fluid Infiltration of the SW Highlands Regional Metamorphic Terrain

A time-integrated fluid flux profile was constructed across the SW Highlands. The profile is illustrated in figure 10.26 and was compiled from figures 10.18 10.23, 10.24 and 10.25. Where three-dimensional time-integrated fluid fluxes are available, these are plotted in preference to one-dimensional fluxes. Otherwise one-dimensional fluxes are plotted to represent minimum fluxes.

On the basis of the distance-flux profiles shown in figure 10.26, it is possible to achieve the following objectives, relating to syn-metamorphic fluid-infiltration, which were posed at the outset of this thesis.

(1) To identify regional-scale structural and lithological controls of syn-metamorphic fluid flow.

(2) To investigate the grain-scale mechanisms of syn-metamorphic fluid flow.

(3) To impose meaningful constraints on the volume of mobile fluid present during. regional metamorphism.

(4) To identify a realistic fluid source.

(5) To develop a quantitative model of fluid-infiltration during regional metamorphism of the Dalradian of the SW Scottish Highlands and to establish the wider significance of such a model.

(6) To assess the role of fluid in advecting heat.

Figure 10.26: 3-D Time-integrated Fluid Flux Profile constructed across the SW Highlands

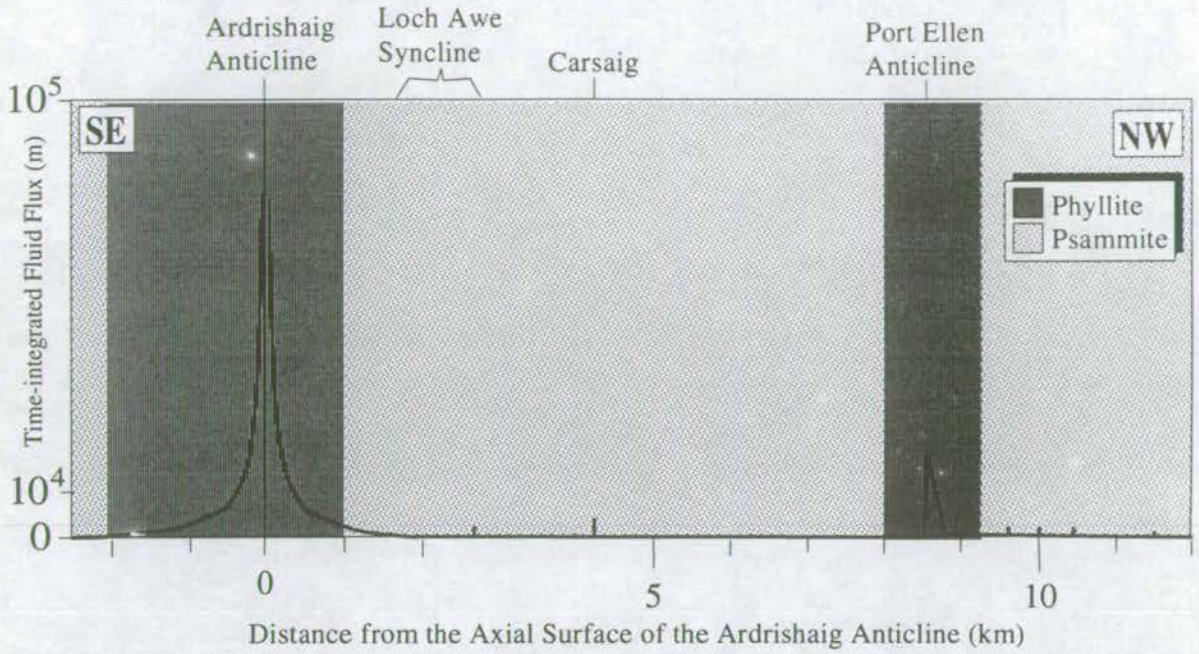

The above graph shows regional variation of the 3-D time-integrated fluid flux. Two major phyllite fluid channels are identified, within the Ardrishaig and Port Ellen Phyllites. Furthermore regions of local channelised flow are developed within the Crinan Grits and Islay-Jura Quartzites, in which fluid is focused along metabasic or phyllitic layers.

10.10.1 Structural and Lithological Controls of Syn-metamorphic Fluid Infiltration

In this sub-section, observations from the time-integrated fluid flux profile shown in figure 10.26 which relates to the structural and lithological controls of syn-metamorphic fluid flow, are stated and discussed.

Observations

(1) Upward fluid flow is channelled through the phyllites.

(2) Within the phyllitic lithologies (Port Ellen Phyllites and Ardrishaig Phyllites), two major (0.6 and 3.0km) channels develop, within which fluid is strongly focused along the axial surfaces of the Ardrishaig and Port Ellen Anticlines. Along the axial surface of the Ardrishaig Anticline the time-integrated fluid flux exceeds 10^4 m^3/m^2.

(3) Within the psammitic lithologies (Crinan Grits and Islay-Jura Quartzite), more localised channelisation of fluid is evident. Fluid is focused on a 5-10m scale along individual phyllitic intercalations or type III metabasic margins. It was only possible to estimate one-dimensional time-integrated fluid fluxes of such locally channelled fluid and therefore the given estimated fluxes of 20-800m^3/m^2 must represent a minimum.

Interpretations

The following interpretations arise from the above observations:

(1) A strong lithological control of syn-metamorphic fluid flow is evident from figure 10.26. Upward transport of syn-metamorphic fluids is strongly focused through the structurally-inclined, phyllitic units (Ardrishaig and Port Ellen Phyllites), despite fluid being driven ***directly upwards*** by buoyancy forces. Furthermore, upwards transport of syn-metamorphic fluids through the psammitic lithologies (Crinan Grits and Islay-Jura Quartzite) is focused through individual phyllitic intercalations or type III metabasite margins. Fluid ***does not*** infiltrate psammites.

(2) Regional folding is a second important control of syn-metamorphic fluid flow. Figure 10.26. Within phyllitic lithologies syn-metamorphic fluid is strongly focused

along the axial surfaces of the Ardrishaig and Port Ellen Anticlines. Hence, upwards transport of syn-metamorphic fluids must be focused through regional-scale antiforms.

(3) Localised shearing and deformation result in intensive focusing of syn-metamorphic fluid flow. In particular, in the Islay-Jura Quartzite, sheared margins of vertical metabasite dykes are inferred to behave as fluid "pipes", through which buoyancy-driven fluids pass through the impermeable psammite. Also, shearing of individual metabasic sills (e.g. Port Cill Maluaig and Traigh Gheighsgeir, localities 37-39 & 5*, map C and localities 12 & 2*, map B in figure 10.9) results in locally anomalous and increased time-integrated fluid fluxes. Furthermore, it is probable that focusing of fluid through the axial-zones of the Ardrishaig and Port Ellen Anticlines is developed in response to shearing and deformation.

An important consideration arising from these interpretations is the need to establish the relative timing of fluid infiltration (and resultant mineral reactions) and shearing deformation. This question was initially posed by Billings & White (1950) regarding the development of type III assemblages at the margins of similar (type I) greenschist facies metabasic dykes emplaced within the Albee Formation, Woodsville Quadrangle, Vermont and New Hampshire, U.S.A.. It is evident, from the above interpretation that shearing deformation pre-dates fluid infiltration within the psammites. However, the situation is not as clear within the phyllites. A spatial correlation between the development of type III assemblages and marginal deformation of metabasites is evident (section 5.3.6). A possibility which must be considered is that marginal-shearing of metabasites, associated with intensified deformation in the axial zones of the Ardrishaig and Port Ellen Anticlines, may enhance permeability of metabasite margins and result in lithology-parallel fluid focusing and development of type III assemblages. However, the observed correlation of reaction and isotope fronts within a broad metabasite sill at Port Ellen (chapter 8) implies that time-integrated fluid fluxes within types I→III assemblages were identical in ***both*** direction and magnitude. Metabasite margins may not

therefore behave purely as "pipes" because there would be no driving force for the observed advection of the isotope front an ***order of magnitude further*** than the reaction front. Therefore, the inferred existence of a lithology-perpendicular component of fluid flow within the Ardrishaig and Port Ellen phyllites is well-founded.

10.10.2 Grain-scale Mechanism of Syn-metamorphic Fluid Flow

In this sub-section, observations from the time-integrated fluid flux profiles shown in figure 10.26, which relate to the grain-scale mechanisms of syn-metamorphic fluid flow, are stated and discussed.

Observations

(1) Psammites are essentially impermeable to syn-metamorphic fluid infiltration.

(2) Calc-phyllites and type III metabasites are permeable to syn-metamorphic fluid infiltration.

(3) Shearing and deformation result in increased permeability.

Interpretations

The following interpretations arise from the above observations:

(1) The observation that psammites are effectively impermeable is consistent with the experimental predictions of Holness (1993), as discussed in sections 2.3.2 and 5.5, that the quartz-fluid-quartz dihedral angle is probably just above the critical value of 60° (***below*** which grain-edge fluid flow is energetically favoured) for a ***CO_2-bearing*** hydrous fluid in the P-T range of SW Highland Dalradian metamorphism (8-10kb, 410-530°C).

(2) The observation that calc-phyllites are permeable is of considerable importance to future experimental studies of grain-scale fluid flow mechanisms. The Ardrishaig and Port Ellen Phyllites are essentially mica-quartz-calcite aggregates. The rock matrices are anisotropic (elongated // D_1-fabric). Therefore, it is probable that addition of mica and/or grain-scale anisotropy result in a significant reduction of the dihedral-angle

and subsequent increase in the connectivity of the pore space. Thus, an essential objective of future experimental studies of grain-scale fluid flow will be to investigate the behaviour of the dihedral angle and the connectivity of pore space in micaceous mineral aggregates and anisotropic matrices.

(3) Increased fluid fluxes associated with localised shearing and deformation may also reflect grain-scale control of fluid flow. An inter-dependence of pore-space connectivity and deformation is possibly inferred.

10.10.3 The Volume of Syn-metamorphic Fluid

In this sub-section, the average time-integrated fluid flux across the entire flux-distance profile illustrated in figure 10.26 is calculated.

Apparent "Infinite" Fluxes

As a result of fitting a logarithmic solution to the fluid flux data, infinite fluxes are predicted in several localities. In figure 10.26, in which the predominant control of fluid flow is assumed to be regional structure, infinite flux is predicted along the axial surface of the Ardrishaig Anticline. This is merely a result of the ***over***-simplification of fitting logarithmic curves to the fluid flux profile. To enable calculation of the mean fluid flux, it is essential to assume the magnitude of the fluid flux where an infinite flux is predicted. A minimum estimate of the flux within the this zone is given by the highest flux observed in the near vicinity of the axial surface of the Ardrishaig Anticline. A value of 10^4 m^3/m^2 is given for Lochead (0.2km NW of the axial surface of the Ardrishaig Anticline) from figure 10.26. This is the assumed flux within 0.2km of the axial zone the Ardrishaig Anticline

Observations

A minimum estimate of the mean syn-metamorphic time-integrated fluid flux Dalradian across the SW Scottish Highlands may be determined from figure 10.26 as follows:

(1) The area under the flux-distance curve shown in figure 10.26 is calculated.

(2) This area is equated with an identical area which is described by a uniform (average) flux.

Calculation

(1) The areas under the flux-distance curve in figure 10.26 is 5×10^6 m^2.

(2) This area may be described by a uniform (average) flux, of $670m^3/m^2$ given that the length of the section is ≈15km.

This value represent a ***minimum*** estimates of the true average time-integrated fluid flux because (i) minimum flux estimates are assumed in zones of apparent "infinite" flux (see above), and (ii) localised channelled fluid fluxes along metabasites and phyllites within the Crinan Grits and Islay-Jura Quartzite are not included in the calculation.

Interpretation

The estimated value of the average time-integrated fluid flux across the SW Highlands, based on the assumption that the predominant control of fluid flow is regional-structure (figure 10.26) is $670m^3/m^2$. This is considerably smaller than time-integrated fluid fluxes estimated from a number of recent studies (e.g. Ferry 1988, Ferry 1992). Ferry (1988) estimated fluid:rock ratios of ≈1.0 during regional metamorphism of the Albee, Giles Mountain and Amonoosuc Volcanics, New England and Ferry (1992) measured time-integrated fluxes in the excess of 2.5×10^3 m^3/m^2 (section 2.3.1) during regional metamorphism of the Waits River Formation, Eastern Vermont. It has proven problematic to establish a physically realistic source reservoir for such large quantities of fluid (section 2.2.3), and therefore the low mean fluid fluxes estimated in this study are encouraging, particularly with a view to identifying the fluid source reservoir.

10.10.4 The Source of Syn-metamorphic Fluid

In this sub-section, the source of syn-metamorphic fluid in the Dalradian of the SW Highlands is evaluated on the basis of the fluid flow morphology described by figure 10.26 and the average fluid flux estimated in section 10.10.3.

Theory

A number of authors have suggested the potential of metamorphic devolatilisation reactions as an important source of syn-metamorphic fluids (e.g. Walther & Orville 1982, Graham *et al.* 1983, Bickle & Baker 1990a). Walther & Orville (1982) attempted to quantify the volumetric contribution of metamorphic devolatilisation reactions to the deep-crustal fluid budget. They calculated that an average pelite may lose a maximum of 5 wt.% (≡ 12 vol.% at 5kb, 500°C) fluid as a result of prograde devolatilisation reactions, much of which will be liberated by chlorite beak-down at the garnet isograd.

Calculation

The minimum thickness of underlying pelites (t) required to undergo metamorphic devolatilisation in order to generate a given time-integrated fluid flux ($\omega\varphi t$) or fluid:rock ratio (F:R) assuming that total devolatilisation liberates ≈12vol.% fluid (F:R=0.12) is given by:

$$t = \frac{wjt}{0.12}, t = \frac{F{:}R\ V}{0.12} \qquad (10.23)$$

where V = total volume of the infiltrated rock. Equation 10.23 is applied to the calculated fluid:rock ratio in Northern New England (Ferry 1988), and to calculate average time-integrated fluid fluxes in E. Vermont (Ferry 1992) and the SW Highlands (this study). Calculation details are tabulated in table 10.7.

Table 10.7: Calculation of minimum thicknesses of underlying pelites which are required to undergo complete metamorphic devolatilisation

Study Area	Reference	$\omega\varphi t$ / F:R, V	t
N. New England	Ferry (1988)	F:R = 1.0, V = 10km	83km
E. Vermont	Ferry (1992)	$\omega\varphi t = 2.5\times10^3$ m^3/m^2	21km
SW Highlands	(this study)	$\omega\varphi t = 670$m^3/m^2	5.6km

Interpretation

Regional metamorphism in New England was at approximately 6-7kb (Ferry 1988, 1992) and regional metamorphism of SW Highlands was at 8-10kb (section 5.3.4). Therefore Acadian Metamorphism (New England) was at about 20km depth and Dalradian metamorphism was at about 30km depth (assuming 3km≡1kb). Crustal thicknesses in New England were about 40km (Ferry 1988) and crustal thicknesses in the SW Highlands were about 60-70km (assuming an orogenic thickness). The thickness of underlying pelites are unlikely to be sufficient to account for ***predicted*** average fluid volumes in all but the SW Highlands. Therefore, metamorphic devolatilisation reactions within underlying phyllites are likely to be a viable source of syn-metamorphic fluid ***only*** in the SW Highlands. Two possibilities exist. Either an additional fluid source is present in New England or the models are flawed. However, it is shown in section 2.2.3 that metamorphic devolatilisation at depth in the crust is the only viable source of hydrous syn-metamorphic fluids. It may thus be concluded that the reaction and isotope front advection models are presently the most meaningful quantitative approaches to interpreting syn-metamorphic fluid infiltration.

10.10.5 A Quantitative Model of Syn-metamorphic Fluid Infiltration in Dalradian rocks of the SW Highlands

In this sub-section a quantitative-model describing syn-metamorphic fluid infiltration affecting Dalradian rocks of the SW Highlands, based on the time-

integrated fluid flux profile constructed across the SW Scottish Highlands (figure 10.27), is presented and examined critically.

Model of Syn-metamorphic Fluid Infiltration

The proposed model of syn-metamorphic fluid infiltration affecting the Dalradian of the SW Scottish Highlands is presented in figure 10.27 and outlined as follows.

(1) Fluid Source

Syn-metamorphic hydrous fluids were derived by devolatilisation reactions at depth in the crust. Much of the CO_2 uptake may have been the result of oxidation of graphite (Graham *et al.* 1983).

(2) Driving Force of Fluid Flow

Upwards movement of syn-metamorphic fluid was buoyancy-driven.

(3) Fluid Flow Patterns

Upwards fluid flow was channelled through (permeable) metabasic and phyllitic units and deflected by (impermeable) psammitic units. Within phyllitic units, large volumes of fluid flowed pervasively upwards, focused at least partly through the axial zones of antiforms. Within psammitic units, upwards fluid flow was locally channelled through narrow layers of intense deformation associated with metabasite emplacement or phyllitic intercalation.

(4) Effects of Syn-metamorphic Fluid Flow

Syn-metamorphic fluid fluxes are clearly sufficient to drive carbonation mineral reactions in metabasites and to transport isotopic tracers. However it is of considerable geological importance to determine whether fluxes were sufficient to

Figure 10.27: Model of Syn-metamorphic Fluid Flow in the SW Scottish Higlhands

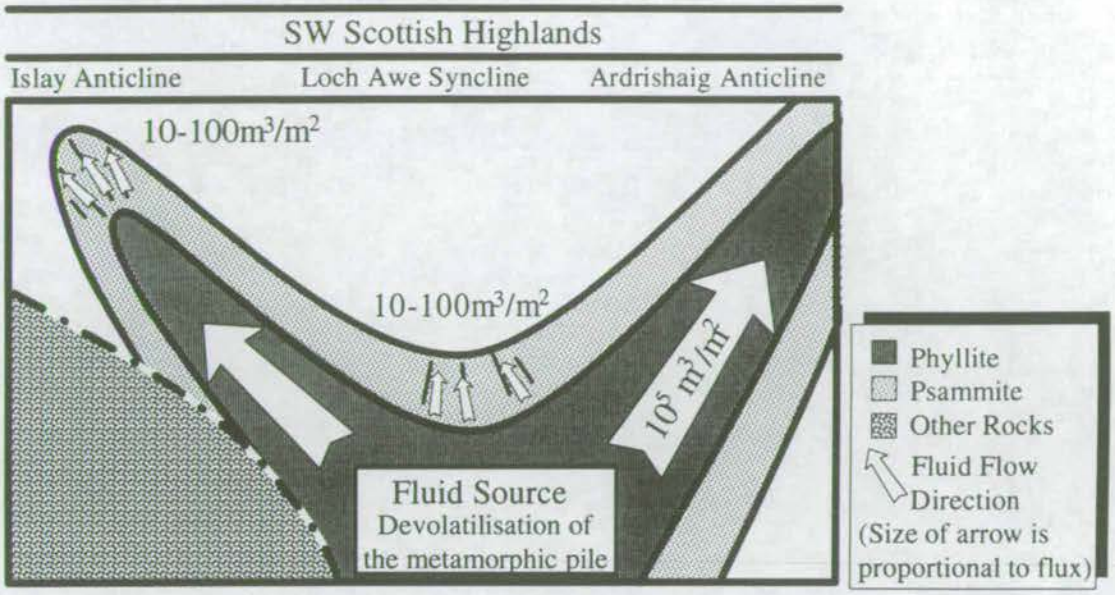

Figure 10.28: Dependence of Transport of Heat and Oxygen on the Fluid Flux Rate
(adapted from Bickle & McKenzie 1987)

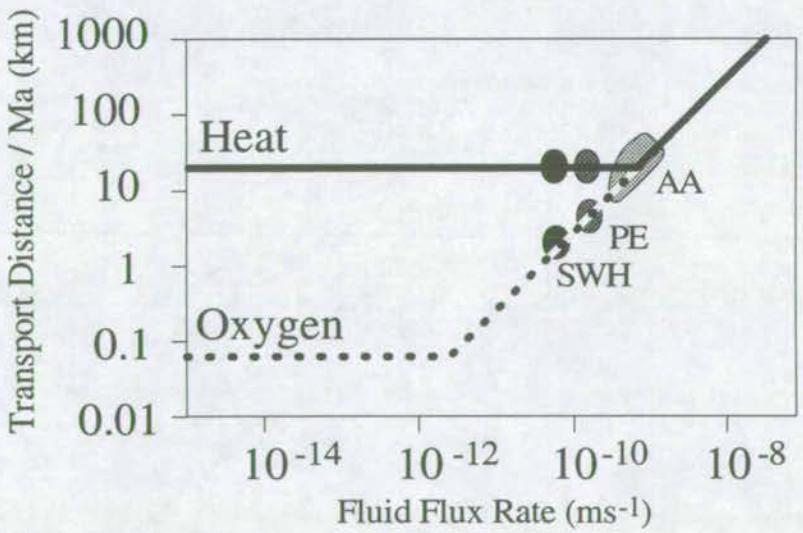

AA = Ardrishaig Anticline
PEA = Port Ellen Anticline
SWH = South West Highlands

advect heat (particularly in zones of high fluid fluxes: e.g. the axial-zone of the Ardrishaig Anticline).

Figure 6 in Bickle & McKenzie (1987) describes the relationship between fluid flux rate ($\omega\varphi$) and the transport distances of heat and chemical components per 1Ma. Regions of diffusion of heat and matter, diffusion of heat and advection of matter and advection of both heat and matter are distinguished. The plot is redrawn in figure 10.28 and calculated values (listed in table 10.8) of $\omega\varphi$ (calculated from $\omega\varphi t$ by assuming $t \leq 10Ma$[12]).

Table 10.8: Fluid Flux Rates at specific localities within the SW Highlands

Locality	**$\omega\varphi t$ (from figure 10.25)**	**$\omega\varphi$ (assuming $t \leq 10Ma$)**
Axial Zone of Ardrishaig Anticline	10^4-10^5 m^3/m^2	10^{-9}-10^{-8}
Mean SW Highland Flux	670 m^3/m^2	10^{-10}

It is evident from figure 10.26 that ***only*** fluid flux rates estimated for the axial-zone of the Ardrishaig Anticline are likely to be sufficient to advect heat. However, extensive advection of a compatible solute (e.g. oxygen) is possible throughout much of the SW Highland phyllites. This conclusion may be tested by examining calcite stable isotope data obtained from the Ardrishaig Phyllites. Carbonate $\delta^{18}O$ data from a 30m (lithology-perpendicular) traverse of calc-phyllites adjacent to a broad metabasite sill at Rubha Garbh (GR753 767) are listed in table 10.9.

Table 10.9 $\delta^{18}O$ Data from Rubha Garbh SW Highland Phyllites

Sample	**Locality**	**Lithology**	**Assemblage**	**$\delta^{18}O$**
RG3	Rubha Garbh	Calc-phyllite	Qz-Chl-Mu-Cc-Ab	**12.42**
RG4	Rubha Garbh	Calc-phyllite	Qz-Chl-Mu-Cc	**12.80**
RG5	Rubha Garbh	Calc-psammite	Qz-Chl-Mu-Cc	**12.68**
RG6	Rubha Garbh	Calc-psammite	Qz-Chl-Cc-Mu-Ab	**12.34**
77-59	Rubha Garbh	Calc-psammite	Qz-Cc-Chl-Ab-Mu	**12.59**
Ag-7-4	Rubha Garbh	Calc-phyllite	Qz-Chl-Cc-Mu-Ab	**11.94**
Ag-7-5	Rubha Garbh	Calc-phyllite	Qz-Chl-Cc-Mu-Ab	**11.56**

[12]The maximum duration of Dalradian metamorphism is estimated to be ≈10Ma on the basis of zircon dating (section 3.4.4).

Carbonate $\delta^{18}O$ are listed for samples RG3, RG4, RG5, RG6, 77-59, Ag-7-4 and Ag-7-5 which were collected on a 30m traverse of calc-phyllites and calc-psammites at Rubha Garbh and found to vary by a mere 1.3‰.

It is evident from table 10.9, that carbonate $\delta^{18}O$ varies by $\pm\approx 0.5$‰. It is likely therefore that regional homogenisation of $\delta^{18}O$ has occurred within the Ardrishaig Phyllites. A useful future objective pertaining from these results would be to construct a regional-scale traverse of $\delta^{18}O$ across the Ardrishaig Phyllites in the view to test the assumed fluid flow geometries (i.e. structural control >> lithological control and vice versa, section 10.9.1) and permeabilities in relation to lithological variations. The zone of highest time-integrated fluid fluxes should coincide with the zone of most extensive isotopic modification. Furthermore, a small, but potentially significant thermal perturbation may be developed in this zone. There is no documented petrological evidence defining the existence of such a zone however the axial region of the Ardrishaig Anticline is very poorly exposed and such a zone if present will be narrow and may easily have been missed.

11. QUANTITATIVE MODELLING AND REGIONAL MAPPING OF FLUID FLOW:

Post-metamorphic Veining and Porphyroblast Growth

11.1 Introduction

This chapter presents a qualitative investigation of the development of dolomite and pyrite-bearing veins and ankerite and pyrite porphyroblasts in response to post-metamorphic fluid infiltration. In the first section the appearance and association of dolomite veining and ankerite porphyroblast is discussed. Subsequently the spatial distribution of dolomite veining and ankerite porphyroblast growth is investigated. Finally, pyritisation is reviewed briefly in the context of its spatial association with dolomite veining and ankerite growth. It is concluded that veins and porphyroblasts developed in response to a single phase of retrograde fluid infiltration under different uplift conditions and/or in different lithologies.

11.2 Dolomite-veining and Ankerite Porphyroblasts

Retrograde dolomite/ankerite develops in two distinct parageneses throughout the Dalradian of the SW Highlands. Dolomite/ankerite is developed in association with K-feldspar ± quartz ± chlorite in veins, and as disseminated porphyroblasts in association with K-feldspar, muscovite, paragonite and quartz in metabasites and calc-phyllites.

Retrograde Dolomite ± K-feldspar ± Quartz ± Chlorite Veining

Retrograde dolomite ± K-feldspar ± quartz ± chlorite veining is widespread throughout the Dalradian of the SW Scottish Highlands. The significance of these veins as monitors of retrograde fluid infiltration was initially recognised by Graham *et al.* (1983) and developed by Fein *et al.* (1993).

Graham *et al.* (1983) observed the stabile assemblages: K-feldspar + dolomite and K-feldspar + chlorite, for which THERMOCALC (Powell & Holland 1988) predicts temperatures below 300°C. Furthermore, veins cross-cut D_1-D_4 structures. Veining must therefore record a third phase of fluid infiltration during retrogression.

Fein *et al.* (1993) undertook a comprehensive study of retrograde fluid infiltration of the Loch Tay Limestone. They determined that the fluid was a CO_2-poor hydrous brine, and that the temperature of infiltration was in the range 200 to 400°C, by analysis of fluid inclusions. Furthermore, they proposed that the grain-scale mechanism of fluid infiltration was either (i) grain-edge flow or (ii) dissolution of host calcite. The study of Fein *et al.* (1993) is discussed in section 4.2.3.

Retrograde Ankerite Porphyroblast Growth

Large, euhedral, irregular and skeletal ankerite porphyroblasts are observed to over-grow type III metabasite and calc-phyllite assemblages. Ankerites are generally observed to replace pre-existing calcite (figure 5.14 and section 5.3.2.5), and to over-grow D1-fabrics (figure 5.6 and section 5.3.2.5). Furthermore, ankerite-calcite pairs record temperatures below 300°C on the basis of the calcite-dolomite-ferrodolomite geothermometer of Annovitz & Essene (1987) (section 5.3.2.5). For these reasons, ankerite porphyroblasts are implied to have developed in response to a third, retrograde phase of fluid infiltration.

Association of Dolomitic Veins and Ankerite Porphyroblasts

Both dolomitic veins and ankerite porphyroblasts are inferred to have developed as a result of retrograde fluid infiltration. Both dolomitic veining and ankeritic porphyroblast growth evidently post-dated both D_1-D_4 deformation and peak metamorphism. Furthermore, dolomitic veining and ankerite porphyroblast growth occurred at similar temperatures in the range 200-400°C. In this study the association of dolomitic veining and ankerite porphyroblast growth was rigorously demonstrated on the basis of field, optical and stable isotopic interpretation. The

approaches are detailed in section 5.3.2.5. It is therefore sufficient to summarise the critical observations:

(1) Ankerite porphyroblast growth is regularly associated with development of a blebs, lenses and veinlets of dolomite/ankerite + quartz + chlorite ± K-feldspar.

(2) Aggregates of ankerite porphyroblasts are observed to originate in veinlets (figure 5.5).

(3) Dolomite-veining is associated with anomalously high $\delta^{18}O$ signatures. Similarly high $\delta^{18}O$ signatures are reflected in ankerite-porphyroblast bearing phyllites.

For these reasons, it was concluded that dolomite-bearing veins and ankerite porphyroblasts developed in response to the same episode of retrograde fluid infiltration.

Fracture-controlled vs. Pervasive Fluid Infiltration

Dolomite-bearing veins must have developed in response to fracture-controlled fluid infiltration, whereas ankerite porphyroblasts must have developed in response to pervasive infiltration. It is of immediate concern to establish the reasons for which pervasive and fracture-controlled flow may have developed as a result of the same phase of fluid infiltration.

Fracture-controlled infiltration is likely to have occurred at higher crustal levels and/or in different lithologies than pervasive infiltration. It remains to investigate the spatial distribution of areas of intense dolomitic veining and areas of extensive ankerite porphyroblast growth, so as to evaluate any spatial relationship with the uplift history of the terrain.

11.3 Spatial Distribution of Dolomitic Veining and Ankerite Porphyroblast Growth

Figure 11.1 describes the spatial distribution of areas of intense dolomitic veining and areas of intensive ankerite porphyroblast growth. Figure 11.1 also

Figure 11.1: Distribution of Retrograde Fluid Alteration

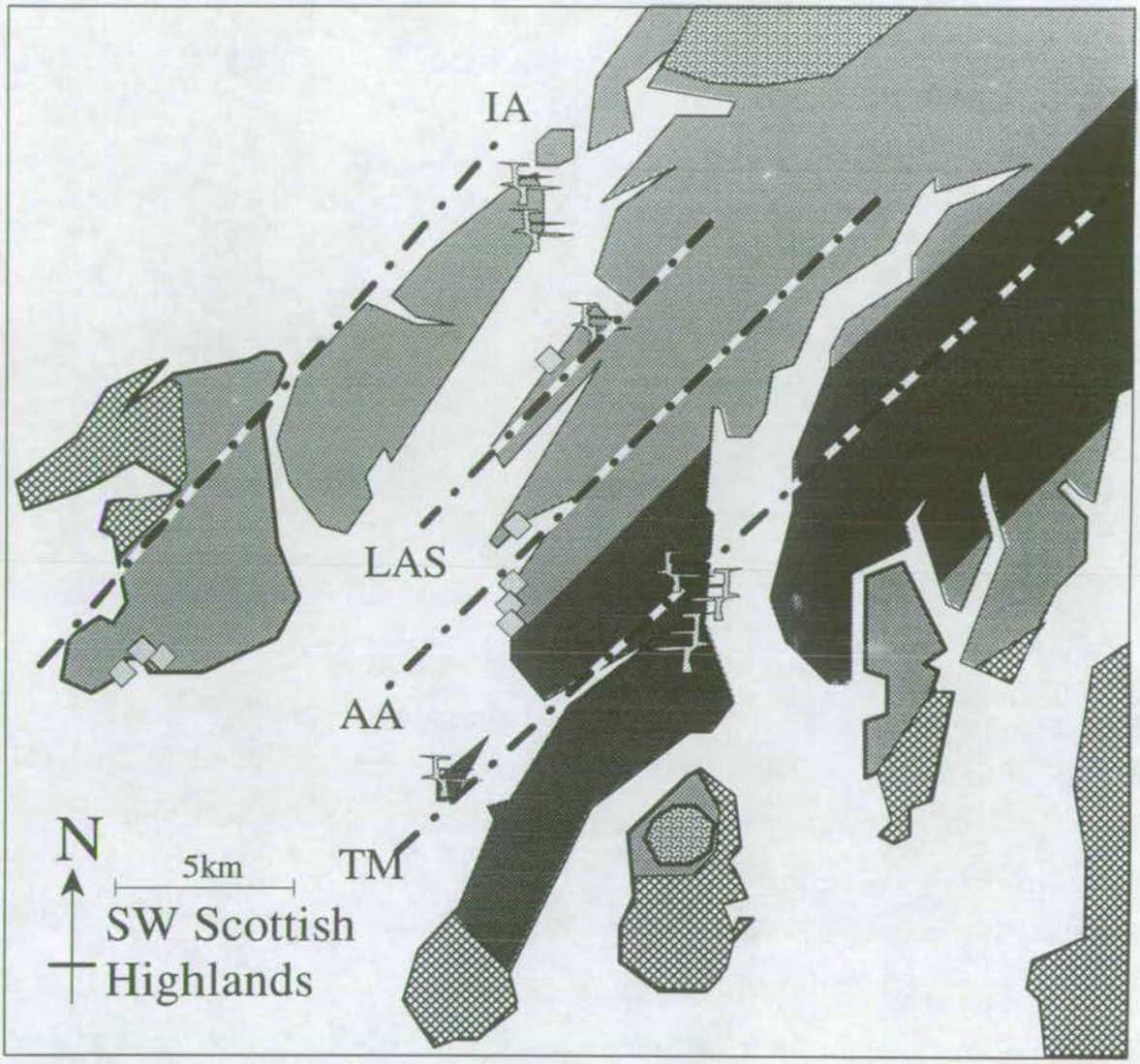

Biotite Zone

Garnet Zone

Retrograde Dol-Qz-Chl Veining

Retrograde Ank-Porphyroblast Growth

IA Islay Anticline

LAS Loch Awe Syncline

AA Ardrishaig Anticline

TM Tarbert Monoform

Additional ornamentation is explained in figure 3.2.

includes the distribution of metamorphic zones and the major deformational fold structures.

Observations

Dolomite veining is most extensively developed in regions of higher-grade metamorphism particularly in garnet-zone rocks in the vicinity of the Tarbert Monoform, although veining is not precluded from regions of lower grade. Ankerite porphyroblast growth is most extensively developed in regions of lower grade, particularly in biotite zone calc-phyllites and metabasites of the Ardrishaig Phyllites, Crinan Grits and the Port Ellen Phyllites. For example mafics at Southbay, near Tarbert (GR869 710) show dolomite veining whereas mafics at Carsaig (GR729 878) and Port Ellen (GR366 447) show pervasive growth of ankerite porphyroblasts.

Interpretations

The observations that fracture-controlled dolomite veins predominate in ***higher-grade*** garnet-zone rocks, whereas pervasive ankerite porphyroblast growth predominates in the ***lower-grade*** biotite-zone rocks is non-intuitive. This apparent problem may be resolved by considering the tectonic evolution of the Dalradian rocks of the SW Scottish Highlands. D_4 deformation resulted in rapid uplift with subsequent formation of the Cowal Antiform and the Tarbert and Ben Ledi Monoforms. The Loch Awe Syncline, although tightened during D_4 deformation, was effectively "anchored" by the dense Tayvallich Volcanics and associated sill complex, and therefore experienced much slower uplift (Dymoke 88). Therefore, garnet-zone rocks, which presently span the Cowal Antiform, underwent considerably more rapid uplift than biotite-zone rocks within the Loch Awe Syncline (figure 11.2). Therefore garnet-zone rocks may have reached lower temperatures more rapidly than the biotite-zone rocks. Retrograde fluid infiltration post-dated D_4 deformation, by which time the garnet-zone rocks were at lower temperatures and may therefore have undergone fracture-controlled infiltration whereas the biotite-zone rocks were at higher temperatures and may therefore have undergone pervasive

Figure 11.2: Differential Uplift Rates during D_4 in the Dalradian

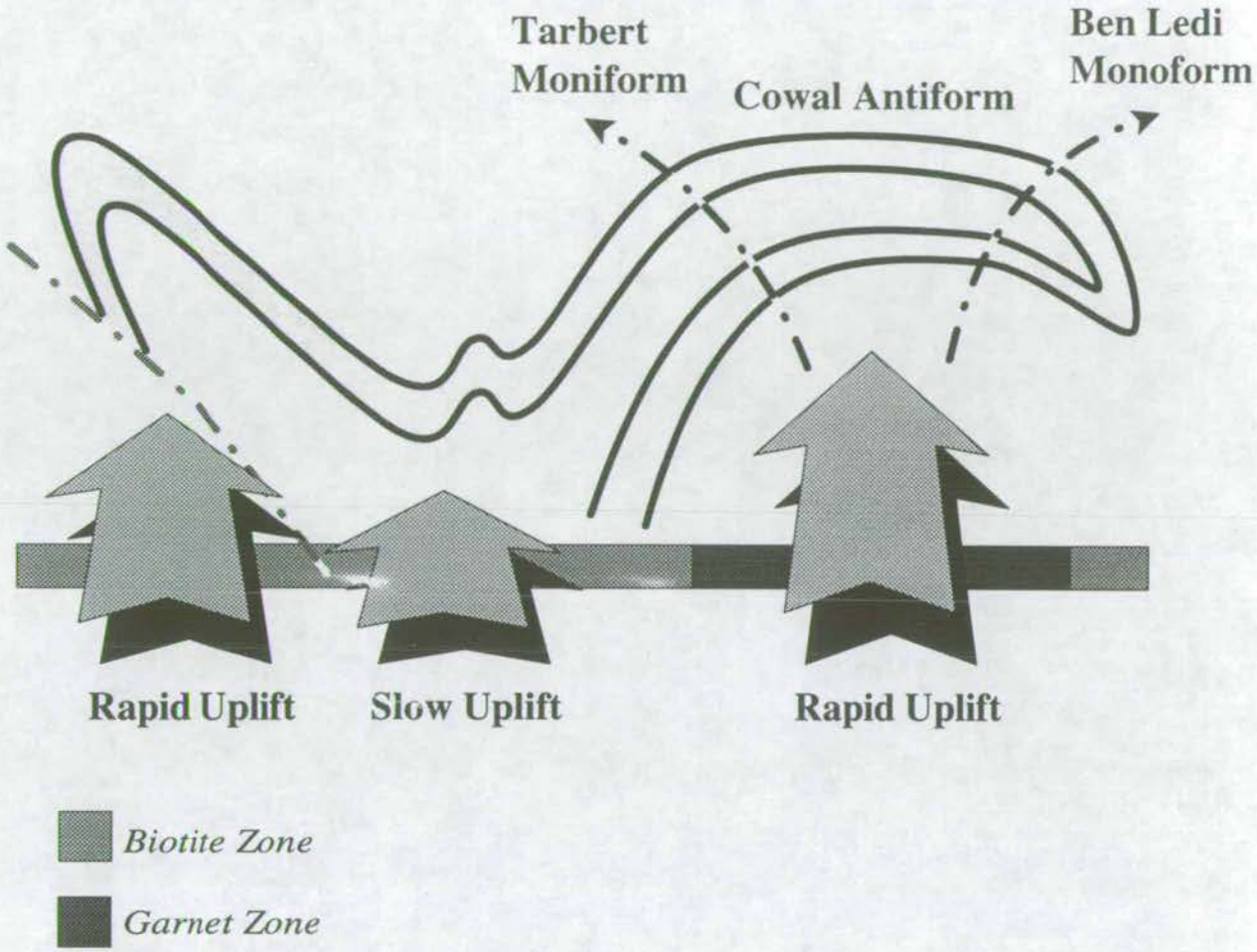

fluid infiltration. Furthermore, the distribution of ankerite porphyroblasts may imply a lithological control. Ankerites are generally observed in phyllites, schists and type III metabasites but rarely observed in psammites. Similar lithological controls to those which affected syn-metamorphic fluid infiltration (section 10.10.1) are inferred.

11.4 Pyritisation

Pyrite is a common accessory phase throughout the Dalradian rocks of the SW Scottish Highlands. It is most commonly found within metabasite lithologies, although its presence has been recorded within phyllites and marbles. Within metabasite sills and dykes, pyrite either occurs as small veinlets or as disseminated grains developed throughout the entire sill/dyke or concentrated in a narrow band at one or other margin.

Parageneses of Pyrite

In thin section, disseminated pyrite is observed to overgrow pre-existing D_1 and D_4 fabrics and pyrite veins are observed to cross-cut individual metamorphic mineral grains. It is likely, therefore that pyritisation is also associated with later retrograde fluid infiltration.

Spatial Distribution of Disseminated Pyrite and Pyrite Veins

The spatial distribution of areas of extensive growth of disseminated pyrite and areas of intensive pyrite veining is illustrated, superimposed on the distribution patterns of dolomite-veining and ankerite porphyroblasts, in figure 11.3.

From figure 11.3, pyrite is developed as disseminated grains in the lower grade biotite zone rocks of West Knapdale and SE Islay and as small veins and veinlets within the higher grade biotite zone rocks of North Jura. The spatial distribution of areas of pyritic veining and areas of disseminated pyrite growth mimics the distribution of areas of ankeritic veining and areas of ankerite porphyroblast growth. It is likely therefore that pyritisation is also developed in response to the same phase of retrograde fluid infiltration and that the distribution

Figure 11.3: Distribution of Retrograde Fluid Alteration

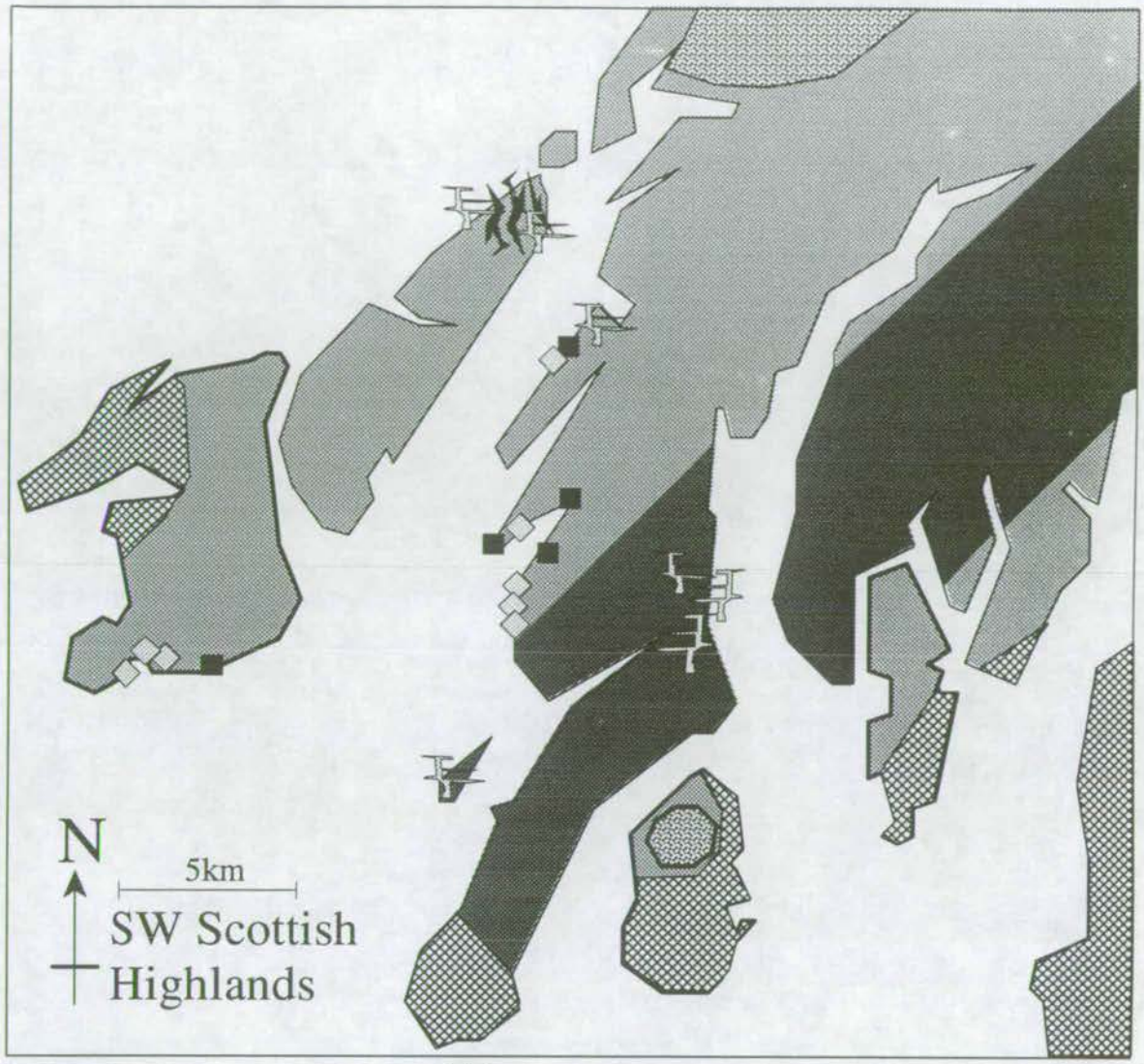

Biotite Zone

Garnet Zone

Retrograde Dol-Qz-Chl Veining

Retrograde Ank-Porphyroblast Growth

Retrograde Pyrite Veining

Retrograde Disseminated Pyrite Growth

Additional ornamentation is explained in figure 3.2.

Figure 11.4: MgO/(MgO+FeO) for Chlorite across a Pyritisation Front at Point of Knap

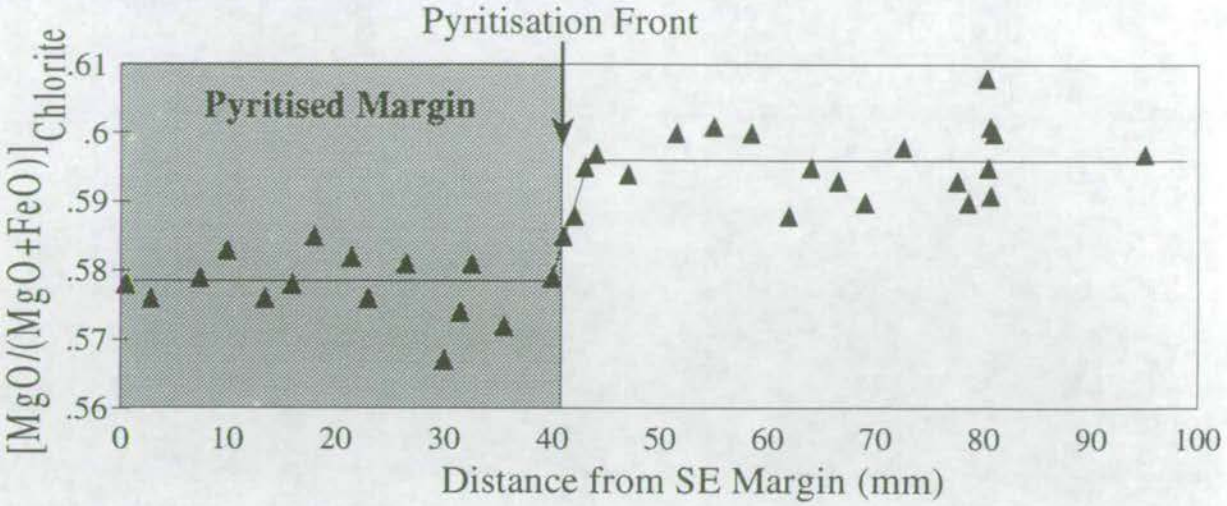

pattern of the distinct pyrite parageneses again reflects differential uplift described in figure 11.2.

Pyrite-enriched Metabasite Margins

Pyrite enriched metabasite margins were identified at Point of Knap, Lochead and Sgeir Figheadair where they were consistently found to be less than 1m wide. Minimal associated compositional variation was identified by XRF analytical techniques (appendix 8). At the Point of Knap, a detailed traverse showing the variation of MgO/(MgO+FeO) of chlorite was constructed across a visibly apparent pyritisation "front" and revealed a subtle increase in FeO content of chlorites in the pyritised margin (figure 11.4). It is likely therefore that pyrite formation was induced by addition of Fe and H_2S from the infiltrating fluid phase.

11.5 Summary

A third phase of fluid infiltration has been identified as having affected the Dalradian of the SW Scottish Highlands. Fluid infiltration during retrogression, at temperatures of 200-400°C resulted in fracture-controlled infiltration-driven dolomite ± K-feldspar ± quartz ± chlorite and pyrite veining and pervasive-infiltration driven growth of ankerite porphyroblasts and disseminated pyrites. The spatial distribution of regions of pervasive and fracture-controlled infiltration was controlled by differential uplift rates during D_4 deformation and host lithology.

CHAPTER 12

CONCLUSIONS

12. CONCLUSIONS

12.1 Layout of Conclusions

To conclude this study, the initial objectives are re-iterated, the project strategy is reviewed, and a semi-quantitative model of deep-crustal fluid flow in the Dalradian of the SW Scottish Highlands is presented.

12.2 Thesis Objectives

The overall objective of this thesis was to further our understanding of fluid infiltration in the crust. More specifically, the aims of the thesis were:

(1) To develop a practical approach by which recent quantitative one-dimensional fluid flow models may be applied in a regional metamorphic terrain.

(2) To apply this approach to measure one-dimensional time-integrated fluid fluxes.

(3) To map regional fluid flow and identify regional fluid flow patterns.

(4) To attempt to quantify for the first time three-dimensional time-integrated fluid fluxes.

(5) To evaluate (i) structural, (ii) lithological, and (iii) grain-scale controls of crustal fluid flow.

(6) To quantify the fluid volume and to identify the fluid source.

(7) To assess the role of fluid flow in heat advection during metamorphism.

(8) To develop an internally-consistent model of crustal fluid flow.

12.3. Project Strategy

In order to achieve the above objectives the following theoretical and practical strategies have been adopted:

(1) A suitable modelling approach for the quantification of fluid flow was selected on the basis of the following criteria (chapter 2):

(i) The model should offer ***meaningful*** constraint on the magnitude ***and*** direction of fluid flow.

(ii) The boundary conditions of the model should be satisfied.

(iii) The model assumptions should be generally applicable.

(iv) The model should have the potential of constraining fluid flow in three-dimensions.

The one-dimensional models of Bickle & McKenzie (1987) and Bickle & Baker (1990b), which calculated one-dimensional time-integrated fluid fluxes from the advection distances of isotope and mineral reaction fronts, satisfy the above criteria and were subsequently implemented in this study.

(2) A suitable field area was selected for regional-scale mapping of fluid flow on the basis of the following criteria (chapters 3, 4 & 5):

(i) The study area should contain abundant suitable marker lithologies which satisfy the boundary conditions of the above fluid flow models. Specifically, suitable permeable marker lithologies should be isotopically and mineralogically distinct from the surrounding rock, such that identifiable isotope and reaction fronts could develop.

(ii) The study area should be well-characterised in terms of structure, deformation and metamorphism.

(iii) The timing of successive phases of fluid infiltration should be constrained relative to deformation and metamorphism.

The Dalradian of the SW Scottish Highlands was found to satisfy all of the above criteria and abundant greenschist facies metabasic sills and dykes were identified as suitable marker lithologies. Three phases of fluid infiltration may be distinguished, the timing of which (relative to deformation and metamorphism) may be unambiguously constrained. Prior to metamorphism, SW Highland rocks underwent spilitisation, associated with redistribution of Na and Ca in basic lithologies. During metamorphism, SW Highland metabasites were infiltrated by CO_2-bearing hydrous fluid which resulted in measurable advection of reaction and isotope fronts. During retrogression and uplift, SW Highland rocks underwent a third phase of fluid

infiltration which resulted in fracture-controlled dolomitic and pyritic veining and pervasive growth of ankerites and pyrites.

(3) The nature of pre-, syn- and post-metamorphic phases of fluid infiltration was interpreted on the basis of field, petrological and geochemical observations, as outlined below:

(i) Pre-metamorphic phase: A tentative qualitative interpretation of the flow mechanisms and source of pre-metamorphic fluid flow was posed on the basis of detailed bulk-chemical profiles, identifying Na-Ca redistribution "fronts".

(ii) Syn-metamorphic phase: A thorough quantitative interpretation of the structural, lithological and grain-scale controls of syn-metamorphic fluid flow was established as follows:

- A detailed modal profile was constructed across a well-exposed metabasic sill at Port Cill Maluaig, West Knapdale, from which the reaction:

$$\mathbf{3Am + 2Ep + 10CO_2 + 8H_2O = 3Chl + 10Cc + 21Qz} \qquad \mathbf{(1)}^{1}$$

was identified. The morphology of the reaction front profile was examined to form criteria on which to base measurement of reaction front advection (chapter 6). Furthermore, a simple geochemical technique for rapid measurement of wt.% calcite ($\propto$ reaction progress) was tested, by comparison with this profile and found to be consistent (chapter 7).

- Time-integrated fluid fluxes were calculated independently using the reaction and isotope front advection models, in a broad metabasic sill at Port Ellen, Islay. The composition of the infiltrating fluid was assumed to be controlled by the mineral assemblage of the host calc-phyllite. Predicted time-integrated fluid fluxes were consistent. Therefore, the models were assumed to be generally applicable, the assumed fluid composition was taken to be generally representative, and the timing of isotopic alteration is shown to be temporally related to syn-metamorphic reaction front advection (chapter 8).

---

[1]Reaction 1 is included in a reference card at the back of the thesis.

• One-dimensional (lithology-perpendicular) time-integrated fluid flux vectors were calculated from measured advection of reaction 1 into the margins of greenschist facies metabasites. The direction of fluid flow was identified in three dimensions from one-dimensional flux measurements from a suite of metabasites in a variety of orientations implementing simplified vector mathematical approach. A regional, three-dimensional time-integrated fluid flux profile was constructed across the SW Highlands terrain, from which the lithological and structural controls of fluid flow were evaluated, the volume of crustal fluids was estimated and the fluid source was identified.

(iii) Post-metamorphic phase: A qualitative interpretation of the post-metamorphic (fracture-controlled) dolomitic and pyritic veining and (pervasive) porphyroblastic ankerite and disseminated pyrite growth was presented on the basis of petrological, field and experimental observations and geothermometric constraints.

A semi-quantitative model of deep-crustal fluid flow in the Dalradian of the SW Scottish Highlands arises from this study and is presented in the following section.

12.4 A Quantitative Model of Deep-crustal Fluid Flow in the Dalradian of the SW Scottish Highlands

Three phases of fluid infiltration may be distinguished which have affected the chemical, mineralogical or isotopic structure of the Dalradian rocks of the SW Scottish Highlands. These are, in chronological order; (1) pre-metamorphic spilitisation, (2) syn-metamorphic pervasive fluid-infiltration, and (3) post-metamorphic fracture-controlled dolomite-Kfeldspar-quartz-chlorite and pyrite veining and pervasive ankerite porphyroblast and disseminated pyrite growth. The model interpretation arising from this thesis is presented below.

Pre-metamorphic Spilitisation

During crustal extension in the early stages of ensialic rifting of the Palaeozoic super-continent, the Tayvallich Volcanics were erupted at the sea-floor

and the associated basic sills were emplaced into consolidating sub-seafloor sediments. The heat associated with volcanism and sill emplacement drove convection of sea-water to shallow crustal depths. Infiltration of sea-water induced Ca/Na exchange reactions (spilitisation) which were most extensive at the centres of the basic sills. Their spatial distribution, within individual sills, may have been brought about by thermal focusing of fluid along the hot interiors of the cooling sills, or, more simply, by thermally enhanced Ca/Na exchange rate in the hot sill interiors.

Spilitic chemical alteration is most common in basic sills and lavas in close proximity to the Tayvallich Volcanics, because these represent the structurally highest rocks at the time of emplacement and were closest to (i) the fluid source (the sea), and (ii) the heat source (the magmatic centre). However, spilitisation is developed elsewhere, presumably as a result of locally developed, thermally-driven fluid-convection cells associated with the emplacement of individual sills.

Syn-metamorphic Fluid Infiltration

At the peak of greenschist facies regional metamorphism, devolatilisation reactions, probably at the garnet isograd, liberated a limited volume of hydrous fluid *(from a layer of phyllites with a minimum thickness of ≈ 5-6km)* which took up CO_2 by oxidation of graphite (the former existence of which is inferred by (i) low $\delta^{13}C$ carbonates within the phyllites, and (ii) graphitic intercalations within the Islay-Jura Quartzite). The CO_2-bearing hydrous fluid migrated upwards through the crust, driven by buoyancy.

Upwards moving fluid was focused through major phyllitic units, and deflected away from major psammitic units, on a regional-scale.

Within phyllites fluid was focused extensively along the axial surfaces of the major regional antiforms *(attaining fluxes in excess of 10^4-10^5 m^3/m^2, which are essentially high enough to advect heat).* Fluid flow was predominantly lithology-parallel *(the ratio of lithology-parallel to lithology-perpendicular flow was at least 10:1).*

Within psammites, fluid flow was localised to zones of intensive deformation associated with (i) emplacement of metabasites and (ii) phyllitic intercalations. Such zones acted as fluid "pipes", along which fluids passed through the psammitic units. Psammites were themselves impermeable to fluid infiltration, as were marbles, in agreement with predicted pore structure of quartz and calcite matrices at high pressures and temperatures.

Syn-metamorphic fluids were in local equilibrium with the host calc-phyllites, but were out of equilibrium with the type I metabasite assemblage: amphibole + epidote, and therefore induced advection of the reaction (1) into the margins of metabasite sills and the subsequent development of the type III assemblage: chlorite + calcite + quartz. Furthermore, syn-metamorphic fluid flow induced isotopic modification of metabasite margins. *(For these reasons, and because time-integrated fluid fluxes are externally-controlled and are therefore identical within phyllites and metabasites, individual metabasite units, are highly effective "flow-meters" of regional syn-metamorphic fluid movement).*

Post-metamorphic Fluid Infiltration

During differential uplift, associated with tightening of the Tay Nappe structure and the development of the Tarbert and Ben Ledi Monoforms during D_4 deformation, the Dalradian rocks of the SW Highlands were subjected to a third and final phase of fluid infiltration. Ankerite-Kfeldspar-quartz-chlorite veining was developed in response to fracture-controlled fluid movement during rapid uplift of the garnet-zone rocks of the Cowal Antiform. Similarly, pyrite veining was developed during rapid uplift of the upper biotite-zone rocks of the Islay Anticline. Ankerite porphyroblasts and disseminated pyrite grew in response to more pervasive flow during slower uplift of the lower biotite-zone rocks of the Loch Awe Syncline and Ardrishaig Anticline. Furthermore, post-metamorphic fluid infiltration was associated with large isotopic shifts.

12.5 Concluding Statements

It has been demonstrated in this thesis that individual phases of fluid infiltration may be unambiguously distinguished on the basis of (i) mineralogical, (ii) isotopic, and (iii) chemical alterations.

Combined theoretical, petrochemical and field studies have been applied in the SW Highlands to investigate the three successive phases of fluid infiltration affecting the Dalradian of the SW Scottish Highlands. Where possible the volume, source and transport mechanisms have been evaluated. These are shown in table 12.1.

Table 12.1 Constraints of Volume, Source and Transport Mechanisms of Fluid Flow in the SW Highlands

Phase of Infiltration	Time-integrated Flux	Source	Transport Mechanisms	Alterations
Pre-metamorphic	???	Sea water	Convection	**Mineralogical:** Ab-enrichment Ep-segregations **Isotopic:** Obscured by later infiltration **Chemical:** Na/Ca-redistribution
Syn-metamorphic	Average = $600 m^3/m^2$ Maximum>10^5 m^3/m^2	Metamorphic devolatilisation	Uni-directional Upwards Flow Channelled through Phyllite Focused through antiforms	**Mineralogical:** Advection of reaction fronts **Isotopic:** Advection of isotope fronts **Chemical:** None: Isochemical
Post-metamorphic	???	???	Fracture-controlled and Pervasive	**Mineralogical:** Dol/Pyrite Veins Ank porphyroblasts Disseminated Pyr **Isotopic:** High $\delta^{18}O$ **Chemical:** Fe-redistribution

12.6 Future Work

Obvious follow-up studies to this work include the following:

(1) Construction of a detailed isotopic traverse across the Ardrishaig Phyllites to confirm the existence of a zone of intense fluid focusing along the axial surface of the Ardrishaig Anticline as depicted in figure 10.26;

(2) A detailed appraisal of the Stotfield Bay section to fully evaluate the direction and magnitude of the three-dimensional time-integrated fluid flux.

(3) To test the more widespread applicability of the fluid flow model which is delineated in figures 10.26 and 10.27, particularly in areas where measurements of high fluid fluxes (or fluid:rock ratios) has proven problematic (e.g. Vermont-New Hampshire, Ferry 1988, 1992).

(4) To determine the grain-scale controls which are inevitably responsible for observed focusing of fluid in anisotropic mica-quartz-calcite phyllites, by examining similar bimineralic matrices by pre-existing and new experimental procedures, including dihedral angle approaches (e.g. Holness 1993) and connectivity experiments (e.g. measurement of transport of an isotopic tracer in bimineralic matrices or measurement of conductivity through an interconnected pore network).

REFERENCES

ANDERTON, R. 1975. Tidal flat and shallow marine sediments from the Craignish Phyllites, Middle Dalradian, Argyll, Scotland. *Geological Magazine* **112**, 337-348.

ANDERTON, R. 1976. Tidal-shelf sedimentation: an example from the Scottish Dalradian. *Sedimentology* **23**, 429-458

ANDERTON, R. 1977. The Dalradian rocks of Jura. *Scottish Journal of Geology* **13**, 135-142.

ANDERTON, R. 1985. Sedimentation and tectonics in the Scottish Dalradian. *Scottish Journal of Geology* **21**, 407-436.

ANNOVITZ, L.M. & ESSENE, E.J. 1987. Phase equilibria in the system $CaCO_3$-$MgCO_3$-$FeCO_3$. *Journal of Petrology* **28**, 389-414.

BAKER, J., BICKLE, M.J., BUICK, I.S., HOLLAND, T.J.B. & MATTHEWS, A. 1989. Isotopic and petrological evidence for the infiltration of water-rich fluids during the Miocene M2 metamorphism on Naxos, Greece. *Geochimica et Cosmochimica Acta* **53**, 2037-2050.

BICKLE, M.J. & McKENZIE, D.P. 1987. The transport of heat and matter by fluids during metamorphism. *Contributions to Mineralogy and Petrology* **95**, 384-392.

BICKLE, M.J. & BAKER, J. 1990a. Advective-diffusive transport of isotope fronts: an example from Naxos, Greece. *Earth and Planetary Science Letters* **97**, 78-93.

BICKLE, M. & BAKER, J. 1990b. Migration of reaction and isotopic fronts in infiltration zones: assessments of fluid flux in metamorphic terrains. *Earth & Planetary Science Letters* **98**, 1-13.

BILLINGS, M.P. & WHITE, W.S. 1950. Metamorphosed Mafic Dykes of the Woodsville Quadrangle, Vermont and New Hampshire. *American Mineralogis*t **35**, 629-643.

BOTTINGA, Y. & RICHET, P. 1981. High Pressure and temperature equation of state and calculation of thermodynamic properties of gaseous carbon-dioxide. *American Journal of Science* **281**, 615-660.

BREISLAK, S. 1818. Institutions geologiques (French translation by P.J.L. Campmas). Institutions geologiques, Milan, 1, 468 p. (3)

BUCHER-NURMINEM, K. 1987. A recalibration of the chlorite-biotite-muscovite geobarometer. *Contributions to Mineralogy and Petrology* **96**, 519-522.

BUICK, I.S. 1988. The metamorphism and structural evolution of the Barrovian overprint, Naxos, Cyclades, Greece. Ph.D. dissertation, (unpublished) University of Cambridge, U.K.

BURGESS J.G., GRAHAM C.M., & HARTE, B. 1981. Kyanite and chloritoid phyllites from the chlorite zone of the SW Scottish Highlands. *Journal of the Geological Society* **138**, Part 5, 634.

DAVY, Sir H. 1822. On the state of water and aeriform matter in cavities found in certain crystals. *Royal Society London Philosophical Transactions* **2**, 367-376.

DEER, W.A., HOWIE, R.A. & ZUSSMAN, J. 1992. An introduction to the Rock Forming Minerals, 2nd edition. Longman Group (FE) Ltd, Hong Kong.

DEMPSTER, T.J. 1985. Uplift patterns and orogenic evolution in the Scottish Dalradian. *Journal of the Geological Society of London* **142**, 111-128.

DYMOKE, P.L. 1988. Geochronological and Petrological studies of the Thermal Evolution of the Dalradian, South West Scottish Highlands. Ph.D (unpublished) Edinburgh.

ELLES, G.L. & TILLEY, C.E. 1930. Metamorphism in relation to structure in the Scottish Highlands. *Transactions of the Royal Society of Edinburgh* **56**, 621-646.

ETHERIDGE, M.A., COX, S.F., & VERNON, R.H., 1984. High fluid pressures during metamorphism and deformation. *Journal of Metamorphic Geology* **1**, 205-226.

EYLES, C.H. and EYLES, N. 1983. Glaciomarine model for upper Precambrian diamictites of the Port Askaig Formation, Scotland. *Geology* **11**, 692-696.

FAIRCHILD, I.J. 1985. Petrography and carbonate chemistry of some Dalradian dolomitic metasediments: preservation of diagenetic textures. *Journal of the Geological Society of London* **142**, 167-185.

FEIN, J.B., GRAHAM, C.M., HOLNESS, M.B. & FALLICK, A.E. 1993. Controls on the Mechanisms of Fluid Infiltration During Regional Metamorphism: An Isotopic and Textural Study of Retrograde Dalradian Rocks of the SW Scottish Highlands. *Journal of Metamorphic Geology* (in press).

FERRY, J.M. 1980. A Case Study of the Amount and Distribution of Heat and Fluid During Metamorphism. *Contributions to Mineralogy & Petrology* **71**, 373-385.

FERRY, J.M. 1983. Applications of the Reaction Progress Variable in Metamorphic Petrology. *Journal of Petrology* **24** (4), 343-376.

FERRY, J.M. 1983. Regional metamorphism of the Vassalboro Formation, south-central Maine, USA: a case study of the role of fluid in metamorphic petrogenesis. *Journal of the Geological Society of London* **140**, 551-576.

FERRY, J.M. 1984. Phase composition as a measure of reaction progress and an experimental model for the high-temperature metamorphism of mafic igneous rocks. *American Mineralogist* **69**, 667-691.

FERRY, J.M. 1986. Infiltration of Aqueous Fluid and High Fluid:Rock Ratios During Greenschist Metamorphism: A Reply. *Journal of Petrology* **27**, 695-714.

FERRY, J.M. 1987. Metamorphic hydrology at 13-Km depth and 400-550°C. *American Mineralogist* **72**, 39-58.

FERRY, J.M. 1988. Contrasting mechanisms of fluid flow through adjacent stratigraphic units during regional metamorphism, south-central Maine, U.S.A. *Contributions to Mineralogy and Petrology* **98**, 1-12.

FERRY, J.M. 1989. Contact metamorphism of roof pendants at Hope Valley, Alpine County, California, USA. *Contributions to Mineralogy and Petrology* **101**, 402-417.

FERRY, J.M. 1992. Regional Metamorphism of the Waits River Formation, Eastern Vermont: Delineation of a New Type of Giant Metamorphic Hydrothermal System. Journal of Petrology 33(1), 45-94.

FERRY,J.M. & SPEAR, F.S. 1978. Experimental calibration of the partitioning of Fe and Mg between biotite and garnet. *Contributions to Mineralogy & Petrology* **66**, 113-117.

FYFE, W.S., PRICE, N.J. & THOMPSON, A.B. 1978. Fluids in the Earth's Crust. Elsevier Science Publications Company, Amsterdam.

GOWER, P.J. 1977. The Dalradian rocks of the west coast of the Tayvallich peninsular. *Scottish Journal of Geology* **13**, 125-133.

GRAHAM, C.M. 1973. Chemical Petrology of Metamorphosed Basic Rocks of the Dalradian Series with particular Reference to the Knapdale area of Argyll. Ph.D thesis (unpublished), Edinburgh.

GRAHAM, C.M. 1976. Petrochemistry and tectonic significance of Dalradian metabasic rocks of the S.W. Scottish Highlands. *Journal of the Geological Society of London* **132**, 61-84.

GRAHAM, C.M. 1986. The role of the Cruachan Lineament during Dalradian Evolution. *Scottish Journal of Geology* **22**, 257-270.

GRAHAM, C.M., GREIG, K.M., SHEPPARD, M.F. & TURI, B. 1983. Genesis and mobility of the H_2O-CO_2 fluid phase during regional greenschist and epidote amphibolite facies metamorphism: a petrological and chemical isotope study in the Scottish Dalradian. *Journal of the Geological Society of London* **140** (4), 577-599.

GRAHAM, C.M. & BORRADAILE, G.J. 1984. The petrology and study of Dalradian metabasaltic dykes of Jura: implications for early Dalradian evolution. Scottish Journal of Geology 20 (2), 257-270.

GRAHAM, C.M. & POWELL R. 1984. A garnet-hornblende geothermometer: calibration, testing and application to the Pelona Schist, Southern California. *Journal of Metamorphic Geology* **2**, 13-31.

GREENWOOD, H.G. 1967. Mineral equilibria in the system MgO-SiO_2-H_2O-CO_2. *In* Abelson, P.H. (Ed.). Researches in Geochemistry II. John Wiley & Sons, New York.

GREENWOOD, H.J. 1975. Buffering of pore fluids by metamorphic reactions. American Journal of Science 275, 573-593.

GREGORY, A.R. & BACKUS, M.M. 1980. Geopressured formation parameters, geothermal well, Brazoria County, Texas. *In* Dorfman, M.H. & Fisher, W.L. (Eds.). Proceedings 4th U.S. Gulf Coast Geopressure-Geothermal Energy Conf.

GREGORY, R.T. & TAYLOR, H.P. 1981. An oxygen isotope profile in a section of Cretaceous oceanic crust, Samail Ophiolite, Oman: evidence of $\delta^{18}O$ buffering of the oceans by deep (>5 Km) seawater-hydrothermal circulation at Mid-Oceanic Ridges. *Journal of Geophysical Research* **86**, 2737-2755.

GREIG, K.M. 1984. Metamorphosed carbonates and fluid behaviour in the Dalradian of S. W. Argyll, Scotland. PhD thesis (unpublished), Edinburgh.

HALL, J. 1985. Geophysical constraints on crustal structure in the Dalradian region of Scotland. *Journal of the Geological Society of London* **142**, 149-155.

HALLIDAY, A.N., GRAHAM, C.M., AFTALION, M. & DYMOKE, P. 1989. The depositional age of the Dalradian Supergroup: U-Pb and Sm-Nd isotopic studies of the Tayvallich Volcanics, Scotland. *Journal of the Geological Society of London* **146**, 3-6.

HARRIS, N.B.W. & BICKLE, M.J. 1989. Advective fluid transport during charnockite formation; an example from southern India. *Earth and Planetary Science Letters* **93**, 151-156.

HARTE, B. & GRAHAM, C.M. 1975. The Graphical Analysis of Greenshist to Amphibolite Facies Mineral Assemblage in Metabasites. *Journal of Petrology* **16** (2), 347-370.

HARTE,B., BOOTH, J.E., DEMPSTER, T.J., MENDUM, J.R. and WATTS, D. 1984. Aspects of post-depositional evolution of Dalradian and Highland Border complex rocks in the Southern Highlands of Scotland. *Transactions of the Royal Society of Edinburgh Earth Science* **75**, 152-163.

HODGES, K.V. & SPEAR, F.S. 1982. Geothermometry and geobarometry and the Al_2SiO_5 triple point at Mount Moosilauke, New Hampshire. *American Mineralogist* **67**, 1118-1134.

HOFMANN, A.W. 1972. Chromatographic theory of infiltration metasomatism and its application to feldspars. *American Journal of Science* **272**, 69-90.

HOLNESS, M.B. & GRAHAM, C.M. 1991. Equilibrium dihedral angles in the system H_2O-CO_2-NaCl-calcite, and implications for fluid flow during metamorphism.

JOHNSON, M.R.W. 1983. Dalradian. *In* CRAIG, G.Y. (Ed.). Geology of Scotland. Second edition. Scottish Academic Press, Edinburgh.

KILBURN, C., PITCHER, W.S. & SHACKLETON, R.M. 1965. The stratigraphy and origin of the Portaskaig Boulder Bed Series (Dalradian). *Geological Journal* **4**, 343-360.

KORZHINSKII, D.S. 1951. Derivation of the equation of infiltration metasomatic zoning (in Russian): *Akad. Nauk SSSR, Doklady* **77**, no. 2, 305-308.

KORZHINSKII, D.S. 1952. The derivation of the equation of a simple diffusion metasomatic zoning (in Russian): *Akad. Nauk SSSR, Doklady* **84**, no. 2, 597-600.

KORZHINSKII, D.S. 1970. Theory of Metasomatic Zoning (translated by Jean Agrell): Oxford, Clarendon Press.

LASSEY, K.R. & BLATTNER, P. 1989. Unidimensional transport of stable isotopes: The shape of geochemical fronts. In MILES (Ed.). Water-Rock Interaction, *Proceedings of the 6th international symposium on water-rock interaction*. Balkema, Rotterdam.

MANSON V., 1967. Geochemistry of basaltic rocks: major elements. Pp. 215-269 *in* Hess, H.H., & Poldervaart, A., (Eds). Basalts: the Poldervaart treatise on rocks of basaltic composition, New York: Interscience.

MASSONNE, H-J. & SCHREYER, W. 1987. Phengite geobarometry based on the limiting assemblage with k-feldspar, phlogopite and quartz. *Contributions to Mineralogy and Petrology* **96**,212-224.

McKENZIE, D.P. 1978. Some remarks on the development of sedimentary basins. *Earth & Planetary Science Letters* **40**, 25-32.

OLIVER, N.H.S., VALENTA, R.K. & WALL, V.J. 1990. The effect of heterogeneous stress and strain on metamorphic fluid flow, Mary Kathleen, Australia, and a model for large-scale fluid circulation. *Journal of Metamorphic Geology* **8**, 311-331

PHILLIPS, F.C. 1930. Some mineralogical and chemical changes induced by progressive metamorphism in the Green Bed Group of the Scottish Dalradian. *Mineralogical Magazine* **22**, 239-256.

PIPER, J.D.A. 1983. Proterozoic palaeomagnetism and single continent plate tectonics. *Geophysical Journal R. Astronomical Society* **74**, 163-197.

POWELL, R. & EVANS, J.A. 1983. A new geobarometer for the assemblage biotite-muscovite-chlorite-quartz. *Journal of Metamorphic Geology* **1**, 331-336.

POWELL, R., CONDICLIFFE, D.M. & CONDICLIFFE, E. 1984. Calcite-dolomite geothermometry in the system $CaCO_3$-$MgCO_3$-$FeCO_3$: an experimental study. *Journal of Metamorphic Geology* **2**, 33-42.

POWELL, R. & HOLLAND, T.J.B. 1988. An internally consistent thermodynamic dataset with uncertainties and correlations: 3. Applications to geobarometry, worked examples and a computer program. *Journal of Metamorphic Geology* **6**, 173-204

RAMSAY, J.G. 1967. Folding and fracturing of rocks. McGraw-Hill, New York.

ROBERTS, J.L. 1974. The structure of the Dalradian rocks in the SW Highlands of Scotland. *Journal of the Geological Society of London* **130**, 93-124.

ROBERTS, J.L. & TREAGUS, J.E. 1977. The Dalradian rocks of the South-west Highlands - Introduction. *Scottish Journal of Geology* **13** (2), 87-99.

ROEDDER, E. 1984. Fluid Inclusions. Reviews in Mineralogy 12, Mineralogical Society of America.

ROGERS, G., DEMPSTER, T.J., BLUCK, B.J. & TANNER, P.W.G. 1989. A high precision U-Pb age for the Ben Vuirich granite: implications for the evolution of the Scottish Dalradian Supergroup. *Journal of the Geological Society of London* **146**, 789-798.

SKELTON, A.D.L., GRAHAM, C.M. & BICKLE, M.J. 1992. Structural controls of fluid flow during regional metamorphism: Application of reaction front advection theory to greenschist facies metabasites in the Scottish Dalradian. In KHARAKA, Y.K. & MAEST, A.S. (Eds.). Water-Rock Interaction, *Proceedings of the 7th international symposium on water-rock interaction*. Balkema, Rotterdam.

SMITH, R.E. 1968. Redistribution of major elements in the alteration of some basic lavas during burial metamorphism. *Journal of Petrology* **9**, 191-219.

SORBY, H.C. 1858. On the microscopic structure of crystals, indicating the origin of minerals and rocks. *Geological Society of London Quarterly Journal* **14**, pt. 1, 453-500.

SPENCER, A.M. 1971. Late Precambrian glaciation in Scotland. *Memoirs of the Geological Society of London* **6**, 100p.

SWEATMAN, T.R. & LONG, J.V.P. 1969. Quantitative electron-probe micro-analysis of rock-forming minerals. *Journal of Petrology* **10**, 332-379.

TAYLOR, H.P. 1968. The Oxygen Isotope Geochemistry of Igneous Rocks. *Contributions to Mineralogy and Petrology* **19**, 1-71.

TAYLOR, H.P. 1977. Water/rock interactions and the origin of H_2O in granitic batholiths. *Journal of the Geological Society of London* **133**, 509-558.

TODHEIDE, K. 1972. Water at high temperatures and pressures. *In*, Franks, F. (Ed). Water, a Comprehensive Treatise **1**, p. 463-514.

VALLANCE, T.G. 1960. Concerning Spilites. *Proceedings of the Linn. Soc. N.S.W.* **85**, 8-52.

VALLANCE, T.G. 1965. On the chemistry of pillow lavas and the origin of spilites. *Mineralogical Magazine* **34**, 8-52.

VALLANCE, T.G. 1969. Spilites again: some consequences of the degradation of basalts. *Proceedings of the Linn. Soc. N.S.W.* **94**, 8-53.

VEIZER, J. & HOEFS, J. 1976. The nature of O^{18}/O^{16} and C^{13}/C^{12} secular trends in sedimentary carbonate rocks. *Geochimica and Cosmochimica Acta* **40**, 1387-1395.

VOLL, G. 1960. New work on petrofabrics. *Liverpool & Manchester geological Journal* **2**, 503-567.

WALTHER, J.V. & ORVILLE, P.M. 1982. Volatile Production and Transport in Regional Metamorphism. *Contributions to Mineralogy and Petrology* **79**, 252-257.

WATKINS, K.P. 1983. Petrogenesis of Dalradian albite porphyroblast schists. *Journal of the Geological Society of London* **140**, 601-618.

WATSON, E.B. 1982. Melt infiltration and magma evolution. *Geology* **10**, 236-240.

WATSON, E.B. & BRENAN, J.M. 1987. Fluids in the lithosphere, 1. Experimentally-determined wetting characteristics of CO_2-H_2O fluids and their implications for fluid transport, host-rock physical properties, and fluid inclusion formation. *Earth and Planetary Science Letters* **85**, 497-515.

WICKHAM, S.M. & TAYLOR, H.P. Jr. 1985. Stable isotopic evidence for large-scale seawater infiltration in a regional metamorphic terrane; the Trois Seigneurs Massif, Pyrenees, France. *Contributions to Mineralogy and Petrology* **91**, 122-137.

WICKHAM, S.M. & TAYLOR, H.P. 1987. Stable isotope constraints on the origin and depth of penetration of hydrothermal fluids associated with Hercynian regional metamorphism and crustal anatexis. *Contributions to Mineralogy & Petrology* **95**, 255-268.

WOOD, B.J. & GRAHAM, C.M. 1986. Infiltration of Aqueous Fluid and High Fluid:Rock Ratios During Greenschist Facies Metamorphism: A Discussion. *Journal of Petrology* **27** (3), 751-761.

WOOD, B.J. & WALTHER, J.V. 1986. Fluid Flow During Metamorphism And Its Implications For Fluid-Rock Ratios. *In* WALTHER, J.V. & WOOD, B.J. (Eds.). Fluid-Rock Interactions during Metamorphism. Springer-Verlag, New York.

YARDLEY, B.W.D. & BOTTRELL, S.H. 1992. Silica mobility and fluid movement during metamorphism of the Connemara schists, Ireland. *Journal of Metamorphic Geology* **10**, 453-464.

Appendix 1: Geobarometry Data

Figure A1.1: Location map of geobarometry sample localities; Clachbreac, Port Ellen and Scarba.

Figure A1.2: Representative mineral analyses from Clachbreac, Port Ellen and Scarba.

Figure A1.3: Mole fraction data, calculated from the mineral analyses presented in figure A1.2 using RECALC (Holland).

Figure A1.4: Graphical representation of the muscovite-biotite-chlorite-quartz geobarometer of Powell & Evans (1983), and pressure estimates from Clachbreac, Port Ellen and Scarba.

Figure A1.5: Compiled geobarometric data from this study and Dymoke (1988).

Figure A1.1: Location Map of Geobarometry Samples

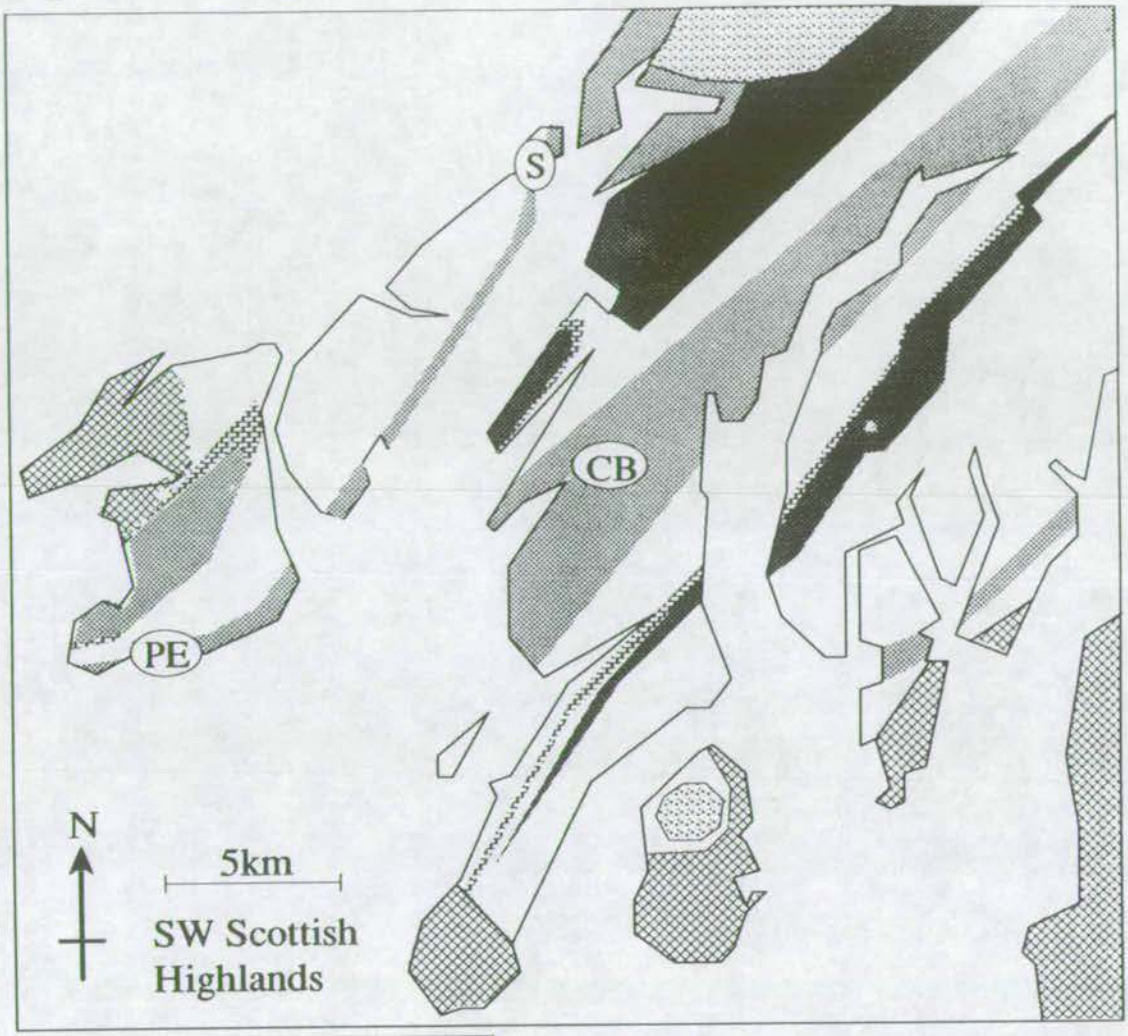

KEY

- Phyllite
- Quartzite
- Volcanics
- Marble
- Other Metamorphic and Sedimentary Rocks
- Other Igneous Rocks

CB = Clachbreac
PE = Port Ellen
S = Scarba

Figure A1.2: Representative Mineral Analyses

Clachbreac

	Mu	Bi	Chl
SI	47.53	36.67	24.98
TI	0.31	1.27	0.05
AL	30.73	17.35	21.08
FE	1.80	18.73	24.39
MN	0.00	0.15	0.30
MG	2.51	10.76	15.80
CA	0.02	0.14	0.18
NA	0.36	0.07	0.04
K	10.60	7.41	0.03
TOT	93.88	92.56	86.86
SI	6.44	5.91	5.31
TI	0.03	0.15	0.01
AL	4.91	3.30	5.28
FE	0.20	2.52	4.33
MN	0.00	0.02	0.06
MG	0.51	2.58	5.00
CA	0.00	0.02	0.04
NA	0.09	0.02	0.02
K	1.83	1.52	0.01
SUM	14.03	16.06	20.06

Port Ellen

	Mu	Bi	Chl
SI	48.67	35.41	25.12
TI	0.03	1.48	0.05
AL	30.77	16.03	19.46
FE	2.46	21.54	27.66
MN	0.00	0.18	0.36
MG	2.40	8.96	13.33
CA	0.00	0.06	0.24
NA	0.18	0.14	0.03
K	11.07	9.28	0.01
TOT	95.57	93.09	86.25
SI	6.50	5.86	5.48
TI	0.00	0.18	0.01
AL	4.85	3.13	5.01
FE	0.27	2.98	5.05
MN	0.00	0.02	0.07
MG	0.47	2.21	4.33
CA	0.00	0.01	0.06
NA	0.05	0.04	0.01
K	1.89	1.96	0.00
SUM	14.04	16.40	20.01

Scarba

	Mu	Bi	Chl
SI	45.81	37.79	26.35
TI	0.35	1.44	0.02
AL	25.37	14.90	19.52
FE	7.34	17.02	20.40
MN	0.02	0.13	0.21
MG	4.43	12.91	19.03
CA	0.02	0.00	0.03
NA	0.28	0.04	0.05
K	9.75	9.59	0.03
TOT	93.36	93.82	85.64
SI	6.45	5.78	5.55
TI	0.04	0.17	0.00
AL	4.21	2.69	4.85
FE	0.86	2.18	3.59
MN	0.00	0.02	0.04
MG	0.93	2.94	5.97
CA	0.00	0.00	0.01
NA	0.08	0.01	0.02
K	1.75	1.87	0.01
SUM	14.32	15.65	20.04

Figure A1.3: Mole Fraction Data: Clachbreac, Port Ellen and Scarba (RECALC, Holland & Powell 1988)

Clach Breac (Recalc, Holland & Powell 1989)

<==== muscovite ====>

	x	sd(x)	%
x(mu)	0.583	0.0122	2.1
x(cel)	0.137	0.00559	4.1
x(pa)	0.0301	0.0045	15
x(ma)	0.00015	0.000376	251.1

<==== biotite ====>

	x	sd(x)	%
x(phl)	0.0465	0.00258	5.5
x(ann)	0.0266	0.0103	38.8
x(east)	0.034	0.0023	6.8
x(naph)	0.000667	0.000484	72.5

<==== chlorite ====>

	x	sd(x)	%
x(clin)	0.0198	0.0128	65
x(daph)	0.00427	0.00527	123.3
x(ames)	0.0198	0.0034	17.2

Scarba (Recalc, Holland & Powell 1989)

<==== muscovite ====>

	x	sd(x)	%
x(mu)	0.335	0.0322	9.6
x(cel)	0.176	0.0436	24.7
x(pa)	0.0146	0.00307	21.1

<==== biotite ====>

	x	sd(x)	%
x(phl)	0.105	0.00512	4.9
x(ann)	0.0261	0.00992	38
x(east)	0.0292	0.003	10.3
x(naph)	0.000666	0.000839	125.9

<==== chlorite ====>

	x	sd(x)	%
x(clin)	0.0642	0.0184	28.6
x(daph)	0.00224	0.00195	86.8
x(ames)	0.0248	0.00344	13.9

Port Ellen (Recalc, Holland & Powell 1989)

<==== muscovite ====>

	x	sd(x)	%
x(mu)	0.588	0.0125	2.1
x(cel)	0.138	0.00563	4.1
x(pa)	0.0145	0.00418	28.8

<==== biotite ====>

	x	sd(x)	%
x(phl)	0.0372	0.0022	5.9
x(ann)	0.056	0.0219	39.1
x(east)	0.0225	0.00234	10.4
x(naph)	0.000852	0.000315	37

<==== chlorite ====>

	x	sd(x)	%
x(clin)	0.00875	0.00786	89.7
x(daph)	0.00832	0.0123	148.1
x(ames)	0.00922	0.00185	20.1

Figure A1.4: Muscovite-Biotite-Chlorite-Quartz Geobarometry (after Powell & Evans 1983)

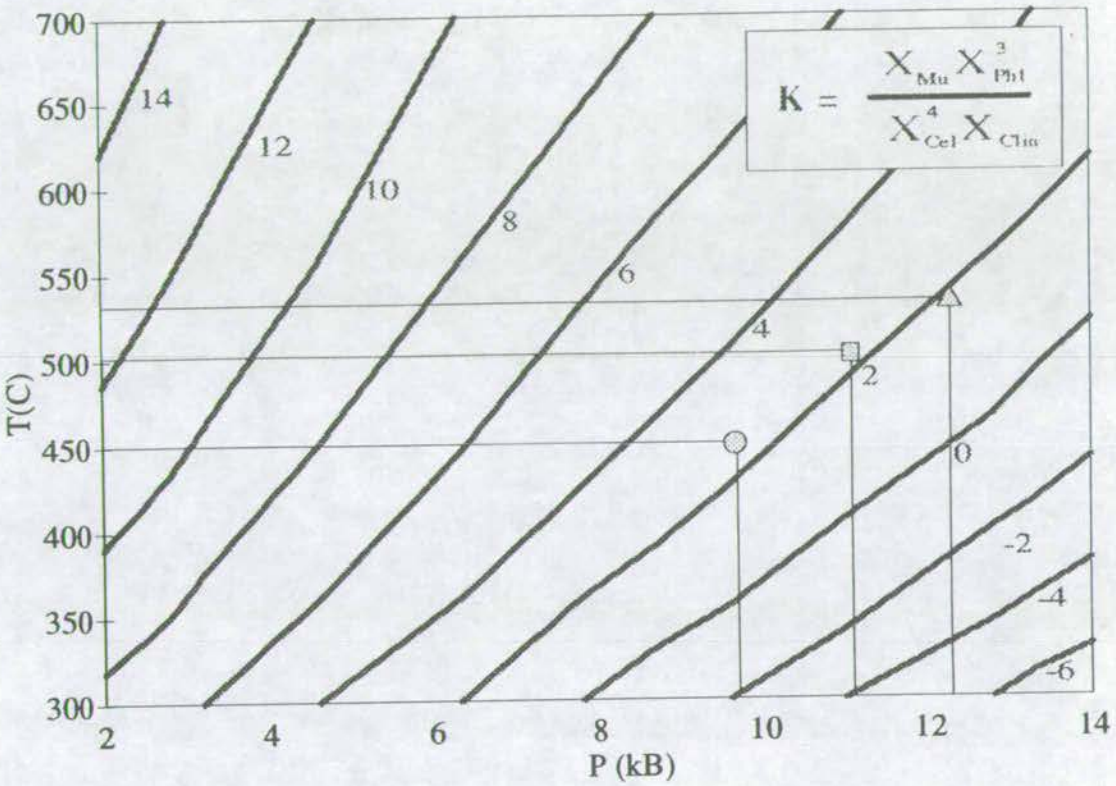

Clachbreac (▨)
Estimated Pressure: 11.0kB

Port Ellen (◎)
Estimated Pressure: 9.7kB

Scarba (△)
Estimated Pressure: 12.3kB

Figure A1.5: SW Highland Geobarometry

	Mu-Bi-Chl-Qz Geobarometry (Powell & Evans 1983)
Clachbreac	11.0
Port Ellen	9.7
Scarba	12.3

	Mu-Bi-Qz-Ksp Geobarometry (Dymoke 1988)
Tayvallich	9-10
Clach Breac	7-8
Stronachullin (North)	7-8
Stronachullin (South)	8-9

	Mu-Bi-Chl-Qz Geobarometry (Dymoke 1988)
Tayvallich	9-10
Clach Breac	11-12
Stronachullin (North)	10.5-11.5
Stronachullin (South)	11-12

Appendix 2: Geothermometry Data

Figure A2.1: Location map of geothermometry sample localities; Traigh Gheighsgeir, Loch Fuar Bheinne, Stronefield, Keppoch Point, Gigha, Loch Stornoway, Scarba and Port Cill Maluaig.

Figure A2.2: Calcite (Fe-Mg) Geothermometry, after Powell *et al.* (1984), at the localities; Traigh Gheighsgeir, Loch Fuar Bheinne, Stronefield and Keppoch Point. Temperatures were estimated graphically.

Figure A2.3: Calcite-Dolomite Geothermometry,after Powell *et al.* (1984), at the localities; Traigh Gheighsgeir, Loch Fuar Bheinne, Stronefield and Keppoch Point. Temperatures were estimated graphically.

Figure A2.4: Calcite-Dolomite-Ferrodolomite Geothermometry,after Annovitz & Essene (1987), at the localities; Traigh Gheighsgeir, Loch Fuar Bheinne, Stronefield and Keppoch Point. Temperatures were estimated using the following equations:

$$T^{CaMg} = A.X_{Cc}^{MgCO_3} + \frac{B}{\left(X_{Cc}^{MgCO_3}\right)^2} + C.\left(X_{Cc}^{MgCO_3}\right)^2 + D\sqrt{X_{Cc}^{MgCO_3}} + E$$

$A = -2360.0$

$B = -0.01345$

$C = 2620.0$

$D = 2608.0$

$E = 334.0$

$$T^{CaMgFe} = T^{CaMg} + a.X_{Cc}^{FeCO_3} + b.\left(X_{Cc}^{FeCO_3}\right)^2 + c.\frac{X_{Cc}^{FeCO_3}}{X_{Cc}^{MgCO_3}} + d\left(X_{Cc}^{FeCO_3}.X_{Cc}^{MgCO_3}\right) + e.\left(\frac{X_{Cc}^{FeCO_3}}{X_{Cc}^{MgCO_3}}\right) + f.\left(X_{Cc}^{FeCO_3}.X_{Cc}^{MgCO_3}\right)^2$$

$a = 1718.0$

$b = -10610.0$

$c = 22.49$

$d = -26260.0$

$e = 1.333$

$f = 0.32837 \times 10^7$

Figure A2.5: Representative mineral analyses from Gigha & Loch Stornoway.

Figure A2.6: Mole fraction data, calculated from the mineral analyses presented in figure A2.5 using RECALC (Holland).

Figure A2.7: Garnet-Biotite Geothermometry, after Ferry & Spear (1977) and Hodges & Spear 1982, at the localities; Gigha and Loch Stornoway. Temperatures were calculated using the following equation:

$$0 = 12454 - 4.662T + 0.057P + RT\ln K$$

$$K = \frac{\left(X_{gt}^{alm}\right)^3.\left(X_{bi}^{phl}\right)^3}{\left(X_{gt}^{py}\right)^3.\left(X_{bi}^{ann}\right)^3}$$

Figure A2.8: Average temperature calculation data, generated by THERMOCALC (Powell & Holland 1988), for the localities; Scarba, Traigh Gheighsgeir, Stronefield and Port Cill Maluaig. Temperature was calculated from the intersections of all possible univariant reaction curves at the chosen pressure.

Figure A2.9: Compiled geothermometric data from this study and Dymoke (1988).

Figure A2.1: Location Map of Geothermometry Samples

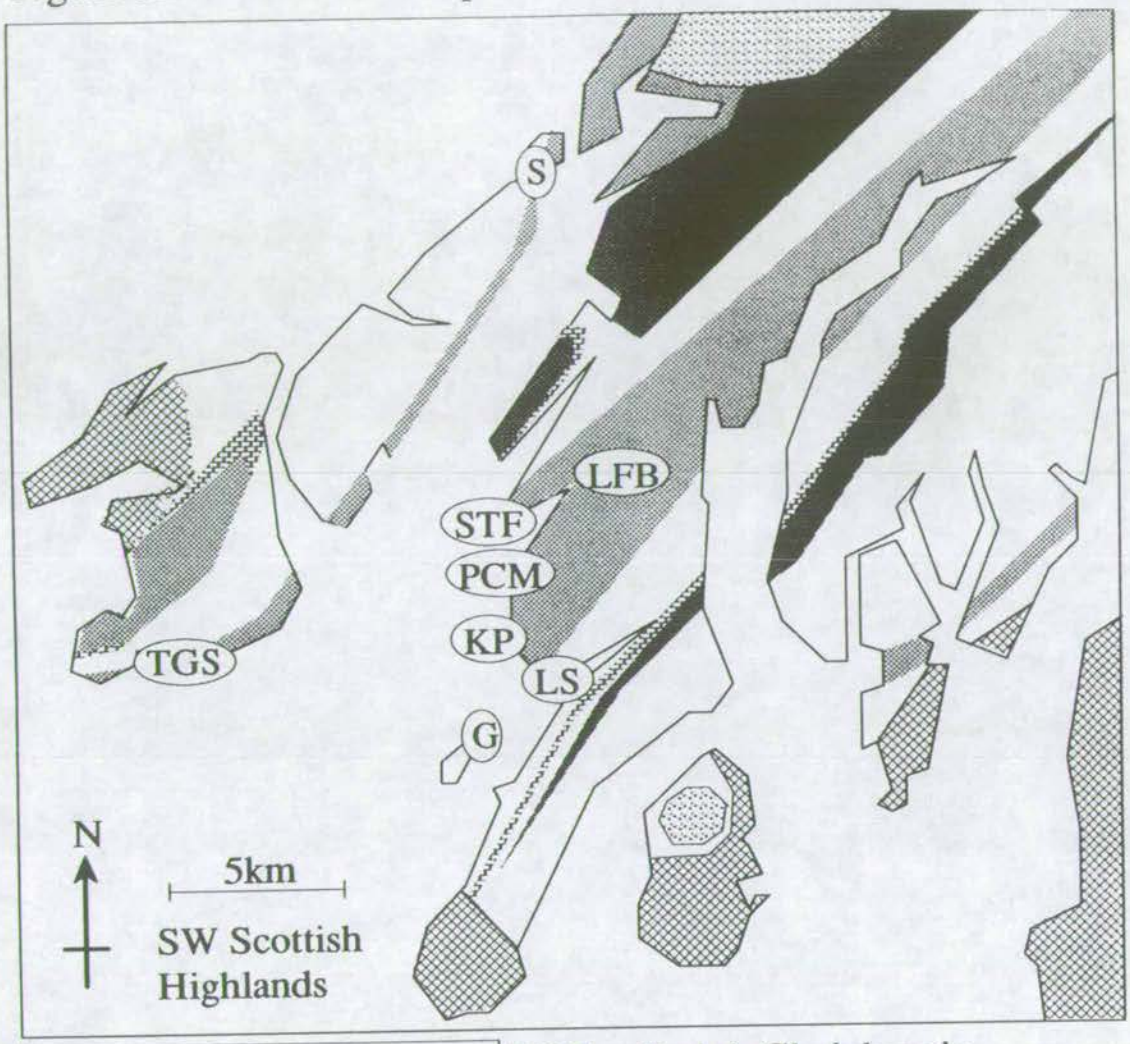

KEY

- Phyllite
- Quartzite
- Volcanics
- Marble
- Other Metamorphic and Sedimentary Rocks
- Other Igneous Rocks

TGS = Traigh Gheighsgeir
LFB = Loch Fuar Bheinne
STF = Stronefield
KP = Keppoch Point
G = Gigha
LS = Loch Stornoway
S = Scarba
PCM = Port Cill Maluaig

Figure A2.2: Calcite (Fe-Mg) Geothermometry
(after Powell et al. 1984)

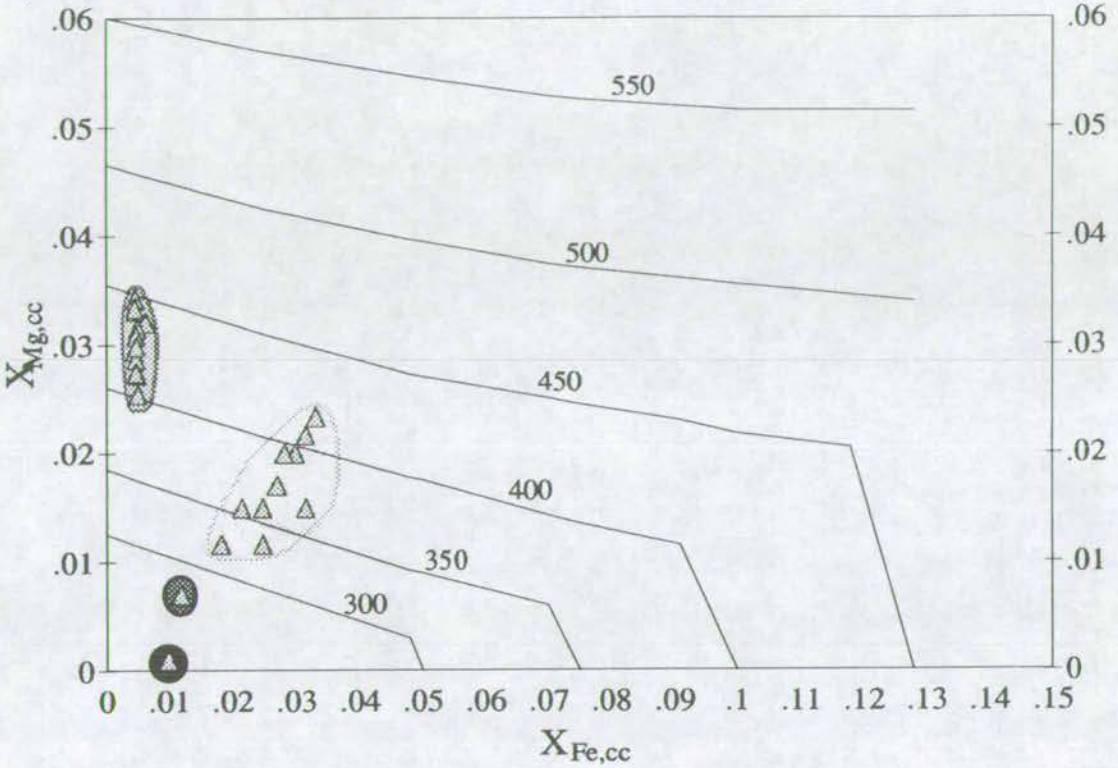

Traigh Gheighsgeir
Estimated Temperature: 320-420C

Loch Fuar Bheinne
Estimated Temperature: 400-450C

Stronefield
Estimated Temperature: 280C

Keppoch Point
Estimated Temperature: <200C

Figure A2.3: Calcite-Dolomite Geothermometry
(after Powell*et al.* 1984)

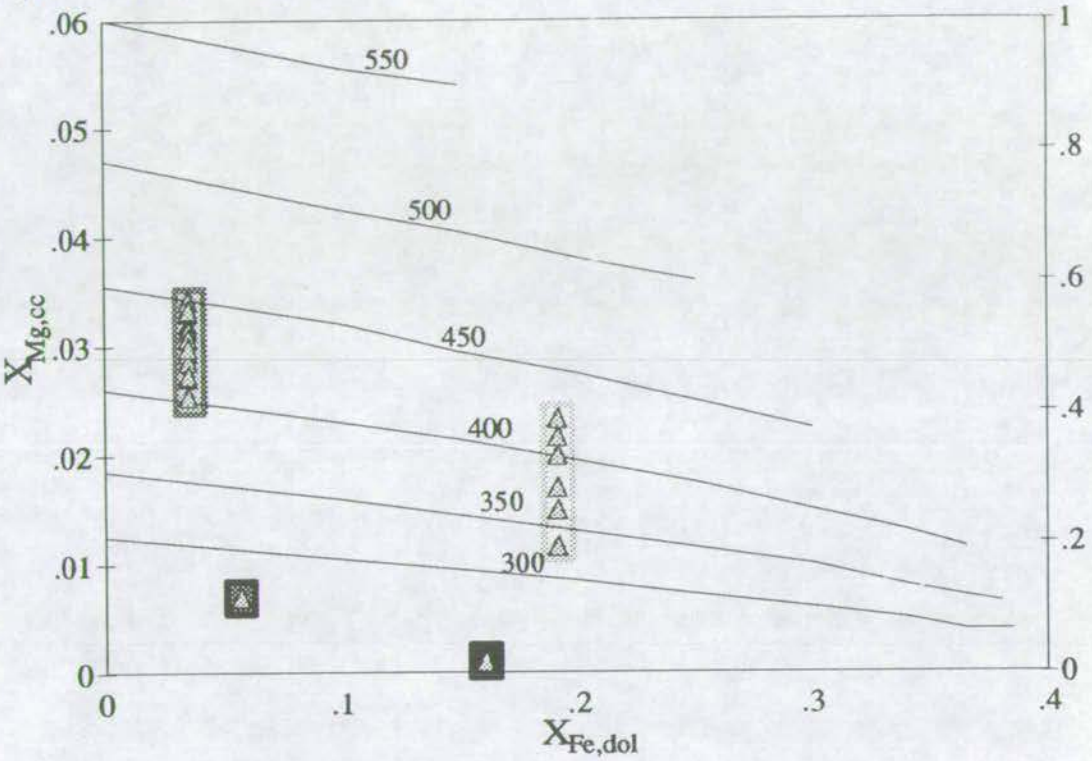

Traigh Gheighsgeir
Estimated Temperature: 330-430C

Loch Fuar Bheinne
Estimated Temperature: 400-450C

Stonefield
Estimated Temperature: 230C

Keppoch Point
Estimated Temperature: <200C

Figure A2.4: Calcite-Dolomite-Ferrodolomite Geothermometry

Annovitz & Essene (1987)

Traigh Gheighsgeir

X(FeCO3,Cc)	0.0317	0.0217	0.0317	0.0183	.025	.025	0.0333	.03	0.0283	0.02722
X(MgCO3,Cc)	0.0217	.015	.015	0.0117	.015	0.0117	0.0233	.02	.02	0.01704
T(Ca-Mg)	**367**	**286**	**286**	**218**	**286**	**218**	**381**	**350**	**350**	**360**
T(Ca-Mg-Fe)	**466**	**362**	**396**	**290**	**374**	**316**	**483**	**446**	**441**	**451**

Stronefield

X(FeCO3,Cc)	0.012
X(MgCO3,Cc)	0.007
T(Ca-Mg)	**-12**
T(Ca-Mg-Fe)	**52**

Keppoch Point

X(FeCO3,Cc)	0.01
X(MgCO3,Cc)	0.001
T(Ca-Mg)	#######
T(Ca-Mg-Fe)	#######

Loch Fuar Bheinne

X(FeCO3,Cc)	0.005	0.005	0.0047	0.0067	0.0054	0.0054	0.0054	0.0051	0.0049	0.0051	0.0051	0.0052	0.0142
X(MgCO3,Cc)	0.0342	0.03317	0.0295	0.032	0.0315	0.0254	0.0272	0.0308	0.0334	0.0287	0.0274	0.0299	0.0152
T(Ca-Mg)	**454**	**448**	**426**	**442**	**439**	**398**	**411**	**434**	**450**	**421**	**412**	**429**	**289**
T(Ca-Mg-Fe)	**470**	**465**	**441**	**463**	**456**	**415**	**428**	**451**	**466**	**437**	**429**	**445**	**339**

Figure A2.5: Representative Mineral Analyses

Gigha

	Gt	Bi
SI	36.51	34.20
TI	0.19	2.11
AL	20.94	15.42
FE	25.70	26.49
MN	6.43	0.14
MG	0.44	7.11
CA	10.25	0.03
NA	0.00	0.05
K	0.00	8.79
TOT	100.45	94.33
SI	5.88	5.72
TI	0.02	0.26
AL	3.98	3.04
FE	3.46	3.71
MN	0.88	0.02
MG	0.11	1.77
CA	1.77	0.01
NA	0.00	0.02
K	0.00	1.88
SUM	16.10	16.43

Loch Stornoway

	Gt	Bi
SI	37.33	35.62
TI	0.11	1.99
AL	20.49	16.17
FE	24.52	22.14
MN	8.15	0.19
MG	0.60	9.84
CA	9.48	0.01
NA	0.00	0.07
K	0.00	9.07
TOT	100.69	95.10
SI	5.99	5.77
TI	0.01	0.24
AL	3.88	3.09
FE	3.29	3.00
MN	1.11	0.03
MG	0.14	2.38
CA	1.63	0.00
NA	0.00	0.02
K	0.00	1.87
SUM	16.06	16.39

Figure A2.6: Mole Fraction Data: Gigha and Loch Stornoway (RECALC, Holland & Powell 1988)

Loch Stornoway (Recalc, Holland & Powell 1989)

<==== garnet ====>

	x	sd(x)	%
x(gr)	0.0184	0.000807	4.4
x(py)	1.25E-05	3.46E-06	27.6
x(alm)	0.133	0.00859	6.4
x(andr)	2.19E-05	1.58E-05	72.4

<==== biotite ====>

	x	sd(x)	%
x(phl)	0.043	0.00255	5.9
x(ann)	0.0532	0.0209	39.4
x(east)	0.0205	0.00283	13.8
x(naph)	0.000505	0.000366	72.5

Gigha (Recalc, Holland & Powell 1989)

<==== garnet ====>

	x	sd(x)	%
x(gr)	0.0239	0.00101	4.2
x(py)	5.08E-06	1.86E-06	36.7
x(alm)	0.175	0.0105	6
x(andr)	8.16E-07	3.53E-06	432.8

<==== biotite ====>

	x	sd(x)	%
x(phl)	0.0175	0.00124	7.1
x(ann)	0.0981	0.0397	40.4
x(east)	0.00875	0.00202	23.1
x(naph)	0.000151	0.000153	101

Figure A2.7: Garnet-Biotite Geothermometry
(Ferry & Spear 1977)

	X(Pyr)	X(Alm)	X(Phl)	X(Ann)	T
Gigha	5.08E-06	0.175	0.0175	0.0981	**502**
Loch Stornoway	1.25E-05	0.133	0.043	0.0532	**495**

Figure A2.8: Average Temperature Calculation Data (THERMOCALC , Powell & Holland 1988)

Output data from THERMOCALC are present herein. Temperatures are calculated at 1kB intervals between 5 and 15kB from the intersections of all univariant reaction curves generated from mineral assemblage data from Scarba (SCARBA), Traigh Gheighsgeir (TGS), Stronefield (STF) and Port Cill Maluaig (PCM).
Actvities (a) were calculated using AX (Holland 1991) from electron microprobe data presented in appendix 7.
The THERMOCALC output includes the following:
1. Input criteria: standard deviation of temperature limit (sd(T) limit), rock name, suggested pressure and fluid composition (x(H2O)).
2. Activities (a) and standard deviations of ln(activity) (sd(ln a)), tabulated for all pure end-member species present in the rock.
3. Independent univariant reactions generated by THERMOCALC.
4. Pressure/temperature calculations; the temperature at the suggested pressure (T(P)), the standard deviation of temperature (sd), the slope of the reaction curve at the estimated P & T (dP/dT) and lnK are tabulated for each independent univariant reaction.
5. Diagnostic information; a variety of parameters are tabulated from which the reliability of each reaction in generating the output data may be established. The parameters, and their significance is explained in the outputs.
6. Average temperature (av T), standard deviation (sd) and fit (f) calculated at 1kb intervals from 5 to 15kb are presented.

To enable identification of electron microprobe data specific to the above P/T calculation, the individual localities are listed below:

Abbreviation	Locality	Distance from Base of Section
SCARBA	Scarba	28.1m
TGS1	Traigh Gheighsgeir	3.18m
TGS2	Traigh Gheighsgeir	0.23m
STF1	Stronefield	-1.6m
STF2	Stronefield	2.0m
STF3	Stronefield	5.2m
PCM1	Port Cill Maluaig	12.2m
PCM2	Port Cill Maluaig	2.8m
PCM3	Port Cill Maluaig	3.9m
PCM4	Port Cill Maluaig	4.22m

Geothermometric data generated from THERMOCALC is unique in that instead of depending on a single calibrated reaction, all the possible reactions in the rock are utilised. Nevertheless some of the temperature estimates presented herein suffer from poorly fitting data, and therefore their application must be treated with caution.

<= AVERAGE PRESSURE/TEMPERATURE CALCULATIONS =>

an independent set of reactions has been calculated for sd(T) limit = 40C :
Rock name : SCARBA (suggested P = 10.0 kbar)(for x(H2O) = 1.0)

	clin	daph	ames	fame	phl	ann	east
a	0.0794	0.00592	0.0205	0.00256	0.107	0.0467	0.0309
sd(ln a)	0.30953	0.60386	0.44059	0.67047	0.27113	0.3685	0.40749

	q	mu	H2O
a	1	1	1
sd(ln a)	0	0	

reactions

1) 2clin + 3mu = ames + 3east + 7q + 4H2O
2) clin + phl + 3mu = 4east + 7q + 4H2O
3) 6clin + 4daph + 15mu = 5fame + 15east + 35q + 20H2O
4) 10clin + 4ann + 21mu = 3fame + 25east + 49q + 28H2O

calculations

	T(P)	sd	dP/dT	ln_K
1	516	35	0.0889	-9.249
2	499	40	0.0961	-9.139
3	514	37	0.0906	-46.245
4	499	37	0.1019	-67.2

Rock SCARBA : average temperatures(for x(H2O) = 1.0)

Diagnostic information

av, sd, fit are result of doubling (first table) /
halving (second table) uncertainty on ln a :
a ln a is suspect if any are v different from lsq values.
e* are ln a residuals normalised to ln a uncertainties :
large absolute values, say >2.5, point to suspect info.
hat are the diagonal elements of the hat matrix :
large values, say >0.40, point to influential data.
For 95% confidence, fit (= sd(fit)) should be less than 1.61

	av	sd	fit
lsq	529	32	0.99

	T	sd	fit	e*	hat
clin	523	37	0.97	0.2	0.19
daph	523	33	0.85	0.8	0.04
ames	517	35	0.8	-0.9	0.11
fame	530	33	0.99	0	0.04
phl	530	32	0.98	0.1	0.01
ann	527	32	0.82	-0.8	0
east	554	42	0.84	0.7	0.41
q	529	32	0.99	0	0
mu	529	32	0.99	0	0
H2O	529	32	0.99	0	0

	T	sd	fit	e*	hat
clin	533	29	1	0.2	0.19
daph	536	31	1.11	0.8	0.04
ames	541	30	1.14	-0.9	0.11
fame	529	31	0.99	0	0.04
phl	529	32	0.99	0.1	0.01
ann	531	32	1.11	-0.8	0
east	516	25	1.06	0.7	0.41
q	529	32	0.99	0	0
mu	529	32	0.99	0	0
H2O	529	32	0.99	0	0

P	5	6	7	8	9	10	11	12
av T	464	478	492	505	517	529	541	553
sd	30	31	31	32	32	32	35	38
f	0.6	0.7	0.8	0.8	0.9	1	1.1	1.1

P	13	14	15
av T	564	575	585
sd	41	44	47
f	1.2	1.3	1.4

<= AVERAGE PRESSURE/TEMPERATURE CALCULATIONS =>

an independent set of reactions has been calculated for sd(T) limit = 40C :
Rock name : PCM1 (suggested P = 10.0 kbar) (for x(CO2) = 0.02 and x(H2O) = 0.98)

	clin	daph	ames	fame	cz	cc	q	H2O
a	0.0114	0.028	0.00726	0.0149	1	1	1	0.98
sd(ln a)	0.47854	0.43647	0.50211	0.5119	0	0	0	

	CO2
a	0.02
sd(ln a)	

reactions

1) 5ames + 8cc + 14q = 4clin + 4cz + 2H2O + 8CO2
2) 5fame + 8cc + 14q = 4daph + 4cz + 2H2O + 8CO2

calculations

	T(P)	sd	dP/dT	ln_K
1	445	22	0.1714	6.743
2	448	24	0.1615	6.742

Rock PCM1 : average temperatures (for x(CO2) = 0.02 and x(H2O) = 0.98)

Diagnostic information

av, sd, fit are result of doubling (first table) /
halving (second table) uncertainty on ln a :
a ln a is suspect if any are v different from lsq values.
e* are ln a residuals normalised to ln a uncertainties :
large absolute values, say >2.5, point to suspect info.
hat are the diagonal elements of the hat matrix :
large values, say >0.22, point to influential data.
For 95% confidence, fit (= sd(fit)) should be less than 1.96

	av	**sd**	**fit**
lsq	**446**	**19**	**0.1**

	T	sd	fit	e*	hat
clin	447	21	0.08	0	0.15
daph	446	20	0.09	0	0.1
ames	447	22	0.07	-0.1	0.25
fame	446	21	0.07	0.1	0.21
cz	446	19	0.1	0	0
cc	446	19	0.1	0	0
q	446	19	0.1	0	0
H2O	446	19	0.1	0	0
CO2	446	23	0.1	0	0.19

	T	sd	fit	e*	hat
clin	446	17	0.11	0	0.15
daph	447	18	0.11	0	0.1
ames	446	16	0.12	-0.1	0.25
fame	447	17	0.12	0.1	0.21
cz	446	19	0.1	0	0
cc	446	19	0.1	0	0
q	446	19	0.1	0	0
H2O	446	19	0.1	0	0
CO2	446	17	0.1	0	0.19

P	5	6	7	8	9	10	11	12
av T	404	415	425	433	440	446	452	457
sd	17	18	18	18	18	19	19	19
f	0.1	0.1	0.1	0.1	0.1	0.1	0.1	0.1

P	13	14	15
av T	462	466	469
sd	19	19	19
f	0.1	0.1	0.2

<= AVERAGE PRESSURE/TEMPERATURE CALCULATIONS =>

an independent set of reactions has been calculated for sd(T) limit = 40C :
Rock name : PCM2 (suggested P = 10.0 kbar) (for x(CO2) = 0.02 and x(H2O) = 0.98)

	clin	daph	ames	fame	phl	ann	east	naph
a	0.0193	0.0291	0.00901	0.0125	0.0436	0.0946	0.0228	3.00E-04
sd(ln a)	0.44501	0.43163	0.49152	0.53057	0.37564	0.26672	0.43259	3.30E+01

	tr	ftr	hb	ed	parg	fhb	cz	ab
a	4.10E+00	04 4.8E-	0004 0.	0127 7.9	E-0004 0	0.0044	0.0146	1
sd(ln a)	0.99015	0.91946	0.47216	0.8674	0.66161	0.51105	0	0

	cc	q	CO2	H2O
a	1	1	0.02	0.98
sd(ln a)	0	0		

reactions (incomplete)

1) 20ames + 3tr + 22cc + 35q = 19clin + 14cz + 22CO2
2) 10clin + 12cc + 28q = 5ames + 6tr + 12CO2 + 14H2O
3) 17ames + 3hb + 22cc + 35q = 16clin + 14cz + 22CO2
4) 10daph + 12cc + 28q = 5fame + 6ftr + 12CO2 + 14H2O
5) 17fame + 3fhb + 22cc + 35q = 16daph + 14cz + 22CO2
6) 4daph + fame + 12cc + 28q = 6fhb + 12CO2 + 14H2O
7) 10clin + tr + 7ab + 12cc = 5ames + 7ed + 12CO2 + 14H2O
8) 5clin + 5phl + 12cc + 28q = 5east + 6tr + 12CO2 + 14H2O
9) 3clin + 2ames + tr + 7ab + 12cc = 7parg + 12CO2 + 14H2O
10) 52clin + 68ann + 72cz + 21ab = 10ames + 68east + 21parg + 51fhb + 132H2O

calculations

	T(P)		sd	dP/dT	ln_K
1	447		39	0.2104	42.565
2	460		23	0.1206	-30.878
3	422		32	0.2155	29.959
4	454		22	0.1029	-32.347
5	428		36	0.2264	30.547
6	506		15	0.1001	-6.841
7	472		24	0.2061	-26.262
8	449		20	0.1286	-30.324
9	459		17	0.178	-8.918
1	0	508	39	0.1132	-268.205

Rock PCM2 : average temperatures (for x(CO2) = 0.02 and x(H2O) = 0.98)

Diagnostic information
av, sd, fit are result of doubling (first table) /
halving (second table) uncertainty on ln a :
a ln a is suspect if any are v different from lsq values.
e* are ln a residuals normalised to ln a uncertainties :
large absolute values, say >2.5, point to suspect info.
hat are the diagonal elements of the hat matrix :
large values, say >0.53, point to influential data.
For 95% confidence, fit (= sd(fit)) should be less than 1.37

	av	sd	fit
lsq	474	15	1.76

	T	sd	fit	e*	hat
clin	473	15	1.75	0.5	0.04
daph	473	15	1.74	0.8	0.02
ames	475	15	1.75	-0.6	0.06
fame	474	15	1.76	-0.2	0.02
phl	474	15	1.76	0.4	0
ann	474	15	1.74	-0.6	0
east	474	15	1.75	0.6	0
tr	476	15	1.71	1.4	0.04
ftr	477	14	1.63	2	0.03
hb	469	13	1.45	-2.9	0.04
ed	475	15	1.74	0.7	0.03
parg	475	15	1.73	1	0.03
fhb	472	14	1.67	-1.5	0.01
cz	474	15	1.76	0	0
ab	474	15	1.76	0	0
cc	474	15	1.76	0	0
q	474	15	1.76	0	0
CO2	479	23	1.75	0.3	0.51
H2O	474	15	1.76	0	0

	T	sd	fit	e*	hat
clin	475	15	1.77	0.5	0.04
daph	475	15	1.78	0.8	0.02
ames	472	14	1.77	-0.6	0.06
fame	474	15	1.76	-0.2	0.02
phl	474	15	1.77	0.4	0
ann	474	15	1.77	-0.6	0
east	474	15	1.77	0.6	0
tr	470	15	1.88	1.4	0.04
ftr	469	16	1.96	2	0.03
hb	480	17	2.08	-2.9	0.04
ed	472	15	1.79	0.7	0.03
parg	471	15	1.81	1	0.03
fhb	476	15	1.84	-1.5	0.01
cz	474	15	1.76	0	0
ab	474	15	1.76	0	0
cc	474	15	1.76	0	0
q	474	15	1.76	0	0
CO2	472	12	1.76	0.3	0.51
H2O	474	15	1.76	0	0

P	5	6	7	8	9	10	11	12
av T	426	438	448	457	466	474	481	488
sd	12	13	13	14	14	15	15	16
f	1.6	1.6	1.6	1.7	1.7	1.8	1.8	1.9

P	13	14	15
av T	494	500	506
sd	17	17	18
f	1.9	2	2.1

<= AVERAGE PRESSURE/TEMPERATURE CALCULATIONS =>

an independent set of reactions has been calculated for sd(T) limit = 40C :
Rock name : PCM3 (suggested P = 10.0 kbar) (for x(CO2) = 0.02 and x(H2O) = 0.98)

	clin	daph	ames	fame	tr	ftr	hb	ed
a	0.0203	0.0229	0.0104	0.0114	0.00127	9.00E-04	0.0187	0.00213
sd(ln a)	0.44119	0.46128	0.48395	0.54007	0.55797	0.85338 0	.44707 0	0.75165

	parg	fhb	cz	ab	cc	q	CO2	H2O
a	0.00557	0.0141	1	1	1	1	0.02	0.98
sd(ln a)	0.63382	0.51516	0	0	0	0		

reactions

1) 20ames + 3tr + 22cc + 35q = 19clin + 14cz + 22CO2
2) 10clin + 12cc + 28q = 5ames + 6tr + 12CO2 + 14H2O
3) 17ames + 3hb + 22cc + 35q = 16clin + 14cz + 22CO2
4) 10daph + 12cc + 28q = 5fame + 6ftr + 12CO2 + 14H2O
5) 17fame + 3fhb + 22cc + 35q = 16daph + 14cz + 22CO2
6) 4daph + fame + 12cc + 28q = 6fhb + 12CO2 + 14H2O
7) 10clin + tr + 7ab + 12cc = 5ames + 7ed + 12CO2 + 14H2O
8) 3clin + 2ames + tr + 7ab + 12cc = 7parg + 12CO2 + 14H2O

calculations

	T(P)	sd	dP/dT	ln_K
1	432	37	0.2218	37.31
2	480	19	0.1145	-23.872
3	415	31	0.2213	27.232
4	469	23	0.0993	-26.702
5	422	37	0.2316	28.366
6	508	16	0.0995	-5.983
7	489	23	0.1943	-20.273
8	459	16	0.1779	-8.835

Rock PCM3 : average temperatures (for x(CO2) = 0.02 and x(H2O) = 0.98)

Diagnostic information

av, sd, fit are result of doubling (first table) /
halving (second table) uncertainty on ln a :
a ln a is suspect if any are v different from lsq values.
e* are ln a residuals normalised to ln a uncertainties :
large absolute values, say >2.5, point to suspect info.
hat are the diagonal elements of the hat matrix :
large values, say >0.50, point to influential data.
For 95% confidence, fit (= sd(fit)) should be less than 1.42

	av	sd	fit
lsq	477	16	1.96

	T	sd	fit	e*	hat
clin	474	16	1.92	1	0.06
daph	476	16	1.95	0.6	0.01
ames	478	17	1.95	-0.5	0.07
fame	477	16	1.95	-0.4	0.01
tr	479	16	1.9	1.2	0.05
ftr	479	16	1.89	1.4	0.03
hb	473	13	1.56	-3	0.02
ed	477	16	1.96	0.2	0.02
parg	478	16	1.91	1.2	0.02
fhb	475	16	1.86	-1.5	0.01
cz	477	16	1.96	0	0
ab	477	16	1.96	0	0
cc	477	16	1.96	0	0
q	477	16	1.96	0	0
CO2	485	25	1.94	0.5	0.54
H2O	477	16	1.96	0	0

	T	sd	fit	e*	hat
clin	479	16	2.01	1	0.06
daph	477	16	1.98	0.6	0.01
ames	475	16	1.97	-0.5	0.07
fame	476	16	1.97	-0.4	0.01
tr	473	16	2.04	1.2	0.05
ftr	474	17	2.07	1.4	0.03
hb	481	19	2.38	-3	0.02
ed	476	16	1.96	0.2	0.02
parg	474	17	2.05	1.2	0.02
fhb	478	17	2.05	-1.5	0.01
cz	477	16	1.96	0	0
ab	477	16	1.96	0	0
cc	477	16	1.96	0	0
q	477	16	1.96	0	0
CO2	474	12	1.97	0.5	0.54
H2O	477	16	1.96	0	0

P	5	6	7	8	9	10	11	12
av T	428	440	451	460	469	477	484	491
sd	14	14	15	15	16	16	17	17
f	1.8	1.8	1.8	1.9	1.9	2	2	2.1

P	13	14	15
av T	497	503	509
sd	18	19	20
f	2.1	2.2	2.3

<= AVERAGE PRESSURE/TEMPERATURE CALCULATIONS =>

an independent set of reactions has been calculated for sd(T) limit = 40C :
Rock name : PCM4 (suggested P = 10.0 kbar) (for x(CO2) = 0.02 and x(H2O) = 0.98)

	ames	fame	tr	ftr	hb	ed	parg	fhb
a	0.0033	0.0121	2.30E-05	1.90E-04	0.00257	9.60E-05	0.00191	0.0139
sd(ln a)	0.53307	0.53377	4.17029	1.00811	0.54067	1.06547	0.75066	0.51713

	gl	fgl	cz	ab	cc	q	CO2	H2O
a	5.00E-06	1.70E-05	1	1	1	1	0.02	0.98
sd(ln a)	8.94427	1.16673	0	0	0	0	-	

reactions

1) 15ames + 64cc + 126q = 12tr + 20cz + 64CO2 + 38H2O
2) 3ames + 10cc + 21q = 3hb + 2cz + 10CO2 + 8H2O
3) fame + 19fhb + 22cc + 35q = 16ftr + 14cz + 22CO2
4) 10ames + 4ftr + 12cc + 28q = 5fame + 10hb + 12CO2 + 14H2O
5) 5ames + tr + 3ed + 7ab + 12cc = 10parg + 12CO2 + 14H2O
6) 27ames + 12tr + 42ab + 76cc = 42parg + 8cz + 76CO2 + 74H2O
7) 3fame + 4fgl + 12cc + 28q = 6fhb + 8ab + 12CO2 + 10H2O
8) 7ames + 145fhb + 4gl + 170cc + 241q = 116ftr + 8ed + 106cz + 170CO2

calculations

	T(P)	sd	dP/dT	ln_K
1	443	34	0.1462	-42.439
2	486	12	0.13	-0.744
3	280	39	0.248	-51.482
4	546	34	0.1337	9.742
5	471	31	0.1592	4.406
6	471	32	0.184	19.533
7	603	24	0.0604	31.518
8	292	39	0.241	-359.417

Rock PCM4 : average temperatures (for x(CO2) = 0.02 and x(H2O) = 0.98)

Diagnostic information

av, sd, fit are result of doubling (first table) /
halving (second table) uncertainty on ln a :
a ln a is suspect if any are v different from lsq values.
e* are ln a residuals normalised to ln a uncertainties :
large absolute values, say >2.5, point to suspect info.
hat are the diagonal elements of the hat matrix :
large values, say >0.50, point to influential data.
For 95% confidence, fit (= sd(fit)) should be less than 1.42

	av	sd	fit
lsq	469	27	2.92

	T	sd	fit	e*	hat
ames	468	31	2.92	0.2	0.17
fame	470	29	2.92	-0.4	0.07
tr	469	27	2.91	0.7	0
ftr	472	27	2.84	1.8	0.04
hb	466	27	2.85	-1.6	0.03
ed	471	27	2.89	1.2	0.03
parg	470	27	2.91	0.6	0.02
fhb	464	25	2.66	-2.7	0.02
gl	469	27	2.91	0.9	0
fgl	468	20	2.14	5.9	0
cz	469	27	2.92	0	0
ab	469	27	2.92	0	0
cc	469	27	2.92	0	0
q	469	27	2.92	0	0
CO2	474	42	2.92	0.3	0.45
H2O	469	27	2.92	0	0

	T	sd	fit	e*	hat
ames	469	25	2.92	0.2	0.17
fame	468	26	2.93	-0.4	0.07
tr	468	27	2.95	0.7	0
ftr	464	27	3.03	1.8	0.04
hb	472	27	2.99	-1.6	0.03
ed	466	27	2.98	1.2	0.03
parg	467	27	2.94	0.6	0.02
fhb	472	29	3.11	-2.7	0.02
gl	469	28	2.98	0.9	0
fgl	471	42	4.47	5.9	0
cz	469	27	2.92	0	0
ab	469	27	2.92	0	0
cc	469	27	2.92	0	0
q	469	27	2.92	0	0
CO2	467	22	2.92	0.3	0.45
H2O	469	27	2.92	0	0

P	5	6	7	8	9	10	11	12
av T	421	433	443	453	461	469	476	483
sd	19	21	22	24	26	27	29	31
f	2.2	2.4	2.5	2.6	2.8	2.9	3.1	3.2

P	13	14	15
av T	489	495	500
sd	32	34	36
f	3.4	3.5	3.7

<= AVERAGE PRESSURE/TEMPERATURE CALCULATIONS =>

an independent set of reactions has been calculated for sd(T) limit = 40C :
Rock name : TGS1 (suggested P = 10.0 kbar) (for x(CO2) = 0.02 and x(H2O) = 0.98)

	clin	daph	ames	fame	cc	dol	fdol	ab
a	0.0113	0.0343	0.00909	0.022	0.925	0.166	0.625	1
sd(ln a)	0.47907	0.41032	0.49104	0.46613	0.00169	0.20867	0.04219	0

	q	pa	CO2	H2O
a	1	1	0.02	0.98
sd(ln a)	0	0		

reactions

1) ames + 6dol + 4q + 4H2O = 2clin + 6cc + 6CO2
2) fame + 6fdol + 4q + 4H2O = 2daph + 6cc + 6CO2
3) 5ames + 30fdol + 20q + 20H2O = 4clin + 6daph + 30cc + 30CO2
4) 5dol + 3q + pa + 3H2O = clin + 5cc + ab + 5CO2

calculations

	T(P)	sd	dP/dT	ln_K
1	519	25	0.0504	6.047
2	433	17	0.0569	-0.58
3	432	16	0.0573	-2.9
4	542	21	0.0454	4.109

Rock TGS1 : average temperatures (for x(CO2) = 0.02 and x(H2O) = 0.98)

Diagnostic information

av, sd, fit are result of doubling (first table) /
halving (second table) uncertainty on ln a :
a ln a is suspect if any are v different from lsq values.
e* are ln a residuals normalised to ln a uncertainties :
large absolute values, say >2.5, point to suspect info.
hat are the diagonal elements of the hat matrix :
large values, say >0.33, point to influential data.
For 95% confidence, fit (= sd(fit)) should be less than 1.61

	av	sd	fit
lsq	493	47	3.7

	T	sd	fit	e*	hat
clin	493	47	3.67	0.8	0
daph	503	42	3.19	2.7	0.04
ames	488	41	3.2	-3.1	0.01
fame	489	47	3.59	-1.4	0.03
cc	493	47	3.7	0	0
dol	481	40	3.02	3.7	0.06
fdol	498	48	3.61	-0.8	0.03
ab	493	47	3.7	0	0
q	493	47	3.7	0	0
pa	493	47	3.7	0	0
CO2	502	76	3.69	0.3	0.54
H2O	493	47	3.7	0	0

	T	sd	fit	e*	hat
clin	492	48	3.73	0.8	0
daph	486	50	4.01	2.7	0.04
ames	499	54	4.27	-3.1	0.01
fame	497	48	3.82	-1.4	0.03
cc	493	47	3.7	0	0
dol	511	55	4.54	3.7	0.06
fdol	491	47	3.73	-0.8	0.03
ab	493	47	3.7	0	0
q	493	47	3.7	0	0
pa	493	47	3.7	0	0
CO2	490	36	3.71	0.3	0.54
H2O	493	47	3.7	0	0

P	5	6	7	8	9	10	11	12
av T	375	400	425	448	471	493	514	535
sd	35	37	40	42	45	47	50	53
f	2.9	3	3.2	3.4	3.5	3.7	3.9	4.1

P	13	14	15
av T	555	575	595
sd	55	58	60
f	4.2	4.4	4.6

<= AVERAGE PRESSURE/TEMPERATURE CALCULATIONS =>

an independent set of reactions has been calculated for sd(T) limit = 40C :
Rock name : TGS2 (suggested P = 10.0 kbar) (for x(CO2) = 0.02 and x(H2O) = 0.98)

	clin	daph	ames	fame	dol	fdol	cc	pa
a	0.0137	0.0318	0.0102	0.0199	0.486	0.514	1	1
sd(ln a)	0.46775	0.42026	0.48509	0.47817	0.07917	0.07095	0	0

	q	ab	CO2	H2O
a	1	1	0.02	0.98
sd(ln a)	0	0		

reactions

1) ames + 6dol + 4q + 4H2O = 2clin + 6cc + 6CO2
2) fame + 6fdol + 4q + 4H2O = 2daph + 6cc + 6CO2
3) 5ames + 30fdol + 20q + 20H2O = 4clin + 6daph + 30cc + 30CO2
4) 5dol + pa + 3q + 3H2O = clin + 5cc + ab + 5CO2

calculations

T(P)	sd	dP/dT	ln_K	
1	450	16	0.0568	0.333
2	451	18	0.055	1.013
3	449	17	0.0554	5.066
4	475	13	0.0507	-0.686

Rock TGS2 : average temperatures (for x(CO2) = 0.02 and x(H2O) = 0.98)

Diagnostic information

av, sd, fit are result of doubling (first table) /
halving (second table) uncertainty on ln a :
a ln a is suspect if any are v different from lsq values.
e* are ln a residuals normalised to ln a uncertainties :
large absolute values, say >2.5, point to suspect info.
hat are the diagonal elements of the hat matrix :
large values, say >0.33, point to influential data.
For 95% confidence, fit (= sd(fit)) should be less than 1.61

	av	sd	fit
lsq	490	28	2.47

	T	sd	fit	e*	hat
clin	496	25	2.14	1.9	0.04
daph	492	26	2.22	1.6	0.01
ames	484	24	2.06	-2.3	0.05
fame	488	25	2.15	-2	0.01
dol	491	31	2.46	-0.1	0.09
fdol	491	29	2.46	-0.1	0.01
cc	490	28	2.47	0	0
pa	490	28	2.47	0	0
q	490	28	2.47	0	0
ab	490	28	2.47	0	0
CO2	503	47	2.42	0.5	0.64
H2O	490	28	2.47	0	0

	T	sd	fit	e*	hat
clin	486	31	2.74	1.9	0.04
daph	489	30	2.64	1.6	0.01
ames	499	33	2.93	-2.3	0.05
fame	493	32	2.79	-2	0.01
dol	490	27	2.47	-0.1	0.09
fdol	490	28	2.47	-0.1	0.01
cc	490	28	2.47	0	0
pa	490	28	2.47	0	0
q	490	28	2.47	0	0
ab	490	28	2.47	0	0
CO2	487	21	2.48	0.5	0.64
H2O	490	28	2.47	0	0

P	5	6	7	8	9	10	11	12
av T	374	400	424	447	469	490	511	532
sd	17	19	22	24	26	28	31	33
f	1.6	1.7	1.9	2.1	2.3	2.5	2.7	2.8

P	13	14	15
av T	552	571	590
sd	36	38	41
f	3	3.2	3.4

<= AVERAGE PRESSURE/TEMPERATURE CALCULATIONS =>

an independent set of reactions has been calculated for sd(T) limit = 40C :
Rock name : TGS2 (suggested P = 10.0 kbar) (for x(CO2) = 0.02 and x(H2O) = 0.98)

	clin	daph	ames	fame	dol	fdol	cc	pa
a	0.0137	0.0318	0.0102	0.0199	0.236	0.264	1	1
sd(ln a)	0.46775	0.42026	0.48509	0.47817	0.17488	0.16255	0	0

	q	ab	CO2	H2O
a	1	1	0.02	0.98
sd(ln a)	0	0		

reactions

1) ames + 6dol + 4q + 4H2O = 2clin + 6cc + 6CO2
2) fame + 6fdol + 4q + 4H2O = 2daph + 6cc + 6CO2
3) 5ames + 30fdol + 20q + 20H2O = 4clin + 6daph + 30cc + 30CO2
4) 5dol + pa + 3q + 3H2O = clin + 5cc + ab + 5CO2

calculations

	T(P)	sd	dP/dT	ln_K
1	501	22	0.0519	4.659
2	500	24	0.0504	5.009
3	499	22	0.0508	25.048
4	524	18	0.0467	2.919

Rock TGS2 : average temperatures (for x(CO2) = 0.02 and x(H2O) = 0.98)

Diagnostic information

av, sd, fit are result of doubling (first table) /
halving (second table) uncertainty on ln a :
a ln a is suspect if any are v different from lsq values.
e* are ln a residuals normalised to ln a uncertainties :
large absolute values, say >2.5, point to suspect info.
hat are the diagonal elements of the hat matrix :
large values, say >0.33, point to influential data.
For 95% confidence, fit (= sd(fit)) should be less than 1.61

	av	sd	fit
lsq	541	31	2.11

	T	sd	fit	e*	hat
clin	544	26	1.81	1.6	0.01
daph	543	27	1.88	1.3	0.01
ames	535	26	1.75	-2	0.04
fame	537	27	1.84	-1.7	0.02
dol	542	35	2.11	-0.2	0.22
fdol	543	33	2.1	-0.3	0.11
cc	541	31	2.11	0	0
pa	541	31	2.11	0	0
q	541	31	2.11	0	0
ab	541	31	2.11	0	0
CO2	553	45	2.06	0.4	0.46
H2O	541	31	2.11	0	0

	T	sd	fit	e*	hat
clin	538	33	2.33	1.6	0.01
daph	539	32	2.25	1.3	0.01
ames	548	35	2.49	-2	0.04
fame	545	34	2.37	-1.7	0.02
dol	539	27	2.11	-0.2	0.22
fdol	539	29	2.12	-0.3	0.11
cc	541	31	2.11	0	0
pa	541	31	2.11	0	0
q	541	31	2.11	0	0
ab	541	31	2.11	0	0
CO2	537	25	2.12	0.4	0.46
H2O	541	31	2.11	0	0

P	5	6	7	8	9	10	11	12
av T	414	441	468	493	517	541	564	586
sd	18	20	23	25	28	31	33	36
f	1.3	1.4	1.6	1.8	1.9	2.1	2.3	2.5

P	13	14	15
av T	608	629	650
sd	39	42	45
f	2.6	2.8	3

<= AVERAGE PRESSURE/TEMPERATURE CALCULATIONS =>

an independent set of reactions has been calculated for sd(T) limit = 40C :
Rock name : STF1 (suggested P = 10.0 kbar) (for x(CO2) = 0.02 and x(H2O) = 0.98)

	clin	daph	ames	fame	mu	cel	q	dol
a	0.0362	0.0146	0.0168	0.00813	0.58	0.107	1	0.595
sd(ln a)	0.39336	0.51385	0.4545	0.5745	0.03411	0.27118	0	0.04923

	fdol	cc	CO2	H2O
a	0.405	1	0.02	0.98
sd(ln a)	0.10617	0		

reactions

1) ames + 4q + 6dol + 4H2O = 2clin + 6cc + 6CO2
2) fame + 4q + 6fdol + 4H2O = 2daph + 6cc + 6CO2
3) 5ames + 20q + 30fdol + 20H2O = 4clin + 6daph + 30cc + 30CO2
4) mu + 4q + 6dol + 4H2O = clin + cel + 6cc + 6CO2

calculations

	T(P)	sd	dP/dT	ln_K
1	453	15	0.0566	0.565
2	460	21	0.0541	1.781
3	458	18	0.0545	8.903
4	480	12	0.0574	-1.888

Rock STF1 : average temperatures (for x(CO2) = 0.02 and x(H2O) = 0.98)

Diagnostic information
av, sd, fit are result of doubling (first table) /
halving (second table) uncertainty on ln a :
a ln a is suspect if any are v different from lsq values.
e* are ln a residuals normalised to ln a uncertainties :
large absolute values, say >2.5, point to suspect info.
hat are the diagonal elements of the hat matrix :
large values, say >0.33, point to influential data.
For 95% confidence, fit (= sd(fit)) should be less than 1.61

	av	sd	fit
lsq	483	28	2.3

	T	sd	fit	e*	hat
clin	492	24	1.86	2	0.07
daph	485	27	2.22	0.9	0.01
ames	481	24	1.96	-1.9	0
fame	484	26	2.11	-1.5	0
mu	483	28	2.29	0.2	0
cel	472	24	1.79	-1.9	0.08
q	483	28	2.3	0	0
dol	484	30	2.3	-0.1	0.06
fdol	483	28	2.3	0.2	0.01
cc	483	28	2.3	0	0
CO2	485	49	2.3	0.1	0.68
H2O	483	28	2.3	0	0

	T	sd	fit	e*	hat
clin	476	31	2.61	2	0.07
daph	482	29	2.37	0.9	0.01
ames	485	32	2.62	-1.9	0
fame	483	31	2.51	-1.5	0
mu	483	28	2.3	0.2	0
cel	489	30	2.52	-1.9	0.08
q	483	28	2.3	0	0
dol	483	28	2.3	-0.1	0.06
fdol	483	28	2.3	0.2	0.01
cc	483	28	2.3	0	0
CO2	483	20	2.3	0.1	0.68
H2O	483	28	2.3	0	0

P	5	6	7	8	9	10	11	12
av T	384	406	427	447	465	483	500	517
sd	30	30	29	29	29	28	28	28
f	2.5	2.5	2.4	2.4	2.3	2.3	2.3	2.2

P	13	14	15
av T	533	549	564
sd	27	27	27
f	2.2	2.1	2.1

<= AVERAGE PRESSURE/TEMPERATURE CALCULATIONS =>

an independent set of reactions has been calculated for sd(T) limit = 40C :
Rock name : STF2 (suggested P = 10.0 kbar) (for x(CO2) = 0.02 and x(H2O) = 0.98)

	clin	daph	ames	fame	mu	cel	q	dol
a	0.00876	0.0127	0.00783	0.0106	0.5	0.101	1	0.0992
sd(ln a)	0.49297	0.52891	0.49852	0.5485	0.05149	0.27877	0	0.24343

	fdol	cc	CO2	H2O
a	0.319	0.961	0.02	0.98
sd(ln a)	0.13921	0.00045		

reactions

1) ames + 4q + 6dol + 4H2O = 2clin + 6cc + 6CO2
2) fame + 4q + 6fdol + 4H2O = 2daph + 6cc + 6CO2
3) 5ames + 20q + 30fdol + 20H2O = 4clin + 6daph + 30cc + 30CO2
4) mu + 4q + 6dol + 4H2O = clin + cel + 6cc + 6CO2

calculations

	T(P)	sd	dP/dT	ln_K
1	561	30	0.0471	9.001
2	468	23	0.0534	2.444
3	466	20	0.0537	12.222
4	602	28	0.0471	7.294

Rock STF2 : average temperatures (for x(CO2) = 0.02 and x(H2O) = 0.98)

Diagnostic information

av, sd, fit are result of doubling (first table) /
halving (second table) uncertainty on ln a :
a ln a is suspect if any are v different from lsq values.
e* are ln a residuals normalised to ln a uncertainties :
large absolute values, say >2.5, point to suspect info.
hat are the diagonal elements of the hat matrix :
large values, say >0.33, point to influential data.
For 95% confidence, fit (= sd(fit)) should be less than 1.61

	av	sd	fit
lsq	538	63	3.63

	T	sd	fit	e*	hat
clin	542	61	3.45	1.7	0.01
daph	554	59	3.22	2.4	0.07
ames	540	56	3.17	-2.7	0
fame	536	62	3.51	-1.4	0
mu	537	63	3.6	0.4	0
cel	521	57	3.14	-2.3	0.05
q	538	63	3.63	0	0
dol	516	58	3.1	3.2	0.14
fdol	561	68	3.37	-1.7	0.17
cc	538	63	3.63	0	0
CO2	532	95	3.62	-0.2	0.41
H2O	538	63	3.63	0	0

	T	sd	fit	e*	hat
clin	534	66	3.77	1.7	0.01
daph	527	66	3.87	2.4	0.07
ames	535	70	4.01	-2.7	0
fame	540	65	3.74	-1.4	0
mu	538	64	3.63	0.4	0
cel	545	66	3.84	-2.3	0.05
q	538	63	3.63	0	0
dol	566	66	4.21	3.2	0.14
fdol	527	60	3.73	-1.7	0.17
cc	538	63	3.63	0	0
CO2	539	53	3.63	-0.2	0.41
H2O	538	63	3.63	0	0

P	5	6	7	8	9	10	11	12
av T	427	452	475	497	518	538	557	575
sd	60	61	61	62	63	63	64	65
f	3.6	3.6	3.6	3.6	3.6	3.6	3.6	3.6

P	13	14	15
av T	593	611	628
sd	65	66	66
f	3.6	3.7	3.7

<= AVERAGE PRESSURE/TEMPERATURE CALCULATIONS =>

an independent set of reactions has been calculated for sd(T) limit = 40C :
Rock name : STF3 (suggested P = 10.0 kbar) (for x(CO2) = 0.02 and x(H2O) = 0.98)

	clin	daph	ames	fame	mu	cel	q	dol
a	0.0191	0.0301	0.00996	0.0143	0.471	0.0881	1	0.447
sd(ln a)	0.44574	0.42738	0.48623	0.5159	0.0591	0.29662	0	0.09168

	fdol	cc	CO2	H2O
a	0.553	1	0.02	0.98
sd(ln a)	0.06	0		

reactions

1) ames + 4q + 6dol + 4H2O = 2clin + 6cc + 6CO2
2) fame + 4q + 6fdol + 4H2O = 2daph + 6cc + 6CO2
3) 5ames + 20q + 30fdol + 20H2O = 4clin + 6daph + 30cc + 30CO2
4) mu + 4q + 6dol + 4H2O = clin + cel + 6cc + 6CO2

calculations

	T(P)	sd	dP/dT	ln_K
1	463	17	0.0555	1.518
2	448	18	0.0553	0.792
3	447	16	0.0557	3.961
4	492	14	0.0562	-0.807

Rock STF3 : average temperatures (for x(CO2) = 0.02 and x(H2O) = 0.98)

Diagnostic information
av, sd, fit are result of doubling (first table) /
halving (second table) uncertainty on ln a :
a ln a is suspect if any are v different from lsq values.
e* are ln a residuals normalised to ln a uncertainties :
large absolute values, say >2.5, point to suspect info.
hat are the diagonal elements of the hat matrix :
large values, say >0.33, point to influential data.
For 95% confidence, fit (= sd(fit)) should be less than 1.61

	av	sd	fit
lsq	488	33	2.49

	T	sd	fit	e*	hat
clin	493	31	2.31	1.5	0.05
daph	493	30	2.21	1.7	0.03
ames	487	28	2.12	-2.1	0
fame	488	31	2.34	-1.4	0
mu	487	33	2.46	0.4	0
cel	475	27	1.95	-2.1	0.08
q	488	33	2.49	0	0
dol	482	35	2.43	0.7	0.1
fdol	489	33	2.45	-0.5	0.01
cc	488	33	2.49	0	0
CO2	490	56	2.49	0.1	0.61
H2O	488	33	2.49	0	0

	T	sd	fit	e*	hat
clin	483	34	2.65	1.5	0.05
daph	484	35	2.68	1.7	0.03
ames	488	38	2.84	-2.1	0
fame	487	35	2.65	-1.4	0
mu	488	33	2.5	0.4	0
cel	495	35	2.74	-2.1	0.08
q	488	33	2.49	0	0
dol	490	32	2.53	0.7	0.1
fdol	487	33	2.51	-0.5	0.01
cc	488	33	2.49	0	0
CO2	487	24	2.49	0.1	0.61
H2O	488	33	2.49	0	0

P	5	6	7	8	9	10	11	12
av T	386	409	430	450	469	488	505	522
sd	34	34	34	34	33	33	33	32
f	2.7	2.7	2.6	2.6	2.5	2.5	2.5	2.4

P	13	14	15
av T	538	554	570
sd	32	32	31
f	2.4	2.3	2.3

Figure A2.9: SW Highland Geothermometry

	Thermocalc (Holland & Powell 1988)
Scarba	529
PCM (Port Cill Maluaig)	446,474,477,469
TGS(Traigh Gheighsgeir)	493,490
STF (Stonefield)	483,538,488

	Cc-Dol-Fdol Thermometry (Annovitz & Essene 1987)
Traigh Gheighsgeir	290,316,362,374,441,446,451,466,483
Stronefield	52
Keppoch Point	########
Loch Fuar Bheinne	339,415,428,429,,437,441,445,451,456,463,465,466,470

	Cc-Dol Geothermometry (Powell et al. 1984)
Traigh Gheighsgeir	330-430
Stronefield	230
Keppoch Point	<200
Loch Fuar Bheinne	400-450

	Cc(Fe-Mg) Geothermometry (Powell et al. 1984)
Traigh Gheighsgeir	320-420
Stronefield	280
Keppoch Point	<200
Loch Fuar Bheinne	400-450

	Cc-Dol Geothermometry (Dymoke 1988)
SW Jura	475,480,441,605
Tayvallich	415,420,339,360,420,434

	Gt-Bi Geothermometry (Dymoke 1988)
Tarbert(East)	501,507,486,490,474,491,491,511,509
Clach Breac	477,507,452,479,528,562

	Gt-Hb Geothermometry (Dymoke 1988)
Stronachullin	557,535,563,562,539,567,550,528,556
Tarbert(East)	527,517,506,497
Tarbert(West)	491,527,546

Appendix 3: T-X_{CO_2} Calculations

Isobaric T-X_{CO_2} sections, calculated at 10kb, are presented together with relevant output data from THERMOCALC, for the the following systems:

- The approximated metabasite systems $NCMASHCO_2$ and $NCFASHCO_2$;
- The approximated phyllite systems $KCMASHCO_2$ and $KCFASHCO_2$;
- The approximated ky-phyllite systems $MASHCO_2$ and $FASHCO_2$;
- The approximated ctd-phyllite systems $MASHCO_2$ and $FASHCO_2$;
- Compiled data from the above systems, including only those reactions which will have modal significance for infiltration of a CO_2-bearing hydrous fluid, in the system $KNCMASHCO_2$ and $KNCFASHCO_2$.
- The T-X_{CO_2} phase relations of the reaction Sph→Ru+Cc+Qz

The THERMOCALC output includes the following:

1. Activites (pure end member reactions, therefore activities = 1)
2. Excluded assemblages.
3. All independent reactions.
4. Tabulated T-X_{CO_2} data.
5. Location and Schreinemakers analysis of stable intersections.

(6. Metastable intersections)

(7. Stability of reactions not involved in invariant points, detailed in 5)

temperature-x(CO2) phase diagram calculations

Unit activities

excluded assemblages | tr dol |

no of reactions = 9, no of intersections = 2,

1) 3clin + 10cc + 21q = 3tr + 2cz + 10CO2 + 8H2O
2) 3clin + 19cc + 11CO2 = 2cz + 3q + 15dol + 11H2O
3) 4cc + 6q + 3pa = 2cz + 3ab + 4CO2 + 2H2O
4) 6tr + 8cc + 21pa + 2H2O = 10cz + 6clin + 21ab + 8CO2
5) 2cz + 2clin + 4q + 5ab = 2tr + 5pa + 2H2O
6) clin + 2cc + 5q + ab = tr + pa + 2CO2 + 2H2O
7) 2clin + 14cc + pa + 6CO2 = 2cz + 10dol + ab + 8H2O
8) 42q + 20dol + 19pa + 2H2O = 10cz + 4clin + 19ab + 40CO2
9) 3q + 5dol + pa + 3H2O = clin + 5cc + ab + 5CO2

Temperatures for NCMASHCO2 in the range 100 <-> 700C; for P = 10.0 kbar
uncertainties at or near x(CO2) = 0.0505

x(CO2)	0.001	0.002	0.005	0.01	0.015	0.02	0.025	0.03	0.04	0.05	0.1	sdT
1	395	418	451	478	495	506	515	523	535	544	570	8
2	300	332	381	423	450	470	486	500	523	541	602	13
3	391	415	448	476	493	505	515	522	535	544	573	9
4	379	404	440	470	488	502	512	521	535	546	579	16

5	549	549	548	545	543	541	539	537	533	529	513	121
6	398	421	453	480	496	507	516	523	535	543	569	8
7	264	299	352	399	430	454	473	490	517	540	619	16
8	366	393	431	462	482	496	508	517	532	544	579	9
9	333	362	406	443	466	484	497	509	528	542	590	11

T-x(CO2) of intersections for NCMASHCO2 : P = 10.0 kbar
window : T 100 <-> 700C; x(CO2) 0.001 <-> 0.1
in excess : CO2 H2O

stable intersection 1 involving tr,cz,clin,cc,q,pa,ab + CO2,H2O or [dol]

	low T	**high T**	**dx/dt**
5) 2cz + 2clin + 4q + 5ab = 2tr + 5pa + 2H2O			
[cc]		stable	-0.00263
4) 6tr + 8cc + 21pa + 2H2O = 10cz + 6clin + 21ab + 8CO2			
[q]		stable	0.0009
3) 4cc + 6q + 3pa = 2cz + 3ab + 4CO2 + 2H2O			
[tr,clin]	stable	stable	0.00102
1) 3clin + 10cc + 21q = 3tr + 2cz + 10CO2 + 8H2O			
[pa,ab]	stable	stable	0.00107
6) clin + 2cc + 5q + ab = tr + pa + 2CO2 + 2H2O			
[cz]		stable	0.00111

T = 534C, x(CO2) = 0.0388

metastable intersection 2 involving cz,clin,cc,q,dol,pa,ab + CO2,H2O or [tr]
T = 548C, x(CO2) = 0.0540

SW Highlands : Metabasites : NCMASHCO2

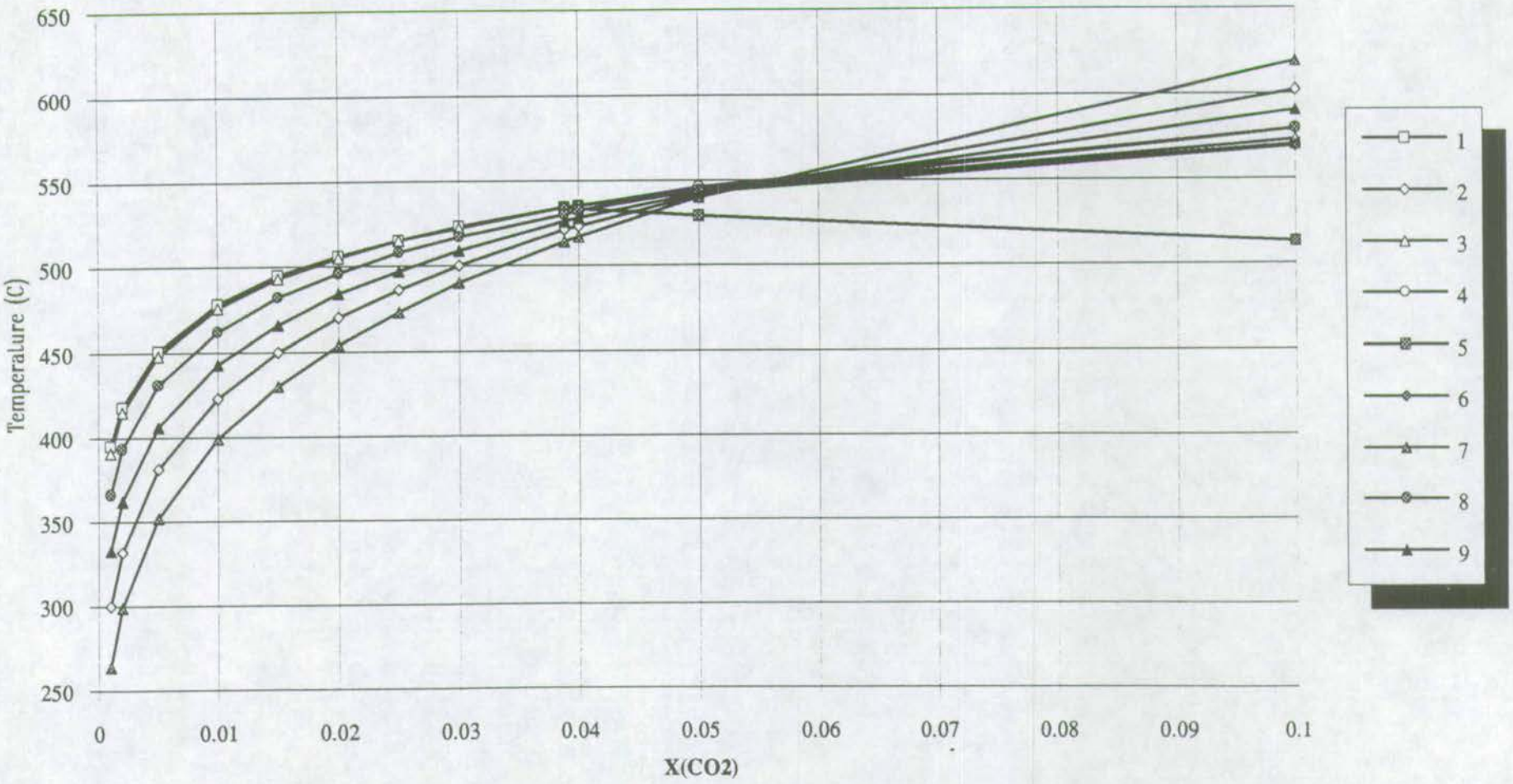

temperature-x(CO2) phase diagram calculations

Unit activities

excluded assemblages |ftr dol|

no of reactions = 9, no of intersections = 1,

1) 3daph + 10cc + 21q = 3ftr + 2cz + 10CO2 + 8H2O
2) 3daph + 19cc + 11CO2 = 2cz + 3q + 15fdol + 11H2O
3) 4cc + 6q + 3pa = 2cz + 3ab + 4CO2 + 2H2O
4) 6ftr + 8cc + 21pa + 2H2O = 10cz + 6daph + 21ab + 8CO2
5) 2cz + 2daph + 4q + 5ab = 2ftr + 5pa + 2H2O
6) daph + 2cc + 5q + ab = ftr + pa + 2CO2 + 2H2O
7) 2daph + 14cc + pa + 6CO2 = 2cz + ab + 10fdol + 8H2O
8) 42q + 19pa + 20fdol + 2H2O = 10cz + 4daph + 19ab + 40CO2
9) 3q + pa + 5fdol + 3H2O = daph + 5cc + ab + 5CO2

Temperatures for NCFASHCO2 in the range 250 <-> 700C; for P = 10.0 kbar
uncertainties at or near x(CO2) = 0.0505

x(CO2)	0.001	0.002	0.005	0.01	0.015	0.02	0.025	0.03	0.04	0.05	0.1	sdT
2	397	419	451	477	493	504	513	520	531	540	566	9
5	283	316	366	409	437	458	475	489	513	532	596	17
6	391	415	448	476	493	505	515	522	535	544	573	8
7	373	400	440	473	493	508	520	530	546	558	596	26

8	494	493	493	492	491	490	489	488	486	485	477	109
12	400	422	453	478	493	504	512	519	530	538	561	12
15	-	273	328	377	410	434	455	472	501	525	610	24
16	363	389	428	460	479	494	505	515	530	541	578	9
17	323	353	398	435	459	477	491	503	522	537	586	13

T-x(CO2) of intersections for NCFASHCO2 : P = 10.0 kbar
window : T 250 <-> 700C; x(CO2) 0.001 <-> 0.1
in excess : CO2 H2O

stable intersection 2 involving ftr,cz,daph,cc,q,pa,ab + CO2,H2O or [fdol]

	low T	high T	dx/dt
5) 2cz + 2daph + 4q + 5ab = 2ftr + 5pa + 2H2O			
[cc]		stable	-0.00542
4) 6ftr + 8cc + 21pa + 2H2O = 10cz + 6daph + 21ab + 8CO2			
[q]		stable	0.000339
3) 4cc + 6q + 3pa = 2cz + 3ab + 4CO2 + 2H2O			
[ftr,daph]	stable	stable	0.000418
1) 3daph + 10cc + 21q = 3ftr + 2cz + 10CO2 + 8H2O			
[pa,ab]	stable	stable	0.00044
6) daph + 2cc + 5q + ab = ftr + pa + 2CO2 + 2H2O			
[cz]		stable	0.000471

T = 491C, x(CO2) = 0.0143

metastable intersection 7 involving cz,daph,cc,q,pa,ab,fdol + CO2,H2O or [ftr]
T = 555C, x(CO2) = 0.0651

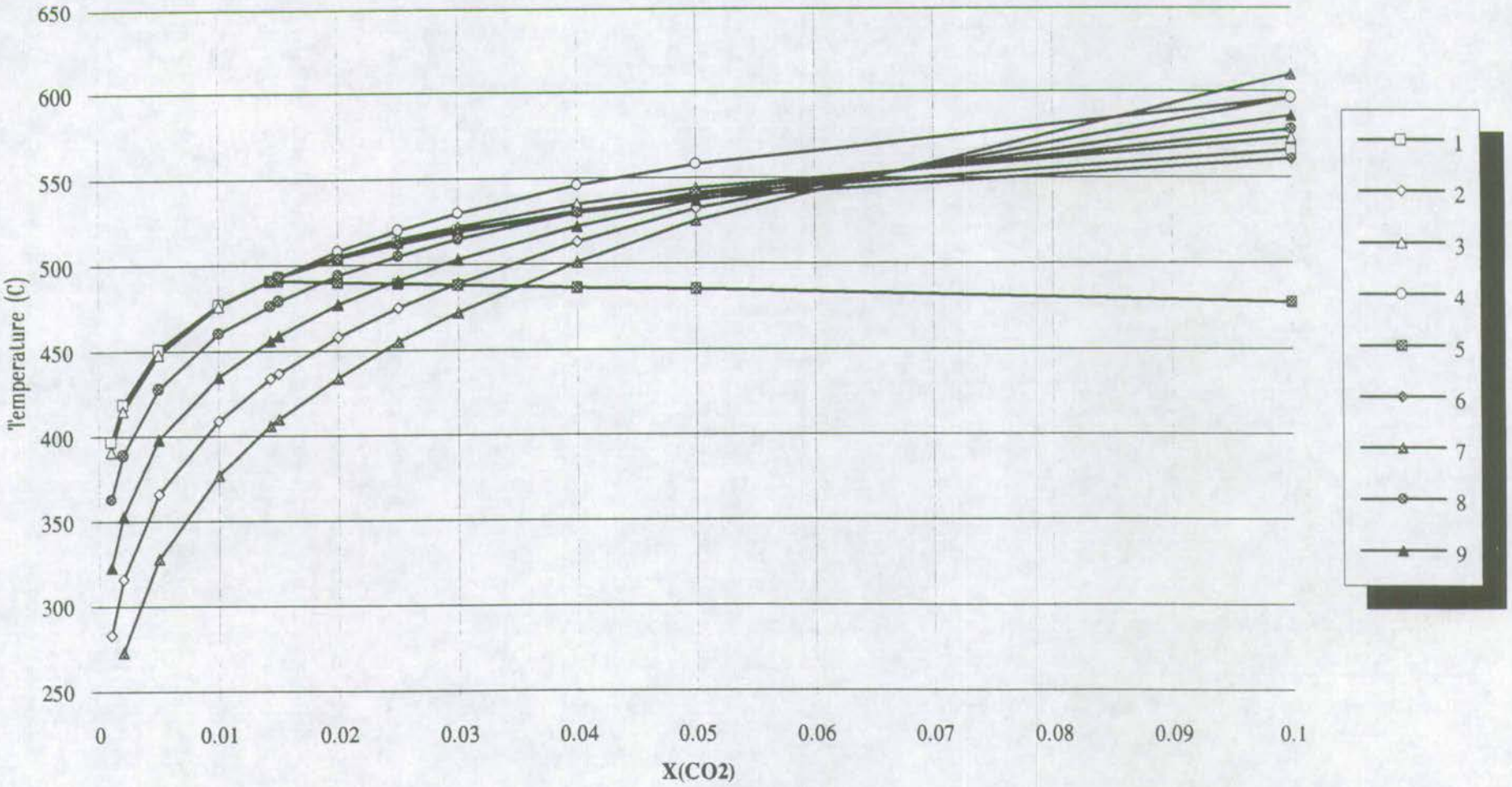
SW Highlands : Metabasites : NCFASHCO2
650
600
550
500
450
400
350
300
250
Temperature (C)
0
0.01
0.02
0.03
0.04
0.05
0.06
0.07
0.08
0.09
0.1
X(CO2)
1
2
3
4
5
6
7
8
9

temperature-x(CO2) phase diagram calculations

Unit activities

no excluded assemblages

no of reactions = 4, no of intersections = 1,

1) 3clin + 8ksp = 5phl + 3mu + 9q + 4H2O
2) ksp + 3dol + H2O = phl + 3cc + 3CO2
3) mu + 3q + 8dol + 4H2O = clin + phl + 8cc + 8CO2
4) mu + 3q + 5dol + 3H2O = clin + ksp + 5cc + 5CO2

Temperatures for KCMASHCO2 in the range 200 <-> 700C; for P = 10.0 kbar
uncertainties at or near x(CO2) = 0.0505

x(CO2)	0.001	0.002	0.005	0.01	0.015	0.02	0.025	0.03	0.04	0.05	0.1	sdT
1	288	288	288	287	287	287	286	286	285	285	282	18
2	335	362	401	434	455	470	482	492	508	521	560	9
3	339	368	410	446	468	485	498	509	527	542	587	10
4	341	371	416	454	477	495	509	521	540	555	605	11

T-x(CO2) of intersections for KCMASHCO2 : P = 10.0 kbar
window : T 200 <-> 700C; x(CO2) 0.001 <-> 0.1
in excess : CO2 H2O
sorry, none in the window

Stability of reactions not involved in intersections :

<= stable => 1) 3clin + 8ksp = 5phl + 3mu + 9q + 4H2O
<= stable => 2) ksp + 3dol + H2O = phl + 3cc + 3CO2
<= stable => 3) mu + 3q + 8dol + 4H2O = clin + phl + 8cc + 8CO2
metastable 4) mu + 3q + 5dol + 3H2O = clin + ksp + 5cc + 5CO2

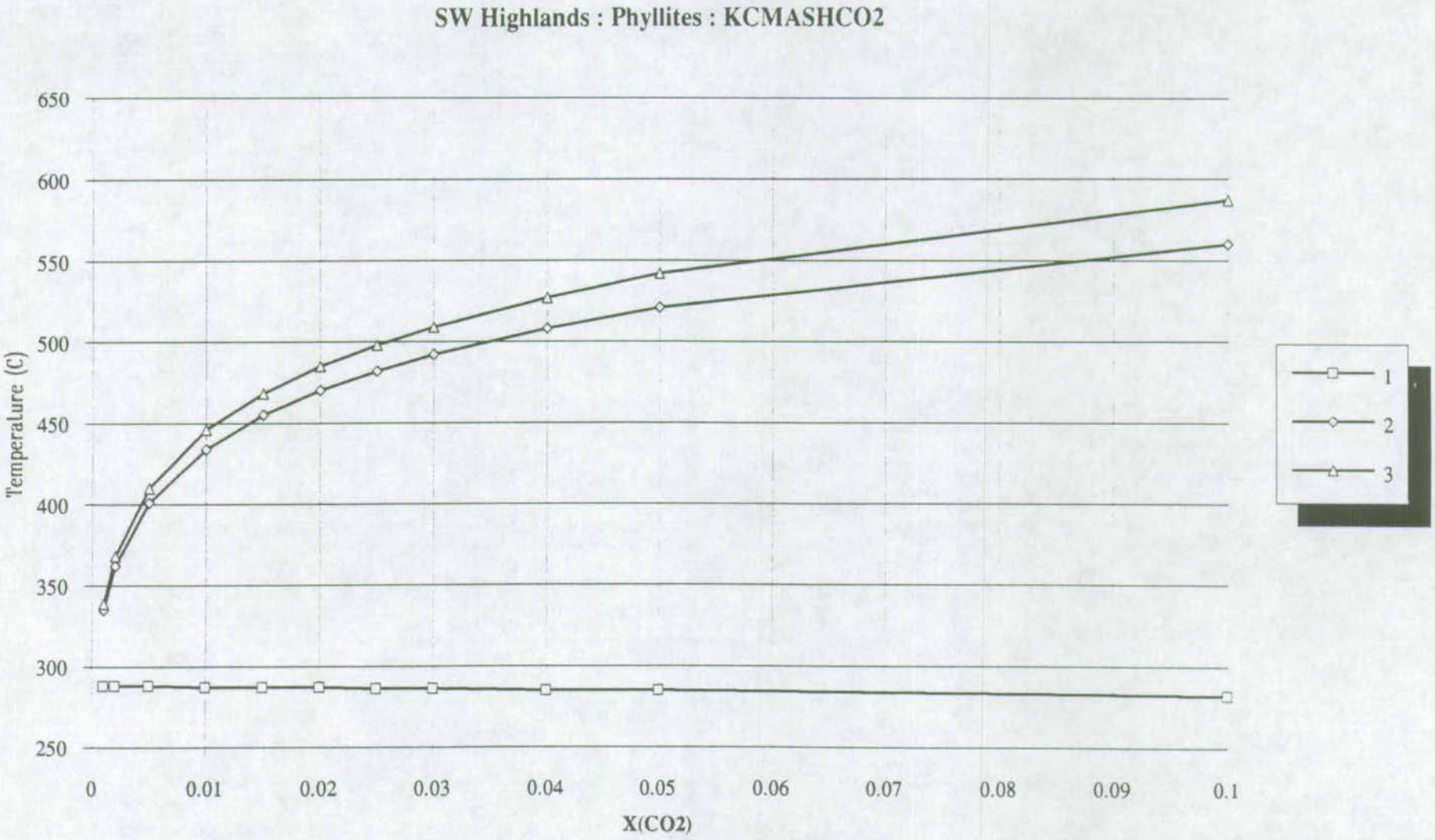
SW Highlands : Phyllites : KCMASHCO2
650
600
550
500
450
400
350
300
250
Temperature (C)
0
0.01
0.02
0.03
0.04
0.05
0.06
0.07
0.08
0.09
0.1
X(CO2)
1
2
3

temperature-x(CO2) phase diagram calculations

Unit activities

no excluded assemblages

no of reactions = 4, no of intersections = 1,

1) 3daph + 8ksp = 5ann + 3mu + 9q + 4H2O
2) ksp + 3fdol + H2O = ann + 3cc + 3CO2
3) mu + 3q + 8fdol + 4H2O = daph + ann + 8cc + 8CO2
4) mu + 3q + 5fdol + 3H2O = daph + ksp + 5cc + 5CO2

Temperatures for KCFASHCO2 in the range 200 <-> 700C; for P = 10.0 kbar
uncertainties at or near x(CO2) = 0.0505

x(CO2)	0.001	0.002	0.005	0.01	0.015	0.02	0.025	0.03	0.04	0.05	0.1	sdT
1	293	293	292	292	292	291	291	291	290	289	287	16
2	327	353	393	425	446	461	473	483	499	512	551	11
3	329	359	402	438	461	478	491	502	520	535	580	12
4	331	362	408	446	471	489	503	515	535	551	601	13

T-x(CO2) of intersections for KCFASHCO2 : P = 10.0 kbar
window : T 200 <-> 700C; x(CO2) 0.001 <-> 0.1
in excess : CO2 H2O
sorry, none in the window

Stability of reactions not involved in intersections :

<= stable => 1) 3daph + 8ksp = 5ann + 3mu + 9q + 4H2O
<= stable => 2) ksp + 3fdol + H2O = ann + 3cc + 3CO2
<= stable => 3) mu + 3q + 8fdol + 4H2O = daph + ann + 8cc + 8CO2
metastable 4) mu + 3q + 5fdol + 3H2O = daph + ksp + 5cc + 5CO2

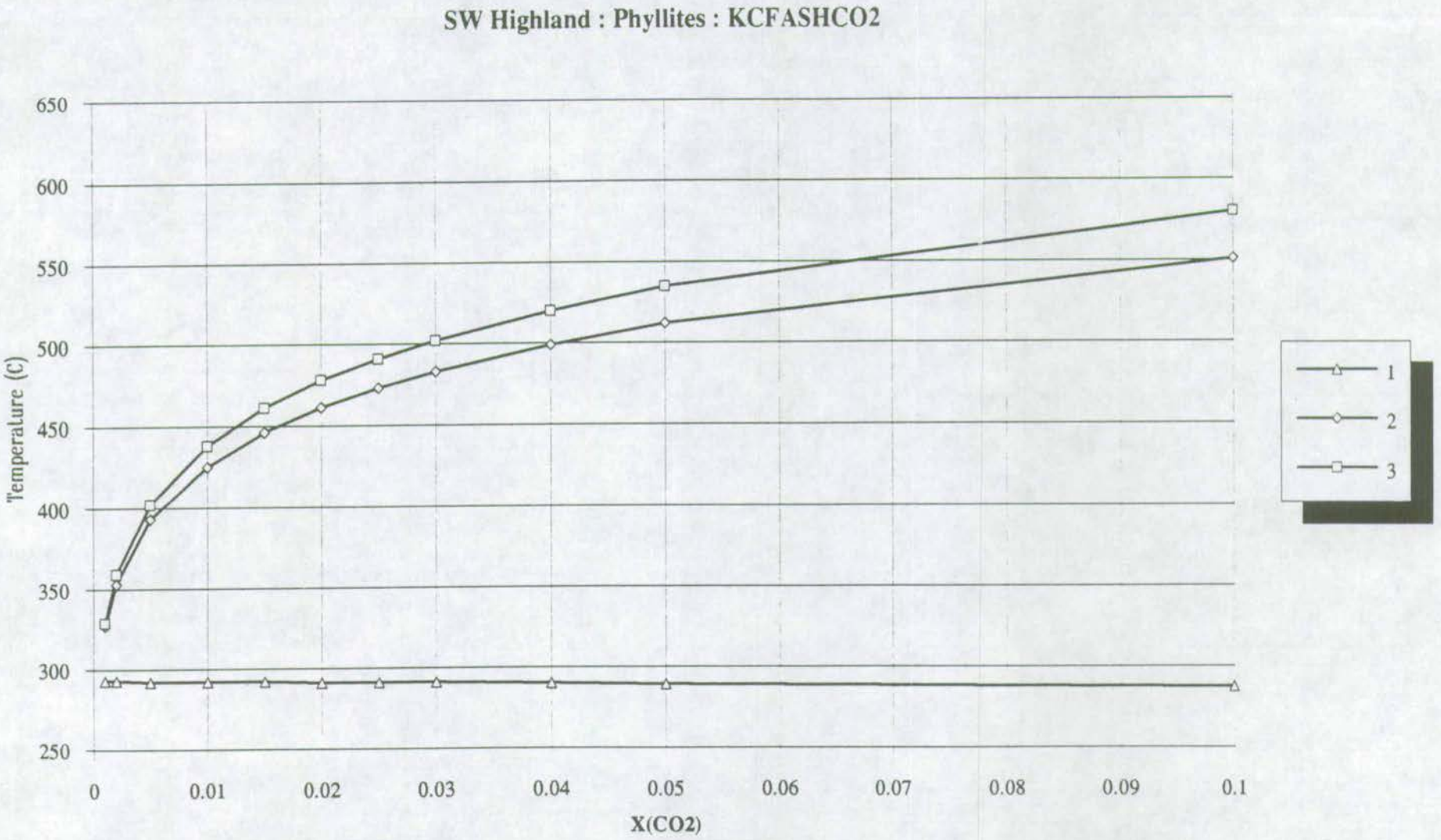
SW Highland : Phyllites : KCFASHCO2
650
600
550
500
450
400
350
300
250
Temperature (C)
0
0.01
0.02
0.03
0.04
0.05
0.06
0.07
0.08
0.09
0.1
X(CO2)
1
2
3

temperature-x(CO2) phase diagram calculations

Unit activities

no excluded assemblages

no of reactions = 4, no of intersections = 1,

1) pyhl = ky + 3q + H2O
2) ky + 5mag + 2q + 4H2O = clin + 5CO2
3) ky + 15mag + 2pyhl + 10H2O = 3clin + 15CO2
4) 5mag + pyhl + 3H2O = clin + q + 5CO2

Temperatures for MASHCO2 in the range 200 <-> 700C; for P = 10.0 kbar
uncertainties at or near x(CO2) = 0.0505

x(CO2)	0.001	0.002	0.005	0.01	0.015	0.02	0.025	0.03	0.04	0.05	0.1	sdT
1	429	429	429	428	428	427	427	426	425	424	419	25
2	260	289	333	370	394	412	426	439	458	474	525	12
3	269	297	339	374	396	413	426	438	456	470	516	11
4	273	300	341	376	397	414	426	437	455	468	512	11

T-x(CO2) of intersections for MASHCO2 : P = 10.0 kbar
window : T 200 <-> 700C; x(CO2) 0.001 <-> 0.1
in excess : CO2 H2O

stable intersection 1 involving ky,clin,mag,q,pyhl + CO2,H2O

	low T	high T	dx/dt
1) pyhl = ky + 3q + H2O			
[clin,mag]	stable	stable	-0.00899
2) ky + 5mag + 2q + 4H2O = clin + 5CO2			
[pyhl]		stable	0.000444
3) ky + 15mag + 2pyhl + 10H2O = 3clin + 15CO2			
[q]	stable		0.000482
4) 5mag + pyhl + 3H2O = clin + q + 5CO2			
[ky]	stable		0.000501

T = 427C, x(CO2) = 0.0250

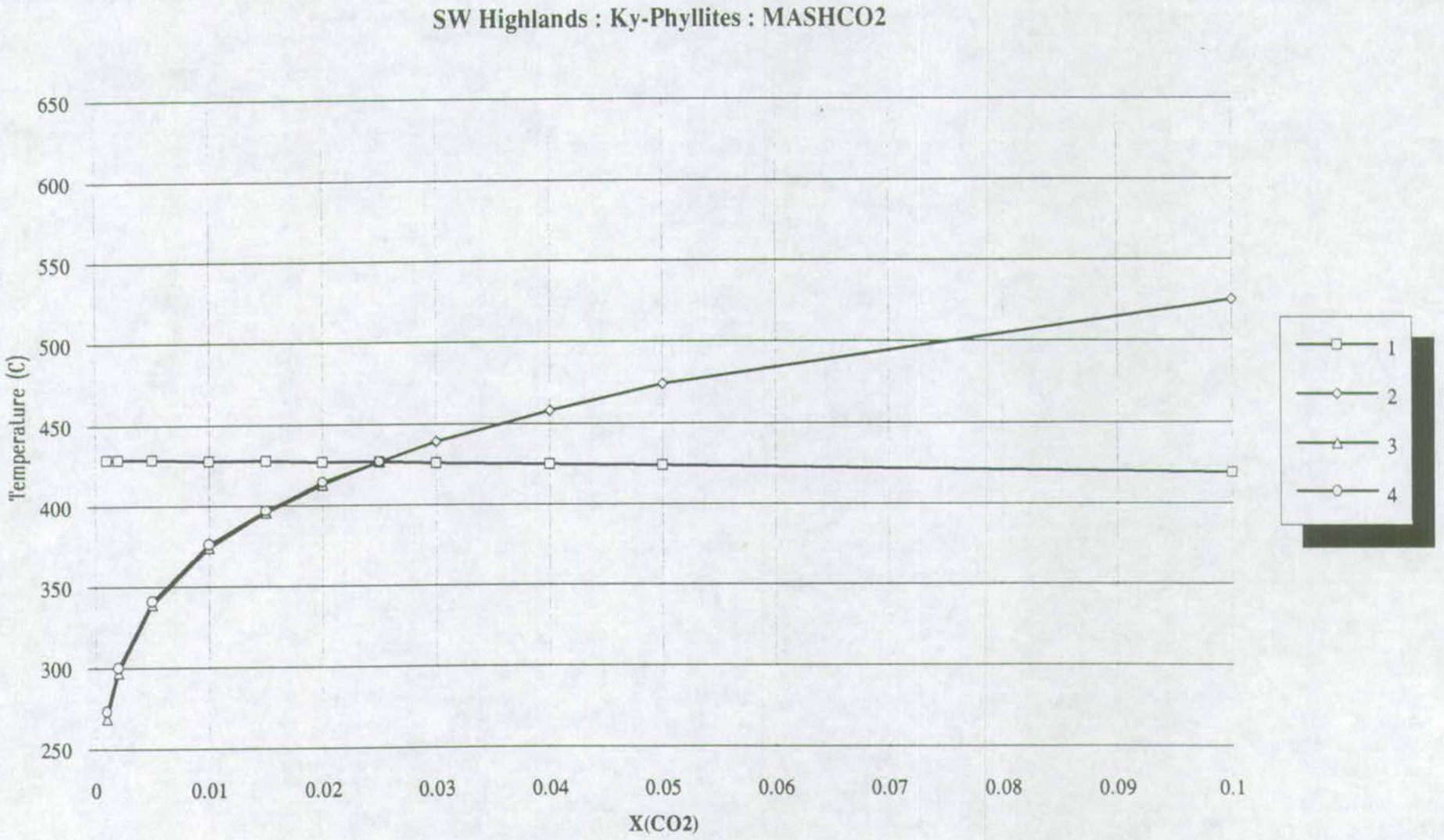
SW Highlands : Ky-Phyllites : MASHCO2
650
600
550
500
450
400
350
300
250
Temperature (C)
0
0.01
0.02
0.03
0.04
0.05
0.06
0.07
0.08
0.09
0.1
X(CO2)
1
2
3
4

temperature-x(CO2) phase diagram calculations

Unit activities

no excluded assemblages

no of reactions = 4, no of intersections = 1,

1) pyhl = ky + 3q + H2O
2) ky + 5sid + 2q + 4H2O = daph + 5CO2
3) ky + 15sid + 2pyhl + 10H2O = 3daph + 15CO2
4) 5sid + pyhl + 3H2O = daph + q + 5CO2

Temperatures for FASHCO2 in the range 200 <-> 700C; for P = 10.0 kbar
uncertainties at or near x(CO2) = 0.0505

x(CO2)	0.001	0.002	0.005	0.01	0.015	0.02	0.025	0.03	0.04	0.05	0.1	sdT
1	429	429	429	428	428	427	427	426	425	424	419	25
2	289	320	368	409	435	455	470	484	505	523	580	13
3	296	327	372	410	434	453	467	479	499	515	566	13
4	300	329	373	411	434	452	466	477	496	511	560	12

T-x(CO2) of intersections for FASHCO2 : P = 10.0 kbar
window : T 200 <-> 700C; x(CO2) 0.001 <-> 0.1
in excess : CO2 H2O

stable intersection 1 involving ky,daph,sid,q,pyhl + CO2,H2O

	low T	high T	dx/dt
1) pyhl = ky + 3q + H2O			
[daph,sid]	stable	stable	-0.00848
2) ky + 5sid + 2q + 4H2O = daph + 5CO2			
[pyhl]		stable	0.000246
3) ky + 15sid + 2pyhl + 10H2O = 3daph + 15CO2			
[q]	stable		0.000265
4) 5sid + pyhl + 3H2O = daph + q + 5CO2			
[ky]	stable		0.000275

T = 428C, x(CO2) = 0.0135

SW Highlands : Ky-Phyllites : FASHCO2

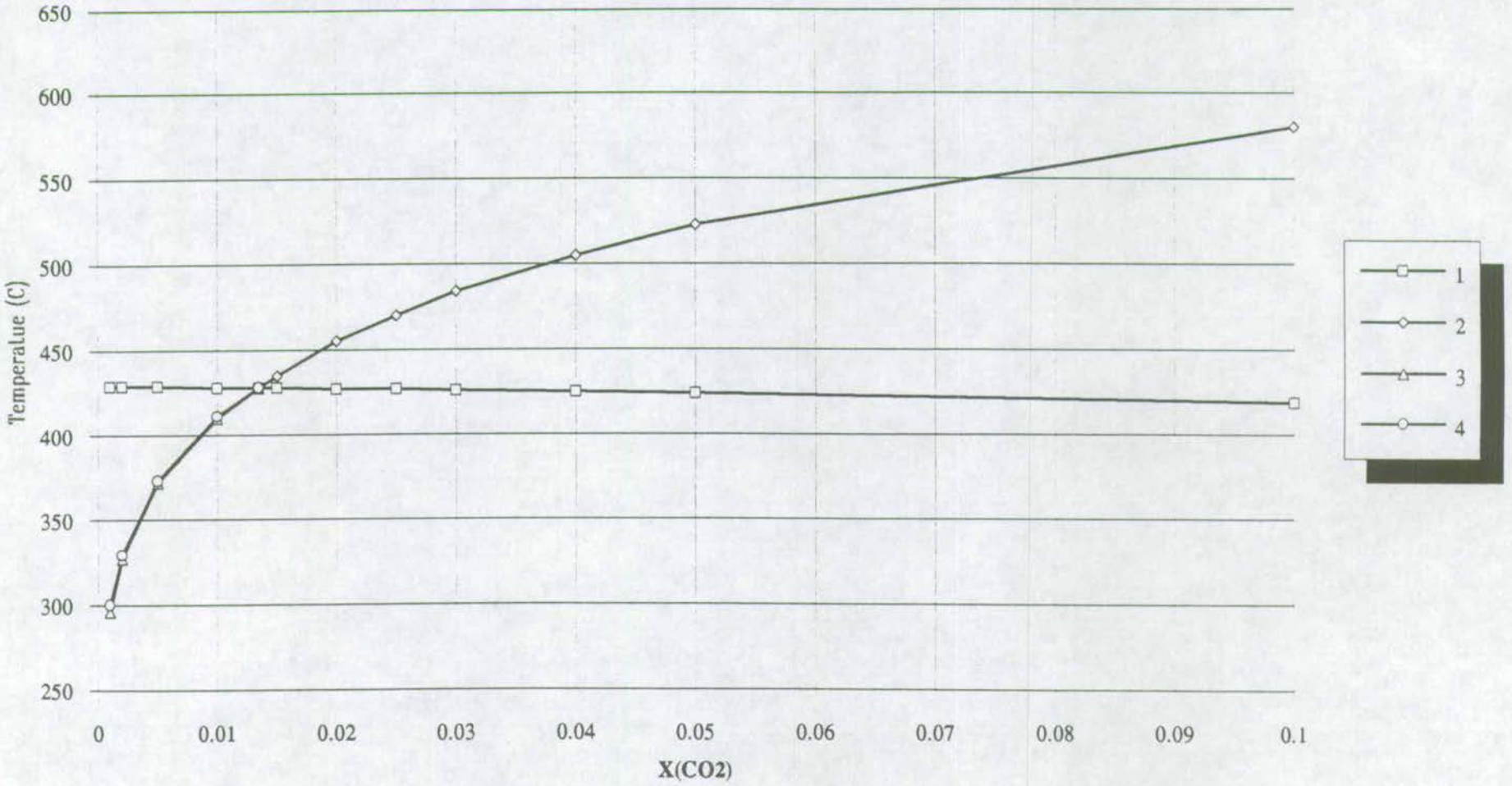

temperature-x(CO2) phase diagram calculations

Unit activities

no excluded assemblages

no of reactions = 1, no of intersections = 0,

1) mctd + 4mag + 2q + 3H2O = clin + 4CO2

Temperatures for MASHCO2 in the range 200 <-> 700C; for P = 10.0 kbar
uncertainties at or near x(CO2) = 0.0505

x(CO2)	0.001	0.002	0.005	0.01	0.015	0.02	0.025	0.03	0.04	0.05	0.1	sdT
1	259	287	329	365	387	404	418	429	447	462	509	11

T-x(CO2) of intersections for MASHCO2 : P = 10.0 kbar
window : T 200 <-> 700C; x(CO2) 0.001 <-> 0.1
in excess : CO2 H2O
sorry, none in the window

Stability of reactions not involved in intersections :

<= stable => 1) mctd + 4mag + 2q + 3H2O = clin + 4CO2

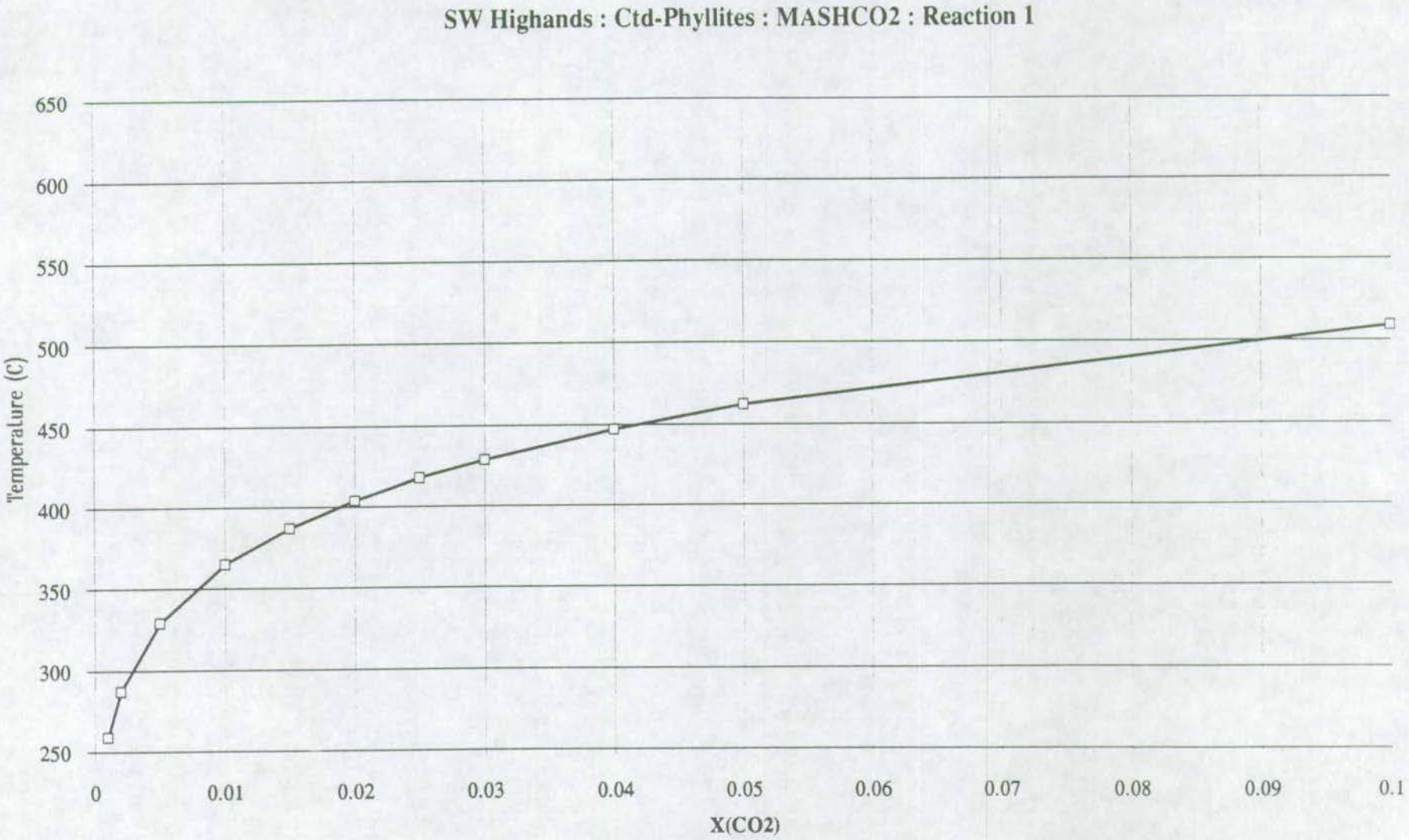
SW Highands : Ctd-Phyllites : MASHCO2 : Reaction 1
650
600
550
500
450
400
350
300
250
Temperature (C)
0
0.01
0.02
0.03
0.04
0.05
0.06
0.07
0.08
0.09
0.1
X(CO2)

temperature-x(CO2) phase diagram calculations

Unit activities

no excluded assemblages

no of reactions = 1, no of intersections = 0,

1) fctd + 4sid + 2q + 3H2O = daph + 4CO2

Temperatures for FASHCO2 in the range 200 <-> 700C; for P = 10.0 kbar
uncertainties at or near x(CO2) = 0.0505

x(CO2)	0.001	0.002	0.005	0.01	0.015	0.02	0.025	0.03	0.04	0.05	0.1	sdT
1	306	338	385	426	452	471	487	500	521	538	594	13

T-x(CO2) of intersections for FASHCO2 : P = 10.0 kbar
window : T 200 <-> 700C; x(CO2) 0.001 <-> 0.1
in excess : CO2 H2O
sorry, none in the window

Stability of reactions not involved in intersections :

<= stable => 1) fctd + 4sid + 2q + 3H2O = daph + 4CO2

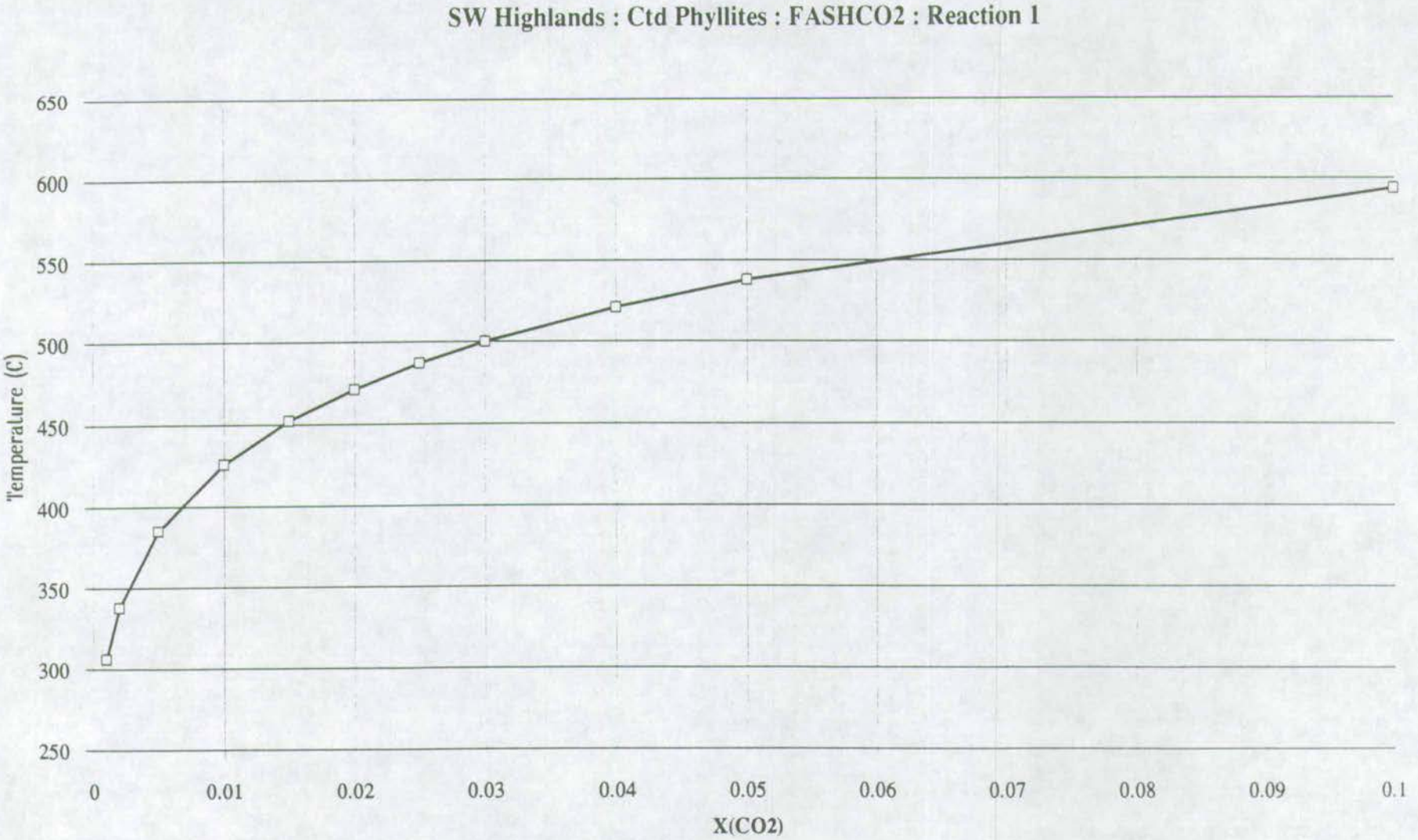
SW Highlands : Ctd Phyllites : FASHCO2 : Reaction 1
650
600
550
500
450
400
350
300
250
Temperature (C)
0
0.01
0.02
0.03
0.04
0.05
0.06
0.07
0.08
0.09
0.1
X(CO2)

Temperature-x(CO2) phase diagram calculations

SW Highland : Metabasites : NCMASHCO2

1) 3clin + 10cc + 21q = 3tr + 2cz + 10CO2 + 8H2O
3) 4cc + 6q + 3pa = 2cz + 3ab + 4CO2 + 2H2O
9) 3q + 5dol + pa + 3H2O = clin + 5cc + ab + 5CO2

Temperatures for NCMASHCO2 in the range 100 <-> 700C; for P = 10.0 kbar
uncertainties at or near x(CO2) = 0.0505

x(CO2)	0.001	0.002	0.005	0.01	0.015	0.02	0.025	0.03	0.04	0.05	0.1	sdT
1	395	418	451	478	495	506	515	523	535	544	570	8
3	391	415	448	476	493	505	515	522	535	544	573	9
9	333	362	406	443	466	484	497	509	528	542	590	11

SW Highlands : Phyllites : KCMASHCO2

1) 3clin + 8ksp = 5phl + 3mu + 9q + 4H2O
3) mu + 3q + 8dol + 4H2O = clin + phl + 8cc + 8CO2

Temperatures for KCMASHCO2 in the range 200 <-> 700C; for P = 10.0 kbar
uncertainties at or near x(CO2) = 0.0505

x(CO2)	0.001	0.002	0.005	0.01	0.015	0.02	0.025	0.03	0.04	0.05	0.1	sdT
1	288	288	288	287	287	287	286	286	285	285	282	18
3	339	368	410	446	468	485	498	509	527	542	587	10

SW Highlands : Ctd-Phyllites : MASHCO2

1) mctd + 4mag + 2q + 3H2O = clin + 4CO2

Temperatures for MASHCO2 in the range 200 <-> 700C; for P = 10.0 kbar
uncertainties at or near x(CO2) = 0.0505

x(CO2)	0.001	0.002	0.005	0.01	0.015	0.02	0.025	0.03	0.04	0.05	0.1	sdT
1	259	287	329	365	387	404	418	429	447	462	509	11

SW Highlands : Ky-Phyllites : MASHCO2

1) pyhl = ky + 3q + H2O
2) ky + 5mag + 2q + 4H2O = clin + 5CO2

Temperatures for MASHCO2 in the range 200 <-> 700C; for P = 10.0 kbar
uncertainties at or near x(CO2) = 0.0505

x(CO2)	0.001	0.002	0.005	0.01	0.015	0.02	0.025	0.03	0.04	0.05	0.1	sdT
1	429	429	429	428	428	427	427	426	425	424	419	25
2							427	439	458	474	525	12

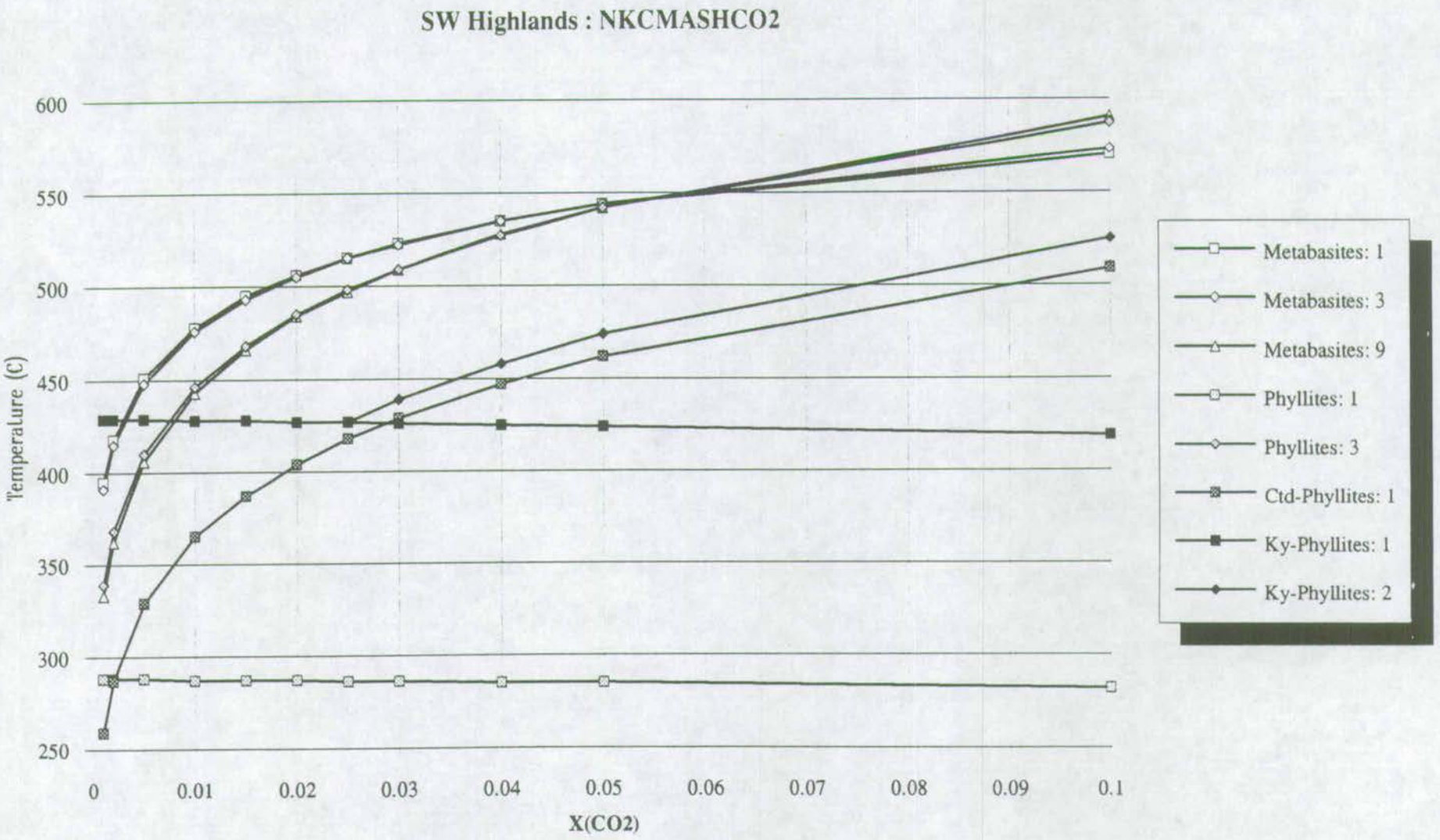
SW Highlands : NKCMASHCO2
Temperature (C)
600
550
500
450
400
350
300
250
0
0.01
0.02
0.03
0.04
0.05
0.06
0.07
0.08
0.09
0.1
X(CO2)
Metabasites: 1
Metabasites: 3
Metabasites: 9
Phyllites: 1
Phyllites: 3
Ctd-Phyllites: 1
Ky-Phyllites: 1
Ky-Phyllites: 2

Temperature-x(CO2) phase diagram calculations

SW Highlands : Metabasites : NCFASHCO2

1) 3daph + 10cc + 21q = 3ftr + 2cz + 10CO2 + 8H2O
3) 4cc + 6q + 3pa = 2cz + 3ab + 4CO2 + 2H2O
9) 3q + pa + 5fdol + 3H2O = daph + 5cc + ab + 5CO2

Temperatures for NCFASHCO2 in the range 250 <-> 700C; for P = 10.0 kbar
uncertainties at or near x(CO2) = 0.0505

x(CO2)	0.001	0.002	0.005	0.01	0.015	0.02	0.025	0.03	0.04	0.05	0.1	sdT
1	397	419	451	477	493	504	513	520	531	540	566	9
3	391	415	448	476	493	505	515	522	535	544	573	8
9	323	353	398	435	459	477	491	503	522	537	586	13

SW Highland : Phyllites : KCFASHCO2

1) 3daph + 8ksp = 5ann + 3mu + 9q + 4H2O
3) mu + 3q + 8fdol + 4H2O = daph + ann + 8cc + 8CO2

Temperatures for KCFASHCO2 in the range 200 <-> 700C; for P = 10.0 kbar
uncertainties at or near x(CO2) = 0.0505

x(CO2)	0.001	0.002	0.005	0.01	0.015	0.02	0.025	0.03	0.04	0.05	0.1	sdT
1	293	293	292	292	292	291	291	291	290	289	287	16
3	329	359	402	438	461	478	491	502	520	535	580	12

SW Highlands : Ctd-Phyllites : FASHCO2

1) fctd + 4sid + 2q + 3H2O = daph + 4CO2

Temperatures for FASHCO2 in the range 200 <-> 700C; for P = 10.0 kbar
uncertainties at or near x(CO2) = 0.0505

x(CO2)	0.001	0.002	0.005	0.01	0.015	0.02	0.025	0.03	0.04	0.05	0.1	sdT
1	306	338	385	426	452	471	487	500	521	538	594	13

SW Highlands : Ky-Phyllites : FASHCO2

1) pyhl = ky + 3q + H2O
2) ky + 5sid + 2q + 4H2O = daph + 5CO2

Temperatures for FASHCO2 in the range 200 <-> 700C; for P = 10.0 kbar
uncertainties at or near x(CO2) = 0.0505

x(CO2)	0.001	0.002	0.005	0.01	0.0135	0.015	0.02	0.025	0.03	0.04	0.05	0.1	sdT
1	429	429	429	428	428	428	427	427	426	425	424	419	25
2					428	435	455	470	484	505	523	580	13

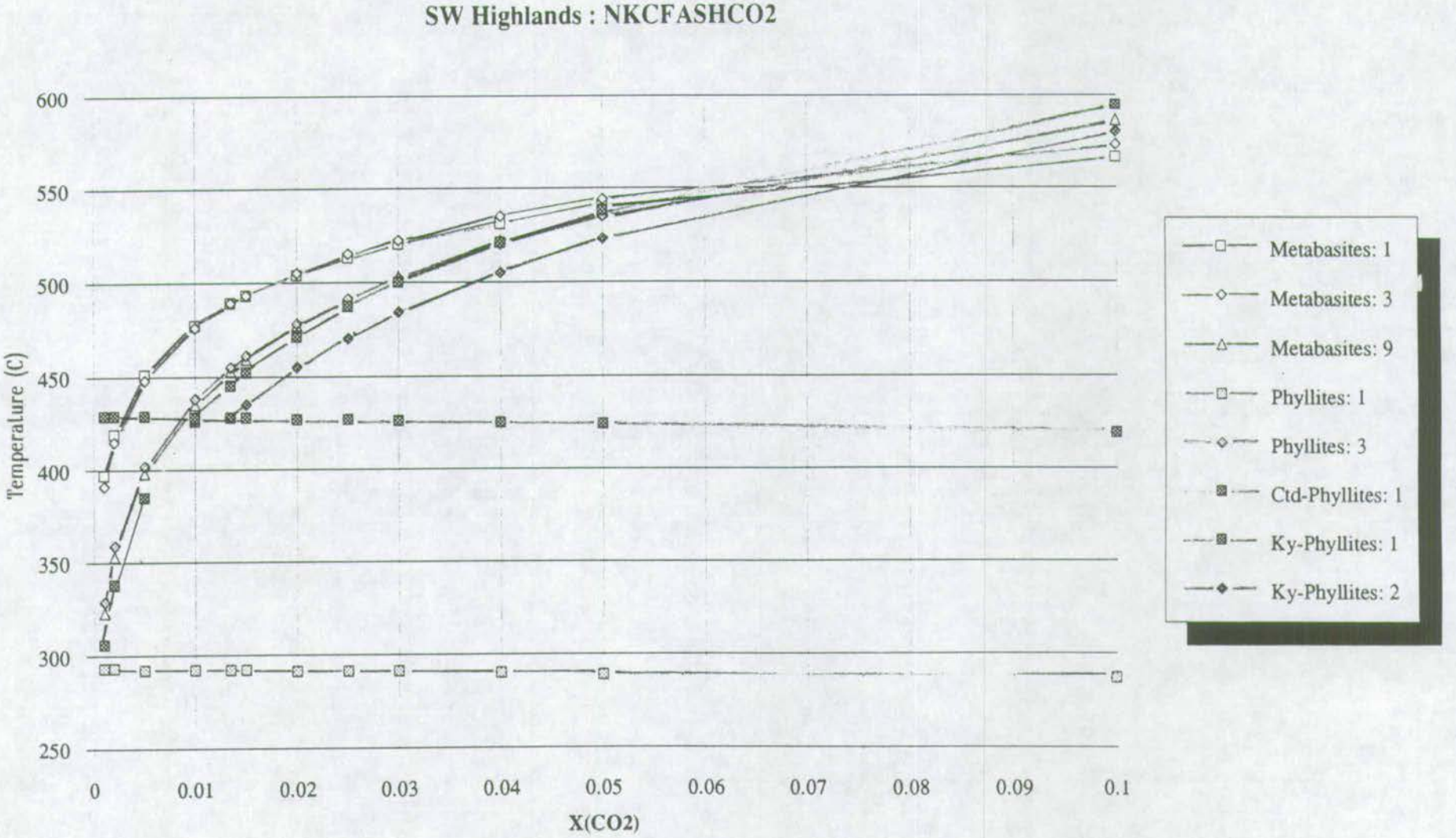
SW Highlands : NKCFASHCO2
Temperature (C)
600
550
500
450
400
350
300
250
0
0.01
0.02
0.03
0.04
0.05
0.06
0.07
0.08
0.09
0.1
X(CO2)
Metabasites: 1
Metabasites: 3
Metabasites: 9
Phyllites: 1
Phyllites: 3
Ctd-Phyllites: 1
Ky-Phyllites: 1
Ky-Phyllites: 2

temperature-x(CO2) phase diagram calculations

Unit activities

no excluded assemblages

no of reactions = 1, no of intersections = 0,

1) ru + cc + q = sph + CO2

Temperatures for Sph-Ru in the range 250 <-> 600C; for P = 10.0 kbar
uncertainties at or near x(CO2) = 0.0505

x(CO2)	0.001	0.002	0.005	0.01	0.015	0.02	0.025	0.03	0.04	0.05	0.1	sdT
1	347	375	415	449	470	486	498	509	525	538	578	10

T-x(CO2) of intersections for Sph-Ru : P = 10.0 kbar
window : T 250 <-> 600C; x(CO2) 0.001 <-> 0.1
in excess : CO2
sorry, none in the window

Stability of reactions not involved in intersections :

<= stable => 1) ru + cc + q = sph + CO2

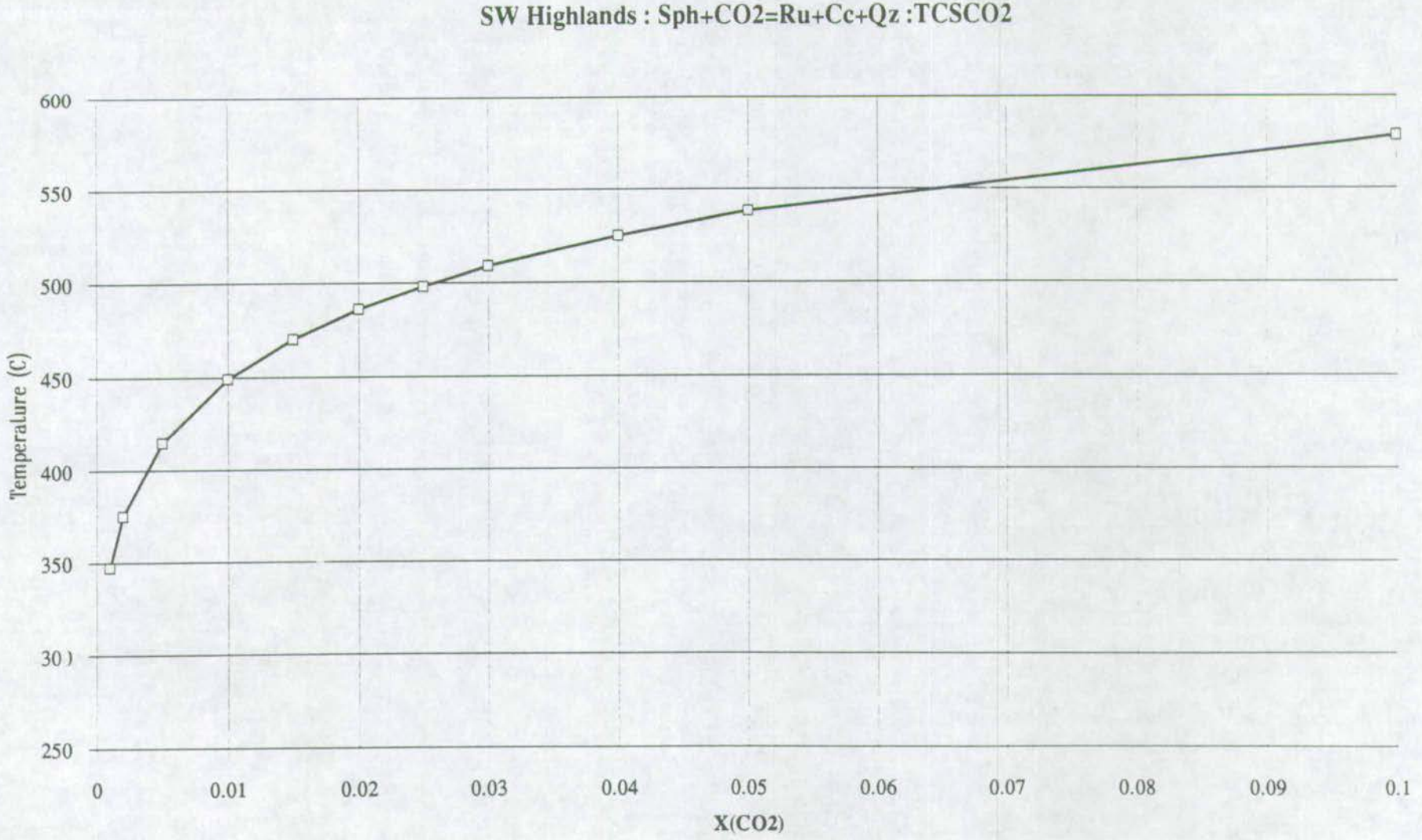
SW Highlands : Sph+CO2=Ru+Cc+Qz :TCSCO2
600
550
500
450
400
350
300
250
Temperature (C)
0
0.01
0.02
0.03
0.04
0.05
0.06
0.07
0.08
0.09
0.1
X(CO2)

A70

Appendix 4: Modal Profiles

Figure A4.1: Location map of modal profiles.

Figures A4.2-A4.3: Modal profiles showing reactions (1) and/or (2) at North Jura and Traigh Gheighsgeir.

Figures A4.4-A4.10: Modal profiles showing reaction 1 in biotite-zone rocks at North Jura, The Ard of Port Ellen, Port Cill Maluaig and Clachbreac.

Figure A4.11: Modal profile showing reaction 1 in garnet-zone rocks at Loch Stornoway.

Figure A4.12: Modal profile showing reaction 1 in the lowest grade, stilpnomelane-bearing, biotite-zone rocks at Carsaig.

Figure A4.1: Location Map of Modal Profiles

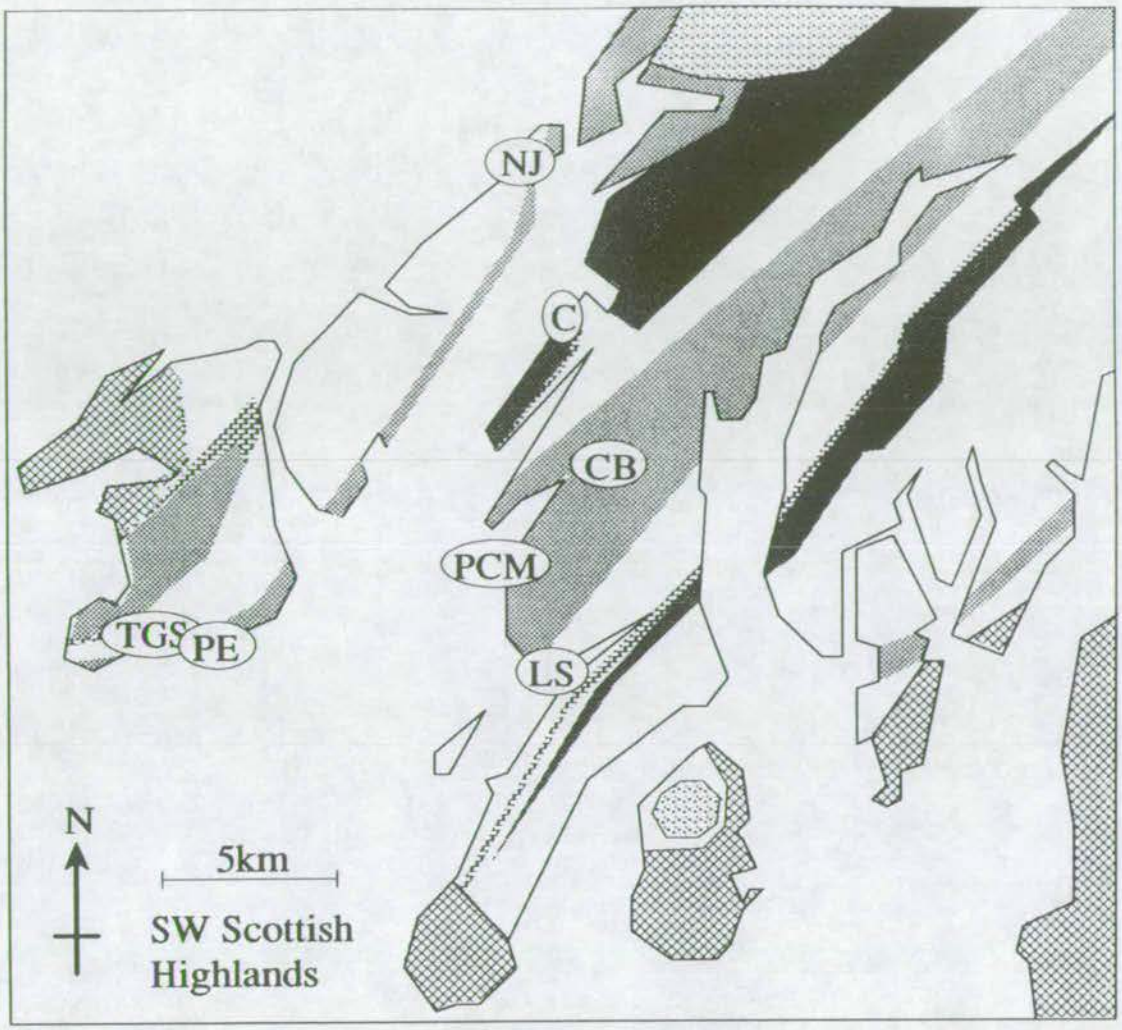

KEY

- Phyllite
- Quartzite
- Volcanics
- Marble
- Other Metamorphic and Sedimentary Rocks
- Other Igneous Rocks

NJ = North Jura
PE = Port Ellen
TGS = Traigh Gheighsgeir
C = Carsaig
PCM = Port Cill Maluaig
LS = Loch Stornoway
CB = Clachbreac

Figure A4.2: Modal Profile of Metabasite (1) at North Jura, showing the reaction:Chl+Cc (+Ab)(+Bi) +CO2=Dol+Mu+Qz+H2O

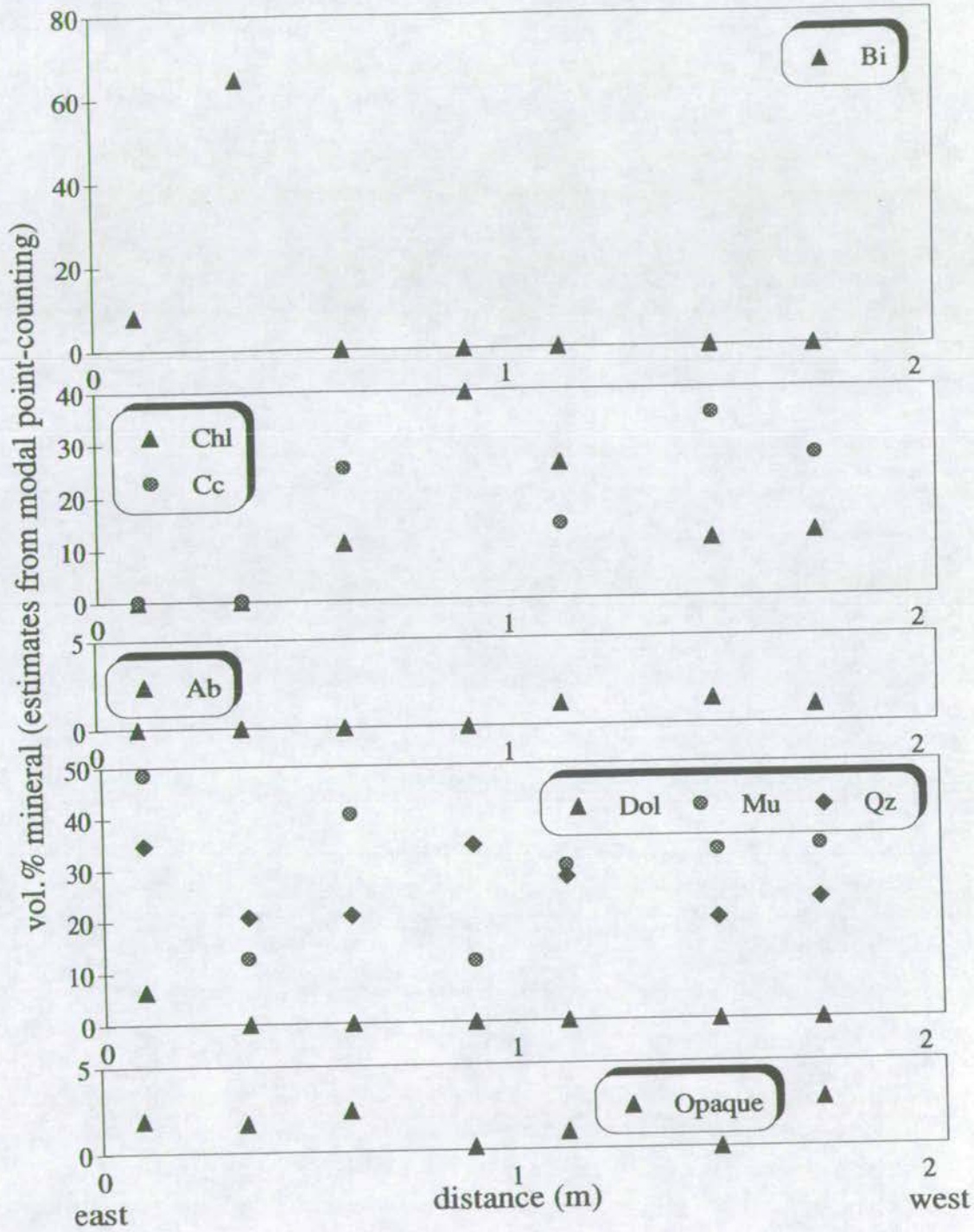

Figure A4.3: Modal Profile at Traigh Gheighsgeir,
showing the reaction: Chl+Cc+Fsp+CO2=Dol+Mica+Qz+H2O

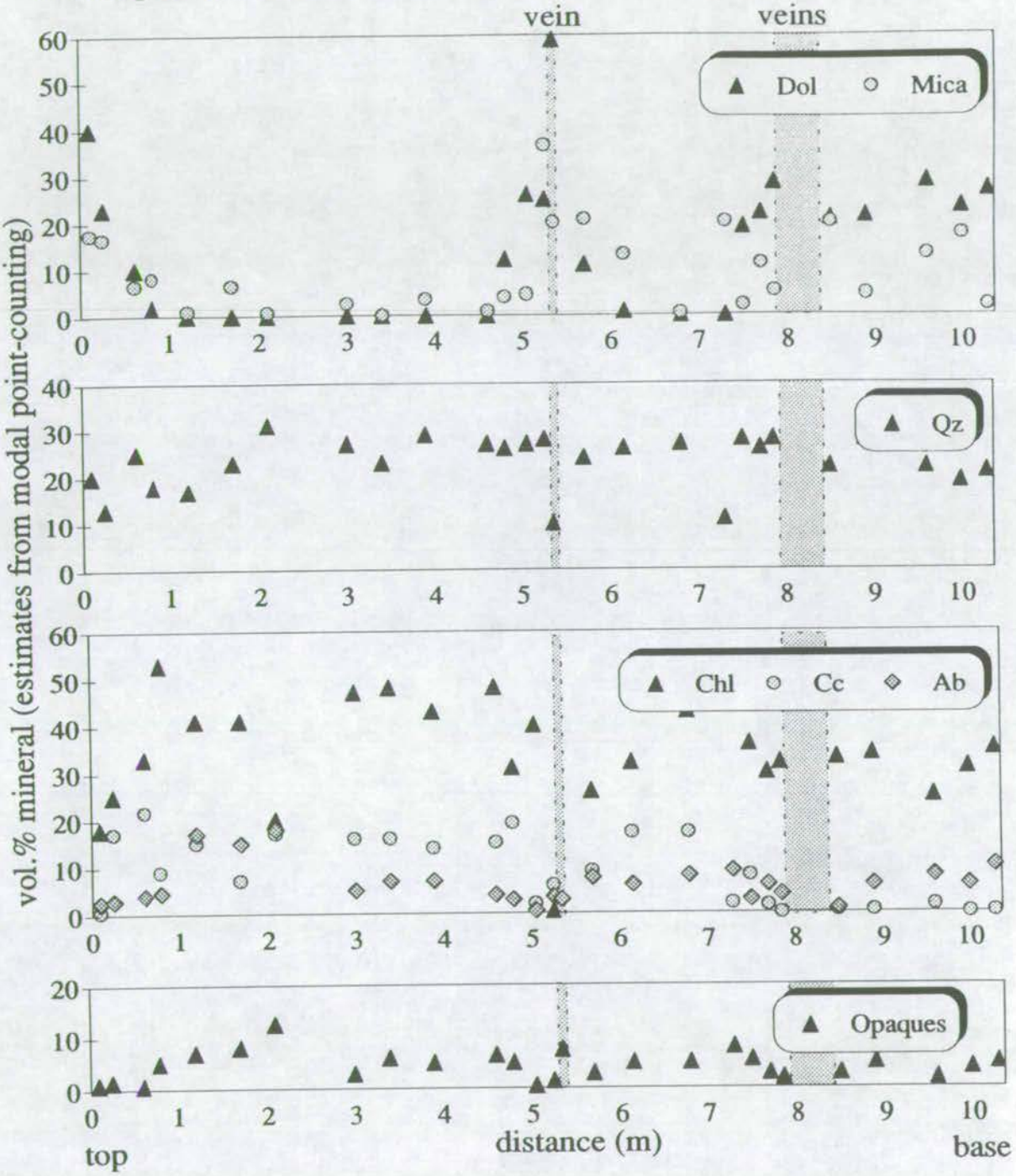

Figure A4.4: Modal Profile of Metabasite (2) at North Jura, showing the reaction: Am+Ep+CO2+H2O=Chl+Cc+Qz

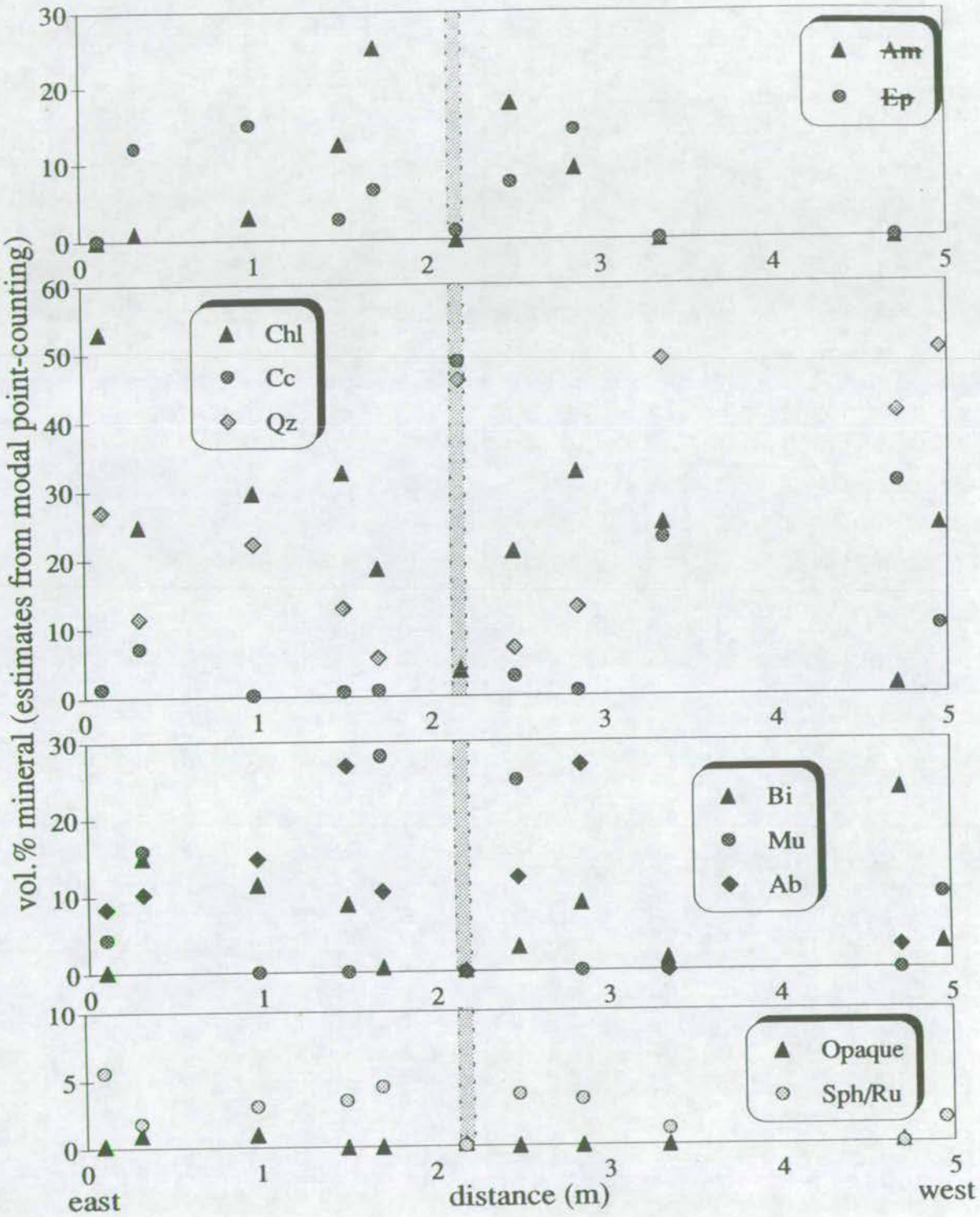

Figure A4.5: Modal Profile of Metabasite (3) at North Jura, showing the reaction: Am+Ep+CO2+H2O=Chl+Cc+Qz

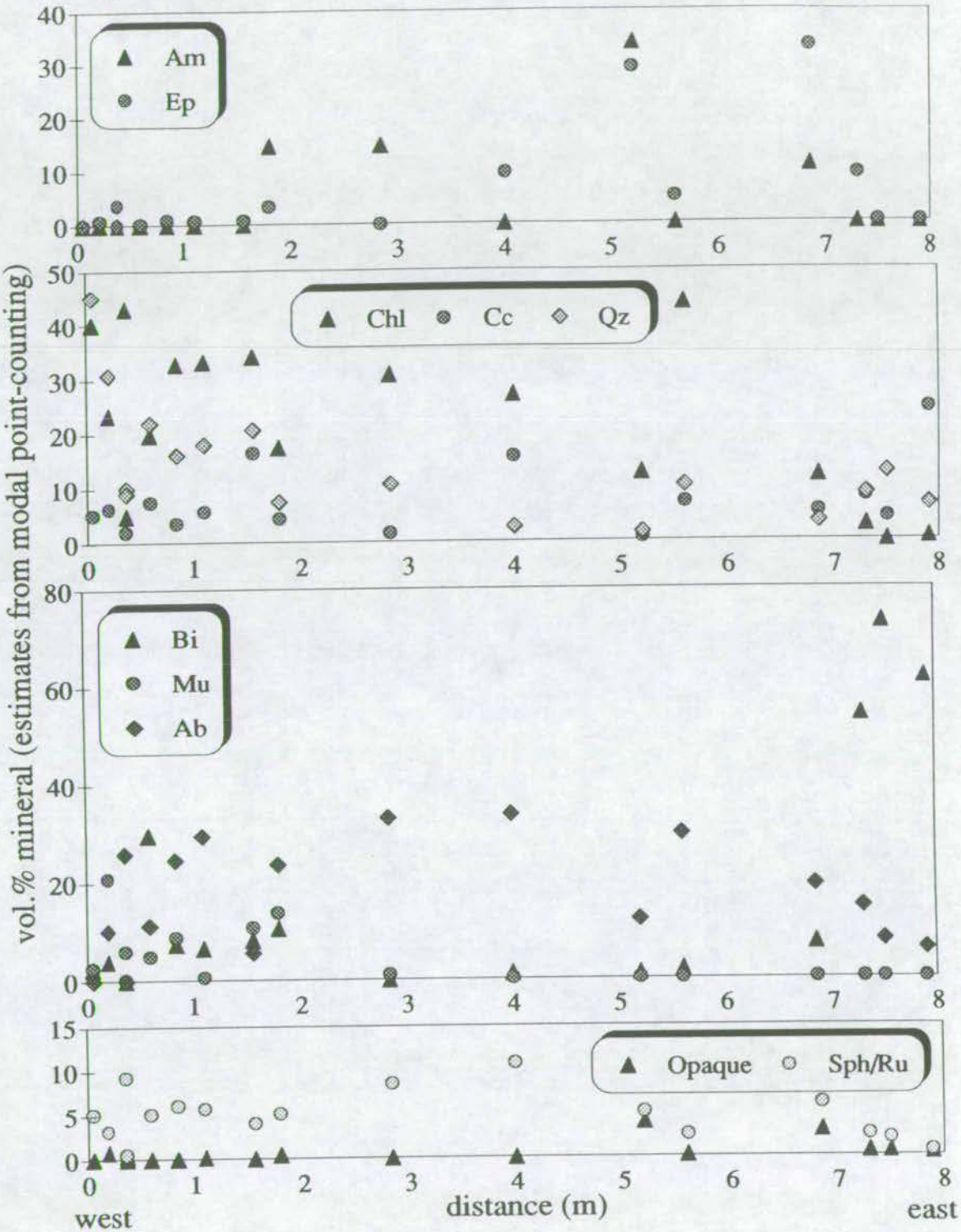

Figure A4.6: Modal Profile of Metabasite (4) at North Jura, showing the reaction: Am+Ep+CO2+H2O=Chl+Cc+Qz

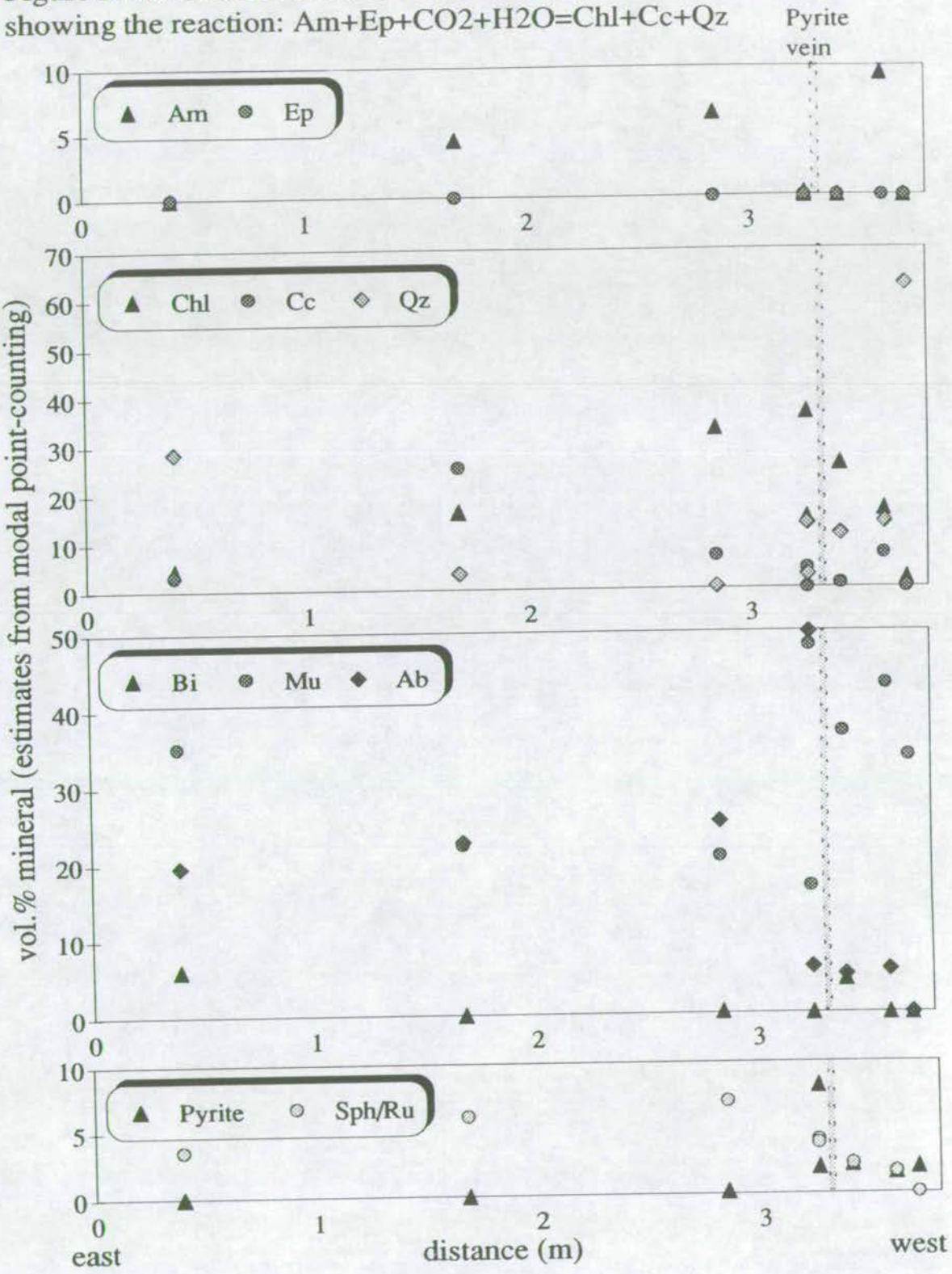

Figure A4.7: Modal Profile at The Ard of Port Ellen: Big Feldspar Sill 1, showing the reaction: Am+Ep+CO2+H2O=Chl+Cc+Qz

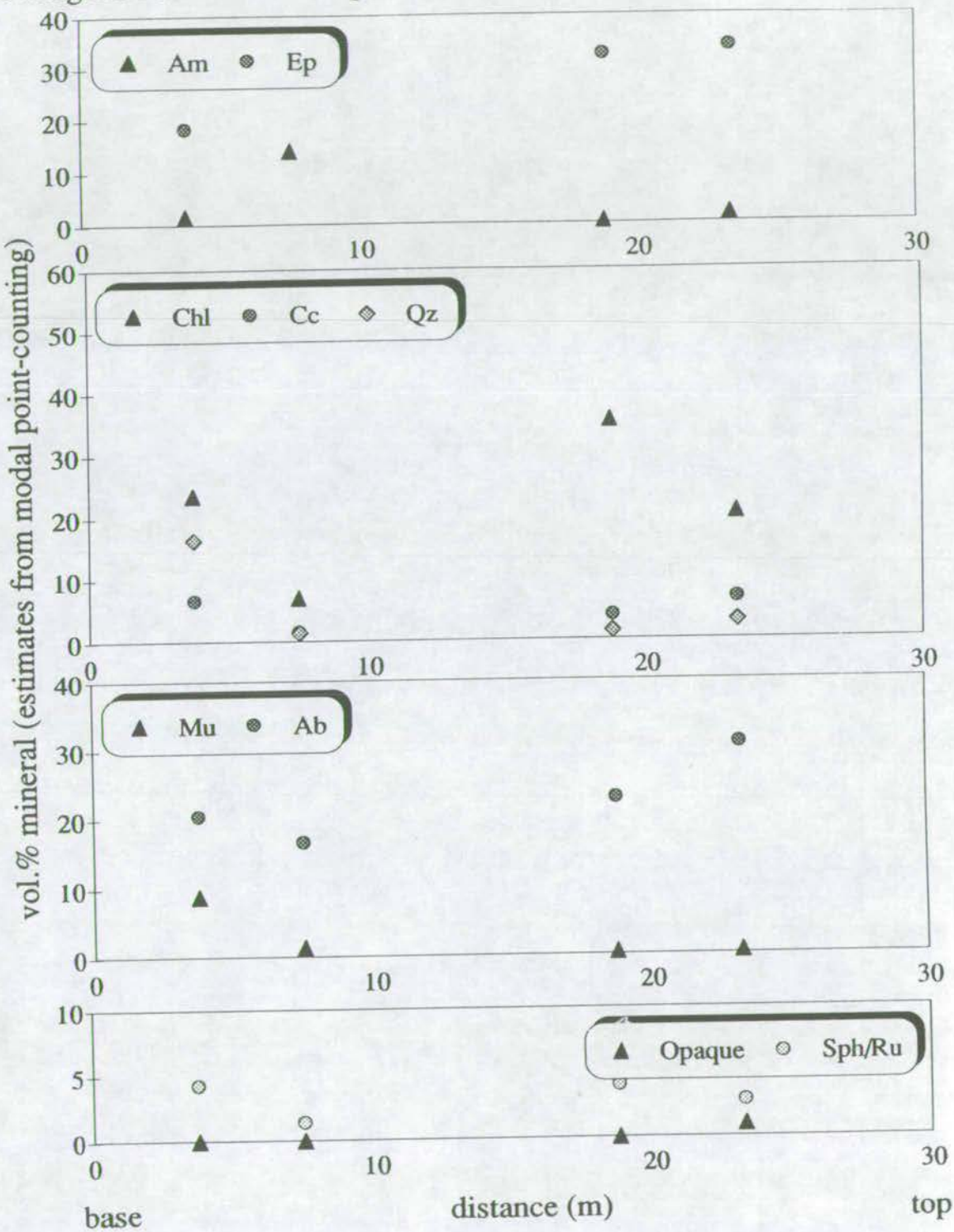

Figure A4.8: Modal Profile at The Ard of Port Ellen: Big Feldspar Sill 2, showing the reaction: Am+Ep+CO2+H2O=Chl+Cc+Qz

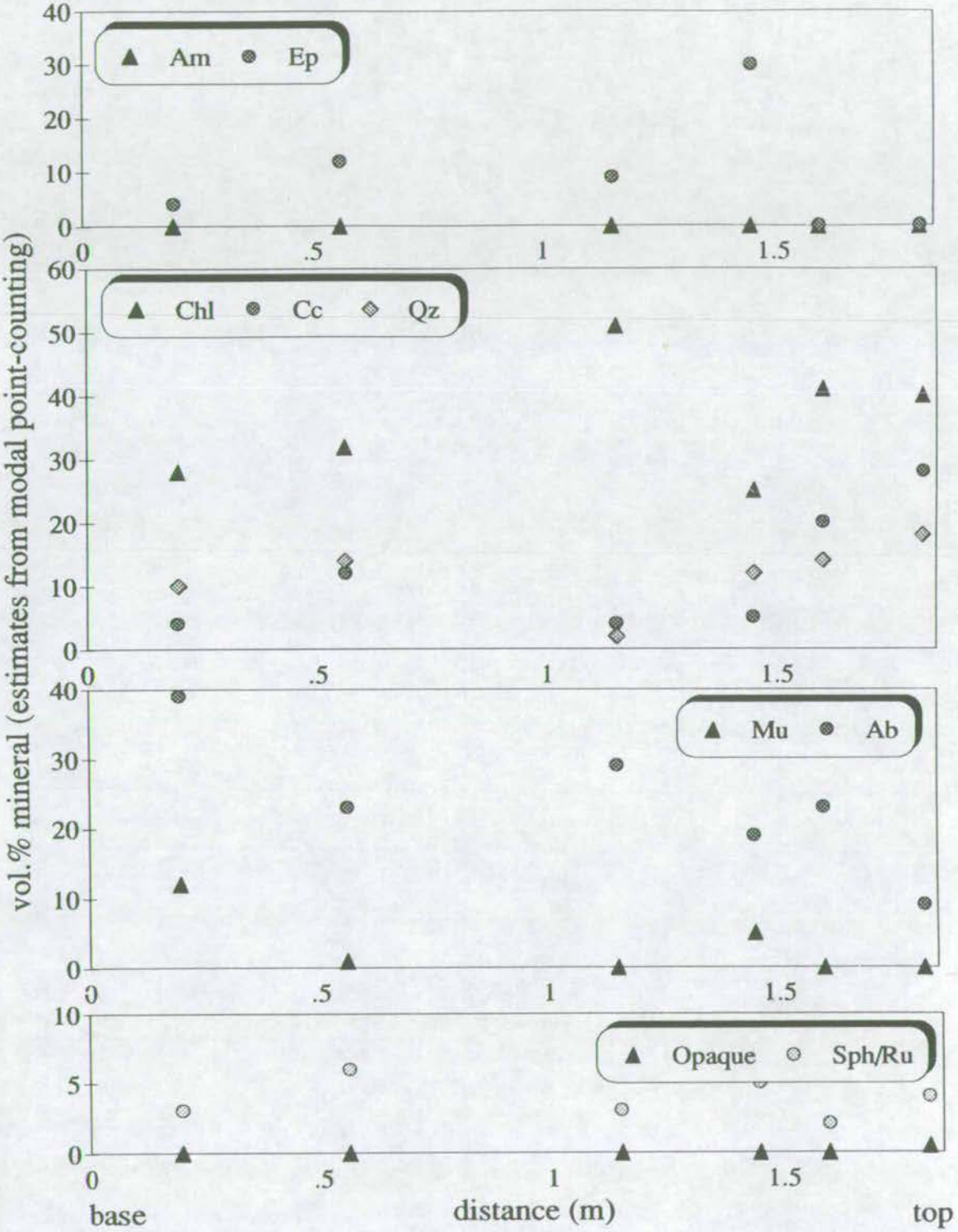

Figure A4.9: Modal Profile at Port Cill Maluaig,
showing the reaction: Am+Ep+CO2+H2O=Chl+Cc+Qz

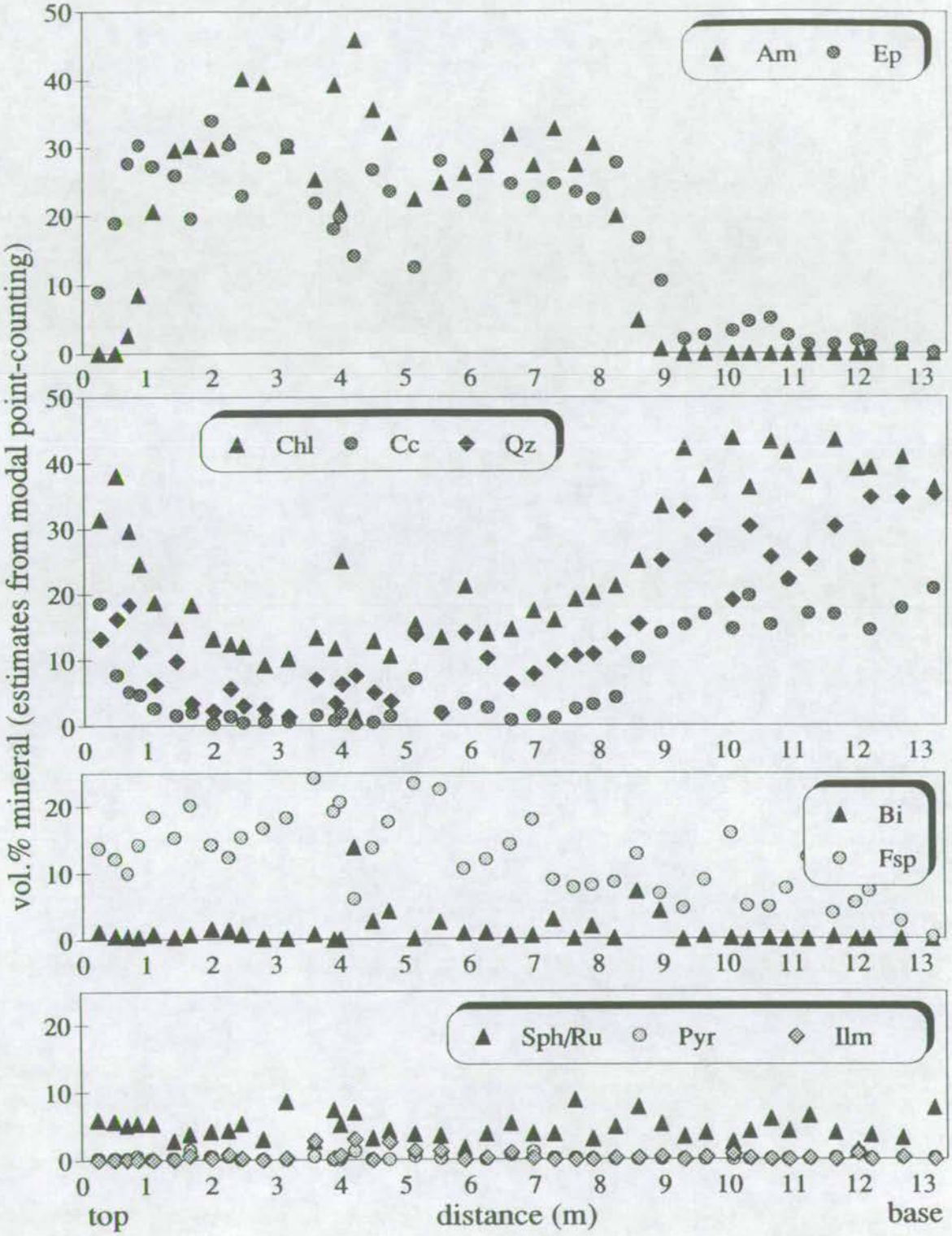

Figure A4.10: Modal Profile at Clachbreac,
showing the reaction: Am+Ep+CO2+H2O=Chl+Cc+Qz

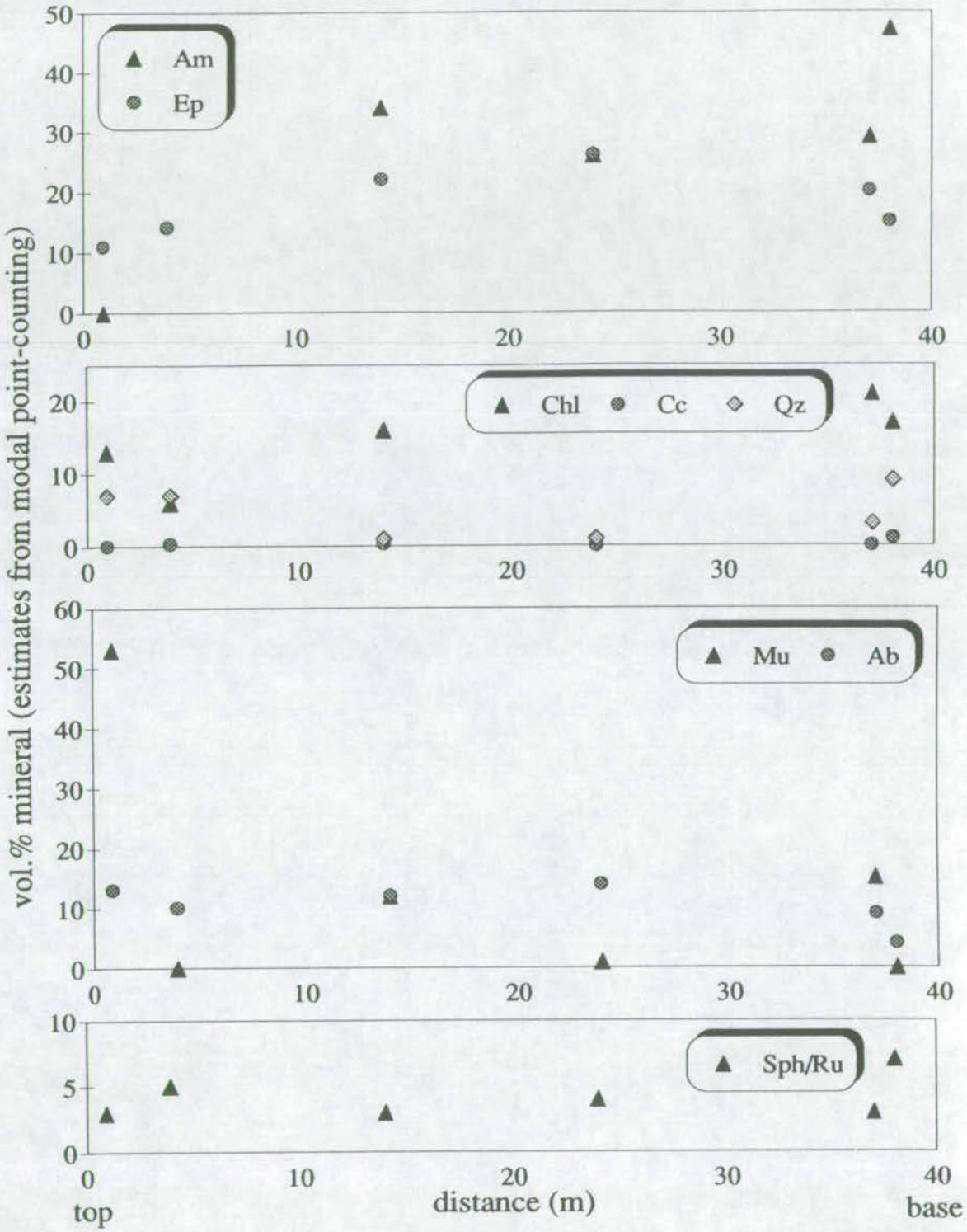

Figure A4.11: Modal Profile at Loch Stornoway,
showing the reaction: Am+Ep+CO2+H2O=Chl+Cc+Qz

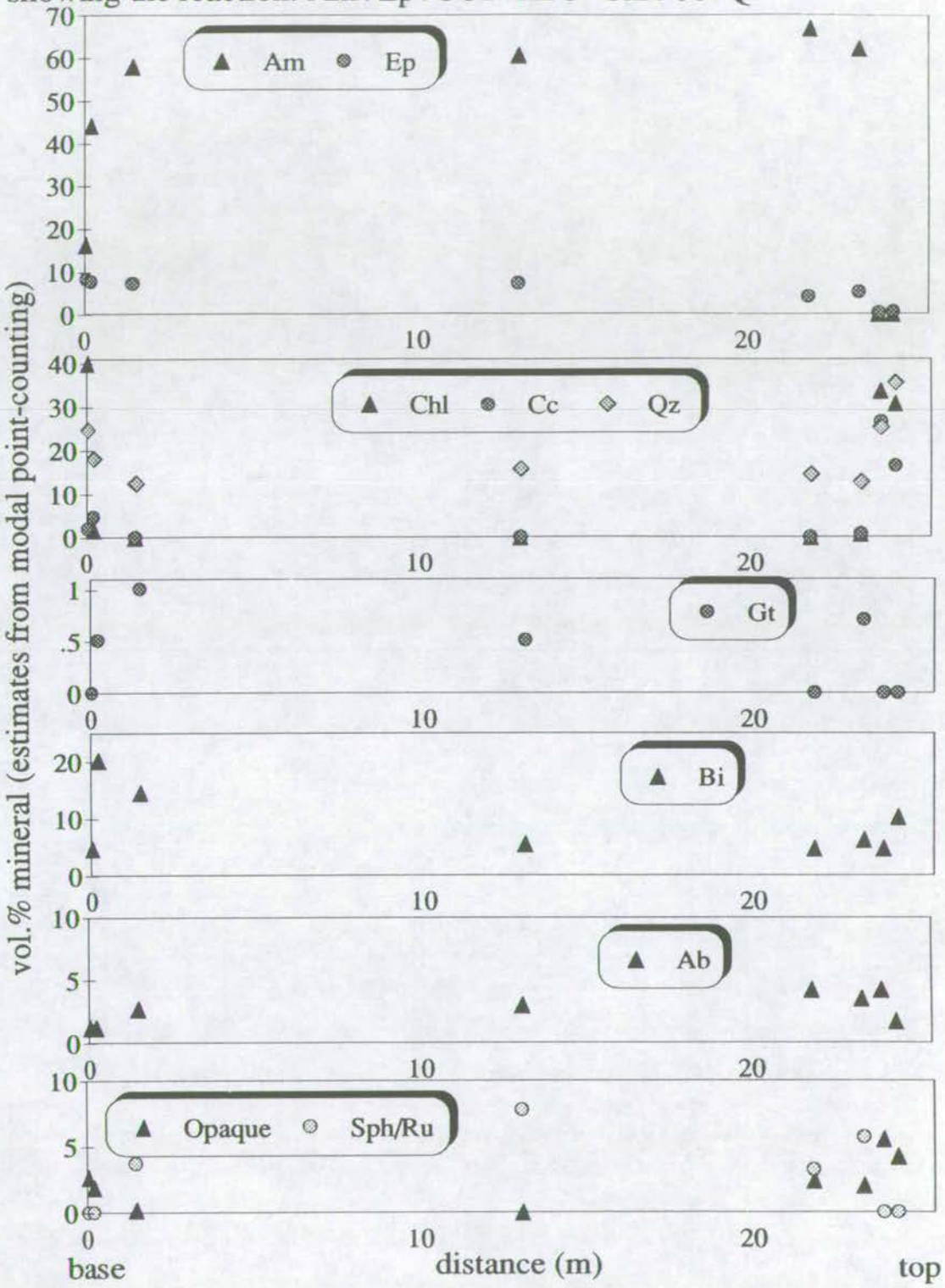

Figure A4.12: Modal Profile at Carsaig,
showing the reaction: Am+Ep+H20+CO2=Chl+Cc+Qz

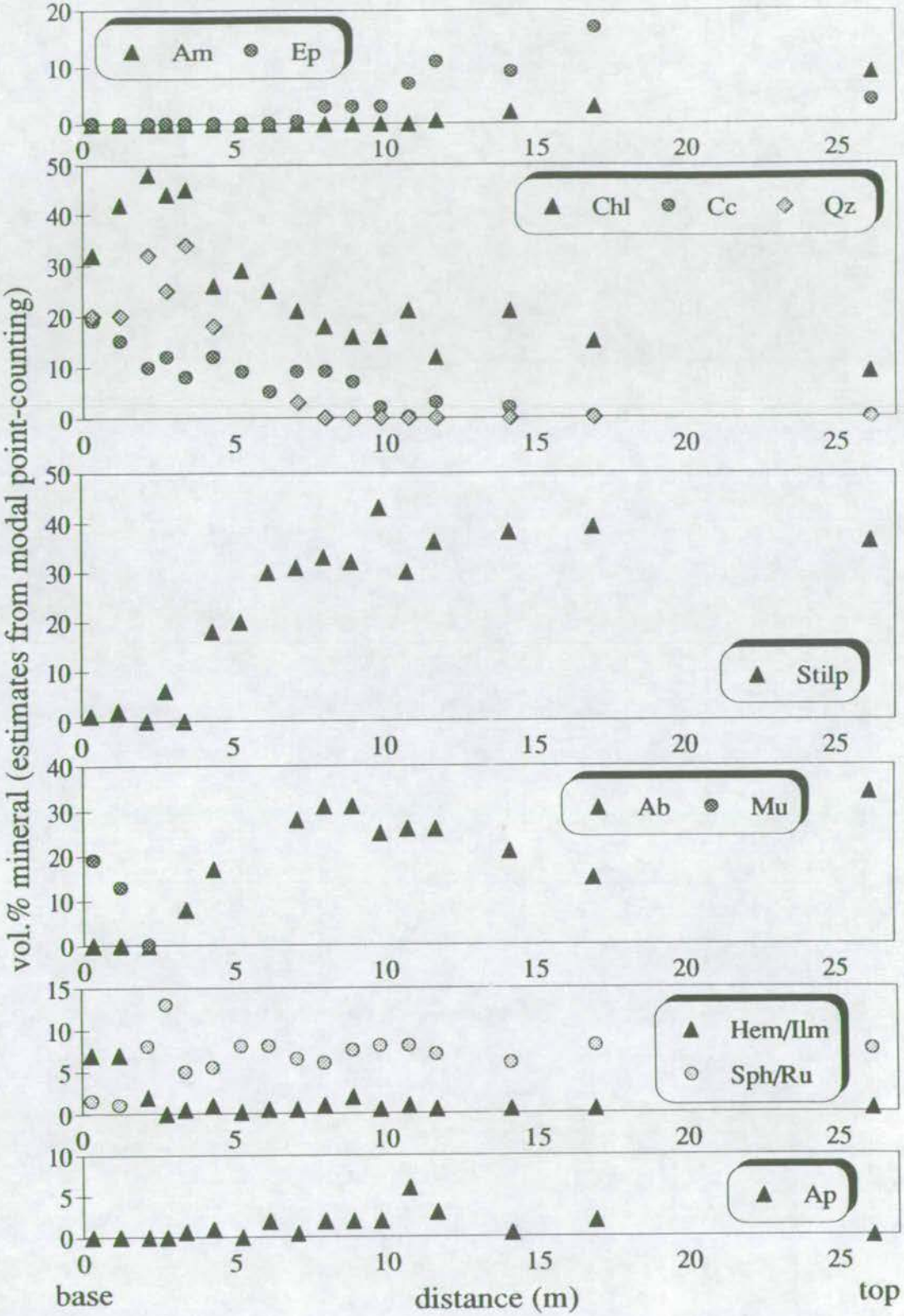

Appendix 5: Reaction Progress Profiles

Figures A5.1-A5.4: ankeritic metbabasites:
Profiles of Dol/(Dol+Cc), Vol.% Cc and Vol.% Dol,
constructed using standard calibrations in figure 4.3.

Figure A5.5-A5.24: reaction (1):
Profiles of Vol.% Cc,
constructed using standard calibrations in figure 4.3.

Reaction progress profiles include information about the host rock types and the local structure.

The host rock types are identified from the key which is presented below:

Host Rock Types

Quartzite

Phyllite

Marble

Local structure is depicted schematically, together with profile data.

Figure A5.1: Reaction Progress Profiles of the Metabasite Dykes on Scarba

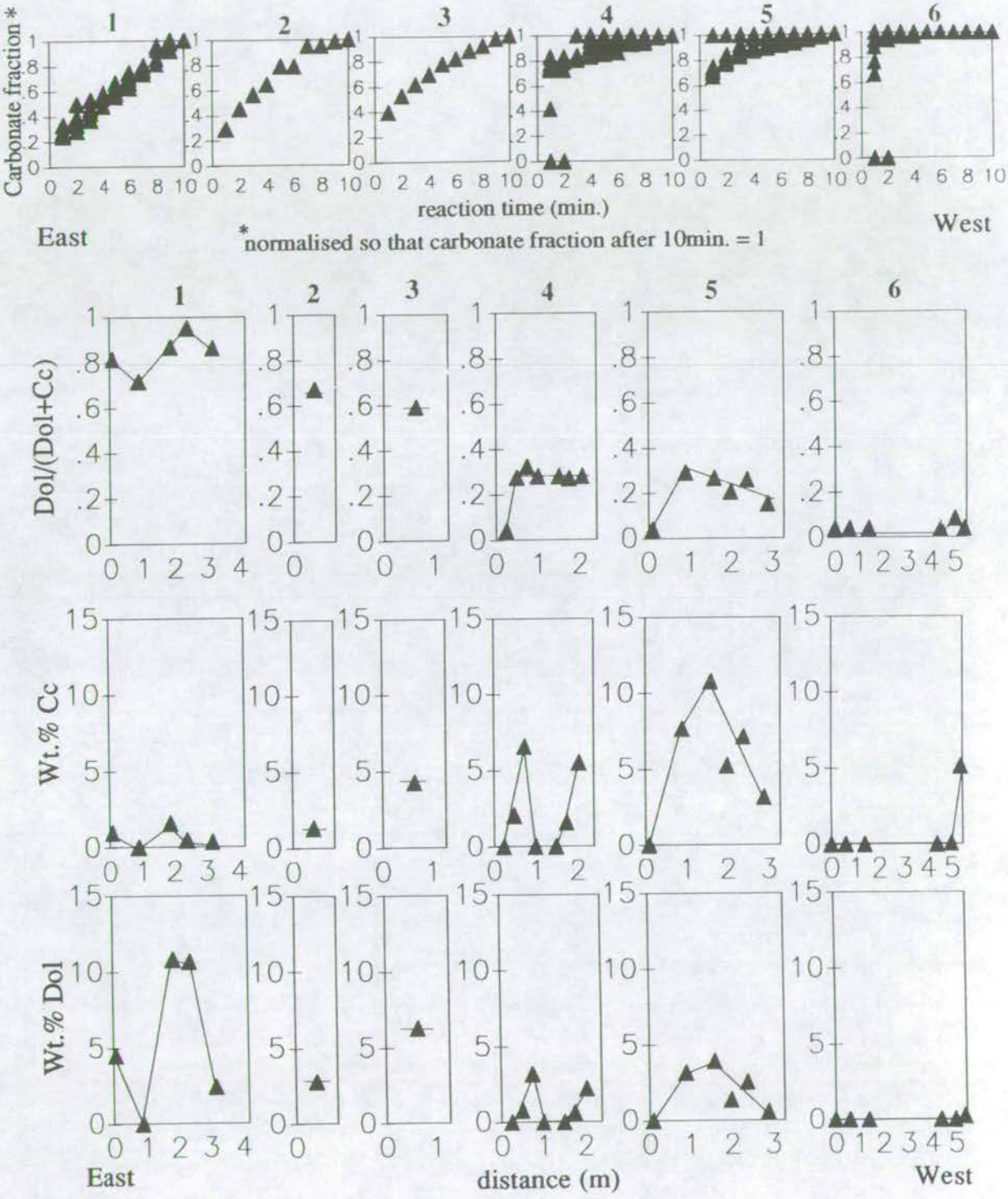

Figure A5.2 Reaction Progress Profiles of the Metabasite Sills at Traigh Gheighsgeir

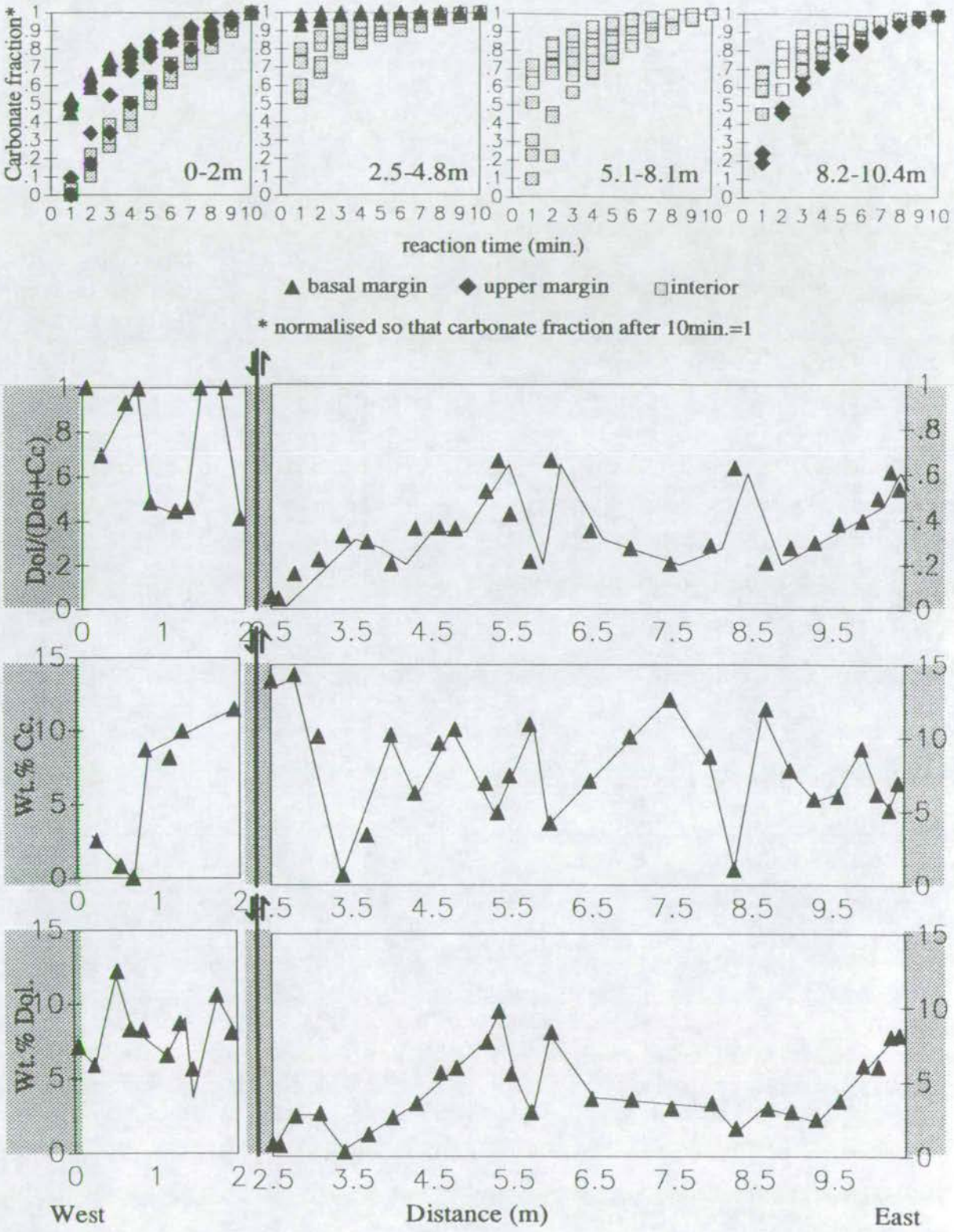

Figure A5.3: Reaction Progress Profile of the Metabasite Sill at Sgeir Figheadair

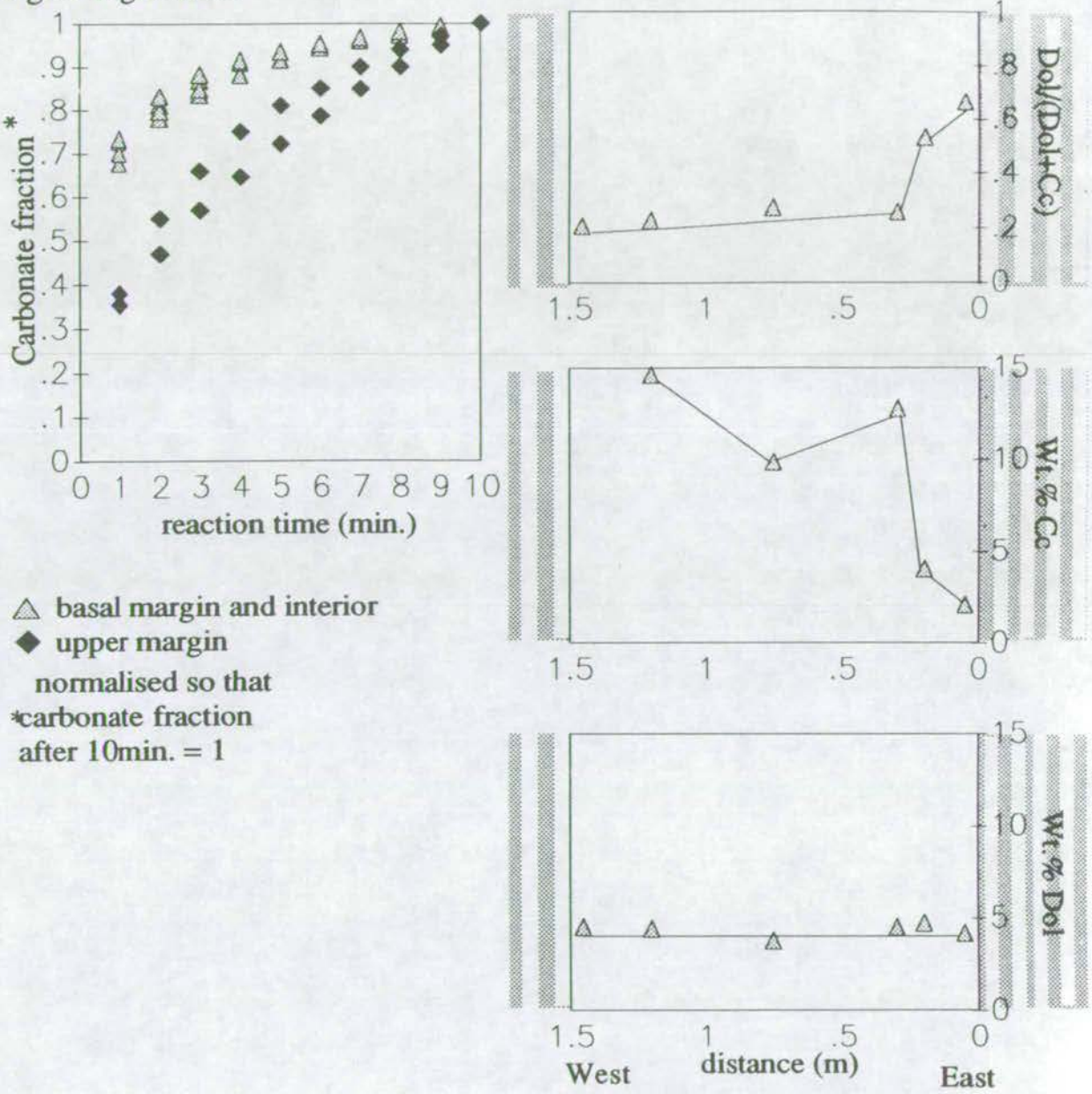

△ basal margin and interior
◆ upper margin

*carbonate fraction normalised so that after 10min. = 1

Figure A5.4: Reaction Progress Profiles of the Metabasite Sill at Keppoch Point

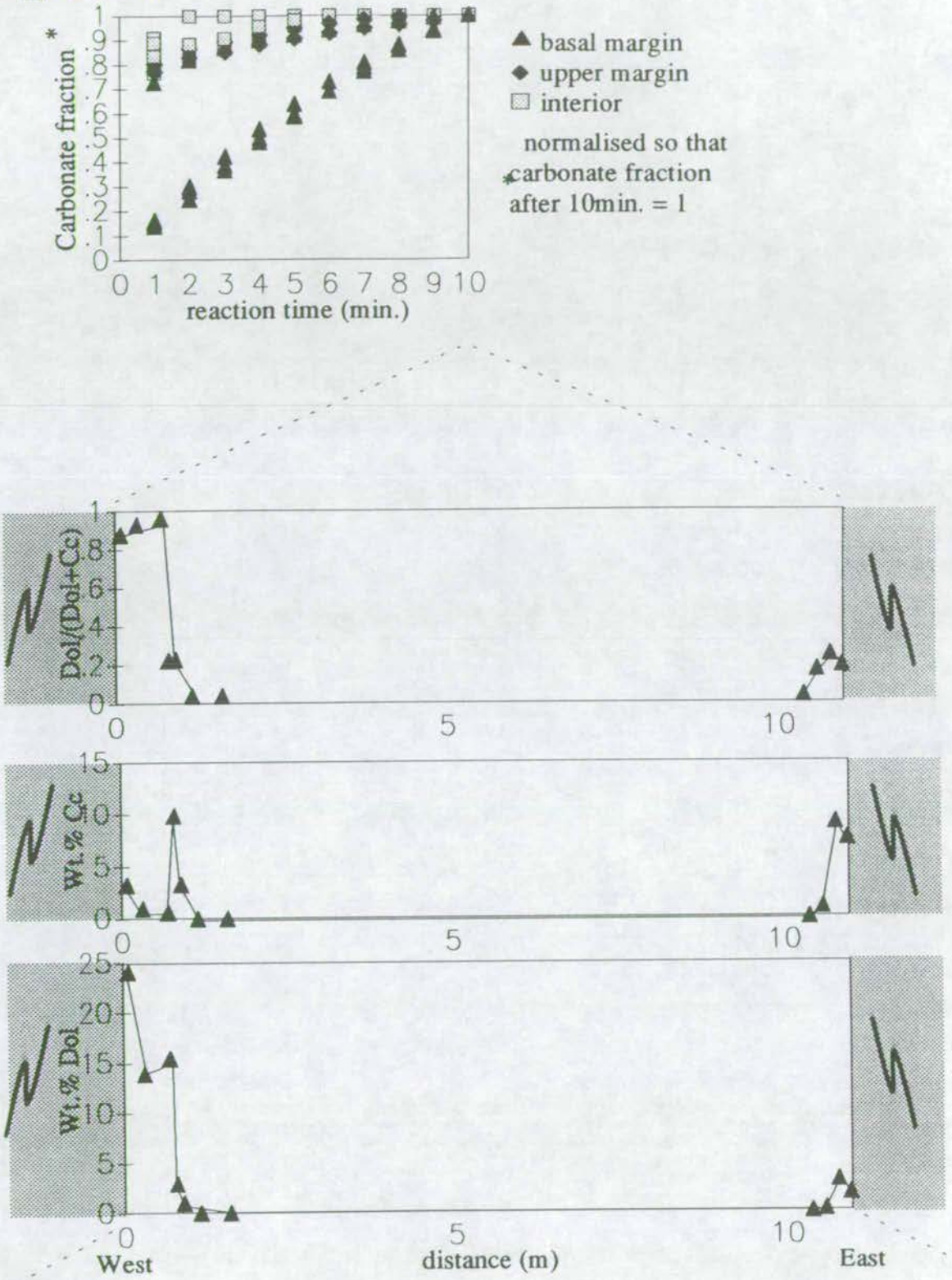

Figure A5.5: Reaction Progress Profiles of the Metabasite Dykes on North Jura

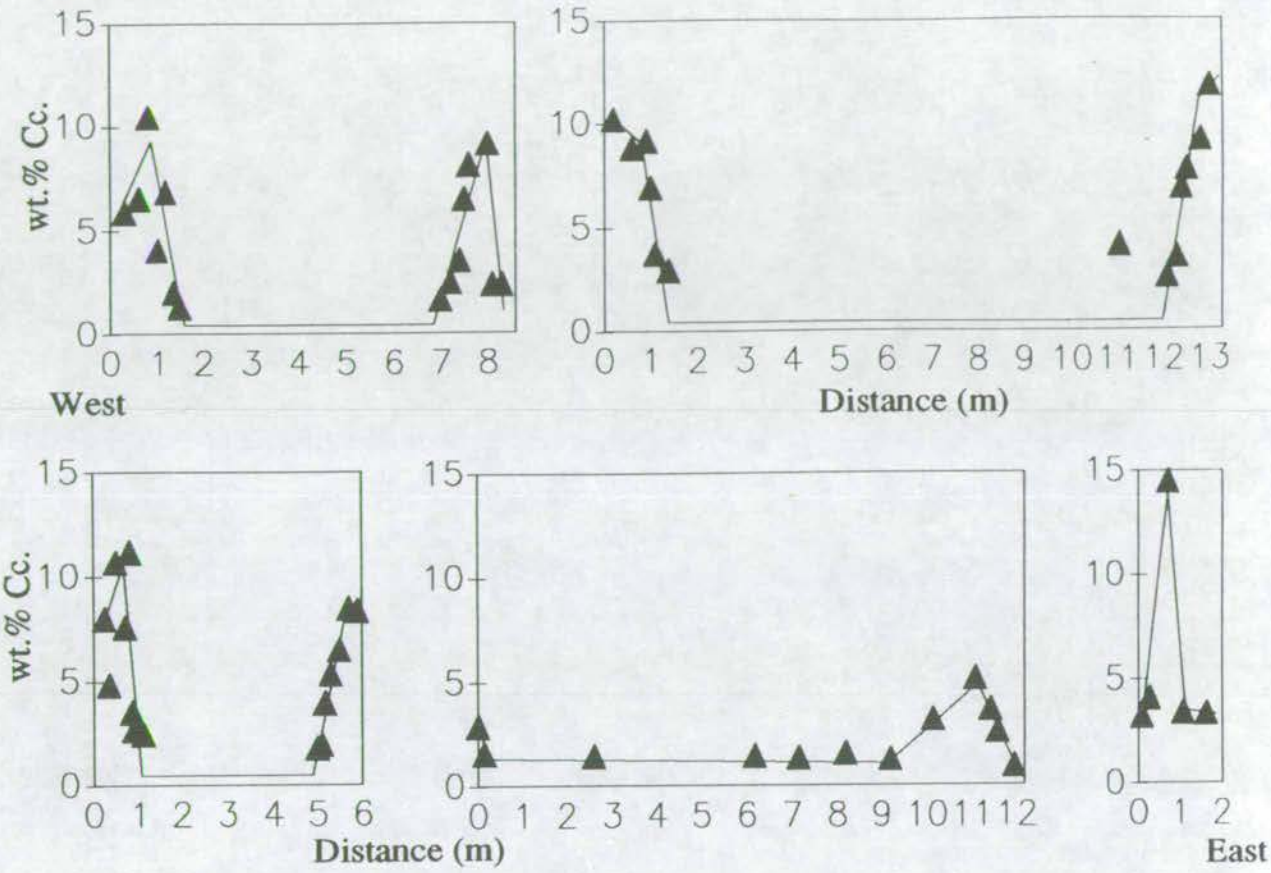

Figure A5.6: Reaction Progress Profiles of the Metabasite Sills at the Ard of Port Ellen

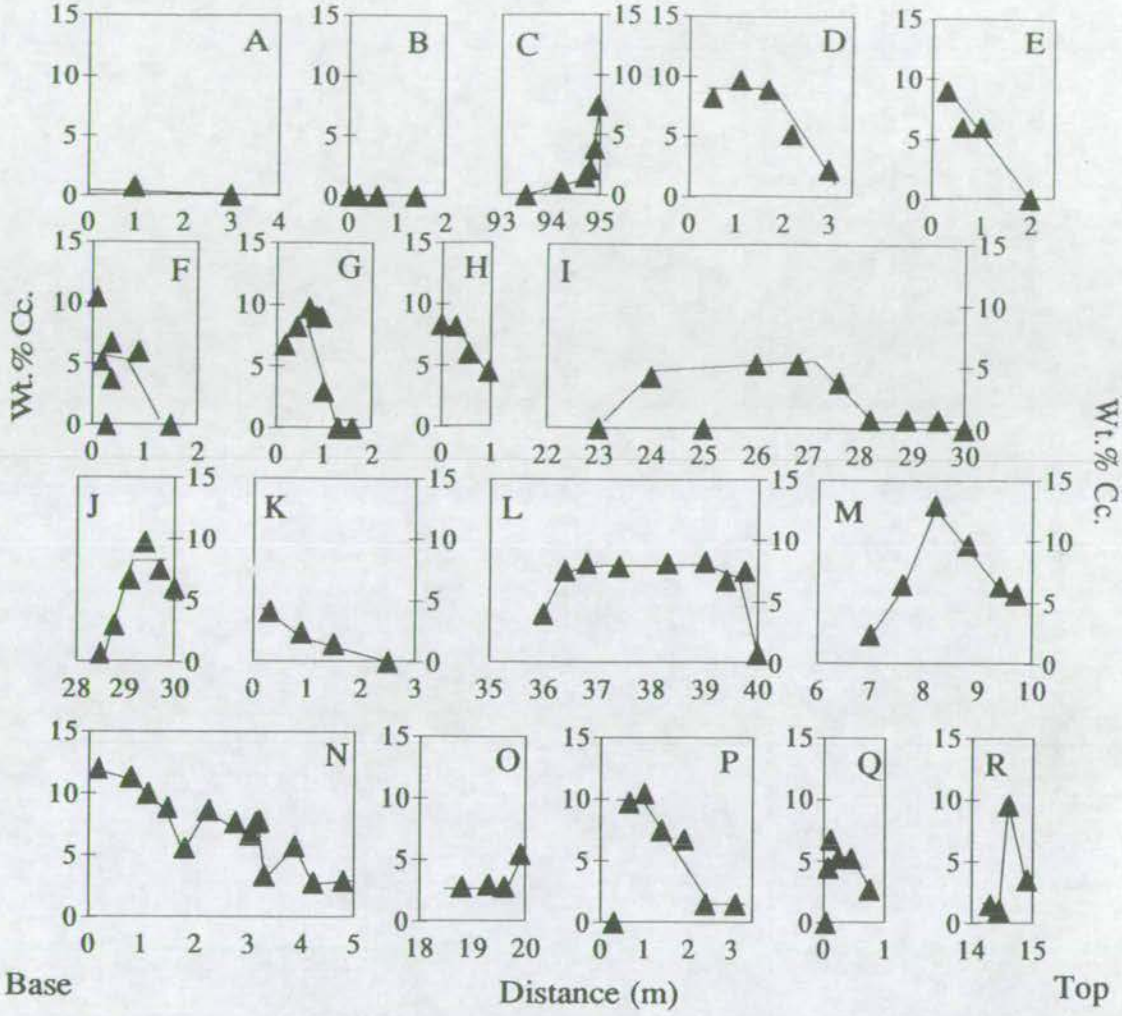

Profile Locations, The Ard of Port Ellen

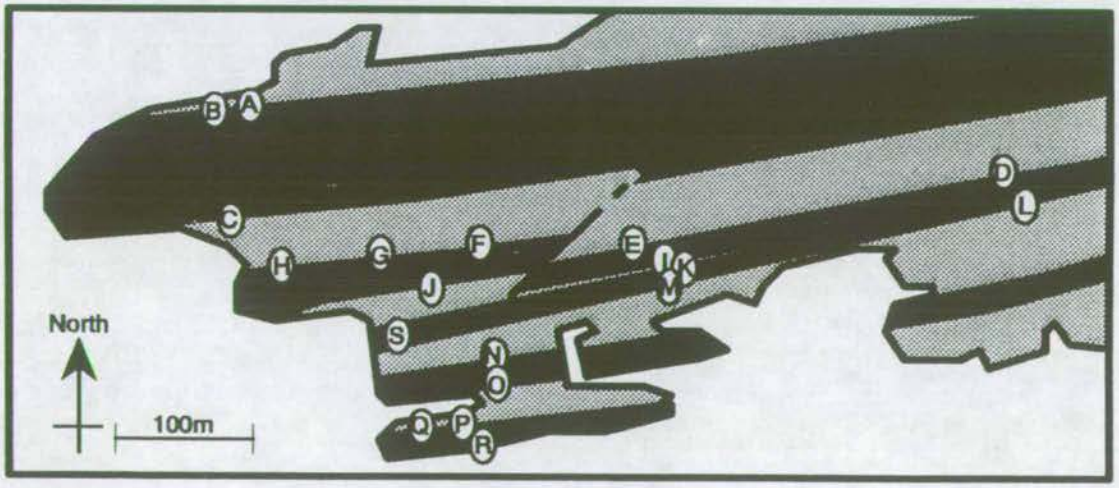

Figure A5.7: Reaction Progress Profile of a Metabasite on the Island of Danna

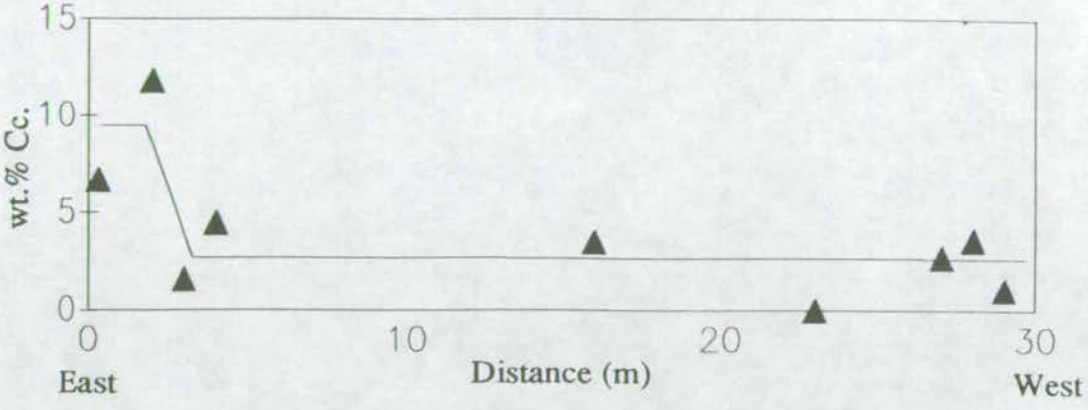

Figure A5.8: Reaction Progress Profiles of the Metabasite Sill at Castle Sween

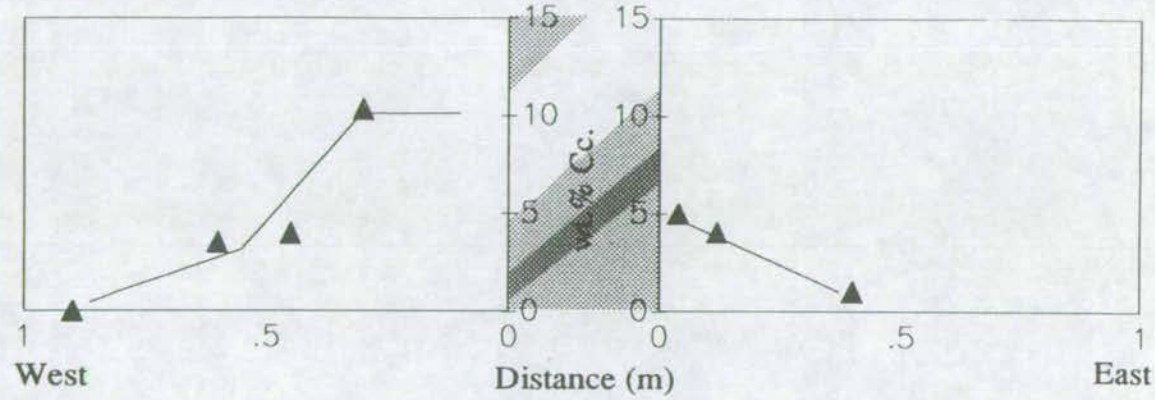

Figure A5.9: Reaction Progress Profiles of the Metabasite Sills at Bagh an Doide

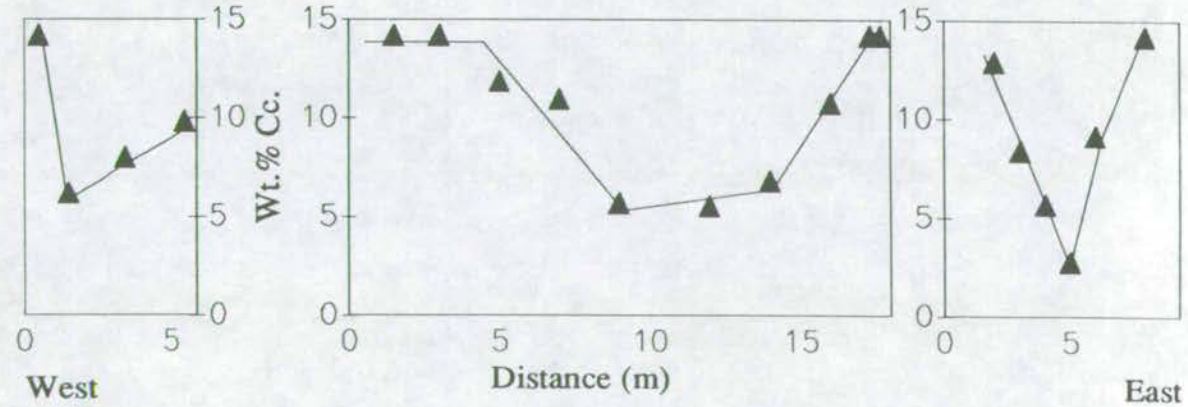

Figure A5.10: Reaction Progress Profiles of the Metabasite Sills at the Point of Knap

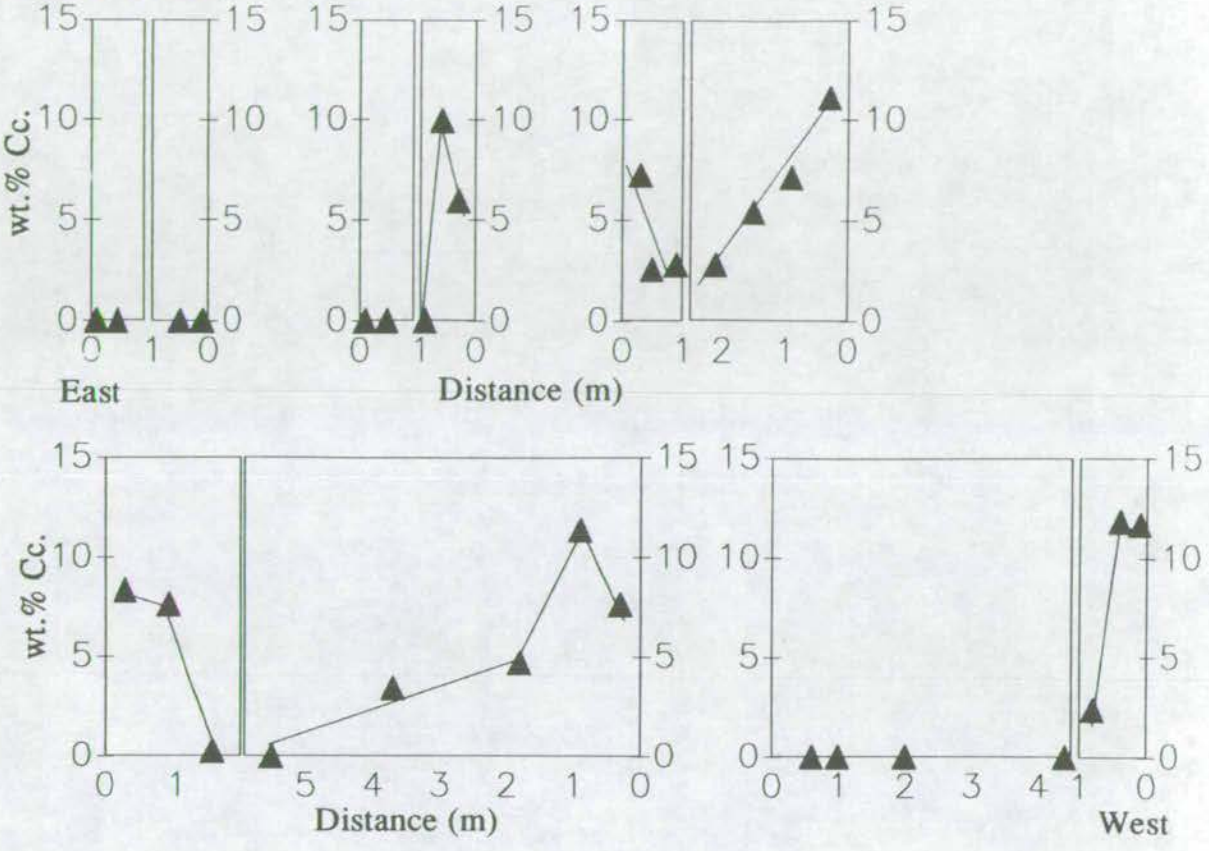

Figure A5.11: Reaction Progress Profiles of the Metabasite Sills West of Stonefield Bay

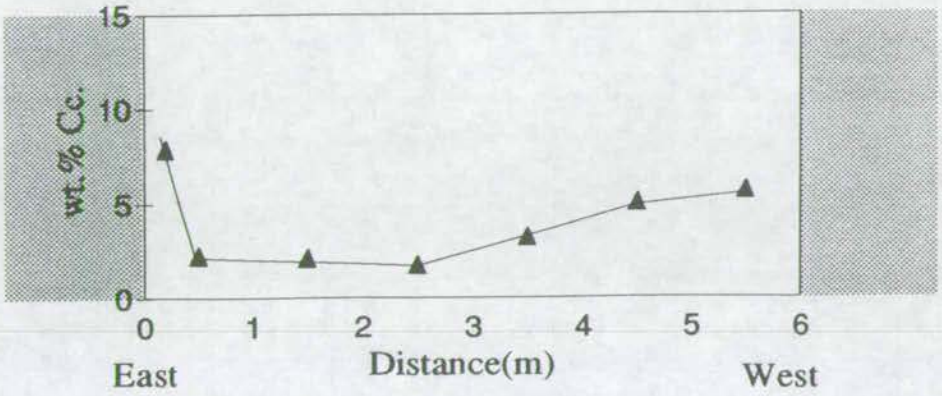

Figure A5.12: Reaction Progress Profiles of the Metabasite Sills East of Stonefield Bay

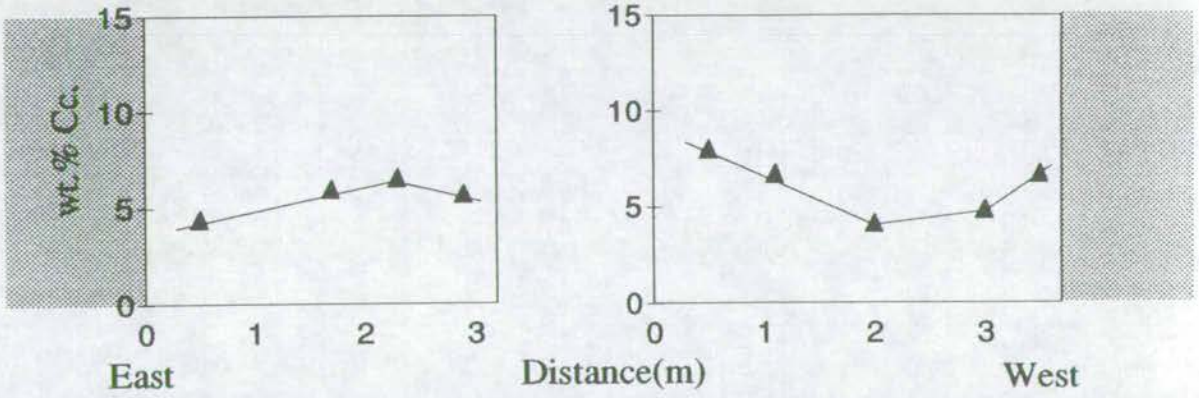

Figure A5.13: Reaction Progress Profiles of the Metabasite Sills at Rubha Garbh

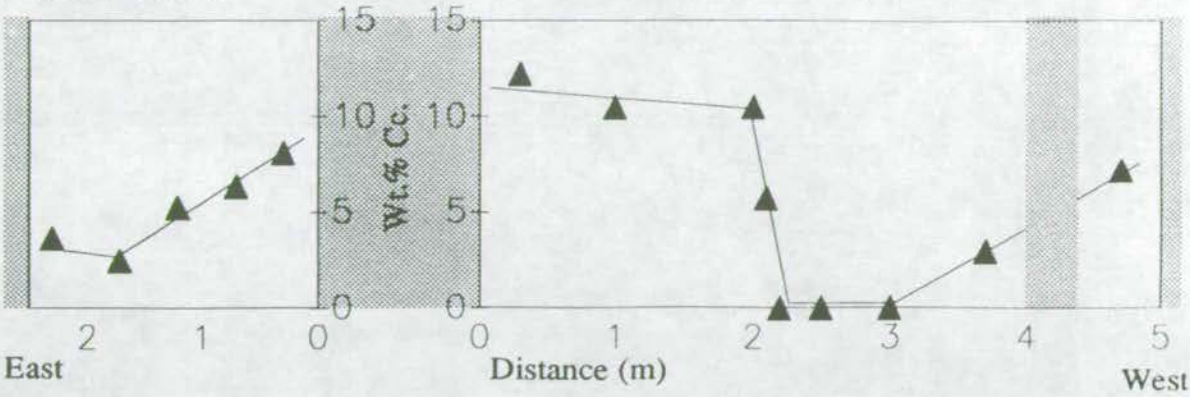

Figure A5.14: Reaction Progress Profiles of the Metabasite Sill at Lochead

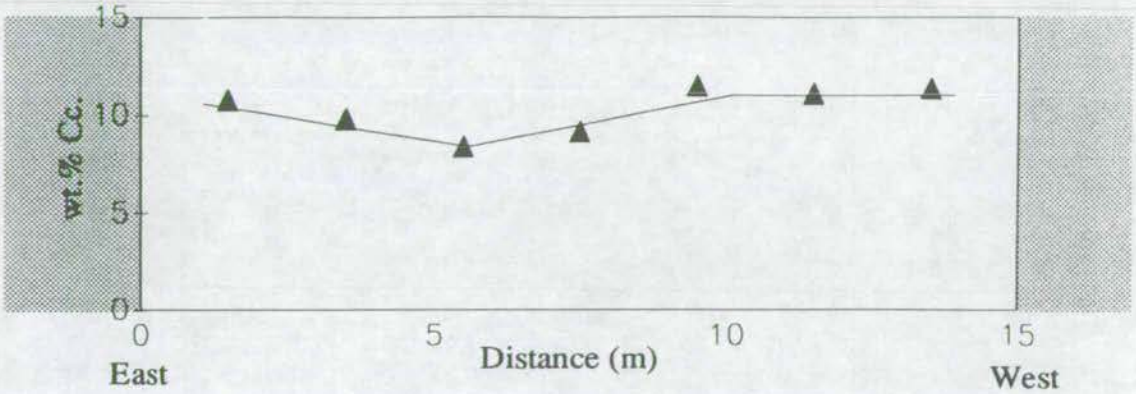

Figure A5.15: Reaction Progress Profiles of the Metabasite Sill at Ormsary

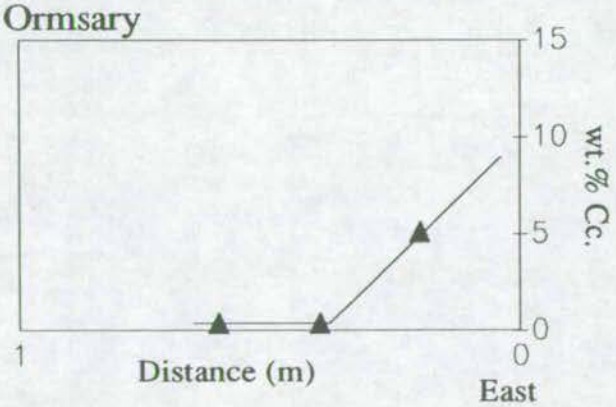

Figure A5.16: Reaction Progress Profiles of the Metabasite at Port Cill Maluaig

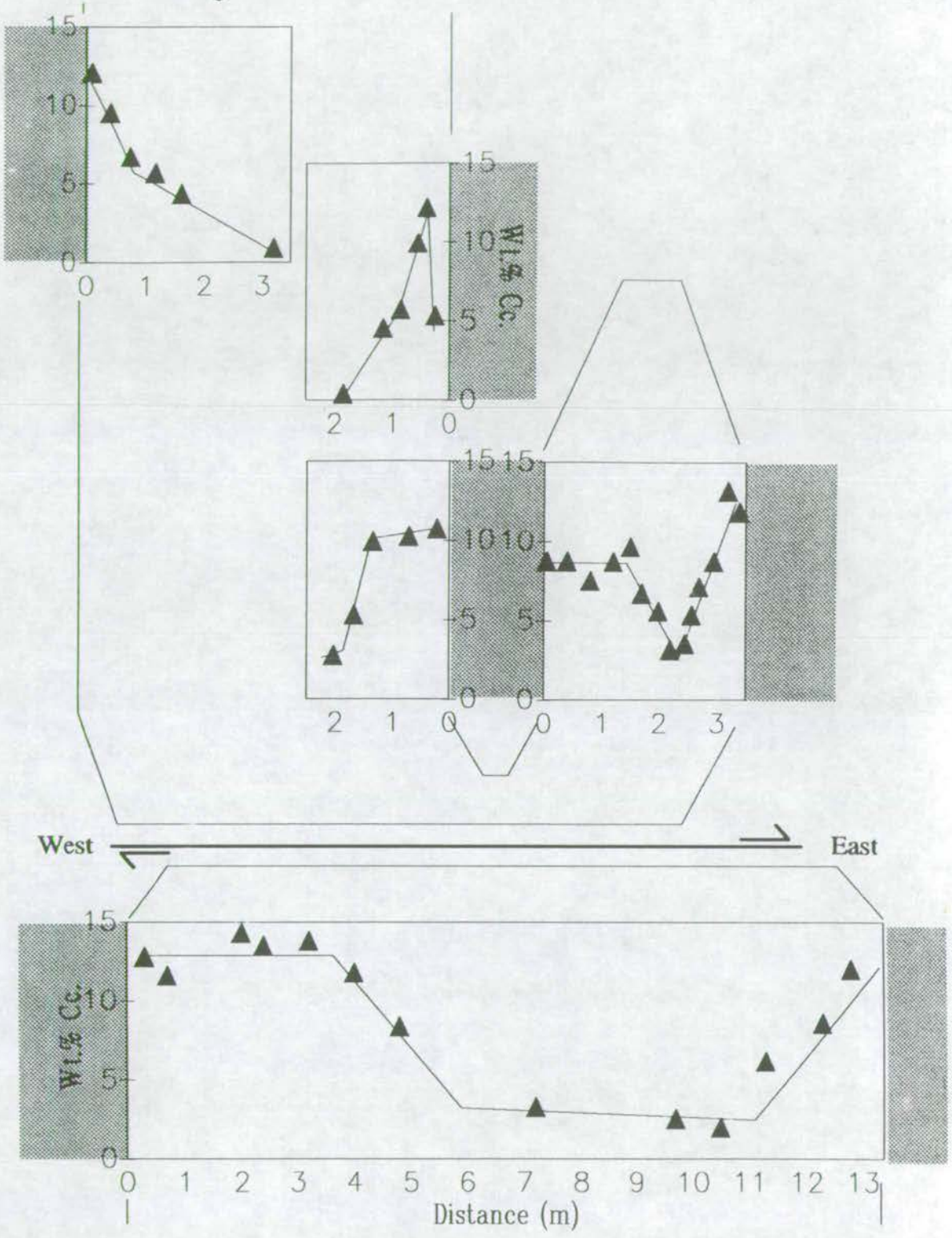

Figure A5.17: Reaction Progress Profiles of the Metabasite at Rubha Cill Maluaig

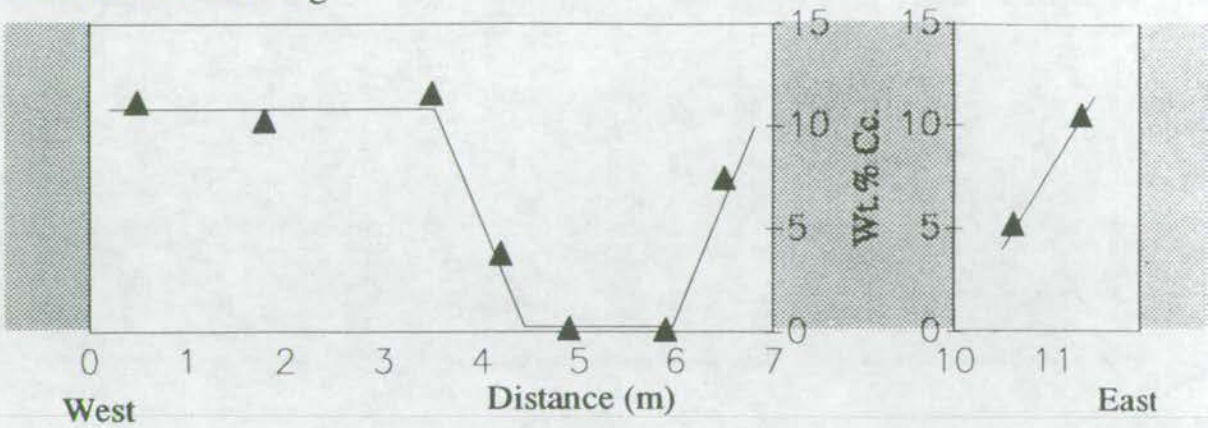

Figure A5.18: Reaction Progress Profiles of the Metabasite Sills at Stotfield Bay and Miller's Bay

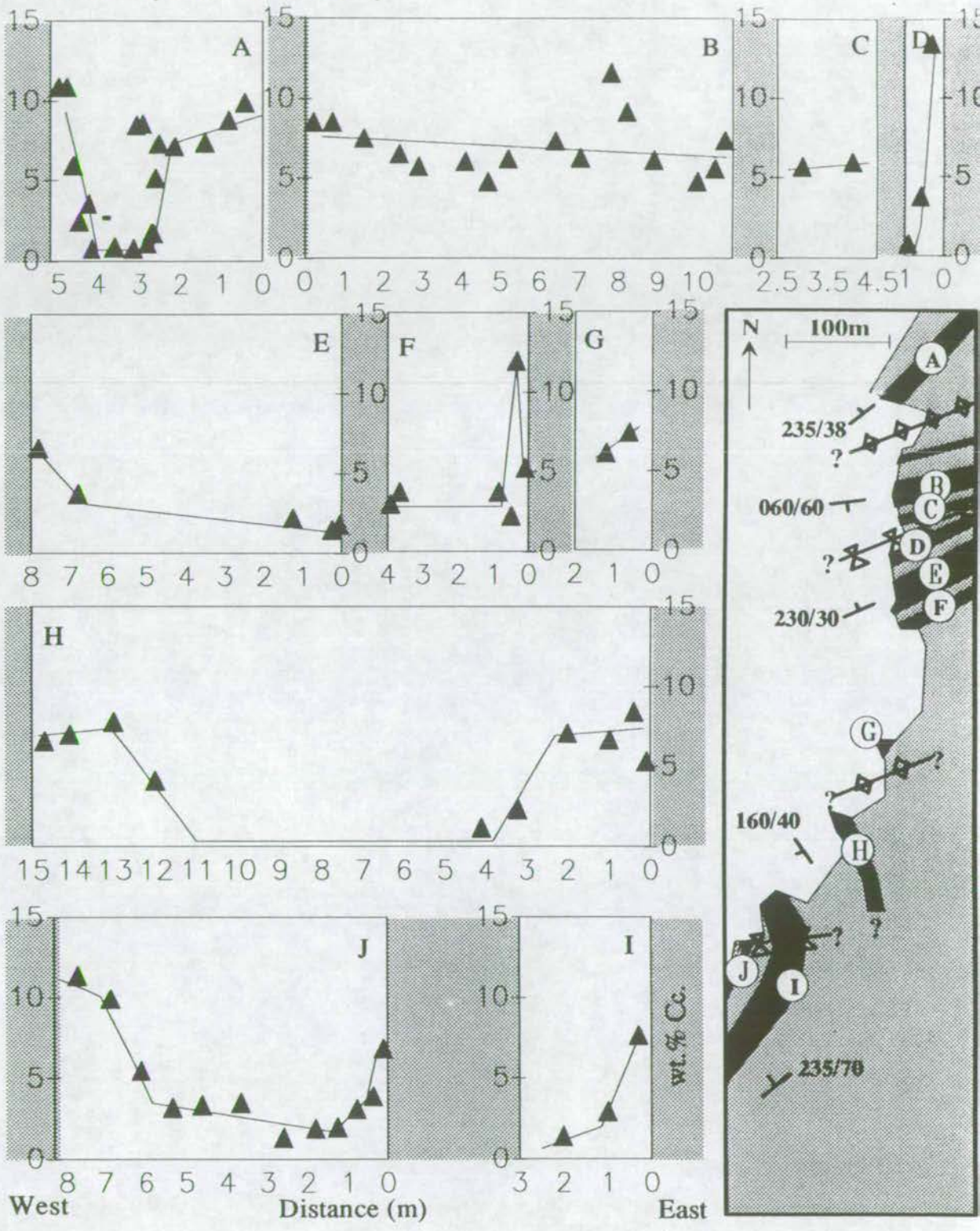

Figure A5.19: Reaction Progress Profiles of the Metabasites at Cretshangen Bay

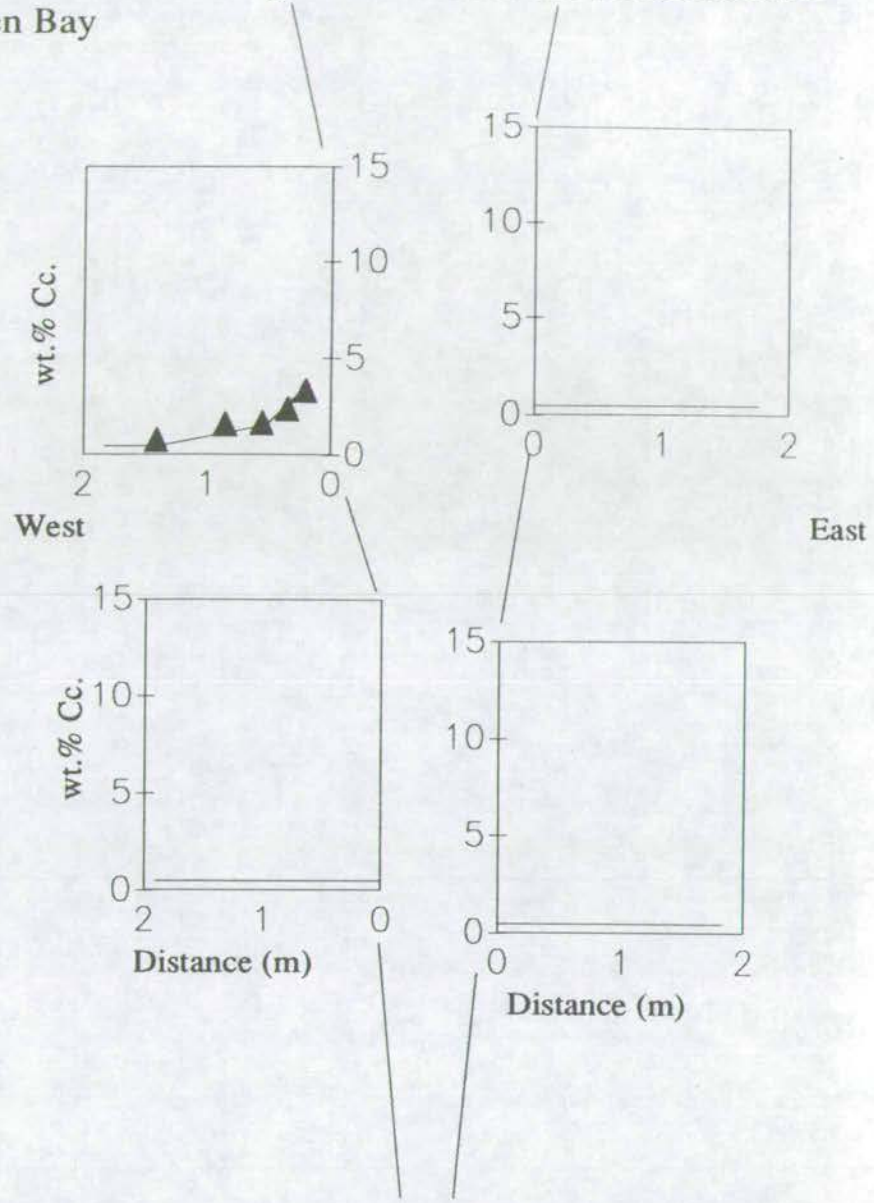

Figure A5.20: Reaction Progress Profiles of the Metabasite Sills at Port Ban

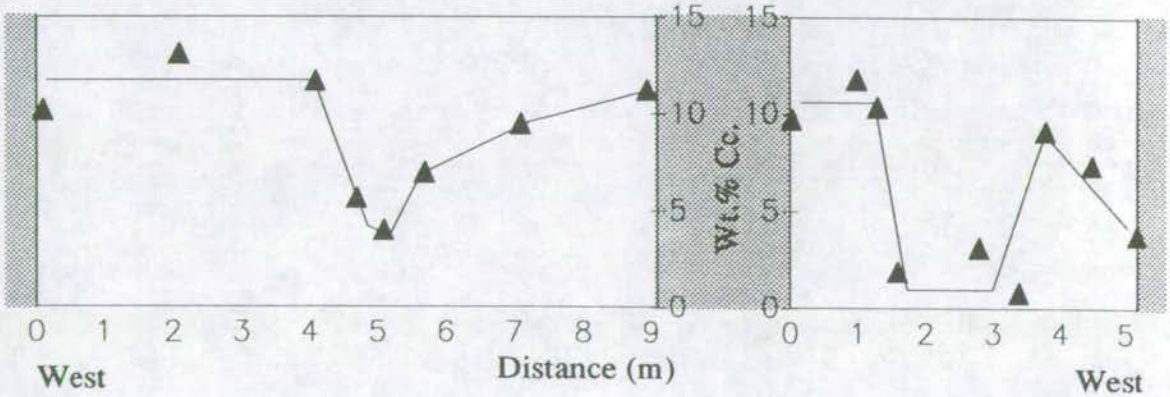

Figure A5.21: Reaction Progress Profiles of a Metabasite Sill at Kilberry Head

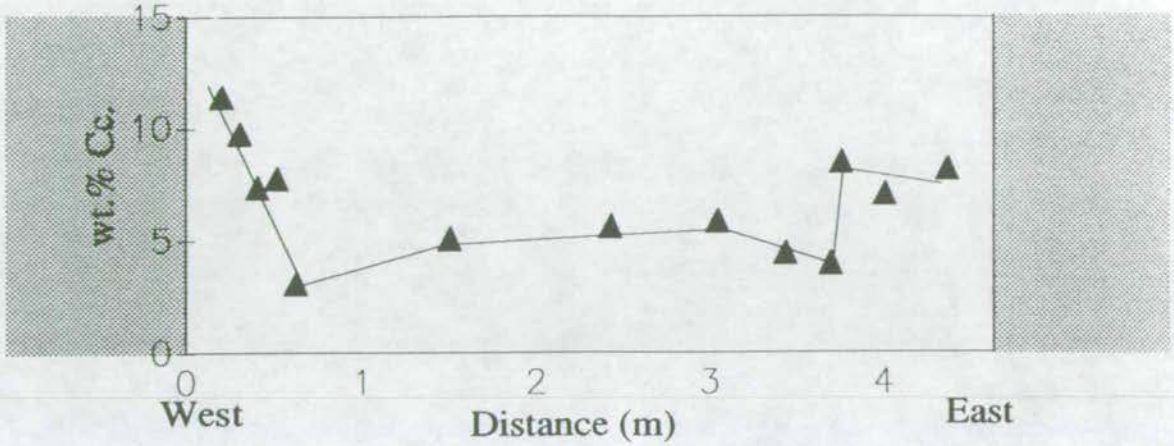

Figure A5.22: Reaction Progress Profile of the Metabasite Sill at Sgeir Maire

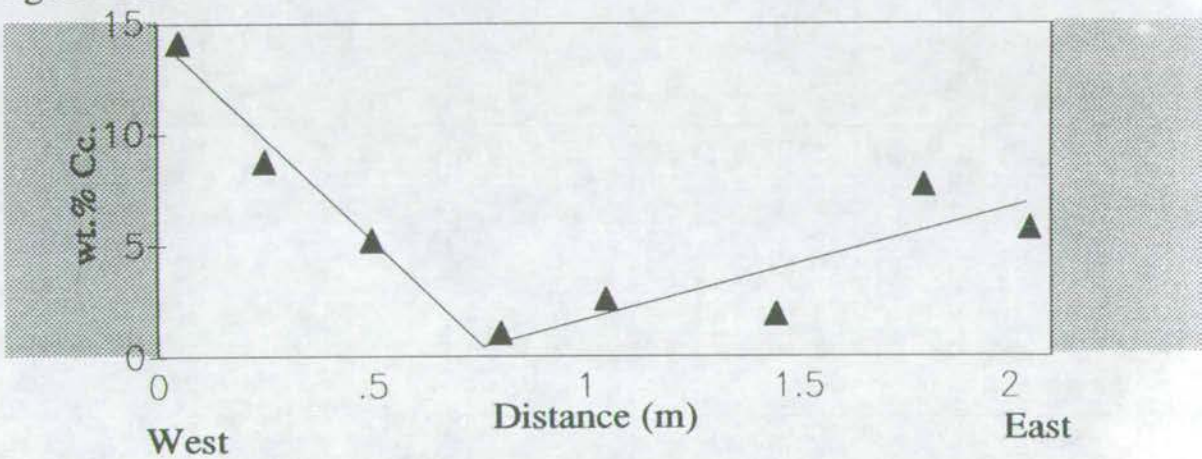

Figure A5.23: Reaction Progress Profiles of the Metabasite Sills at Loch Stornoway

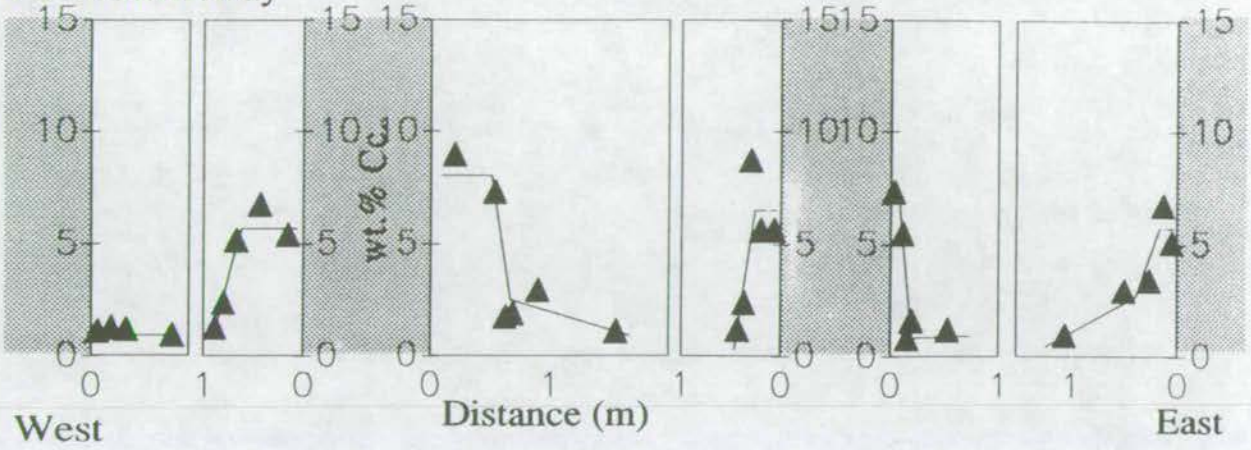

Figure A5.24: Reaction Progress Profile of Metabsite Sill at Rudh a' Bharr Ruaidh

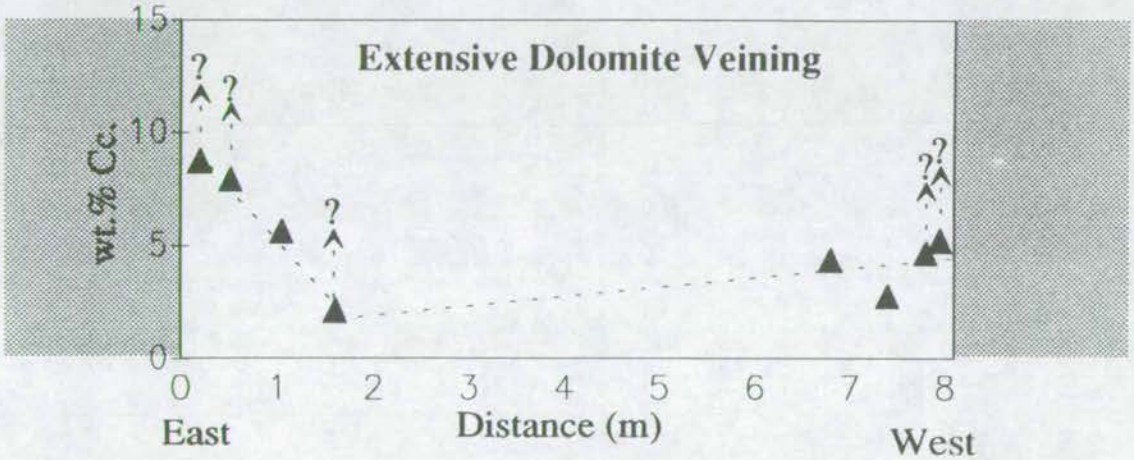

Appendix 6: Stable Isotope Data

Figure A6.1: Location map of stable isotope sample traverses.

Figure A6.2: Stable isotope traverse at Port Ellen

Figure A6.3: Stable isotope traverse at Mull of Oa

Figure A6.1: Location Map of Stable Isotope Sample Traverses

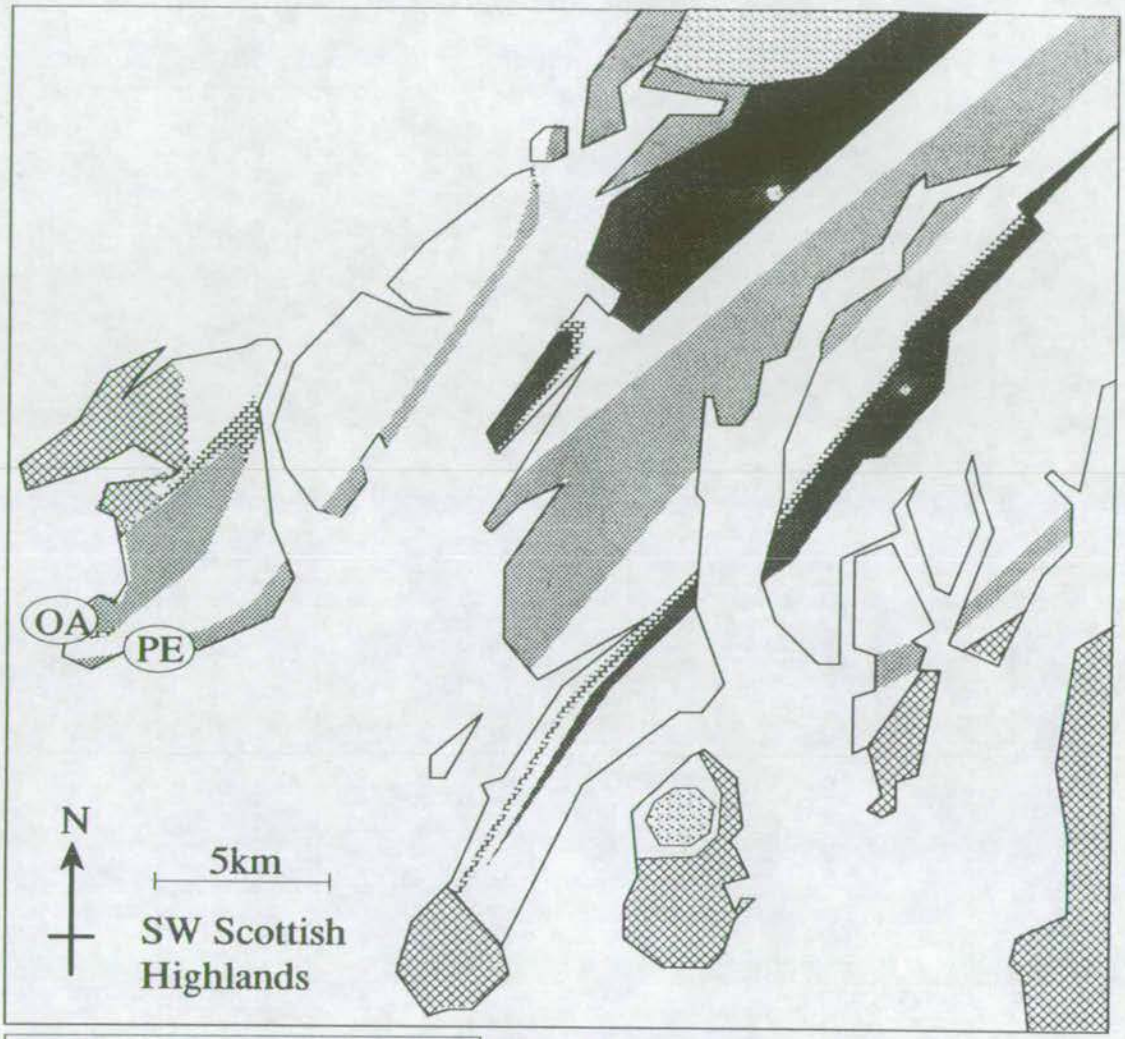

KEY

- Phyllite
- Quartzite
- Volcanics
- Marble
- Other Metamorphic and Sedimentary Rocks
- Other Igneous Rocks

PE = Port Ellen
OA = Mull of Oa

Figure A6.2: Oxygen Isotope Profile at The Ard of Port Ellen

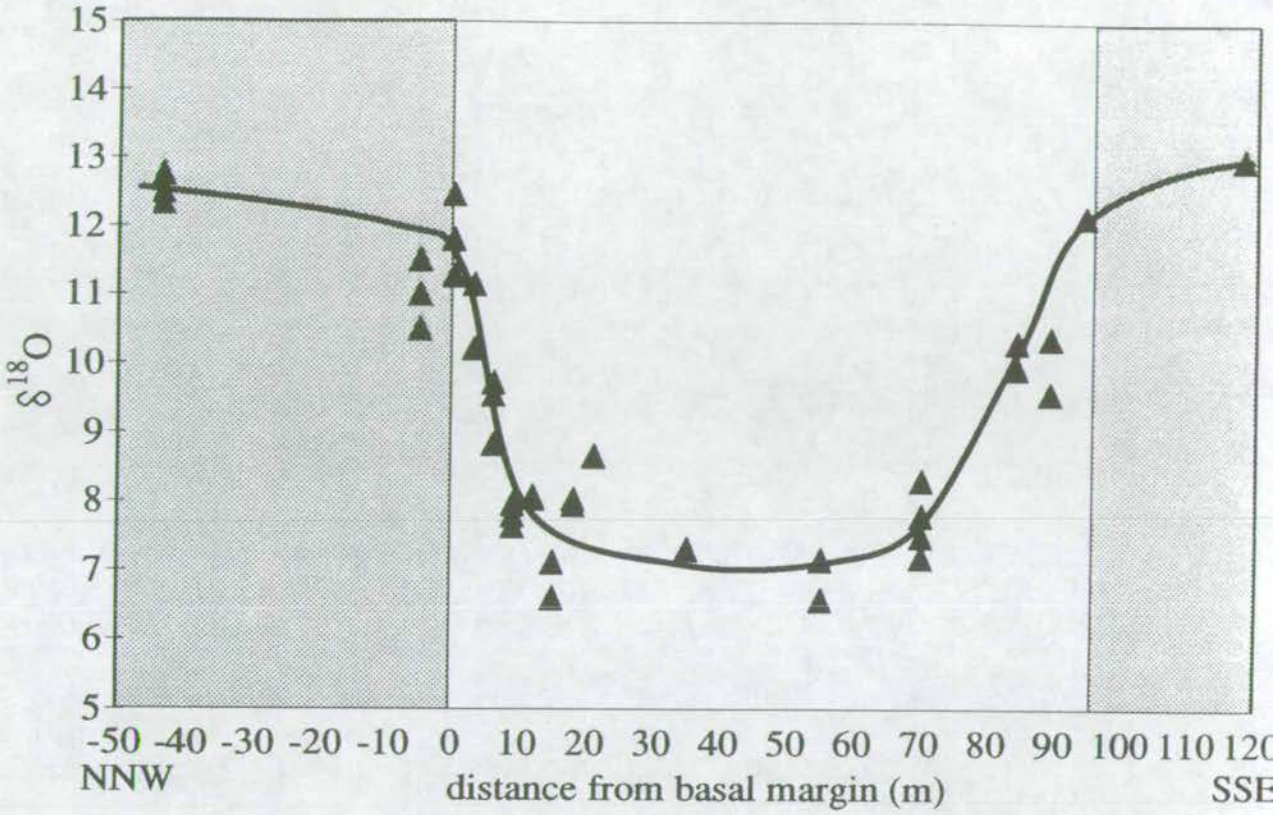

Stable Isotope Data: Port Ellen

Distance from basal margin (m)	-43	-5	0	3	6	9	12	15	18	21	35	55	70	84	89	94	118
O(SMOW)	12.337	11.504	11.27	10.21	9.537	7.96	8.07	7.12	8.033	8.657	7.32	6.589	7.202	10.31	9.565	12.134	12.98
O(SMOW)	12.76	10.502	12.46	11.14	9.718	7.643	8.044	6.608	7.947	8.65		7.17	7.501	9.934	10.367		
O(SMOW)	12.5	11.0	11.8		8.824	7.801							8.312				
O(SMOW)													7.803				

Figure A6.3: Stable Isotope Data from the Mull of Oa

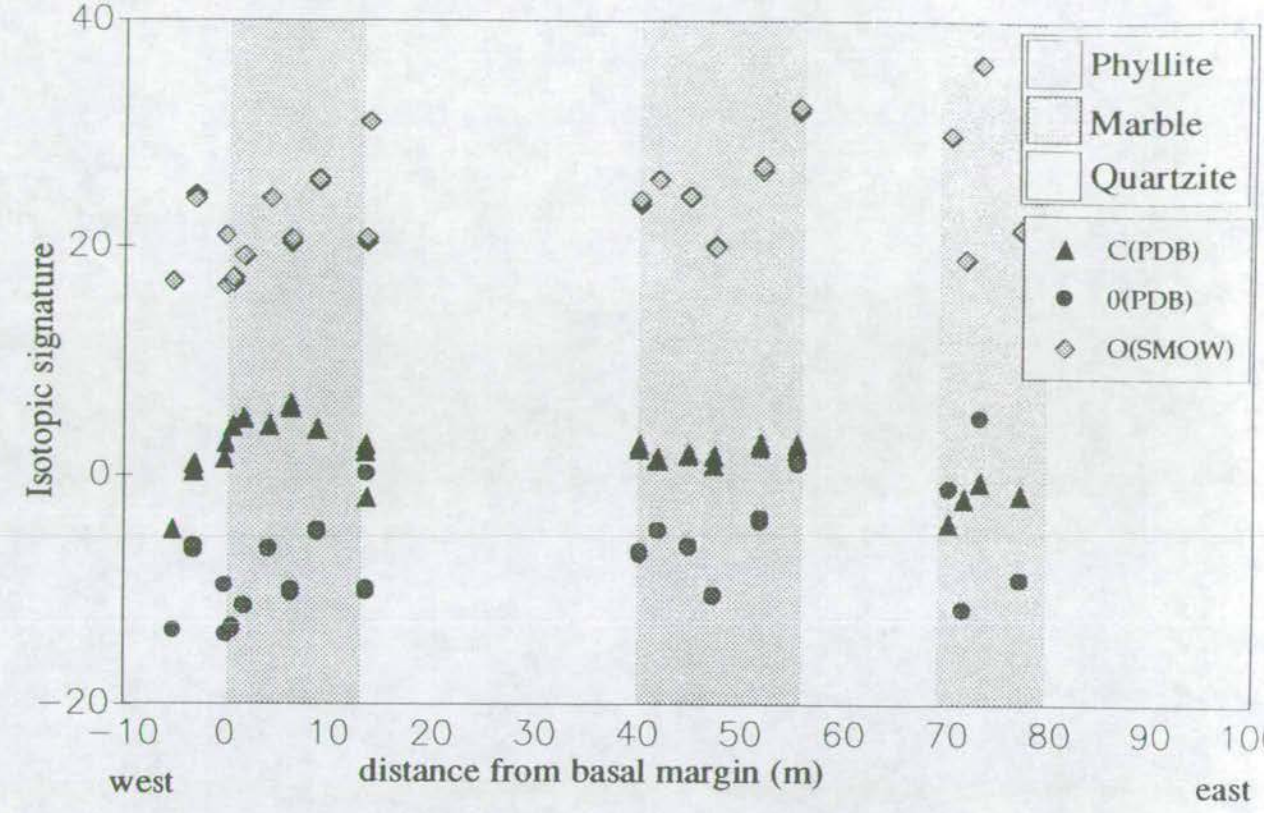

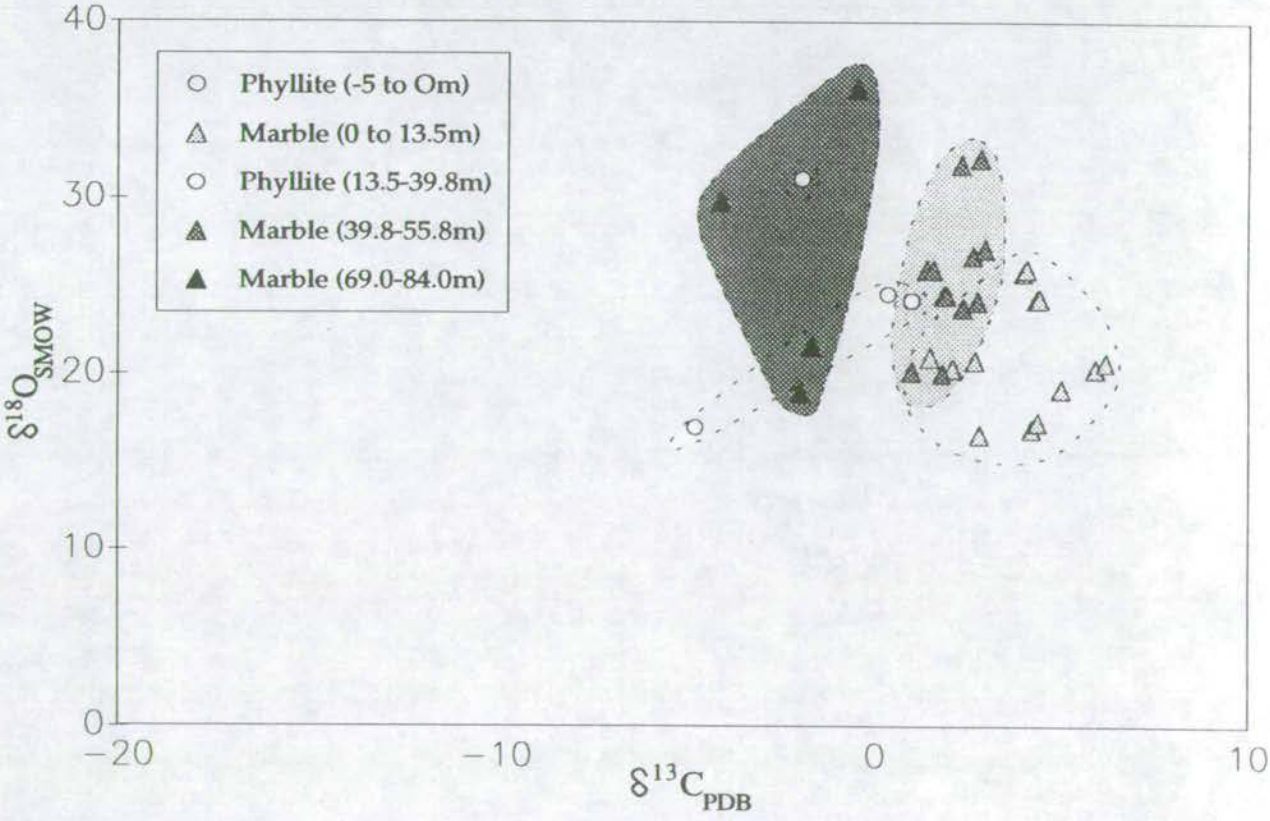

Stable Isotope Data: Mull of Oa

Distance from base of NNW-most Marble	-5	-3	-3	-.1	.05	.75	.75	1.8	4.2	4.2	6.3	6.3
C(PDB)	-4.708	.335	.976	1.478	2.784	4.182	4.336	4.961	4.32	4.397	5.881	6.154
O(PDB)	-13.591	-6.555	-6.19	-9.671	-13.92	-13.612	-13.235	-11.397	-6.455	-6.414	-10.27	-9.914
O(SMOW)	16.899	24.529	24.152	20.94	16.56	16.877	17.265	19.161	24.255	24.298	20.322	20.689
Distance from base of NNW-most Marble	8.8	8.8	13.5	13.5	13.6	40	40	41.8	41.8	44.8	44.8	47.3
C(PDB)	3.971	4.046	2.077	2.678	-1.936	2.346	2.731	1.366	1.551	1.85	1.916	.988
O(PDB)	-4.943	-4.778	-10.224	-9.811	.163	-6.892	-6.553	-4.802	-4.82	-6.202	-6.242	-10.406
O(SMOW)	25.815	25.984	20.37	20.786	31.078	23.805	24.154	25.96	25.941	24.516	24.475	20.182
Distance from base of NNW-most Marble	47.3	51.8	51.8	55.3	55.3	70	71.5	73	77			
C(PDB)	1.798	2.617	2.919	2.276	2.79	-4.046	-1.948	-0.48	-1.647			
O(PDB)	-10.529	-4.039	-3.653	1.012	1.335	-1.066	-11.653	5.143	-9.068			
O(SMOW)	20.056	26.747	27.144	31.954	32.286	29.811	18.897	36.212	21.561			

Appendix 7: Electron Microprobe Data

Electron microprobe data are presented from Scarba, Traigh Gheighsgeir, Stonefield, Port Cill Mauaig, Keppoch Point, and Point of Knap. Distances (z) refer to the following lithological sections:

Scarba:

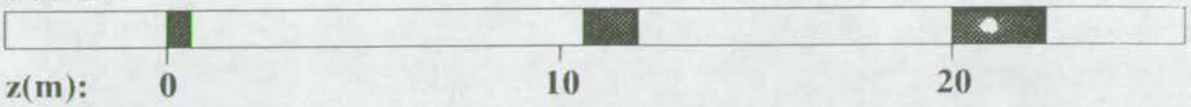

Traigh Gheighsgeir:

Stonefield:

Port Cill Maluaig:

Keppoch Point:

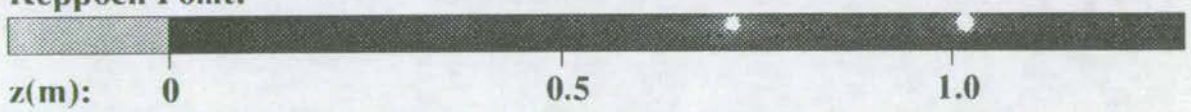

Point of Knap:

Analyses of Chlorites to enable identification of pyritisation front (figure 11.4)

- **Psammite**
- **Phyllite**
- **Metabasite**
- **Marble**

Scarba: Chlorites

z(m)	-4	28.1	28.1	28.1
SI	35.26	26.27	26.44	26.35
TI	.36	.04	.03	.02
AL	29.04	19.75	19.66	19.52
FE	9.15	20.49	20.73	20.4
MN	0	.19	.2	.21
MG	7.53	19.01	19	19.03
CA	.26	.03	.03	.03
NA	2.81	.03	.03	.05
K	.02	.02	.04	.03
TOT	84.43	85.83	86.16	85.64
SI	6.84	5.52	5.54	5.55
TI	.05	.01	0	0
AL	6.64	4.89	4.86	4.85
FE	1.48	3.6	3.63	3.59
MN	0	.03	.04	.04
MG	2.18	5.95	5.93	5.97
CA	.05	.01	.01	.01
NA	1.06	.01	.01	.02
K	0	.01	.01	.01
SUM	18.32	20.03	20.04	20.04

Scarba: Biotites

z(m)	-4	-4	-4	16	8.7	8.7	8.7	16	16	28.1	28.1	28.1
SI	35.47	35.28	29.47	34.79	27.88	31.95	31.5	38.4	39.9	37.07	37.62	37.79
TI	1.74	1.69	.79	1.21	1	1.2	1.23	1.58	.99	1.39	1.38	1.44
AL	14.87	15	16.23	14.05	15.52	16.54	16.47	14.31	18.51	15.1	14.8	14.9
FE	19.04	19.32	25.98	15.77	18.93	19.31	20.43	15.35	13.2	17.15	17.4	17.02
MN	.08	.09	.06	.12	.08	.12	.14	.14	.08	.12	.13	.13
MG	13.14	12.79	12.96	14.42	13.85	15.43	14	14.78	11.35	12.77	12.89	12.91
CA	.04	.02	.06	.18	.11	.15	.15	.03	.04	0	.06	0
NA	.05	.07	.05	.03	.01	.02	.02	.04	.03	.19	.13	.04
K	7.36	7.3	3	6	2.06	3.08	3.17	8.58	7.33	9.47	9.45	9.59
TOT	91.79	91.56	88.6	86.57	79.44	87.8	87.11	93.21	91.43	93.26	93.86	93.82
SI	5.57	5.56	4.91	5.67	5	5.16	5.16	5.83	5.98	5.72	5.76	5.78
TI	.21	.2	.1	.15	.13	.15	.15	.18	.11	.16	.16	.17
AL	2.75	2.79	3.19	2.7	3.28	3.15	3.18	2.56	3.27	2.75	2.67	2.69
FE	2.5	2.55	3.62	2.15	2.84	2.61	2.8	1.95	1.65	2.21	2.23	2.18
MN	.01	.01	.01	.02	.01	.02	.02	.02	.01	.02	.02	.02
MG	3.07	3	3.22	3.5	3.7	3.71	3.42	3.34	2.54	2.94	2.94	2.94
CA	.01	0	.01	.03	.02	.03	.03	0	.01	0	.01	0
NA	.02	.02	.02	.01	0	.01	.01	.01	.01	.06	.04	.01
K	1.47	1.47	.64	1.25	.47	.63	.66	1.66	1.4	1.86	1.85	1.87
SUM	15.6	15.59	15.72	15.46	15.46	15.45	15.43	15.55	14.98	15.71	15.68	15.65

Traigh Geighsgeir, South: Chlorites

z(m)	5.38	5.38	5.38	5.23	5.23	5.23	5.03	5.03	5.03	5.23	5.23	5.23	5.03	5.03	5.03
SI	22.78	22.97	22.67	25.59	23.6	25.03	23.76	23.18	23.73	23.69	23.51	23.87	23.66	23.54	31.03
TI	.31	.05	.05	.03	.11	.1	.07	.08	.06	.07	.05	.22	.1	.02	.03
AL	21.87	21.32	20.76	23.49	21.28	22.33	21.46	21.06	21.17	21.85	22.11	21.74	21.45	22.4	28.07
FE	27.97	27.72	26.78	27.61	30.51	25.81	29.77	28.99	28.97	29.8	28.61	28.39	28.9	29.08	20.21
MN	.09	.08	.12	.07	.09	.17	.1	.26	.14	.05	.09	.09	.08	.1	.03
MG	12.82	12.34	12.41	8.99	11.02	12.1	11.16	11.85	12.44	10.78	12.02	11.91	11.64	11.2	7.14
CA	.03	.08	.05	.03	.03	.04	.08	.07	.04	.03	.02	.03	.05	.07	.06
NA	.05	.4	.24	.01	.01	.05	.01	.01	.01	.07	.07	.02	.06	.04	2.83
K	.01	.17	.12	0	0	.02	0	0	0	.03	.03	.02	.02	.02	.43
TOT	85.93	85.13	83.2	85.82	86.65	85.65	86.41	85.5	86.56	86.37	86.51	86.29	85.96	86.47	89.83
SI	5.01	5.11	5.14	5.54	5.2	5.41	5.23	5.15	5.19	5.21	5.13	5.22	5.21	5.15	6.1
TI	.05	.01	.01	0	.02	.02	.01	.01	.01	.01	.01	.04	.02	0	0
AL	5.67	5.59	5.55	5.99	5.53	5.69	5.57	5.52	5.46	5.67	5.69	5.6	5.57	5.78	6.51
FE	5.14	5.15	5.08	5	5.62	4.66	5.48	5.39	5.3	5.48	5.22	5.19	5.32	5.32	3.32
MN	.02	.02	.02	.01	.02	.03	.02	.05	.03	.01	.02	.02	.01	.02	0
MG	4.2	4.09	4.19	2.9	3.62	3.9	3.66	3.93	4.06	3.53	3.91	3.88	3.82	3.65	2.09
CA	.01	.02	.01	.01	.01	.01	.02	.02	.01	.01	0	.01	.01	.02	.01
NA	.02	.17	.11	0	0	.02	0	0	0	.03	.03	.01	.03	.02	1.08
K	0	.05	.03	0	0	.01	0	0	0	.01	.01	.01	.01	.01	.11
SUM	20.12	20.2	20.15	19.46	20.02	19.74	19.98	20.07	20.07	19.96	20.03	19.95	20	19.97	19.23

z(m)	5.03	4.73	4.73	4.73	4.5	4.5	4.5	4.08	4.08	4.08	3.58	3.58	3.58	3.18	3.18
SI	25.79	23.6	23.87	24.13	23.8	23.49	23.72	23.74	23.62	23.45	24.29	23.54	23.67	24.05	23.19
TI	.09	.04	.05	.06	.07	.05	.04	.03	.03	.08	.06	.05	.03	.04	.08
AL	23.25	22.1	21.49	21.11	21.94	21.15	21.29	21.53	21.92	21.57	22.07	21.92	21.48	21.57	21.32
FE	26.27	28.63	28.37	27.91	28.52	27.95	27.47	27.39	27.78	28.02	26.73	27.89	27.63	27.37	27.57
MN	.08	.16	.16	.2	.25	.28	.27	.24	.25	.27	.24	.26	.25	.16	.21
MG	10.76	12.05	12.11	12.78	12.49	12.62	12.8	12.41	12.13	12.46	12.23	12.45	12.55	12.31	12.42
CA	.05	.03	.03	.01	.03	.04	.08	.05	.03	.04	.01	.04	.19	.03	.08
NA	.61	.02	.03	.03	.02	.04	.03	.01	.01	.01	.27	.07	.05	.02	.04
K	.06	0	.01	.01	0	.01	0	0	0	.01	.04	.04	.03	.01	.02
TOT	86.96	86.63	86.12	86.24	87.12	85.63	85.7	85.4	85.77	85.91	85.94	86.26	85.88	85.56	84.93
SI	5.49	5.15	5.23	5.27	5.16	5.18	5.21	5.22	5.18	5.15	5.28	5.14	5.19	5.27	5.15
TI	.01	.01	.01	.01	.01	.01	.01	0	0	.01	.01	.01	0	.01	.01
AL	5.83	5.68	5.55	5.43	5.6	5.5	5.51	5.58	5.67	5.59	5.66	5.65	5.55	5.57	5.58
FE	4.07	5.22	5.2	5.09	5.17	5.15	5.04	5.04	5.1	5.15	4.86	5.1	5.07	5.02	5.12
MN	.01	.03	.03	.04	.05	.05	.05	.04	.05	.05	.04	.05	.05	.03	.04
MG	3.41	3.92	3.95	4.16	4.03	4.15	4.19	4.07	3.97	4.08	3.96	4.05	4.1	4.02	4.11
CA	.01	.01	.01	0	.01	.01	.02	.01	.01	.01	0	.01	.04	.01	.02
NA	.25	.01	.01	.01	.01	.02	.01	0	0	0	.11	.03	.02	.01	.02
K	.02	0	0	0	0	0	0	0	0	0	.01	.01	.01	0	.01
SUM	19.72	20.01	19.99	20.01	20.03	20.07	20.04	19.98	19.98	20.05	19.94	20.05	20.04	19.94	20.06

z(m)	3.18	2.28	2.28	2.28	1.88	1.88	1.88	1.38	1.38	1.38	.68	.68	.68	.48	.48
SI	23.64	23.07	24.17	23.58	23.96	23.63	23.41	23.83	23.51	23.57	24.03	23.9	23.94	23.81	23.9
TI	.05	.02	.05	.03	.05	.14	.05	.06	.04	.06	.05	.04	.05	.07	.06
AL	21.94	21.78	21.45	21.51	21.4	21.47	21.54	21.36	21.24	21.51	21.32	22.05	21.3	21.46	21.34
FE	27.67	27.64	26.98	27.41	27.26	27.37	27.53	27.77	27.29	27.69	27.45	28.15	27.93	27.82	27.72
MN	.21	.16	.21	.21	.22	.2	.21	.2	.18	.21	.21	.17	.2	.21	.2
MG	12.05	11.78	12.22	12.09	12.78	12.72	12.29	12.69	12.73	12.64	12.75	12.29	12.71	12.7	12.41
CA	.09	.06	.08	.06	.01	.02	.04	.03	.03	.03	.08	.05	.04	.05	.07
NA	.02	.01	.01	0	.01	.03	.02	.03	.01	.01	.11	.01	.02	0	.04
K	.01	0	.01	.01	0	0	0	.01	0	0	.03	0	0	0	.01
TOT	85.68	84.52	85.18	84.9	85.69	85.58	85.09	85.98	85.03	85.72	86.03	86.66	86.19	86.12	85.75
SI	5.19	5.14	5.31	5.22	5.25	5.19	5.18	5.22	5.2	5.18	5.25	5.19	5.23	5.2	5.24
TI	.01	0	.01	0	.01	.02	.01	.01	.01	.01	.01	.01	.01	.01	.01
AL	5.68	5.73	5.56	5.62	5.52	5.56	5.62	5.51	5.54	5.57	5.49	5.65	5.49	5.53	5.52
FE	5.08	5.15	4.96	5.08	4.99	5.03	5.09	5.08	5.05	5.09	5.01	5.11	5.1	5.09	5.09
MN	.04	.03	.04	.04	.04	.04	.04	.04	.03	.04	.04	.03	.04	.04	.04
MG	3.94	3.91	4	3.99	4.17	4.16	4.05	4.14	4.19	4.14	4.15	3.98	4.14	4.14	4.06
CA	.02	.01	.02	.01	0	0	.01	.01	.01	.01	.02	.01	.01	.01	.02
NA	.01	0	0	0	0	.01	.01	.01	0	0	.05	0	.01	0	.02
K	0	0	0	0	0	0	0	0	0	0	.01	0	0	0	0
SUM	19.97	19.99	19.9	19.97	19.99	20.01	20.01	20.02	20.03	20.03	20.02	19.98	20.02	20.02	19.99

z(m)	.48	.23	.23	.23
SI	23.58	23.99	23.76	23.37
TI	.05	.06	.05	.04
AL	21.81	21.77	21.59	21.3
FE	27.46	27.28	27.32	26.82
MN	.19	.21	.13	.19
MG	12.33	12.94	12.52	12.78
CA	.03	.08	.08	.11
NA	.01	.01	.02	.03
K	.01	.01	0	.01
TOT	85.47	86.35	85.47	84.65
SI	5.18	5.21	5.22	5.18
TI	.01	.01	.01	.01
AL	5.65	5.57	5.59	5.57
FE	5.05	4.95	5.02	4.97
MN	.04	.04	.02	.04
MG	4.04	4.19	4.1	4.22
CA	.01	.02	.02	.03
NA	0	0	.01	.01
K	0	0	0	0
SUM	19.98	20	19.98	20.03

Traigh Geighsgeir, South: Dolomites

z(m)	.23	.04	4.5	4.08	3.58	3.18	2.28	1.88	1.38	.68	.48
SI	.54	.46	0	.03	.01	.04	0	.03	.03	.01	.01
FE	14.66	13.29	2.07	2.14	2.38	1.73	1.72	1.33	2.12	1.51	2.1
MN	1.63	1.16	1.18	1.2	1.12	1.07	1.17	.94	.43	1.02	1.1
MG	13.88	13.94	.85	.78	.9	.46	.61	.47	.57	.55	.85
CA	24.69	25.27	53.48	52.32	51.37	52.14	52	53.91	50.09	51.03	49.6
SR	0	.04	.04	.06	.07	.03	.02	0	.11	.03	.06
TOT	55.4	54.16	57.62	56.53	55.85	55.47	55.52	56.68	53.35	54.15	53.8
SI	.09	.08	0	0	0	0	0	0	0	0	0
FE	1.98	1.83	.17	.18	.2	.15	.15	.11	.19	.13	.19
MN	.22	.16	.1	.1	.1	.09	.1	.08	.04	.09	.1
MG	3.34	3.41	.12	.12	.14	.07	.09	.07	.09	.09	.13
CA	4.28	4.45	5.61	5.59	5.56	5.68	5.66	5.74	5.67	5.69	5.5
SR	0	0	0	0	0	0	0	0	.01	0	0
SUM	9.91	9.92	6	6	6	6	6	6	6	6	6

Stonefield: Chlorites

z(m)	-.4	-.4	-1.6	-1.6	-1.6	-3.6	-3.6	-3.6	-4.6	-4.6	-4.6	5.2	5.2	5.2	5
SI	24.91	25.33	26.57	25.03	24.92	22.76	24.75	24.79	24.85	24.83	25.34	24.84	24.88	25.12	25.03
TI	.05	.1	.05	.06	.02	.02	.04	.06	.03	.04	.04	.05	.05	.06	.04
AL	21.29	21.16	22.01	21.06	21.28	19.53	21.54	21.38	21.14	20.77	21.06	21.23	20.81	21.34	21.03
FE	24.32	23.96	22.27	23.8	23.67	22.45	23.81	23.42	23.53	23.13	23.3	26.47	26.53	26.43	27.09
MN	.14	.12	.11	.12	.13	.12	.12	.1	.12	.13	.11	.1	.11	.13	.11
MG	15	14.85	14.7	15.9	15.71	14.3	15.35	15.45	16.13	16.19	15.7	13.93	14.22	14.01	13.88
CA	.06	.03	.01	.01	.07	1.63	.09	.04	.06	.04	.02	.06	.09	.11	.03
NA	.17	.07	.01	.04	0	.01	.15	0	.01	.04	.01	.01	.02	.03	0
K	.04	.04	.6	.04	.01	.01	.08	.13	.01	0	.17	.06	.04	.07	0
TOT	85.98	85.66	86.33	86.06	85.81	80.83	85.93	85.37	85.88	85.17	85.75	86.75	86.75	87.3	87.21
SI	5.34	5.43	5.59	5.34	5.33	5.22	5.3	5.33	5.31	5.34	5.41	5.33	5.35	5.35	5.36
TI	.01	.02	.01	.01	0	0	.01	.01	0	.01	.01	.01	.01	.01	.01
AL	5.38	5.35	5.46	5.3	5.37	5.28	5.43	5.42	5.33	5.27	5.3	5.37	5.27	5.36	5.31
FE	4.36	4.3	3.92	4.25	4.23	4.31	4.26	4.21	4.21	4.16	4.16	4.75	4.77	4.71	4.85
MN	.03	.02	.02	.02	.02	.02	.02	.02	.02	.02	.02	.02	.02	.02	.02
MG	4.79	4.74	4.61	5.06	5.01	4.89	4.9	4.95	5.14	5.19	5	4.46	4.56	4.45	4.43
CA	.01	.01	0	0	.02	.4	.02	.01	.01	.01	0	.01	.02	.03	.01
NA	.07	.03	0	.02	0	0	.06	0	0	.02	0	0	.01	.01	0
K	.01	.01	.16	.01	0	0	.02	.04	0	0	.05	.02	.01	.02	0
SUM	20	19.9	19.76	20.01	19.98	20.14	20.02	19.97	20.03	20.02	19.95	19.98	20.02	19.97	19.98

z(m)	5	5	2	.6
SI	24.85	24.98	28.94	24.12
TI	.05	.05	.06	.04
AL	21.17	20.92	20.83	21.21
FE	26.42	26.68	25.44	28.09
MN	.1	.1	.14	.17
MG	13.97	13.95	13.25	13.02
CA	0	.01	0	.08
NA	.01	.01	.01	.01
K	0	0	.38	.01
TOT	86.57	86.7	89.05	86.75
SI	5.34	5.37	5.95	5.24
TI	.01	.01	.01	.01
AL	5.37	5.3	5.05	5.43
FE	4.75	4.8	4.37	5.1
MN	.02	.02	.02	.03
MG	4.48	4.47	4.06	4.21
CA	0	0	0	.02
NA	0	0	0	0
K	0	0	.1	0
SUM	19.97	19.97	19.57	20.04

Stonefield: Muscovites

z(m)	-.4	-1.6	-3.6	-4.6	5.6	5.2	5	5	5	4.3	1.9
SI	47.91	47.81	47.47	42.92	48.31	46.06	48.99	47.9	47.98	47.08	47.71
TI	.41	.35	.39	.37	.39	.39	.28	.37	.64	.35	.39
AL	31.04	30.72	31.05	28.73	30.67	30.77	30.6	31.45	30.45	30.45	30.64
FE	2.82	2.44	2.25	5.87	2.79	4.52	1.82	2.49	2.43	3.12	3.83
MN	.03	.01	0	.03	.02	.02	0	.02	.02	.06	.03
MG	1.72	1.94	1.69	3.62	1.54	2.27	1.98	1.6	1.6	1.95	2.21
CA	.09	0	.01	.02	.02	.06	0	.01	0	1.61	.03
NA	.65	.47	.32	.43	.61	.52	.13	.46	.45	.66	.42
K	9.72	10.38	10.41	8.53	9.92	9.49	11.05	10.49	10.27	9.49	9.92
TOT	94.39	94.12	93.59	90.52	94.27	94.1	94.85	94.79	93.84	94.77	95.18
SI	6.46	6.47	6.45	6.15	6.52	6.3	6.57	6.44	6.51	6.37	6.42
TI	.04	.04	.04	.04	.04	.04	.03	.04	.07	.04	.04
AL	4.93	4.9	4.98	4.86	4.88	4.96	4.83	4.99	4.87	4.86	4.86
FE	.32	.28	.26	.7	.31	.52	.2	.28	.28	.35	.43
MN	0	0	0	0	0	0	0	0	0	.01	0
MG	.35	.39	.34	.77	.31	.46	.4	.32	.32	.39	.44
CA	.01	0	0	0	0	.01	0	0	0	.23	0
NA	.17	.12	.08	.12	.16	.14	.03	.12	.12	.17	.11
K	1.67	1.79	1.81	1.56	1.71	1.66	1.89	1.8	1.78	1.64	1.7
SUM	13.95	14	13.96	14.22	13.94	14.08	13.95	13.99	13.94	14.07	14.02

Stonefield: Dolomites

z(m)	-.6	-4.6	-3.6	-1.6	5.6	5.6	5.6	5.2	5.2	5.2	5	.6	2
SI	.07	.01	0	0	0	0	0	.1	.92	.1	.04	.57	.13
FE	11.4	10.41	9.55	9.41	2.62	3.14	2.6	13.52	13.87	13.97	2.48	3.69	.9
MN	.91	.75	1.31	1.17	.74	.78	.8	.96	.93	.97	.78	.81	.96
MG	12.62	13.63	13.49	13.82	16.78	16.27	17.22	11.85	11.22	11.26	16.9	16.56	.28
CA	28.54	29.25	29.61	29.16	32.78	33.3	32.72	29.33	28.92	29.58	33.35	32.1	57.35
SR	.11	.07	.14	.07	0	0	.05	.1	.15	.16	0	0	.07
TOT	53.65	54.12	54.1	53.63	52.92	53.49	53.39	55.86	56.01	56.04	53.55	53.73	59.69
SI	.01	0	0	0	0	0	0	.02	.15	.02	.01	.09	.02
FE	1.59	1.43	1.31	1.3	.35	.42	.34	1.84	1.87	1.91	.33	.48	.12
MN	.13	.1	.18	.16	.1	.1	.11	.13	.13	.13	.1	.11	.13
MG	3.14	3.33	3.3	3.39	3.97	3.84	4.03	2.87	2.7	2.74	3.95	3.86	.07
CA	5.11	5.13	5.2	5.14	5.58	5.64	5.51	5.11	5	5.17	5.61	5.38	9.64
SR	.01	.01	.01	.01	0	0	0	.01	.01	.02	0	0	.01
SUM	9.99	10	10	10	10	10	10	9.98	9.85	9.98	9.99	9.91	9.98

Port Cill Maluaig: Chlorites

z(m)	.25	.25	.25	.5	.5	.5	.75	.75	.75	.88	.88	.88	1.11	1.11	1.11
SI	23.74	23.45	23.41	23.93	23.8	23.79	24.08	23.4	24.1	25.02	24.39	25.01	25.59	25.36	25.17
TI	.06	.05	.07	.05	.05	.05	.03	.03	.05	.05	.05	.05	.05	.05	.04
AL	19.66	19.99	20.48	19.33	19.67	20	20.03	20.15	19.16	20.47	20.04	19.93	20.45	20.61	20.52
FE	27.56	28.04	28.23	27.35	27.2	27.39	26.52	26.44	26.17	26.74	26.7	26.37	27.15	26.88	27.03
MN	.31	.34	.33	.32	.34	.32	.32	.33	.33	.35	.36	.33	.38	.39	.4
MG	12.99	12.79	13.05	13.47	13.2	13.55	13.88	13.79	13.84	14.4	14.31	14.49	14.44	14.5	14.71
CA	.02	.02	.02	.04	.07	.04	.09	.05	.06	.05	.06	.06	.03	.02	.07
NA	.04	.05	.03	.03	.03	.02	.08	.09	.19	.02	.01	.02	.02	.03	.04
K	0	0	.01	.01	.03	0	.03	.03	.07	0	0	.05	0	0	.01
TOT	84.38	84.73	85.63	84.53	84.39	85.16	85.06	84.31	83.97	87.1	85.92	86.31	88.11	87.84	87.99
SI	5.31	5.24	5.18	5.34	5.32	5.27	5.31	5.22	5.39	5.37	5.32	5.41	5.43	5.39	5.35
TI	.01	.01	.01	.01	.01	.01	0	.01	.01	.01	.01	.01	.01	.01	.01
AL	5.19	5.27	5.34	5.09	5.18	5.22	5.21	5.3	5.05	5.18	5.15	5.08	5.11	5.17	5.14
FE	5.16	5.24	5.22	5.11	5.08	5.07	4.89	4.93	4.89	4.8	4.87	4.77	4.82	4.78	4.81
MN	.06	.06	.06	.06	.06	.06	.06	.06	.06	.06	.07	.06	.07	.07	.07
MG	4.33	4.26	4.3	4.48	4.4	4.47	4.56	4.58	4.61	4.6	4.65	4.67	4.56	4.59	4.66
CA	0	0	0	.01	.02	.01	.02	.01	.01	.01	.01	.01	.01	0	.02
NA	.02	.02	.01	.01	.01	.01	.03	.04	.08	.01	0	.01	.01	.01	.02
K	0	0	0	0	.01	0	.01	.01	.02	0	0	.01	0	0	0
SUM	20.09	20.12	20.14	20.11	20.09	20.12	20.1	20.15	20.13	20.04	20.09	20.05	20.01	20.02	20.08

z(m)	1.43	1.43	1.43	1.68	1.68	1.68	2	2	2	2.27	2.27	2.27	2.47	2.47	2.47
SI	25.04	25.41	25.15	25.24	24.85	24.63	24.71	24.55	25.09	24.62	24.58	24.75	29.79	24.84	24.83
TI	.05	.06	.05	.05	.04	.05	.05	.04	.09	.05	.05	.05	.05	.05	.05
AL	20.5	20.23	20.39	20.08	19.97	20.3	20.62	21.06	20.22	20.15	20.43	20.59	20.11	19.83	19.93
FE	26.38	26.92	26.6	26.92	27.08	26.76	27.65	27.63	27.5	26.9	26.85	27.37	24.44	26.89	27.2
MN	.37	.38	.35	.38	.37	.37	.39	.38	.38	.34	.35	.34	.33	.38	.37
MG	14.54	14.37	14.78	14.34	14.28	14.01	13.44	13.72	13.73	13.97	13.87	13.67	11.83	14.11	13.83
CA	.09	.09	.06	.05	.09	.03	.05	.07	.04	.05	.06	.06	.13	.07	.09
NA	.04	.02	.03	.02	.03	.02	.04	.04	.05	.09	.02	.06	1.12	.13	.24
K	0	0	0	0	0	0	0	.02	.24	.02	0	.08	0	.08	.08
TOT	87.01	87.48	87.41	87.08	86.71	86.17	86.95	87.51	87.34	86.19	86.21	86.97	87.8	86.38	86.62
SI	5.37	5.43	5.37	5.42	5.38	5.35	5.34	5.27	5.4	5.36	5.34	5.34	6.19	5.4	5.39
TI	.01	.01	.01	.01	.01	.01	.01	.01	.01	.01	.01	.01	.01	.01	.01
AL	5.18	5.1	5.13	5.09	5.09	5.2	5.25	5.33	5.13	5.17	5.23	5.24	4.92	5.08	5.1
FE	4.73	4.81	4.75	4.84	4.9	4.86	5	4.96	4.95	4.89	4.88	4.94	4.25	4.88	4.94
MN	.07	.07	.06	.07	.07	.07	.07	.07	.07	.06	.06	.06	.06	.07	.07
MG	4.65	4.58	4.7	4.59	4.6	4.54	4.33	4.39	4.4	4.53	4.49	4.4	3.66	4.57	4.47
CA	.02	.02	.01	.01	.02	.01	.01	.02	.01	.01	.01	.01	.03	.02	.02
NA	.02	.01	.01	.01	.01	.01	.02	.02	.02	.04	.01	.03	.45	.05	.1
K	0	0	0	0	0	0	0	.01	.07	.01	0	.02	0	.02	.02
SUM	20.04	20.02	20.06	20.03	20.08	20.04	20.03	20.07	20.06	20.07	20.04	20.05	19.57	20.1	20.12

z(m)	2.8	2.8	2.8	3.17	3.17	3.17	3.6	3.6	3.6	3.9	3.9	3.9	4.05	4.05	4.05
SI	25.46	24.77	24.84	24.45	24.58	25.27	24.81	25.04	25.02	24.34	24.88	24.7	24.8	24.89	24.9
TI	.17	.05	.06	.04	.05	.05	.04	.05	.06	.23	.05	.06	.05	.07	.03
AL	19.64	19.94	20.32	20.1	20.66	20.53	20.03	20.28	20.08	19.93	20.35	20.54	20.43	20	20.22
FE	27.28	27.17	27.12	27.1	27.03	25.46	25.96	26.42	25.62	26.79	27.02	26.78	26.7	26.97	26.6
MN	.34	.33	.33	.36	.35	.37	.3	.3	.31	.31	.32	.33	.36	.34	.35
MG	12.97	13.66	13.84	13.39	13.76	12.22	14.78	14.37	14.89	13.86	14.11	14.19	14.08	14.24	14.5
CA	.28	.17	.04	.11	.1	1.1	.05	.05	.05	.19	.06	.04	.11	.04	.02
NA	.07	.09	.01	.44	.11	.43	.02	.08	.02	.18	.02	.01	.04	.03	.04
K	.62	.01	0	.16	.05	.15	0	.01	0	.05	0	.06	0	0	0
TOT	86.83	86.19	86.56	86.15	86.69	85.58	85.99	86.6	86.05	85.88	86.81	86.71	86.57	86.58	86.66
SI	5.52	5.4	5.38	5.35	5.32	5.51	5.38	5.4	5.41	5.32	5.37	5.33	5.36	5.39	5.37
TI	.03	.01	.01	.01	.01	.01	.01	.01	.01	.04	.01	.01	.01	.01	0
AL	5.02	5.12	5.19	5.18	5.27	5.28	5.12	5.15	5.11	5.14	5.18	5.23	5.2	5.1	5.14
FE	4.95	4.95	4.91	4.95	4.89	4.64	4.71	4.76	4.63	4.9	4.87	4.83	4.83	4.88	4.8
MN	.06	.06	.06	.07	.06	.07	.06	.05	.06	.06	.06	.06	.07	.06	.06
MG	4.19	4.44	4.47	4.36	4.44	3.97	4.77	4.62	4.79	4.52	4.54	4.56	4.53	4.59	4.66
CA	.07	.04	.01	.03	.02	.26	.01	.01	.01	.04	.01	.01	.03	.01	0
NA	.03	.04	0	.19	.05	.18	.01	.03	.01	.08	.01	0	.02	.01	.02
K	.17	0	0	.04	.01	.04	0	0	0	.01	0	.02	0	0	0
SUM	20.04	20.05	20.02	20.17	20.07	19.96	20.06	20.04	20.03	20.11	20.04	20.06	20.04	20.06	20.06

z(m)	4.22	4.22	4.22	4.22	4.22	4.5	4.5	4.5	4.5	4.5	4.5	4.76	4.76	4.76	4.76
SI	24.74	28.5	24.75	25.17	24.79	24.25	24.99	24.63	29	24.94	24.88	24.67	34.03	24.7	24.64
TI	.08	.05	.06	.12	.14	.06	.05	.04	.12	.05	.06	.07	.06	.05	.06
AL	20.37	19.39	19.65	19.84	19.56	19.94	19.65	20.05	19.84	20.08	19.64	20.1	17.28	20.02	20
FE	29.43	26.07	29.61	30.06	29.28	27.67	27.99	28.02	25.89	27.89	27.79	27.39	25.2	27.47	27.55
MN	.43	.33	.42	.4	.41	.38	.36	.39	.34	.38	.39	.38	.34	.34	.36
MG	12	10.18	12.28	11.74	12.25	13.52	12.9	13.44	12.3	13.9	13.55	14.13	12.04	13.96	13.78
CA	.11	.11	.06	.15	.13	.05	.29	.05	.08	.06	.02	.07	.08	.05	.05
NA	.04	2.78	.04	.02	.13	.02	.07	.03	2	.05	.03	.06	.07	.11	.13
K	.06	0	.02	.25	.55	.05	.12	0	.54	.03	.05	0	.03	.01	.07
TOT	87.26	87.41	86.89	87.75	87.24	85.94	86.42	86.65	90.11	87.38	86.41	86.87	89.13	86.71	86.64
SI	5.38	6.07	5.42	5.47	5.42	5.32	5.46	5.36	5.97	5.37	5.42	5.34	6.9	5.36	5.35
TI	.01	.01	.01	.02	.02	.01	.01	.01	.02	.01	.01	.01	.01	.01	.01
AL	5.23	4.87	5.07	5.08	5.04	5.16	5.06	5.14	4.82	5.1	5.05	5.13	4.13	5.12	5.12
FE	5.36	4.64	5.42	5.46	5.35	5.08	5.11	5.1	4.46	5.03	5.07	4.96	4.27	4.98	5.01
MN	.08	.06	.08	.07	.08	.07	.07	.07	.06	.07	.07	.07	.06	.06	.07
MG	3.89	3.23	4.01	3.8	3.99	4.42	4.2	4.36	3.78	4.46	4.4	4.56	3.64	4.51	4.46
CA	.03	.03	.01	.03	.03	.01	.07	.01	.02	.01	0	.02	.02	.01	.01
NA	.02	1.15	.02	.01	.06	.01	.03	.01	.8	.02	.01	.03	.03	.05	.05
K	.02	0	.01	.07	.15	.01	.03	0	.14	.01	.01	0	.01	0	.02
SUM	20.01	20.06	20.05	20.01	20.14	20.1	20.03	20.07	20.07	20.08	20.05	20.1	19.05	20.1	20.11

z(m)	4.76	5.15	5.15	5.15	5.55	5.55	5.55	5.92	5.92	5.92	6.26	6.26	6.26	6.98	6.98
SI	24.64	24.92	24.97	24.23	24.75	24.8	24.63	24.4	24.81	24.7	24.47	25.07	24.68	24.89	24.73
TI	.05	.05	.05	.04	.05	.03	.06	.04	.04	.05	.03	.03	.04	.04	.03
AL	19.99	20.06	19.85	20.51	20.07	20.09	20.09	20.39	19.97	19.83	19.45	19.57	20.08	19.98	19.37
FE	27.44	26.81	27.18	26.84	26.33	26.12	26.56	26.57	26.41	26.52	24.86	25.47	26.07	25.52	25.73
MN	.35	.36	.35	.35	.33	.33	.35	.39	.37	.35	.33	.33	.35	.34	.33
MG	13.76	14.52	14.03	14.55	14.62	14.78	14.54	14.4	14.81	14.6	15.23	15.08	14.52	15.28	15.01
CA	.05	.09	.04	.09	.07	.09	.07	.06	.04	.05	.04	.09	.05	.04	.05
NA	.05	.07	.06	.1	.02	.04	.03	.03	.02	.02	.04	.03	.03	.04	.03
K	.07	.02	.01	.04	.02	.03	.08	0	0	.11	0	0	.01	0	0
TOT	86.4	86.9	86.54	86.75	86.26	86.31	86.41	86.28	86.47	86.23	84.45	85.67	85.83	86.13	85.28
SI	5.36	5.37	5.41	5.24	5.36	5.36	5.34	5.3	5.36	5.36	5.39	5.44	5.37	5.37	5.41
TI	.01	.01	.01	.01	.01	0	.01	.01	.01	.01	0	0	.01	.01	0
AL	5.13	5.1	5.07	5.23	5.13	5.12	5.13	5.22	5.09	5.08	5.05	5.01	5.15	5.09	4.99
FE	5	4.83	4.93	4.86	4.77	4.72	4.81	4.82	4.77	4.82	4.58	4.62	4.74	4.61	4.71
MN	.06	.07	.06	.06	.06	.06	.06	.07	.07	.06	.06	.06	.06	.06	.06
MG	4.46	4.66	4.53	4.69	4.72	4.76	4.7	4.66	4.77	4.73	5	4.88	4.71	4.92	4.89
CA	.01	.02	.01	.02	.02	.02	.02	.01	.01	.01	.01	.02	.01	.01	.01
NA	.02	.03	.03	.04	.01	.02	.01	.01	.01	.01	.02	.01	.01	.02	.01
K	.02	.01	0	.01	.01	.01	.02	0	0	.03	0	0	0	0	0
SUM	20.08	20.09	20.06	20.16	20.07	20.08	20.1	20.1	20.09	20.11	20.09	20.05	20.06	20.08	20.09

z(m)	6.98	7.3	7.3	7.3	8.25	7.63	7.63	7.63	7.9	7.9	7.9	8.25	8.25	8.25	8.6
SI	24.87	25.04	25	24.76	17.89	25.14	24.71	24.81	24.94	25.59	25.19	25.09	24.82	25.18	25.09
TI	.03	.12	.03	.06	.05	.04	.04	.05	.04	.05	.04	.04	.04	.03	.04
AL	19.4	19.51	19.06	19.87	19.92	20.04	19.95	20.04	20.16	19.45	19.71	19.39	19.87	19.94	19.23
FE	25.35	25.97	25.76	26.14	22.28	25.89	25.59	25.01	25.69	25.81	25.35	25.77	25.77	25.34	25.61
MN	.33	.33	.35	.34	.31	.34	.34	.33	.32	.31	.33	.34	.34	.34	.3
MG	15.41	14.53	14.8	14.78	15.36	14.72	14.88	14.72	14.56	14.9	15.02	14.75	14.72	15.13	14.65
CA	.06	.08	.03	.06	.05	.03	.04	.03	.05	.06	.04	.03	.06	.03	.05
NA	.05	.11	.04	.13	.04	.02	.02	.01	.08	.11	.07	.03	.04	.04	.03
K	.01	.32	0	.06	.02	0	0	0	.01	.05	.02	.07	.02	0	0
TOT	85.51	86.01	85.07	86.2	75.92	86.22	85.57	85	85.85	86.33	85.77	85.51	85.68	86.03	85
SI	5.41	5.44	5.48	5.37	4.43	5.43	5.38	5.41	5.41	5.52	5.46	5.47	5.4	5.43	5.5
TI	0	.02	0	.01	.01	.01	.01	.01	.01	.01	.01	.01	.01	0	.01
AL	4.98	5	4.93	5.08	5.82	5.1	5.12	5.16	5.15	4.94	5.03	4.98	5.1	5.07	4.97
FE	4.61	4.72	4.72	4.74	4.62	4.67	4.66	4.56	4.66	4.65	4.59	4.7	4.69	4.57	4.69
MN	.06	.06	.07	.06	.07	.06	.06	.06	.06	.06	.06	.06	.06	.06	.06
MG	5	4.71	4.84	4.78	5.67	4.74	4.83	4.79	4.7	4.79	4.85	4.79	4.77	4.87	4.78
CA	.01	.02	.01	.01	.01	.01	.01	.01	.01	.01	.01	.01	.01	.01	.01
NA	.02	.05	.02	.05	.02	.01	.01	0	.03	.05	.03	.01	.02	.02	.01
K	0	.09	0	.02	.01	0	0	0	0	.01	.01	.02	.01	0	0
SUM	20.11	20.1	20.06	20.12	20.66	20.02	20.06	20	20.03	20.03	20.04	20.05	20.06	20.03	20.02

z(m)	8.6	8.6	8.96	8.96	8.96	9.32	9.32	9.32	9.65	9.65	9.65	10.07	10.07	10.07	10.33
SI	25.52	25.54	24.95	25.24	25.09	25.13	24.73	24.94	23.99	24.39	23.89	24.2	23.97	23.88	23.79
TI	.04	.04	.06	.04	.07	.04	.05	.06	.05	.12	.05	.04	.05	.04	.05
AL	19.64	19.39	20.25	19.94	19.87	20.08	20.16	20.24	19.68	19.16	19.76	19.12	18.98	19.02	19.63
FE	25.73	25.03	26.27	26.32	26.14	26.6	26.66	26.7	27.06	27.07	26.75	27.28	27.36	27.3	27.43
MN	.31	.26	.29	.26	.28	.26	.25	.26	.26	.22	.26	.26	.26	.25	.27
MG	14.91	15.4	14.43	14.76	14.57	13.98	13.99	14.11	13.85	14.33	13.8	13.64	13.61	13.7	13.32
CA	.07	.03	.03	.03	.03	.06	.04	.03	.07	.09	.02	.02	.03	.08	.07
NA	.02	.02	.11	.09	.1	.04	.02	.03	.02	.03	.04	.03	.02	.03	.11
K	.08	0	.03	.03	.02	0	0	0	0	0	0	.01	0	0	.03
TOT	86.32	85.71	86.42	86.71	86.17	86.19	85.9	86.37	84.98	85.41	84.57	84.6	84.28	84.3	84.7
SI	5.5	5.52	5.39	5.43	5.43	5.44	5.38	5.4	5.31	5.37	5.31	5.39	5.37	5.35	5.3
TI	.01	.01	.01	.01	.01	.01	.01	.01	.01	.02	.01	.01	.01	.01	.01
AL	4.99	4.94	5.15	5.06	5.07	5.13	5.17	5.16	5.14	4.97	5.18	5.02	5.01	5.02	5.16
FE	4.64	4.52	4.74	4.73	4.73	4.82	4.85	4.83	5.01	4.99	4.97	5.08	5.12	5.11	5.11
MN	.06	.05	.05	.05	.05	.05	.05	.05	.05	.04	.05	.05	.05	.05	.05
MG	4.79	4.96	4.64	4.73	4.7	4.51	4.54	4.55	4.57	4.7	4.57	4.53	4.54	4.57	4.43
CA	.02	.01	.01	.01	.01	.01	.01	.01	.02	.02	0	0	.01	.02	.02
NA	.01	.01	.05	.04	.04	.02	.01	.01	.01	.01	.02	.01	.01	.01	.05
K	.02	0	.01	.01	.01	0	0	0	0	0	0	0	0	0	.01
SUM	20.02	20.01	20.05	20.06	20.05	19.99	20.02	20.02	20.11	20.13	20.1	20.1	20.12	20.14	20.14

z(m)	10.33	10.33	10.66	10.66	10.66	10.93	10.93	10.93	11.25	11.25	11.25	11.65	11.65	11.65	12
SI	24.54	24.18	23.65	24.16	24.12	23.47	23.97	23.82	23.43	24.37	23.84	23.98	23.96	23.9	23.86
TI	.07	.06	.04	.06	.06	.06	.05	.05	.06	.04	.04	.04	.06	.05	.05
AL	19.41	19.61	19.3	19.19	19.57	19.8	19.96	19.72	20.44	19.67	19.6	19.32	19.92	19.78	20.09
FE	27.28	27.47	28	27.93	27.93	27.43	28.09	27.83	27.89	28.04	28	27.98	28.26	28.01	28.73
MN	.26	.27	.27	.27	.27	.24	.27	.26	.26	.29	.24	.28	.28	.27	.29
MG	13.7	13.48	13.46	13.59	13.61	13.29	13.29	13.48	12.95	13.55	13.5	13.1	12.88	13.09	12.96
CA	.09	.06	.04	.04	.04	.03	.05	.12	.07	.05	.05	.06	.06	.05	.07
NA	.07	.03	.02	.05	.03	.14	.09	.07	.34	.08	.14	.24	.1	.46	.03
K	.01	0	0	0	0	.03	.04	0	.08	.01	.02	.14	.04	.09	0
TOT	85.43	85.16	84.78	85.29	85.63	84.49	85.81	85.35	85.52	86.1	85.43	85.14	85.56	85.7	86.08
SI	5.4	5.35	5.29	5.36	5.32	5.25	5.28	5.28	5.19	5.35	5.28	5.34	5.3	5.29	5.26
TI	.01	.01	.01	.01	.01	.01	.01	.01	.01	.01	.01	.01	.01	.01	.01
AL	5.04	5.12	5.09	5.02	5.09	5.22	5.19	5.15	5.34	5.09	5.12	5.07	5.2	5.16	5.22
FE	5.02	5.08	5.23	5.18	5.15	5.13	5.18	5.16	5.17	5.15	5.19	5.21	5.23	5.18	5.3
MN	.05	.05	.05	.05	.05	.05	.05	.05	.05	.05	.05	.05	.05	.05	.05
MG	4.5	4.45	4.48	4.49	4.48	4.43	4.37	4.45	4.28	4.43	4.46	4.35	4.25	4.32	4.26
CA	.02	.01	.01	.01	.01	.01	.01	.03	.02	.01	.01	.01	.01	.01	.02
NA	.03	.01	.01	.02	.01	.06	.04	.03	.15	.03	.06	.1	.04	.2	.01
K	0	0	0	0	0	.01	.01	0	.02	0	.01	.04	.01	.03	0
SUM	20.08	20.09	20.17	20.14	20.13	20.16	20.14	20.15	20.21	20.12	20.18	20.19	20.11	20.24	20.13

z(m)	12	12	12.2	12.2	12.2	12.7	12.7	12.7	13.2	13.2	13.2	6.63	6.63	6.63
SI	23.94	23.75	24.23	23.74	23.65	22.52	22.13	22.85	23.02	23.19	23.18	23.26	23.81	24.25
TI	.06	.05	.05	.06	.08	.04	.04	.06	.04	.08	.07	.05	.15	.03
AL	19.82	19.73	19.71	19.96	20.09	18.73	18.2	19.33	19.26	19.43	19.68	19.4	19.58	19.92
FE	28.6	28.63	28.42	28.97	28.61	28.36	27.55	28.84	28.94	28.95	29.06	26.57	26.37	25.96
MN	.27	.32	.3	.33	.31	.32	.29	.32	.35	.33	.3	.34	.32	.33
MG	12.86	12.59	12.91	12.65	12.81	12.11	11.59	12.29	12.49	12.61	11.97	14.11	14.66	14.98
CA	.08	.12	.07	.05	.07	.04	.05	.06	.04	.03	.06	.19	.15	.04
NA	.03	.03	.09	.05	.06	.39	.28	.51	.25	.07	.31	.04	.01	.06
K	0	0	0	.01	.01	.08	.07	.08	.05	0	.09	0	0	0
TOT	85.66	85.22	85.78	85.82	85.69	82.59	80.2	84.34	84.44	84.69	84.72	83.96	85.05	85.57
SI	5.3	5.29	5.35	5.26	5.24	5.22	5.28	5.19	5.22	5.23	5.23	5.22	5.26	5.3
TI	.01	.01	.01	.01	.01	.01	.01	.01	.01	.01	.01	.01	.02	0
AL	5.17	5.19	5.13	5.22	5.25	5.12	5.12	5.18	5.14	5.16	5.24	5.14	5.1	5.13
FE	5.3	5.34	5.25	5.37	5.3	5.5	5.49	5.48	5.48	5.46	5.48	4.99	4.87	4.74
MN	.05	.06	.06	.06	.06	.06	.06	.06	.07	.06	.06	.06	.06	.06
MG	4.24	4.18	4.25	4.18	4.23	4.19	4.12	4.16	4.22	4.24	4.03	4.72	4.82	4.88
CA	.02	.03	.02	.01	.02	.01	.01	.01	.01	.01	.01	.05	.04	.01
NA	.01	.01	.04	.02	.03	.18	.13	.22	.11	.03	.14	02	0	.03
K	0	0	0	0	0	.02	.02	.02	.01	0	.03	0	0	0
SUM	20.11	20.11	20.1	20.13	20.14	20.31	20.23	20.34	20.27	20.19	20.22	20.21	20.17	20.15

Port Cill Maluaig: Amphiboles

z(m)	.7	.88	.88	.88	.88	1.11	1.11	1.11	1.43	1.68	1.68	1.68	2	2	2
SI	35.34	50.44	43.6	34.13	30.04	45.59	41.74	49.48	45.12	47.63	47.6	46.33	46.8	44.56	47.87
TI	.12	.73	.22	.59	.97	.38	.62	.17	.82	.79	.62	.23	.23	.18	1.1
AL	22.59	5.27	11.8	5.86	4.51	8.76	9.92	5.35	8.76	6.16	6.54	8.63	7.63	10.2	6.56
FE	11.52	15.29	10.6	13.97	12.88	18.64	20.22	17.09	19.07	18.71	17.77	18.2	18.3	19.51	17.37
MN	.21	.28	.26	.41	.61	.31	.29	.31	.34	.42	.35	.36	.33	.32	.31
MG	.02	11.7	5.63	7.11	7.13	10.93	11.74	13.13	10.18	10.19	11.46	9.8	9.83	9.07	10.63
CA	22.75	10.15	14.52	22.85	24.35	9.76	6.39	9.72	10.51	10.86	10.04	10.77	11.56	10.83	11.78
NA	.04	.59	.72	.79	.82	.91	.82	.57	1.16	1.09	.73	1.27	1.2	1.32	.98
K	0	.83	2.36	.47	.42	1.13	.87	.56	.7	.42	1.41	.3	.29	.5	.44
TOT	92.59	95.28	89.71	86.18	81.73	96.41	92.61	96.38	96.66	96.27	96.52	95.89	96.17	96.49	97.04
SI	5.6	7.55	6.98	6.15	5.83	6.92	6.63	7.38	6.86	7.23	7.19	7.04	7.11	6.8	7.17
TI	.01	.08	.03	.08	.14	.04	.07	.02	.09	.09	.07	.03	.03	.02	.12
AL	4.22	.93	2.23	1.24	1.03	1.57	1.86	.94	1.57	1.1	1.16	1.55	1.37	1.83	1.16
FE	1.53	1.91	1.42	2.1	2.09	2.37	2.69	2.13	2.43	2.38	2.24	2.31	2.32	2.49	2.18
MN	.03	.04	.04	.06	.1	.04	.04	.04	.04	.05	.04	.05	.04	.04	.04
MG	0	2.61	1.34	1.91	2.06	2.47	2.78	2.92	2.31	2.31	2.58	2.22	2.23	2.06	2.37
CA	3.86	1.63	2.49	4.41	5.06	1.59	1.09	1.55	1.71	1.77	1.62	1.75	1.88	1.77	1.89
NA	.01	.17	.22	.28	.31	.27	.25	.16	.34	.32	.21	.37	.35	.39	.28
K	0	.16	.48	.11	.1	.22	.18	.11	.14	.08	.27	.06	.06	.1	.08
SUM	15.28	15.07	15.23	16.34	16.72	15.49	15.58	15.26	15.5	15.33	15.4	15.38	15.39	15.51	15.31

z(m)	2.27	2.27	2.27	2.27	3.17	3.17	3.17	2.8	2.8	2.8	2.47	2.47	2.47	4.05	4.05
SI	45.67	48.72	53.11	44.48	46.18	41.84	46.5	44.03	44.35	48.79	49.09	40.27	47.06	44.43	53.8
TI	.28	.72	.51	.2	.6	.21	1.03	.27	.35	.43	.25	.39	1.24	.25	.25
AL	9.62	4.83	3.77	10.19	7.8	11.96	6.93	10.35	10.9	5.3	5.46	14.06	5.09	11.51	3.04
FE	18.53	19.28	15.46	19.13	18.34	20.29	18.28	19.43	19.45	17.25	17	20.9	16.13	19.62	15.19
MN	.34	.42	.29	.29	.31	.3	.32	.3	.34	.32	.33	.31	.26	.33	.28
MG	9.1	10.23	11.73	8.83	9.82	7.23	9.81	8.24	8.21	11.18	11.3	6.23	13.19	8.29	13.09
CA	11.09	10.54	11.74	11.34	11.46	11.55	11.19	11.43	10.88	11.64	11.58	11.38	10.6	11.22	11.67
NA	1.39	1.02	.58	1.35	1.14	1.56	1.14	1.53	1.6	.87	.82	1.74	1.7	1.61	.41
K	.37	.41	.11	.46	.44	.64	.57	.51	.46	.32	.18	.78	.16	.41	.05
TOT	96.39	96.17	97.3	96.27	96.09	95.58	95.77	96.09	96.54	96.1	96.01	96.06	95.43	97.67	97.78
SI	6.93	7.4	7.75	6.8	7.04	6.53	7.11	6.77	6.76	7.36	7.39	6.28	7.15	6.7	7.8
TI	.03	.08	.06	.02	.07	.02	.12	.03	.04	.05	.03	.05	.14	.03	.03
AL	1.72	.87	.65	1.84	1.4	2.2	1.25	1.88	1.96	.94	.97	2.59	.91	2.05	.52
FE	2.35	2.45	1.89	2.45	2.34	2.65	2.34	2.5	2.48	2.18	2.14	2.73	2.05	2.48	1.84
MN	.04	.05	.04	.04	.04	.04	.04	.04	.04	.04	.04	.04	.03	.04	.03
MG	2.06	2.32	2.55	2.01	2.23	1.68	2.24	1.89	1.87	2.51	2.53	1.45	2.99	1.86	2.83
CA	1.8	1.72	1.84	1.86	1.87	1.93	1.83	1.88	1.78	1.88	1.87	1.9	1.72	1.81	1.81
NA	.41	.3	.16	.4	.34	.47	.34	.46	.47	.25	.24	.53	.5	.47	.12
K	.07	.08	.02	.09	.09	.13	.11	.1	.09	.06	.03	.16	.03	.08	.01
SUM	15.42	15.27	14.96	15.5	15.41	15.65	15.37	15.54	15.5	15.28	15.24	15.72	15.52	15.52	14.98

z(m)	4.05	3.9	3.9	3.9	3.6	3.6	3.6	4.22	4.22	4.22	4.22	4.22	4.5	4.5	4.5
SI	50.02	46.43	40.56	47.34	52.78	48.11	50.83	40.57	42.28	41.28	40.21	41	42.72	43.87	43.87
TI	.59	.17	.22	.22	1.94	.85	1.38	.25	.34	.31	.26	.28	.19	.27	.16
AL	4.58	9.56	15.43	8.15	4.63	6.24	4.75	13.71	12.6	13.42	14.15	14.82	11.28	11.29	10.65
FE	16.48	19.69	20.82	18.39	14.03	16.71	15.7	22.31	21.75	22.12	22.1	21.82	20.77	19.77	20.22
MN	.3	.31	.29	.29	.17	.23	.28	.36	.36	.38	.32	.38	.27	.34	.32
MG	12.69	9.42	6.24	10.49	11.33	13.44	12.52	5.65	6.29	6.01	5.38	5.05	7.41	7.72	8.01
CA	11.81	11.98	11.65	11.67	8.77	9.95	12.43	11.21	11.16	10.71	11.42	10.38	11.69	11.03	11.38
NA	.63	1.24	1.73	1.21	.37	.57	.64	1.74	1.81	1.76	1.71	2.07	1.5	1.66	1.46
K	.11	.36	.82	.31	.1	.12	.13	.88	.54	.7	.82	.78	.51	.49	.52
TOT	97.21	99.16	97.76	98.07	94.12	96.22	98.66	96.68	97.13	96.69	96.37	96.58	96.34	96.44	96.59
SI	7.41	6.89	6.2	7.04	7.82	7.18	7.39	6.33	6.51	6.41	6.29	6.36	6.61	6.72	6.73
TI	.07	.02	.03	.02	.22	.1	.15	.03	.04	.04	.03	.03	.02	.03	.02
AL	.8	1.67	2.78	1.43	.81	1.1	.81	2.52	2.29	2.46	2.61	2.71	2.06	2.04	1.93
FE	2.04	2.44	2.66	2.29	1.74	2.09	1.91	2.91	2.8	2.87	2.89	2.83	2.69	2.53	2.6
MN	.04	.04	.04	.04	.02	.03	.03	.05	.05	.05	.04	.05	.04	.04	.04
MG	2.8	2.08	1.42	2.33	2.5	2.99	2.71	1.31	1.44	1.39	1.25	1.17	1.71	1.76	1.83
CA	1.87	1.9	1.91	1.86	1.39	1.59	1.94	1.87	1.84	1.78	1.91	1.72	1.94	1.81	1.87
NA	.18	.36	.51	.35	.11	.17	.18	.53	.54	.53	.52	.62	.45	.49	.43
K	.02	.07	.16	.06	.02	.02	.02	.18	.11	.14	.16	.15	.1	.1	.1
SUM	15.23	15.47	15.72	15.42	14.62	15.26	15.15	15.73	15.63	15.66	15.72	15.64	15.61	15.53	15.55

z(m)	4.5	4.5	4.76	4.76	4.76	4.76	4.76	5.15	5.15	5.15	5.55	5.55	5.55	5.92	5.92
SI	41.24	46.08	41.34	44.11	44.88	42.43	42.04	51.91	46.22	43.99	50.26	43.96	42.06	46.91	56.46
TI	.29	2.14	.25	.26	.27	.28	.27	.13	.22	.25	.2	.3	.24	.23	.94
AL	13.05	7.56	13.1	11.18	10.1	12.33	13.17	3.7	9.25	11.9	7.86	10.92	12.06	7.79	4.87
FE	21.02	18	20.77	19.7	19.62	20.58	20.67	16.19	18.68	19.29	16.59	19.48	19.59	17.95	13.7
MN	.29	.3	.3	.33	.32	.33	.31	.3	.34	.37	.28	.32	.28	.33	.26
MG	6.72	9.48	6.54	8.04	8.66	7.08	6.57	12.47	9.53	8.09	9.63	8.58	8.2	10.46	8.86
CA	11.67	12.35	11.39	10.89	11.26	11.33	11.15	11.47	11.06	10.73	10.5	11.43	11.15	11.51	11.12
NA	1.53	1.18	1.74	1.68	1.53	1.75	1.89	.65	1.39	1.78	1.25	1.5	1.64	1.21	.71
K	.62	.3	.68	.41	.38	.61	.69	.13	.33	.47	.28	.45	.55	.28	.14
TOT	96.43	97.39	96.11	96.6	97.02	96.72	96.76	96.95	97.02	96.87	96.85	96.94	95.77	96.67	97.06
SI	6.4	6.94	6.43	6.73	6.82	6.53	6.47	7.66	6.96	6.68	7.42	6.69	6.51	7.07	8.09
TI	.03	.24	.03	.03	.03	.03	.03	.01	.02	.03	.02	.03	.03	.03	.1
AL	2.39	1.34	2.4	2.01	1.81	2.24	2.39	.64	1.64	2.13	1.37	1.96	2.2	1.39	.82
FE	2.73	2.27	2.7	2.51	2.49	2.65	2.66	2	2.35	2.45	2.05	2.48	2.54	2.26	1.64
MN	.04	.04	.04	.04	.04	.04	.04	.04	.04	.05	.04	.04	.04	.04	.03
MG	1.55	2.13	1.52	1.83	1.96	1.62	1.51	2.74	2.14	1.83	2.12	1.95	1.89	2.35	1.89
CA	1.94	1.99	1.9	1.78	1.83	1.87	1.84	1.81	1.79	1.75	1.66	1.87	1.85	1.86	1.71
NA	.46	.34	.52	.5	.45	.52	.56	.19	.41	.52	.36	.44	.49	.35	.2
K	.12	.06	.13	.08	.07	.12	.14	.02	.06	.09	.05	.09	.11	.05	.03
SUM	15.66	15.35	15.67	15.52	15.51	15.64	15.65	15.11	15.42	15.53	15.08	15.56	15.66	15.41	14.51

z(m)	5.92	6.26	6.26	6.26	6.98	6.98	6.98	7.3	7.3	7.3	7.63	7.63	7.63	7.9	7.9
SI	57.39	53.46	52.8	49.62	76.91	58.37	51.71	60.67	45.14	48.57	50.85	47.25	56.63	52.38	51.73
TI	.1	.32	.74	.49	.91	.28	1.31	.13	.14	.19	.21	.78	.61	.37	.37
AL	3.54	3.71	3.86	4.28	1.86	3.57	3.15	5.48	5.85	5.34	6.32	5.31	4.66	3.54	4.13
FE	14.12	14.38	14.1	15.46	6.79	13.2	14.04	13.28	16.37	16.34	16.18	16.26	13.97	15.23	15.18
MN	.3	.28	.26	.31	.11	.23	.3	.17	.28	.3	.28	.26	.22	.31	.29
MG	10.89	12.18	13.11	13.2	5.51	11.26	12.94	10.19	13.06	13.73	11.5	14.02	11.03	13.52	12.82
CA	10.32	10.36	10.17	10.84	5.79	9.37	12	5.93	11.19	10.32	9.55	9.18	8.06	11.72	11.6
NA	.53	.54	.48	.61	.22	.47	.55	.46	.72	.67	.88	.42	.49	.57	.69
K	.08	.05	.07	.09	.01	.08	.04	.12	.12	.12	.15	.04	.07	.06	.11
TOT	97.27	95.28	95.59	94.9	98.11	96.83	96.04	96.43	92.87	95.58	95.92	93.52	95.74	97.7	96.92
SI	8.19	7.88	7.76	7.48	9.89	8.29	7.64	8.48	7.06	7.3	7.53	7.24	8.15	7.63	7.6
TI	.01	.04	.08	.06	.09	.03	.15	.01	.02	.02	.02	.09	.07	.04	.04
AL	.6	.64	.67	.76	.28	.6	.55	.9	1.08	.95	1.1	.96	.79	.61	.72
FE	1.69	1.77	1.73	1.95	.73	1.57	1.73	1.55	2.14	2.05	2	2.08	1.68	1.86	1.87
MN	.04	.03	.03	.04	.01	.03	.04	.02	.04	.04	.04	.03	.03	.04	.04
MG	2.32	2.68	2.87	2.96	1.06	2.38	2.85	2.12	3.05	3.08	2.54	3.2	2.36	2.94	2.81
CA	1.58	1.64	1.6	1.75	.8	1.43	1.9	.89	1.88	1.66	1.52	1.51	1.24	1.83	1.83
NA	.15	.15	.14	.18	.05	.13	.16	.12	.22	.2	.25	.12	.14	.16	.2
K	.01	.01	.01	.02	0	.01	.01	.02	.02	.02	.03	.01	.01	.01	.02
SUM	14.58	14.84	14.9	15.19	12.91	14.46	15.02	14.13	15.5	15.31	15.03	15.25	14.47	15.11	15.11

z(m)	7.9	8.25	8.25	8.25	8.6	8.6	8.6	6.63	6.63
SI	52.37	52.03	49.62	51.41	61.75	50.36	55.74	50.64	51.84
TI	.51	.61	2.28	.16	.47	.81	.16	.81	1.1
AL	3.32	3.32	4.43	3.49	2.7	5.12	4.31	3.83	2.94
FE	14.92	14.96	14.85	14.87	11.82	15.85	11.7	15.51	14.37
MN	.29	.32	.27	.29	.19	.29	.25	.29	.3
MG	13.81	12.92	12.2	13.11	10.96	11.64	8.26	12.79	12.53
CA	11.19	12.34	12.85	12.02	9.92	11.91	15.41	11.62	12.1
NA	.48	.6	.72	.59	.51	.99	.84	.56	.54
K	.03	.05	.09	.06	.04	.4	.13	.05	.05
TOT	96.92	97.15	97.31	96	98.36	97.37	96.8	96.1	95.77
SI	7.66	7.64	7.32	7.63	8.53	7.43	8.06	7.53	7.69
TI	.06	.07	.25	.02	.05	.09	.02	.09	.12
AL	.57	.57	.77	.61	.44	.89	.73	.67	.51
FE	1.83	1.84	1.83	1.85	1.37	1.96	1.41	1.93	1.78
MN	.04	.04	.03	.04	.02	.04	.03	.04	.04
MG	3.01	2.83	2.68	2.9	2.26	2.56	1.78	2.84	2.77
CA	1.75	1.94	2.03	1.91	1.47	1.88	2.39	1.85	1.92
NA	.14	.17	.21	.17	.14	.28	.24	.16	.16
K	.01	.01	.02	.01	.01	.08	.02	.01	.01
SUM	15.06	15.1	15.15	15.14	14.27	15.21	14.68	15.12	15.01

Port Cill Maluaig: Biotites

z(m)	.25	.25	.5	.7	1.11	2.27	2	1.68	2.47	2.8	3.17	4.22	4.5	4.76
SI	4.86	29.66	33.18	31.61	36.44	36.08	35.4	35.63	35.69	35.69	35.64	35.65	35.78	35.76
TI	.19	1.3	1.34	1.32	1.41	1.62	1.59	1.56	1.59	1.56	1.45	1.78	1.53	1.63
AL	3.31	16.75	15.03	15.09	16.18	15.53	15.48	15.62	15.4	15.6	15.68	15.12	15.4	15.16
FE	4.97	23.31	21.73	20.87	21.67	21.9	21.96	20.69	22	22.01	21.8	24.06	22.55	22.38
MN	.08	.22	.2	.17	.23	.22	.2	.2	.21	.19	.22	.24	.24	.19
MG	2.51	12.59	10.03	11.07	10.45	9.74	9.58	10.08	9.54	9.54	9.92	8.73	9.64	9.66
CA	43.46	.18	.14	.15	.1	.75	.04	.77	.16	.15	1.02	.16	.04	.56
NA	0	.17	.09	.18	.42	.07	.08	.05	.77	.04	.03	.1	.05	.07
K	.21	3.3	7.91	6.55	8.51	7.18	8.94	7.26	7.72	8.76	6.28	8.95	9.09	8.16
TOT	59.59	87.48	89.65	87.01	95.41	93.09	93.27	91.86	93.08	93.54	92.04	94.79	94.32	93.57
SI	1.52	4.95	5.47	5.33	5.59	5.65	5.59	5.63	5.62	5.61	5.62	5.6	5.61	5.62
TI	.04	.16	.17	.17	.16	.19	.19	.19	.19	.18	.17	.21	.18	.19
AL	1.22	3.3	2.92	3	2.93	2.87	2.88	2.91	2.86	2.89	2.91	2.8	2.84	2.81
FE	1.3	3.25	2.99	2.94	2.78	2.87	2.9	2.73	2.9	2.89	2.87	3.16	2.95	2.94
MN	.02	.03	.03	.02	.03	.03	.03	.03	.03	.03	.03	.03	.03	.03
MG	1.17	3.13	2.46	2.78	2.39	2.27	2.26	2.37	2.24	2.24	2.33	2.04	2.25	2.26
CA	14.53	.03	.02	.03	.02	.13	.01	.13	.03	.03	.17	.03	.01	.09
NA	0	.06	.03	.06	.12	.02	.02	.02	.24	.01	.01	.03	.02	.02
K	.08	.7	1.66	1.41	1.67	1.43	1.8	1.46	1.55	1.76	1.26	1.79	1.82	1.64
SUM	19.87	15.62	15.75	15.74	15.68	15.46	15.69	15.47	15.65	15.64	15.39	15.7	15.71	15.61

Keppoch Point: Chlorites

z(m)	.1	.1	.1	.4	.4	.4	.5	.5	.5	.6	.6	.6	.7	.7	.7
SI	24.72	24.76	24.92	24.74	25.37	24.34	24.98	25.04	24.51	24.43	24.14	23.9	24.66	23.93	24.22
TI	.05	.04	.04	.04	.06	.05	.05	.05	.07	.04	.05	.05	.06	.06	.06
AL	20.68	20.59	20.79	20.38	20.35	20.43	20.42	20.65	20.58	19.79	20.1	20.2	20.1	20.74	20.59
FE	26.6	26.51	26.59	27.94	28.07	28.16	27.85	27.9	27.97	27.57	27.74	27.8	27.71	27.85	27.68
MN	.35	.36	.36	.3	.28	.34	.25	.32	.3	.34	.3	.36	.31	.34	.34
MG	14.15	14.29	14.05	13.37	13.25	12.92	13.47	13.14	13.17	13.43	13.64	12.99	13.48	13.3	13.12
CA	.01	0	0	.01	.01	.01	0	0	0	.03	.02	.02	.03	.02	.02
NA	.02	.02	.03	.01	.03	.03	.01	.03	.02	.03	.02	.02	.03	.03	.01
K	0	0	0	0	0	0	0	0	0	.01	.01	0	.01	0	0
TOTAL	86.58	86.57	86.78	86.79	87.42	86.28	87.03	87.13	86.62	85.67	86.02	85.34	86.39	86.27	86.04
SI	5.33	5.34	5.36	5.36	5.45	5.32	5.39	5.4	5.33	5.37	5.29	5.29	5.37	5.23	5.3
TI	.01	.01	.01	.01	.01	.01	.01	.01	.01	.01	.01	.01	.01	.01	.01
AL	5.26	5.24	5.27	5.21	5.15	5.27	5.2	5.25	5.27	5.13	5.19	5.27	5.16	5.35	5.31
FE	4.8	4.78	4.78	5.07	5.04	5.15	5.03	5.03	5.08	5.07	5.09	5.14	5.05	5.09	5.07
MN	.06	.07	.07	.06	.05	.06	.05	.06	.06	.06	.06	.07	.06	.06	.06
MG	4.55	4.59	4.5	4.32	4.24	4.21	4.33	4.22	4.27	4.4	4.46	4.28	4.38	4.33	4.28
CA	0	0	0	0	0	0	0	0	0	.01	0	0	.01	0	0
NA	.01	.01	.01	0	.01	.01	0	.01	.01	.01	.01	.01	.01	.01	0
K	0	0	0	0	0	0	0	0	0	0	0	0	0	0	0
SUM	20.03	20.04	20	20.03	19.97	20.04	20	19.98	20.03	20.06	20.11	20.07	20.05	20.09	20.04

z(m)	.8	.8	.8	.9	.9	.9
SI	25.17	25.01	24.91	24.09	23.98	23.84
TI	.05	.03	.05	.05	.04	.05
AL	20.68	20.8	20.84	20.42	20.46	19.97
FE	27.19	27.15	28	27.95	28.22	28.41
MN	.32	.34	.35	.35	.33	.34
MG	13.86	13.6	13.42	13.11	13.04	12.72
CA	.05	.02	.06	.04	.04	.02
NA	.01	.01	.02	.02	.03	.02
K	.01	.01	0	.01	.01	.01
TOTAL	87.34	86.97	87.65	86.04	86.15	85.38
SI	5.39	5.38	5.34	5.28	5.26	5.29
TI	.01	0	.01	.01	.01	.01
AL	5.22	5.28	5.27	5.28	5.29	5.23
FE	4.87	4.88	5.02	5.13	5.18	5.27
MN	.06	.06	.06	.07	.06	.06
MG	4.42	4.36	4.29	4.29	4.26	4.21
CA	.01	0	.01	.01	.01	0
NA	0	0	.01	.01	.01	.01
K	0	0	0	0	0	0
SUM	19.99	19.98	20.02	20.07	20.09	20.09

Keppoch Point: Amphiboles

z(m)	.8	.9	1	1	1
SI	26.04	27.76	46.11	45.63	46.23
TI	.69	1.31	.24	.26	.24
AL	2.78	9.38	10.93	11.23	10.08
FE	2.35	9	19.05	18.55	18.99
MN	.38	.18	.4	.37	.4
MG	1.03	3.4	8.67	8.54	8.85
CA	33.77	23.12	10.1	10.63	10.39
NA	.05	.08	1.77	1.59	1.51
K	.99	3.31	.41	.48	.45
TOT	68.08	77.54	97.68	97.28	97.14
SI	6.07	5.61	6.89	6.85	6.95
TI	.12	.2	.03	.03	.03
AL	.76	2.24	1.93	1.99	1.79
FE	.46	1.52	2.38	2.33	2.39
MN	.08	.03	.05	.05	.05
MG	.36	1.02	1.93	1.91	1.98
CA	8.43	5.01	1.62	1.71	1.67
NA	.02	.03	.51	.46	.44
K	.29	.85	.08	.09	.09
SUM	16.59	16.51	15.41	15.41	15.39

Keppoch Point: Biotites

z(m)	.8	.8	.9	1
SI	40.25	38.72	50.01	35.88
TI	.04	.24	.24	1.53
AL	18.26	17.62	14.67	16.4
FE	20.78	19.86	12.61	22.23
MN	.02	.03	0	.23
MG	7.68	7.58	4.74	8.91
CA	.18	.19	.36	.04
NA	.08	.08	.04	.05
K	4.08	3.91	9.14	8.79
TOT	91.37	88.23	91.81	94.06
SI	6.13	6.1	7.33	5.61
TI	0	.03	.03	.18
AL	3.28	3.27	2.53	3.02
FE	2.64	2.62	1.54	2.9
MN	0	0	0	.03
MG	1.74	1.78	1.03	2.07
CA	.03	.03	.06	.01
NA	.02	.02	.01	.02
K	.79	.79	1.71	1.75
SUM	14.64	14.64	14.24	15.59

Keppoch Point: Dolomites

z(m)	.1	.1	.1	.4	.4	.4	.5	.5	.5	.5	.5	.5	.5	.5	.6
SI	0	0	0	0	0	0	0	0	0	0	0	0	.07	0	.02
FE	6.62	11.08	10.18	8.96	9.39	8.82	4.65	7.35	4.78	6.74	9.6	8.14	4.63	7.85	5.17
MN	.78	.91	.82	.78	.81	.78	.63	.51	.65	.44	.71	.92	.62	.84	.73
MG	15.36	11.64	11.73	11.7	12.01	12.96	16.34	15.21	16.4	15.28	11.96	14.18	16.43	14.76	16.59
CA	30.7	31.14	31.12	32.37	31.82	31.71	30.44	30.15	30.97	30.22	30.09	30.39	30.29	30.36	29.89
SR	0	0	0	0	0	0	0	0	0	0	0	0	0	0	.03
TOT	53.46	54.77	53.85	53.81	54.03	54.27	52.06	53.22	52.8	52.68	52.36	53.63	52.04	53.81	52.43
SI	0	0	0	0	0	0	0	0	0	0	0	0	.01	0	0
FE	.89	1.53	1.42	1.24	1.3	1.2	.63	1	.64	.92	1.37	1.11	.63	1.06	.7
MN	.11	.13	.12	.11	.11	.11	.09	.07	.09	.06	.1	.13	.09	.12	.1
MG	3.69	2.86	2.91	2.89	2.96	3.15	3.97	3.68	3.93	3.72	3.04	3.45	3.98	3.56	4
CA	5.31	5.49	5.55	5.75	5.63	5.54	5.31	5.25	5.34	5.29	5.49	5.31	5.28	5.26	5.19
SR	0	0	0	0	0	0	0	0	0	0	0	0	0	0	0
SUM	10	10	10	10	10	10	10	10	10	10	10	10	9.99	10	10

z(m)	.6	.7	.7	.7	.8	.8	.8
SI	.05	.03	.03	0	.14	.03	.07
FE	7.46	8.6	5.99	5.29	1.76	1.61	1.79
MN	.58	.79	.78	.7	.95	.86	.92
MG	14.59	12.96	15.54	15.95	.62	.62	.64
CA	30.67	30.29	29.91	30.15	52.06	53.21	53.45
SR	.05	.12	.1	.05	.36	.34	.41
TOT	53.4	52.79	52.35	52.14	55.89	56.67	57.28
SI	.01	.01	0	0	.02	0	.01
FE	1.02	1.2	.82	.72	.25	.22	.25
MN	.08	.11	.11	.1	.14	.12	.13
MG	3.54	3.23	3.8	3.89	.16	.15	.16
CA	5.35	5.43	5.25	5.29	9.38	9.46	9.41
SR	0	.01	.01	0	.04	.03	.04
SUM	9.99	9.99	10	10	9.98	10	9.99

Point of Knap: Chlorites

Analysis	1	2	3	4	5	6	7	8	9	10	11	12	13	14	15
SI	25.7	25.23	25.38	25.35	24.77	24.8	25.21	25.41	25.41	25.59	25.06	24.63	28.32	25.49	24.91
TI	.04	.02	.03	.04	.03	.04	.02	.03	.02	.03	.03	.04	.03	.02	.02
AL	20.32	19.44	20.34	19.93	20.17	19.75	20.26	19.83	19.67	19.19	19.39	18.19	17.96	18.77	18.64
FE	22.39	22.3	22.24	22.35	21.82	22.31	22.59	21.95	22.27	22.27	21.98	22.73	21.93	22.13	22.4
MN	.26	.25	.25	.24	.24	.23	.25	.25	.23	.24	.25	.25	.24	.25	.25
MG	17.19	17	17.34	17.22	17.14	17.02	17.38	17.38	17.39	17.01	17.08	16.67	16.56	17.21	16.81
CA	.02	.04	.04	.05	.03	.02	.04	.02	.05	.04	.05	.06	.04	.04	.03
NA	.02	.03	.03	.02	.01	0	.1	.01	.02	.02	0	.08	.02	.04	.03
K	0	0	0	0	0	0	.01	0	0	0	0	0	0	0	0
TOT	85.94	84.31	85.65	85.2	84.21	84.17	85.86	84.88	85.06	84.39	83.84	82.65	85.1	83.95	83.09
SI	5.45	5.47	5.4	5.43	5.36	5.39	5.37	5.45	5.45	5.54	5.46	5.49	6.02	5.55	5.5
TI	.01	0	0	.01	0	.01	0	0	0	0	0	.01	0	0	0
AL	5.08	4.97	5.11	5.04	5.15	5.06	5.09	5.02	4.98	4.9	4.98	4.78	4.5	4.82	4.85
FE	3.97	4.04	3.96	4.01	3.95	4.06	4.02	3.94	4	4.03	4	4.23	3.9	4.03	4.13
MN	.05	.05	.05	.04	.04	.04	.05	.05	.04	.04	.05	.05	.04	.05	.05
MG	5.43	5.49	5.5	5.5	5.53	5.51	5.52	5.56	5.56	5.49	5.54	5.53	5.25	5.58	5.53
CA	0	.01	.01	.01	.01	0	.01	0	.01	.01	.01	.01	.01	.01	.01
NA	.01	.01	.01	.01	0	0	.04	0	.01	.01	0	.03	.01	.02	.01
K	0	0	0	0	0	0	0	0	0	0	0	0	0	0	0
SUM	20	20.05	20.04	20.05	20.06	20.07	20.1	20.03	20.06	20.01	20.05	20.13	19.73	20.05	20.08

Analysis	16	17	18	19	20	21	22	23	24	25	26	27	28	29	30
SI	24.53	25.06	23.83	24.47	24.59	24.33	24.86	24.11	24.43	23.2	24.3	24.17	27.13	27.51	26.87
TI	.02	.05	.06	.21	.05	.06	.02	.04	.03	.08	.02	.02	.04	.04	.05
AL	19.54	19.78	20.29	20.51	20.16	20.58	20.48	20.52	20.31	20.07	20.75	20.91	21.6	21.75	21.34
FE	22.39	22.07	21.85	21.74	21.43	21.88	22.28	21.92	22.1	21.47	21.9	22.15	21.93	21.35	22.18
MN	.24	.25	.26	.24	.25	.25	.25	.24	.26	.24	.24	.26	.25	.25	.27
MG	17.3	18.36	17.97	18.33	18.22	18.44	17.81	18.09	18.04	17.34	18.25	18.14	18.53	18.6	18.02
CA	.06	.02	.03	.11	.03	.08	.07	.06	.1	.06	.03	.04	.04	.07	.04
NA	.03	.02	0	0	.08	.01	.15	.01	.07	.29	.07	.04	.12	.05	.18
K	0	0	0	0	0	0	0	0	.02	.11	.04	.01	0	.03	.03
TOT	84.11	85.61	84.29	85.61	84.81	85.63	85.92	84.99	85.36	82.86	85.6	85.74	89.64	89.65	88.98
SI	5.35	5.35	5.17	5.22	5.28	5.19	5.29	5.19	5.24	5.14	5.19	5.16	5.47	5.52	5.47
TI	0	.01	.01	.03	.01	.01	0	.01	0	.01	0	0	.01	.01	.01
AL	5.02	4.97	5.19	5.15	5.11	5.18	5.14	5.2	5.13	5.24	5.22	5.26	5.14	5.15	5.13
FE	4.06	3.94	3.97	3.88	3.85	3.9	3.97	3.94	3.96	3.98	3.91	3.95	3.7	3.58	3.78
MN	.04	.05	.05	.04	.05	.05	.05	.04	.05	.05	.04	.05	.04	.04	.05
MG	5.62	5.84	5.82	5.82	5.83	5.86	5.65	5.8	5.76	5.72	5.81	5.77	5.57	5.56	5.47
CA	.01	0	.01	.03	.01	.02	.02	.01	.02	.01	.01	.01	.01	.02	.01
NA	.01	.01	0	0	.03	0	.06	0	.03	.12	.03	.02	.05	.02	.07
K	0	0	0	0	0	0	0	0	.01	.03	.01	0	0	.01	.01
SUM	20.14	20.16	20.22	20.17	20.17	20.21	20.17	20.21	20.21	20.31	20.22	20.22	19.98	19.91	19.99

Appendix 8: X-Ray Fluorescence Data

Figure A8.1: Location map of XRF sample traverses.

Figures A8.2-A8.8: XRF data from sample traverses across selected SW Highland metabasites is presented in the following format:

1. Tabulated XRF data: Sample localities are specified by their distance from the basal margin of the metabasite.

2. Weight % Oxides as a function of distance from the basal margin of the metabasite.

3. Weight % Volatiles as a function of distance from the basal margin of the metabasite.

4. Plots of $\frac{MgO}{MgO+FeO}$ and $\frac{Na_2O}{Na_2O+CaO}$ as a function of distance from the basal margin of the metabasite.

Figure A8.1: Location Map of XRF Sample Traverses

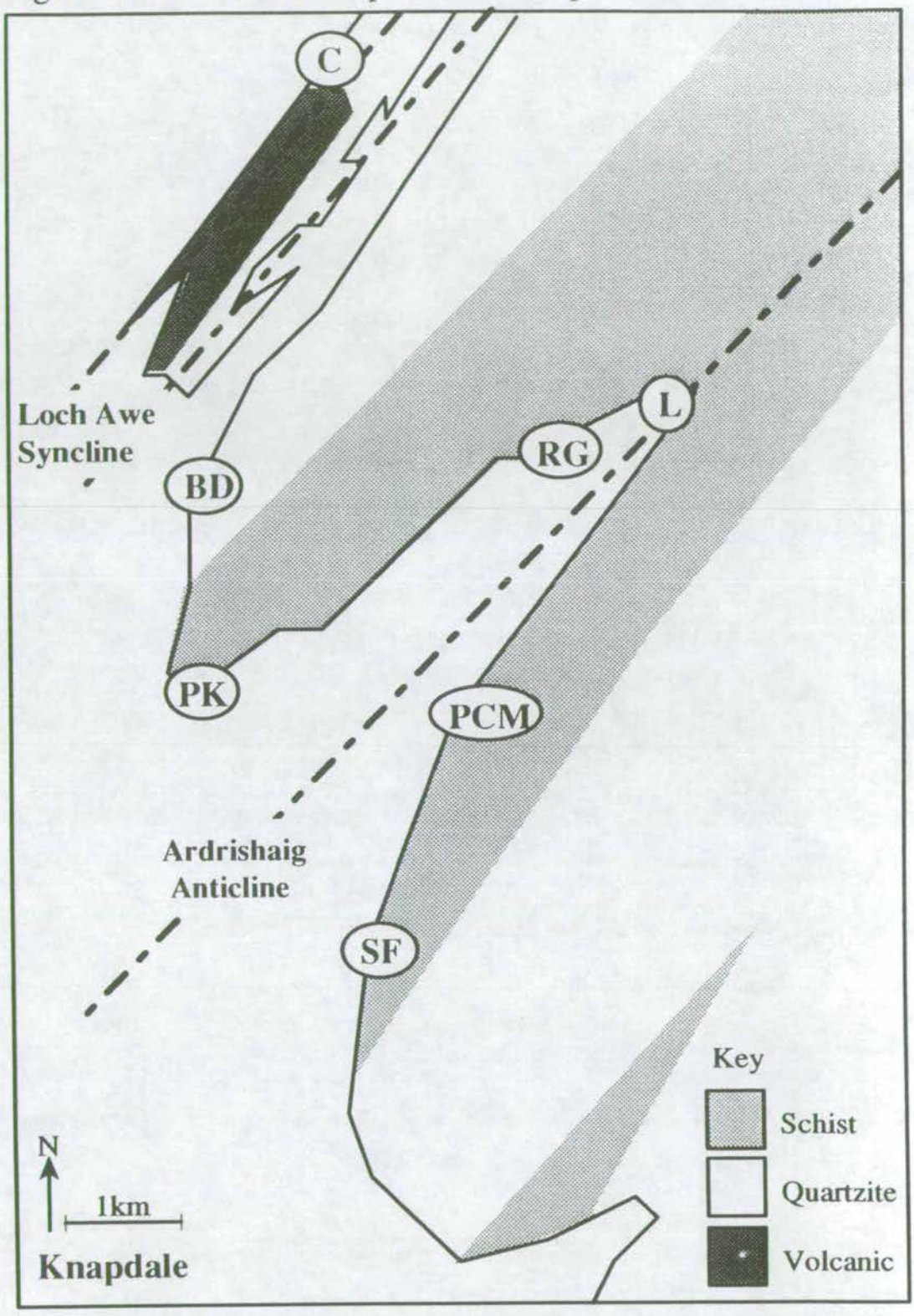

C = Carsaig, BD = Bagh an Doide, PK = Point of Knap, RG = Rubha Garbh L = Lochead, PCM = Port Cill Maluaig, and SF = Sgeir Figheadair

Figure A8.2: XRF data. Carsaig

z(m)	SiO2	Al2O3	Fe2O3	MgO	CaO	Na2O	K2O	TiO2	MnO	P2O5	Fluid	Total
1	43.19	12.10	14.88	4.70	8.88	1.04	.859	3.326	.195	1.638	8.93	99.73
2	42.44	12.43	15.80	4.07	8.76	2.52	.072	3.393	.219	1.662	8.00	99.36
3	39.78	12.34	15.52	5.81	9.33	2.01	.137	3.526	.238	1.753	9.26	99.71
4	42.51	12.42	16.78	4.84	7.15	2.88	.318	3.516	.223	1.877	6.54	99.05
5	42.32	12.86	16.77	4.42	7.46	3.67	.517	3.736	.235	1.996	5.42	99.40
6	43.41	12.46	16.79	4.72	7.42	3.29	.537	3.574	.237	1.871	5.50	99.81

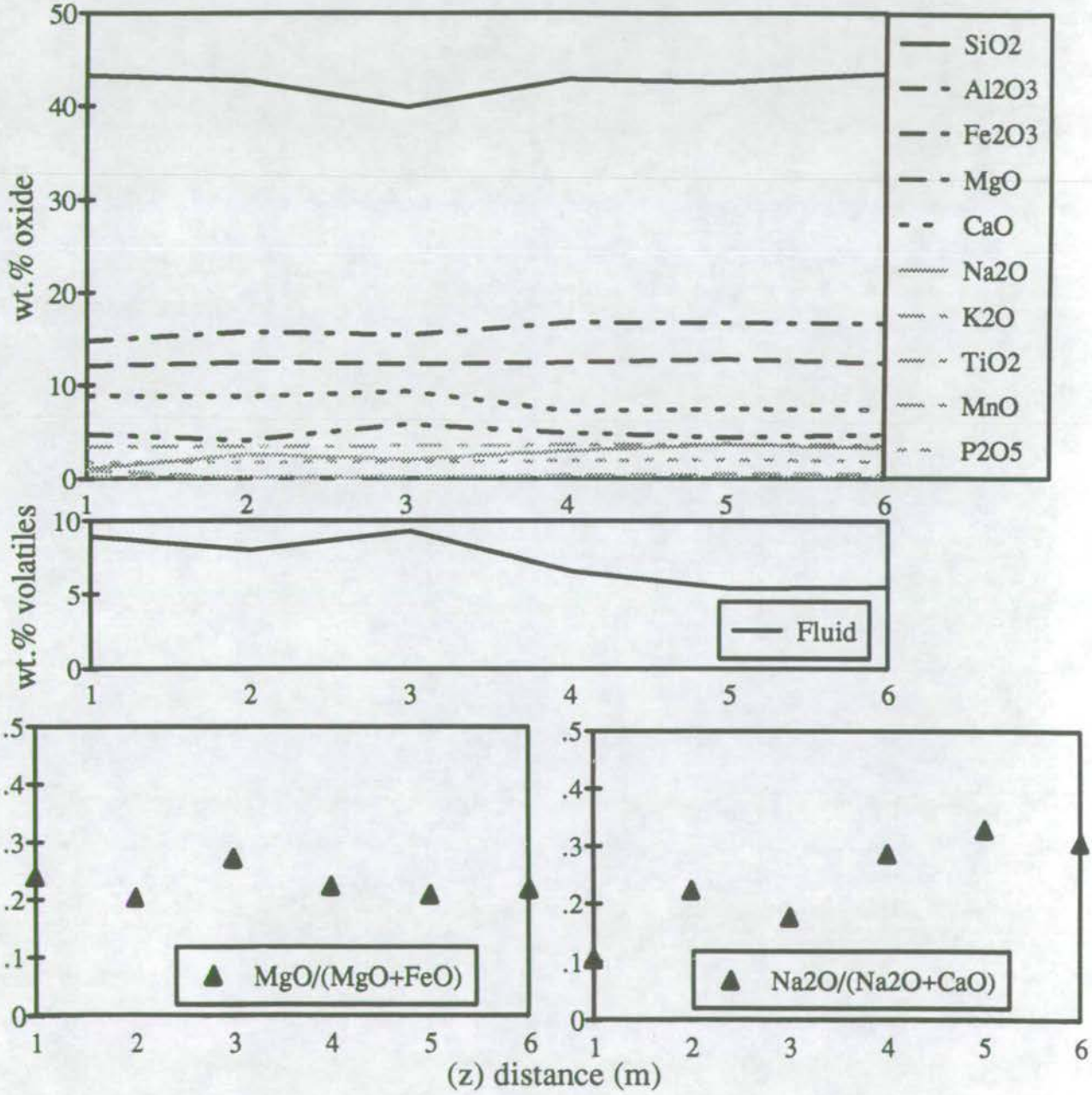

Figure A8.3: XRF Data: Bagh an Doide

z(m)	SiO2	Al2O3	Fe2O3	MgO	CaO	Na2O	K2O	TiO2	MnO	P2O5	Fluid	Total
.4	33.74	11.79	15.75	3.55	13.78	3.05	.050	3.700	.279	.495	13.20	99.39
1.6	38.20	11.28	16.79	6.22	9.90	1.73	.018	3.372	.199	.446	9.88	98.03
3.5	41.38	11.69	15.99	5.86	7.88	1.88	.104	3.723	.194	.463	9.92	99.09
6	42.81	12.58	15.24	6.36	5.36	3.07	.160	3.624	.223	.404	9.40	99.22
8.5	42.61	12.17	15.16	6.47	5.80	2.97	.161	3.449	.231	.405	10.07	99.50
11	42.85	11.01	16.54	6.76	7.50	.27	.042	3.835	.163	.505	9.81	99.29
12	43.28	12.13	13.63	3.92	8.92	2.73	.259	3.829	.163	.617	9.26	98.74
13.7	33.67	11.94	16.17	3.60	13.22	3.09	.045	3.842	.273	.466	12.75	99.06
15.8	39.57	12.63	17.82	4.49	8.67	2.24	.113	3.513	.230	.641	9.48	99.41
17.4	37.20	12.60	15.84	3.81	10.68	2.98	.261	3.864	.255	.499	10.01	97.99
17.8	40.16	12.96	12.87	3.35	10.83	3.68	.217	3.932	.229	.512	10.04	98.79

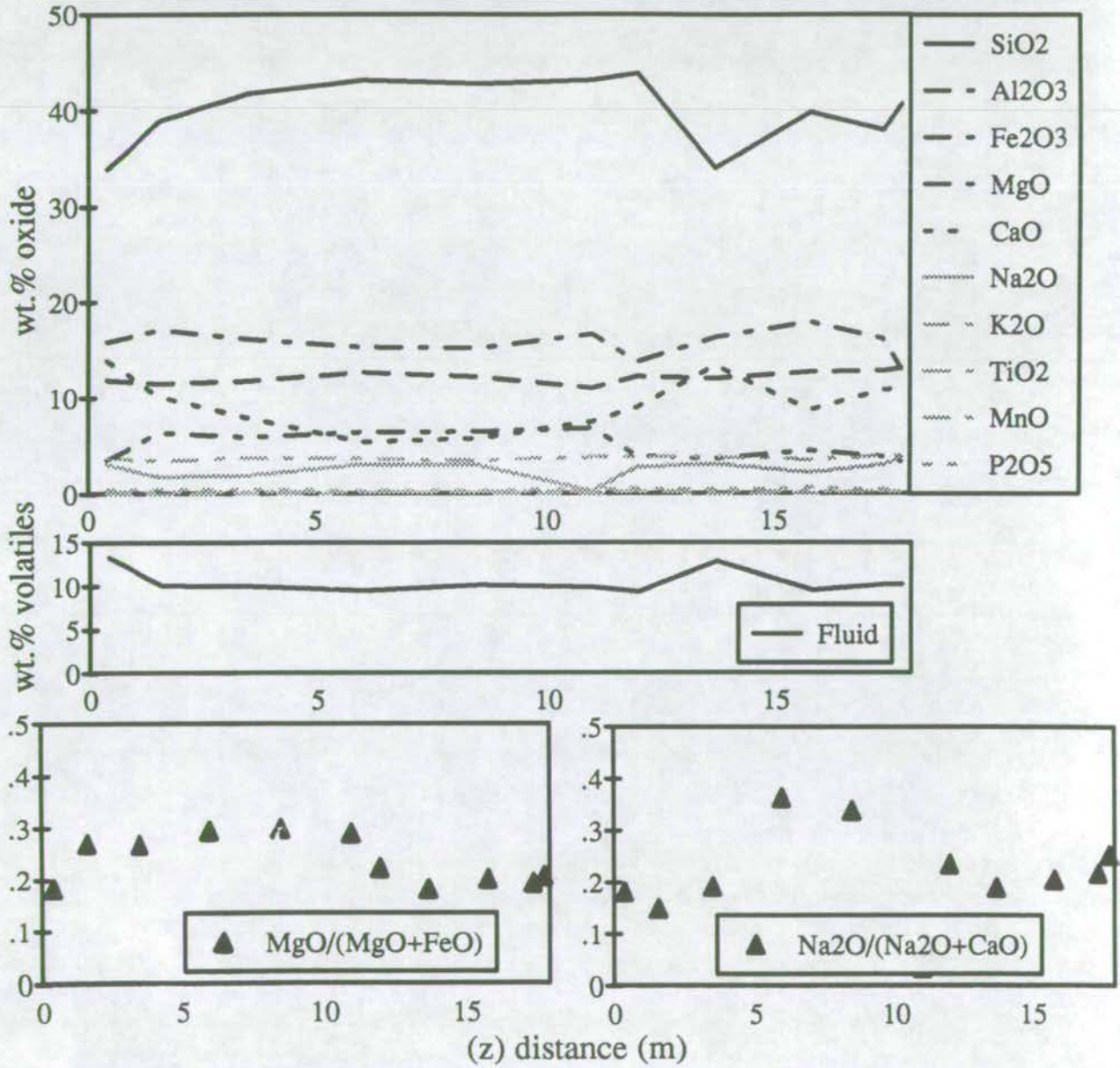

Figure A8.4: XRF Data: Point of Knap

z(m)	SiO2	Al2O3	Fe2O3	MgO	CaO	Na2O	K2O	TiO2	MnO	P2O5	Fluid	Total
.01	45.11	14.29	13.05	7.96	7.08	1.95	.571	1.391	.143	.176	7.73	99.40
.03	45.87	14.10	12.90	7.92	6.71	1.90	.591	1.392	.139	.175	7.23	98.94
.05	46.20	14.13	12.75	7.98	6.57	1.90	.560	1.408	.142	.177	7.01	98.82
.07	43.79	14.28	13.18	8.29	7.77	1.77	.460	1.447	.158	.179	8.29	99.61
.09	43.25	14.11	13.01	8.22	8.29	1.70	.422	1.500	.160	.196	8.79	99.66

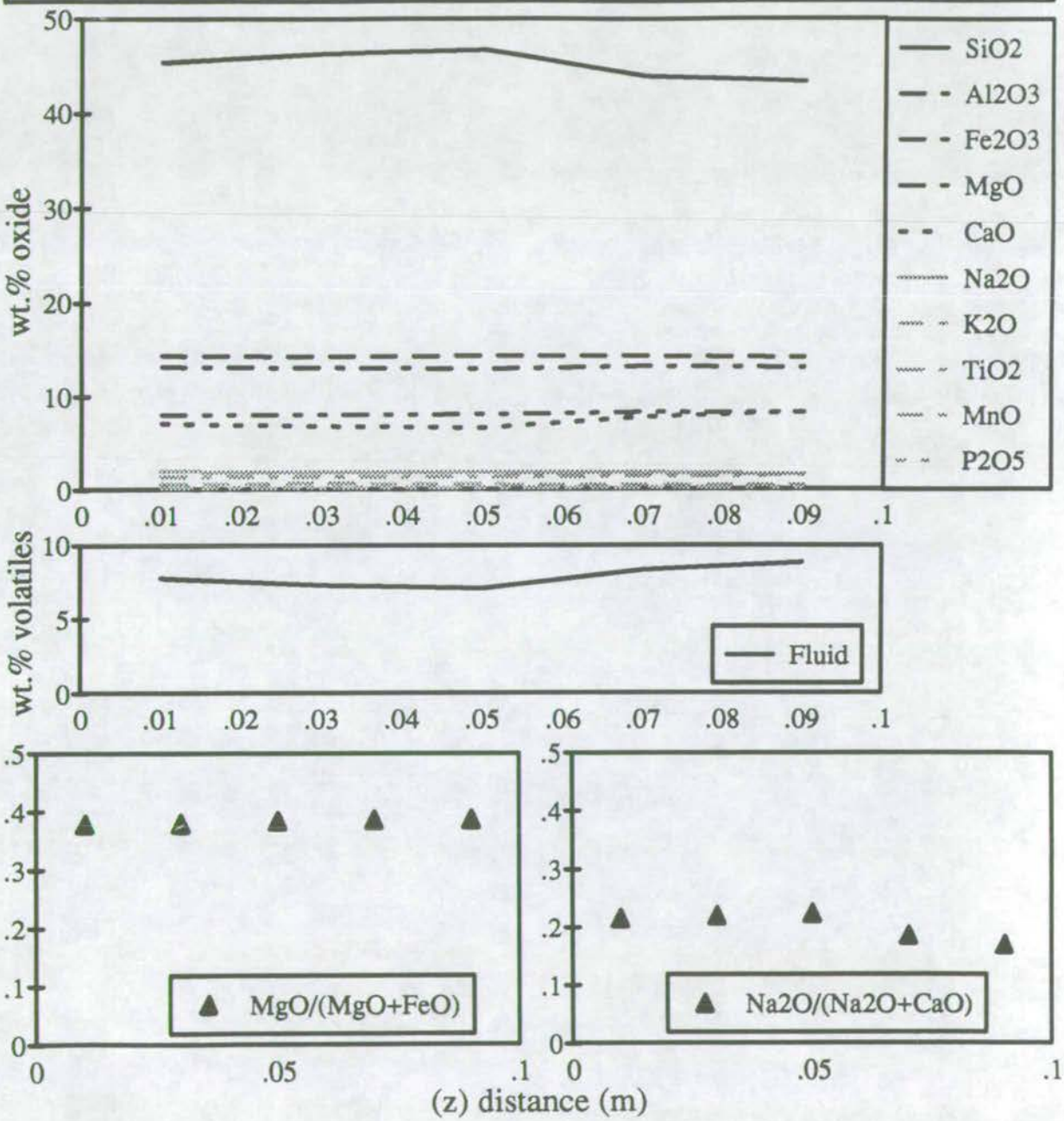

Figure A8.5: XRF Data: Rubha Garbh

z(m)	SiO2	Al2O3	Fe2O3	MgO	CaO	Na2O	K2O	TiO2	MnO	P2O5	Fluid	Total
3	44.49	13.62	12.60	5.73	8.35	3.6	.015	1.786	.204	.217	9.02	99.63
13	47.2	15.63	12.37	6.43	6.26	4.37	.019	1.736	.158	.217	6.2	100.59
28	44.73	12.36	17.81	4.26	6.96	3.73	.017	2.697	.271	.296	7.25	100.38
46	47.7	16.69	12.09	7.25	5.00	4.92	.028	1.949	.163	.252	3.25	99.3
73	48.79	15.78	11.85	6.59	6.21	4.93	.035	1.734	.161	.211	3.21	99.5
102	47.47	14.84	12.17	5.05	7.25	5.11	.033	1.731	.215	.287	7.16	101.33
135	46.59	13.67	14.33	5.46	6.87	3.97	.018	1.707	.159	.225	6.45	99.44
162	38.15	15.53	15.66	5.89	9.12	4.35	.019	1.769	.209	.211	9.76	100.67

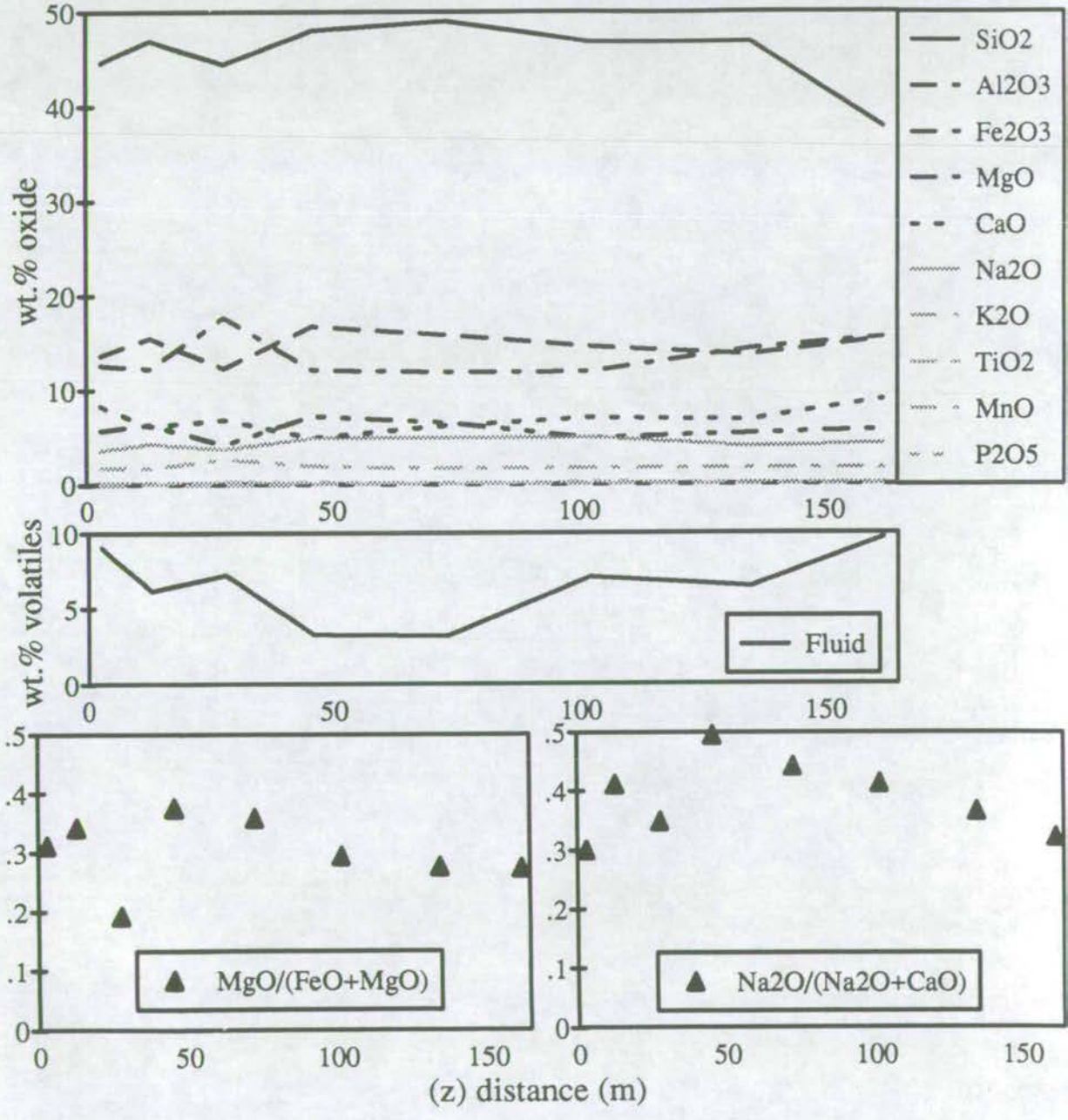

Figure A8.6: XRF Data: Lochead

z(m)	SiO2	Al2O3	Fe2O3	MgO	CaO	Na2O	K2O	TiO2	MnO	P2O5	Fluid	Total
.2	43.39	14.52	11.42	7.65	7.63	3.01	.01	1.482	.155	.201	9.13	98.61
.5	43.86	14.71	11.32	7.54	7.52	2.01	.678	1.48	.138	.206	9.07	98.53
.9	43.62	14.29	10.68	7.23	8.39	2.15	.71	1.467	.144	.204	10.31	99.19
1.4	42.83	13.54	10.25	6.82	9.77	1.96	.618	1.404	.151	.189	11.35	98.89

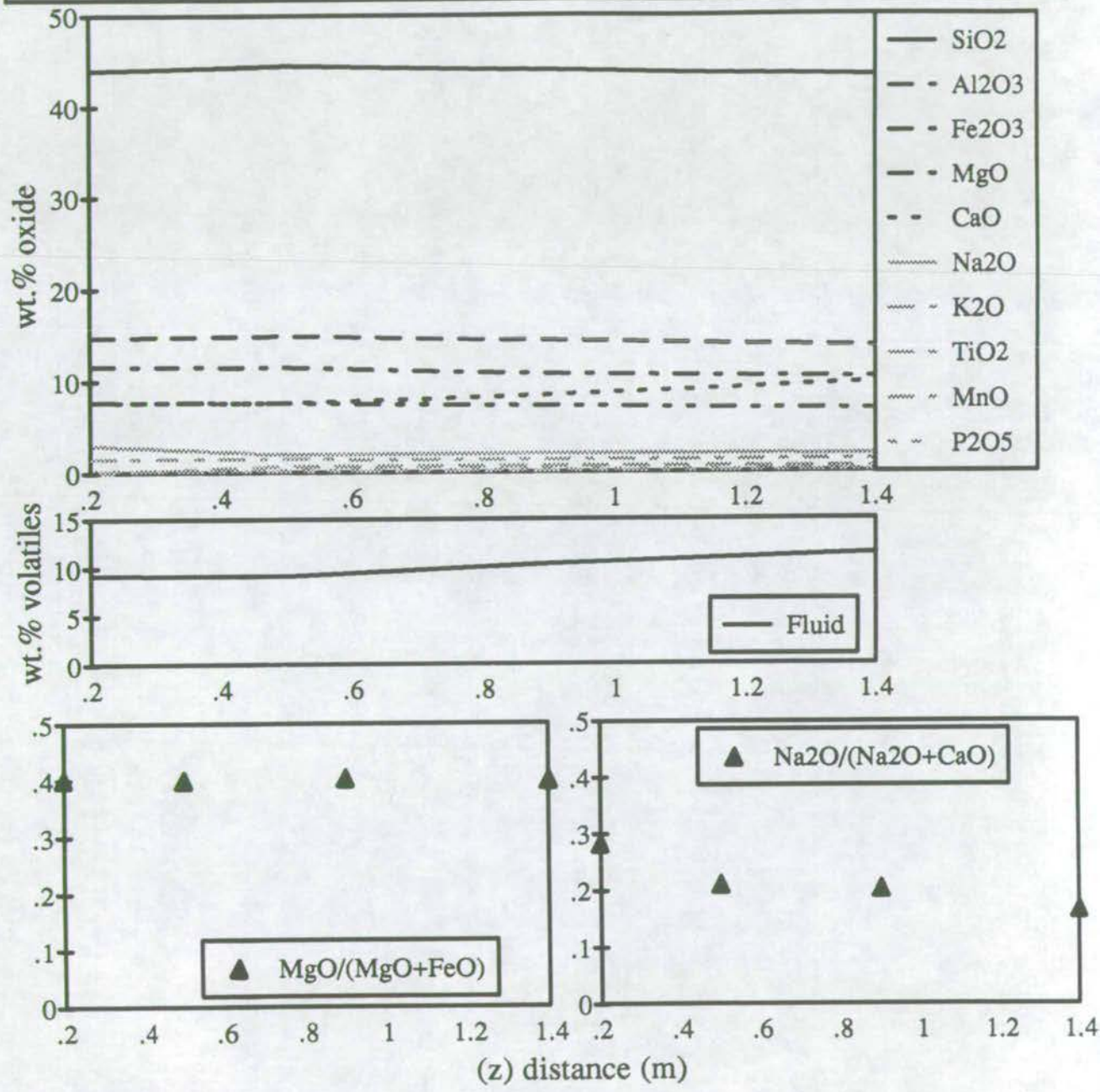

Figure A8.7: XRF Data: Port Cill Maluaig

z(m)	SiO2	Al2O3	Fe2O3	MgO	CaO	Na2O	K2O	TiO2	MnO	P2O5	Fluid	Total
.25	44.99	14.24	12.49	5.06	8.81	2.88	.22	2.13	.187	.228	7.48	98.71
.7	47.91	15.58	13.29	5.35	9.06	1.35	.207	2.182	.157	.238	5.34	100.66
1.11	47.95	15.61	13.25	5.40	9.72	1.72	.166	2.241	.161	.240	3.78	100.24
1.43	47.61	15.19	13.52	5.21	10.12	1.66	.197	2.265	.179	.238	3.51	99.7
1.68	46.5	14.43	14.04	5.04	9.40	2.25	.159	2.301	.195	.250	2.93	97.49
2.27	50.31	16.04	13.59	6.06	9.38	2.30	.354	2.285	.179	.265	2.75	103.52
2.47	47.64	15.15	13.58	5.28	10.05	2.03	.278	2.296	.189	.236	2.61	99.34
2.80	47.48	15.04	13.70	5.33	9.99	1.95	.315	2.285	.187	.240	2.58	99.09
3.60	47.52	14.52	13.54	5.88	9.65	1.91	.280	2.217	.178	.230	3.12	99.05
3.90	47.71	15.74	12.86	5.28	10.15	2.31	.159	2.072	.167	.215	2.85	99.52
4.05	48.90	15.28	13.87	5.89	7.73	2.16	.093	1.940	.181	.180	3.75	99.99
4.22	48.17	10.81	17.21	4.36	9.83	.64	1.333	3.657	.196	.406	2.39	99
4.50	46.82	14.09	15.35	6.27	8.91	1.91	.261	2.423	.194	.236	2.78	99.25
4.76	47.47	13.68	14.93	5.56	9.55	1.68	.527	2.698	.196	.273	2.65	99.21
5.15	52.66	13.50	10.94	4.99	8.09	2.66	.063	1.885	.168	.219	6.04	101.22
5.92	57.03	17.53	16.56	7.53	11.15	2.59	.222	2.746	.238	.255	3.19	119.04
6.26	47.45	14.79	13.17	6.04	10.23	2.04	.216	2.136	.174	.222	2.96	99.42
6.63	47.22	14.49	13.51	6.38	9.64	1.78	.234	2.166	.172	.227	2.83	98.65
7.30	47.28	14.62	14.05	6.63	9.25	1.73	.259	2.190	.170	.222	3.1	99.51
7.63	47.83	14.58	13.92	6.53	9.28	1.60	.213	2.234	.166	.233	3.16	99.74
7.90	47.78	14.38	13.66	6.12	10.18	1.72	.182	2.235	.185	.235	3.1	99.78
8.60	46.08	14.06	13.88	6.24	8.76	1.28	.574	2.213	.177	.228	5.84	99.34
9.32	46.31	13.75	13.17	6.04	8.42	2.53	.099	2.123	.167	.232	8.26	101.11
9.65	45.08	13.30	12.50	5.72	10.40	2.48	.089	2.033	.178	.226	9.87	101.88
10.07	44.03	13.14	12.88	5.57	9.52	2.39	.094	2.092	.177	.219	9.23	99.32
10.33	44.74	13.04	13.04	5.63	9.16	2.22	.108	2.110	.170	.225	8.84	99.28
10.66	44.74	13.07	13.04	5.60	9.05	2.26	.143	2.137	.171	.221	8.97	99.39
10.93	44.06	13.21	12.72	5.42	9.73	2.50	.149	2.066	.178	.221	9.26	99.52
11.25	44.62	13.45	12.60	5.43	8.90	2.72	.209	2.089	.173	.221	8.81	99.23
12.00	44.95	14.01	12.91	5.25	8.59	3.07	.114	2.103	.172	.233	8.56	99.95
12.20	43.94	13.63	12.27	4.82	9.41	3.25	.149	2.146	.187	.224	8.92	98.95
12.70	44.24	13.71	12.58	4.76	9.04	3.31	.097	2.120	.193	.223	8.97	99.26
13.20	44.63	13.73	12.50	4.85	8.94	3.25	.081	2.195	.201	.233	8.68	99.29

Figure A8.7: XRF Data: Port Cill Maluaig

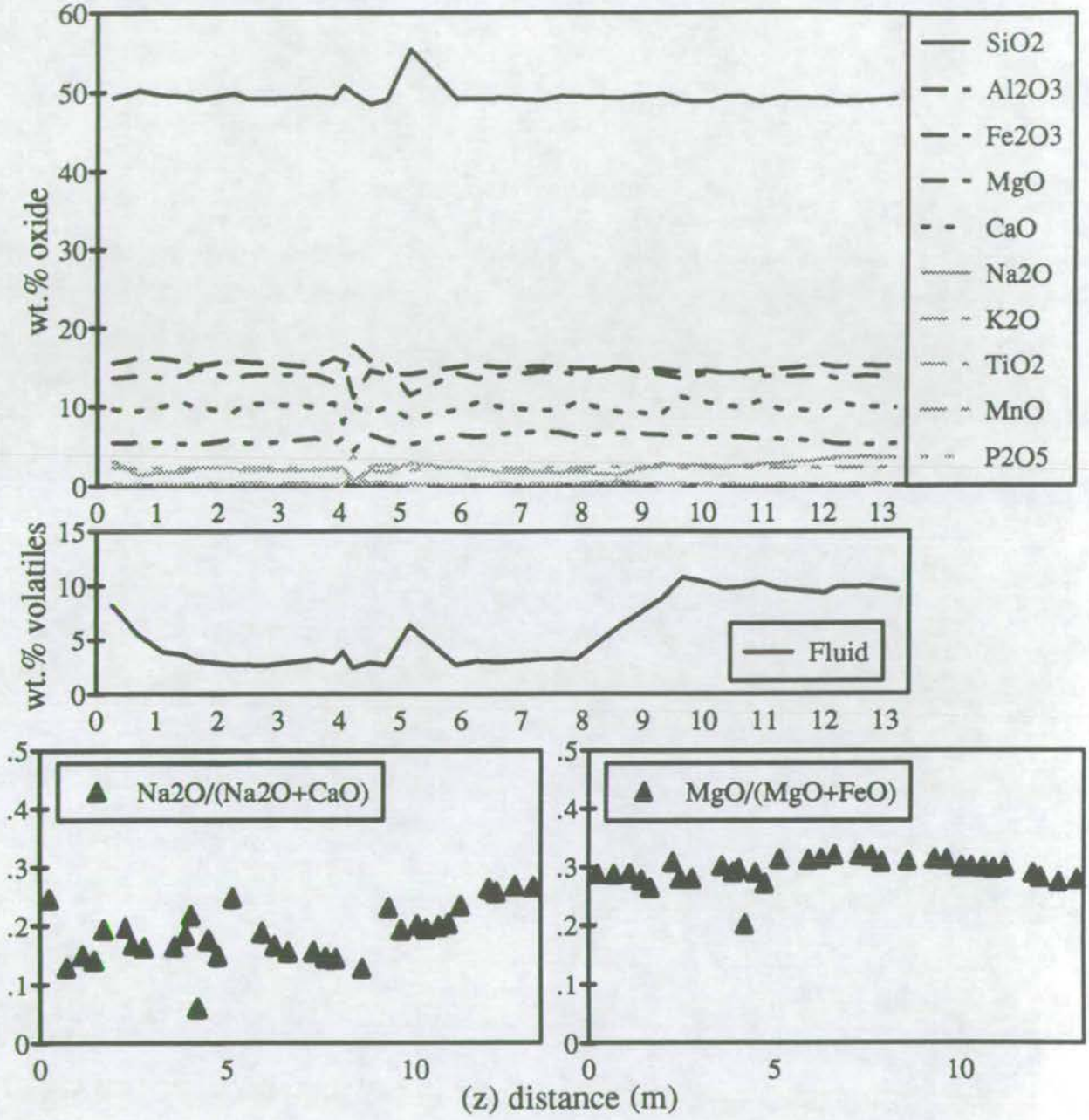

Figure A8.8: XRF Data: Sgeir Figheadair

z(m)	SiO2	Al2O3	Fe2O3	MgO	CaO	Na2O	K2O	TiO2	MnO	P2O5	Fluid	Total
.015	49.53	13.11	15.67	6.87	2.99	1.61	.595	2.305	0.196	0.240	6.50	99.61
.055	42.63	12.12	13.41	5.31	8.02	1.51	.929	2.037	0.202	0.218	10.10	96.49
.095	42.79	11.46	13.77	5.86	9.70	1.22	.544	1.986	0.256	0.217	11.47	99.27
.125	42.88	11.40	13.98	6.58	8.21	1.26	.518	2.022	0.244	0.216	10.85	98.16

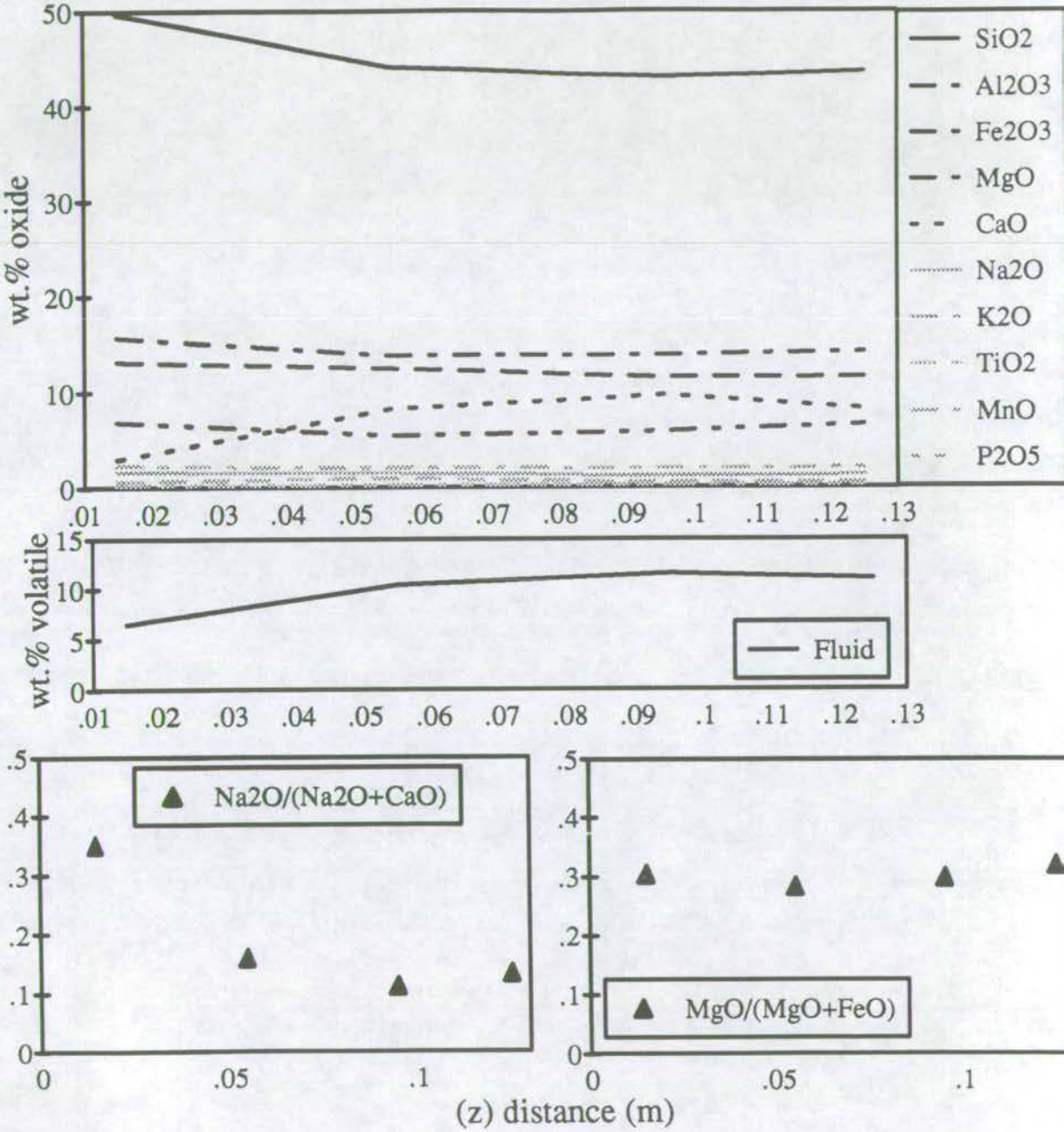

Water-Rock Interaction, Kharaka & Maest (eds) © 1992 Balkema, Rotterdam. ISBN 90 5410 075 3

Structural controls of fluid flow during regional metamorphism: Application of reaction front advection theory to greenschist facies metabasites in the Scottish Dalradian

A. D. L. Skelton & C. M. Graham
Department of Geology and Geophysics, University of Edinburgh, UK

M. J. Bickle
Department of Earth Sciences, University of Cambridge, UK

ABSTRACT: Infiltration of H_2O-CO_2 fluids during greenschist facies regional metamorphism in Dalradian rocks of the SW Scottish Highlands has driven calcite- and dolomite- forming reactions at the margins of metabasic sills. A simple geochemical technique has enabled reaction fronts to be identified in the field. Time integrated fluid fluxes have been calculated from the distances which these fronts have been advected into sill margins. Fluid flow directions have been constrained from the asymmetry of front profiles. Regional scale mapping of directionally-constrained time-integrated fluid fluxes has revealed large-scale fluid flow patterns. Fluid flow was channelised along both regional and outcrop-scale antiformal hinge zones. Time-integrated fluid fluxes vary reciprocally with distance from the axial plane of a regional recumbent anticline, and average fluxes across the sampled area of about 75 m^3/m^2 are consistent with derivation of the fluid from devolatilisation of underlying, higher grade lithologies, without recourse to extraneous fluid sources.

1. INTRODUCTION

Crustal metamorphism must be accompanied by movement of substantial volumes of H_2O-CO_2 fluids in order to remove fluid lost during prograde devolatilisation reactions (eg Walther and Orville 1982). The movement of such fluids through metamorphic rocks may result in systematic changes in the stable isotopic compositions, mineral assemblages and mobile element chemistry of rocks along the flowpath. Isotopic, petrological and trace element data may thus provide important constraints on fluid sources, fluid pathways, fluid volumes and transport mechanisms, but results of such studies have remained controversial (eg Wood and Graham 1986). Estimates of fluid volumes in metamorphic terrains vary from small volumes consistent with fluid derived purely through devolatilisation reactions (Baker et al 1989; Bickle and Baker 1990a) to large volumes sufficient to modify the geochemical and thermal structure of metamorphic terrains (eg Wickham and Taylor 1985, Ferry 1988). Such large fluid volumes could only be derived from an external source such as surface waters convected to depths of metamorphism which is physically implausible (eg Wood and Walther 1986), or if fluid is channelised.

Quantities of fluid interacting with rocks undergoing metamorphism have commonly been calculated from reaction progress or isotopic mass balance equations in terms of volumetric fluid:rock ratios. The basis and significance of such calculations have been criticised by several authors (eg Wood and Graham 1986, Wood and Walther 1986). Calculations based purely on mass-balance equations provide no constraints on the direction of fluid flow, and imply significant and implausible departures from local chemical equilibrium along the (unconstrained) flowpath.

Where a potential tracer of fluid flow such as oxygen isotopes has been homogenised on a regional scale (eg Wickham and Taylor 1985), information on fluid flow paths and fluid fluxes cannot be deduced. However, where advective displacement of isotopic or petrological discontinuities (eg lithological boundaries) from their original, pre-metamorphic location may be identified

and quantified, advective movement of fluid may be unambiguously demonstrated, and fluid fluxes in the direction of front advection computed (eg Bickle and Baker 1990a,b). Such studies yield directionally-constrained, time-integrated fluid fluxes which can be used as meaningful indicators of fluid volumes and transport directions, thus aiding in the identification of fluid sources.

Here we outline the application of reaction front theory to the infiltration of CO_2-bearing, H_2O-rich fluid into greenschist facies metabasic rocks in the Dalradian of the SW Scottish Highlands. Directionally constrained, time-integrated fluid fluxes have been mapped on a regional scale for the first time, the relationship of local and regional structure to fluid flow pathways investigated, and fluid sources constrained.

2. GEOLOGY AND INFILTRATION HISTORY

The rocks of the SW Scottish Highlands comprise a series of psammites, phyllites, calc-pelites, marbles and metabasic sills, dykes, lavas and tuffs, all metamorphosed in the greenschist and epidote amphibolite facies and isoclinally folded on a regional scale during the Caledonian Orogeny. NW and SE facing recumbent antiforms (Fig 1) are separated by a synformal root-zone (the Loch Awe Syncline). These rocks show evidence of three chronologically distinct episodes of infiltration (Graham et al 1983): (i) Metabasites proximal to the Loch Awe Syncline show mineralogical and geochemical evidence of pre-metamorphic spilitic alteration, probably resulting from sub-seafloor hydrothermal activity during emplacement of sills and volcanics; (ii) The majority of metabasites show marginal alteration resulting from infiltration of CO_2-bearing hydrous fluid during metamorphism, documented by the metamorphic carbonation/hydration reactions: (1) Amph + Epid + CO_2 + H_2O = Chl + Cc + Qz, or, more rarely and at higher X(CO2) (2) Chl + Cc + Ab + CO_2 = Dol + Parag + Qz + H_2O (Fig 2); (iii) Many lithologies are locally retrogressed and altered by vein-controlled H_2O-CO_2 fluid. The results of a study of the peak-metamorphic infiltration event are now presented and discussed.

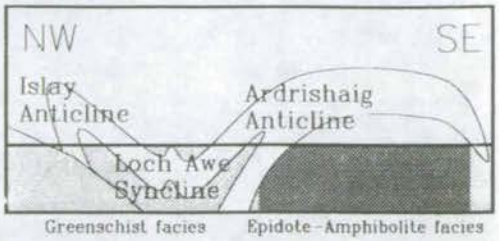

Figure 1: Structural and Metamorphic Section of the S.W. Scottish Highlands.

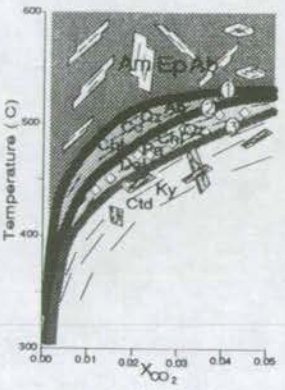

Reaction 1 is the calcite-forming reaction: Am+Ep+CO2+H2O =Chl+Cc+Qz. Reaction 2 is the dolomite-forming reaction: Chl+Ab+Cc+CO2 =Dol+Pa+Qz+H2O. Reactions 2 and/or 3 buffer the infiltrating fluid composition within the host phyllites.

Figure 2: T-X(CO2) phase relations (adapted from Holland and Powell 1988)

3. METHODOLOGY

The advection distances of carbonation reaction fronts from metabasite lithological boundaries were measured using a simple field-based geochemical technique. Samples taken at intervals across metabasites were crushed, and a known volume was reacted in a portable, sealed reaction vessel with an excess of 10% HCl. The volume of CO_2 evolved was measured from the pressure recorded on a built-in manometer. The reaction vessel was previously calibrated in the laboratory for samples containing calcite, dolomite, and calcite + dolomite, the relative amounts of coexisting calcite and dolomite being estimated from reaction rate differences.

Using these data, the progress of calcite and dolomite generating carbonation reactions (1) and (2) was calculated. Reaction progress was plotted against distance from metabasite contacts, and steps in reaction progress constrained the location of reaction fronts (Fig 3). Results of this approach were found to be in good agreement with location of reaction fronts from point

counting. The ease and rapidity of this technique, without recourse to laboratory work, allows a comprehensive regional picture of fluid flux in relation to structure and lithology to be constructed for the first time.

The advection distance of a reaction front ($V_f t$) measured as above is given by Baker and Bickle (1990a) as:

$$V_f t = \frac{w\phi t\,(X_{CO2,2} - X_{CO2,1})}{v_{CO2}(1 - X_{CO2,2}) - v_{H2O} X_{CO2,2}} \quad (3)$$

where v_{CO2} and v_{H2O} are the stoichiometric coefficients of CO_2 and H_2O, respectively, absorbed by reaction (1) or (2) at the reaction front, and $X_{CO2,2}$ and $X_{CO2,1}$ are the volume fractions of CO_2 in the fluid downstream and upstream of the reaction front respectively. V_f is the velocity of the front, t is time, and therefore $V_f t$ is the (time-integrated) distance which the front has travelled. w is the velocity of the fluid, ø is the porosity (instantaneous fluid volume), and thus wø is the fluid flux and wøt the time-integrated fluid flux. v_{CO2} and v_{H2O} can be estimated from the reaction stoichiometry. $X_{CO2,2}$ is the equilibrium fluid composition for the reaction (1) or (2), computed from calculated T-$X(CO_2)$ phase relations (Fig 2; Holland and Powell 1988). $X_{CO2,1}$ is the composition of the infiltrating fluid and has been shown to be that which is buffered by the host phyllite assemblage and is computed from similar calculated T-$X(CO_2)$ phase relations.

The measured advection distance, $V_f t$, must be corrected for diffusive broadening of the front, which should be symmetrical on each side of infiltrated metabasic sills, and can readily be deduced for example from Fig 3. If suitable assemblages are not available to constrain the $X(CO_2)$ of infiltrating fluid, values can be obtained by simultaneously solving equation (3) for two reaction fronts ((1) and (2)) in the same sill. From equation (3), we calculate $V_f t = 0.2 w\phi t$ for reaction (1) and $V_f t = 0.1 w\phi t$ for reaction (2). Calculated fluxes are directionally constrained by the asymmetry of reaction zones, the thicker margin being on the infiltration side and the thinner margin resulting from diffusive front broadening (Fig 3).

4. DISCUSSION

The fluid flux map constructed for the abundant metabasic sills in the greenschist facies of the SW Scottish Highlands (Fig 4) shows a remarkable correlation between flux direction and geological structure over the whole region. Fluid flow direction has a major component outwards from antiformal axial surfaces and inwards towards synformal axial surfaces. Of particular interest is the observation that the magnitude of the time-integrated fluid flux shows a strong linear correlation with reciprocal distance from the axis of the major regional antiformal structure - the Ardrishaig Anticline (Fig. 5). Fluid is thus strongly channelised along both local and regional antiforms.

The time-integrated fluid flux as constrained in a NW-SE direction and averaged across the area sampled in the SW Highlands (18km x 12km) is about 75 m^3/m^2. A flux of this magnitude could be generated, for example, by metamorphic devolatilisation of about 2-3km thickness of underlying metabasites and metasediments along the fluid flow path undergoing prograde dehydration at a greenschist to epidote-amphibolite transition comparable to that exposed at the garnet isograd to the SE of the study area, where breakdown of chlorite liberates about 3-4 vol.% water. The volumes of fluid required are consistent with the known geological and

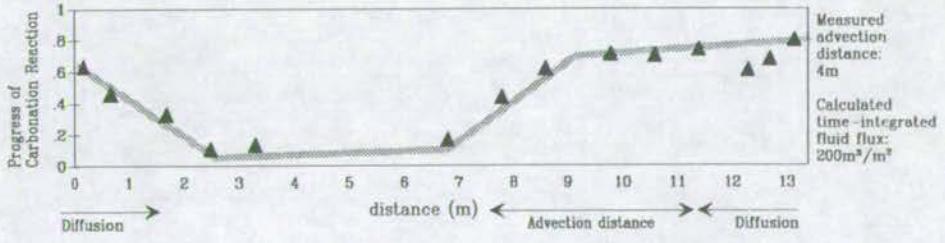

Figure 3: Profile of Field Estimates of Reaction Progress across a Metabasite Sill at Port Cill Maluaig in Knapdale S.W. Scottish Highlands

lithological structure of the area, and no external sources of fluid are required.

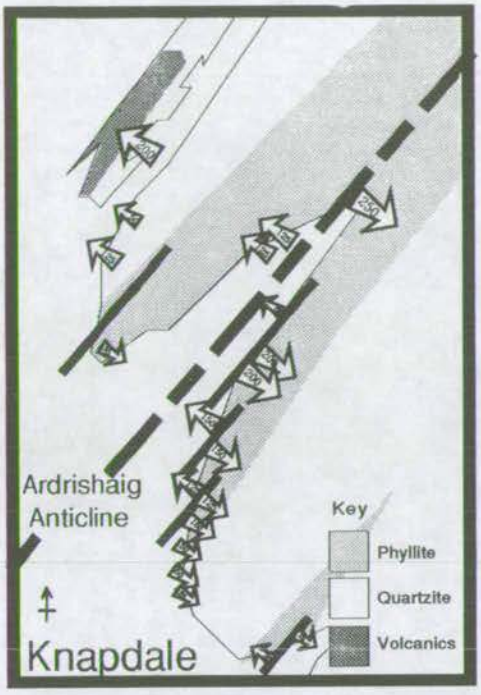

Figure 4; Map showing directionally constrained Time-integrated fluid fluxes

Arrows indicate the direction and magnitude of fluid flow. Dashed Lines are anticlinal axes. Fluid is seen to flow outwards from anticlinal axes suggesting that they act as fluid channels. The magnitude of the time-integrated fluid flux decreases with distance from the Ardrishaig anticline implying that it acts as a regional fluid channel.

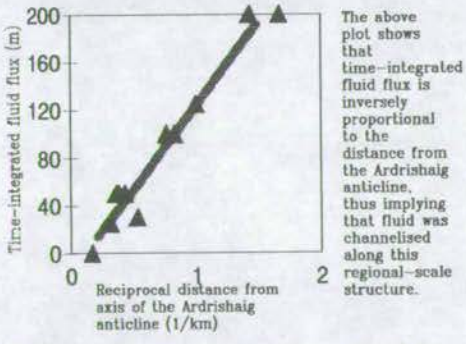

Figure 5 ; Fluid-channelisation along the Ardrishaig Anticline

5. REFERENCES

Baker J, Bickle M J, Buick I S, Holland T J B and Matthews A (1989) Isotopic and petrological evidence for the infiltration of water-rich fluids during the Miocene M2 metamorphism on Naxos, Greece. Geochim Cosmochim Acta 53, 2037-2050.

Bickle M J and Baker J (1990a) Migration of reaction and isotopic fronts in infiltration zones: assessments of fluid flux in metamorphic terrains. Earth Planet Sci Letters 98, 1-13.

Bickle M J and Baker J (1990b) Advective-diffusive transport of isotopic fronts: an example from Naxos, Greece. Earth Planet Sci Letters 97, 78-93.

Ferry J M (1988) Infiltration-driven metamorphism in Northern New England. J Petrol 29, 1121-1159.

Graham C M , Greig K M, Sheppard S M F and Turi B (1983) Genesis and mobility of the mobility of the H_2O-CO_2 fluid phase during regional greenschist and epidote amphibolite facies metamorphism: a petrological and stable isotope study in the Scottish Dalradian. J geol. Soc. London 140, 577-599.

Powell R and Holland T J B (1988) An internally consistent thermodynamic dataset with uncertainties and correlations: 3. Applications to geobarometry, worked examples and a computer program. J Metam Geol 6, 173-204.

Walther J V and Orville P M (1982) Rates of metamorphism and volatile production and transport in regional metamorphism. Contrib Miner Petrol 79, 252-257.

Wickham S M and Taylor H P (1985) Stable isotope evidence for large-scale seawater infiltration in a regional metamorphic terrain: the Trois Seigneurs massif, Pyrenees, France. Contrib Miner Petrol 91, 122-137.

Wood B J and Graham C M (1986) Infiltration of aqueous fluid and high fluid:rock ratios during greenschist facies metamorphism: a discussion. J Petrol 27, 751-761.

Wood B J and Walther J V (1986) Fluid flow during metamorphism and its implications for fluid-rock ratios. In J V Walther and B J Wood (eds). Fluid-rock interactions during metamorphism, Advances in Physical Geochemistry 5, 89-108, Springer-Verlag: New York.

REFERENCE CARD

Mineral Reactions

Reaction (1): $3am+2ep+8H_2O+10CO_2 = 3chl+10cc+21qz$
Reaction (2): $sph+CO_2=ru+cc+qz$
Reaction (3): $2cz+3ab+4CO_2+2H_2O = 3pa+4cc+6qz$
Reaction (4): $ab+chl+5cc + 5CO_2 = pa+5ank+3qz+3H_2O$
Reaction (5): $bi+chl+8cc+8CO_2 = mu+8ank+3qz+4H_2O$
Reaction (6): $5bi+3mu+9qz+4H_2O = 8Kfsp+3chl$
Reaction (7): $chl+4CO_2 = ctd+4sid+2qz+3H_2O$
Reaction (8): $chl+5CO_2 = ky+5sid+2qz+H_2O$
Reaction (9): $ky+3qz+H_2O = pyhl$

1-D Isotope Front Advection Model

$$V_f.t = \frac{\omega\varphi t}{\left(\frac{\rho_s K_d}{\rho_f}\right)}$$

1-D Reaction Front Advection Model

$$V_f t = \frac{\omega_1.\varphi_1.t.\left(X_{CO2,2} - X_{CO2,1}\right)}{R_{CO2}.\left(1 - X_{CO2,2}\right) - R_{H2O}.X_{CO2,2}}$$

Mineral Abbreviations

ab = albite
am = amphibole
ames = amesite
an = anorthite
ank = ankerite
ann = annite
bi = biotite
cc = calcite
cel = celadonite
chl = chlorite
clin = clinochlore
cz = clinozoisite
daph = daphnite
dol = dolomite
east = eastonite
ed = edenite
ep = epidote
fame = ferro-amesite
fdol = ferro-dolomite
fgl = ferro-glaucophane
fhb = ferro-hornblende
fsp = felspar
ftr = ferro-tremolite
gl = glaucophane
hb = hornblende
Kfsp = K-feldspar
mag = magnesite
mu = muscovite
pa = paragonite
parg = pargasite
phl = phlogopite
sid = siderite
q = quartz
tr =tremolite

Modal Profile of Reaction (1)

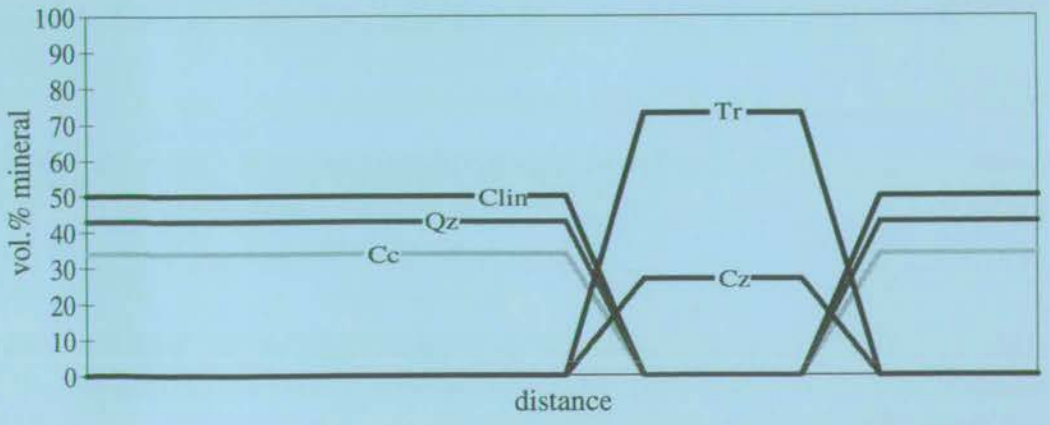

Map Legend

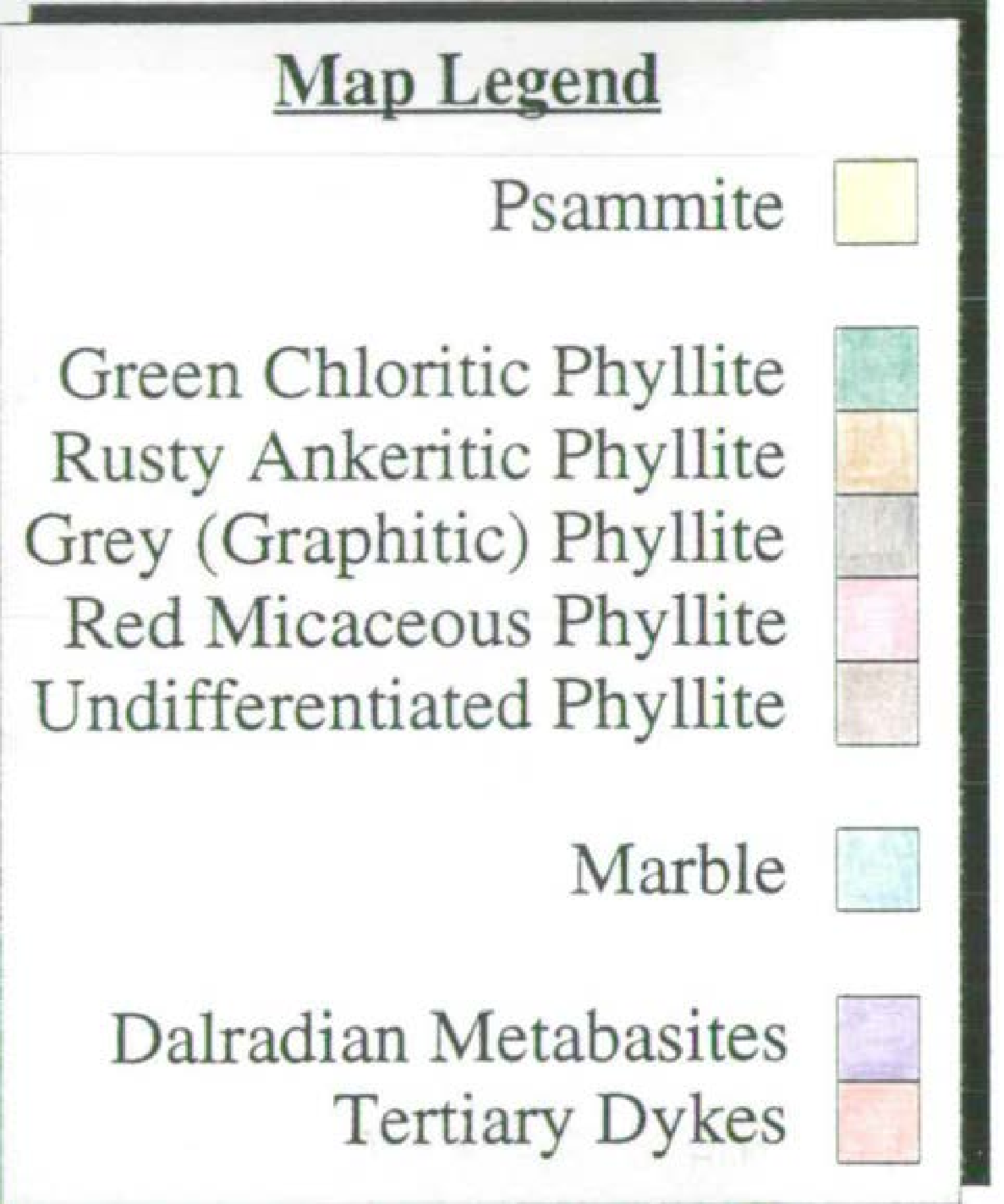
Psammite
Green Chloritic Phyllite
Rusty Ankeritic Phyllite
Grey (Graphitic) Phyllite
Red Micaceous Phyllite
Undifferentiated Phyllite
Marble
Dalradian Metabasites
Tertiary Dykes

Scarba

whirlpool

Jura

N

≈1:18000

Field Slips: Carrydreckan

Field Slips: Islay

N

≈1:12500 (Upper Map)
≈1:18000 (Lower Maps)

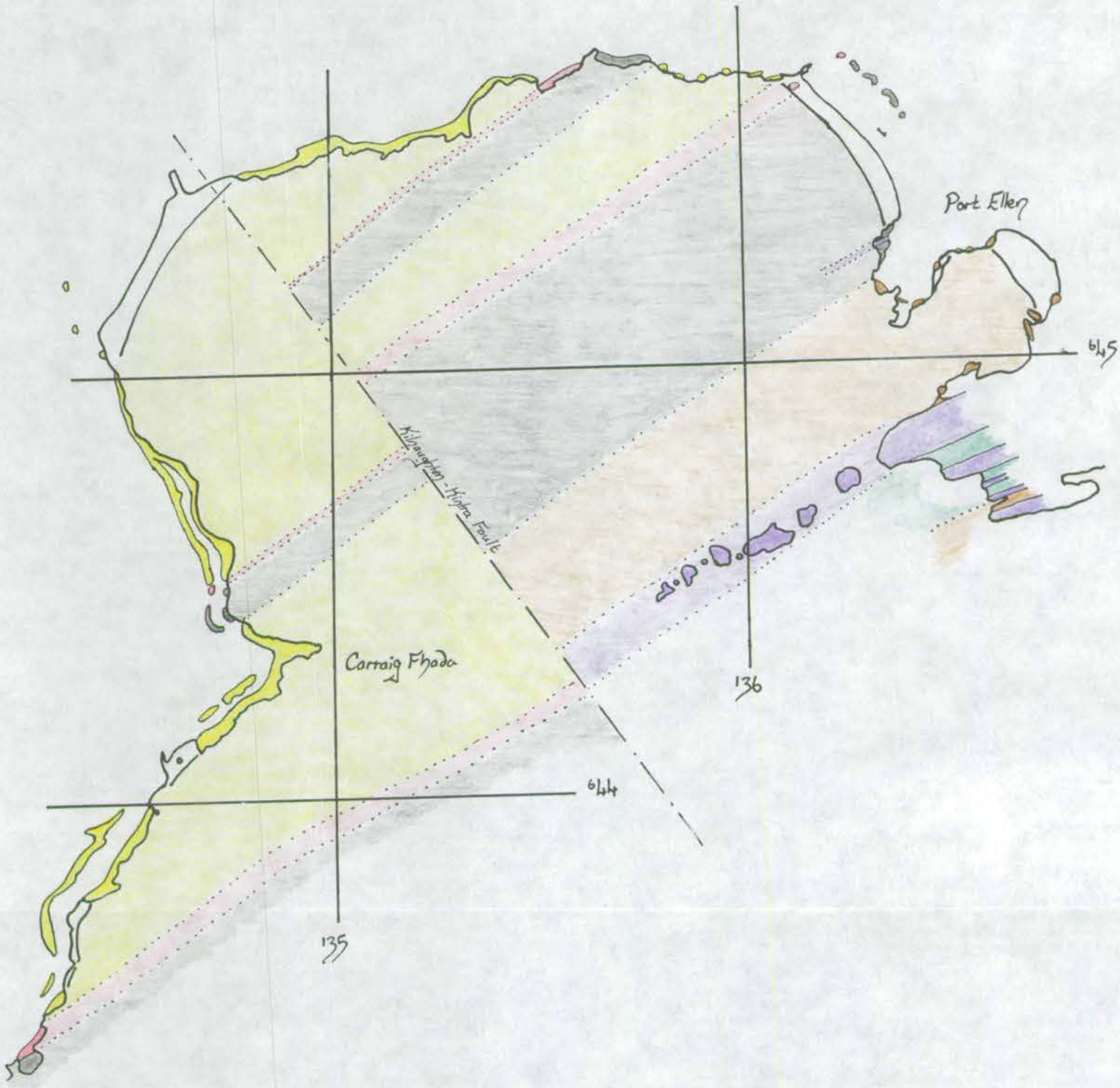

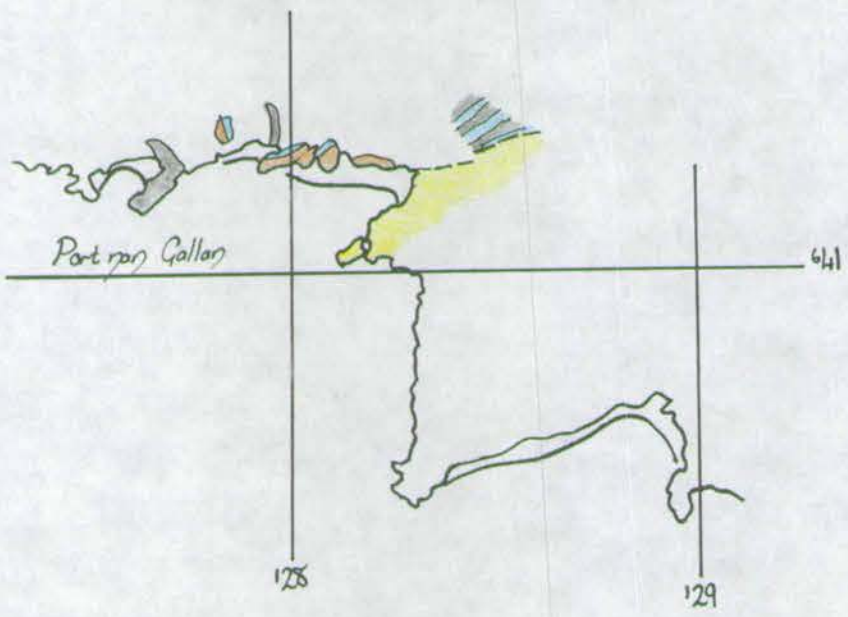

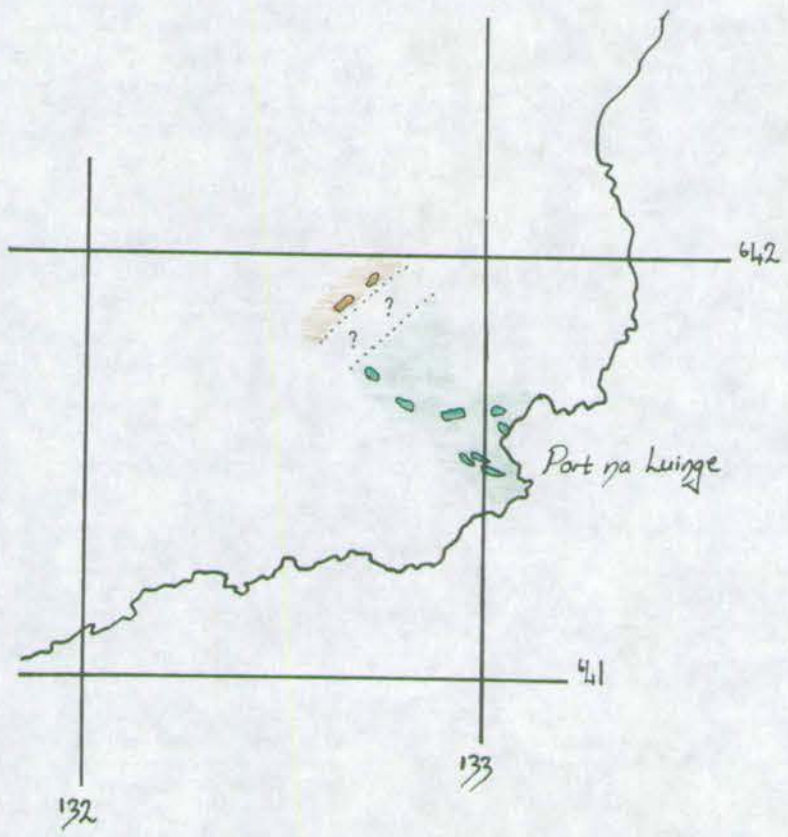

Field Slips : Keills

N

≈1:18000

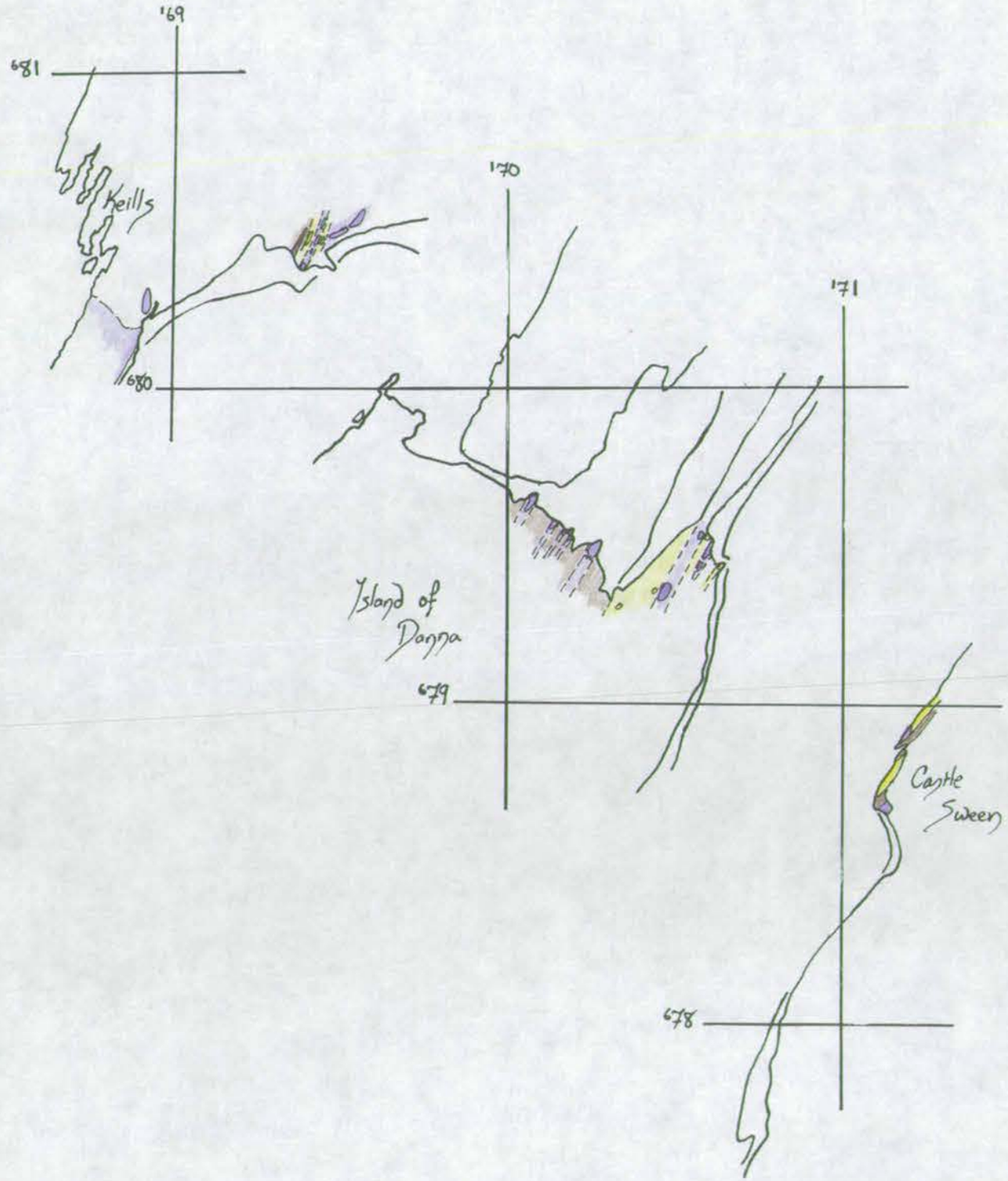

Field Slips: Kilmory

N

≈1:18000

677

676

675

674

673

672

171

170

175

176

174

173

Bagh an Doide

Stronefield Bay

Point of Knap

Rubha Garbh

Ellory

Rubha an Tuithe

Field Slips: Kilberry

N

≈1:18000

Port Cill Maluaig

670

669

172

Stotfield Bay

668

667

666

Port Bàn

665

664

171

Kilberry Head

674

Àrd Dùn

673

174

663

Sgeir Mòire

662

Port Mòr

171

661

172

173

Loch Stornoway